1051-A

Faculteit Wetenschappen
Vakgroep Geologie en Bodemkunde
Academiejaar 2001 - 2002

Development of coral banks in Porcupine Seabight (SW Ireland) A multidisciplinary approach

Ontwikkeling van koraalbanken in de Porcupine Seabight (SW Ierland) Een multidisciplinaire studie

Ben De Mol

Promotor: Prof. Dr. J.-P. Henriet
Co-promotor: Prof. Dr. R. Swennen

Proefschrift ingediend bij de Faculteit Wetenschappen van de Universiteit Gent voor het verkrijgen van de graad van Doctor in de Wetenschappen

UNIVERSITEIT GENT

Faculteit Wetenschappen
Vakgroep Geologie en Bodemkunde
Academiejaar 2001 - 2002

UNIVERSITEIT GENT
RCMG-Seismostratigrafie
inventarisnummer : .....
.....1051(A).....

Development of coral banks in Porcupine Seabight (SW Ireland) A multidisciplinary approach

---

Ontwikkeling van koraalbanken in de Porcupine Seabight (SW Ierland)
Een multidisciplinaire studie

Ben De Mol

Promotor: Prof. Dr. J.-P. Henriet
Co-promotor: Prof. Dr. R. Swennen

Proefschrift ingediend bij de Faculteit Wetenschappen van de Universiteit Gent voor het verkrijgen van de graad van Doctor in de Wetenschappen

It would not be a poem
What I am going to say
Neither I know if it is worth
To try to describe you

The Sea
The Sea

Here I am have been standing
Only to be able to see it
And I ve been getting older
Never understanding it

The Sea
The Sea

Pedro Ayres Magalhães

Acknowledgments

Dit doctoraatsonderzoek kende zijn start-up in de zomer van 1997 tijdens een seismische campagne met "onze" R/V Belgica. Het was mijn eerste expeditie naar de Procupine Seabight. Wat er tussen die start-up fase ligt en na deze regels geschreven te hebben, de give-up fase, reikt veel verder dan het eenzaam uitdoctoren van het onstaan van koraalbanken. En dit heb ik allemaal aan jullie te danken. Toch wil ik even enkele mensen, instituten en geldschieters in het bijzonder bedanken.

Eerst en vooral wil ik de "godfather" van dit initieel mound-onderzoeksproject en het brein achter de nationale (Bijzondere Onderzoeks Fonds, RUG), Europese (5th Framework projects: GEOMOUND) en internationale (IODP) projecten en tevens mijn promotor, Prof. Dr. J.P. Henriet bedanken. Hij draagde ertoe bij om van mij een cosmopoliete burger te maken met een rijke baggage aan levenservarigen: expedities met Prof. Logachev, R/V Belgica en R/V Poseidon, duiken naar de bodem van het meer van Genève, het organiseren van een congres, het werken aan een IODP projectvoorstel, studenten door de Alpen en de Ardennen loodsen en niet te vergeten de talrijke congressen en workshops waar ik mocht aan deelnemen. Daarnaast heeft hij me getoloreerd tot zijn give-up fase om mijn doctoraat te lezen. Bedankt!

Mijn co-promoter Prof. Dr. Rudy Swennen (KULeuven) draagde bij tot het sedimentologisch deel van dit werk. Zowel op de Prof. Logachev als daarbuiten heeft hij me geholpen en enkele elementaire begrippen van de sedimentology aangeleerd. Ik was steeds welkom op zijn departement en hij was ook steeds bereid om even te discussiëren over moundjes.

Al mijn collega's hebben uiteraard op een of andere manier bijgedragen tot dit werk. Onze ingenieurs: Tom, Hans, Koen Wim C en Peter. Zonder hun hulp en vakkennis was dit werk niet mogelijk geweest. Marcske was er altijd om te helpen met administratie, het organiseren van congressen, reizen, etc. Wim V. hielp bij het processen van de data en was altijd te vinden voor een gezellige babbel. Mijn naaste collega was Veerle, die ik toch wel wil bedanken voor de vele uren dat we gediscusieerd hebben en voor de hulp bij de literatuur, briefingen, interpretaties en het nalezen van sommige delen van dit manuscript. Den Deevid wist me dan weer alles te vertellen over drifts, Heinrich events en andere sedimentaire zaken. Het laatste jaar echter was Pieter mijn vaste room-mate, criticus van mijn figuren, structureel adviseur en luisterpaal. Hij draagde ook bij tot de uiteindelijk terminologie van de mound-evolutie. Vera en Geert wil ik bedanken voor de hulp bij de interpretatie en mooie figuurtjes van de sidescan sonar. Tist (Prof. Dr. De Batist) voor de hulp bij het zoeken van literatuur en het organiseren van het reilen en

zeilen van de dienst. Herlinde voor de mysterieuze nacht, Yannick als fietspartner en Rob als vaste tafelgenoot. Daarnaast wil ik de volgende licentiaatsstudenten bedanken voor hun bijdrage tot dit werk: David, Sigrid, Kris, Wim L. en 'el Hugo'.

Daarnaast zijn er vele mensen betrokken geweest bij de verschillende analysis en monster voorbereidingen:

- De afdeling fysico-chemische geologie van de KULeuven zou ik willen bedanken voor hun gastvrijheid en de goede samenwerking. In bijzonder Maarten VG voor de hulp bij de CT-scans en Danny voor de chemische analysis.
- Prof. Dr. Dullo (Geomar Kiel) and Prof. Dr. Freiwald (Institut für Paläontologie, Universität Erlangen) for their support and discussion throughout this study.
- I would like to thank Geirr Haarr (former Exploration manager Statoil Exploration Ireland Ltd.) for the interest and providing data. Peter Croker of Petroleum Affairs Division, Dublin Ireland to provide data and sediment samples but also for the discussion.
- Dr. M. Hovland (Statoil) supported me in my initial steps in the mound research and the discussions.
- Prof. Dr. Ann Vanreusel en de afdeling Marine Biolgie (RUG) wil ik van harte bedanken voor de nauwe en aangename samenwerking.
- Prof. Dr. E. Van Ranst en Nicole zou ik willen bedanken voor het uitvoeren van de chemische analysis en XRD.
- Prof. Dr. Keppens en zijn team (VUB) voor de isotopische metingen.
- Dr. M. White (UCG Galway) for his input of the oceanographic data and the support with the interpretation of the oceanographic data. Thanks Martin.
- Special thanks to the crew and staff of the research vessels Belgica, Prof. Logachev and Poseidon.
- Prof. Hans Werner Schenke en Andreas Beyer for providing the bathymetric maps of the Belgica mound province.
- Eddy Van der Meersch voor de fantastische foto's.
- Prof. Dr. Micheal Ivanov (MSU), I would like to thank him for his enthusiasm and the organisation of the TTR7 and TTR8 expedition. It was a wonderfull expierence on board of

the Prof. Logachev. Off course I would like to thank all the Russian students and staff for the collaboration and support out at sea.

- The people of UCD Vik, Prof. Dr. Shannon for their hospitality and interest in my reseach. Angela for her help in the final interpretation of the seismic profiles and the interesting discussions.
- I would like to thank all the GEOMOUND, EOCMOUND and ACES partners for the discussions, workshops and cruises.

Al mijn café vrienden en sportmaatjes, bedankt voor de leuke ontspannende momnenten!

Daarnaast wil ik nog een woordje richten aan mijn ouders en familie die me altijd hebben gesteund tijdens de laatste jaren en begrip hadden voor het feit dat ik af en toe afwezig was tijdens belangrijke familiereunies.

Eén persoon wil ik toch in het bijzonder bedanken: ze was er altijd, thuis om me te voeden, op de dienst om te helpen bij de correcties, de lay-out en het printwerk. De laatste maanden waren misschien slopend maar nu is het voorbij…..bedankt Sabine !

This study was initiated in the framework of the two European Mast III projects ENAM and CORSAIRES and carried out in co-operation with the UNESCO-IOC "Training Through Research" programme. It became later the central theme of the "Porcupine-Belgica" project of Ghent University (BOF). Methodological developments were funded by the Belgian Antarctic Research Programme. This research will be continued in the framework of the FP5 research projects GEOMOUND, ECOMOUND and ACES of the OMARC cluster.

Tot slot wens ik het IWT te bedanken voor de financiële steun in de vorm van een doctoraatsbeurs.

Mei, 2002

Ben

Table of content

Abstract I

Nederlandse samenvatting III

Inleiding III
Koraalbanken in de Porcupine Seabight IV
Milieu voorwaarden voor koraalbanken in de Porcupine Seabight VI
Begravingsfase VII
Interne structuur van de Porcupine Seabight mounds VII
De oorsprong van de koraalbanken VIII
Interne controle IX
Externe controle IX
Conclusie XI

1 Introduction 1

1.1 History 3
1.2 General aspects of the mounds in Porcupine Seabight 6
1.3 Discussion topics 7

2. State of the art 9

2.1 Deep-water corals 11
2.1.1 Framework builders 11
2.1.2 Coral framework 12
2.1.3 Terminology 14
2.1.4 Biozonation 15
2.1.5 Biodiversity 17
2.1.6 Coral banks in the Porcupine Seabight 18
2.1.7 Environmental requirements 18
2.1.7.1 Ocean boundary conditions 19
2.1.7.2 Are deep-water corals related to seepage? 21

2.2 Gas migration and Seepage 27
2.2.1 Seepage model for the Porcupine Seabight 27
2.2.2 Hydrocarbons 29
2.2.2.1 Origin of gas in shallow sediments 30
2.2.3 Seepage patterns 32
2.2.3.1 Halo and apical anomalies 33
2.2.3.2 Fault related anomalies 33
2.2.4 Seabottom expression of seeps 34
2.2.4.1 Acoustic techniques 34
2.2.4.2 Geochemical observations 38

2.3 Geological setting of Porcupine Seabight 45
2.3.1 Geometry 45
2.3.2 Geology 45
2.3.2.1 Genesis of the basin 47

2.3.2.2 Faults 47
2.3.2.3 Sediment record 47
2.3.2.4 Pre rift sequence 49
2.3.2.5 Porcupine Median High 49
2.3.2.6 Rift sequences 49
2.3.2.7 Seismostratigraphy in the Porcupine Basin 52
2.3.2.8 Pleistocene-Holocene 53
2.3.3 Hydrocarbon potential 56

2.4 Hydrodynamic setting 57
2.4.1 Water masses 57
2.4.2 Currents 58
2.4.2.1 Northward flowing currents 58
2.4.2.2 Near-surface currents 60
2.4.2.3 Near-seabed currents 60
2.4.3 Slope specific process 62
2.4.3.1 Internal waves 62
2.4.3.2 Bottom friction 65
2.4.3.3 Nepheloid layers 66

3 Data 69

3.1 High-resolution seismic data 59
3.1.1 Acquisition 72
3.1.2 Vertical resolution 74
3.1.3 Scattering near the seabed 74
3.1.4 Velocity pull-ups below the mounds 76
3.1.5 Processing of seismic data 77
3.1.6 Interpretation of seismic profiles 78

3.2 Sidescan sonar 79

3.3 Echosounding 80

3.4 Multi beam 80

3.5 Oceanographic data or CTD profiles 81

3.6 Shallow cores 81
3.6.1 Training Through Research Programme (UNESCO-IOC)-CORSAIRES-ENAM (EC MAST 3 programme) 81
3.6.2 Belgica 83
3.6.3 Pelagia 83
3.6.4 Poseidon 84
3.6.5 Petroleum Affairs Division Ireland cores 84
3.6.6 Statoil cores 84

3.7 Underwater TV profiler 86

4. Belgica mound province 87

4.1 Introduction 89

4.2 Mapping of the Belgica mounds 91
4.2.1 General bathymetry 92
4.2.2 Distribution of the mounds 96
4.2.2.1 General water depth mound analysis 96
4.2.2.2 Water depth - mound type 97
4.2.2.3 Water depth - mound - zone relation 98

4.3 Geometry of the Belgica mounds 101
4.3.1 General geometry per mound type 104
4.3.1.1 Width 104
4.3.1.2 Height 105
4.3.2 Mound shape in plan view 110
4.3.2.1 EW profiles 110
4.3.2.2 NS profiles 111
4.3.2.3 General plan view of the mounds 111
4.3.2.4 Detailed plan view shape of the surface mounds 112
4.3.2.5 Mound area 115
4.3.3 Summary 115

4.4 Geological record 117
4.4.1 Unconformities 117
4.4.1.1 Mound base 119
4.4.2 Facies description 122
4.4.2.1 Facies Ba 122
4.4.2.2 Facies Bb 122
4.4.2.3 Facies Bc 126
4.4.2.4 Facies Bd 128
4.4.2.5 Mound substratum 131
4.4.2.6 Facies Be 132

4.5 Seismic properties of the mounds 137

4.6 Case studies 141
4.6.1 BEL26, Challenger mound 141
4.6.1.1 Bathymetry 141
4.6.1.2 Geometry 142
4.6.1.3 Geology 144
4.6.2 BEL35 - Thérèse mound and friends 146
4.6.2.1 Bathymetry 146
4.6.2.2 Geometry 147
4.6.2.3 Geology 151

4.7 Sidescan sonar images 155
4.7.1 Northern zone 157
4.7.2 Southern part 161

4.8 Sedimentology 165

4.8.1 Off-mound sediment samples 165
4.8.1.1 Sandwaves field 165
4.8.1.1 NS channel 167
4.8.2 Near-mound sediment samples 167
4.8.3 On-mound sediment samples 168
4.8.3.1 Southern Belgica mound province 168
4.8.3.2 Central Belgica mound province 172
4.8.4 Grain size analysis 174
4.8.4.1 Paleoclimatology 176
4.8.5 Mineralogy 182
4.8.6 Contourites 186

4.9 Biological results 189
4.9.1 Biological zonation 189
4.9.1. Description of the video transect 192
4.9.2 Biodiversity on the mounds 193
4.9.2. General observations 194
4.9.2. Microhabitats 196

4.10 Oceanography 199

5. Hovland mound province 207

5.1 Mapping of the Hovland-Magellan mounds 209
5.1.1 General bathymetry in the Hovland-Magellan mound province 213
5.1.2 Distribution of the mounds in the Hovland mound province 215
5.1.2.1 General depth analysis 215

5.2 Geometry of the Hovland mounds 217
5.2.1 General mound geometry 217
5.2.1.1 Width 217
5.2.1.2 Height 219
5.2.1.3 Development of the mound 221
5.2.1.4 Detailed mound geometry 224
5.2.2 Magellan mounds 232
5.2.2.1 General observations 232
5.2.2.2 Mound geometry 234

5.3 Geological record 237
5.3.1 Unconformities 238
5.3.1.2 Facies Ha 244
5.3.1.3 Facies Hb 245
5.3.1.4 Facies Hc 246
5.3.1.5 Facies Hd 251
5.3.1.6 Facies He 252
5.3.1.7 Mound facies 256
5.3.2 Mound / facies relation 257
5.3.3 Mound / faults relation 258
5.3.4 Pockmarks and migration structures 260

5.4 Sedimentology 265
5.4.1 Off-mound samples 265
5.4.1.1 Magellan mound province 265
5.4.1.2 Hovland mound province 268
5.4.2 Moats 268
5.4.3 On-mound cores 269
5.4.3.1 Magellan mound 269
5.4.3.2 Cores on HOV02 271
5.4.3.3 Cores on HOV03 275
5.4.3.4 Cores on HOV04 275
5.4.3.5 Cores on HOV05 277
5.4.4 Sediment characterization 279
5.4.4.1 Clay mineralogical analysis 279
5.4.4.2 Binocular analysis 283
5.4.4.3 Scanning electron microscopy 284
5.4.4.4 Cathodoluminescence microscopy 285
5.4.4.5 Petrographic microscopy 285
5.4.5 Isotopic analysis 287
5.4.5.1 Isotopic analysis of TTR7-AT-16G 288
5.4.5.2 Isotopes of corals 290
5.4.6 Gas analysis 293
5.4.6.1 Headspace gas 293
5.4.6.2 Occluded gas 295
5.4.6.3 Gas isotopes 295
5.4.6.4 Gas chromatography - Mass spectrometry 297
5.4.6.5 Carbonate isotopic values 298
5.4.6.6 Summary 298

5.5 Biological results 301
5.5.1 Biological zonation 301
5.5.1.1 Introduction 301
5.5.1.2 Results 302
5.5.1.3 Biological zonation based on boxcore samples. 304

5.6 Oceanography 309

6 Discussion 317

6.1 Present setting 317
6.1.1 Coral bank distribution 317
6.1.1.1 Surface coral banks 317
6.1.1.2 Buried coral banks 318
6.1.2 Coral bank geometry 318
6.1.2.1 Circular banks 318
6.1.2.2 Elongated banks 319
6.1.2.3 Sediment pressure 319
6.1.3 Framework builders 319
6.1.3.1 Associated fauna 320
6.1.3.2 Site specific associated fauna 320
6.1.3.3 Microhabitat 321

6.1.3.4 Sponges 321
6.1.3.5 Bioeroders 321
6.1.3.6 Distribution of living corals 322
6.1.3.7 Baffling of sediment 322
6.1.3.8 Zonation 323
6.1.4 Oceanographic environment 323
6.1.4.1 Origin of MOW 324
6.1.4.2 Nutrients 325
6.1.4.3 Model of the present 326

6.2 Initial coral bank development and triggering 327
6.2.1 Paleo-environment before the coral bank initiation 327
6.2.1.1 Contourites 328
6.2.2 Coral bank base 329
6.2.2.1 Dating 329
6.2.2.2 Origin of the erosion 329
6.2.2.3 MOW in the past 330
6.2.3 Internal structure of the coral bank 330
6.2.4 Coral bank triggering 331
6.2.5 Coral bank development 332
6.2.5.1 Start-up 332
6.2.5.2 Catch-up 335
6.2.5.3 Keep-up 336
6.2.5.4 Give-up 336
6.2.5.5 Evolutional Stadia 336

6.3 Are coral banks related to seeps? 338
6.3.1 Critical evaluation of the models 340

7 Conclusion and perspectives 345

7.1 Conclusion 345

7.2 Perspectives 346
7.2.1 EU 5th Framework projects 346
7.2.2 IODP 347

References 349

Abstract

This multidisciplinary study describes the morphology, seismic facies, sedimentology, biology and oceanography of large deep-water coral banks and their geological setting in the Porcupine Seabight offshore Ireland. Coral banks in the Porcupine Basin are larger than most of their North Atlantic counterparts. They are about 1 km wide, can be up to 3 km long and attain heights of almost 200 m above the seafloor. The banks are mound-shaped elevations, hosting living deep-water coral and associated fauna on their upper flanks. This biological active layer covers a dead assemblage of corals, filled with terrigeneous mud similar to the surrounding seabed. The coral banks in the Porcupine Basin occur in two geographical provinces, each characterized by a typical mound shape: complex flatted topped seafloor mounds in the Hovland mound province, partly buried mounds in the Belgica mound province, and a large numbers of smaller NS elongated buried mounds of various shapes in the Magellan mound province.

All coral banks, buried or outcropping, occur in association with current-induced features such as moats, sediment tails and sediment dunes indicating their location in regions of strong currents. Only few mounds are still outcropping today, which suggests that environmental conditions were more favourable fro the mound growth in the past. The depth range of these outcropping mounds coincides with the top of the dense Mediterranean Outflow Water, where current enhancement through internal tidal waves could control coral growth. Mound growth started simultaneously, probably since the Late Pliocene and after a period of erosion and non-deposition. Various phases of mound development in the past few millions years may have occurred and be related to important fluctuations in oceanographic conditions, where the MOW can play a major role. Though the genesis and initial control of mound settings in this basin might be related to hydrocarbon seeps, it appears that the major development of the Porcupine coral banks in recent geological times has most likely been controlled by oceanic circulation and dynamics in water masses and nutrient supply. No conclusive evidence has yet been found for either hypothese.

Sediment stress, largely controlled by currents, plays an important role in the mound development. Coral banks accrete by active baffling of sediment by the biological framework and extension of the biological cap (Catch-up). Once this fragile system between sedimentation and biological growth is out of balance, the framework will progressively be filled with sediment (Keep-up) with only a few living patches. Once the sediment dominates the structure the coral banks get buried and draped by sediment (Give-up).

Nederlandse samenvatting

Inleiding

Koudwaterkoraalecosystemen staan sedert enkele jaren in het brandpunt van de belangstelling van zee-onderzoekers. Biologen waren sinds de eerste beschrijving in de 19de eeuw (cf. Thomson, 1873) al geïntrigeerd door deze mysterieuze koudwaterkoralen. Geologen en vooral petroleumgeologen kregen pas recent interesse in deze materie toen er een relatie bleek te bestaan tussen het voorkomen van koudwaterriffen en onderzeese methaanbronnen of 'seeps' (Hovland, 1990). Ondanks de groeiende belangstelling van Europese laboratoria en de offshore industrie hebben de diepzeeriffen hun diepste geheimen nog niet prijs gegeven. In februari 1997 werd in Gent dan ook het eerste internationaal congres georganiseerd door onze onderzoeksgroep met als thema koudwaterkoralen en de relatie "deep-biosphere-geosphere". Dit was de aanzet tot uitgebreide internationale acties (TTR-cruises, Belgica-cruises, etc.) en lag aan de basis van 3 succesvolle Europese projecten: GEOMOUND, ECOMOUND en ACES in de OMARC cluster, naast een nationaal project: Porcupine-Belgica (BOF, RUG).

De meest voorkomende azooxanthellate soort is *Lophelia pertusa* (Linné) die algemeen aangetroffen wordt langs de randen van de Noordatlantische Oceaan. Ook al zijn deze koralen beschreven als niet rifopbouwend, toch komen ze voor in grote koloniale structuren en bedekken ze vaak verheven structuren op de zeebodem (e.g. Stetson *et al.*, 1962, Neumann et al, 1977, Freiwald and Henrich, 1997).

Uit onderzoek van koudwaterriffen voor de Noorse kust blijkt dat verschillende externe factoren (stromingspatronen, seizoenaal voedseltransport en zeespiegelschommelingen) en interne factoren (benthische associaties, afbraak van organisch materiaal, bacteriën, bio-erosie) een rol kunnen spelen in de vorming en de stabilisatie van zulke systemen (Freiwald *et al.*, 1999; Mortensen, 2000). Maar ook geologische factoren spelen een belangrijke rol: de riffen worden in deze setting duidelijk geassocieerd met post-glaciale structuren (tills, morenen en ijsberggroeven (Freiwald and Wilson, 1998)) en misschien ook met methaanbronnen (Hovland and Thomsen, 1997). Langs de Faeroer eilanden en Rockall Trough komen gelijkaardige riffen voor in waterdiepten tot 450m (Frederiksen *et al.*, 1992). Uit de resultaten van deze auteurs blijken ook hier oceanografische factoren (stromingen, watermassa's,...) een belangrijke rol te spelen in de ruimtelijke organisatie van deze koralen.

In de Porcupine Seabight (ten SW van Ierland) zijn op industriële seismische profielen (Hovland *et al.*, 1994) en op hoge-resolutie seismische profielen enkele tientallen zeer grote "mounds" waargenomen met afmetingen tot 2km doormeter en 200m hoogte, langs de continentale rand opdomende "mounds" en kleinere bedolven structuren, in een waterdiepte van 600 tot 1200m (Henriet *et al.*, 1998; Henriet et

al., 2001; De Mol et al., in press). De grote mounds zijn gekoloniseerd door een uitzonderlijk rijke biologische niche. De Porcupine "mounds" onderscheiden zich dan ook duidelijk van de eerder besproken riffen in Noorwegen en rond de Faeroer eilanden door hun dimensie en het milieu waarin ze voorkomen, merkwaardig genoeg in een dieper deel van het oceanisch bekken. In deze setting werd een vrij systematische relatie waargenomen tussen de inplanting van deze diepwaterriffen en diepere tectonische breuken, die als aanvoerwegen van methaan uit dieperliggende koolwaterstofreservoirs kunnen fungeren (Hovland *et al.*, 1994).

Toch is het niet duidelijk of er een relatie bestaat tussen de opbouw van deze zeebodemstructuren en migratie van fluida. Eveneens is de rol van de koralen en hun geassocieerde fauna als actieve onderzeese structuurbouwers niet achterhaald, of dat daarentegen mounds opgebouwd worden door andere processen al dan niet geassocieerd met methaanopwelling - eventueel van bacteriologische aard- en de koralen gewoon "mound-minnend" zijn. Een geologische controle op de verdeling van deze diepe "mounds" in het Porcupine bekken lijkt aldus evident, maar de ware toedracht ervan en de wisselwerking tussen geologische factoren en fysisch-oceanografische (stromingen, watertemperaturen) of ecologische (plankton-benthos koppeling, interactie tussen bacteriën, algen, azooxanthellate koralen, sponsen, enz.) blijft een kernvraag.

In dit doctoraal onderzoek wordt getracht een grondige analyse te maken naar de aard en toedracht van de geologische, fysisch-oceanografische en ecologische factoren die de genese, ontwikkeling en ruimtelijke verdeling van diepwaterkoralen kunnen bepalen in de Porcupine Seabight. Deze geologische controle zelf is complex en dient dan ook vanuit diverse invalshoeken bestudeerd te worden: bekkendynamica, opbouw van biogene en niet-biogene sedimenten, migratie van fluïda en diagenese, geofysische en geochemische karakterisatie, paleoceanografische evolutie en paleoklimatologische controle.

Koraalbanken in de Porcupine Seabight

De koraalbanken in de Porcupine Seabight komen voor in drie goed afgelijnde geografische provincies (Henriet et al., 1998; Henriet et al., 2001; De Mol et al, in press). Elke provincie is gekenmerkt door een typische bankmorfologie. De Hovland provincie, gelegen in het meest noordelijk gedeelte van het bekken, is gekarakteriseerd door grote kegelvormige mounds of langwerpige ruggen geassocieerd met diepe grachtstructuren. Ten noordwesten en in het noorden van de Hovland mound provincie komt de Magellan mound provincie voor. Deze provincie is gekenmerkt door bedolven structuren die een grotere vormenvariëteit vertoont dan de Hovland mounds. Deze 2 nabijgelegen mound provincies zijn van elkaar gescheiden door een zone waar geen banken voorkomen. De Belgica mound provincie is gelegen langs de oostelijke continentale helling van de Porcupine Seabight en is gekenmerkt door

grote morfologische zeebodemstructuren. Hellingafwaarts zijn de flanken van de banken gevrijwaard van begraving. De hellingopwaartse zijde daarentegen is meestal begraven.

Deze variëteit van structuren maakt van de Porcupine Seabight een uniek studiegebied voor het bestuderen van de vorming en ontwikkeling van dergelijke diepzeebouwsels.

De resultaten beschrijven grote topografische structuren in het Porcupine bekken waar diepzeekoralen (*Madrepora oculata*, *Lophelia pertusa*, *Desmophyllum en Stylestris*) voorkomen geassocieerd met een rijke diepzeefauna op kegelvormige of langwerpige structuren.

De belangrijkste observaties zijn:

- het voorkomen van drie mound provincies
- de dimensie van de koraalbanken
- de relatief hoge concentratie van benthische fauna op de heuvels
- de asymmetrie in het biologisch leven
- het voorkomen van een koraalconstructie gevuld met siliciklastisch materiaal
- de erosieve basis van de koraalbanken
- het voorkomen van de koraalbanken nabij de bovengrens van MOW
- de indicaties van sterke stromingen
- het voorkomen van koralen in warme periodes.
- geen evidentie van rechtstreekse observatie van koolwaterstoffen

Met de verworven gegevens kan een beeld gevormd worden van het geografisch voorkomen, de geologische plaatsing, de ondiepe sedimentologie en de oppervlakkige biologische zonatie. Wat betreft de interne opbouw van deze structuren is er een gebrek aan informatie: tot nu toe zijn er geen diepe kernen beschikbaar; de koraalbanken vertonen een akoestische transparantie. Desalniettemin is de beschrijving van deze structuren gelijkend op de definitie van een koraalbank elders in de Noordatlantische Oceaan (Cairns and Stanley, 1981; Hovland et al., 1998; Pratje, 1924; Reed, 1992; Stetson et al., 1962; Teichert, 1958). De term koraalbank is gedefinieerd als een topografische hoogte hoofdzakelijk bestaande uit koralen. De koraalbank is de laatste fase in de evolutie van diepzeekoraalstructuren. Een koraalbank is gekenmerkt door drie goed te onderscheiden eenheden: (1)

een zone van levende koraalkolonies, die (2) rusten op een open geraamte van dode koraalconstructies en een afbraakzone, en (3) een zone waar het koraalgeraamte en fragmenten zijn gevuld en begraven met sedimenten. In werkelijkheid kan herkolonisatie op deze 3 zones voorkomen. De grootste dichtheid van de levende koraalkolonies komt voor nabij de top van de structuur (Mortensen et al., 1995).

Door hun grootte en modderige matrix verschillen de koraalbanken in het Porcupine bekken van andere azooxanthellate (voornamelijk *Lophelia*) koraalbanken. De beschreven azooxanthellate koraalbanken in de literatuur zijn voornamelijk opgebouwd uit een koraalgeraamte al dan niet ondersteund door sponzen (Freiwald et al., 1999), gevuld met biogeen en terrigeen materiaal. In het algemeen komen ze voor bovenop een reeds bestaande structuur op de zeebodem zoals glaciale sills, moreenruggen, ijsberggroeven en seamounds (Cairns and Stanley, 1981; Freiwald et al., 1999).

Milieu voorwaarden voor koraalbanken in de Porcupine Seabight

Voorkomen van diepwaterkoralen

De kernbeschrijvingen en de biologische gegevens tonen aan dat de koralen een belangrijke rol spelen in de evolutie van de koraalbanken. De meest voorkomende koralen zijn *Lophelia* en *Madrepora*. Beide koraalspecies zijn zeer verbreid in de Atlantische Oceaan en komen voor in dezelfde ecologische niche (Strömgren, 1971; Le Danois, 1948; Freiwald, 1998). De voorwaarden voor de groei van *Lophelia* en *Madrepora* koralen zijn: een hard substraat, voldoende voedsel (copepoden, zoöplankton) en een bescherming tegen begraving. Concentraties van koralen zijn voornamelijk gevonden nabij sterke stromingen (upwelling, interne golven tussen gestratificeerde watermassa's etc.) die de afzetting van fijnkorrelige sedimenten onderdrukken en de voorzieningen van voedsel bevorderen (Cairns and Stanley, 1981; Freiwald, 1998). In deze gunstige gebieden kunnen azooxanthellate koralen zich nestelen als een hard substraat aanwezig is. Als deze ecologische voorwaarden zich wijzigen, sterft de koraalstructuur af en wordt ze opgevuld met sedimenten.

In de Porcupine Seabight blijken de koraalbanken voor te komen na een periode van erosie, langs de flanken van een lokale depressie, met uitzondering van de Magellan mounds. Tijdens of net na zo een periode van niet-afzetting zijn talrijke harde substraten aanwezig en zijn de stromingen voldoende groot om de koraalbouwsels te vrijwaren van overtollige sedimentatie en te voorzien van voedsel. De Magellan mounds zijn minder ontwikkeld en blijken groter op de randen van de provincie waar de dikte van het bovenliggend sedimenten pakket afneemt. De gunstige omstandigheden in de Magellan mounds hebben vermoedelijk minder lang plaatsgevonden dan in de andere provincies.

Oceanografisch regime

Zeebodemstructuren geïnduceerd door stromingen zoals grachten, sedimentstaarten en sedimentgolven zijn nauw verbonden met koraalbanken in de Porcupine Seabight. Textuuranalyse van sidescan sonar beelden van de Hovland en Belgica mounds bevestigen de sterke stromingen nabij de zeebodem maar suggereren dat de stromingen in de Hovland mounds zwakker zijn dan in de Belgica mounds. (Huvenne et al, submitted.). Dit reflecteert zich ook in het biolgisch leven dat veel rijker is aan de bekkenwaartse randen van de Belgica mounds dan aan eender welke flank in de Hovland mound provincie. Diepzeestromingen in het bekken zijn gemeten (Rice et al., 1991) en voorspeld door een mathematisch model (New et al., 2001.). Interne getijdengolven komen voor in de overganszone tussen het MOW en het bovenliggende ENAW, die op hun beurt verantwoordelijk zijn voor de sterke lokale stromingsregimes. Het MOW uit zich in een zone van maximale saliniteit. De invloed van hogere saliniteit is zichtbaar in de CTD profielen voor beide gebieden. Interne getijdengolven langs de continentale helling van de Porcupine Seabight zijn geanalyseerd door Rice et al. (1990) in functie van de helling van de zeebodem en hellingen van de golfstralen. Stromingen langs de helling worden versterkt door de breking van de interne getijdengolven waar de helling van de straalweg van de golf groter is dan de helling van de zeebodem (Rice et al., 1990). Deze kritische helling is tegengesteld evenredig met het dichtheidsgradient tussen de verschillende watermassa's (Sherwin and Taylor, 1987). Wegens het densiteitsverschillen tussen ENAW en MOW lijkt het ook evident dat dergelijke stromingen voorkomen aan deze grens.

De koraalbanken komen juist in deze grenszone voor. Nogmaals blijkt uit de CTD-profielen dat het effect van MOW kleiner is in de Hovland mounds dan in de Belgica mounds, wat de zwakkere stromingen zou kunnen verklaren. De gemiddelde hellingsgradient in de Hovland mound provincie is vermoedelijk kleiner dan de kritische helling voor het breken van de interne golven (Rice et al., 1990), maar de lokale depressie op de flanken waar de koraalbanken zitten, heeft een veel sterker gradient dat de kritische waarde mogelijk overschrijdt.

Begravingsfase

Bedolven koraalbanken zoals de Magellan en enkele Belgica mounds zitten in de huidige omstandigheden in gebieden waar de sedimentdruk relatief groot is (dikker driftpakket), wat overeenkomt met vlakkere zones en relatief zwakkere stromingen. In de aanvangsfase van de ontwikkeling van de koraalbank zullen de ecologische voorwaarden voldaan geweest zijn voor de opbouw. Als de sedimentatie-input toenam na een periode van niet-afzetting waren de stromingen op deze lokaties te zwak om de koraalbank te vrijwaren van begraving.

Het is echter paradoxaal dat sedimentatie de groei van de koralen zou verhinderen en tegelijkertijd de ontwikkeling van de koraalbank positief zou beïnvloeden. Het koraalraam vangt als

het ware de sedimenten in suspensie. De hoge concentraties van micro- en macro fauna (sponzen etc.) die geassocieerd zijn met de structuur, stabiliseren dan op hun beurt het volledige raamwerk (Freiwald et al., 1999). Dergelijke bouwsels kunnen verder evolueren zolang de koraalgroei gelijke tred houdt met de sedimentatie en er nieuwe ruimte vrijkomt om het sediment te vangen. De vraag blijft evenwel hoe dit alles gestart is.

Interne structuur van de Porcupine Seabight mounds

Zoals hierboven reeds vermeld, is er geen direkte informatie aangaande de interne structuur van de koraalbanken. De basis van de koraalbanken is continue en meestal erosief. In de Belgica en Hovland mound provincie is deze onregelmatig met diepe insnijdingen maar in de Magellan mound provincie blijkt de basis zwak hellend, zonder enige onregelmatigheden. Met uitzondering van enkele erosiestructuren, zijn er geen aanwijzingen van onderliggende breuken, slumps of moddervulkanen die een initiaal topografisch reliëf zou vormen onder de koraalbanken.

In vergelijking met de Sula Ridge in Noorwegen is de ruimtelijke verdeling van de koralen in het Porcupine Seabight gelijkaardig ondanks het verschil in schaal. De Sula Ridge is een koraalbank met een lengte van 13km, die bestaat uit de versmelting van relatief kleine koraalmounds. De koraalmounds van de Sula Ridge hebben een gemiddelde hoogte van 20-25m en een breedte van 50m. Ze bestaan uit bolvormige koraalkolonies met een hoogte van 1.5 m, die een subeenheid in het moundbouwsel vormt (Henrich et al., 1996; Freiwald, 1998; Freiwald and Wilson, 1998; Freiwald et al., 1999). De Porcupine koraalbanken vertonen een gelijkaardige opbouw maar ze zijn verder ontwikkeld in vertikale zin. De Sula Ridge heeft zich gevormd op reeds aanwezige reliëfvormen op de zeebodem en is verder geëvolueerd langs deze structuur. In de Porcupine Seabight hebben de koraalbanken hoogstwaarschijnlijk zelf de topografische structuur opgebouwd en hebben ze zich verder ontwikkeld in vertikale zin.

De oorsprong van de koraalbanken

Verschillende observaties pleiten voor een korte en snelle initiële groei van de koraalbanken. Dit blijkt uit de onlapping van de driftsedimenten in de Belgica mound provincie. Het massaal voorkomen van Magellan mounds op een horizont is een andere aanwijzing.

Uit de oceanografische en biologische resultaten blijkt dat de huidige verspreiding van levende *Lophelia* en *Madrepora* koralen en koraalbanken overeenkomen met specifieke omstandigheden (sterke stromingen, trage sedimentatiesnelheden). Toch is het niet duidelijk waarom de koraalbanken zijn beginnen ontwikkelen in zo grote aantallen op enkele specifieke locaties.

De belangrijkste observaties in dit verband zijn:

- een snelle initiële groei ongeveer gelijktijdig in elke provincie
- geen aanwijzingen voor verschillende opstartfasen binnen eenzelfde provincie
- de moundinitiatie is begrensd binnen de mound provincie
- de moundgroei komt in iedere provincie voor na een periode van erosie.

Deze observaties suggereren dat de beginfase binnen elke provincie veroorzaakt is door een drastische verandering in het milieu, die de ontwikkeling van de koraalbanken aanmoedigt in het bekken. Deze veranderingen kunnen van geologische (interne controle) of oceanografische (externe controle) aard zijn.

Interne controle

Hovland (1990), Hovland et al. (1994) en (1998) suggeren een causale relatie tussen de diepwaterkoralen en koolwaterstof, 'seeps'. Door de lokale fertilisatie van gefocusseerde 'seeps', kunnen aan alle voorwaarden (extra voedsel, cementatie tot hardsubstraat) voor koraalgroei voldaan zijn. In de Hovland mound provincie interpreteerde Hovland et al. (1994) op basis van industriële seismische profielen dat de koraalbanken onmiddellijk boven grote breuken geplaatst zijn, die kunnen fungeren als migratiepaden voor koolwaterstoffen. Geen directe aanwijzingen gevonden in deze studie om deze theorie te bevestigen. Uit de literatuur blijkt ook dat de meeste koraalbanken niet voorkomen in dergelijk omstandigheden.

De potentiële rol van methaan in de opstartfase van de koraalbanken wordt ook naar voorgebracht door Henriet et al. (1998; 2001) In dit model wordt voor de Magellan mound provincie een mogelijke relatie tussen methaanmigratie, hellingsinstabiliteiten en moundgroei voorgesteld. Zo een model veronderstelt verschillende fasen van gashydraatvorming en destabilisatie in een milieu onder extreme variatie van bodemstromingen en van temperatuur in recente ijstijden en glaciale-interglaciale perioden. Om deze theorie te bekrachtigen zijn geen aanwijzingen gevonden in deze studie.

Externe controle

Uit de resultaten van deze studie werd een derde scenario ontwikkeld. In deze hyptohese wordt het ontstaan van de koraalbanken in verband gebracht met de initiatie van het MOW in de Noordatlantische Oceaan. De evolutie van oceanische toevoerswegen in het Neogeen en Quartair hadden een grote impact op de globale oceaan circulatie. De sluiting van de Isthumus van Pananama, startte 4.6Ma geleden (Haug and Tiedemann, 1998) en splitste de grote watermassa's van de tropische zone van de Atlantische Oceaan van het noorden. Deze gebeurtenis controleert nog steeds de huidige

oppervlakteparameters van de NE Atlantische Oceaan. Waarschijnlijk zijn door het latente warmtetransport in de oceaan de ijstijden in de noordelijke hemisfeer ontstaan, die de advectie in de diepere waterlagen verhoogde. Dit in combinatie met het MOW dat zich herinstalleerde in de Atlantische Oceaan na de Laat Miocene-Vroeg Pliocene Messinaanse saliniteitscrisis in de Middellandse Zee (Maldonado and Nelson, 1999). Een regionaal hiaat van Laat Pliocene ouderdom is beschreven in het Rockall-Goban Spur profiel en geïnterpreteerd als de herinstalatie van het MOW (Pearson and Jenkins, 1986). Op basis van microfossielassociaties van diepe boorkernen van de Noordatlantische Oceaan (ten westen van de Rockall Bank en in de Western Approaches), verondersteld Schnitker (1986) dat de huidige waterstratificatie in het Noordatlantisch diepwater (NADW) zich ontwikkelde bij het begin van de moderne ijstijden ongeveer 2-2.5 Ma geleden. De klimaatfluctuaties en eustatische zeespiegelschommelingen blijken een dominerende controle te hebben op het MOW sinds het Laat Plioceen (Cremer and Faugères, 1993; Nelson et al., 1993; Caralp, 1988; Grousset et al., 1998). De oudste fossiele optekeningen van *Lophelia en Madrepora* in het Noordatlantisch gebied dateren van Vroeg Pliocene ouderdom en komen voor in de Middellandse Zee (Chevalier, 1961; Cairns and Stanley, 1981; Esteban, 1996; Pérès, 1985).

Diepwaterkoralen komen onder verschillende vormen voor langs de Europese continentale randen van Gibraltar tot Noorwegen (Freiwald, 1998). Daarom is het mogelijk dat de larven van de azooxanthellate koralen geïntroduceerd zijn in de NE Atlantische Oceaan samen met het MOW en het voordeel namen van de randeffecten die deze veroorzaken (stromingen ten gevolge van hogere densiteitsverschillen) om de continentale randen te koloniseren. Het effect van het MOW komt niet verder dan de meest noordelijk deel van de Porcupine Bank in de Rockall Trough (New et al., in press, van Aken, 2000). Het transport van de larven naar de meest noordelijke gebieden kan verzekerd zijn door andere noordwaartse stromingen gerelateerd aan de NAC (Freiwald et al., 1999). In dit scenario zijn verschillende startfasen mogelijk, door het al dan niet voorkomen van MOW in de Porcupine Seabight. Deze cylus is beïnvloed door klimatologische veranderingen. In warmere perioden en bij hoge zeespiegelstand zal het MOW een grotere invloed hebben. Een eerste periode van koraalbankontwikkeling zou plaats gevonden hebben in de Belgica mound provincie die zich ontwikkelde op Miocene afzettingen, terwijl een tweede fase zich afspeelde op de grens tussen het Plio-Pleistoceen in de Magellan en Hovland mound provincies. De geschatte ouderdom van een Hovland mound past in dit scenario. De sterke erosie oppervlakten weerspiegelen waarschijnlijk drastische veranderingen in het oceanografisch regime met hoge stromingssnelheden zoals op het einde van het Mioceen en begin Pleistoceen. Kleinere variaties zijn waarschijnlijk terug te brengen naar ijstijden cyclussen en kleinere klimaatsveranderingen. De microfossielenassemblages in kernen van de koraalbanken (Coles et al., 1996) en de driftsedimenten (Van Rooij, pers. com.) tonen ook een variatie van soorten die exclusief in de Middellandse Zee voorkomen in de sedimenten, die overeenkomen met koraalrijke lagen en warme periodes vertegenwoordigen.

Conclusie

Deze studie beschrijft de morfologie, de seismische facies, de sedimentologie en de biologie van grote diepzeekoraalbanken en hun oceanografische en geologische setting in de Porcupine Seabight (SW Ierland). De koraalbanken in de Porcupine Seabight zijn groter dan de meeste beschreven banken in de Noordatlantische Oceaan. Ze zijn ongeveer 1km breed, ze kunnen een lengte bereiken van 3km en een hoogte van 200m. De banken zijn topografische hoogtes waar levende diepzeekoralen en geassocieerde fauna voorkomen op de bovenste flanken. De biologische actieve laag overdekt een dode gemeenschap van koralen, gevuld met terrigeen, fijn, korrelig sediment.

De koraalbanken in de Porcupine Seabight komen voor in drie provincies, elke gekenmerkt door een typische mound vorm: kegelvormige oppervlaktemounds in de Hovland mound provincie, gedeeltelijk bedolven kegelvormige mounds in de Belgica mound provincie, en talrijke kleinere bedolven mounds in de Magellan mound provincie.

Alle banken zijn geassocieerd met stromingsstructuren zoals, grachten, sedimentstaarten en zandgolven die verwijzen naar een dynamisch stromingsregime. Slechts enkele koraalbanken komen voor aan de oppervlakte. Dit laat veronderstellen dat de omstandigheden voor de opbouw van de koraalbanken gunstiger waren in het verleden. De bathymetrische zone waar deze oppervlaktemounds voorkomen valt samen met de top van het MOW, waar de stromingen worden versterkt door interne getijde golven, die een gunstig klimaat vormen voor de ontwikkeling van de koraalbanken.

De ontwikkeling van de koraalbanken startte gelijktijdig in elke provincie, waarschijnlijk in het Laat Plioceen, na periodes van erosie en niet-afzetting. De koraalbanken hebben verschillende ontwikkelingsfasen (start-up, catch-up, keep-up en give-up) ondergaan die samenhangen met veranderingen van de oceanografie in het bekken.

Naast een duidelijke link tussen de oceanografie en de ontwikkeling van de koraalbanken is het niet duidelijk wat de voorwaarden voor de genese van de koraalbanken zijn. De aanvangsfase (Start-up) laat drastische veranderingen in het bekken veronderstellen die een gunstig klimaat vormen voor lokale groei van koralen dat leidt tot een koraalbank. Deze drastische wijzigingen in het milieu kunnen veroorzaakt zijn door veranderingen in de oceanografische circulatiepatronen, zoals de instalatie van het MOW in de Porcupine Seabight. Geen aanwijzingen zijn gevonden voor mogelijk link met koolwaterstoffen.

1 Introduction

1

1.1 History 3
1.2 General aspects of the mounds in Porcupine Seabight 6
1.3 Discussion topics 7

1 Introduction

This study finds its origin in a high-resolution seismic cruise in 1997 with R/V Belgica in the Porcupine Seabight, SW of Ireland (Fig. 1.1). During that cruise large mound structures were for the first time recorded with high-resolution seismics. These mound structures have been associated with deep-water corals and occur in well-defined areas in the Seabight. The aim of this research is to study the mounds in the Porcupine Seabight; to investigate their distribution and detailed morphology, their stratigraphic and sedimentological setting and the role of geological, biological and oceanographic processes controlling the origin and development of the large seabed structures.

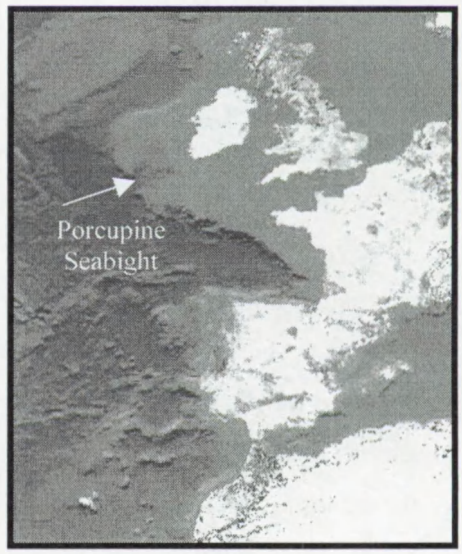

Fig. 1.1: Location of the Porcupine Seabight.

This study is based on high-resolution seismic profiles, sidescan sonar images, shallow sediment cores, oceanographic data and biological studies.

1.1 History

In 1869 and 1870, three famous British scientists Wyville-Thomson, Carpenter and Gwyn Jeffreys embarked on the small navy vessel H.M.S. Porcupine. The aim of this scientific cruise was to prove that life exists in the deep-sea. During that cruise they deployed several dredge hauls to the west of Ireland and in the Gulf of Biscay. These dredge samples recovered a wide range of unidentified deep-sea fauna including deep-water corals. This was a significant step in the discovery of the deep-sea fauna and the first description of the deep-water corals on the Porcupine bank and in the Porcupine abyssal plain. The Porcupine Seabight had been surveyed by the same some seven years earlier (Thomson, 1873) (Fig. 1.2). It is immediately adjacent to the northern part of the Bay of Biscay.

Fig. 1.2: *Lophelia pertusa* is for the first time reported in the Porcupine Seabight by Wyville Thomson (1873).

During the succeeding 50 years it was visited by a variety of scientists. Most of these expeditions obtained only a small number of samples in the region, but the Helga and Helga II worked out an extensive series of stations, particularly on the eastern and northern flanks of the Seabight, though no deeper than about 1600 m (Le Danois, 1948).

After WW I only the French research trawler Président Théodore Tissier visited the Seabight. Nevertheless, by 1948 Le Danois was able to provide a superb synoptic account of the continental slope fauna off the coasts of northwestern Europe, including a remarkable amount of details on the general facies in the Porcupine Seabight. He made a facies interpretation of different European continental slopes and found at several locations large quantities of corals. These occurred mostly in a narrow bathymetric zone between 500-1000 m along the continental slope and formed, according to Le Danois, huge belts up to several hundreds of meters high and thousands of meters long. In the Porcupine Seabight he reported such a band of coral on the eastern flank and named it "massif de la Baie de Dingle".

After the work of Le Danois the corals and coral structures in the Porcupine Seabight fell out of interest of marine research. Still, research on the stony framework building cold-water corals *Lophelia, Madrepora, Desmophyllum, Dendrophyllia*, etc. continued in the cradle of cold-water corals research, in Norway. Since the very first description of deep-water structures and more specific of *Lophelia pertusa* (Gunnerus, 1768; Rasch, 1836; Sars, 1865) in Norwegian water, they were subject of many research projects on their biology and their geomorphological expression on the seafloor (Freiwald, 1998; Hovland and Mortensen, 1999; Mortensen, 2000). Also in other areas of the European margin, *Lophelia* was studied but less intensively than in Norway.

Coral structures have been found along the northwest continental margin in the fjords and offshore Norway (Freiwald, 1998; Hovland and Mortensen, 1999; Mortensen, 2000), around the British Isles (Wilson, 1975; Wilson, 1979a; Wilson, 1979b), the Faeroer Islands (Frederiksen et al., 1992; Jensen and Frederiksen, 1992), the Rockall Bank (Scoffin et al., 1980; Wilson, 1979c), the Rockall Trough (de Haas et al., 2000; Kenyon et al., 1998), the Gollum channels (Tudhope and Scoffin, 1995), the Porcupine Bank (Scoffin and Bowes, 1988) and in the Mediterranean Sea (Zibrowius, 1980). Besides the northeastern Atlantic, corals and coral structures have also been reported along the margin of West Africa (Zibrowius and Gili, 1990), in the northwest Atlantic Blake Plateau (Reed, 1992; Stetson et al., 1962), near the Bahamas (Messing et al., 1990; Mullins et al., 1981; Neumann et al., 1977; Neumann and Paull, 1998), on Hatteras Slope (Paull et al.,

2000), in the Gulf of Mexico (Moore and Bullis, 1960) and from a few scattered records from the Pacific (Squires, 1965) and Indian Ocean (Rogers, 1999).

It is clear that the deep-water corals are cosmopolitan even though they are more frequently observed in the Northeastern Atlantic. This might suggest a privileged habitat for *Lophelia pertusa* but it might also reflect the more intensive deep-water coral research efforts in this part of the ocean. Though, most of these studies are biologically orientated, Teichert (1958) drew the attention of geologists to the fact that coral frameworks thrive in high latitudes and/or deep environments and emphasized the similarities. He also pointed out the importance of deep reefs to the geologist in the interpretation of similar fossil structures. Nevertheless, one had to wait till the nineties for more geological interest.

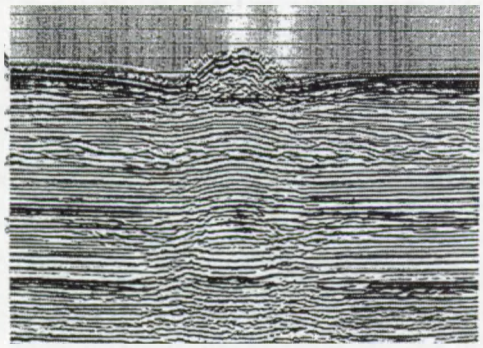

Fig. 1.3: Seismic profile of the dome like structure on the seafloor of the Porcupine Seabight, possibly linked hydrocarbon seepage (Hovland et al., 1994).

In the early nineties the deep-water coral structures of the Porcupine Seabight were brought in the spotlights of geologists. This was indirectly the result of extensive seismic and sampling surveys for oil exploration, which lead to the publication of Hovland et al. (1994) who described for the first time on conventional 2D seismic profiles dome-like structures on the seafloor, in the central part of the Porcupine Seabight (Fig. 1.3). The gravity cores taken on these structures yielded the deep-sea coral *Lophelia pertusa* besides muddy sediment. Another key observation was the remarkable relation between mounds and interpreted deeper faults underneath the mounds. The authors proposed a model in which hydrocarbon seeping played a role in the occurrence and evolution of the mound structures. This was one of the first models to explain the occurrence and patchy distribution of modern deep-water coral structures by geologists.

These observations and the proposed model were the immediate cause of a renewed academical interest in the subsurface of the Porcupine Seabight. The first cruise to the mounds in the Porcupine Seabight was organized by the RCMG (Renard Centre of Marine Geology) in the framework of the E.U. MAST 3 projects CORSAIRES and ENAM II to study slope instabilities along the eastern flank of the Porcupine Seabight with high-resolution seismic profiles. This survey of RV Belgica resulted in the discovery of partly buried mounds creating a terrace-like morphology of the eastern flank of the basin. During the same cruise the mounds reported by

Hovland et al. (1994), have been visited and imaged by high-resolution seismic profiles. In addition, a few extra lines have been sailed to the north and a field of buried mounds has been discovered. This first successful seismic survey was followed by a Training Through Research-CORSAIRES cruise (Kenyon et al., 1998) on which shallow sediment cores and sidescan sonar data have been collected in the different mound provinces. Three European projects, GEOMOUND, ECOMOUND and ACES, which study respectively the internal and external control of coral build-ups and the biology of the deep-water corals along the NE European margins, and the cruises mentioned above form the base of this work.

1.2 General aspects of the mounds in Porcupine Seabight

The coral banks in the Porcupine Basin reach spectacular sizes, up to 200 m height and 5 km length. They occur in three mound provinces (Fig. 1.4), each with a different mound type displaying distinct morphological features (Henriet et al., 1998;De Mol et al. in press).

- The "Hovland" mound province, in the central part of the basin, is characterized by large conical mounds or elongated ridges associated with deep moat structures at the seafloor. They are called after the first author of the paper that described these structures for the first time.

- The "Magellan" mound province occurs north to northwest of the "Hovland" mound province and is characterized by buried mounds in a large variety of shapes. These mounds had been reported in a site survey by the commercial survey ship R/V "Svitzer Magellan", a few months before the Belgica cruise.

- The "Belgica" mound province is located on the continental slope in the east of the basin. Large mounds, which display a well-exposed downslope side in the bathymetry but an almost entirely buried upslope side, characterize this province. These mound structures were called "Belgica mounds" after their discovery by the RV Belgica on high-resolution seismic profiles. They corresponded approximately to the "Massif de la Baie de Dingle" of Le Danois (1948).

The variety in structures in well-delineated provinces makes the Porcupine Basin a unique site to study the environmental and geological control on the origin and evolution of deep-water coral banks.

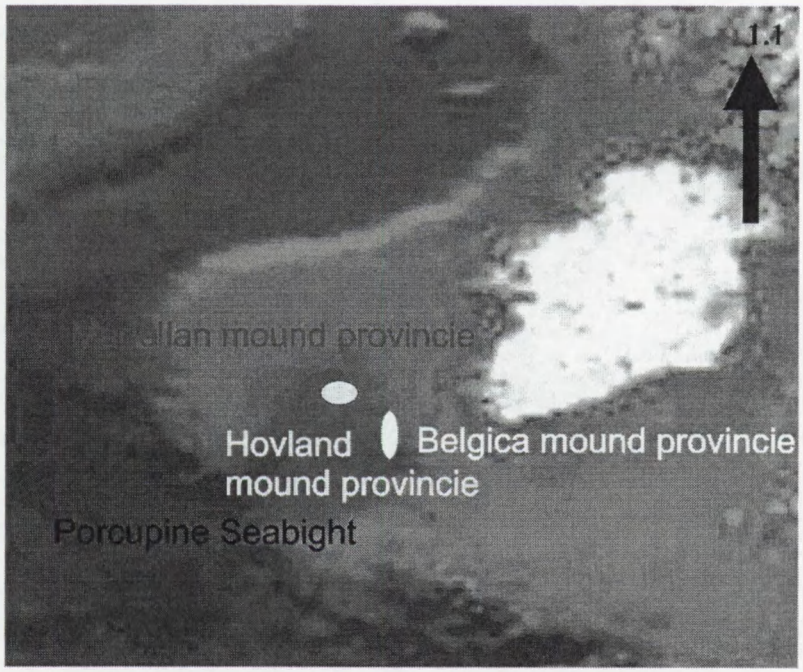

Fig. 1.4: Location map of the three mound provinces in the Porcupine Seabight.

1.3 Discussion topics

The presence of deep-water coral banks is considered to be closely related to oceanographic conditions favourable for the azooxanthellate corals, for which nutrient supply, current activity, and slow sedimentation rates seem to be the most important controlling parameter (Stetson et al., 1962; Cairns and Stanley, 1981; Mullins et al., 1981; Frederiksen et al., 1992; Freiwald et al., 1999; Mortensen et al., 1995; De Mol et al., in press). Hovland (1990) and Henriet et al. (1998) suggest that some deep-water coral banks in hydrocarbon basins may initially form in areas of seepage. These hypotheses will be tested in the discussion for the mounds of the Porcupine Seabight.

2. State of the art 9

2.1 Deep-water corals 11
2.1.1 Framework builders 11
2.1.2 Coral framework 12
2.1.3 Terminology 14
2.1.4 Biozonation 15
2.1.5 Biodiversity 17
2.1.6 Coral banks in the Porcupine Seabight 18
2.1.7 Environmental requirements 18
2.1.7.1 Ocean boundary conditions 19
2.1.7.2 Are deep-water corals related to seepage? 21

2.2 Gas migration and Seepage 27
2.2.1 Seepage model for the Porcupine Seabight 27
2.2.2 Hydrocarbons 29
2.2.2.1 Origin of gas in shallow sediments 30
2.2.3 Seepage patterns 32
2.2.3.1 Halo and apical anomalies 33
2.2.3.2 Fault related anomalies 33
2.2.4 Seabottom expression of seeps 34
2.2.4.1 Acoustic techniques 34
2.2.4.2 Geochemical observations 38

2.3 Geological setting of Porcupine Seabight 45
2.3.1 Geometry 45
2.3.2 Geology 45
2.3.2.1 Genesis of the basin 47
2.3.2.2 Faults 47
2.3.2.3 Sediment record 47
2.3.2.4 Pre rift sequence 49
2.3.2.5 Porcupine Median High 49
2.3.2.6 Rift sequences 49
2.3.2.7 Seismostratigraphy in the Porcupine Basin 52
2.3.2.8 Pleistocene-Holocene 53
2.3.3 Hydrocarbon potential 56

2.4 Hydrodynamic setting 57
2.4.1 Water masses 57
2.4.2 Currents 58
2.4.2.1 Northward flowing currents 58
2.4.2.2 Near-surface currents 60
2.4.2.3 Near-seabed currents 60
2.4.3 Slope specific process 62
2.4.3.1 Internal waves 62
2.4.3.2 Bottom friction 65
2.4.3.3 Nepheloid layers 66

2.1 Deep-water corals

The principal framework builder in the deep-water coral structures in the NE-Atlantic is the scleractinia (stone coral) *Lophelia pertusa* supported by *Madrepora oculata*, *Desmophyllum dianthus* and *Dendrophyllia cornigera*. However the latter species are never found alone in a coral framework, and they are less abundant (Table 2.1) (Dons, 1944; Frederiksen et al., 1992; Rogers, 1999). All these corals are able to live at great waterdepth under cold and dark water conditions. They lack photosymbionts in their endodermal tissue and zooxanthellae (endosymbiotic microalgea), which leads to their classification under the azooxanthellate corals. Azooxanthellate corals are found in a wide bathymetric range from 0-6200 m depths and at temperatures between 1° to 29°C (Stanley and Cairns, 1988). They have thus a wider distribution than zooxanthellate corals (tropical corals). Seventy five percent of the azooxanthellate coral species are solitary, while the remaining are colonial or pseudocolonial. Pseudocolonial corals produce a skeleton by clonal reproduction, but they have polyps living as individuals, without interconnected neural network (Freiwald, 1998).

2.1.1 Framework builders

Fig. 2.1: Zig-zag budding of *Lophelia pertusa* (photo: E. Van der Meersche).

Only a few of these pseudocolonial azooxanthellate structures are capable to create a rigid framework, among them *Lophelia pertusa*. The morphology of the colonies, in this context used as a practical term for the assemblage for clonal polyps occurring on a common skeleton, can be quite different. Freiwald (1998) studied the branching mode of *Lophelia* through a submersible dive at Sula Ridge (off Norway) and found two types of branching. A first type forms elongated branches with a zig-zag budding. These are rather weak forms of *Lophelia* (Fig. 2.1). The other end member of the morphological type is hemispherical massive aggregations of colonies, which are common on the Sula Ridge.

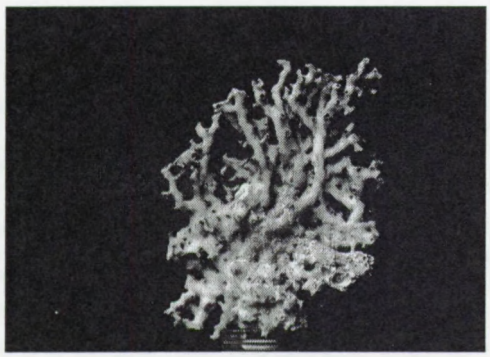

Fig. 2.2: Bushy colonies of *Madrepora*, resulting in fan shape colonies.

They form cauliflower-shaped framework with a circular outline up to 1.5 m height and a diameter of 3 m, as also observed by Wilson (1979) on the Rockall Bank and Mortensen (2000) at other locations in Norway. This branching mode deviates more from the parent growth direction and can be described as dendroid or bushy (Fig. 2.2). Furthermore neighbouring colonies commonly grow together and considerably increase the architectural stability of the framework. Mortensen (2000) suggests that the varieties are genetically or environmentally controlled (Freiwald and Henrich, 1997). Other coral species observed in the coral structures in the NE-Atlantic as *Madrepora* and *Dendrophyllia profunda* predominantly form bushy colonies with outward growing branches through the continuous budding of polyps. This mode of continuous growth results in 30-50 cm high, fan-shaped colonies. The potential for framework building of this fragile growth habit is however limited (Freiwald, 1998; Stetson et al., 1962).

Fig. 2.3: *Eunice norvegicus* play an important role in the strengthening of the coral framework (photo: A. Vanreusel).

Inside the framework construction of *Lophelia,* mucus sheets play an important role to make it more rigid (Freiwald, 1998). This mucus forms sheets along the surface of the skeletons, suppressing the epizoic growth and boosting the skeleton with extra-calcification. This process creates calcification in the form of the selective thickening and the multiplication of fusion-points to adjacent corallites, and even between different coral species (Freiwald, 1998). *Madrepora oculata* also displays this form of thickening and extra calcification. An extra strengthening in the framework is provided by the calcification of the tubes of the polychaete *Eunice norvegicus* (Fig. 2.3). These tubes are primarily made out of parchment, but the mucus sheet of the coral calcifies the tube and integrates the tubes in the framework (Freiwald, 1998). In between the branches and the tubes a significant free space is still available, which creates space for other organisms and/or sediment infill.

2.1.2 Coral framework

The development of a coral framework results from the interaction between growth and decay. The degradation of the structure by borings of predominantly sponges and other endoliths (e.g. foraminiferan) fragilize the coral framework and may even cause a collapse (Freiwald and Wilson, 1998).

Wilson (1979) proposed a hypothesis for the development of coral framework on the Rockall Bank. He suggested that the corals settle down on a favourable place, forming a branching colony. In the next step pieces break off form the original colony and form new settlements for larvae or continued growth as a new colony (Fig. 2.4). Frequently, the initial colony becomes too large to keep confined on the original site or the framework gets weaker by bioerosion. This can result in circular thickets of colonies, surrounded by coral debris, which are called "Wilson rings" (Freiwald, 1998). Such debris rings can be recolonized and form a coppice consisting of concentric rings of colonies. This model is confirmed for the coral coppice formation in the Norwegian waters (Freiwald et al., 1999).

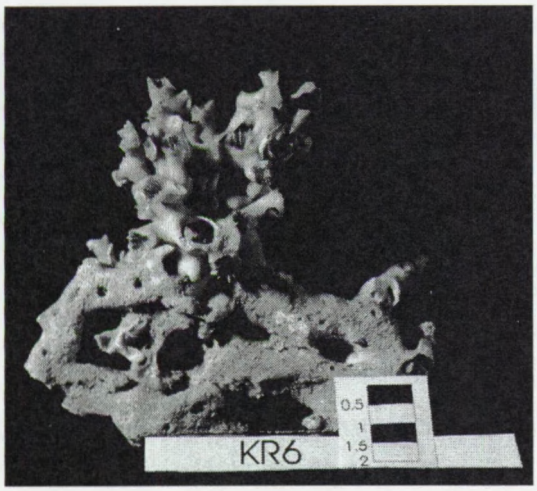

Fig. 2.4: New settlement of *Lophelia* on a bioeroded coral colony.

The coral framework gets later filled with sediments. The origin of the sediment can be diverse. If no external source is involved, the sediments are mostly composed of coral rubble (Scoffin et al., 1980; Wilson, 1979) in addition with calcareous and siliceous biodetritus of associated fauna. During the evolution of the coral structure, the framework will baffle sediment in suspension from an external source, which fortifies the framework.

Freiwald and Wilson (1998) recognized two additional processes that will help the preservation of such structures: sponge-induced stabilization and lithification. Sponges may fill the caves in the framework and will trap sediment, which yields a more rigid and stable construction. In bioclastic material with a high porosity and in high current regimes, interstitial precipitation of fine-grained magnesium calcite can create muddy micrite in mud free sediments. Although the micrite cement is originally deposited as a paste, sustained crystal growth from sequential precipitation results in dense lime muds, as happens in the lithoherms in the Straits of Florida (Wilber and Neumann, 1993). The end member of this process can be compared with bioherms and biodetrical mud mounds, such as the Frasnian reefs in Belgium (Boulvain, 2001).

2.1.3 Terminology

Many terms are proposed to describe coral clusters and mound structures hosting deep-water corals (Table 2.1). In the early years of deep-water coral research, only the names bank or reef were used to describe the mound structures. The last decades, however, a higher diversity of terms is being used. This trend is clearly related to the improvement of research methods and the increased knowledge of the structures. All terms have in common that they describe well-limited elevated structures, partly or completely built of organisms, with a dominance of deep-water corals.

In the Porcupine Seabight different terms are used for -in principle- the same seabed structures. Le Danois (1948) described the coral facies in the eastern margin of the Seabight as "Massif coralline de Dingle". Hovland et al. (1994) called the structures in the central part seabed mounds, carbonate knolls and bioherms. The same structures are called by Henriet et al. (1998) deep-water reefs, bioherms and later carbonate mounds (De Mol, 1998; De Mol et al., 1999; Henriet et al., 2001). On the end, a third term is introduced by De Mol et al. (in press.) who called the structures coral banks. All these different terms denote slightly different perspectives, as summarized below:

- **Mound**: "*a low rounded natural hill, generally of earth; a knoll, or an organic structure built by fossil colonial organism*" (Bates and Jackson, 1980). A **carbonate** mound or **carbonate mud mound** refers to the high carbonate and/or mud content. The carbonate mud mound is a term defined for fossil build-ups.

  Mud mounds are essentially made of muddy carbonate sediments, namely mudstone, wackstone and, to a less extent, packstone. Although they may reach substantial sizes, they are **not framework-supported**. Mud mounds possess a background matrix that may be pure micrite, or a micrite, which incorporates peloid, small bioclasts or larger skeletal fragments (Monty et al., 1995). A subdivion is made in:

  - **microbial** mud mounds: in which the dominant texture, microfabric and composition is considered to have a more or less *in situ* microbial origin and
  - **biodetrial** mud mounds, in which the dominant component is broken and transported skeletal debris.

This terminology is originally used to describe ancient structures without any framework. The general term of mound denotes a carbonate build-up having depositional relief and being composed predominantly of carbonate mud, peloidal mud or micrite. (Monty et al., 1995). This concept excludes partly or completely the involvement of framework builders.

- A **bioherm** is in the definition of Bates and Jackson (1980) "a mound-like, dome-like, reef-like mass of rock, built by sedimentary organisms (such as corals), composed almost exclusively of their calcareous remains, and enclosed or surrounded by rocks of a different lithology. This term has originally been defined in a structural context although it generally implies a calcareous composition". A bioherm refers to a fossil structure with a framework.

- The term **coral bank** is widely used to describe deep-water coral structures (Cairns and Stanley, 1981; De Mol et al., in press; Hovland et al., 1998; Pratje, 1924; Reed, 1992; Squires, 1965; Stetson et al., 1962; Teichert, 1958). It refers to an elevation on the seafloor consisting partly or completely of corals. It can be partly supported by a framework, but this is not a requirement. Teichert (1958) introduced this term to avoid the term reef for his deep-water structures because the term reef implicates also a rigid structure in the wave-base zone.

  The term coral reef is also used for topographically highs on the basis of skeletal framework accretion enhanced by biologically controlled cementation (Freiwald, 1998). The reefs studied in Norway have a framework building capacity which leads to elevated structures on the seafloor, supporting a highly diverse associated fauna with biodiversity indices similar to those found in tropical shallow water reefs (Freiwald, 1998; Mortensen, 2000). Reef is here defined as a discrete carbonate structure formed in-situ, or bound organic compounds that developed a topographic relief on the seafloor.

2.1.4 Biozonation

Different studies of coral structure show a biozonation on these structures. Messing et al. (1990) illustrate a biozonation across lithoherms in the northeastern Straits of Florida. The lithoherms are elongated mound structures oriented parallel to prevailing northerly bottom current. These lithoherms exhibit a consistent faunal zonation characterized by attached, suspension-feeding invertebrates. The four most abundant macro-epibenthic groups (alcynorians, crinoids, sponges

and stylasterid hydrocorals) dominate the structures except at the stoss side and the crest. Three faunal zones have been observed on these mounds, related to the current regime and the available substratum. Mortensen et al. (1995) studied isolated reefs in the Sula Ridge complex and identified three distinct zones: living *Lophelia*, dead *Lophelia* and *Lophelia* rubble. The diversity of taxa increases from the living *Lophelia* zone to the rubble zone. Sponges are more common in the dead *Lophelia* zone, *Gorgonians* in the living *Lophelia* zone and squad lobster in the rubble zone. The diversity and the densities of *Gorgonian* and erect *sponges* are the highest on the stoss side of the reefs. This indicates that the near bottom patterns are important for the faunal distribution on the reefs, besides the substratum.

Freiwald et al. (1997) described in detail the biozoantion of a *Lophelia* reef mound from Stjernsund (West Finnmark, Northern Norway). The reef mound geometry is both laterally and vertically zoned. Vertical zonation is expressed by a living outer rim of pillow shaped satellite coral colonies and by a dead, highly porous core of coral framework. Secondary reef dwellers in the living outer rind are highly adapted sessile species; the dead framework core bears a more diversified epi-fauna. The lateral zonation is expressed by an upcurrent growing stage and a downcurrent dying stage. The dying reef mound section is characterised by a cluster of *in situ* collapsing coral frameworks. The remnants are densely colonised by octocorals and sponges.

This basic zonation of the coral frameworks described by Freiwald et al. (1997) is modified in the description of the biological results for the specific data of the Belgica and Hovland mound provinces.

Four zones refer to the occurrences of deep-water corals:

- **Living coral zone**: in this zone the corals have a red to white colour and are relatively easy to distinguish on the footage. In the lower part dead coral functions as substratum for new settlements of corals and get filled with sediments.

- **Dying coral zone**: this zone is characterized by dead coral constructions. On top a few patches of living coral can colonise the framework. This zone shows a greater diversity than the living corals zone, which almost exclusively consist of deep-water corals. The coral framework gets partly filled with sediment. The faunal assemblage

attached to these degraded and dying frameworks comprises octacoralia and sponges, as far as can be inferred form the video tracks.

- **Proximal coral rubble zone**: is characterized by dead coral framework largely filled with sediments. Sponges colonize this debris zone in the Belgica mound province. The corals show a larger desintegration than the dying coral zone. Nevertheless still some coral colonies can be recognized.

- **Distal coral rubble zone**: in this zone only a few coral branches stick out of the sediment. At some patches the coral framework is still visible in the sediment. The dominant component in this zone is sediment, clogged in the dead coral framework. Small coral fragments are spread on the seabed.

2.1.5 Biodiversity

Preliminary results of the biodiversity of the deep-water coral frameworks in the NE Atlantic suggest species richness similar to tropical reefs (Jensen and Frederiksen, 1992; Mortensen et al., 1995; Rogers, 1999). The diversity of the macrofauna is higher within coral rubble zone of the *Lophelia* reef than in the living zone (Jensen and Frederiksen, 1992; Mortensen et al., 1995). The high species diversity with these reefs is probably best explained by the great habitat diversity in a framework (Mortenson, 2000).

However these studies discuss site-specific results and are based on limited spatial sampling on a global and local scale, which does not allow a good quantification of the biodiversity in the deep-water coral settings. The quantification of the biodiversity is one of the objective in the EU fifth Framework Research Program research project: The Atlantic Coral Ecosystem Study (ACES) which will adopt a whole ecosystem approach to the study of the poorly known but widely distributed European deep-water cold coral province.

2.1.6 Coral banks in the Porcupine Seabight

Coral banks in the Porcupine Seabight occur as morphologically well-delineated, mound-shaped structures. The highest density of living deep-water biological associations is observed at the upper flanks of the mound. From subsurface sediment samples it seems that the cover of dead assemblage of corals is filled with terrigeneous mud, with a similar composition as the surrounding sediments.

This description is comparable with the definition of coral banks in the North Atlantic Ocean, as reported by different authors (Pratje, 1924; Teichert, 1958; Stetson et al., 1962; Cairns and Stanley, 1981; Reed, 1992; Hovland et al., 1998). The coral bank represents an advanced evolutionary step in the formation of deep-water coral structures and shows many similarities to shallow-water coral reefs. In principle, a coral bank is characterized by three distinct units: (1) a cap of living coral colonies which, (2) rests on an open-spaced but dead coral framework and debris zone, and (3) a zone of coral framework and debris that is clogged solidly with sediment. In reality, however, recolonisation by corals takes place on each of these three delineated zones. The greatest density of living coral colonies is observed on the top and upper flanks of the bank (Mortensen et al., 1995).

This term leaves more freedom when more information is available about the inner structure than reef or carbonate mud mound. In this work the term "mound" will be used for a morphological description of the coral banks in the Porcupine Basin.

2.1.7 Environmental requirements

The distribution of *Lophelia pertusa* and other deep-water corals encompasses a variety of geographic locations and bathymetric zones (Table 2.1). Basically, the environmental conditions for deep-water corals to settle down can be reduced to two requirements:

- A first requirement is a suitable substratum. The corals are found on hard substrates like dropstones, outcropping rocks, carbonate crusts, pebbles, worm tubes, shells and coral debris (Table 2.1). A hard substratum is believed to be a primary requirement for settling of *Lophelia*, giving a stable anchorage in a dynamic environment.

- A second requirement is the availability of food. Till recently, little was known about the feeding habits of azooxanthellate. The observations made by Freiwald (1998) of *Lophelia*

pertusa during his submersible dives on Sula Ridge and aquarium experiments of Mortensen (2000) are crucial in understanding the feeding biology of *Lophelia*. Both authors demonstrated that *Lophelia* is preferentially a carnivore. The polyps are able to capture and ingest living zooplankton such as copepods, chaetognaths and crustacea ranging from 1 mm to 2 cm, drifting over the corals. The observation suggests that *Lophelia* has a wide range of invertebrates in its diet, and that it rejects unsuitable food and sediment. The size of food particles that Lophelia is able to capture is probably related to the current velocity. Large food items are probably captured at the highest rate of current velocities. The corals utilise fine-grained organic particles as a food source in addition to zooplankton in low current speed settings. This illustrates that currents are important in obtaining food. The extended tentacles are motionless until a tactile stimulus, that is triggered by the contact between the copepod prey and the tentacle, induces the capture process. Once stimulated, all tentacles try to fix the prey, which is then paralyzed by the nematocyst array. Next, the tentacle crown with the prey is completely retracted into the calyx. The release of the remains of the consumed prey was not observed but the digested remains may become utilised by the polycheate *Eunice norvegicus*, that lives closely associated to the living polyps (Mortensen, 2000).

The corals occur in general in a broad variety of environmental conditions; regionally, they occur in well-defined depth ranges parallel to the shelf break, continental margin or rim of offshore banks and seamounds and in a narrow range of oceanographic parameters (temperature, salinity, current regime) (Table 2.1). This implies that certain environments are more favourable than others. To explain the regional distribution of these structures, two main hypotheses are proposed, which comply with the basic requirements.

The first hypothesis relates the distribution to oceanographic conditions while a second focuses on the distribution to seepage.

2.1.7.1 Ocean boundary conditions

Freiwald (1998) plotted the occurrence of *Lophelia* corals against oceanographic parameters for the NE-Atlantic from Cape St Vincent (Portugal) to the Norwegian Sea. This analysis resulted in an apparent correlation between coral appearance and specific temperature, salinity and oxygen level in the water column. The dominant temperature of *Lophelia* occurrences in the NE-Atlantic

ranges between 6 and 12.5° C. The temperature range gradually decreases from the south (8.5° C to 12.5° C) to the north (6° C to 8° C).

A positive correlation is also found between the coral occurrence and relatively high salinity waters. The source for high salinities is for the southern part of the north Atlantic the Mediterranean Outflow Water, which influences the intermediate waters from Cape St. Vincent till the Porcupine Seabight and the Rockall Trough (see 2.4). The salinity range is quite broad (35-37 $^{0}/_{00}$), but the corals are preferentially located near the core of the high salinity zone. Near the Faeroer Islands and Norway the salinity window is narrower and controlled by different water masses and currents.

A third important factor is the dissolved oxygen content, which is a factor for heterotrophic life in the oceans. Almost all coral structures are found in the oxygen minimum zone, which means that in this particular level no oxygen is added to the system by phytoplankton or by mechanical mixing. Instead, oxygen is consumed through decomposition of sinking organic matter. This might indicate an increased availability of digested food for the corals at these levels. However in the Norwegian waters, the *Lophelia* corals have their largest density about 200m higher than the oxygen minimum zone (Mortensen, 2000). This analysis relates the occurrence of corals to oceanographic conditions, via an increase in food available for the corals.

Frederiksen et al. (1992) related the occurrence of *Lophelia* on the shelf around the Faeroer Islands with seabed slopes critical to internal tidal waves. The breaking of these waves will increase the local current velocity, which might increase the food supply to the corals. They suggested that an increase in current regime induces resuspension of organic matter from the seabed, leading to an increased food supply downslope of the mixing region. A second source of food is the increase in vertical nutrient flux through the thermocline, due to mixing by internal tidal waves. This flux should increase the phytoplankton production, and the flocculent organic particulate matter. The supply of organic particles can be important under certain conditions for the nutrition of the corals.

Mortensen et al. (2001) related the coral distribution in mid-Norway to escarpments and rugged seabed topography. This might increase the local currents, which in their turn may help to concentrate food particles. These two local models brought the concentration of food in relation to enhanced currents, which keeps the bottom free of sedimentation and safeguards the corals from sediment burial.

2.1.7.2 Are deep-water corals related to seepage?

Hovland (1990); Hovland et al. (1994); Hovland et al. (1998) and Hovland and Thomsen (1997) suggest a causal relationship between deep-water coral banks and hydrocarbon seeps. Based on a literature review in the North Atlantic, Hovland (1990) and on their own geological, geochemical, geophysical and biological results off Norway (Hovland, 1990; Hovland et al., 1998; Hovland and Thomsen, 1997), Australia and the Porcupine Basin (Hovland et al., 1994), a number of authors proposed a provocative model for the formation of carbonate reefs (including deep-water coral banks). Whereby they suggest that coral banks are preferentially located at seepage sites, supporting high concentration of microorganisms suspended in the water column. They assume that seepage sites provide the energy basis and carbon source for the buildup of ecosystems, independent of photosynthesis. Higher organisms, most frame- and shell-forming organisms, should utilize this local fertilization and gradually accumulate at the seepage site. Depending on the nature of the seeping compounds (CH_4, CO_2 and/or H_2S), early diagenetic mineral precipitation may also occur, whereby sediment grains and skeletal remains are cemented to produce a firm and solid substratum. In this way, the corals are provided with a hard substrate to settle. The model tries to explain the distribution pattern of deep-water coral banks as a consequence of local fertilization that results from focused hydrocarbon seepage. After the initialisation, the coral bank evolution may remain controlled by the seepage evolution. Episodes of seeping can control stacking of series of banks. A direct corollary of this model is that, if and when the source of the local hydrocarbon seep is cut off, the coral banks will die (Hovland, 1990).

In this thesis, data are gathered in function of both hypotheses and tested for each province in the Porcupine Seabight. For this reason a brief overview will be given on hydrocarbon migration (see 2.2), the general geology and the hydrocarbon potential of the Porcupine Seabight (see 2.3) and the hydrodynamic regime in the basin (see 2.4).

Reference	Locality	Depth (m)	Temperature (°C)	Oceanography	Dimension	Classification	Predominant coral	Substratum
Norwegian coast (Mikkelsen et al., 1982)	Drøbak, Oslofjord	20-40				bush	*Lophelia pertusa*	
West Finnmark (Dons, 1935)	Stjernsund and Oksfjord	250-260	8-6	S=33,3‰	L=10			hard substrate
Norwegian fjord (Strømgren, 1971)	Trondheimfjord	50-250	6-10	S=32-35‰ strong currents	H=30		*Lophelia pertusa*	
Norway (Dons, 1944)	Off Norway57°-70°N	57-300	4-6.5-8.4		H=60	banks, coppice	*Lophelia pertusa* *Madrepora oculata*	
Northern Norway West Finnmark (Freiwald and Henrich, 1997; Henrich et al., 1996)	Stjernsund sill upper western slope 70°N	235-260	5-6	CS=40 cm/s S=34.5 ‰ Estuarine circulation pattern	80° slope till 15° H=10 , 100 across W=60 domed reef	framework thickness 10 m	*Lophelia pertusa*	morainic basement, fjord
North Brattholmen (Burdon-Jones and Tambs-Lyche, 1960)	Near Bergen 60°N24'30" 5°07'E	90-110				patch	*Lophelia pertusa* *Madrepora sp.*	
Norwegian Shelf (Mortensen et al., 1995)	64°N Haltenbanken-Frøyabanken	240-290	250 m 7.5 320 m 6.3	S= 35.1-35.2 ‰ CS= 4-5 cm/s at 300 m	H=2-31 1500-50600 m^2	bioherm	*Lophelia pertusa* Associated fauna is not typical for only this habitat (Jensen & Frederikson 1992; Burdon-Jone and Tambs-Lyches 1960)	soft bottom, mixed (>10% stones), dead, living *Lophelia* and *Lophelia* rubble
Sula Ridge (Freiwald et al., 1999)	64°N	270-310	7.8	NAC S=35.05 ‰	L=13000 H=20-35 W=300	coral reef	*Lophelia pertusa*	sill, iceberg plough marks
Sula Ridge (Henrich et al., 1996)	64°N between Frøyabank and Haltenbank NE plunging	280-310			chain of coalesced coral mounds of L=4000 H=20-45	reef	*Lophelia pertusa* and less common *Madrepora sp.*	sill
Mid Norway (Hovland and Thomsen, 1997)	64°N 01' 7°58'E	100-350			H=Up 30 , W=150 L=400 NNW-SSE 50-40°slope	bank	*Lophelia pertusa*	clay ridge
Mid Norway coral banks (Hovland et al., 1998; Mortensen, 2000)	Continental shelf off Mid Norway 63°55'N, 7°53'E 62°30'-65°30'N	220-310		Up and down current, Norwegian Atlantic current	H= 31 57, 5-35m individual banks in local clusters of up to 9 bank/ km^2	coral bank or bioherm or coral reef	*Lophelia pertusa*	subcropping bedrock, light hydrocarbon micro seepage of thermogenic HC

Mid Norway coral banks (Hovland et al., 1998; Mortensen, 2000)	Continental shelf off Mid Norway 63°55'N, 7°53'E 62°30'-65°30'N	220-310		Up and down current, Norwegian Atlantic current	H= 31 57, 5-35m individual banks in local clusters of up to 9 bank/ km^2	coral bank or bioherm or coral reef	*Lophelia pertusa*	subcropping bedrock, light hydrocarbon micro seepage of thermogenic HC
European margin (Le Danois, 1948)	Off Ireland to Bay of Biscay 54°-44°N	180-200	9-12			thickets, massive	*Lophelia pertusa* *Madrepora oculata*	
Bay of Biscay (Wilson, 1979a)	Biscay	250-1000			10-50 across	Lophelia colonies	*Lophelia pertusa* *Madrepora oculata* *Desmophyllum cristagalli*	
European margin (Le Danois, 1948)	Bay of Biscay to Cape Verde 44°-15°N	600-1500	Up to 11				*Lophelia pertusa* *Madrepora oculata*	
European margin (Le Danois, 1948)	Ireland to Northeast Africa	200-450	Up to 13				*Desmophyllum cristagalli*	
Faeroer Shelf (Frederiksen et al., 1992; Jensen and Frederiksen, 1992)	61°43'4"N, 5°43'4"W 60°33'3'N' 6°32'1"W	252-260	6-8	Tidal currents CS=50 to 47 cm/s 35cn/s	H=10 W=110	bank	*Lophelia pertusa*	
Around the Faeroer Isands Faeroer shelf (Frederiksen et al., 1992)	Shelf and upper slope`	220-300		Shelf break and upper slope internal tidal waves		bank	Living and dead *Lophelia pertusa*	
Faeroes (Frederiksen et al., 1992)	Faroe Bank	110-slope 210-446	6-8.6				*Stylasteridae* *Lophelia pertusa*	
Faeroes (Frederiksen et al., 1992)	Bill Baily Bank slope and Lousy Bank	500-1000 730					Living *Lophelia pertusa* *Madrepora oculata*	
Rockall Bank (Wilson, 1979c)		130-400			H=1-1.5 10-50 m across		*Lophelia pertusa*	
Rockall Trough (Kenyon et al., 1998)	Both margins,53°45'-54°15'N and 14°15'-13°45'W 55°20'-55°45' N and 16°-15°W	500-1000		Strong bottom currents	H=up to 350, L= up to 2000 sub circular NE-SW ridge	Carbonate mud mounds	*Lophelia pertusa* *Madrepora oculata*	Upper slope, volcanic? Erosive surface
Porcupine Basin (Le Danois 1948)			8-12°		H=61	Massif Bank	*Lophelia pertusa* *Madrepora* *Caryophyllia* *Desmophyllum* *Dendrophylia* *Solenosmilia*	

Porcupine Bank (Scoffin and Bowes, 1988)		100-200 250-500			5.5 m across, H=1 m	coral patches	*Lophelia pertusa* *Stylaster sp.*	Coarse lithic fragments near the margin of the bank. Tens to hundred meters apart 250-500
Porcupine Basin This paper, (Henriet et al., 1998)	Belgica mounds 51°10'N - 51°35'N and 11°45'W-11°30'W	600-900	9.5-8.5	Strong bottom currents MOW seepage?	H=70-190 L=4 km W=1 km	coral banks, carbonate mounds	*Madrepora oculata* *Lophelia pertusa*	
Porcupine Basin This paper, (Hovland et al., 1994)	Hovland mound 52°30'-52°N and 12-13°W	725-900	9-8.5	Strong currents MOW? seepage?	H=100 m L=5.m composite W=1 km Across=1 km total thickness 250 m	coral bank, carbonate knolls, pseudobioherm	*Madrepora oculata* *Lophelia pertusa* *Desmophylieum*	
Porcupine Seabight (Tudhope and Scoffin, 1995)	Gollum Channel 11°10W 50°40'N	725-920			25m across	patches	*Lophelia pertusa*	
British waters (Wilson, 1979b)	Scottish and Inner Hebrides	190-300			H=Up 18m		*Lophelia pertusa*	
Gulf of Mexico (Moore and Bullin, 1960)	Mississippi Delta (27N)	450-550	10.4		H=55m small hillock	banks	*Lophelia pertusa*	
Gulf of Mexico (Moore and Bullis, 1960 in Stetson et al., 1962)		512	10.4		320 m diameter H =55m	hillock	*Lophelia pertusa* *Caryophyllia sp.*	
Gulf of Mexico (Ludwick and Walton, 1957 in Stetsonet al. 1962)		100-180	18	S=32-37‰	400 m across H=9m	pinnacle		
Off Central Eastern Florida (Reed, 1992)	Off Florida 27.5-28.5	70-100	7.5-15-26.5		about 25 m	banks and thickets	*Oculina varicosa*	
Straits of Florida (Neumann et al., 1977)	Off little Bahama Bank (28.5°N)	500-700	5.5-10			lithoherm	*Enallospammia profunda*	
Straits of Florida (Neumann & Ball, 1970)	Off Miami 26°N	825				thickets	*Enallospammia profunda* *Lophelia pertusa*	
Lithoherms in Blake – Bahama (Neumann and Paull, 1998)	Florida-Hatteras slope and extending 440 m-800 m on the inner blake plateau.	400-800		CS= 100 cm/sec	lithoherm complex: W=400 m, 4.4 km long and H=150 m-50 m 30-60°	lithoherm	*Lophelia pertusa*	

Lithoherms in Blake – Bahama (Neumann and Paull, 1998)	Florida-Hatteras slope and extending 440 m-800 m on the inner blake plateau.	400-800		CS= 100 cm/sec	lithoherm complex: W=400 m, 4.4 km long and H=150 m-50 m 30-60°	lithoherm	*Lophelia pertusa*	
Lithoherms Northeastern Straits of Florida (Messing et al., 1990)	western margin of Little Bahama Bank	500-700	10-12	Northerly bottom CS=10-20 cm/sec crest 100 cm/sec	Elongated L=300 m H=50 60° slopes till scarps	lithoherm	*Gerardia sp.* *Lophelia pertusa*	hardground of authigenic carbonate
Little Bahama Bank (Mullins et al., 1981)	North of Little Bahama bank 27.5°N	1000-1300	4-6		H=5-40	banks	*Solenosmilia variabilis*	
North of Little Bahama Bank (Mullins et al., 1981)	Patchy distribution in 2500 km^2	1000-1300	4-6	Antilles Current flows SE-NW Florida current to form the Gulf stream, CS=50 cm/sec. S= 34.5-35.5 $^0/_{00}$	H= 5-40	Colony, thicket to coppice to bank	*Bathypsammia* *Caryophyllias* *Deltocyathus* *Desmophyllum* *Enallopsammia* *Javania* *Madrepora Polymyces* *Solenosmilia* *Stepahnocyathus* absent *Lophelia* and *Dendrophyllum*	
Little Bahama Bank (Paull et al., 2000)	Hatteras Slope	440			H=150 L=4400 W=400	lithoherm	*Lophelia pertusa*	
Blake Plateau (Stetson et al., 1962)	Blake Plateau (30°-34°N)	670-840	6-10		L=146	coral bank	*Enallospammia (Dendrophyllia) profunda* *Lophelia pertusa*	
Coral banks on the Blake Plateau (Stetson et al., 1962)	265 km southeast of Charleston, South Carolina3108-3885 km^2 31°45'N- 32°10'N/ 77°45'W and 77°20'W	510-870	7-10	S=35 $^0/_{00}$	200 features H=10- 150 L=1200 800 across	coral banks	*Lopheli pertusa* *Dendrophyllia Lophelia pertusa* is dominant on the top of the bank, *Dendrophyllia* in general	North south trend on the crest of an escarpment smaller banks surrounding the escarpment. Substratum carbonate rock

Table 2.1: Deep-water coral occurrences in the North Atlantic.

Legend:
S= salinity in $^0/_{00}$
CS = current speed cm/s
L= length in m
H= height in m
W= Width in m

2.2 Gas migration and Seepage

2.2.1 Seepage model for the Porcupine Seabight

Hovland's general seepage model for coral reefs (1990) has a variant for the coral banks in the Porcupine Seabight. Hovland et al. (1994) published the first descriptions of the coral banks in the Porcupine Seabight. Based on seismic profiles they mapped 31 separate "knolls" which correspond with the mound cluster since then commonly referred to as "Hovland mound province". Most of the "knolls" have associated circular moats and the mounds are framing two major bathymetric lows. The moats range 60-90m in depth. The authors suggested that these moats could be produced by bottom current erosion or by the escape of pore water and gases. They identified deep faults below some of the structures, which might have acted as migration paths for deeper hydrocarbons (Fig. 2.5). Furthermore, they found apparent polarity reversal and locally strong reflectors. These features could be related either to the presence of local gas accumulations, or to acoustic artefacts caused by multiple reflections.

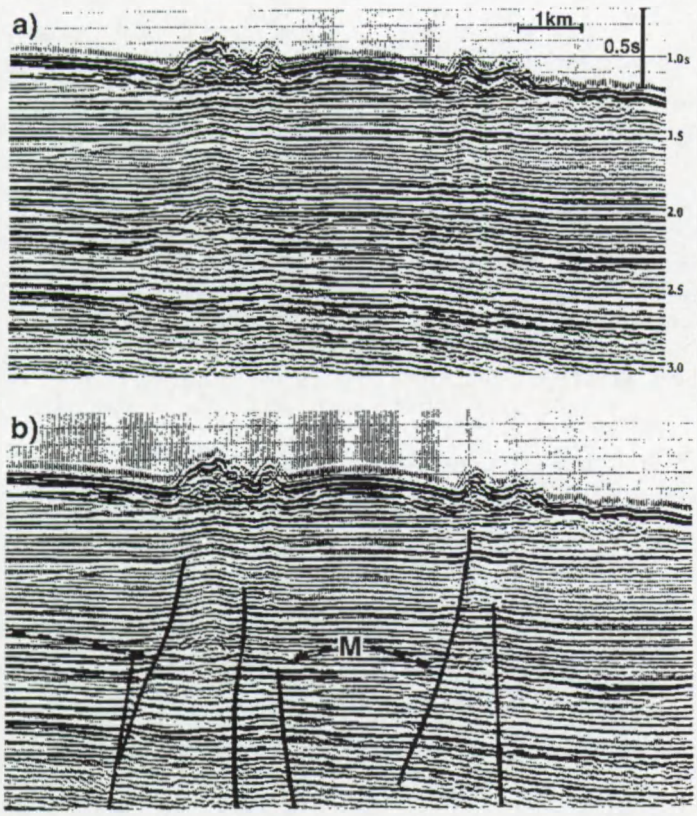

Fig. 2.5: a) seismic profiles of the Hovland mounds b) interpretation of the line showing inferred fault planes and suspected migration routes of hydrocarbons, feeding the mounds (Hovland et al., 1994).

The geochemical results of interstitial and absorbed gas (C_1-C_3) concentrations for the on-mound samples are very variable with the lowest and highest values comparable to those in the inter-mound and off-mound areas (Table 2.2).

The authors interpreted these results in terms of both active methane seepage and active methane consumption by biological activity. Results of stable carbon isotope analysis of absorbed methane $\delta^{13}C_1$ varied from -37 $^0/_{00}$ in off-mound to -35 $^0/_{00}$ PDB in on-mound areas (Table 2.2). The latter have been interpreted by the authors as an overmature thermal methane type without any contribution of biogenic components.

	Off-mound (n=20)		Inter-mound (n=20)		On-mound (n=37)	
	Range	Mean	Range	Mean	Range	Mean
Interstitial methane (ppm v/v)	4.7-8.9	6.8	7.0-15.9	9.8	2.1-21.9	7.0
Interstitial ethane (ppm v/v)	0-0.2	0.1	0.1-0.3	0.1	0.1-0.3	0.2
Interstitial propane (ppm v/v)	0.05-0.14	0.08	0.08-0.23	0.11	0.05-0.27	0.1
Absorbed methane (ppbw)	98-965	625	442-977	655	49-922	437
Absorbed ethane (ppbw)	61-114	87	61-100	79	32-109	65
Absorbed propane (ppbw)	31.6-56.2	43.5	31.8-47.8	39.5	18.8-55.2	34.9
Mean $\delta 1^3C_1$ ($^0/_{00}$)	(n=3) –37.2		(n=5) -37.1		(n=4) 35.	

Table 2.2: Interstitial and absorbed gas concentrations from shallow core samples in Porcupine Basin. The results compare on-mound and off-mound measurements without a significant difference (Hovland et al., 1994).

Based on these results, Hovland et al. (1994) made a conceptual model (Fig. 2.6) in which the first condition for formation of the coral banks is the generation of hydrocarbons at depth (Fig. 2.6 A). A second step is that some of hydrocarbons find their way to the surface in a focused manner, through faults and fissures (Fig. 2.6 B). The seabed is there locally eroded by seepage and the local seawater is provided with nourishment on which bacteria and microorganisms depend ("cloud" in water column). As time passes by, organisms and their skeletal remains accumulate, whereas authigenic carbonates precipitate locally, cementing the sediments and skeletal debris (Fig. 2.6.C). This results in the formation of the coral banks in the Hovland mound province.

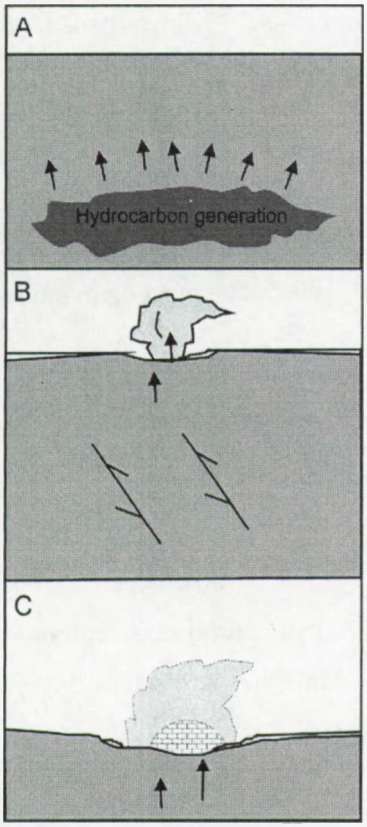

Fig. 2.6: Model for mound formation in the Hovland mound province. See text for explanation (Hovland et al., 1994).

A second model relates the formation of the coral banks in the Magellan mound province to the decay of gashydrate layers (Henriet, 1998; Henriet, 2002). In principle, the model is similar to the proposed model of Hovland et al. (1994) with the exception that the hydrocarbons are stored close to the seabed in a gashydrate layer. This accumulation of gases got released during the decay of the gashydrate layer in periods with warm water bottom currents.

In order to evaluate this hypothesis in the Hovland-Magellan mound province, it is useful to get a better understanding of migration and origin of hydrocarbon gases and detection techniques near the seabed surface to come to a discussion of own data, confronted with published and non-published data of the area. Besides this overview, a summary of the geology of the Porcupine Basin is given in 2.3.

2.2.2 Hydrocarbons

The occurrence of methane gas in seabed sediments is not rare, especially not in continental margins. A primary requirement for the existence of such gas is the availability of sufficient organic matter in the seafloor and either anoxic conditions for biogenic gas or high temperatures for thermogenic gas. Obviously, an appropriate time is needed for the generation of sufficient gas molecules for the accumulation of free gas. Furthermore, a sufficient permeability of the sediment is required for the gas to collect as bubbles. Vertical faults and tilted permeable sedimentary layers are two common examples of possible migration pathways from deeper source rocks to shallower depths. Upward migrating gas can eventually escape form the seafloor unless a less permeable layer blocks upward migration.

At shallow depths below the sediment-water interface, the concentration of hydrocarbons generally increases downwards (Abrams, 1996a). This general increase is subject to considerable

variation and local reversals. This is due to the migration of thermogenic hydrocarbons to the near surface and production of biogenic hydrocarbons in that subsurface zone.

2.2.2.1 Origin of gas in shallow sediments

The gases found in shallow marine sediments include carbon dioxide, hydrogen sulphide, ethane and methane (Claypool and Kaplan, 1974; Floodgate and Judd, 1992). The most common shallow hydrocarbon gas is methane. Methane gas can either be biogenic or thermogenic in origin.

Biogenic gas is created by bacterial activity mainly within the top few meters of sediment. The generation of methane and higher homologues within the sulphate-reducing zone by anaerobic respiration can mask hydrocarbons migrated from the deep horizons. *In situ* generated, non-migrated hydrocarbons can often be mistaken for migrated hydrocarbons. Moreover, interpretation of migrated hydrocarbon gas should refer only to hydrocarbon concentrations that are significantly above background levels (Abrams, 1996a). For this reason it seems important to discuss the origin of methane in the subsurface sediments (Fig. 2.7).

Organic matter in sediments

Any organism that dies can become the focus for bacterial reworking in the sediment. The basis of all living organisms at the surface of the Earth is photosynthesis, which uses solar energy to fix carbon from atmospheric carbon dioxide. All primary productivity is therefore from photosynthetic origin: algae, higher land plants, and some specialized photosynthetic bacteria such as the so-called "blue-green algae" and the purple bacteria (Clayton, 1994; Floodgate and Judd, 1992). These are the main contributors to sedimentary organic matter. Secondary production consists of organisms, which feed on the primary producers. Copepods are the most important group and contribute a little to the sediments although not very much. Finally, much of the organic matter in sediments consists of bacteria themselves, oxidizing primary organic matter and converting some of this to bacterial biomass.

Biogenic methane generation:

Biogenic (bacterial) gas is formed in organic-rich environments by a specialized group of bacteria, the methanogens. These bacteria require anoxic-, nitrate, Fe (III), Mn (IV) and sulphate-free conditions at temperatures below 75 ° C (Ehrlich, 1996). Two distinct metabolic processes

contribute to methane generation; **fermentation** and **CO_2-reduction** using hydrogen. In the first mechanism, simple organic substrates such as acetate are fermented to CH_4 and CO_2

$$CH_3COOH \text{ -= } CH_4 + CO_2$$

In the second mechanism, CO_2 from other bacterial reactions is reduced by hydrogen from the environment

$$CO_2 + 4H_2 = CH_4 + 2\ H_2O$$

The latter reaction tends to be the dominant pathway in marine environments. These reactions are discussed in more detail in (Ehrlich, 1996).

Thermogenic gas

Thermogenic gas is produced from organic compounds at high temperature and pressure, and consequently normally at depths greater than 1000m. This gas and other petroleum compounds may migrate towards the surface to be trapped as shallow gas accumulations (Floodgate and Judd, 1992). Organic matter buried within the sediment is diagenically transformed into fluid by-products of bacterial decay and is expelled along with water. With time, and as the depth of burial and consequently the temperature and pressure increase, the potential for hydrocarbon generation increases, which leads to a mature, organic-rich source rock.

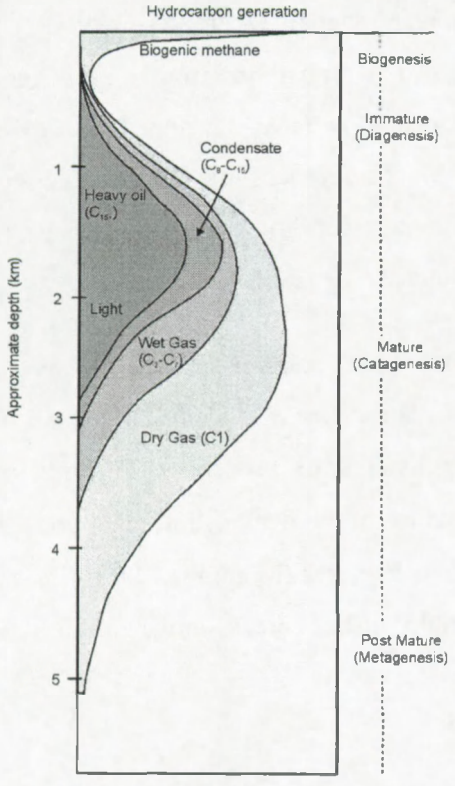

Fig 2.7: Generation of hydrocarbons with depth (Floodgate, 1992).

The type of hydrocarbon generated depends upon the nature of the original organic matter. Kerogen is the organic material in sedimentary rocks, which is insoluble in normal organic solvents. Kerogen is a highly complex, high molecular weight "geopolymer" (Clayton, 1994; Floodgate and Judd, 1992). Given time and appropriate temperature conditions, most kerogen components break down to produce hydrocarbons.

Thermogenic hydrocarbons can be classified into four categories (Floodgate and Judd, 1992):

I. **Oil** (C_{15+}): crude oil includes a wide range (>260) of hydrocarbon compounds, which are in liquid form at surface temperature and pressure.

II. **Condensate** (C_8-C_{15}): hydrocarbons in gaseous form under temperature and pressure conditions found at depth within the sediments, but which condense as a liquid at surface temperature and pressure.

III. **Associated "wet" gas** (C_2-C_7): wet gases are produced in association with methane, and may also be associated with condensates or oil. The wet gases, ethane (C_2), propane (C_3) etc. normally represent more than 5% of the total hydrocarbon gas produced from a source.

IV. **Non-associated "dry" gas**: methane (C_1).

2.2.3 Seepage patterns

Hydrocarbon seeps in marine sediments can be classified in two types: **active** and **passive**.

- **Active seeps** occur where gas bubbles, pockmarks, or bright spots are visible on seismic profiles and where chemosynthetic communities are present in conjunction with large concentrations of migrated hydrocarbons (**macro seeps**) (Abrams, 1996a). These generally occur where generation and migration of hydrocarbons from source rocks are ongoing today or where significant migration pathways have developed due to recent tectonic activity. Link (1952) studied worldwide occurrences of **macro seepage** and deducted that they occur dominantly along high-permeability pathways such as faults, fractures, unconformities, and pore networks in outcropping reservoirs.

- **Passive** seeps occur where concentrations of migrated hydrocarbons are usually low (**micro seeps**) with few or no geophysical anomalies. These occur typically in areas where generation and expulsion is relict or where regional seals prevent significant vertical migration (Abrams, 1996a). **Micro seeps** studies often demonstrate the preferential pathway concept, in particular the role of faults and fractures (Mattews, 1996). It is shown that gas micro seepage along faults occur in spatially distinct areas similar to those shown for gas macro seepage.

Seeps vary in shape, size, and form (Hovland and Judd, 1988). They cause anomalous (significantly higher than background) hydrocarbon concentration patterns to alow petroleum accumulations. These patterns align into halo (doughnut), apical (focal), crescent, or linear (straight-line) shapes. The hydrocarbon concentration pattern may be related to structural features such as seafloor highs, subsurface highs, diapirs, faults, unconformities, and spill points (which may result from structural failure of trapping components).

2.2.3.1 Halo and apical anomalies

Several authors (Abrams, 1996a) observed halo micro seepage patterns and noted that, in selected cases, hydrocarbon anomalies do not appear directly above the subsurface accumulations. This suggests that fluid flow within the near-surface region may affect hydrocarbon movement and should be taken into consideration when interpreting surface geochemical data. This is in contrast to macro seeps, which are usually associated with faults or fractures.

2.2.3.2 Fault related anomalies

In several places in the world were seepage occurs, a direct link is observed between faults and hydrocarbon concentrations in the surface sediments (Abrams, 1996a). In some cases, no geophysical or geochemical anomalies were found in the water column or at the ocean surface. Local shallow (less than 30m) stratigraphical and lithological variations can strongly control the distribution and type of hydrocarbons at such sites. This can be explained by localized subsurface barriers that appear to prevent movement into sediments. Low molecular weight hydrocarbons (C_1 to C_{5+}) and carbon dioxide move up the major fault system into near-surface sediments where local barriers prevent movement into the very near-surface sediments. Hydrocarbon and carbon dioxide anomalies can be found only where the localized barriers are not present or breached. Similar observations have been made in surface geochemical and high-resolution seismic surveys, especially in areas where hydrates are present (Abrams, 1996a). Clayton (1994) comments that although gas may appear to leak from distinct fractures within subsurface sediments, it is actually more dispersed within the shallow sediments.

Some physical barriers, faults, and fractures may prevent a detectable migration hydrocarbons into surface sediment. Faults and fractures can act as migration conduits, but do not always reach the water-sediment interface.

2.2.4 Seabottom expression of seeps

Till now shallow cores and shallow high-resolution seismic are available to evaluate the migration potential and history of the study area together with published results concerning the hydrocarbon potential of the Porcupine Basin. The lack of data from the deeper part, as the base of the coral banks, forces us to use subsurface indicators for gas migration. In this part the applied techniques used in this study will be discussed for recognition of seepage in the study area.

2.2.4.1 Acoustic techniques

With acoustic techniques it is possible to get direct or indirect information of fluid migration. Differences in acoustic impedance can cause changes in amplitude, which might be indicative for fluids in the sediment column (Judd and Hovland, 1992).

Gas characterization on seismic profiles

When free gas is present in seafloor sediments, several modifications of seafloor geoacoustic properties are commonly observed such as compressional wave velocity is reduced below the value for water saturated sediments, attenuation of acoustic waves propagating through the gassy sediment is increased, and acoustic reflection and/or scattering from the gassy sediment is increased. All of these geoacoustic characteristics (sound speed, attenuation, reflectivity and scattering strength) exhibit frequency dependent variations. In gassy sediments, there is a higher attenuation of high frequencies versus low frequencies (Wilkins and Richardson, 1998). Attenuation in gassy sediments includes scattering from bubbles, frame frictional absorption and internal absorption due to bubblewall motion (damping losses) (Anderson and Hampton, 1980). The reduction of sound speed in gassy sediments is similar to the reduced sound speed for propagation through a cloud of gas bubbles in water. For low frequency sound waves, the composite compressibility of the gas bubble/water mixture is essentially controlled by the compressibility of the gas alone. This low bulk compressibility results in the low propagation speed of the sound wave in the mixture. The maximum absorption is near the bubble resonance frequency (Anderson and Bryant, 1990). Several acoustic features indicate the possible appearance of gas or fluid and its migration. Those features are listed below.

Bubble trains in the water column, revealed by echo sounders and side scan sonar indicate that in many cases the transport of gases is an active process. Side scan sonar shows that these gas

plumes in the water column often originate from pockmarks or mounds on the seafloor, arranged along what often appears to be their surface trace of faults.

On the seismic profiles, acoustic **turbidity** or acoustic blanking appears on shallow reflection seismic profiles as zones where all seismic reflections from deeper layers are wiped out. This effect is caused by the absorption of the major part of the acoustic energy by fluids and gas in the sediments (Hovland and Judd, 1988). But also coarse grain beds, shell beds and peat have been identified as causing acoustic turbidity. Gravel scatters the acoustic energy whereas shell and peat either scatter it or absorbe it as they do with the trapped gas. Anyhow, most commonly acoustic turbidity is caused by the absorption of acoustic energy by interstitial gases. Pull down of reflections is often seen at the edge of such zones. This is an indication of the decrease in seismic velocity, which is caused by increased gas content, but not to the point at which acoustic turbidity will occur. This effect may occur when there is as little as 1% of gas present (Fannin, 1980).

Bright spots are high-amplitude negative phase reflections mainly seen on sparker and air gun records. They appear as discontinuous dark layers. Gas accumulations, which cause bright spots, are normally at depths of more than 100m and may be at relatively high pressure (Hovland and Judd, 1988).

Enhanced reflections are discontinuous high amplitude events. Although absolute correlations between individual reflections and lithological horizons are normally not possible, it is probable that these enhanced reflections represent increases in gas content in relatively porous horizons within a dominantly impermeable muddy sediment sequence.

Another type of seismic feature of possible gas occurrences are restricted columnar patches in which no reflections apparently occur. Most commonly they are found directly beneath the seafloor or buried pockmarks. They interrupt reflections as if they had been erosive; however, there is no indication that they have been infilled. The preferred explanation is that they are zones in which individual mineral particles have been rearranged disturbing the acoustic layering. It is supposed that fluids, migrating vertically through the sediments may have been responsible. Hovland and Judd (1988) called this seismic anomaly **columnar disturbance.**

Beneath some pockmarks updoming individual reflectors are sometimes observed. Hovland and Judd (1988) interpreted this as an acoustic effect of vertical gas migration. They occur often in association with columnar disturbances. Most commonly reflections are unaffected by the

occurrence of a pockmark above them, so that the seismic velocities must be closely matched. This excludes the hypothesis that **intra-sedimentary doming** is a velocity effect.

Pockmarks

Pockmarks are shallow seabed depressions formed by the expulsion of fluids (gas and/or water) generally in soft, fine-grained sediments (Hovland and Judd, 1988). They were first described off Nova Scotia by King and MacLean (1970). In muddy sediment environments, pockmarks have often been pointed out as the most prominent visible signature of gas seepage (Hovland and Judd, 1988). For this reason it is important to pay more attention to this phenomena.

Pockmarks can be recognized on seismic profiles by their **erosional nature**. The internal reflectors of the uppermost sediments are truncated by the V-shaped incisions of the pockmarks. The shape of the pockmarks cannot be described as a simple inverted cone. The disadvantage of 2D profiles is that they can cross the feature in a random way. Pockmark sides are rarely smooth, but commonly show several breaks in slope or changes in the angle of the slope. Frequently, pockmarks are frequently asymmetric, with one side considerably steeper than the other (Hovland and Judd, 1988).

The **density** and size of pockmarks is depending of the surface sediments. The highest density occurs in areas with relatively coarse sediments. The pockmarks size in these sediments is rather small and rarely exceeds 50m. Lower densities occur in muddy sediments but the **size** of the pockmarks is much larger (100-150m) (Hovland and Judd, 1988). In the Norwegian trench the density varies from 0 to about 60 per km^2 (Hovland, 1982).

The distribution of pockmarks is in general neither uniform nor random; it is therefore likely to conclude that their distribution is influenced by some other factor. Three parameters have been identified which characterize the pockmark distribution; namely: the number of individual pockmarks, the size of individual pockmarks and the proportion of the seabed actually occupied by pockmarks (Hovland and Judd, 1988). In general, pockmarks range between 50 and 100m in diameter and depths are in the range of 2-3m. The deepest pockmark recorded in the Norwegian Trench is 5.8m deep with an inner slope of 12? (Hovland, 1982).

Pockmarks display a considerable variety in shape and size, both between areas and within an individual area. Hovland and Judd (1988) published a catalogue of different pockmarks and their properties:

- **Unit pockmarks** are very small (<5m in diameter) seabed depressions, which are found in groups as isolated units and in association with larger pockmarks.

- **Fresh pockmarks** are unusually large features, which are surrounded by unit pockmarks.

- **Asymmetric** pockmarks are pockmarks with on one side a gentler slope; the minimum difference of at least 1.5° qualifies a pockmark as asymmetric. The ratio between the angles of the two slopes in asymmetric pockmarks has an average of 1/2.4.

- **Standard circular and elliptical pockmarks** are perhaps the most common. Length-to-width ratios vary considerably form 1 to 1.25 or more. At some locations a relation between the dominant tidal current and the longest axes of the pockmarks has been observed.

- **Composite pockmarks** occur where individual standard pockmarks merge. This can result in a single feature with a complex shape.

- **Pockmark strings.** In the Norwegian Trench, chains or strings of individual pockmarks with a diameter of 10-15m have been observed. The strings often have an extension of several hundreds of meters. These strings are mostly oriented in the direction of the dominant currents and may form a single feature by the growth and merger of the pockmarks in time.

- **Elongated pockmarks and troughs**: some pockmarks tend to be elongated to the extent that they resemble gullies or troughs rather than standard pockmarks. Inside these troughs, the topmost sediment layers are absent and older sediments are exposed at the seabed. A single trough of more than 1 km in length and about 200m width has been located in the Norwegian Trench near the foot of the Western Slope. It is composed of a series of large interlinked pockmarks aligned approximately north-south. This feature is related to a furrow, which might have its origin in an iceberg ploughmark (Hovland and Judd, 1988).

The formation of pockmarks is closely related to fluid migration and escape. Hovland and Judd (1988) developed a model to explain the formation of pockmarks in petroleum basins based on data mainly gathered in the North Sea and literature examples from all over the world. In the original pockmark paper, King and MacLean (1970) suggest that the main agent responsible for the formation of pockmarks is either ascending gas or water. Hovland and Judd (1988) found evidence of a close relation with gas expulsion in petroleum basins.

However, pockmarks have been* observed in areas without gas in the seabed sediments. Furthermore gas-rich areas without pockmarks on the seabed also exist. In the Eckenförde Bay, Baltic Sea, several pockmarks occur in locations of freshwater discharge aquifers (Albert et al., 1998; Whiticar and Werner, 1981) and others at vent sites of biogenic methane (Albert et al., 1998). This illustrates that pockmarks are not only formed by the migration of thermogenic gas. In general, pockmarks are most common in soft, muddy sediments. Within those areas that are pockmarked, acoustic turbidity is sometimes present but it is not common. Any acoustic turbidity beneath a pockmark may represent a potential future activity of gas expulsion, but it cannot have been responsible for past activity (Hovland and Judd, 1988). Where acoustic turbidity is not present, there is at least circumstantial evidence arguing for the previous passage of gas or fluids through the sediments. This may take the form of features such as the zone of columnar disturbances (Hovland, 1992).

2.2.4.2 *Geochemical observations*

Surface geochemical observations can be made close to the end of the subsurface migration path. They offer the advantage of a virtually complete spatial availability of sampling locations, but they are subject to certain boundary conditions that must be considered in interpretation of data.

The type of seepage controls the distribution of migrated hydrocarbons in the near-surface sediments and should dictate the sampling equipment and approach used to detect seeps. Active seeps are usually detected near the water-sediment interface, in the water column or at the sea surface, and at relatively large distances (few tens of meters) from major leak points. Most conventional sediment samplers can capture active seeps (Abrams, 1996a).

Passive seeps can only be detected relatively far below the water-sediment interface and requires samples collected near potential leak points. Sampling equipment must penetrate the zone of maximum disturbance or any shallow migration barriers in fine-grained sediment. Gravity cores are the best sampling devices. Precise location of samples using seismic profiles to locate leak points is critical to detect passive hydrocarbons seep (Abrams, 1996a).

In the near surface, many processes act to modify the seepage, particularly biogenic activity and diffusion (both chemical and mechanical). Bacteria in sediments above hydrocarbon accumulations play a profound role in the oxidation of migrating hydrocarbons. Their activities are directly or indirectly responsible for the varied and often confusing surface manifestation of hydrocarbon seepage (Abrams, 1996b; Clayton, 1994). In addition to the many varieties of

aerobic bacteria that oxidize hydrocarbons, important anaerobes also exist (e.g. sulphate-reducing bacteria and denitrifying bacteria). The most obvious result of hydrocarbon oxidation is a decrease in the concentration of free gas hydrocarbons (interstitial), hydrocarbons dissolved in pore fluids, occluded hydrocarbons, and absorbed hydrocarbons.

Long-term leakage of hydrocarbons, either as macro-seepage or micro-seepage, can set up near-surface oxidation-reduction zones that favour the development of a diverse array of chemical and mineralogical changes. The bacterial oxidation of light hydrocarbons can directly or indirectly cause significant changes in the pH and Eh of the surrounding environment, thereby also changing the stability fields of the different mineral species present in that environment. These changes result in the precipitation or solution and remobilization of various mineral species and elements, so that the rock column above a leaking petroleum accumulation becomes significant. This can be detected and measurably different from laterally equivalent rocks (Abrams, 1996a; Oehler and Sternberg, 1984). In this setting, bacteria can produce new mineral phases either through passive growth or as a result of metabolic activity (Clayton, 1994).

Alteration of hydrocarbons

Two processes mainly control the microbial alteration of migrating hydrocarbon in the near surface: fermentation and respiration.

Fermentation

Fermentation is a simple dissociation reaction yielding energy of a complex organic molecule into two simpler molecules. This process only occurs in the absence of oxygen. Methanogenesis is the most important dissociation process of acetate into methane and CO_2.

$$CH_3COOH = CH_4 + CO_2$$

Respiration

In contrast to fermentation, respiration is an energy yielding process in which the organic, or in some cases the inorganic, substrate is oxidized by means of an external oxidizing agent. The external agent is usually **oxygen** but may also be **sulphate**, **nitrate** or even **ferrous iron** or **manganese**. Respiration is much more energy efficient than fermentation and hence dominates microbial reactions when a suitable oxidant is available. This is also the pathway, which gives rise to most of the by-products, which we find as mineral precipitates in sediments. The electron

acceptors in the environment play an important role in the entire reaction path. In **aerobic** oxidation, oxygen plays this role and is converted to water, for example. Under progressively more **reducing** conditions, then nitrate, manganese, iron and, eventually, sulphate take over. This sequence is not arbitrary. It is dictated by the free energy yield obtained in the process. The dominant reaction will be the most efficient of the possible pathways available.

Hydrocarbon-induced alteration

Passive microbial biomineralization includes bacterial formation of some forms of authigenic iron oxides, phosphates, carbonates and clays (Krumbein, 1983). Still other mineral phases precipitate directly from bacterial enzyme action, such as magnetite particles formed inside the cells of magnetotactic bacteria (Krumbein, 1983). This illustrates that bacteria in seeps are not only responsible for the destruction of hydrocarbons, but they are also responsible for the formation of large volumes of authigenic minerals, including carbonates, elemental sulphur, and iron oxides and sulphides.

Passive microbial mineralization has a larger impact on the surface sediments and is easier to detect. For this reason, the most important processes are briefly discussed below.

Carbonates

Diagenetic carbonate and carbonate cements are among the most common hydrocarbon-induced alterations associated with petroleum seepage (Alexandersson, 1974; Berner, 1968; Bohrmann et al., 1998; Clayton, 1994; Coleman and Raiswell, 1981; Paull et al., 1992; Peckman et al., 1999; Roberts and Aharon, 1994). The carbonates can form as slabs and rubble, large mounds and pillars, hardgrounds, or pore-filling carbonate cement (Clayton, 1994; Schumacher, 1996). These near-surface diagenetic carbonates are formed principally as by-product of hydrocarbon oxidation, particularly of methane, using one of the two reaction pathways, summarized below (for more details see Ehrlich, 1996):

Aerobic

$$CH_4 + 2O_2 + Ca^{2+} = CaCO_3 + H_2O + 2H^+$$

Anaerobic

$$CH_4 + SO_4^{2-} + Ca^{2+} = CaCO_3 + H_2S + H_2O$$

When these reactions occur, carbon dioxide evolves and reacts with water to produce bicarbonate. The bicarbonate binds with calcium and magnesium in seawater and precipitates as carbonate, or carbonate cement, that has an **isotopic signature** that refers to the parent hydrocarbons (Clayton, 1994).

Carbon isotope signals of authigenic carbonate formed during methanogenesis are one of the best indications. There are two fractionation mechanisms with control $\delta^{13}C$ of methane and carbon dioxide during methanogenesis. The **kinetic fractionation** depends on the relative reaction rates of molecules containing only ^{12}C and those, which contain a ^{13}C atom. During CO_2 reduction, the first formed methane is enriched in ^{12}C and the residual CO_2 becomes enriched in ^{13}C (about 25 to 60 $^0/_{00}$ heavier than the CH_4). Methane formed later, contains more ^{13}C, but is still lighter than the CO_2 from which it came (Clayton, 1994). In natural environments, the original CO_2 derived from microbial decomposition of organic matter is typically in the order of -20 to -30 $^0/_{00}$. The first formed methane therefore has $\delta^{13}C$ between -50 and -90 $^0/_{00}$. As methanogensis proceeds, both CO_2 and CH_4 become progressively enriched in ^{13}C until the consumption of CO_2 is balanced by addition from other sources and a steady state is reached. The net result is a range of natural methane isotope ratios typically is between - 55 and -80 $^0/_{00}$ (Abrams, 1996b; Claypool and Kaplan, 1974; Clayton, 1994).

Normal calcite, whether carbon is derived from the atmosphere, freshwater or the marine environment, has a carbon isotopic value of about -10 to +5 $^0/_{00}$ relatively to the PDB standard (Schumacher, 1996)). Calcite formed from oxidized petroleum incorporates carbon form the organic source. It has a typical carbon isotopic composition **more negative than -20** $^0/_{00}$. Depending on the proportion of oxidized hydrocarbon incorporated, the isotopic composition of the resultant carbonate can range form **-10 to -60** $^0/_{00}$ (Schumacher, 1996).

Schumacher (1996) illustrates that not all hydrocarbon seep areas possess isotopically anomalous carbonates and the result is therefore often consistent with a non-petroleum carbon source. It is tempting to relate near-surface carbonate diagenesis to leakage of reservoir hydrocarbons, but we should keep in mind that geochemical anomalies caused by abnormal amounts of carbon dioxide are non-specific for petroleum (Schumacher, 1996).

Abnormal CO_2 concentrations in sediments can result form processes other than microbial oxidation of hydrocarbons such as hydrothermal activity, volcanic activity, catagenesis of organic matter, micropore filtration, and thermochemical sulphate reduction (e.g. Matthews, 1996).

Nevertheless in the study area only **catagenesis of organic matter** can be an alternative process of carbonate isotopic depletion, if it occurs.

The sites of intense methanogenic activity are frequently marked in ancient sediments by authigenic ferroan dolomites and ankerites (Cavanga et al., 1999; Conti and Fontana, 1999; Kelly et al., 1995; Paull et al., 1992; Theil et al., 1999). These are usually attributed to **fermentation** although the picture is not quite this simple. Methane associated carbon dioxide isotopic ratios show a dramatic spread in $\delta^{13}C$. Probably the most significant point to note however is that the +15 $^{0}/_{00}$ end member value assumed in many diagenetic studies (e.g. Irwin and Curtis, 1977) is achieved only in exceptional circumstances (less than 1 % of the samples). Values between +2 and -22 $^{0}/_{00}$ are dominant. It is thus the anomalous situation, which gives rise to the extensive carbonate cementation. This makes sense if we consider the carbonate equilibrium system. During fermentation, CO_2 is released, which in the absence of any other buffer, leads to slightly acidic conditions, which would inhibit carbonate precipitation. This effect, however, is usually buffered to some extent by other bacterial and mineralogical reactions, which keep the sediments at a more or less neutral pH. If, however, CO_2 reduction takes over, after a time the CO_2 will be partially removed, lowering acidity and eventually promoting precipitation of what is left of the dissolved carbonate (Clayton, 1994).

Sulphides

The formation of secondary **pyrite** and other sulphides has been documented in many petroleum fields (Schumacher, 1996). Pyrite is the dominant sulphide mineral in these hydrocarbon induced alteration zones, but pyrrhotite, marcasite, galena, sphalerite and native sulfur are also found and may locally be abundant. The mechanisms responsible for the formation of sulphides in the hydrocarbon seeps environment have been discussed by (Ehrlich, 1996; Oehler and Sternberg, 1984; Sassen et al., 1989). Pyrite can be precipitated in a reducing environment, given a source of sulfur and iron is available. The major source of sulfur in a petroleum province is hydrogen sulfide gas from the petroleum itself, from anaerobic bacterial activity or from the oxidation of petroleum in the near-surface. Source of iron includes iron oxide grain coatings in sandstone, pore-filling clays such as chlorite, rock fragments, etc. The reaction of hydrogen sulphide and iron (in the reaction from hematite) to precipitate pyrite or marcasite can be summarized as follows:

$$Fe_2O_3 + 4H_2S = 2FeS_2 + 3H_2O + 2H^+ + 2e^-$$

The development of a pyrite alteration zone depends on the sulfur content of the oils, the geology and groundwater geochemistry of the sedimentary sequence and the nature of the bacterial degradation (Ehrlich, 1996).

2.3 Geological setting of Porcupine Seabight

2.3.1 Geometry

The Porcupine Seabight, off the west coast of Ireland, forms a N-S oriented, pear-shaped embayment in the Irish Atlantic shelf (Fig. 2.8a). Water depth increases from 150 m in the north to over 3000 m in the south. It is approximately 400 km long, 65 km wide in the north and widening to 150 km in the south. The feature can be subdivided into a north-south trending area of relatively shallower water and a trapezoidal-shaped northeast-trending area of very deep water, the mouth of the Porcupine Seabight, which opens out into the Porcupine Abyssal Plain in the southwest (Fig. 2.8a). The bathymetry of the seabight reflects clearly the underlying geology of the sedimentary basin. The continental slope, bordering the broad shelf of Ireland is steep with a typical 0.05 gradient or 2-3° and is indented with canyons in the northeastern part of the study area.

2.3.2 Geology

The Porcupine Seabight Basin has a broadly symmetrical profile bounded at Jurassic level by basinward-dipping faults (Croker and Shannon, 1987; Shannon, 1991) (Fig. 2.8c). This intracratonic extensional sedimentary basin is bound on three sides by shallow Pre-Cambrian and Lower Paleozoic metamorphic basement platforms, the Porcupine Ridge to the west, the buried Slyne Ridge to the north, and the Irish Mainland Shelf to the east. Goban Spur, a basement high of continental crust (Masson and Miles, 1986) forms the southern limit (Fig. 2.8b).

The Porcupine Seabight Basin is divided into 2 subbasins at about 51°N by a northeast-southwest trending basement structure known as the Clare Lineament (Shannon, 1991; Tate, 1993) (Fig. 2.8b). To the north, the Main Porcupine Basin is a north-south trending basin with water depths ranging from 300 m to 2000 m. The Seabight Basin is a southward extension of the Main Porcupine Basin across the Clare Lineament and has a more elliptical outline, which forms a deep present-day bathymetric embayment. An east-west ridge separates the North Porcupine Basin from the Main Porcupine Basin (Naylor and Shannon, 1982) (Fig. 2.8c). This structure is characterized by an associated geothermal anomaly, which suggests relatively recent movement facilitating the passages of fluids from depth (Croker and Shannon, 1987). This zone is the only part of the region where evidence of transcurrent features has been found and strike-slip transfer faults have been identified (McCann et al., 1995b; Tate et al., 1993). This argues for a complex history of repeated movements from Early Mesozoic to Early Tertiary times, which are probably

located along a deep-seated Caledonian fault zone (McCann et al., 1995b). This basement ridge is also the northern limit of the significant basin extension in the Main Porcupine Basin (Tate et al., 1993).

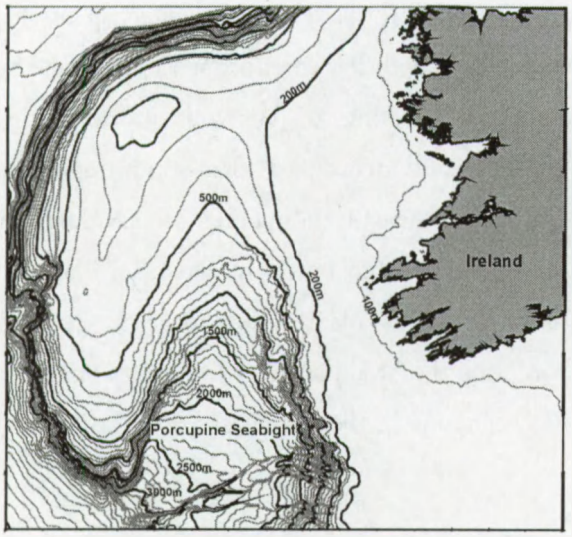

Fig. 2.8a: Geographic location and bathymetric map of the Porcupine Seabight.

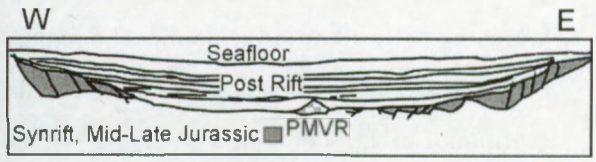

Fig. 2.8c: Synthetic profile of the Main Porcupine Basin (see Fig. 2.8b for location).

Fig. 2.8b: Geological subdivision and structures of the Porcupine Seabight.

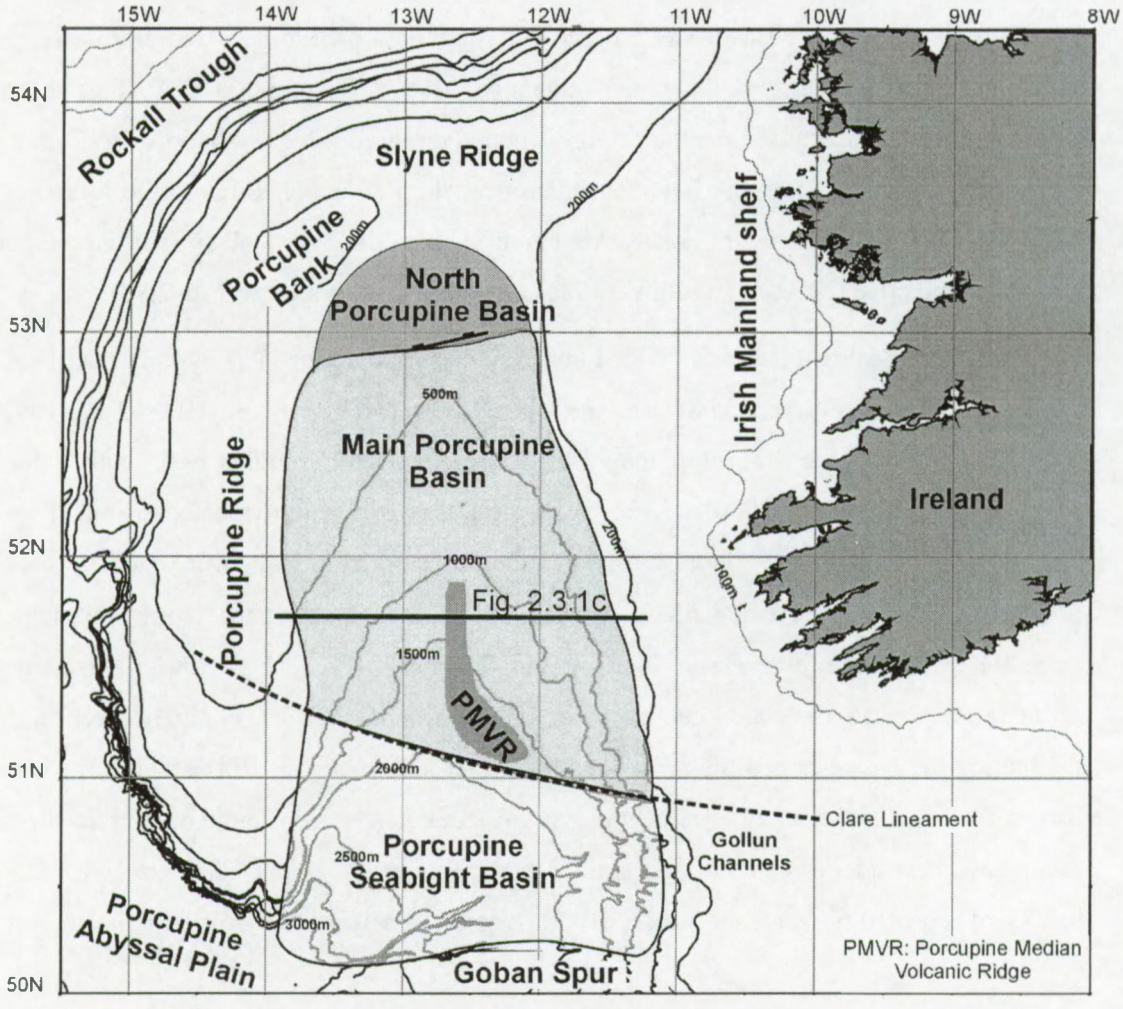

2.3.2.1 Genesis of the basin

The origin of the basin relates to a Middle to Late Jurassic failed rift of the proto-North Atlantic (Croker and Shannon, 1987; Shannon, 1991; Sinclair et al., 1994). It was formed in response to three east-west extensional stresses (rift episodes) separated by thermal subsidence during the opening of the North Atlantic in the Mesozoic (Croker and Shannon, 1987; Max, 1987; Shannon, 1991; Sinclair, 1995; Sinclair et al., 1994; Tate et al., 1993): Triassic to Early Jurassic, Tithonian to Mid-Valanginian (Late Cimmerian) and Mid-Aptian to Albian (Fig. 2.9). This complex structural history of the basin has been interpreted as being related to the interplay of episodic rift events, basinwide thermal subsidence, North Atlantic seafloor spreading dynamics and Alpine orogenesis (McCann et al., 1995a).

2.3.2.2 Faults

The basin-bounding faults and the syn-rift tectonic faults are the primary faults in the basin, determing the overall basin shape and form (Croker and Shannon, 1987; Max, 1987; McCann et al., 1995b; Shannon, 1991; Shannon et al., 1995; Sinclair et al., 1994) (Fig. 2.8c). The dominance of these faults is reflected in the observed orientations of younger faults, which tend to follow these inherited trends. The major basin-bounding faults were also reactivated during later rifting episodes.

2.3.2.3 Sediment record

Mesozoic and Cenozoic deposits reach a maximum thickness up to 10 km, thinning to the north and to the flanks of the basin. Sedimentation within the Porcupine Seabight Basin resulted form the interplay of tectonic and eustatic changes (Max, 1987; McCann et al., 1995b) (Fig. 2.9.). The fault-sediment analysis of McCann et al. (1995) show that tectonic activity was primarily responsible for producing subsiding depocentres.

The sedimentological and structural history of the basin will be discussed in more details with special emphasis to faults and hydrocarbon potential of the mound provinces.

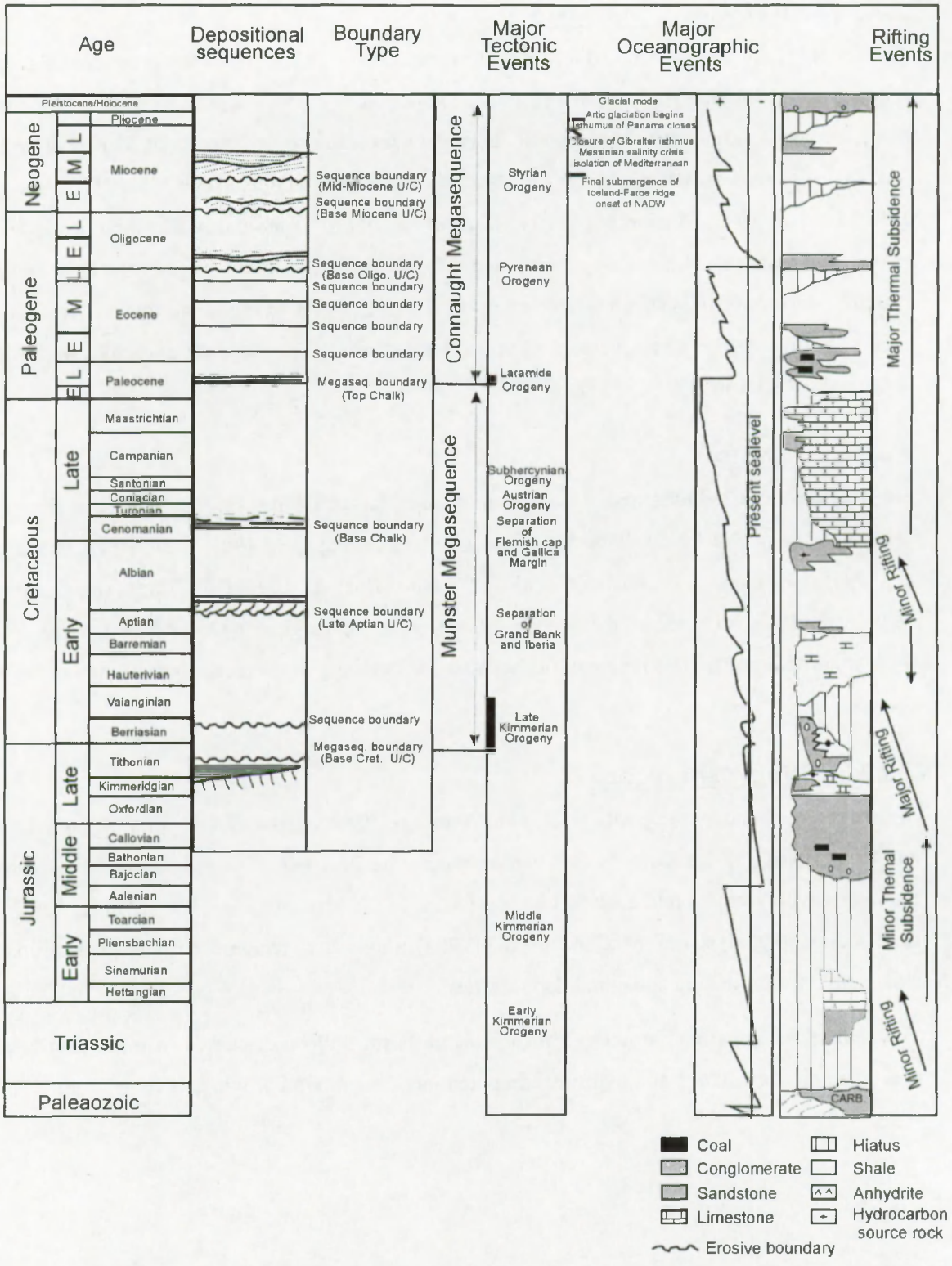

Fig. 2.9: Stratigraphic column, showing the sequence stratigraphy (Moore and Shannon, 1995). Major tectonic oceanographic events (Haq and Van Eysinga, 1998), sea level curve (Shannon , 1991; Moore and Shannon, 1995), lithocolumn (Sinclaire) and rifts (Shannon, 1991).

2.3.2.4 Pre rift sequence

Before the major rifting episode, the region of the Porcupine Seabight Basin was an east-west oriented basin, probably extending onshore in the Shannon Trough, which existed during the Carboniferous (Croker, 1995). The pre-rift succession comprises Devonian clastics overlain by Tournaisian and Visean carbonates and clastic deposits (Croker and Shannon, 1987). The Upper Carboniferous succession is predominantly composed of deltaic deposits (Fig. 2.9).

2.3.2.5 Porcupine Median High

Several studies in the Porcupine Basin have identified the Porcupine median volcanic ridge in the centre of the basin. The ridge is thought to consist of basaltic flows overlying the rift sequence (Tate et al., 1993). (Reston et al., 2001) suggested that the rise may instead represent a series of highs related to mantle serpentinization and for this reason he called the structure the Porcupine Median High. The Porcupine Median High appears as a slight uplift of the faulted sequence, perhaps caused by the volume increase accompanying serpentinization of the underlying mantle.

2.3.2.6 Rift sequences

The **first rifting episode**, in the Triassic-Earliest Jurassic, produced a series of small rift basins, which nucleated along reactived, generally Caledonian, structures (Croker and Shannon, 1987; McCann et al., 1995b; Sinclair, 1995). Continental siliciclastic sediments have been deposited in the geographically isolated, but tectonically linked, NE-SW trending basins (Croker and Shannon, 1987; Sinclair, 1995). This deposition has been followed by precipitations of variable thicknesses of evaporitic minerals and finally by deposition of marine carbonate beds (Fig. 2.9).

The **second rifting episode**, in the Late Jurassic - Early Cretaceous, represents a period of crustal extension and rifting. The amount of stretching increases steadily southwards along the axis of the basin. A change in the extensional direction, from NE-SW to EW in Middle-Late Jurassic times, has had important implications for the opening of the basin (Shannon, 1991; Tate et al., 1993). It suggests that the Porcupine Ridge rotated about 20° from the Irish shelf. (Tate, 1993) Middle Jurassic strata are widespread and dominantly continental, with marine sediments occurring towards the top of the succession as a result of a northward-progressing transgression (Croker and Shannon, 1987) (Fig. 2.9). Faulting was extensive in the main rift phase (Late Jurassic-Early Cretaceous) with predominantly large faults, particularly along the eastern and western margins (McCann et al., 1995b). Fault orientations are mainly parallel to the eastern and western basin margins, although they are more variable in the north. This variability is possibly related to the rotation of the Porcupine Ridge away from the Irish shelf (McCann et al., 1995b).

Growth faulting, with associated shallow marine fans and scarp deposits along the basin margins, occurred during the Tithonian in response to a further major rifting episode, while in the basin centre sequences of sand-rich mass flow deposits were generated and alternate with deep-water hemipelagic shales (McCann et al., 1995b; Tate, 1993).

Cretaceous strata, deposited at the onset of the major thermal stage of basin development, unconformably overlie the faulted Jurassic succession (Croker and Shannon, 1987) (Fig. 2.9). Some faulting continued in the Early Cretaceous (Moore, 1992; Moore and Shannon, 1995)

The **third phase** of rifting reflects thermal subsidence of Cretaceous and Tertiary age, and coincides with seafloor spreading in the North Atlantic (Max, 1987; McCann et al., 1995b; Shannon, 1991; Tate, 1993). Deep-marine sediments are overlain by pro-deltaic shales (Croker and Shannon, 1987). A minor Aptian-Albian rift phase led to the production of local sand-rich deltas with associated beach complexes, fault-bounded clastic fans and turbidite/mass flow deposits (Moore and Shannon, 1995). These, in turn, are overlain by deep-marine chalks deposited during the Upper Cretaceous marine transgression (Moore and Shannon, 1995). In the youngest rifting episode (Aptian), faults were more localized and concentrated mainly in the north of the basin. Fault orientations were predominantly N-S (McCann et al., 1995a; McCann et al., 1995b).

The **final thermal subsidence episode** (Late Cretaceous-Late Tertiary) generated the largest number of faults. An anomalous increase in subsidence occurred in the Early Tertiary, accompanied by igneous activity (Tate et al., 1993). The rapid increase in subsidence, which follows Paleocene magmatism, is explained by a small amount of stretching. Although minor amounts of normal faulting occurred during the Tertiary, this faulting represents negligible horizontal extension and is Late Oligocene in age and hence postdates both the increase in subsidence and much of the igneous activity (Tate et al., 1993).

A Paleogene extensional phase has been proposed by White et al. (1992) on the basis of subsidence analysis. The throw on individual faults is small, and the fault distribution pattern is interpreted by Shannon et al. (1993) in terms of normal thermal subsidence with superimposed basin margin uplift and accelerated basin center subsidence related to ridge-push effects in the Atlantic Ocean. The large number of small faults is interpreted as being the response of brittle lithologies to deformational stresses (e.g. Upper Cretaceous-Danian chalk and Eocene sandstones) rather than to a real rifting event. A number of areas within the basin contain clusters of small faults within the Paleogene section. These are associated with large Miocene slump

features which moved basinwards in response to basin-center thermal subsidence (Moore and Shannon, 1991).

Chalk deposition continued into the Danian (Early Paleocene) and was followed by a regression phase. Pro-delta shales are overlain by Paleocene and Eocene sandy delta lobes in the north of the basin (Croker and Shannon, 1987; Moore and Shannon, 1992), with submarine fan sediments and contourites being deposited further south (Shannon, 1991; Shannon, 1992). Following the Late Eocene to Oligocene unconformity, a thick succession of deep-water shales, with associated channelized sandstones, was deposited (Moore and Shannon, 1992) (Fig. 2). Widespread Mid-Tertiary unconformities, by analogy with the northeast Atlantic stratigraphy, probably relate to changes in oceanic circulation, particularly in the inception of Arctic-derived bottom water across the Eo-Oligocene stage boundary, becoming more vigorous during the Early Miocene (Tate, 1993) (Fig. 2.9). This is illustrated by a basinwide, large erosional unconformity particularly clear on the upper slope (Roberts et al., 1981). The Neogene deposition is thinner than the Paleogene and consists of deep-water sediments. Rapid basin subsidence combined with high sedimentation rates made the depositions unstable (Moore and Shannon, 1991). On the basin margins, there is a good evidence for slumping and migrating channel/levee systems (Moore and Shannon, 1991), while further out in the basin, turbiditic sediments accumulated (Shannon, 1992).

The Paleogene-Neogene deposits in the northern Main Porcupine Basin (Hovland mound province) are up to 2100 m thick (Croker and Shannon, 1987). The Paleocene transgressive sequences generally comprise a basal chalk overlain by a marly and shaly series with clastic incursions. The Late Paleocene-Eocene contains a series of major prograding alluvial fans and deltas from the upper margin. The sequence appears to be thickest on the eastern margin where up to 1400 m have been drilled (Croker and Shannon, 1987). In all instances, a prodelta sequence is succeeded by a sand-prone stacked coarsening-upward delta-front serie with distributary mouth-bar sandstones, and capped by a variable delta-top sequence of channel-fill, point-bar, crevasse-splay and coal-bearing swamp sequences (Shannon, 1992). Deltaic progradation occurred in series of pulses during the Late Paleocene and Eocene, and the prograding delta front migrated northward through time, during a relative sea level rise.

In the southeastern part of the basin, the Eocene contains a series of irregular paleotopographic features. A conceptional interpretation is that these features simply represent an erosive hill and valley paleotopography similar to that seen at the present-day seabed. However, some of the highs, while undoubtedly sculptured by erosion, appear to be mounded features, thinning toward the valleys, which are infilled with horizontally bedded, onlapping, probably low-energy deposits.

These are interpreted as sandy turbidite lobes with the intermound areas being interfan low-energy shales (Croker and Shannon, 1987).

2.3.2.7 Seismostratigraphy in the Porcupine Basin

The Tertiary sedimentary record in the Porcupine Basin and the adjoining basins can be subdivided into two megasequences on seismic profiles (Mc Donnell, 2001; Stoker et al., 2002). Megasequence 1 covers the sediment successions of Paleocene and Eocene age and is subdivided into six sequences (Fig. 2.10). Similarly, Megasequence 2 of Oligocene to recent age is subdivided into seven sequences. The sequence boundaries are delimited by unconformity surfaces of which three are regional and recognised in the Rockall Trough and the Porcupine Basin (Mc Donnell, 2001; Stoker et al., 2002):

- Near Base Tertiary (C40),
- approximate Base Oligocene (C30)
- and Intra Pliocene (C10).

Each of these three surfaces marks a distinct change in sedimentation patterns. A fourth notable unconformity of Late Miocene age (C20) define in the Rockall Trough (Stoker et al., 2002) corresponded to a series of unconformities in the Porcupine Basin (C20a-d) of which C20c is the most comparable to C20 of the Rockall basin (Mc Donnell, 2001).

On the high-resolution seismic profiles, discussed in this thesis only the sediments sequences of Megasequence 2 are imaged. Seven sequences are defined in Megasequence 2 based on Industrial airgun profiles in the Porcupine Basin (Mc Donnell, 2001). Two main unconformities are recognised in this Megasequence 2: Base Oligocene (C30) and Early Pliocene (C10). Four closely spaced unconformities are of Late Early Miocene to Early Middle Miocene age are identified (C20a-C20d) that correspond in time to the C20 unconformity recognised by Stoker et al. (2001) in the Rockall Basin. The dating of the upper two unconformities (C10 and C20) is based on seismic facies correlation with profiles in the Rockall Basin. No absolute neither relative dating is performed on wells in the seismic survey area.

This Megasequence 2 is dominated by marine sediments deposited by along-slope processes i.e. contourite depositions as opposed to the down slope dominated Early Tertiary depositions (Mc Donnell, 2001). The Base Oligocene event (C30) created shelf incisions and canyons in the basin. The Late Mid Oligocene erosional event is locally intense and creates shelf margin incision in the

southeast near the Belgica mound province. These canyons are infilled by Late Oligocene turbidites and pelagic deposition. This intra-Oligocene unconformity forms the basal scour of the first contourite deposits recognised in the basin. Contourite development dominated the later Oligocene of the basin until a relative sea level fall in the Early Miocene brought an end to drift development. The fall in relative sea level probably slowed down circulation in the basin, or may have shut off supply of drift forming bottom currents (Mc Donnell, 2001).

The subsequent earliest Miocene records reflect hemipelagic marine deposition that infill the erosional topography. Depositional style changed in later Early Miocene times with three pulses of slope progradation from the east. Slope failures are also identified in the east. In the west, progradation is not evident but a large sediment slide is identified. A change in environment in post Early Miocene times triggered the re-imitation of drift development. Initially scouring was the most prominent in the north and less on the flanks. The subsequent main phase of drifting is focused along the eastern basin margin (Mc Donnell, 2001).

Contourite drift development continues to the present-day. The youngest unconformity is interpreted to be near Base Pliocene, likely the youngest phase of channel development form the eastern basin margin. These channels were subsequently infilled by drift sediments (Mc Donnell, 2001).

2.3.2.8 *Pleistocene-Holocene*

Few studies concern the Quaternary sedimentation in the Porcupine Basin. The upper sediments in the basin have been studied on and along the Porcupine Ridge by Scoffin and Bowes (1988) and in the Seabight by Rice et al. (1991) and Tudhope and Scoffin (1995), and in the northern part of the Main Porcupine Basin by (Coles et al., 1996). All these studies are based on dredge samples and shallow cores down to 3m. The subbottom sediments consist of a mixture of two suites of sediments: one terrigeneous, of presumed Pleistocene age and glacial origin, composed of fine angular quartz sand and rounded lithic pebbles, cobbles and boulders; the other one consisting of carbonate sands and gravels of modern aspect, built of skeletal fragments of pelagic and benthic organisms.

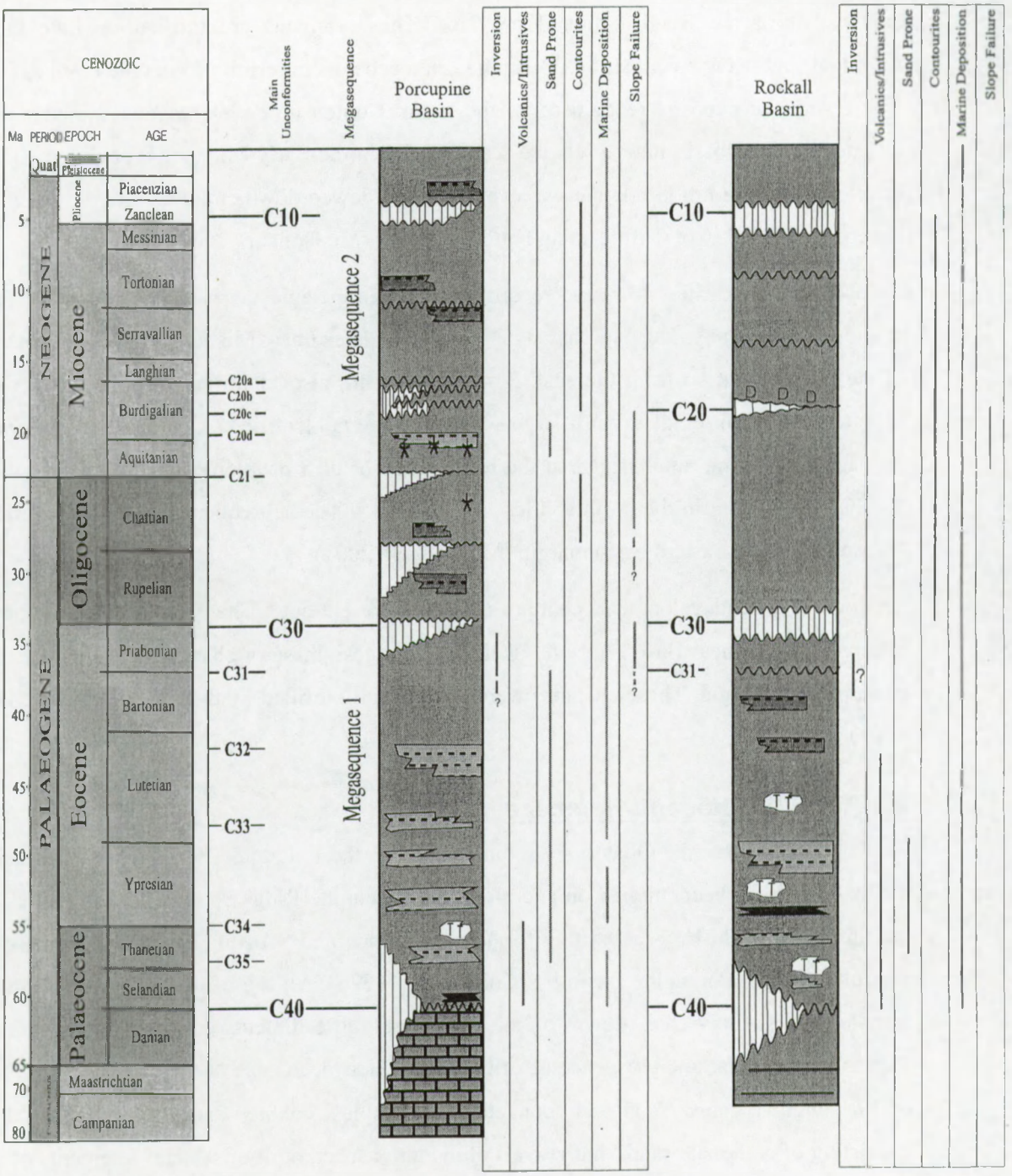

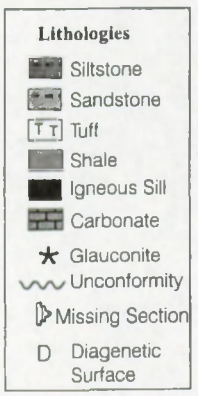

Fig. 2.10: Seismic stratigraphy of Mc Donnell (2001) in the Porcupine and Rockall Basins. The Rockall column is based on well data. It seems that there is a broad comparison in timing and interpretation in sand input, initiation of contourite development and volcanic activity (Mc Donnell, 2001).

The seabottom showed a hummocky seabed configurations consisting of bioturbated terrigenous and carbonate silts and sands with scattered boulders. The greatest abundance of boulders is recorded on the crest of the Porcupine Bank (Scoffin and Bowes, 1988). In the seabed, the many biogenic structures include roughly circular hollows and pits. Probably crustaceans and bottom feeding fish are though responsible for the larger depressions, with burrowing anemones and soft-bodied worms responsible for the smaller pits (Scoffin and Bowes, 1988).

Only in the southern part of the basin a well-developed channel system, the Gollum Channel, occurs on the slope and basin floor (Fig. 2.8). The Gollum Channel forms the downstream component of a large fluvial system, which extended onto the southern Irish shelf during sea level lowstands in glacial periods. Wallace et al. (1988) measured in cores from the abyssal plain at the mouth of the Seabight an abrupt decrease in sedimentation rate from 13 cm/1000 yr during the last Glacial to 3.5 cm/1000 yr in the Holocene. Some channels remain active, transporting sediments at present (Wheeler et al., 1998). The Gollum Channel terminates in the Porcupine Abyssal Plain, but there is little evidence for a large fan system. According to Rice et al. (1991) sediment may have been reworked and redistributed in drift deposits by strong sea bottom currents in the Porcupine Abyssal Plain.

Minor channels are observed further north on the eastern slope of Porcupine Basin. These channels probably originated from glacio-fluvial erosion on the western Irish shelf during glacial periods but are most likely not active today (Wheeler et al., 1998). Iceberg ploughmarks on the seafloor (between 140 – 500 m water depth) of the Porcupine Bank, Slyne Ridge (Belderson et al., 1973) and on the northern slope of the Porcupine Basin (300 m) (Colpaert, 2000) demonstrate the glacial influence on Quaternary sedimentation. The maximum extent of the ice sheets on the western shelf of Ireland is uncertain, due to the nature of the continental shelf and to the fact that Ireland is known to have been wholly glaciated at least on occasion (Graham and Straw, 1992).

2.3.3 Hydrocarbon potential

Mature source rocks are present at various levels within the basin. Oil flowed on test from four wells (BP 26/28-1, BP 26/28-2, Phillips 35/8-1 and Philips 35/8-2) and there have been oil shows in numerous other wells (Croker and Shannon, 1987; Croker and Shannon, 1995; Moore and Shannon, 1995). The Late Jurassic contains the main source rock in the basin (Croker and Shannon, 1987). The Middle Jurassic has some source potential from non-marine shales and the oil present in the Lower Cretaceous of Phillips well 35/8-1 may have been partly sourced from that interval (Croker and Shannon, 1987). Other reservoir quality sandstones occur in Late Carboniferous (fluvio-deltaic), Triassic (non-marine), Early Cretaceous (fluvio-deltaic) in the central and southern parts of the basin (Moore and Shannon, 1995) and Early Tertiary (turbidites and fluvio-deltaic) sequences (Croker and Shannon, 1987; Croker and Shannon, 1995).

Cap rocks are available at Carboniferous, Permo-Triassic, Jurassic, Cretaceous and Tertiary levels. However, the Tertiary is immature around the basin margins, and is likely to have reached maturity only where deeply buried in the central part of the basin. Potential traps, including tilted fault blocks at Carboniferous and Jurassic levels, and stratigraphic onlaps, pinchouts and differential compaction features in the Jurassic, Cretaceous and Tertiary, are known to exist (Croker and Shannon, 1987; Croker and Shannon, 1995; Moore and Shannon, 1995). Most of the potential plays described should have adequate cap rocks/seals. However, some leakage along basin margin faults might occur. Charging the structures with hydrocarbons is probably the greatest uncertainly (Moore and Shannon, 1995).

The Connemara (block 26/28) discovery, present in a tilted fault block (MacDonald et al., 1987), contains an estimate of 195 million barrels of oil in place (Croker and Shannon, 1995). The main oil-bearing reservoir occurs within the widespread Mid-Jurassic continental sandstones. A secondary reservoir flowed oil from the thin updip edge of a Tithonian sandstone wedge (Sinclair et al., 1994).

Recently, test drilling in the vicinity of the Magellan-Hovland mound province proved dry wells (Martin Hovland, Sarah Johnson, pers comm.), despite the acoustic characterization of the deeper part was very promising for oil and gas.

2.4 Hydrodynamic setting

As already mentioned, the Porcupine Seabight forms a deep embayment in the Irish shelf surrounded by steep slopes. The upper slope (<1000 m) settings have generally a complex hydrodynamic regime. The major processes are interactions of tidal currents, vertical mixing, northward flow along the northeastern continental slopes, eddies, cascading, flows, internal tides and waves and the effect of the topography. Beside the major geometry of the slope, smaller features such as coral banks and local irregularities in the topography (canyons and local steep parts) influence the local hydrodynamic regime on a smaller scale. Hydrodynamic processes along the continental margin steer the exchange of nutrients and sediments between the shelf, the deeper part of the basin and the sediment structures. All these processes might play a role in the development of the coral banks and the related sediment structures. For this reason a general oceanographic overview of the basin is summarized.

2.4.1 Water masses

The general hydrography of the Porcupine Seabight is described by Hargreaves (1984), Ellet et al. (1986), Hargreaves (1984) and Vangriesheim (1985) and reviewed by Rice et al. (1991) and White (2001). **Eastern North Atlantic Water** (**ENAW**) is found at a depth of about 750 m in the mouth of the Porcupine Seabight and along the eastern flank of the Porcupine Bank, where it overlies the salinity maximum of the **Mediterranean Outflow Water** (**MOW**) (Fig. 2.11). The ENAW is a winter mode water, formed by strong cooling of water at the northwest of Spain (Pollard et al., 1996). The winter cooling forms the ENAW water mass that is denser and more saline at a particular temperature than the **North Atlantic Central Water** (**NACW**) of the North Atlantic Current and which has clearly a strong influence of Mediterranean Water (Ellet et al., 1986; Pollard, 1996). The MOW is characterized by a salinity maximum (up to 35.7 $^{0}/_{00}$ psu) and an oxygen minimum below 700m, with a core at 800-1100 in depth. van Aken (2000) suggests that the effects of

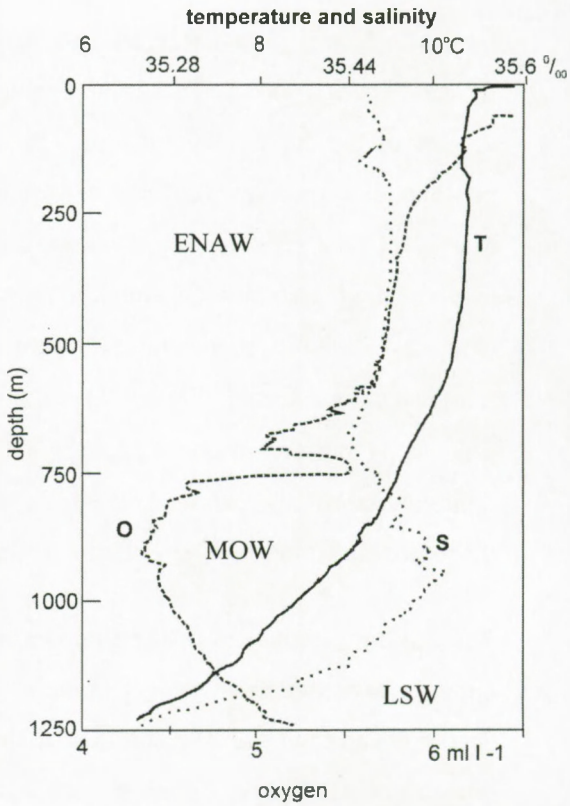

Fig. 2.11: CTD (Conductivity, Temperature, Depth) profile in the Porcupine Seabight mouth showing the water mass characteristics (Rice et al., 1991); T: Temperature, O: Oxygen, S: Salinity.

the MOW in the Porcupine Seabight seasonally change due to the deep winter convection and supported by the cascading of winter water from the Celtic continental shelf. The ENAW and MOW are grouped under the term **Sub Polar Mode Water (SPMW).** These water masses are essentially derived from modification of North Atlantic Central Water (NACW) with a source in the western Atlantic and Mediterranean Outflow Water (White, 2001). Below the Mediterranean Outflow Water, the influence of the **Labrador Sea Water (LSW)** is expressed by a salinity minimum and an oxygen maximum at about 1700 m depth in the mouth of the Porcupine Seabight. There is a permanent thermocline from about 10°C to about 4°C at a water depth from 600 m to 1400 m. A seasonal thermocline has been observed at about 50 m depth (Fig. 2.11).

2.4.2 Currents

2.4.2.1 Northward flowing currents

Based on historical and recently gathered current data of a few ECOmound and ACES moorings in the Rockall Trough and the Porcupine Seabight region, White (2001) produced a map with the mean current vectors of the depths 200-1400 m (Fig. 2.12). This plot of the mean values does not take into account interannual variability nor seasonal variability due to different measurement periods, recording lengths of individual time series. It is clearly imaged that a poleward flowing current has been recorded at all depth levels along the continental slope, in particular close to the seabed. Along the entire eastern margin of the Northeast Atlantic, a general poleward flowing slope current has been observed, to varying degrees (Huthnance and Gould, 1989; Pingree and LeCann, 1989; Pingree and LeCann, 1990; Huthnance, 2001). This slope current is an eastern boundary current (Smith, 1989) comprising at the upper levels a relatively warm and saline shelf edge current (SEC) between depths of 150-400 m. Below this level the MOW and deep ocean re-circulation boundary also flows poleward (Dickson et al., 1985).

The driving mechanism of the slope current is the poleward decline in sea-surface height, caused by the increase of water density with latitude. The rate of reduction in sea-surface height is greater over the deeper ocean than over the continental shelf, so that a difference in sea-surface height is generated across the continental margin, which becomes larger further to the north (Huthnance and Gould, 1989; Pingree, 1989; Huthnance, 2001). Beside the baroclinic effect friction also plays a role in the current pattern, which results in different characteristics in the slope flow at different locations along the Atlantic margin (Pingree and LeCann, 1990). Friction slows down the effect of continuously increasing current further northwards along the slope due to the baroclinic effect (White, 2001).

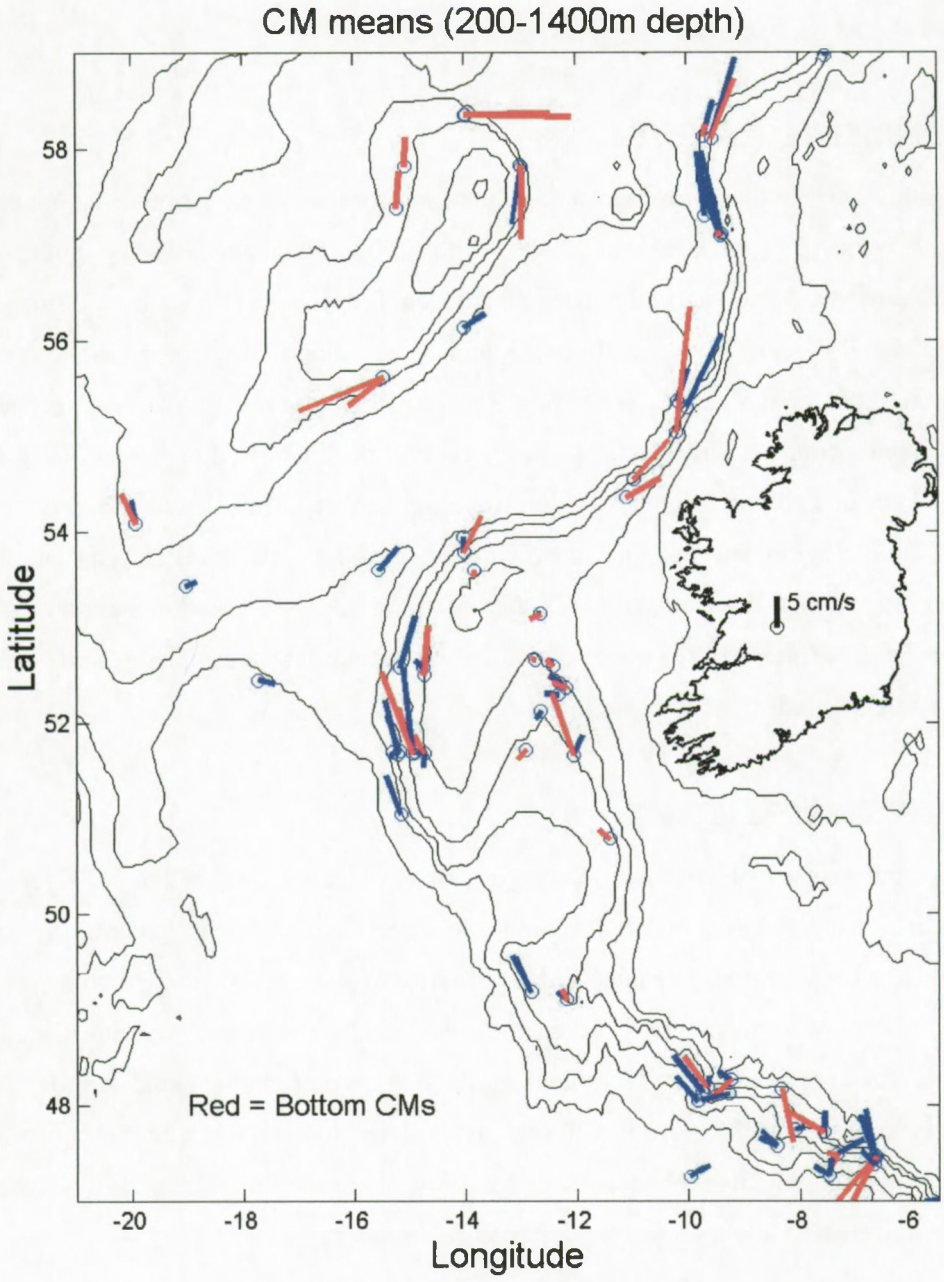

Fig. 2.12: Mean current vectors of bottom and surface currents in the NE Atlantic (White, 2001).

In general, mean poleward currents of about 5 cm/s have been measured along the Celtic Sea slope (Pingree and LeCann, 1990; Huthnance, 2001). Closer to the seabed, mean currents were generally stronger, persistent and directed more along-slope, as one might expect with a greater topographic steering influence for currents closer to the seabed (White, 2001). In the Porcupine Seabight, a mean poleward current is less readily observed, except in the near- bottom current meters on the eastern flank (Pingree

and LeCann, 1990). At the northern end of the Porcupine Seabight, currents are relatively weaker (1-5 cm/s) with some evidence of a topographic steering of the mean flow, cyclonically (anticlockwise) along the slope to the Porcupine Seabight.

2.4.2.2 Near- surface currents

The mean monthly currents in the upper water column indicate seasonality in the slope current regime at certain locations (Pingree and LeCann, 1990; White, 2001; Huthnance, 2001). South of the 53°N, maximum poleward slope and shelf edge currents are found in winter (December-February) with strong flows west of the Porcupine Bank (>10 cm/s) and at the slope of the eastern Porcupine Seabight (Huthnance et al., 2001; White, 2001; White and Bowyer, 1997). At the northern part of the Seabight the poleward flow is the strongest through the deeper portion of the Irish shelf in January/February. The flow first turns on-slope in February/March and then reverses in April/May. Mean monthly speeds are also weakest at this time. The reverse and significant weakening in the upper level currents are not apparent in the lower layer current measurements although minimum current were found in summer in the Porcupine region. Pingree and LeCann (1990) relate this effect partly to changes in large scale density/pressure forcing or a change in wind stress at these times.

2.4.2.3 Near-seabed currents

The near-seabed currents are of particular interest in terms of this research. White (2001) produced a table summarizing the current stability in the Porcupine Seabight (Table 2.3). In general, the stability of the current is stable to a large degree. The most stable currents are associated with the strongest current speeds and generally the greatest mean flows. Taken as a whole, the northern Porcupine Seabight moorings adjacent to the Hovland mound province have the lowest current stability and speeds. This might be expected as it is located near the barrier of the relatively deep shelf between the Porcupine Bank and the Irish continental margin, which is a barrier to flows below about 350 m (White, 2001). Data is somewhat scarce, so little information about cross zonation of currents can be inferred.

The decrease and reversal of the current in the northern mound province might be explained by the considerable overlap in salinity and temperature of the intermediate water masses (ENAW and MOW), which allows both diapycnal and isopycnal mixing. The proximity of the continental shelf edge may enhance the diapycnal mixing (Garrett, 1991) and force the circulation near the margin to be aligned with the topography (van Aken, 2000).

Location	Ref No	Latitude	Longitude	Water depth	Height asb (m)	%exceed. 20cm/s	%exceed. 30cm/s	Stability R (%)
N Porcupine Bank								
	6671	53.78	-14.01	930	10	15%	7.80%	94
W Porcupine Bank								
	5323	51.69	-14.9383	786	29	39.40%	8.20%	95
	5374	51.6967	-14.955	778	40	13%	0.80%	88
	5376	51.6933	-14.7383	500	29	2.90%	0.10%	52
	5378	51.7033	-14.915	741	29	22%	4.80%	98
	5475	51.685	-15.2117	1537	50	2.20%	0%	71
	547	53.6	-13.8383	280	25	20.60%	0.60%	22
SW Rockall Bank								
	6662	55.606	-15.462	818	10	37.20%	8.90%	93
E Porcupine Seabight								
Belgica mound province	1122	50.79	-11.408	960	8	2.20%	0.10%	57
	1142	51.675	-12.043	1000	8	35.80%	11.10%	98
N Porcupine Seabight								
Hovland mound province	5705	52.415	-12.295	500	9	1.30%	0%	73
	10350	53.135	-12.652	360	10	7.70%	0%	60
	30489	52.661	-12.748	500	11	4.70%	0.30%	9
	40471	52.598	-12.420	485	14	1.70%	0%	57

Table 2.3: Percentage exceedance of two speeds (20 cm/s, 30 cm/s) and current stability (R=vector/arithmetic mean current) for some locations to the west of Ireland (White, 2001).

2.4.3 Slope specific process

Due to the geometry of the continental slope and the interaction between the water masses and the slope, two main slope specific processes play an important role in the sedimentation and hydrodynamic settings of the slope:

- the reflection of internal waves on the sloping seabed
- the vertical mixing of water masses at the seabed on a slope, which is gravitationally unstable and which has a tendency to collapse under gravity in a layer away from the slope boundary (Thorpe and White, 1988; White, 2001).

These oceanographic processes will influence the bottom layer of the slope and may play an important role in the evolution of the coral banks. It will consequently be discussed in detail.

2.4.3.1 *Internal waves*

Internal waves are periodic energetic oscillations of the water column through disturbances in the vertical density stratification. These layers meet at the thermocline or pycnocline, which is marked by a sharp change in water temperature or salinity with depth. As a result, the internal layers at the interface of two water masses become periodically unstable and the resulting pressure gradients cause internal wave motion. This is driven by an externally forced acceleration caused by a change in density, in vertical component of the barotropic currents or a change in topography (Wunsch, 1975).

The wave formula can be written in terms of the difference in density (ρ) and the layer depths h_1 and h_2. The cerinity (C= wave velocity), the gravity (g) and the wave number (κ) will give the following equation:

$$C^2 = \frac{(\rho_2 - \rho_1)}{\rho_2 \coth \kappa h_2 + \rho_1 \coth \kappa h_1} \frac{g}{\kappa}$$

In this case we consider a two-layer ocean, which helps to conceptualise a number of internal wave properties and which is a useful approximation in a number of situations such as isolated basins with a pronounced pycnocline, as in the Porcupine Seabight. The real ocean is not a two-layer ocean. It is continuously stratified and internal waves can occur anywhere within the water column. In a continuous

stratification ocean, it is not required that such waves travel only horizontally. The only prerequisite is a density gradient along the path of the wave.

Tidal flow across the **shelf edge** is a known method for generating these internal motions, with subsequent propagation of the internal tidal energy both on and off shelf (New, 1987). Essentially, the continuity of flow across the shelf edge causes the thermocline to depress and this depression propagates away from the shelf edge region as a wave. Numerous observations of internal waves have been made along the Celtic Sea and Biscay Shelves (Huthnance, 1989; New, 1987; Druon, 2001). Internal waves with a tidal period are called **internal tides**.

The distribution of internal tide energy around the Northwest European shelf edge has been discussed in Sherwin and Taylor (1987). They placed the largest signals at the edge of the Celtic Sea. A significant internal tide is also found bordering the Rockall Trough.

Internal wave may not always be of the principal tidal period. Shorter period internal waves may be generated by the flow over rough topography (Thorpe, 1992; White, 2001). Holt and Thorpe (1997) suggested that this form of internal wave generation might happen at the canyons, which intersect the Celtic Sea continental slope. Propagation of these small internal waves in the larger oceanic internal wave field may result in significant mixing and small scale velocity shears (Thorpe, 1989). Elevated structures and scarps on the seabed can also cause such a change in topography.

Unlike surface waves, internal wave **energy propagates** in a different direction (at right angles to) the direction in which the wave crests/troughs move. The angle (β) at which the internal wave energy propagates is given by:

$$\sin^2 \beta = (\omega^2 - f^2)/(N^2 - f^2)$$

ω: wave frequency
N: vertical stratification (density gradient)
f: Coriolis parameter

Reflection of internal waves from a sloping boundary results in a change of wave number normal to the slope. Over sloping topography, bottom intensified flows associated with internal waves can occur when the slope of the topography ($\alpha=\Delta h/\Delta x$) is similar to that of the internal wave :

$$s = \pm\sqrt{\frac{\omega^2 - f^2}{N^2 - \omega^2}}$$

$$N^2 = \frac{-g}{\rho}\frac{d\rho}{dz}$$

Such slopes are termed **critical slopes** (e.g. Holloway, 1985). When the slope of the seabed (α) matches the wave characteristic β, i.e. for a critical wave frequency σ_c, waves reflect along the boundary and the wave number normal to the slope become very large (Fig. 2.13). These intensified flows may well be the dominant process contributing to bottom shear stresses on continental slopes and hence be important in determining sediment resuspension and transport (Eriksen, 1982).

The **bottom current intensification** behaves differently depending on the curvature of the seabottom. Energy enhancement is considerably more likely above locally convex than concave topography (Gilbert and Garrett, 1989). In most cases there are two regions on the continental margin where the slope is critical: one convex near the shelf break and one concave near the base of the slope, where the effect is consequently less than in the previous situation.

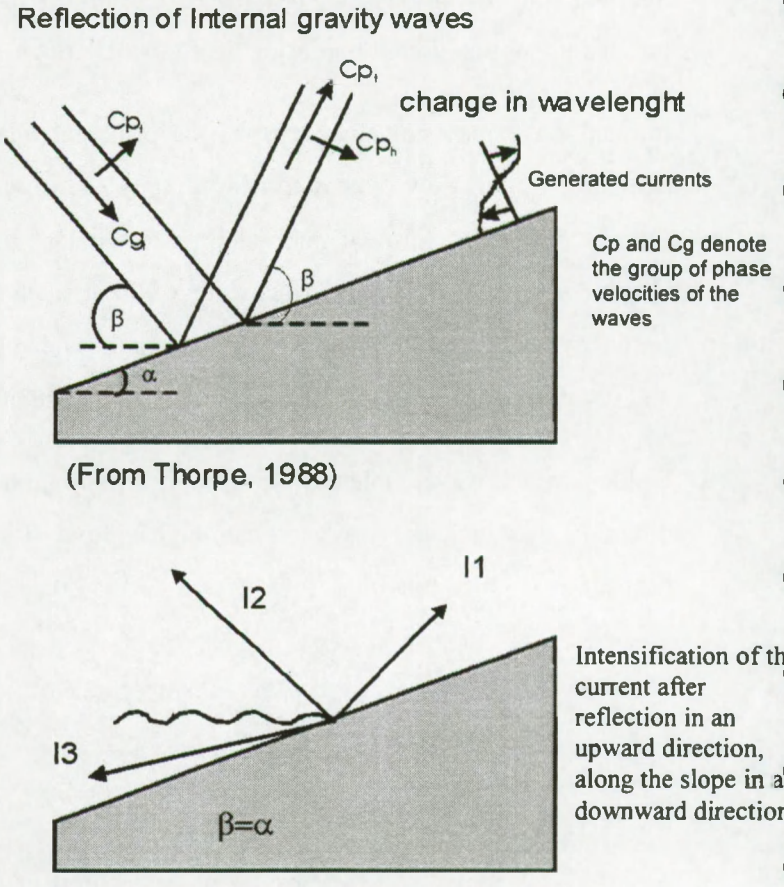

Fig. 2.13: Reflection of internal gravity wave from Thorpe, 1998.

Enhanced mixing near steeply-sloping boundaries has also been observed near **seamounts**. Toole et al., (1994) observed enhanced internal wave energy and enhanced deep mixing near the flank of Fieberling Guyot, as did Mudge and Lueck (1994) near Cobb Seamount (in relatively shallow water). The following processes have been attributed to internal waves: intensification of tidal currents near the seabed near the shelf edge, enhanced internal mixing of the thermocline and creation of nepheloid layers in the deeper parts.

Resonance may also be caused when incoming critical waves reflect from the seabed at other angles of energy propagation. Internal waves focusing and therefore mixing, will first take place near the seabottom. Rather than being an isotropic process along the boundary, resonance of reflected internal waves by geometric focusing (attractor) suggests that there are specific locations where mixing occurs first: i.e. topographic irregularity. Near such an attractor place at the seabottom, intermitted, intermediate turbid layers have recently been observed due to enhanced bottom currents. These have been interpreted as an isotropic mixing due to (near) critical reflection (and amplification) of internal waves, which presumably originated at breaks in the seafloor topography (Maas and Lam, 1995).

Breaking internal waves results in an upslope current, which can be induced by the passage of a decaying wave after it has been broken. A downslope return flow is set up by the passage of the breaker. Both types of currents may be capable of transporting sediment in sand waves and ripples (Fig. 2.13).

2.4.3.2 *Bottom friction*

The ability of internal waves and tides to resuspend and affect sediment over continental slope regions has theoretically been investigated by Ribbe and Holloway (2001). Internal waves that generated bottom layer shear stresses are large enough to resuspend sediment. This effect results in the creation and maintenance of a thin nepheloid layer. The thickness of the suspended sediment layer is controlled by vertical diffusion that is large within the bottom boundary layer, but very small outside. The residual velocity and the asymmetry associated with the velocity field, resulting in both down- and upslope net sediment flux, is found to be sensitive to the formation of vertical mixing. On the western slope of the Porcupine Bank, such conditions have been postulated as the cause for generation of nepheloid layers observed in the water adjacent to the slope (Dickson and McCave, 1986).

2.4.3.3 Nepheloid layers

Nepheloid layers are regions of suspended sediment in the water column. The sediment has been lifted into suspension by the mixing processes at the seabed, forming bottom or benthic nepheloid layers (**BNL**) or intermediate nepheloid layers (**INL**), layers detached from the seabed in mid water. On the Porcupine bank, a direct relation has been found between the BNL formation and the resultant INL (Dickson and McCave, 1986). The BNL had been detached from the seabed and subsequently transported into the ocean as mixed water containing the sediment. The generated BNL spreaded away from the bank along density isopycnals. The BNL had been formed where the internal waves of M2 period (principal lunar tides with a period of 12.42 solar hours) were critical in the slope. The INL resulting from the propagating BNL, have been observed out to a distance of 16 km from the slope (White, 2001).

The potential zones for the generation of internal gravity waves near the Irish shelf break, the Porcupine Bank and at the interface between the MOW and ENAW are specific for the Porcupine Seabight. Based on a biological and oceanographic study, Rice et al. (1990) suggest that such internal waves are breaking on the eastern continental slope of the Porcupine Seabight. The strongest across-slope near-bottom tidal currents in the Porcupine Seabight are probably of the order of 15-20 cm/s and occur in a water depth range between 500-1000 m depth contours on the eastern flank. Such currents are certainly sufficiently powerful to resuspend flocculent phytodetrital material and might even resuspend less flocculent sediment material (Rice et al., 1990).

3 Data

69

3.1 High-resolution seismic data 59
3.1.1 Acquisition 72
3.1.2 Vertical resolution 74
3.1.3 Scattering near the seabed 74
3.1.4 Velocity pull-ups below the mounds 76
3.1.5 Processing of seismic data 77
3.1.6 Interpretation of seismic profiles 78
3.2 Sidescan sonar 79
3.3 Echosounding 80
3.4 Multi beam 80
3.5 Oceanographic data or CTD profiles 81
3.6 Shallow cores 81
3.6.1 Training Through Research Programme (UNESCO-IOC)-CORSAIRES-ENAM (EC MAST 3 programme) 81
3.6.2 Belgica 83
3.6.3 Pelagia 83
3.6.4 Poseidon 84
3.6.5 Petroleum Affairs Division Ireland cores 84
3.6.6 Statoil cores 84
3.7 Underwater TV profiler 86

3 Data

The core samples and seismic data collected in the period from 1997 till 1999 have been acquired in the framework of two European Mast III projects: ENAM and CORSAIRES, in cooperation with the UNESCO-IOC "Training Through Research" program. The data acquired from 1998 till 2002 with the R/V Belgica is partly funded by the "Porcupine-Belgica" project of Ghent University (BOF, GOA). The later cruises are part of the 5th framework European projects GEOMOUND, ECOMOUND and ACES, which respectively focus on internal controls on mound genesis, external controls on mound development and on the role of deep-water corals in mound formation.

The data available for this study includes high-resolution seismic profiles collected with R/V Belgica in the period from 1997 till 2001 (Belgica 1997/12, 1998/11, 1999/13, 2000/16-17 and 2001/12 cruises). Sidescan sonar images (TTR7 CORSAIRES and TTR8 cruise), short gravity cores taken during the TTR7 and TTR8 cruises, cores provided by the Petroleum Affairs Division Ireland and Statoil Exploration Ireland (Ltd.), piston cores taken during an ENAM-cruise with R/V Pelagia in 1999, box cores taken during the TTR7, TTR8, Belgica 00/13 and Pelagia M2000 cruises, benthos TV-profiles recorded during the TTR7-CORSAIRES cruise, CTD profiles and detailed echosounding grids recorded during the Poseidon 265 cruise in the framework of the EC 5th Framework projects, ACES and ECOMOUND (Fig. 3.1). The data will be discussed per mound province and have been listed in a table per province. In this chapter the general characteristics of the data have been discussed together with the aim of sampling.

3.1 High-resolution seismic data

About 2600 km of high-resolution seismic data have been obtained of the Porcupine Basin during five seismic surveys with R/V Belgica, in the period spanning 1997 till 2001. All the cruises were planned in the best weather window for the Porcupine Basin, i.e. May-June. Nevertheless, mostly a few days of the acquisition time were lost due to bad weather conditions.

Two major seismic grids have been acquired: one in the Belgica mound province, along the eastern slope of the basin, and another one in the Hovland-Magellan mound province in the central part of the Basin. In the Belgica mound province a total of 1125 km seismic lines have been recorded, covering an area of 1666 km^2. This results in a 0.675 km/km^2 line density, with an average spacing of 3 km. A detailed grid has been sailed in the Belgica mound province in the

vicinity of Thérèse mound, consisting of 153 km of seismic lines covering an area of 15 km^2 or a 10.2 km/km^2 line density with a spacing of 200m. In the Hovland-Magellan mound province a total of 1446 km of seismic lines has been shot covering an area of 4322 km^2, which results in a density of 0.335 km/km^2 or an average line spacing of 6 km. A dense grid of 88 km seismic lines has been sailed in the Magellan mound province in an area of 57 km^2 with a line density of 1.5 km/km^2, or an average line spacing of 1.2 km.

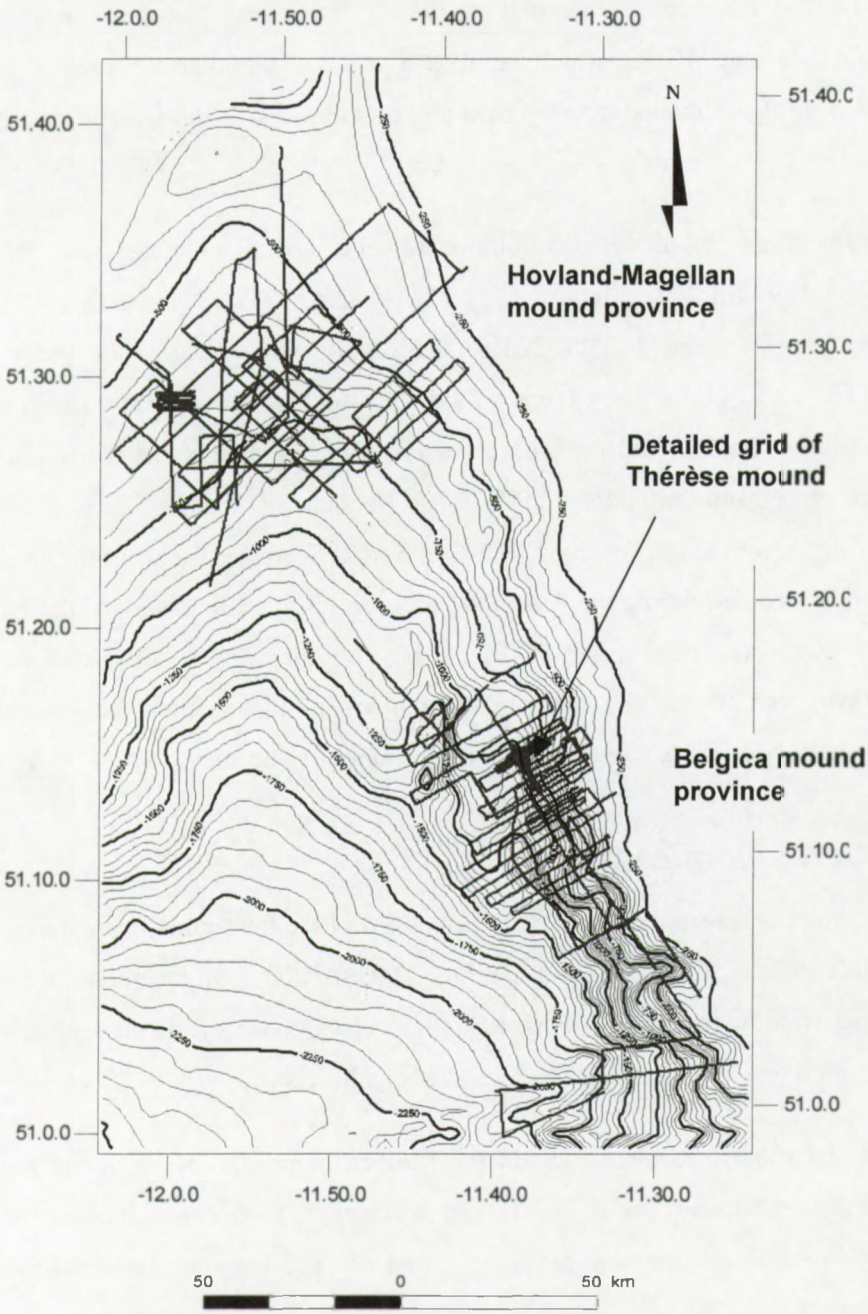

Fig. 3.1: An overview map of the available high-resolution 2D seismic data gathered with the R/V Belgica in the period from 1997-2001, RCMG.

The geometry of the acquisition is explained in figure 3.2. Source and receivers are towed approximately 20-25 m behind the vessel, at about ¼ wavelength below the surface. The source is towed on one side of the vessel and the streamer on the other. The configuration during the different surveys was the same and has been summarized in table 3.1. The shot interval and recording length have been adapted to the circumstances (water depth) and ranged between 1.6-3s.

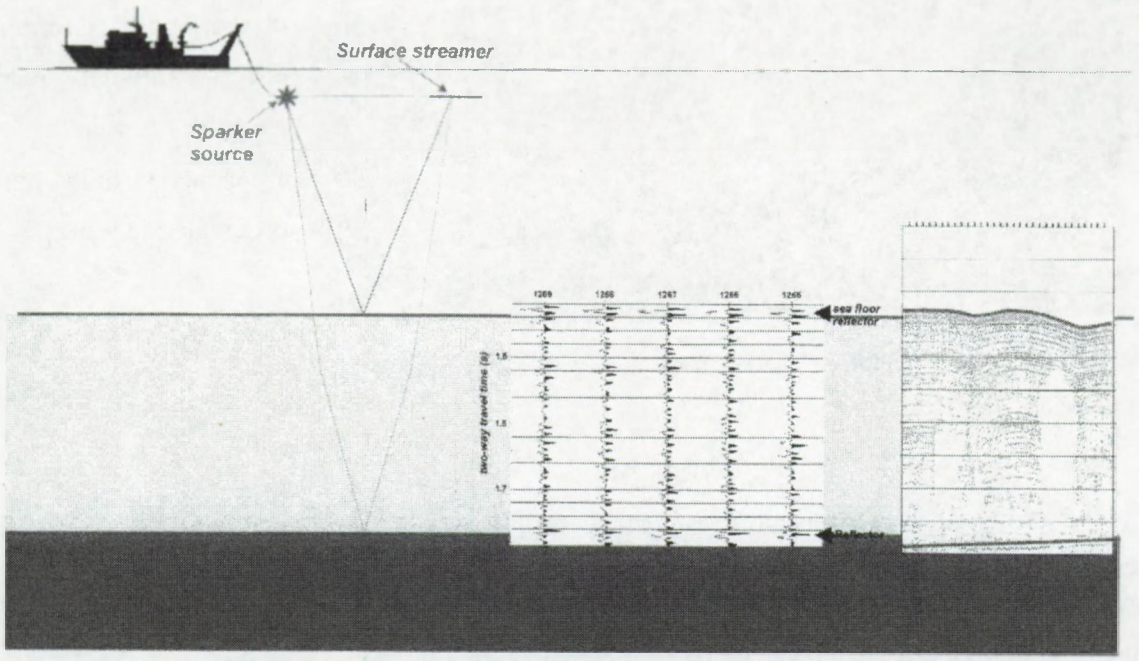

Fig. 3.2: Geometry of the 2D high-resolution acquisition with the RV Belgica.

Vessel	**Source**	**Receiver**	**Seismic Acquisition System**
R/V Belgica	SIG sparker 80 or120 tips Sodera T-water gun Type S15 Model 01	SIG.16.10.5 Single channel streamer	Elics Deph2X
Navigation: Magnavox Mx200 DGPS **Speed**: 2-5 knots **Propulsion**: diesel - electric	**Towing cable**: 15-20m **Energy sparker**: 500J **Energy water gun:** 140bar **Depth**: 0.5-2.5m	**Towing cable**: 15-20m **Depths** 0.5-1m **Length** of active section 5m **Hydrophones**: 10 **Spacing of hydrophones**: 0.3m	**Filter**: low cut filter: 200 **High cut filter**: antialias **Sampling rate** 0.125ms

Table 3.1: Configuration of the high-resolution data.

The seismic source that was used, is a SIG multi-tip sparker (80-120) fired at 500 J (Fig. 3.3) (excepted for 27 water gun profiles: 2 lines in 1999 (P99024, 29 and 30), 18 lines in 2000 (P000502-19) and 7 lines in 2001 (P010541, 42, 43, 44, 50, 51, 52)).

A sparker is an explosive source that generates a steam bubble by discharging electrical energy through point electrodes surrounded by a conductive fluid (salty water, marine water).

Fig. 3.3: A SIG multi-tip sparker used during the acquisition at R/V Belgica.

Input energy used in this seismic investigation is 500J. At this energy level, the seismic signal frequency ranges from 200 to 3000 Hz.

The T-water gun is a pneumatic source using compressed air with a chamber volume of 0.24l. The water gun is towed about 2.5 m under the water surface, which creates frequencies between 150-600 Hz. The air pressure during the operation was 140 bar.

In heavy weather (swell), there is a time difference in the arrivals of the shots depending on the relative position of the source and streamer inside of the wave-swell noise due to the fact that the source and receiver are towed on different sides of the vessel. Swell noise is mainly manifested as a non-alignment due to relative differences in position of the source and the receiver between different shots.

3.1.1 Acquisition

In this study all the seismic data has been recorded digitally with an Elics® Delph2X acquisition system. A sampling rate of 0.125ms has been used i.e. a sampling frequency of 8kHz. The data has been recorded in the field in Elics format and converted to SEG-Y. The seismic profiles are

named with a P, referring to Porcupine, followed by the year and month of acquisition and the number of lines in succession (e.g. P000615 = Porcupine 2000, June, line 15).

The horizontal resolution is defined as the smallest feature that can be discerned in a seismic profile. The horizontal resolution can be calculated by the first Fresnel radius. Two reflecting points that fall within this zone are generally considered as indistinguishable. The Fresnel zone depends on the wavelength and also on the frequency. With high frequency signals, the radius will be considerably reduced. Besides frequency, lateral resolution also depends on the velocity and the depth of the interface. For the sparker data the dominant frequency is around 600 ± 50Hz and for the water gun around 350 ± 50Hz. The estimated velocity of the unconsolidated sediment is around 1650 m/s ± 50 m/s. With such data, an event near the seabed at a two way reflection time of 1.2s would present a Fresnel radius of:

$$r = \frac{v}{2}\sqrt{\frac{t}{f}} = \frac{1650 \pm 50 m/s}{2}\sqrt{\frac{1.2s}{600 \pm 50 s^{-1}}} \approx 37 \pm 7m \quad \textbf{sparker}$$

$$r = \frac{v}{2}\sqrt{\frac{t}{f}} = \frac{1650 \pm 50 m/s}{2}\sqrt{\frac{1.2s}{350 \pm 50 s^{-1}}} \approx 45 \pm 7m \quad \textbf{water gun}$$

For deeper reflectors, at about 1.5 s two way reflection time, with a slightly lower dominant frequency around 400±50 Hz for the sparker source and 250±50 Hz for the water gun (due to the preferential attenuation of high frequency) the Fresnel radius will increase to:

$$r = \frac{v}{2}\sqrt{\frac{t}{f}} = \frac{1750 \pm 50 m/s}{2}\sqrt{\frac{1.5s}{400 \pm 50 s^{-1}}} \approx 54 \pm 7m \quad \textbf{sparker}$$

$$r = \frac{v}{2}\sqrt{\frac{t}{f}} = \frac{1750 \pm 50 m/s}{2}\sqrt{\frac{1.5s}{250 \pm 50 s^{-1}}} \approx 68 \pm 7m \quad \textbf{water gun}$$

3.1.2 Vertical resolution

Vertical resolution can be defined as the closest vertical spacing of two reflectors allowing their identification as independent events. In general, this depends on the wavelength, which is a function of the dominant frequency and velocity. For a sonic velocity of 1700 m/s ±50 m/s and a dominant frequency of 600±50Hz for the sparker and 350±50Hz for the water gun, the dominant wavelength is:

$$\lambda = \frac{v}{f} = \frac{1700 \pm 50 m/s}{600 \pm 50 Hz} \approx 2.8 \pm 0.5 m \quad \textbf{sparker}$$

$$\lambda = \frac{v}{f} = \frac{1700 \pm 50 m/s}{350 \pm 50 Hz} \approx 4.8 \pm 0.5 m \quad \textbf{water gun}$$

The distance defines the tuning thickness, which is the minimum distance between two layers to be distinguished. In general, the vertical resolution is considered to be ranging from ?/3 to ?/8. For the sparker data with a dominant wavelength of 3 m and 5 m of the water gun, the expected resolution will be between **0.4-1 m** and **0.6-1.7 m** respectively. As depth increases, the resolution will decrease due to the preferential loss of high frequencies and the increase of velocity.

3.1.3 Scattering near the seabed

On some locations of the seismic profiles, the reflectors loose their coherence and form almost acoustic transparent areas. One of the best examples has been found in the Belgica mound province; more exactly on the first recordings of Thérèse mound (BEL35) (Fig. 3.4).

- The scattering near the seafloor on seismic profiles can be due to phenomena like seeping of fluids. These fluids can be gassy or mixtures of gas and water, which absorb energy, producing the acoustic blanking as seen in 2.2.

- The roughness of the seabed can invoke scattering of the waves and results in a significant loss of energy.

A quantitative expression is given by Urick (1982):

$$R.C._s = R.C. \times e^{-\left(\frac{4\pi h \sin\theta}{\lambda}\right)^2} = R.C. \times e^{-\left(\frac{4\pi \times 1m \times \sin 90}{3m}\right)} = R.C \times 0.015$$

The reflection coefficient RC depends on the density, compressibility, rigidity, absorption and layering of the seabed materials, while the exponential term depends on the roughness characteristics of the seabed and the angle of incident. We consider e.g. a mound structure with on the surface a large amount of benthic fauna (e.g.. corals, molluscs, etc.), creating a framework of approximately 1 m of thickness, shaping roughness on the seabed. If all the parameters are inserted and a wavelength of 3 m is used for the sparker data, the reflection coefficient is reduced to 1.5% of the normal coefficient for a smooth seafloor. This process might explain the loss of energy and the acoustic facies of a few mounds.

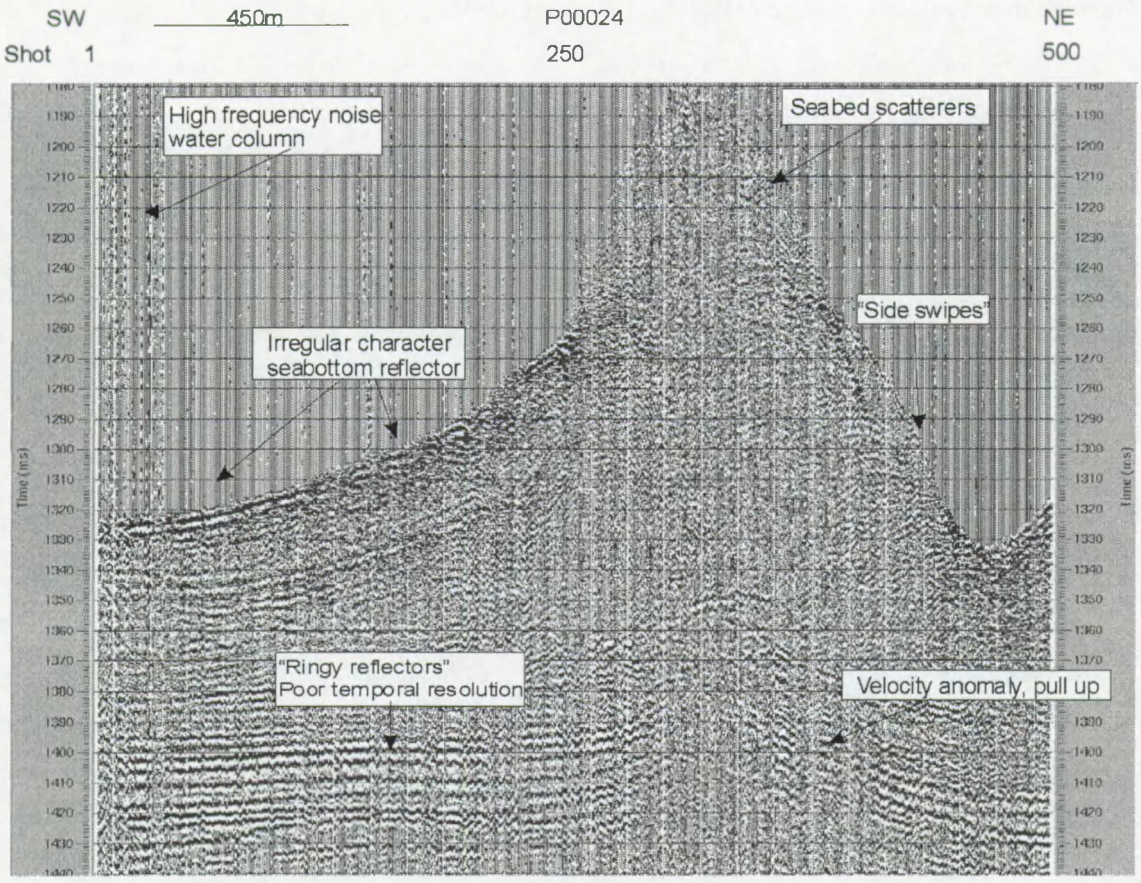

Fig. 3.4: The different noise factors and artifacts on the seismic profiles such as ringing reflectors; swell noise disrupting the horizontal continuity of reflectors, side echoes, diffraction hyperbolae, high frequency noise near the seabotttom, seabed scattering, velocity pull-ups (Galanes-Alvarez, 2001).

3.1.4 Velocity pull-ups below the mounds

Underneath some mound structures a pull-up of reflectors can be observed. Velocity pull-ups occur when units of lower seismic velocity surround a seismic unit with higher seismic velocity (Fig. 3.4). The pull-up underneath has two reasons:

(1) the mound forms a sharply limited elevated structure with respect to the surrounding seafloor. This means that from the reference level (sea level) more water is crossed till the seabed above the surrounding seafloor than above a mound. For a certain reflector underneath the mound the travel time is longer in the water column than in the sediment. For this reason the reflections underneath the mound arrive earlier.

(2) This cannot explain the entire velocity pull-up. What suggests that the velocity inside many mounds is higher than in the surrounding sediments.

Because no direct data is available about the sonic velocity in the mound structures, only a relatively difference between the velocities inside and outside the mound accounting for the difference in arrival times can be calculated for a same depth on the profile.

3.1.5 Processing of seismic data

The raw data contained many types of noise, analyzed in the MSc thesis of Galanes-Alvarez (2001) on profiles in the Belgica mound province (Fig. 3.4). Because the acquisition parameters are not different for the other provinces, similar artefacts and noise-effects have been observed in the seismic lines of the Hovland and Magellan mound province. The seismic data have been processed with a Landmark ProMAX™ 2D 8.0 "98 release". The processing flow used for all the seismic lines is schematically represented in the left panel of figure 3.5.

- To increase the continuity of the reflection in the data and reduce the irregular character of the seabottom reflector, the swell has been removed of the seismic profiles using a filter. This "swell" filter is applied to the profiles in detail grids and a few key profiles in the Hovland mound province. Due to the intensive computer calculation and time consuming process (more than 22hours for a 2500 shot) it was not opportune to apply this filter on the entire data set. The swell filter consists of several processing steps as shown in figure 3.5, which are explained in more details in Galanes-Alvarez (2001).

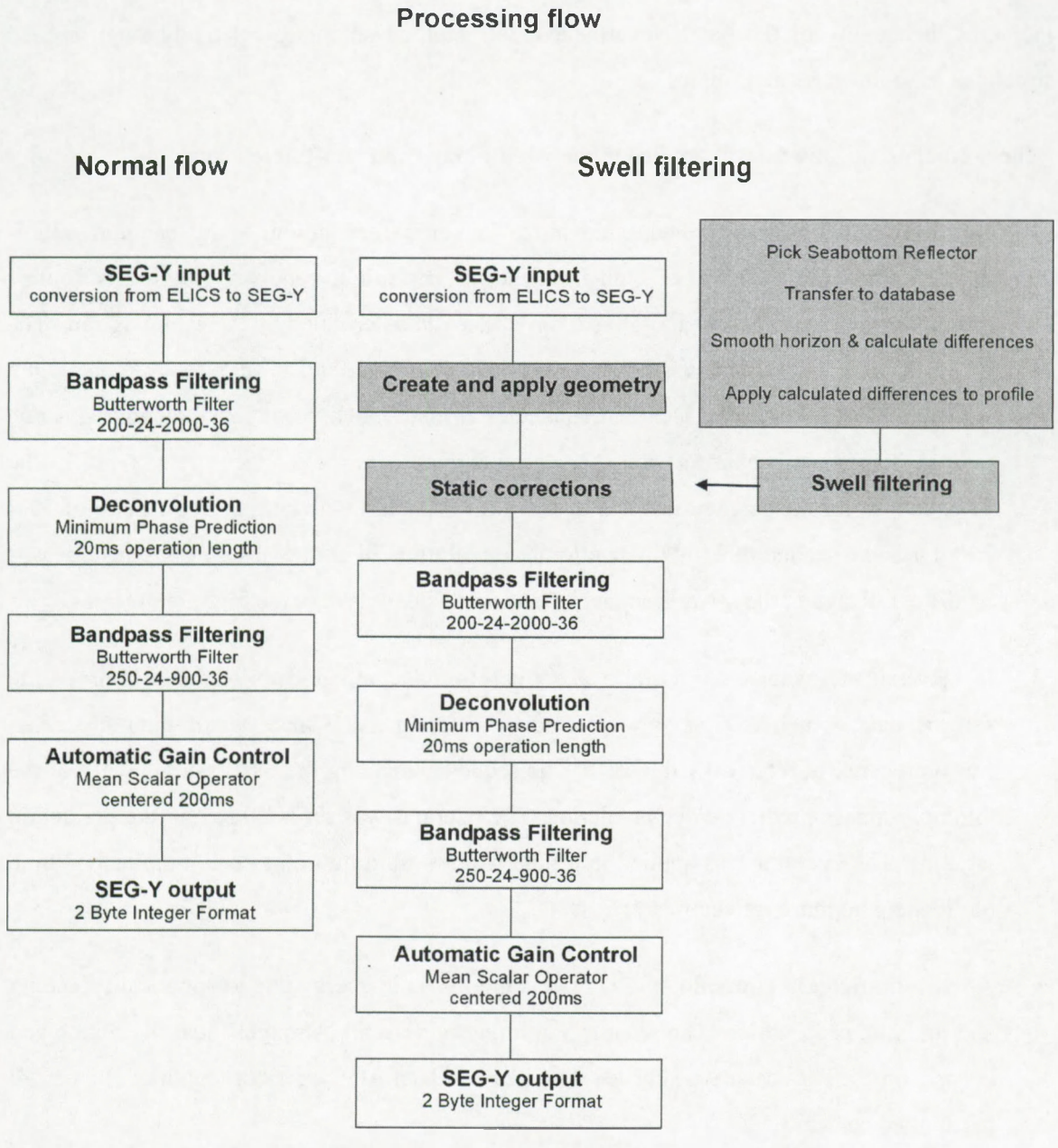

Fig. 3.5: Processing flow for 2D high-resolution seismic profiles.

A first step in the filtering is creating an arbitrary geometry of the seismic profile in order to be able to manipulate the databases and to have a reference for the position of the traces. The geometry of the single channel seismics is calculated out of the total number of shots, shot intervals and the vessel speed. A second step is to calculate the differences between the actual position and the position where the trace should be. The seabed horizon is picked in all traces. Then averaging the relative position of the adjacent traces is followed by calculation of the difference between the averaged value and the original. Finally, this difference is applied as a static correction to the trace (Galanes-Alvarez, 2001). This gives a very satisfactory result and

increases the quality of the data. Nevertheless, this method smoothes relatively small seabed structures as sand waves and ripples.

The normal processing filter is applied to the swell filtered and non-filtered data.

- **Bandpass filtering** was applied to maximize the vertical resolution. A high sampling rate is used to allow the recovery of high frequencies. The initial bandpass filtering is applied during the acquisition as an anti-alias filter, automatic determined by the sampling rate. The range of frequencies of the sparker is between 250 and 900Hz, and for the water gun between 0 and 600Hz. The lack of frequencies around 700Hz for the sparker source is due to a ghost present because of the sparker immersion depth. (Versteeg, pers comm.). The filter chosen for the sparker data is a butterworth bandpass with cutting frequencies of 200-2000Hz and a second of 250-900Hz after deconvolution. In both cases the chosen slope was 24 dB per octave in the lower frequencies and 36dB per octave in the high frequencies.

- In between the bandpass filtering a **deconvolution** is applied. This step can improve the seismic data, which is adversely affected by filtering and which occurs naturally when seismic energy is filtered by the earth. The sequence offering the best results involves the minimum phase predictive deconvolution. The operator was set at 20ms and the prediction lag 2ms. The operator was applied in a time window starting at the seabottom arrival time until where no more reflectors are present.

- An **automatic gain control** (AGC) corrects the losses in energy due to spherical spreading and inelastic propagation. The seismic amplitudes are usually strongest near the source and at early times. The scalar type chosen was Mean with an AGC operator length of 200 or 250 ms applied centered.

For the water gun data a similar processing flow is made with slightly different parameters. Only the bandpass filtering is changed to 70-300Hz.

3.1.6 *Interpretation of seismic profiles*

After processing, the profiles are loaded together with the navigation in an interpretation system of Landmark: the Geographix discovery^{tm} suite. The reflectors have been picked and mapped with the Seisvision module. The same reflectors or horizons were followed from section to section using the intersections of lines. Below the mounds and in the vicinity of the mounds, it is

frequently hard to correlate the reflectors from line to line. Where possible the reflectors have been mapped from section to section till the other side of the same profile. According to the reflectors terminations, patterns and acoustic facies have been grouped in series and units according to the principles of seismic stratigraphy.

Gridding of the picked horizons was applied with the Geoatlas tool of the Discovery suite. With the Geoatlas tool, time maps have been created to show the lateral extension of each horizon. This tool is also used for interactive mapping of the gathered information and to create the final maps. Cores and the mounds have been positioned in Wellbase and plotted as a well layer. The Seisbase is used as a database with all information of the seismics and sidescan sonar data.

The seismic profiles have first been used to map the mound structures and to deduce the geometry of the mounds, moats and discordance horizons and pockmarks. Out of the stratigraphic units and patterns, the recent geological history of the area has been deducted as well as ways in which the mounds can interact with the surrounding sediments.

3.2 Sidescan sonar

During the TTR7 and TTR8 CORSAIRES cruises (Kenyon et al., 1998; Kenyon et al., 1999), 127 km of sidescan sonographs have been recorded: 80 km in the Hovland-Magellan mound province and approximately 47 km in the Belgica mound province. The OREtech system was operated at 30 kHz and towed about 130 m above the seafloor during the TTR7 cruise. The seabed has been imaged over 1 km at either side of the track line with a resolution of 0.4 m.

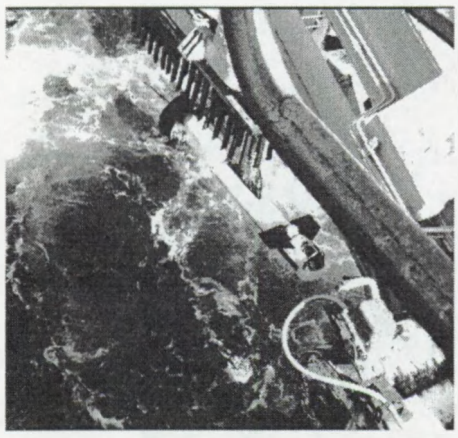

Fig. 3.6: OREtech sidescan sonar fish on RV Logachev operated during the TTR7-CORSAIRES cruise.

For the sonographs recorded during the TTR8 cruise, the OREtech sidescan sonar operated with a frequency of 100 kHz. The swath on either side of that nadir line is 500 m and the resolution is 0.2 m. The processing of the sidescan sonar data has been done by Moscow State University (Pavel Shashkin).

3.3 Echosounding

During the Poseidon 265 cruise in September 2000, a detailed grid of echosounding lines have been sailed in the Hovland mound province. The navigation of these lines was made on the shipboard GPS and a 30 kHz echosounder. The entire XYZ data set gathered in the area is included in the grid. The depth of the first (bottom) echo was stored in the ships automated recording system. The bathymetry data was stored every 10 seconds. This data has to be corrected for false bottom detections due to side echoes in areas with highly variable bottom relief. This echosounding data has been loaded in Geoatlas for further mapping.

3.4 Multi beam

During the Polarstern cruise ANTXVII/4 in June 2000, a multi beam map is made by the Alfred Wegner Institute Bremerhaven. After processing, this map has been kindly made available as a map with a 100m-grid spacing. The data has been inserted in Geoatlas and used as a map in the central Belgica mound province.

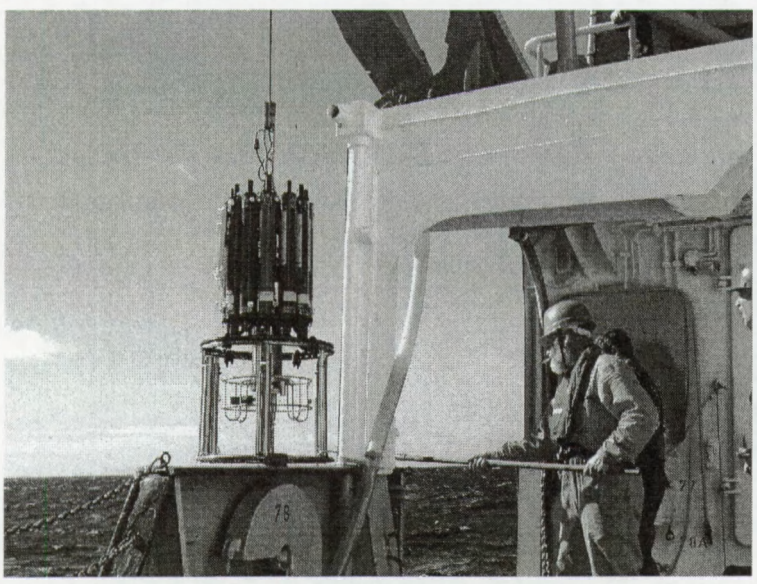

Fig. 3.7: CTD deployment during the Poseidon 265 cruise (September 2000) (photo: Andre Freiwald).

3.5 Oceanographic data or CTD profiles

CTD profiles have been gathered during the Poseidon 265 cruise using a General Oceanics Neil Brown Mark III CTD, equipped with a 12-bottled rosette, but without extra sensors except a bottom trip indicator (Fig. 3.7). The raw data have been analyzed and plotted with Ocean Data View (Schlitzer, 2001). In the Belgica mound province, one CTD has been collected. In the Hovland mound province a detailed CTD transect of 13 CTD profiles has been made around the Hovland mound HOV02 (Freiwald et al., 2000). Two CTD profiles have been collected during ANTXVII/4 with the R/V Polarstern with a Seacat profile SBE 19 CTD in the Belgica mound province.

Shallow cores

Shallow cores and core data have been collected from different sources. All shallow cores are summarized in tables per mound province in the specific chapters.

3.6.1 Training Through Research Programme (UNESCO-IOC)-CORSAIRES-ENAM (EC MAST 3 programme)

During the TTR7 cruise, a total of 25 gravity cores, with a recovery of 1 to 4 m, were taken at the top and flanks of several mounds and in the adjacent moats and sediment (Kenyon et al, 1998). In addition, two dredges and a TV-controlled grab have been taken in the Hovland mound province. In the Belgica mound province a TV-controlled grab sample has been taken to sample the general fauna. In total 14 gravity cores have been taken in the Hovland mound province and 11 in the Belgica mound province. In table Appendix C1 and F1 the identification name, location, water depth, recovery, target structure and brief description have been listed for each province.

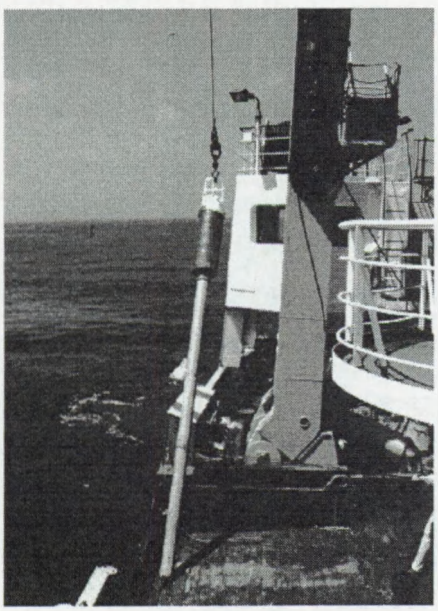

Fig. 3.8: Gravity corer used during the TTR7 and TTR8 cruise.

The gravity core used has a length of 6 m and a weight of approximately 800 kg with an outer diameter of 146 mm, and an inner diameter of 133 mm (Fig. 3.8). The samples were retrieved on deck during the TTR7 cruise. Therefore the gravity corer was laid on its side and the core catcher removed. Then the plastic liner inside got removed and the

sediments extruded. The extruded sediments were cut in sections of 60cm. These sections were cut into 2 halves using a wire and knives. One halve is used for sampling while the other half is cut in 2 pieces whereby one quarter was sent to Moscow State University and the other half was given to the CORSAIRES consortium (Kenyon et al., 1998).

During the TTR8, two gravity cores have been taken on the top of a mound in the Hovland mound province (HOV02) and two on top of a Belgica mound (BEL41). One of each set has been treated as described above for the TTR7 cores. The other part of the set has been kept in the liner and cut in pieces of 1 m and shipped to Belgium. First, these cores have been scanned with a medical X-ray computer tomography system at the University hospital of Leuven, Gasthuisberg. The core taken on top of the Hovland mound was full of corals and has been frozen before cutting with a diamond saw in two half's. One half has been stored and the other has been used for subsampling.

Besides gravity cores, also box cores have been collected during TTR8. The dimension of the box corer is 50x50x50 cm. It allows obtaining undisturbed samples from the seafloor, weighting approximately 185 kg. Only the upper sediment layer can be recovered. Two cores have been taken in the Belgica mound province. These box cores have been analysed in a MSc thesis for the macro benthos diversity and distribution at the Marine Biology unit of the University Ghent (De Bergé, 2000). Eight box cores have been taken in the Magellan mound province in the framework of an engineering survey. This engineering survey showed typical sedimentation of pelagic sediments without any anomaly (Kenyon et al., 1999).

Additionally, two dredge samples and two TV-controlled grab samples have been taken during TTR7. The dredging has been carried out with a 75 cm diameter dredge with a length of 60 cm and wall thickness of 1.5 cm. The weight of the dredge is 200kg and it is towed using a 250 kg depressor fixed on the cable at 1 m from the dredge. Teeth are present at the mouth of the dredge to scrape hard surfaces. There is a net on the bottom for preventing the loss of small clasts. Two crests of Hovland mounds have been sampled, i.e. HOV10 and HOV12.

Two controlled grab samples have been taken on the crest of two mounds. The GTVS-2 TV controlled grab sampler system consists of two principle parts: the grab module and the onboard control unit with monitor and videotape. The grab module is fitted with a monochrome TV camera and four flood lights, which allow selection of the sampling site by the operator. Six hydraulic arms, tipped by hard wearing steel, form an onion shaped hollow body when closed. To

perform closing, each arm is equipped with a hydraulic cylinder. The grab can recover a volume of 1.1 m^3 seabed sediments. The position of the grab, relatively to the ship, is determined by a Sigma 1000 underwater navigation system. One grab sample has been taken on a Hovland mound (HOV10) and another one on a Belgica mound (BEL42). The dredges and grab samples have been used to get a general impression of the benthos fauna on the mounds (Kenyon et al., 1998).

3.6.2 Belgica

During the Belgica cruise of 2000 (Belgica 00/13) box core samples have been taken for analysis of the meiobenthos. This was performed by a Dutch type box corer with a diameter of 32 cm. Four box core samples have been taken close to the crests of BEL35 and BEL32. These samples have been used in a biodiversity study of macrofauna associated with the mounds in the Belgica mound province in the department of Marine Biology of the University Ghent (Van Gaever, 2001).

3.6.3 Pelagia

During the Pelagia cruise M2000 (64PE165) (de Haas et al., 2000), biological sampling has been done with a 600 kg cylindrical box corer with a diameter of 50 cm and a maximum penetration depth of 55 cm. The box corer is equipped with a lid on top that closes at the moment of retrieval, to retain the overlying bottom water and to obtain rather undisturbed core sample. These samples have also been used in the MSc study of Van Gaever (2001) about the biodiversity of the mounds.

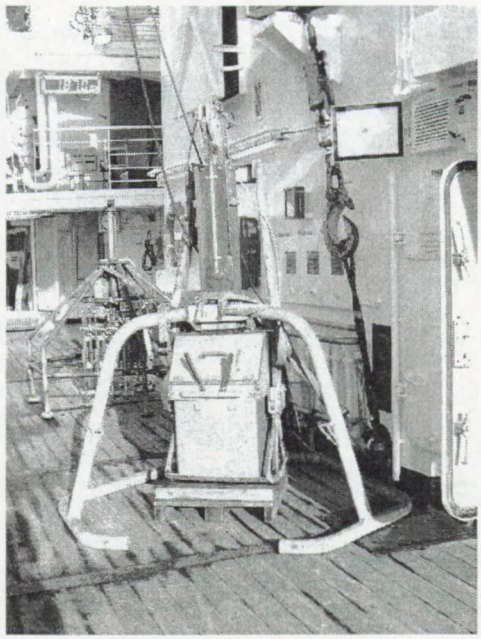

Fig. 3.9: Box corer used during the Poseidon cruise 265.

Piston cores have been taken with the NIOZ piston corer, with a corer head weight of 1500 kg and a 6 or 12 m long core barrel with a 9 cm inner diameter liner. Sections of 110 cm (or less) were cut on deck, capped and labelled. The downcore magnetic susceptibility was measured using a 12 cm diameter Bartington MS2 magnetic susceptibility sensor.

This core data has been used in a MSc thesis of Wim Lekens (Lekens, 2000). Grain size analysis and geochemistry provided information about the sediments around the mound.

3.6.4 Poseidon

The box corer used during the Poseidon cruise 265 (September 2000) has a sampling area of 50x50x50 cm (Fig. 3.9). It has been used at 14 stations (Freiwald et al., 2000). The core recovery was variable due to the nature of the sampled material. The box cores have been used for biological studies done by the teams of the Institute of Geosciences, Tübingen University and the Marine Biology Unit of the University of Ghent (Van Gaever, 2001). The data and descriptions are used for a general overview of the coral distribution and sediment occurrences.

3.6.5 Petroleum Affairs Division Ireland cores

A data set of a shallow coring (3 m-gravity cores) geochemical survey in the Hovland mound province was kindly provided by Petroleum Affairs Division (PAD), Ireland (Peter Croker). Four on-mound cores of this survey have been described and sampled during a visit in PAD Dublin. Two cores (one on-mound and one off-mound) kept in the liner have been taken to Belgium for further investigation. The cores have been sampled during the survey for gas analysis. The samples for gas analyses were not frozen. These samples are used for carbon and oxygen isotopic analyses of methane gas, in view of the determination of the origin of the methane gas (thermogenic or biological). Absorbed gas and total gas content have been determined, considering their role on the carbon isotopic composition of the analyzed methane gas. These cores have been used in the general sediment description of the Hovland mound province and used for geochemical interpretations.

3.6.6 Statoil cores

Statoil Exploration Ireland Ltd has provided a second geochemical data set. This set includes brief core descriptions and geochemical analyses of 140 3 m-gravity cores in the Hovland and Magellan mound province, taken with the SGS vessel R/V Geoboy in 1996. Subsamples were taken in each core, one in the bottom section (A) and one at 1.5 m (section B). 266 samples have been canned and 269 bagged and analysed by SGS in Trondheim, Norway. All samples were frozen at a temperature of -80° C to preserve the absorbed and interstitial gas in the sediments during the transit of the study area to the laboratory. Unfortunately, the majority of the remaining material has been thrown overboard and only some of the bagged samples were left. These

samples have been investigated and described at the core store place in Dublin of CSA Group with the permission of Statoil Exploration Ireland Ltd. (Geirr Haarr). Seven of the samples with the highest potential for gas or on mound samples have been selected and subsampled for mineralogical and additional geochemical analysis. The analysis of the samples carried out by SGS is described below:

- Headspace gas analysis on 266 canned samples
- 90 samples with relatively high headspace gas concentrations have been selected for interstitial gas analysis
- Gas Chromatography (GC): 269 samples extracted
- Total Scanning Fluorescence (TSF): 89 of the GC extracted evaluated
- Gas Chromatography-Mass Spectrometry 30 carried out on a subset of the GC/TSF samples
- Isotopic analysis of carbonates on/near mounds on 5 samples

On a small number of samples, apparently containing abundant mineral carbonate, analyses have been carried out to attempt to identify the presence of carbonate minerals produced by bacterial oxidation of seeping hydrocarbons (authigenic?). The carbonate fraction was characterized with $\delta^{13}C$ and $\delta^{18}O$. The entire report including the analytical techniques is under license of PAD Ireland (internal report: Statoil Seabed Coring, Porcupine License 8/95, offshore Ireland 1996, report No 6096/7).

Two approaches have been taken in the interpretation of the analytical data. The first is based on the search of anomalies in methane content, in the sum of C_2 to C_6 alkanes and in the sum of cyclic alkanes.

The second approach is to look for geographical clustering within the data. This data set has been reinterpreted and used together with the other data. Additional samples have been taken from the samples with a high gas content, looking for characteristics in the mineralogy.

3.7 Underwater TV profiler

An underwater TV survey of the seabed in the Hovland mound province has been carried out from 52.186° N, 12.752° W to 52.116° N, 12.788° W covering HOV10 and HOV02. A second line has been sailed in the Belgica mound province: from 51.467° N, 11.704° W to 51.397° N, 11.703° W covering the mounds: BEL37, BEL41, and BEL42. The photo and television system (FTA) is a towed construction with an open-frame shape based on an OREtech design. It contains deep-sea boxes with electronic equipment such as TV cameras, lights and flashes, external storage batteries from the "Benthos" deep-sea photo system as well as an echosounder and built-in navigation system (SYGMA), which are attached to the frame. FTA is towed 2-8 m above the seabed. Video recording is carried out in both discrete and continuous modes, either together or separately. The high sensitive colour TV camera CCS-5 and the video recorder BR-6200, which are installed in the electronic equipment box, carry out the continuous record. The profiles have been interpreted by the Marine Biology unit of the University of Ghent in a MSc Thesis (De Bergé, 2000). This data is than reinterpreted together with bathymetry data and subbottom samples.

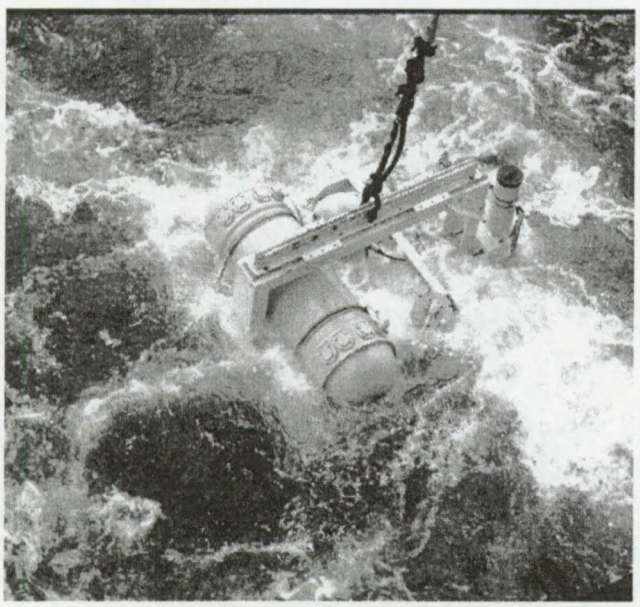

Fig. 3.10: OREtech photo and television system used during the TTR7 cruise.

4. Belgica mound province

87

4.1 Introduction 89

4.2 Mapping of the Belgica mounds 91
4.2.1 General bathymetry 92
4.2.2 Distribution of the mounds 96
4.2.2.1 General water depth mound analysis 96
4.2.2.2 Water depth - mound type 97
4.2.2.3 Water depth - mound - zone relation 98

4.3 Geometry of the Belgica mounds 101
4.3.1 General geometry per mound type 104
4.3.1.1 Width 104
4.3.1.2 Height 105
4.3.2 Mound shape in plan view 110
4.3.2.1 EW profiles 110
4.3.2.2 NS profiles 111
4.3.2.3 General plan view of the mounds 111
4.3.2.4 Detailed plan view shape of the surface mounds 112
4.3.2.5 Mound area 115
4.3.3 Summary 115

4.4 Geological record 117
4.4.1 Unconformities 117
4.4.1.1 Mound base 119
4.4.2 Facies description 122
4.4.2.1 Facies Ba 122
4.4.2.2 Facies Bb 122
4.4.2.3 Facies Bc 126
4.4.2.4 Facies Bd 128
4.4.2.5 Mound substratum 131
4.4.2.6 Facies Be 132

4.5 Seismic properties of the mounds 137

4.6 Case studies 141
4.6.1 BEL26, Challenger mound 141
4.6.1.1 Bathymetry 141
4.6.1.2 Geometry 142
4.6.1.3 Geology 144
4.6.2 BEL35 - Thérèse mound and friends 146
4.6.2.1 Bathymetry 146
4.6.2.2 Geometry 147
4.6.2.3 Geology 151

4.7 Sidescan sonar images 155
4.7.1 Northern zone 157
4.7.2 Southern part 161

4.8 Sedimentology 165
4.8.1 Off-mound sediment samples 165
4.8.1.1 Sandwaves field 165
4.8.1.1 NS channel 167
4.8.2 Near-mound sediment samples 167
4.8.3 On-mound sediment samples 168
4.8.3.1 Southern Belgica mound province 168
4.8.3.2 Central Belgica mound province 172
4.8.4 Grain size analysis 174
4.8.4.1 Paleoclimatology 176
4.8.5 Mineralogy 182
4.8.6 Contourites 186

4.9 Biological results 189
4.9.1 Biological zonation 189
4.9.1. Description of the video transect 192
4.9.2 Biodiversity on the mounds 193
4.9.2. General observations 194
4.9.2. Microhabitats 196

4.10 Oceanography 199

4.1 Introduction

The Belgica mound province is situated on the eastern flank of the continental slope, north of the Gollum Channel system, between 51°10'N - 51°35'N and 11°30'W-11°45'W in water depths from 550 m to 1025 m (Fig. 4.1). The Belgica mounds are named after the oceanographic research vessel R/V Belgica, which discovered the mounds during a survey in May 1997. The occurrence of high concentrations of cold-water corals (e.g. *Madrepora*, *Lophelia*) on the eastern continental slope of the Porcupine Basin has earlier been described by Thomson (1873) and Le Danois (1948) who, however, did not recognize the coral banks as such. The Belgica mounds are outcropping or buried conical mounds (single, or in elongated clusters). The province has an elongated shape with an overall length of 45 km and a maximum width of 10 km.

This chapter includes seismic, sidescan sonar and multi beam data to describe the mound geometry and the surrounding geology. Furthermore, oceanographic and biological data have been discussed to get a general picture of the ongoing processes in the Belgica mound province.

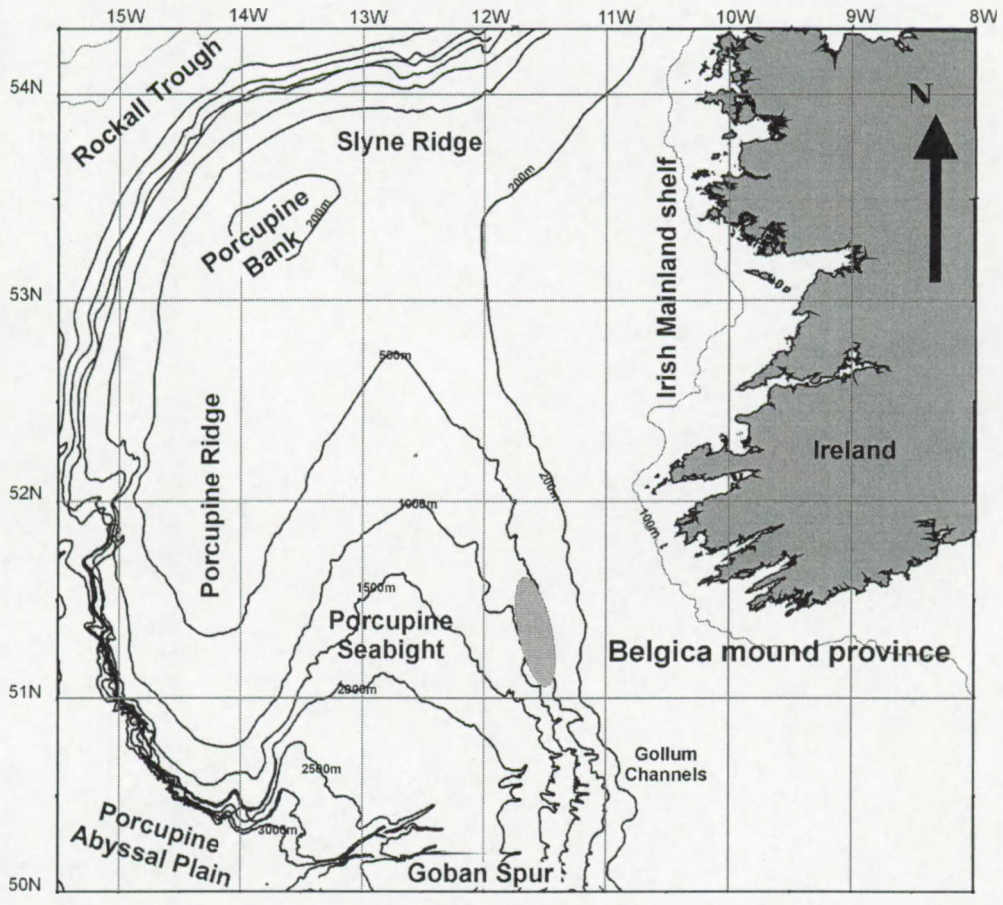

Fig. 4.1: Location map of the Belgica mound province.

4.2 Mapping of the Belgica mounds

The mapping of the mounds is based on 2D high-resolution seismic (Fig. 4.2), sidescan sonar and multi beam data. All the available data, imaging the mounds and their position, have been brought together in a database (Table A.1). In this database the mound number, mound type, available data and mound location in geographic and UTM coordinates have been provided. The highest point or the crest of the mound on the seismic profiles is used for locating of the mound. For the mounds covered with multi beam bathymetry, the apex has been corrected if the seismic profiles did not cross the real crest of the mound.

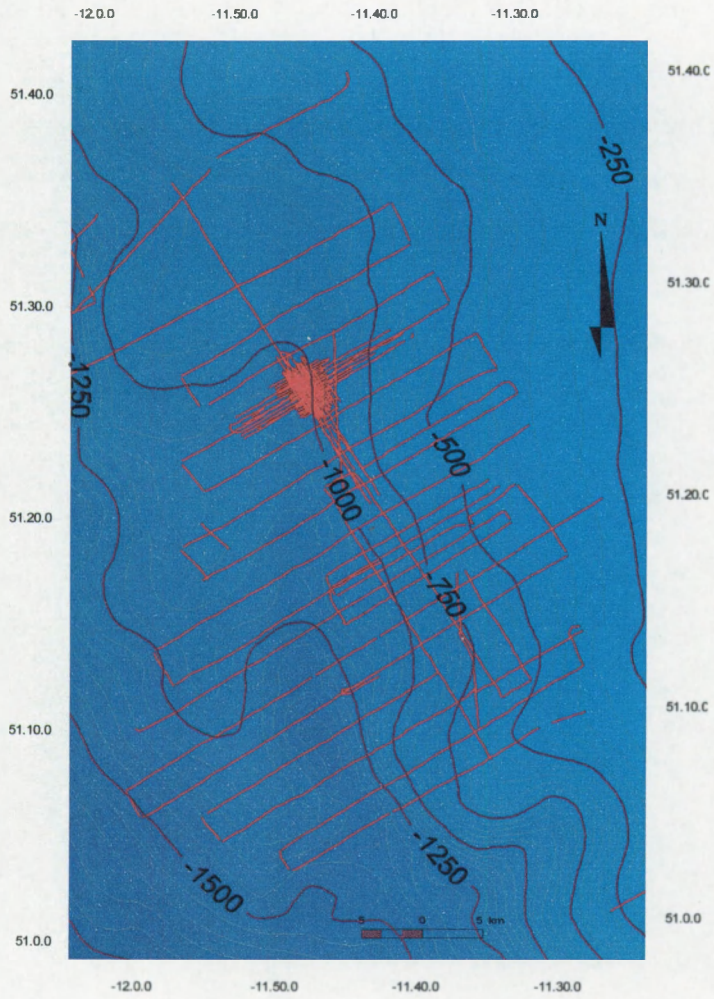

Fig. 4.2: Available high-resolution seismic profiles in the Belgica mound province (RCMG).

A second part of the database illustrates the geometric parameters per mound (see Appendix A). In this list the measured width and height per seismic profile has provided besides the sediment cover above the crest of the mound, the maximum width and height on the profiles and the length ratio between sections on NS and EW profiles. This data is only measured on the seismic profiles because this gives a more faithful mound shape than the surface methods multi beam and sidescan sonar.

The multi beam and sidescan data show the surface expressions of the mounds, which do not always mirror the real shape, due to sedimentation on the flanks. Nevertheless, the sidescan sonar images and multi beam map show clearly the general trend of the mounds and their distribution. The combination of all acoustic techniques

allows analyzing the mounds in a general bathymetric framework. This data set covers 48 of 64 mounds (74%), or 26 surface mounds (SM) and 22 buried mounds (BM).

4.2.1 General bathymetry

A general bathymetric map has been made based on seafloor information from seismic profiles and a selection of multi beam data, the latter made available by AWI Bremerhaven. The highest points of the mounds have been plotted on this map (with a diameter of 800 m) to study the general depth distribution (Fig. 4.3).

Two mound types have been recognized on the seismic profiles: surface mounds (SM) or mounds with a surface expression and buried mounds (BM), which are covered with sediments on the crest of the mounds and which are only seen on the seismic profiles.

Some of the buried mounds have only been imaged on one seismic profile, which does not exclude that these mounds have a surface expression. At least all listed mounds have been crosschecked on the multi beam data. If no surface expression is observed, they have been catalogued as buried mounds.

In total 64 mounds have been recognized in the Belgica mound province. Of this set 48 mounds have been recorded on seismic profiles and 39 on multi beam. 18 surface mounds have only been observed on multi beam.

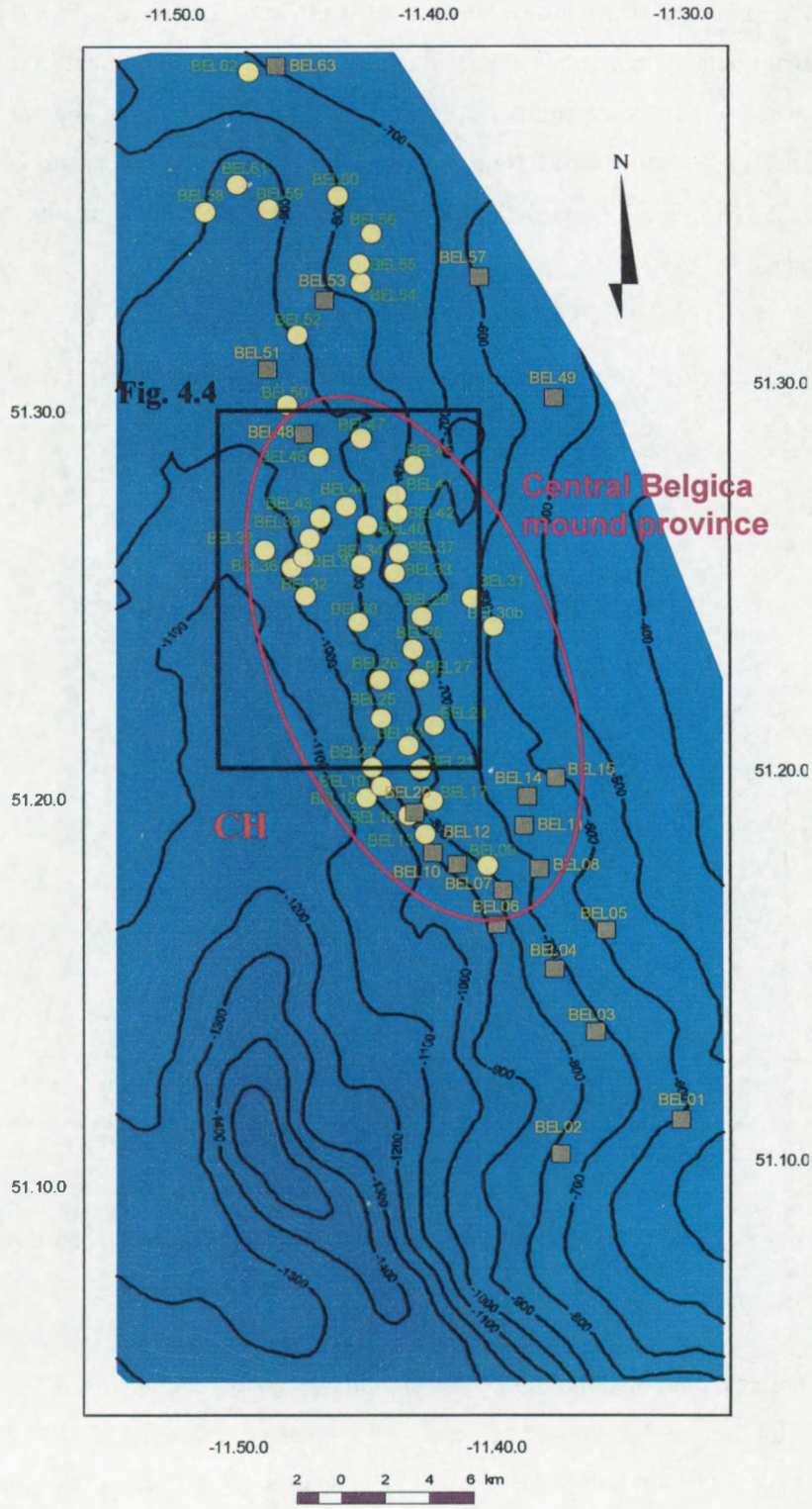

Fig. 4.3: A bathymetric map with the mound locations based on multi beam, seismic and GEBCO data. The squares refer to buried mounds, the dots to surface mounds. The mound number refers to the database (Appendix A.1). CH indicates a NS trending channel bounding the province in the west.

The surface expression of the **mounds** is the most obvious feature recognized on the sonographs and multi beam data. The mounds appear on sonographs as high backscatter (black) patches with large shadows (white) away from the beam (see Appendix C). On the multi beam map the mounds appear as steep sloped topographic heights. Out of the multi beam map and the sonographs, 2 NNE-SSW ranges of mounds have been recognized in the central part of the mound province (Fig. 4.3).

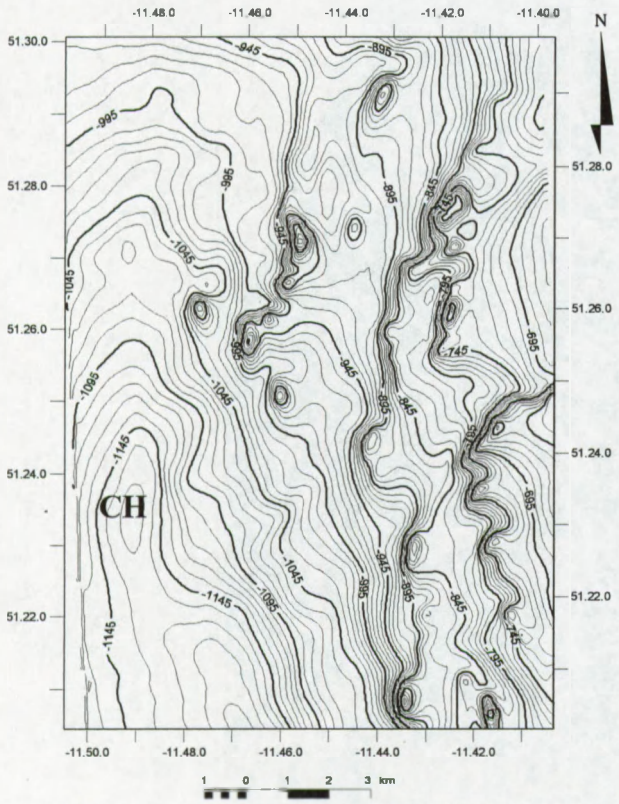

Fig. 4.4a: Multi beam map of a selected area in the Belgica mound province. The mounds are lined up along two NNE-SSW ridges intercepted by downslope channels (source: AWI Bremerhaven).

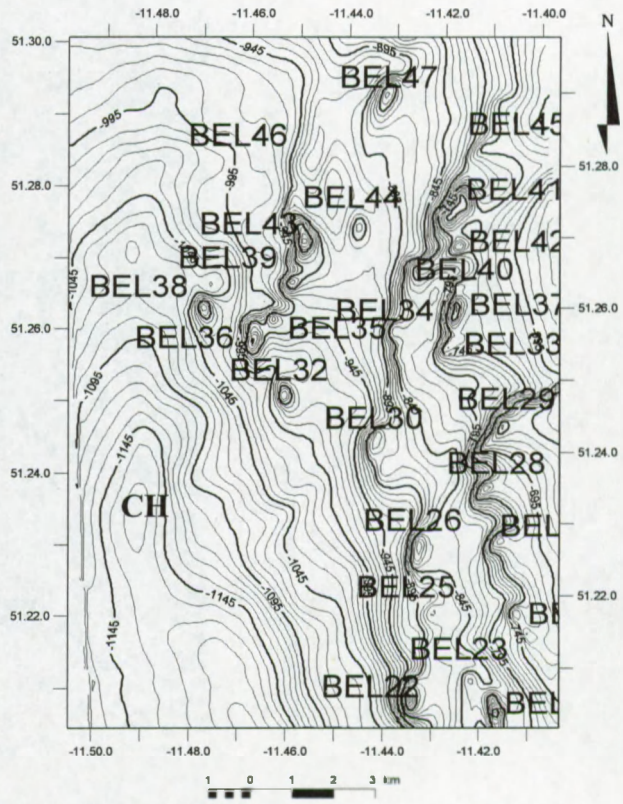

Fig. 4.4b: Multi beam bathymetric map with mound database numbers (source: AWI Bremerhaven).

The most eastern and upslope range of mounds is seated at one of the steep parts of the continental slope around 750m water depth. This break in the slope seems to be formed by the mounds and partly by underlying structures. The seafloor has a low slope gradient between the mound ranges and on the eastern side of the mounds. This coincides with a zone where sediments get trapped between the continental slope and the mounds or between two mounds aligned in a downslope direction (E-W direction). The western side of the mounds has not been covered with

sediments and is generally steeper. This results in a kind of terrace-like profile of the slope in E-W direction.

The steep slopes of the western side display a strong backscattering on the sonographs (see Appendix C and Fig. 4.4). The eastern side of the mounds mostly feature a shadowing effect if the beam of the sidescan sonar was on the western side, or a uniform backscattering, representing a flat zone, if the beam was on the eastern side. The mounds in this zone mostly show a NNE-SSW elongation in their surface expression and build a sequence of summits oriented in a NE-SW direction. On the sonographs the mounds have a surface expression between 2 and 4 km in length, and a width of 0.5 to 1 km. The height above the seafloor of the mounds is up to 150 m.

The continental slope in the Belgica mound province is characterized by downslope channels (Fig. 4.3 and 4.4). Most channels have an E-W orientation but in the vicinity of the mounds they change direction, more northwards or southwards. Some of the channels have a connection to more upslope channels; others are only expressed around the mounds, probably due to local turbulence. Some mounds appear on the flanks of the downslope channels and follow the channel orientation (Fig. 4.4).

Further to the west and downslope, a range of smaller mounds is located around 950 m water depth in a less steep zone and closer to the center of the N-S trending furrow (**CH**) (Fig. 4.3 and Fig. 4.4). This N-S trending depression in the continental slope acts as a break between 900 m and 1500 m water depth. The mounds located on the lower flanks of the furrow are less complex in geometry (single mounds with a N-S orientation) (Fig. 4.4).

In the deepest part of CH, the mounds have a NNW-SSE orientation. These mounds have a diameter from 200 to 700 m. Depressions have been observed around the flanks of the mounds, but they are less expressed than in the eastern range. Compared with the more upslope mounds, these mounds have a steeper slope to the west. Nevertheless, the mounds in the north at this depth level have steeps flanks on either side. In between the two mound ranges the seabed is smooth, with low slope gradients.

Out of the bathymetric analysis it is clear that there is a close relationship between the NS furrow (CH) and the mounds. Most of the mounds are located on the steeper flank of the furrow and are less dense where the flanks of CH get smoother. The mounds show a more complex shape on the steeper flanks than on the smooth zones.

4.2.2 Distribution of the mounds

The different types of mounds in the Belgica mound province can be subdivided in three major geographical areas. This subdivision has been made to illustrate that surface mounds are for 86% located in a narrow zone in the center of the province. The northern and southern areas of the province seem to act as transition zones to the normal seafloor and contain almost exclusively buried mounds (50% of the total population). The surface mounds in these two extremities are generally smaller than in the central zone. The northern area includes the mounds with database number BEL01-BEL05, the central and largest part BEL06-BEL48 and the northern part BEL 49-BEL63 (Fig. 4.3).

4.2.2.1 General water depth mound analysis

The present-day water depth zone of the mounds ranges between 522 and 1017 m (see Appendix A.1 and Table A.2.1). The mean water depth of the mounds is 790 ± 14 m. The 95% confidence range is only 57 m, between 762m and 819 m. This range of values, based on the sample mean, includes a population mean with a likelihood of 95%. The standard deviation of this analysis is 112 m. These statistic parameters show that most of the mounds occur in a narrow depth range around 800 m. Nevertheless, the total bathymetric range of the Belgica mounds is almost 500 m (495 m). A few mounds are located in the periphery (Table A.2.1). For the general depth analysis the skewness is negative, which means that most of the mounds cluster around greater depths and only a few appear in shallow depths. The stem-leaf diagram illustrates the wide range of data points, as well as the mean and the asymmetry of the data (Fig. 4.5).

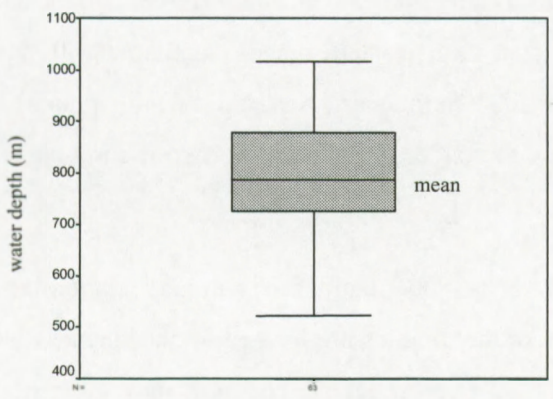

Fig. 4.5: Stem-and-leaf diagram of the overall mound water depth relation. The grey box indicates the 95% confidence and the stem data distribution.

4.2.2.2 *Water depth - mound type*

The **buried mounds** (BM) have a large water depth distribution. The mean water depth over all the samples is 726 m ± 28 m in a 95% confidence range between 667-785 m. The total data range is 438 m between 522 and 960 m. The histogram in figure 4.6 shows that the buried mounds have no specific depth range and that only a few of them appear in greater depths. Two clusters appear in the distribution, one around the mean general depth of 800m and another around 600m, the shallowest level where mounds occur. This is also illustrated in the large negative value of the kurtosis, which shows that clustering of the data does not occur. The skewness shows that the mounds have a right tail with some outliers to greater depth (Table A.2.2).

The **surface mounds** (SM) show a completely different pattern and appear in greater depths than the more scattered distribution of the buried mounds (Fig 4.6). The overall mean for the surface mounds is 821 m ±14 m with a 95% confidence range of 793-849 m, or 56 m depth zone (Table A.2.2). This very narrow range illustrates that the surface mounds prefer a certain depth. In more details the mounds cluster in two zones: around 700 m and around 900 m. The mounds in the 700 m zone are sitting in a steep part of the continental slope as discussed in the general bathymetry. The mounds in the 900 m clusters are located in a flatter area, more to the center of the CH. The two clusters show an almost normal distribution with each about 50% of the total mound population (Fig. 4.6).

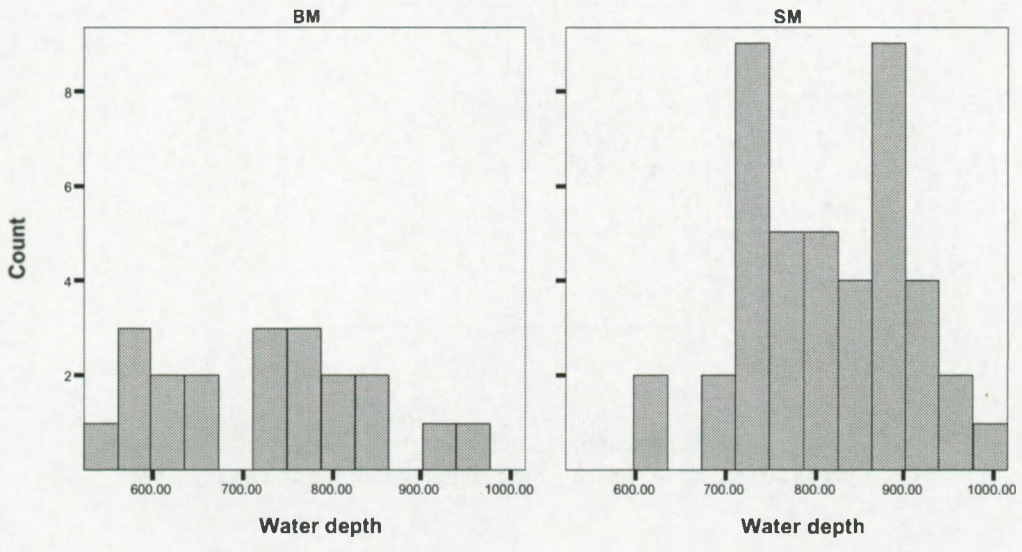

Fig. 4.6: Histograms of the seafloor distribution of the different mound types.

4.2.2.3 Water depth - mound - zone relation

A similar analysis is performed on the three subareas of the mound province to illustrate the spatial depth and the mound type distribution. The central zone (C) contains 43 mounds, the northern zone (N) 15 and the southern zone (S) 5 (Fig. 4.2). The first analysis in the distribution starts with the depth distribution for all the mounds per zone.

In the **central** zone the mound occur in a depth range between 605 and 1017 m. The mean depth of all the mounds located in the central zone is 803 ± 15 m with a 95% confidence zone between 772 and 834 m (Table A.2.3). Even the total range of depths is broad (412 m), most of the mounds cluster in a narrow depth range around 800 m (Fig. 4.7).

The 15 mounds of the **northern** part appear in a depth range between 522 m and 950 m with a mean of 795 ± 34 m, or in a 95% confidence area between 723 and 867 m (Table A.2.3). In this zone the mounds are spread out over a broader depth range than in the central part of the province. The mounds are also located around 800 m. The skewness indicates that greater depths accommodate more mounds than shallower depths.

In the **southern** part only five mounds occur in a depth range between 565-770 m. The mean is 670 ± 41 m. The 95% confidence range is between 556-785 m. (Table A.2.3). The mounds of this zone occur in a broader and shallower depth range than in the other zones. There is neither real clustering nor symmetry observed in the data (Fig. 4.7).

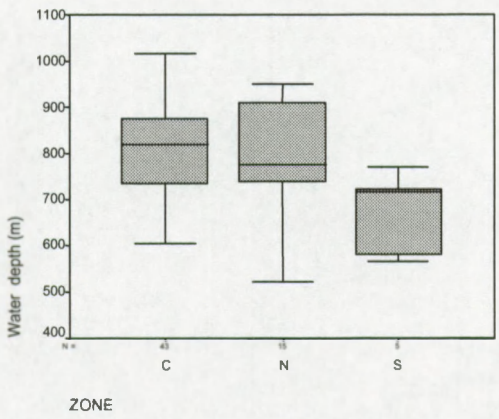

Fig. 4.7: Stem-and-leaf diagram illustrating the depth variation and the means of the three subareas defined in the Belgica mound province.

The next step in the analysis is the discrimination between surface and buried mounds in the three zones.

Southern zone

The southern zone only contains buried mounds. For this reason no extra analysis was necessary.

Central zone

In the central zone 33 surface mounds and 10 buried mounds have been recognized. The **buried mounds** have a mean depth of 762 ± 38 m in a 95 % confidence range for the mean between 675 and 848 m (Table A.2.4). The data cluster at two depths: around 633 m, with 6 samples and 847 m with 4 samples. The latter is approximately the general mean of the mounds. One sample is lying in a depth of 950 m. These observations illustrate that the buried mounds are lying at the water depth extremities of this zone (deepest and most shallowest parts), with a few of them in the mean water depth of the central zone (Fig. 4.8).

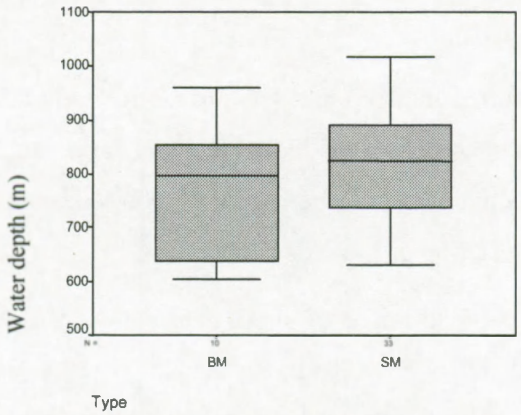

Fig. 4.8: Depth distribution of the BM and SM in the central mound zone. The BM appear in a broad range preferring shallow depths, the SM appear in a narrow zone around the mean.

The **surface mounds** show a large negative skewness, which indicates that the values cluster to greater depths (Table A.2.4). The mean depth is 837 ± 28 m, with a 95% confidence range for the mean between 774-901 m. The total depth range is 412 m in a zone between 605-1017 m. Two clusters appear around 730 m (15 samples) and another at 887 m (18 samples). This illustrates the two series of mounds recognized from the general bathymetry in the central zone (Fig. 4.9).

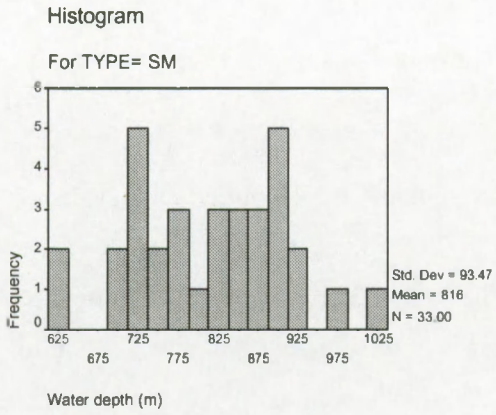

Fig. 4.9: Histogram of the surface mound depth distribution in the central mound zone. The mounds cluster in two narrow zones.

Northern zone

In the northern zone five buried mounds and ten surface mounds have been mapped. The five **buried** mounds appear in a zone between 522 and 922 m (Table A.2.5). This illustrates that the mounds have no preferred depth in the northern part. The buried mounds appear in the two depth extremes of this zone. No clustering of mounds is observed.

The **surface** mounds have a broad range of depth distribution of 228 m (between 722-950 m) (Table A.2.5). The mean depth is 837±28 m, with a 95 % range of confidence for the mean between 774 and 901m. The distribution of the population shows two clusters: the first cluster is located around 757 m and a second around 918m. Both clusters include five samples. Mounds apparently shift to greater depths in comparison with the central province.

- In total 44 surface mounds and 20 buried mounds have been observed.
- The surface mounds occur in the steep the flank of the furrow CH in a narrow depth range around 750 and 900 m. They shift to greater depth from south to north.
- The concentration of the mounds decreases and more buried mounds occur at the tail ends of the province. These mounds appear in a broader geographic distribution where the bathymetry is gentler.

4.3 Geometry of the Belgica mounds

The data obtained with multi beam and sidescan sonar illustrate the surface geometry of the mounds. Although, these techniques do not always represent the real mound shape because the mounds are partly buried. A good estimation can be made out of the mapping of the typical acoustic facies of the mounds on the seismic profiles. The disadvantage of this method is the spatial distribution of the seismic lines (see 3). Even where the seismic profiles do not cross the crest of the mounds, they still convey the best representation of the mound dimension, available with the present data set. All measured parameters concerning the geometry of the mounds have been derived of the seismic profiles (Table A.1).

For the statistic analysis 19 BM (90% of the BM) and 26 SM (59% of the SM) mounds have been taken into account. For each mound the maximum height (in milliseconds two way travel time), width (in meter) along the profile (diameter) and the sediment cover above the mound (in ms TWT) was measured. These results have been analyzed in function of the profile orientation, the maximum measured height and width per mound. The ratio of the width and height of the mounds crossed by two inverse oriented profiles has been calculated to derive the theoretical plan view of the mound.

The geometry analysis of the mounds is based on the mapped mound facies on the seismic profiles. The seismic character of the mound is semi-transparent, which shows a well-delineated acoustic facies with the surrounding semi-parallel reflectors of the sediments (Fig. 4.10). The mounds are bounded with diffraction hyperbolae and side echoes of nearby mounds, which can mask the real shape of the mounds. For this reason the shape is inferred from the termination of the sediment beds on the flanks of the mounds. The width is measured at the base of the mounds, which represent the maximum horizontal size. The maximum height along the profile is measured from the apex of the diffraction hyperbolae to the base of the mounds. The base of the mounds is inferred from the appearance of underlying reflectors and surrounding profiles. The geometry data have been summarized in appendix A.1.

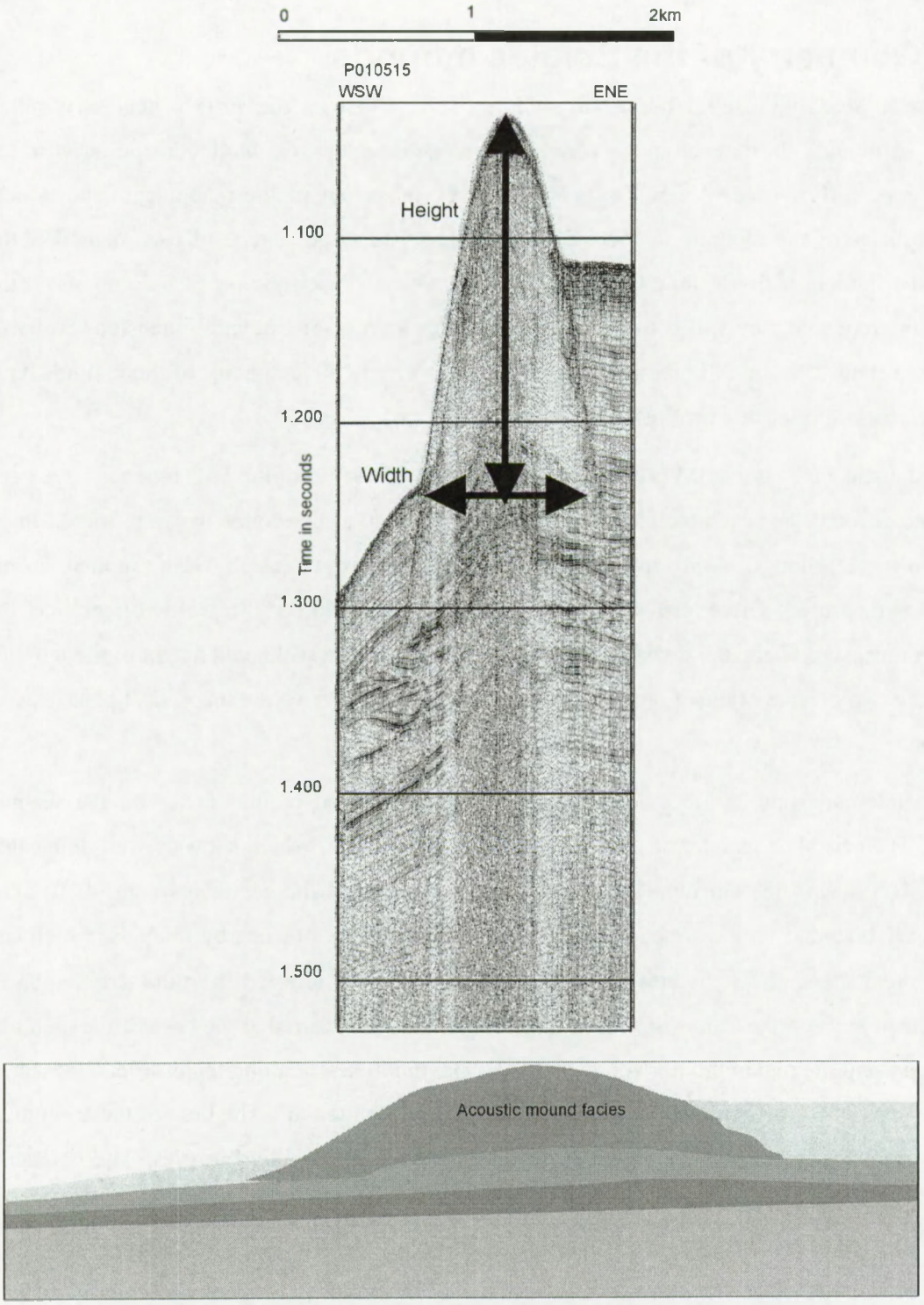

Fig. 4.10: The seismic profiles illustrate better the real mound shape than the surface techniques. The lower image illustrates the mound geometry without vertical exaggeration.

4.3.1 General geometry per mound type

Per mound type the maximum measured height and width have been analyzed to get a general picture shape and dimension.

4.3.1.1 Width

The mean width of the **buried mounds** is 709 m±61m. The 95% area of confidence from the mean is the range bounded by 581 and 837 m (A.3.1) The total range is large, between 267-1092 m. The data cluster around the mean and also at both extremities of the data range (Fig. 4.11). Remarkable is that smaller widths (smaller than 400m) and greater widths (above 900m) represent almost 50% (47.4%) of the measured data. This illustrates the large variation (high variance).

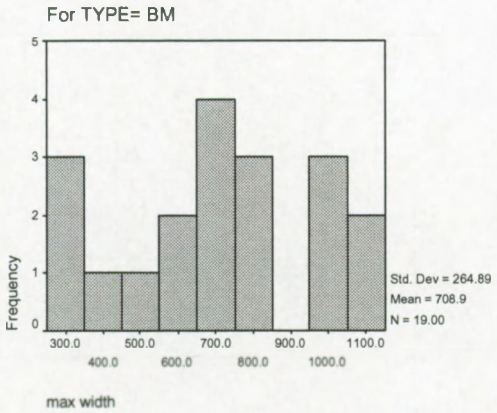

Fig. 4.11: Histogram of the maximum measured width of the BM.

The measured width for the **surface mounds** has a much broader range of values than that of the buried mounds: from 570-2130 m. The mean is 1114 ±77 m and the 95% confidence range is between 955-1274 m, i.e. a range of 319 m. The distribution of the data shows an asymmetry with a tail to greater lengths, or a positive skewness (Table A.3.1 and Fig 4.12). This means that the large lengths above 1500m are exceptional. The width of the mounds cluster between 600 m and 1500 m in a lognormal distribution.

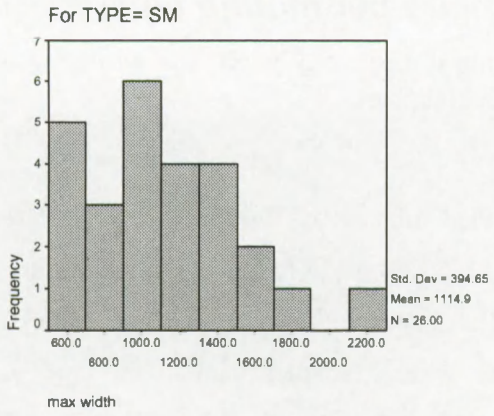

Fig. 4.12: Maximum width of the surface mounds.

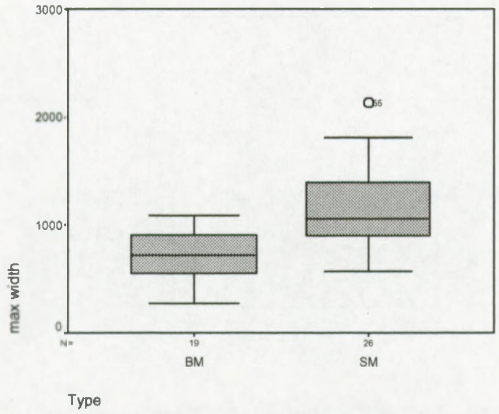

Fig. 4.13: Stem-leaf diagram comparison between the max width of the SM and BM. The SM are clearly larger than the BM.

In general, the width of the buried mounds is smaller. The surface mounds have a mean of approximately 1100 m and the buried mounds of 700 m. The large range of widths is due to the relative location of the seismic profiles with respect to the mound structure.

4.3.1.2 Height

The maximum measured height of the **buried mounds** ranges from 5 to 160 ms TWT with a mean of 54±8 ms (Table A.3.2, Fig. 4.14). The data cluster around the mean and have a right tail to higher values. These large buried mounds (BEL8 and BEL14) are rather exceptional and seem to be recently buried. The highest buried mound is BEL14, sitting on the flank of the continental slope between surface mounds, with a sediments cover of 40 ms (Table A.1). This mound shows no surface expression on the multi beam and is located at a depth of 660 m. The smallest buried mound, BEL49, with a height of 5 ms, stands on the continental slope in a water depth of 556m. The width of this mound is 724 m, which suggests that this mound is profiled at the flanks, so that

only the foot of the mound is recorded on the seismic profile. The relation between the height of the buried mounds and the thickness of the sediment on top of the mound has been presented in figure 4.15.

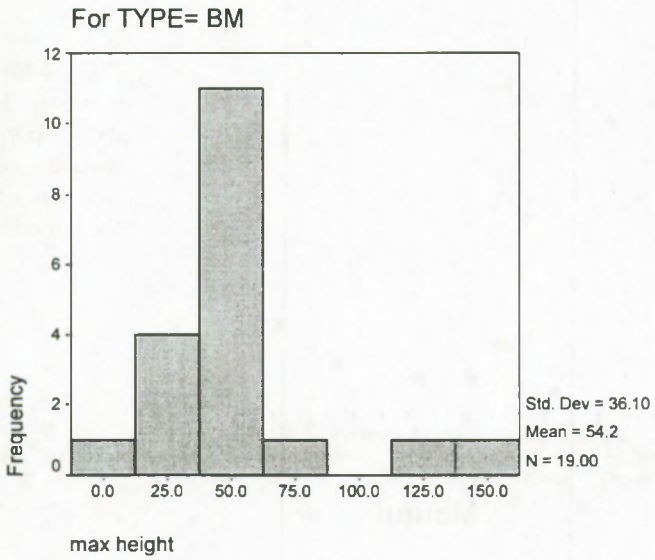

Fig. 4.14: Histogram of the maximum height distribution of the buried mounds.

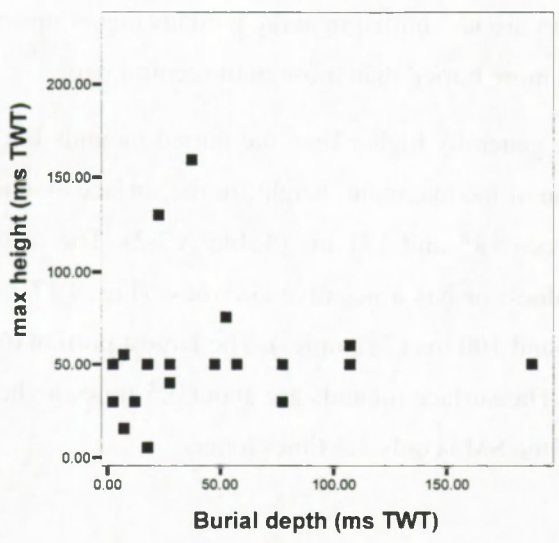

Fig. 4.15: Maximum height-sediment cover plot for the buried mounds.

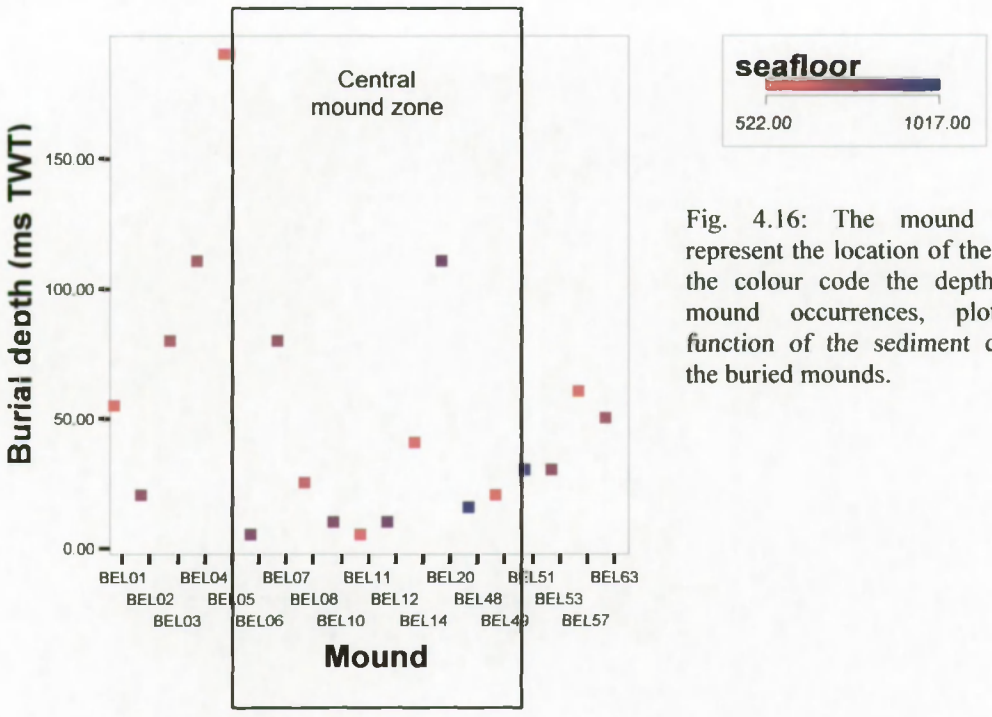

Fig. 4.16: The mound number represent the location of the mound, the colour code the depth of the mound occurrences, plotted in function of the sediment cover of the buried mounds.

The highest buried mounds have a thin sediment cover (Fig. 4.15). The smaller mounds are covered with a variable sediment thickness, from a thin layer to more than 100 ms. It seems that the buried mounds stopped developing approximately at a similar stage of development. The sediment thickness covering the mound depends on the location, as seen in the Figure 4.16. The mounds in the deepest part are less buried than the mounds higher upslope and the mounds at the edges of the province are more buried than those in the central part.

The **surface** mounds are generally higher than the buried mounds but they appear in a broader range of values. The mean of the maximum height for the surface mounds is 153 ± 8 ms in a 95% area of confidence between 135 and 171 ms (Table A.3.2). The distribution of the heights is asymmetric to higher values, or has a negative skewness (Fig. 4.17). Nevertheless, a cluster of lower values appears around 100 ms (7 samples). The largest portion of the population, 18 of 25, clusters around 178 ms. The surface mounds are about 3.5 times higher than the buried mounds (Fig. 4.18). The width of the SM is only 1.5 times longer.

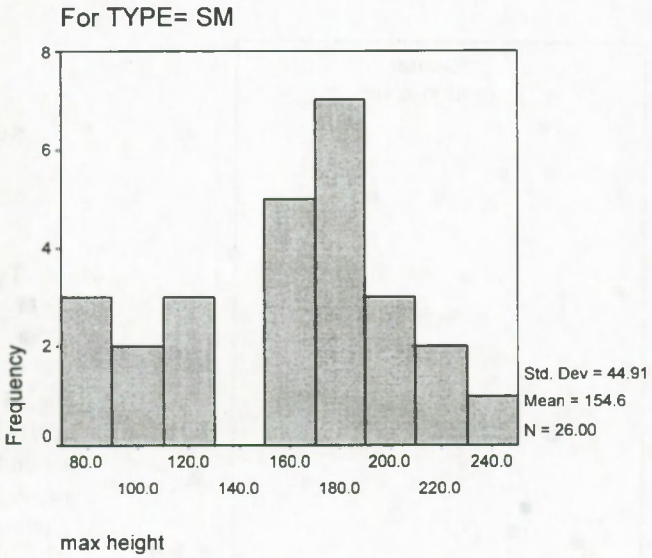

Fig. 4.17: Height distribution of the surface mounds. The height of the mounds cluster around 155 ms TWT.

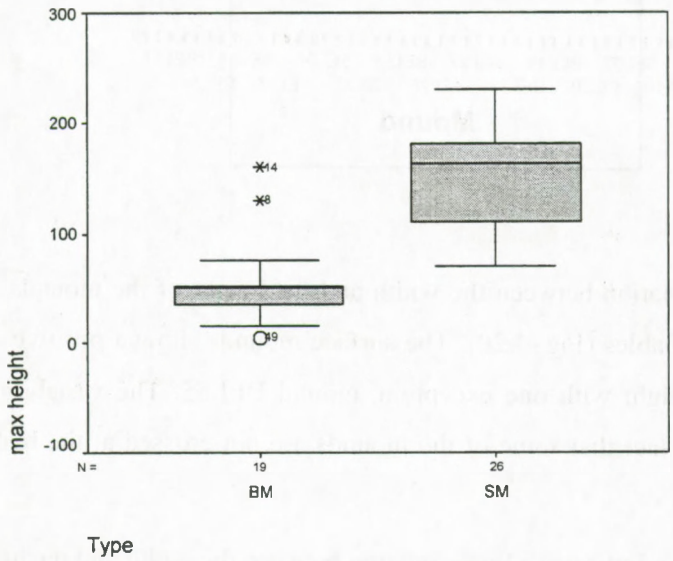

Fig. 4.18: Stem-leaf diagrams of the max height of the buried and surface mounds. The buried mounds have all a similar height with outliers. The surface mounds cluster near 155 ms TWT.

The relation between the mound location and height of the mounds is plotted in Fig. 4.19. The highest mounds appear and in deepest part and in the central part of the Belgica mound province, where also the highest concentration of SM appears. The smallest surface mounds are located in the transition zone between the central and the northern and southern part. The largest mounds appear in the greatest depths.

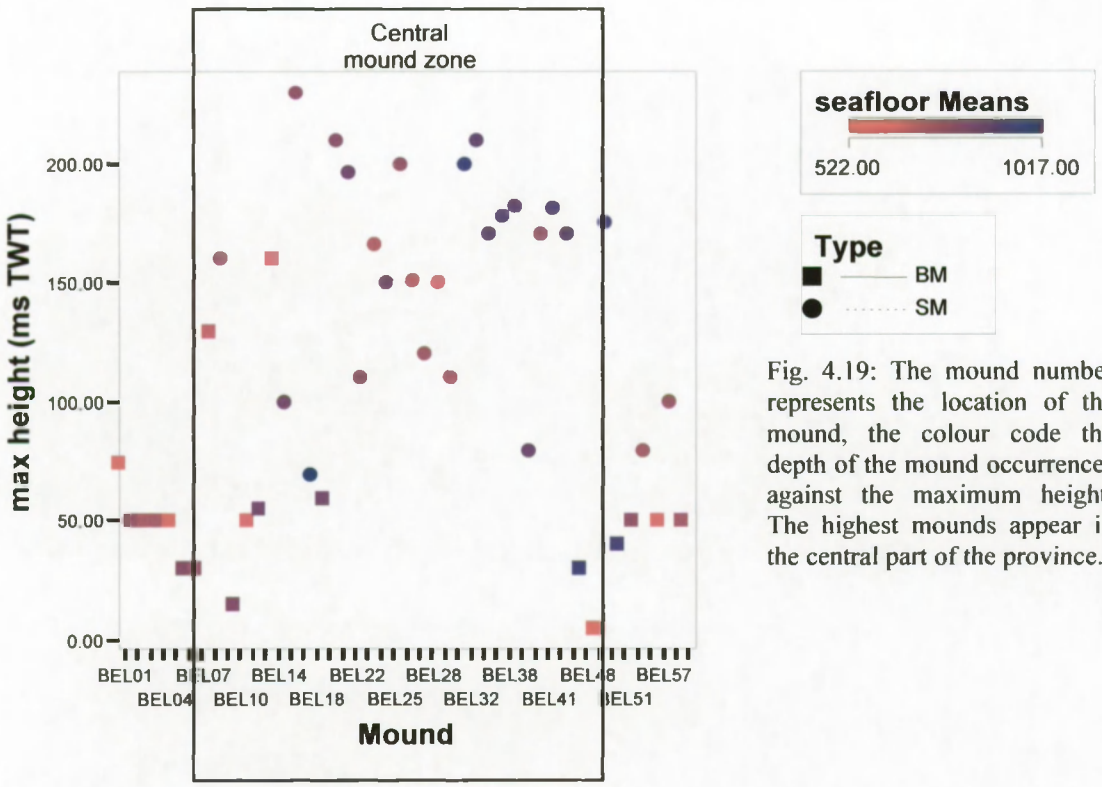

Fig. 4.19: The mound number represents the location of the mound, the colour code the depth of the mound occurrences against the maximum height. The highest mounds appear in the central part of the province.

To analyse the relation between the width and the height of the mounds, a scatter plot has been made of both variables (Fig. 4.20). The surface mounds show a positive correlation between the width and the height with one exception, mound BEL55. The variability in the values can be explained by the fact that some of the mounds are not crossed at the really highest point by the seismic profile.

The data scattering indicates a linear relation between the width and the height of the mounds. For statistical reasons the buried mounds and mound BEL55 have been excluded from the regression calculation. The linear regression between the height and width is calculated through the origin inside a 95% confidence zone. The height in ms TWT is about 14% of the width in meter. Or if the internal sonic speed of 1850 m/s is used as the average speed for the seismic waves inside the mound, a relation of 13% between the width and the height in meter has been found.

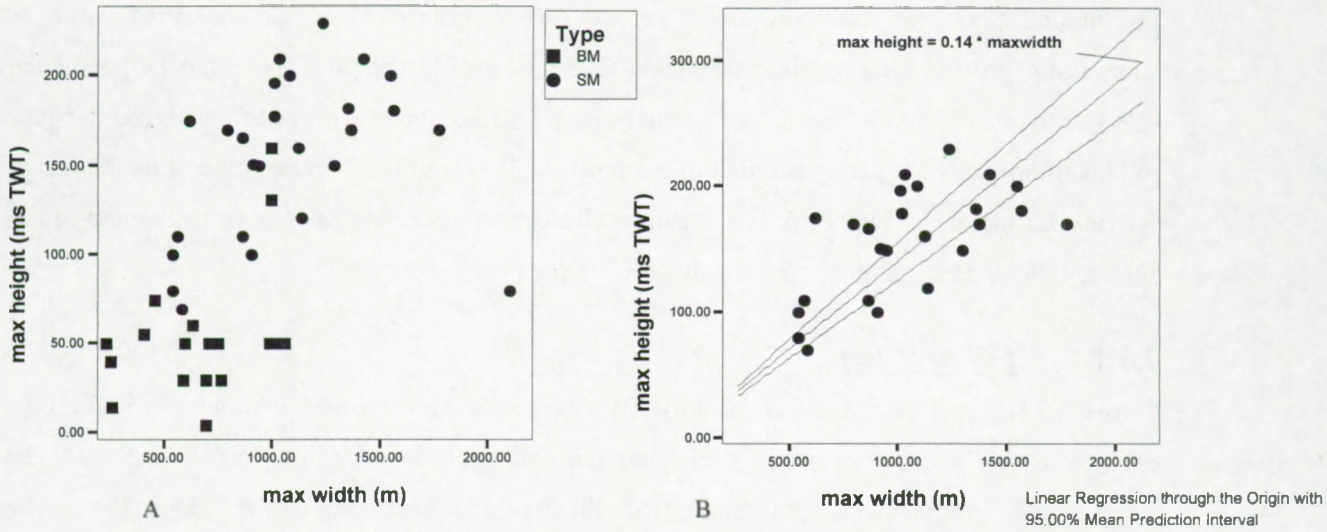

Fig. 4.20: Maximum height and width relationship. A. Illustrates the linear correlation between both parameters for all mounds. The buried mounds appear all at approximately the same height but with variable widths. B. SM have a linear correlation between the width and the height.

- In general, the mounds have a broad base, even if the height is limited. This might indicate an initial horizontal development of the mounds followed by a vertical development.
- The most favourable conditions for the mound development were found in the central part of the Belgica mound province. To the edges the mounds had a limited development, possibly under a larger sediment pressure.

4.3.2 Mound shape in plan view

The mound shape in plan view at the mound base is inferred from the measured width on intersecting profiles. All profiles are subdivided into profiles parallel (NS) and perpendicular (EW) to the continental slope. In a first analysis, all measurements have been analyzed per type and taken into account per orientation of the profiles. This results in a mean mound dimension of the Belgica mound province. A few mounds with crossing seismic lines have been analyzed in more details to derive a more specific shape and to test the earlier findings.

4.3.2.1 EW profiles

In total 15 BM and 21 SM are crossed by EW oriented seismic profiles. The mean width on the EW profiles is 741m ±67m for the buried mounds and 1031±86m for the SM (Table A.3.3). The range of 95% confidence is quite large, what illustrates the scattering of the values (Fig. 4.21). The BM cluster around the mean in a lognormal distribution but with a higher number of values to greater widths (Fig. 4.21). The mean for the EW profiles is slightly larger than the mean of the maximum width discussed above in the buried mounds but the 95% confidence zone is also larger (Table A.3.3).

The SM width distribution shows an opposite image: the absolute values are larger than those of the buried mounds (Fig.4.21 and Fig. 4.22). The mean of the SM in EW direction is smaller than the mean of the max width (Table A.3.1). This demonstrates that the BM observed in this data set have an EW elongation and the SM a NS elongation.

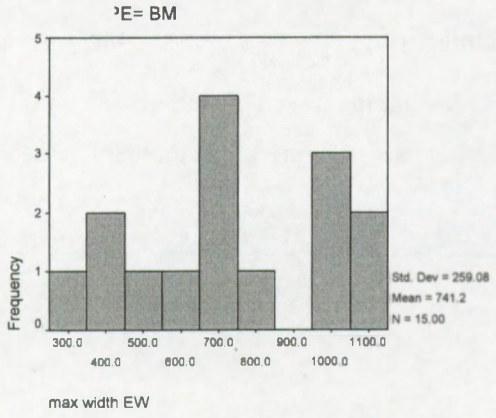

Fig. 4.21: Maximum width distribution on the EW profiles of the buried mounds.

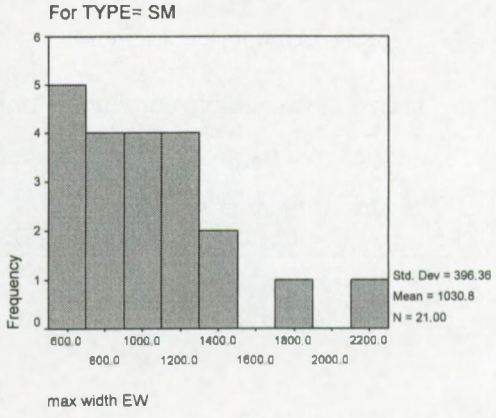

Fig. 4.22: Maximum width distribution on the EW profiles of the surface mounds.

4.3.2.2 NS profiles

On the NS oriented profiles, 5 BM and 16 SM have been imaged. The distribution of the width in NS orientation of the buried mounds shows two clusters: one around 300 m and a second around 800 m. The mean is 554 m with a standard error of 117 m. (Table A.3.4, Fig. 4.23)

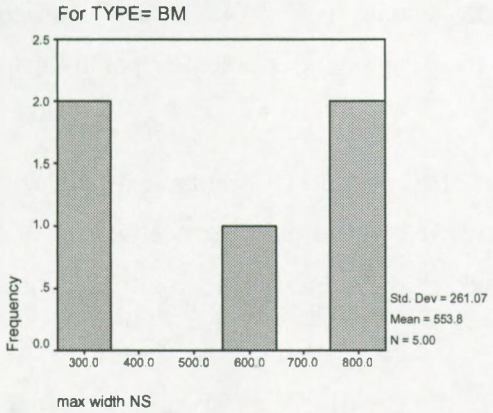

Fig. 4.23: Maximum width of the buried mounds on the NS profiles.

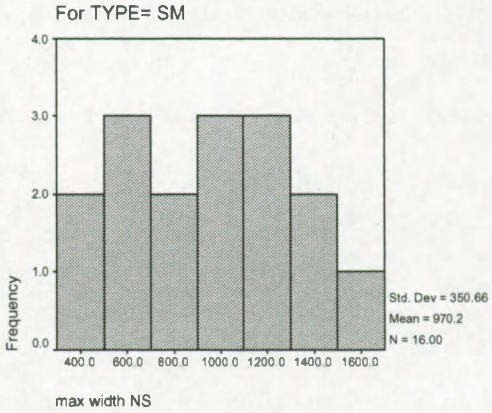

Fig. 4.24: Maximum width of the surface mounds on the NS profiles.

The measurements for the SM show a broad range of values between 374-1578 m (or 1200 m) (Fig. 4.24). The mean is 970 m ± 88 m in a 95% confidence zone between 783-1157 m (374 m). The mean for the max width is larger (1120 m) than the width in NS-direction. The distribution of the data does not cluster or form a real asymmetry.

In comparison with the BM mounds, the SM are larger and have a better defined range.

4.3.2.3 General plan view of the mounds

The ratio of the mean maximum NS over EW width is calculated per mound type to deduce a mean plan view of the mounds.

Buried mounds have a ratio of 0.748 ± 0.172. This suggests that the mounds have an EW or downslope elongation. Due to the asymmetric distribution in the data to greater values for the EW direction, the shape of the buried mounds vary from circular to elliptical, with the longest axis in EW direction in plan view.

For the surface mounds the NS/EW ratio is 0.958±0.121. This means that the mean plan view is almost perfect circular. This shape, based on the means of all measured widths along the profiles, is only an indication for the mean shape. A better approach would be to evaluate the NS/EW ratio per mound. Nevertheless, this is only possible with a select group of surface mounds profiled in two directions.

4.3.2.4 Detailed plan view shape of the surface mounds

Only 10 surface mounds are covered with profiles in both directions, which allows an individual mound shape evaluation. The greatest width and height in one direction was measured if different profiles of one specific mound were available.

To evaluate the relative position of the profiles on the mound, the NS/EW ratio of the height measured on the profiles is calculated. If the profiles cross the mound at a similar point, then the ratio of the heights should be around 1 (Fig. 4.25).

The mounds BEL09, BEL26, BEL30, BEL32, BEL35, BEL36, and BEL39 have a height ratio near 1, varying from 0.86 till 1.12. These mounds are well spread over the central part of the province. The NS/EW ratios for the width measured on the same profile for these selected mounds vary from 0.78 till 1.34. (Fig. 4.25)

Mounds BEL09 and BEL39 have a circular shape in plan view. BEL26 and BEL35 their longest axis is NS oriented and that of BEL30, BEL32 and BEL36 EW oriented. BEL30 and BEL36 show a positive correlation between the width and height ratio. These mounds can be considered as almost **circular** in plan shape because the mounds show a small offset from a height and length ratio of 1.

BEL32 has an EW elongation but has only a small offset of the circular shape. BEL26 shows a positive correlation with between the height and width ratio. For this reason BEL26 has a slight NS elongation but differ a little of the circular shape. BEL35 has a height ratio of 1, which allows to make a good shape estimation based on two profiles. The mound shows a clear elongation in a NS direction with a ratio of 1.3.

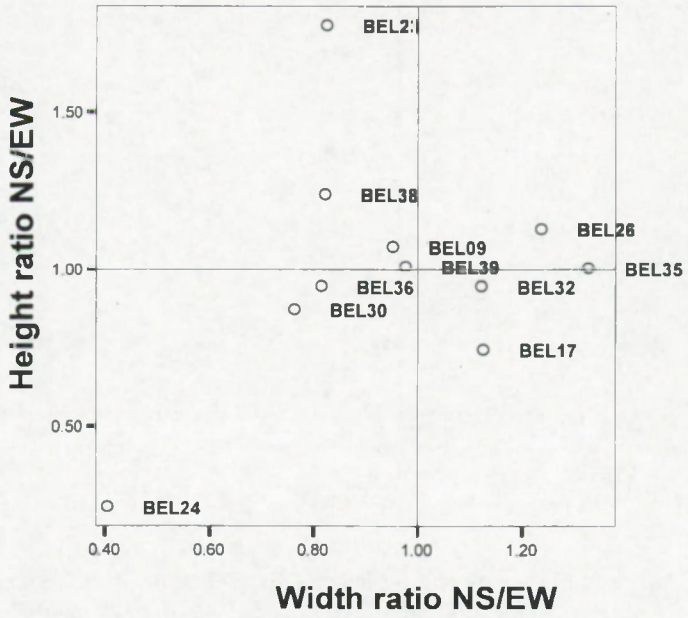

Fig. 4.25: The height and width ratio for the main profile orientation.

BEL17 has a length ratio of 1.14. This means that the NS width of this mound is longer even of the profile does not cross the highest point of the mound, which suggests an NS elongation. BEL24 has a width ratio of 0.42 and a height ratio of 0.24. This mound is excluded of further geometric interpretation because these values are out of the range taken into consideration.

Two mounds show a height ratio greater than 1. BEL38 has a height ratio of 1.24 and a width ratio of 0.84. This means that the longest width has been observed on a NS profile and the highest height on an EW profile. This might imply that the mound shows an EW elongation. BEL23 has a similar length ratio as BEL38 but it has a higher height ratio, which implies also an EW elongation.

The mounds seem to show a circular plan view, although a few mounds have a NS or EW elongation. To find a relation between the shape and the location of the mounds, they have been plotted in function of the depth and the geographic distribution.

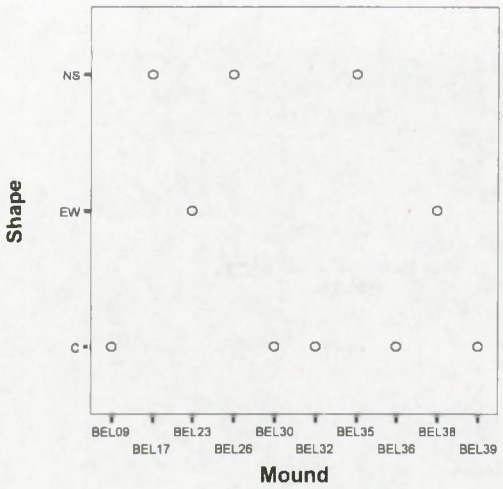

Fig. 4.26: The mound shape in plan view is indicated with a C (circular). The EW elongation and NS elongation versus the mound location have been represented with the mound number.

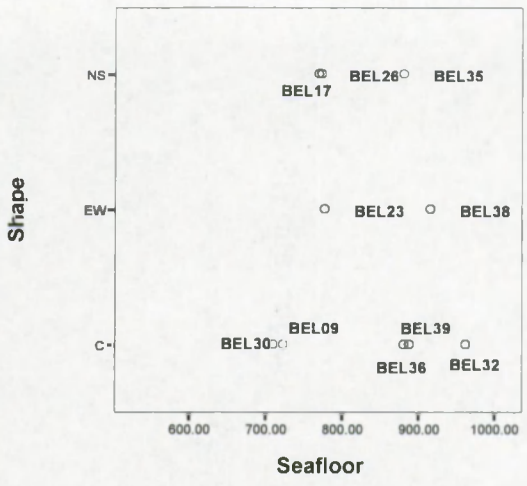

Fig. 4.27: Plot of the mound shape in function of the depth. The mound number represents the geographic location of the mounds.

Figure 4.26 shows the inferred mound shape plotted versus the mound number, which represents the geographic location of the mounds. The circular mounds do not have a specific location in the Belgica mound province. The elongated mounds show no preferential location and neighboring mounds show opposite elongations.

A possible environmental factor that influenced the shape is the depth of occurrences (Fig 4.27). Circular mounds seem to cluster in the two most common depth levels. The elongated mounds are concentrated between those two ranges, but they appear also in the two most common depth levels. This means that the shape of the mounds is not conclusively relation with depth and the geographic location, and that local factors might have played a major role in the mound shape.

The bathymetric map (Fig. 4.2) illustrates that the circular mounds are surrounded by surface mounds and that they seem to occur in "protected" zones. The circular mounds are not limited by incisions as the more elongated mounds.

BEL23 and BEL38, with an EW elongation, show on the multi beam data an elongation in NNW-SSE. BEL23 is sitting higher on the slope and seems to be shaped by local incisions on the northern side. A larger mound, BEL17, shows a clear elevation and a NS elongation. Probably these two features limited the development of BEL23 and forced to develop in an EW direction.

Mound BEL38 is sitting in the deeper part on the lower flank of the furrow and is not surrounded by other mounds. The slope of the mound is probably steered by the current flowing in the furrow. The surface expression of the mound shows an NS elongation formed by sediment deposition on the southern and eastern flank of the mound.

BEL35 shows a clear NS elongation on the multi beam and is flanked by BEL36, which is almost circular. This mound is sitting on the flank of the furrow but in a steeper zone than BEL38, and is bordered by a channel to the south. The mound developed probably toward the north.

BEL26 mound is sitting in a downslope series of mounds and is flanked in the east by large mounds. The mound is flanked by incisions, which might have limited the mound development in an EW direction.

4.3.2.5 Mound area

The area occupied with mounds is estimated to be 40 km^2, based on the inferred geometry of 75% of the total mounds (excluding the mounds recognized on multi beam data) (Table A.1). The total mound surface (including the ones on multi beam data) is estimated to be 55 km^2. This means that about 13% of the total province is occupied by mounds. The total area of buried mounds is estimated to be 8 km^2 or 14 % of the total mound surface.

4.3.3 Summary

The mounds seem to be partly lined up along downslope channels and seem to follow the orientation of the channels. These turbidity channels [Van Rooij, accepted #475] transport sediments from the shelf to the deeper part of the basin and have an enhanced expression near the mounds. The mounds located on the western and deeper side of the province are more freestanding with less sediment accumulation on the flanks than the mounds located higher on the slope. In the lower part the slope of the mound is controlled by the vigorous current in the channel. Most of the mounds have an almost circular shape in plan view and in the surface expression mostly an N-S elongated shaped due to the accumulation of sediments on the flanks. In some cases the sediment accumulation forms a bridge between the mounds, which creates a complex structure with several mound summits.

- The largest mounds cluster around the steepest part of the flank with heights around 180 ms or 166 m (calculated with an internal velocity of 1850 m/s). Mounds in the upper mound range are generally smaller, about 90m high.
- The surface mounds have a mean width of approximately 1100 m and an average height of about 150 ms or 139 m (calculated with an internal velocity of 1850 m/s).
- The most ideal observed shape of the mounds is circular in plan view. The elongation of some mounds is controlled by local factors, most possibly current and seafloor topography.

4.4 Geological record

The sediment record imaged on the high-resolution seismic profiles is limited to the sediments of the upper Megasequence 2 in the seismostratigraphy of Mc Donnell (2001) (see 2.3). These depositions cover a period of Miocene to recent age. In the North Atlantic this period is generally characterized by drift deposition (Faugères et al., 1999; Faugères et al., 1993; Stoker, 1998; Stoker et al., 2002) as reported in seismic studies of the Porcupine Basin (Lekens, 2000; Mc Donnell, 2001; Van Rooij, 1998; Van Rooij et al., accepted). The geological sequences are analysed in order to find a possible relationship between the substratum and the mounds and between the mound development and the burial processes. The geometry of the geological sequences allows estimating the environmental changes from the mound initiation to the mound evolution.

On industrial seismic profiles the underlying sequences have been interpreted as contourite deposits, which are thinning towards the basin margin (Lekens, 2000; Mc Donnell, 2001). They suggest an upslope progradation of the sequences and a source of reworked sediments out of the basin. The high-resolution seismic grid provides more details on the sedimentation processes inside the drift sequences, in order to inferred hydrodynamic regimes. The profiles referred to in the text have been collected in appendix B.

4.4.1 Unconformities

In total five different seismic facies have been recognized on the high-resolution seismic profiles (appendix B). The facies have been indicated with a B for the Belgica mound province and from the base to the top with a, b, c, d and e (Fig 4.28 and Fig. 4.29).

The bounding reflectors for each of these facies have been indicated on the seismic profiles. A short description of each bounding unconformity has been given:

- The upper boundary reflector of the lowermost facies Ba is labelled R1. This reflector is characterized by a high amplitude. This unconformity truncates the lowermost reflectors seen on the profiles. It is difficult to correlate this reflector through the area due to the limited penetration of the seismic profiles and the poor data quality in the southern part. An indirect indication is the downlap of the overlying facies and the truncation of facies Ba. This boundary is illustrated on the profiles e.g. P980549, P000644, 10521, P010528. This reflector corresponds with the C20 reflector of Mc Donnell (2001), with an assigned age of Mid Miocene.

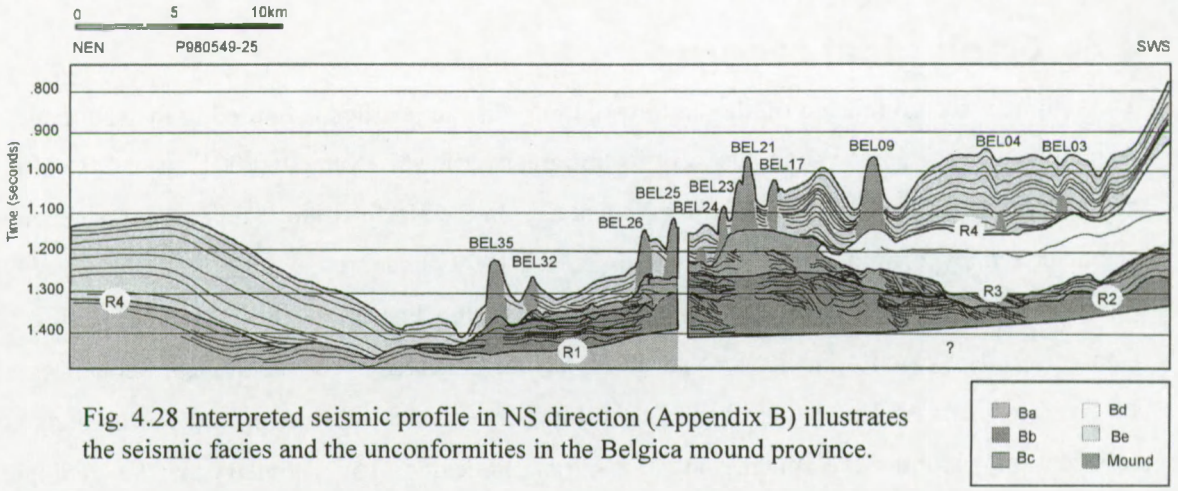

Fig. 4.28 Interpreted seismic profile in NS direction (Appendix B) illustrates the seismic facies and the unconformities in the Belgica mound province.

- Reflector R2 has an erosive character as seen on the profiles P010517 and P010521, P980523, P010528. This unconformity is the top of facies Bb, composed of sets of sigmoidal reflectors. It clearly truncates the sigmoidal reflectors. This reflector could be traced over a large surface in the survey area.
- Unconformity reflector R3 is the upper boundary of facies Bc. This reflector is characterized by a high amplitude. This reflector shows no significant erosion on the EW profiles (Fig 4.29). On the NS profile R3 is more irregular in geometry arguing for a local erosion in the lower part of the slope (Fig 4.28).
- R4 is the last erosive event in this sequence. This unconformity truncates all described facies below (Fig. 4.28, Fig. 4.29). R4 forms a typical erosional, angular unconformity. The expression of the reflector is commonly irregular. R4 is interpreted as the base of the mounds, for this reason a more detailed description is given in the next paragraph.

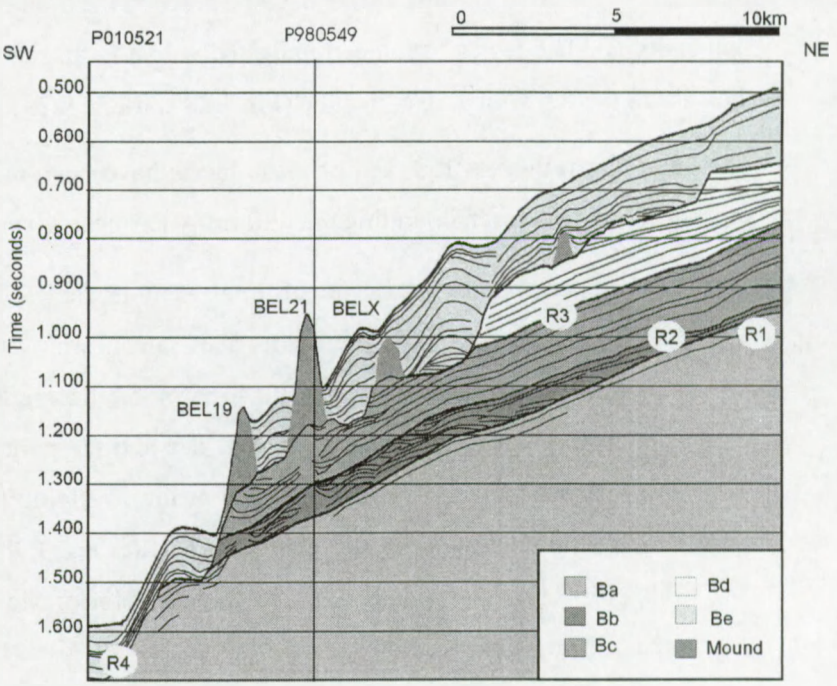

Fig. 4.29: Interpreted SW-NE seismic profile (Appendix B).

4.4.1.1 Mound base

All the mounds in the Belgica mound province root on one base reflector, R4 (Appendix B). The acoustic facies separated by R4 are clearly different and argue for a change in the sedimentary environment after a period of erosion and non-deposition. A vigorous pulse of deep-water circulation might have been responsible for the erosion.

This uppermost erosional reflector R4 may correspond with the C10 reflector (Mc Donnell, 2001) defined by Stoker et al. (2002) for the Rockall Trough. Mc Donnell (2001) assigns an Intra-Early Pliocene age to this reflector, supporting an Intra-Neogene major regional unconformity (Stoker et al., 2002). The dating of the sequences is based on a seismic stratigraphic interpretation within the basin and on correlation of seismic facies with the Rockall Trough sequences.

The very limited well control of the Neogene in the Porcupine Basin is largely due to the lack of cutting returns in the early stage (pre-casing) of exploration drilling. The youngest certain date in the Porcupine Basin is Base Miocene. The Miocene to younger ages of the Porcupine Basin have largely been proposed on the basis of seismic comparison with the Rockall Basin where the Neogene succession has been more confidently dated from ODP and DSDP wells (Mc Donnell, 2001; Stoker et al., 2002).

The correlation of this reflector R4 from industrial data to high-resolution sparker data is hard. It is not always clear that the same reflector is picked due to the converging of the reflector toward the basin margin. Due to these uncertainties the dating of the mound base is suggested to be Intra Pliocene. The erosive character of the reflector suggests a long period of non-deposition and erosion.

Incisions with a NNE-SSW direction have been recognized in the central mound zone and on the eastern upper slope (Fig. 4.30). Further to the north the surface gets smoother and is less influenced by erosion. In the deepest part of the province a large NS furrow (CH) has been eroded (see 4.1). This furrow has its steepest flanks in the southern part of the province and gets smoother to the north, to grade finally into the normal morphology of the mound province. This furrow is still present in the present-day seabed, which suggests that a similar current regime has been active for a long period in this region (see 4.1). A bottom current with a NS direction shaped CH. A few downslope channels have been observed with a NE-SW to almost NS trend, depending on the location of the slope (Fig. 4.30). The occurrence of the mounds has been plotted on the surface of R4 and shows that the large surface mounds of the central zone appear in a zone with enhanced slopes.

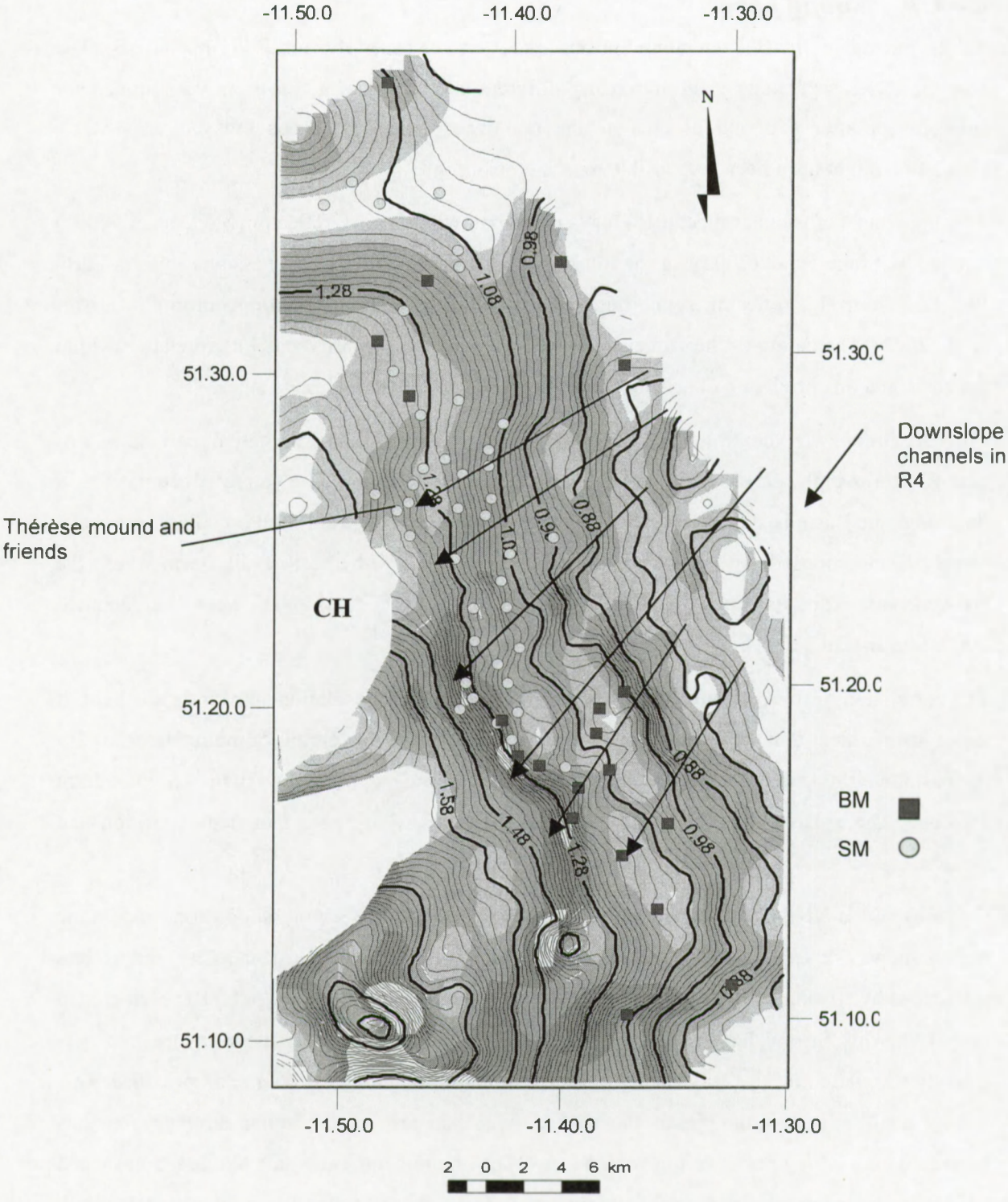

Fig. 4.30: The time structural map (two way reflection time) of R4 shows a surface dip to the west and trend comparable to the present-day bathymetric contours. Slopes have been indicated in a greyscale: darker colours indicate steep zones; lighter almost flat areas or grid cells where the calculations were not performed. The mounds correlate with steeper slopes, related to the NS furrow (CH) or downslope channels.

The steepest slopes are not occupied with mounds and are located on the western side of the mounds (Fig. 4.30, Appendix B, e.g. P010521, P010512, P010528, P980521 and P980523). The mound distribution on the R4 surface shows that the mounds are lined up along EW to NE-SW incisions, where the mounds are sitting on the flanks. The downslope channels have been interpreted as turbidite channels generated at the shelf, which are still active at some locations in the present setting (Van Rooij et al., accepted). It is not clear if these channels have been formed during the main erosion creating R4 or in a later erosional event. This illustrates two trends in the mound distributions:

- the mounds line up along downslope incisions in the erosional reflector in a EW to NE-SW direction,
- the mounds are located along the relative steep flanks of the NS furrow CH.

The mounds around Thérèse mound (BEL35) shift more to the central axis of CH (Fig. 4.30). These mounds developed in higher energetic conditions than the mounds higher on the continental slope.

The buried mounds in the southern part of the province line up with the downslope channels. In the northern part the buried mounds are more spread out and they are not clearly linked to topographic features. In this area the data density is also smaller than in the other parts, which might mask possible local irregularities in the mound base.

The time structural map illustrates the terrace-like geometry of the R4 reflector in the upper part of the slope (Fig. 4.30). Two major escarpments have been identified by a darker band in a NW-SE direction, parallel to the geometry of the basin. They are clearly visible on the seismic profiles P980521, P010521 (Fig 4.29), P980523, P010517. The escarpments have a height of 50-100 ms TWT and they are linked the erosion during R4 in facies Bd. Mc Donnell (2001) suggests that this erosion is closely linked with a phase of shelf edge incision.

4.4.2 Facies description

Five different seismic facies have been recognized on the seismic profiles and mapped. A subcrop map at the R4 level has been made to show the distribution of the facies versus the mound distribution. A short description of each of the facies has been given in this section.

4.4.2.1 Facies Ba

This lowermost facies is characterized by subparallel continuous reflectors with a moderate to low amplitude. The acoustic basement forms the lower limit of this facies. The reflections are dipping to the west on the EW profiles (Fig. 4.29) and show a wavy geometry on the NS profiles (Fig. 4.30). The upper boundary (R1) seen on profiles of the deepest part and on the lower slope is erosive (P980525, P010528, P010512, P000644). This facies Ba might be correlated with seismic facies 9 in the seismostratigraphy of Mc Donnell (2001). This facies is characterized by a NW-SE progradational set of reflectors, thinning towards the basin margin. In the northern part of the province the base mound reflector, R4, erodes this facies and forms the substratum for a few mounds. On some profiles this facies shows the same characteristics of higher sequences, as seen on profile P980523. The distinction between these seismic facies is not always easy to make with the available data set due to the occurrence of the facies near the penetration limits of the high-resolution seismics. In cases of uncertainty of the lateral extension of the below discussed facies due to limited acoustic penetration, it has been decided to classify these as facies Ba.

4.4.2.2 Facies Bb

Facies Bb is characterized by reflectors with a high amplitude and a high lateral continuity reflectors. The reflectors show a sigmoid geometry on the NS profiles (Fig. 4.28, P980549, P010528, P000644) and hummocky to wavy subparallel reflectors on the EW profiles (Fig. 4.29, P010512). On the NS profiles the reflectors are downlapping to the north on the erosive reflector R1, or on smaller local erosional surfaces. The facies geometry changes, depending on the location on the slope.

The sigmoidal geometry has been observed in the lower part of the slope and a hummocky to wavy geometry higher on the slope (P010521). The reflectors onlap on the steepest parts of R1 on the EW profiles. They show a wavy to subparallel configuration in areas where the incisions are filled or where the slope gradient decreases. The upper boundary of this facies is in the north of the basin and on the flank of CH R4, in the southern part and more upslope R2.

Figure 4.31 illustrates the extension and thickness of the facies Bd with the mound distribution in the actual setting. The facies thins to the north and upslope to the east.

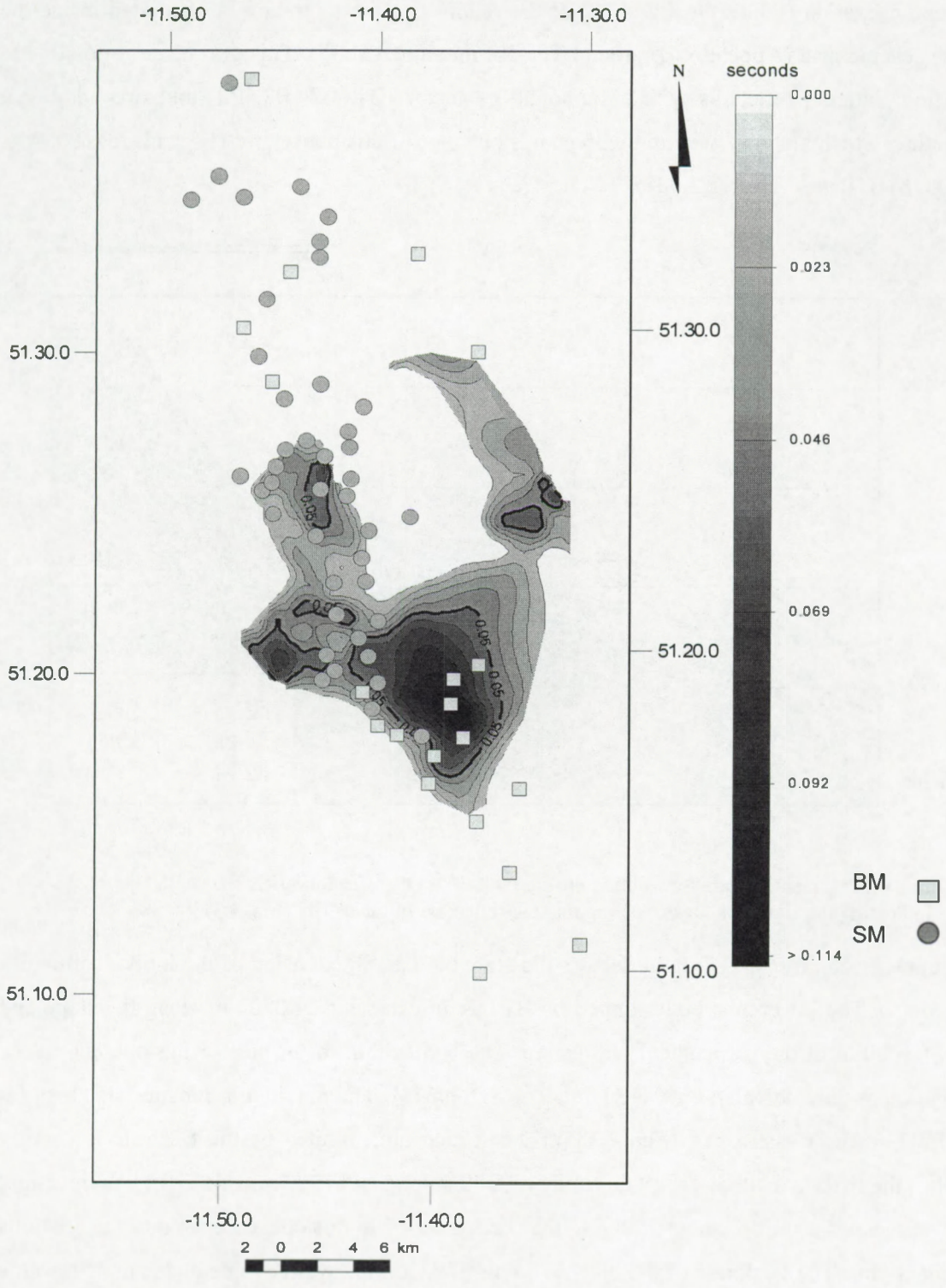

Fig. 4.31: Isopach map of facies Bb with the mound distribution.

Migration of sigmoidal reflectors

The general geometry of the sigmoidal forms in this facies suggests a northward (P010528) and upslope migration (P000644, Fig. 4.32) of the sediment. This migration is illustrated inside the dense seismic grid (Appendix B) around Thérèse mound (BEL35). This grid made it possible to map four internal reflectors with a sigmoidal geometry (B1, B2, B3, B4) and two additional reflectors, which are only seen in the most upslope part of this dense grid (B5 and B6) (P06044, P010528) (Galanes-Alvarez, 2001).

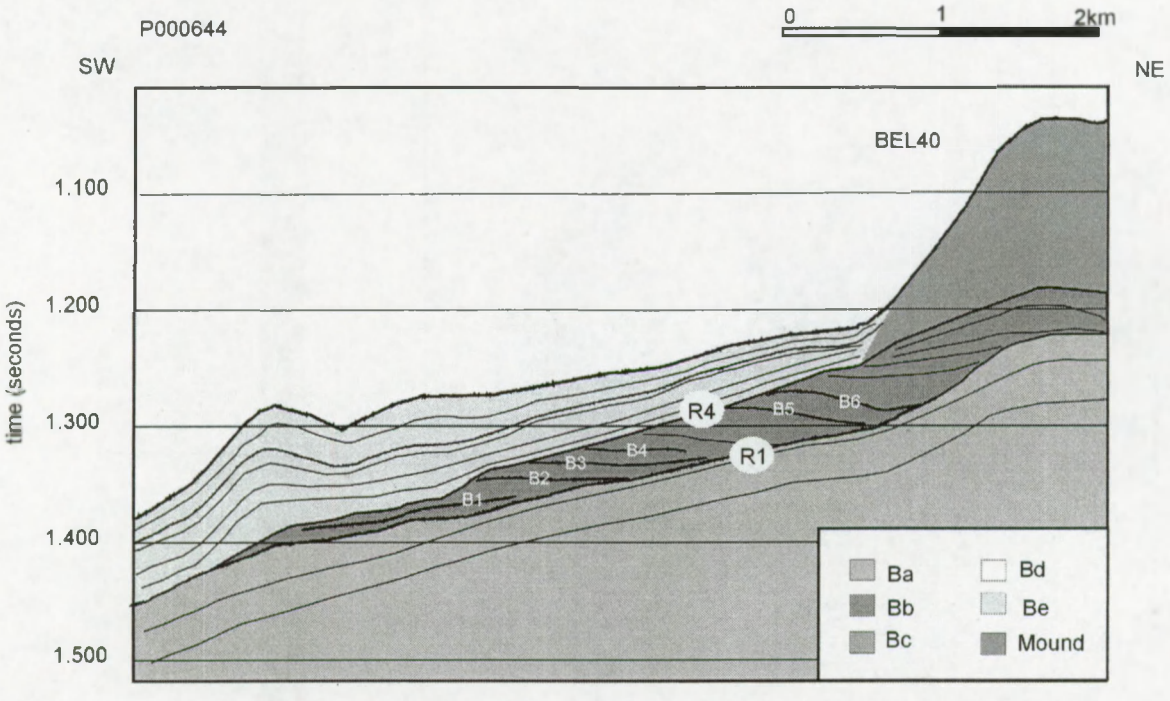

Fig. 4.32: Interpreted high-resolution profile P000644. The reflector labels start with B, indicating the sigmoidal upslope progradating reflectors of facies Bb. (Fig. 4.31)

The time structural maps of the reflectors illustrate the lateral extension of the individual bodies (Fig. 4.33). The lowermost body limited by B1 has an extension of 2700 m along the slope and one of 1700 m in the perpendicular direction. The bodies thin to the east or upslope and to the north, where they downlap on the R1 reflector (P000644). The maximum thickness is about 20 ms TWT in the western part (Fig. 4.33a). The second unit, limited by the B2 reflector, partly overlies the first. In a NS direction this body is 3300 m long and 1000 m wide in an EW direction. This unit shows a shift of about 700 m to the north and 600 m upslope, compared to the previous sediment unit. The thickness of the body is 40 ms TWT on the western side and it thins towards the north and upslope (Fig. 4.33b). Unit B3 shows a more elongate NS shape, extending 3600 m in NS direction and 1300 m in EW direction. This body shifts about 300 m more to the north and

500 m more upslope compared to B2 (Fig. 4.33c). The seismic grid boundaries limit the investigation of the extension of this body. Reflector B4 occurs on top of the B3 reflector with a dimension of 1300 m in NS direction and 500 m in EW direction (Fig. 4.33d). The sigmoidal forms started to migrate from the deepest part of the lower furrow flank and shifted to the north and upslope under a SN flowing current.

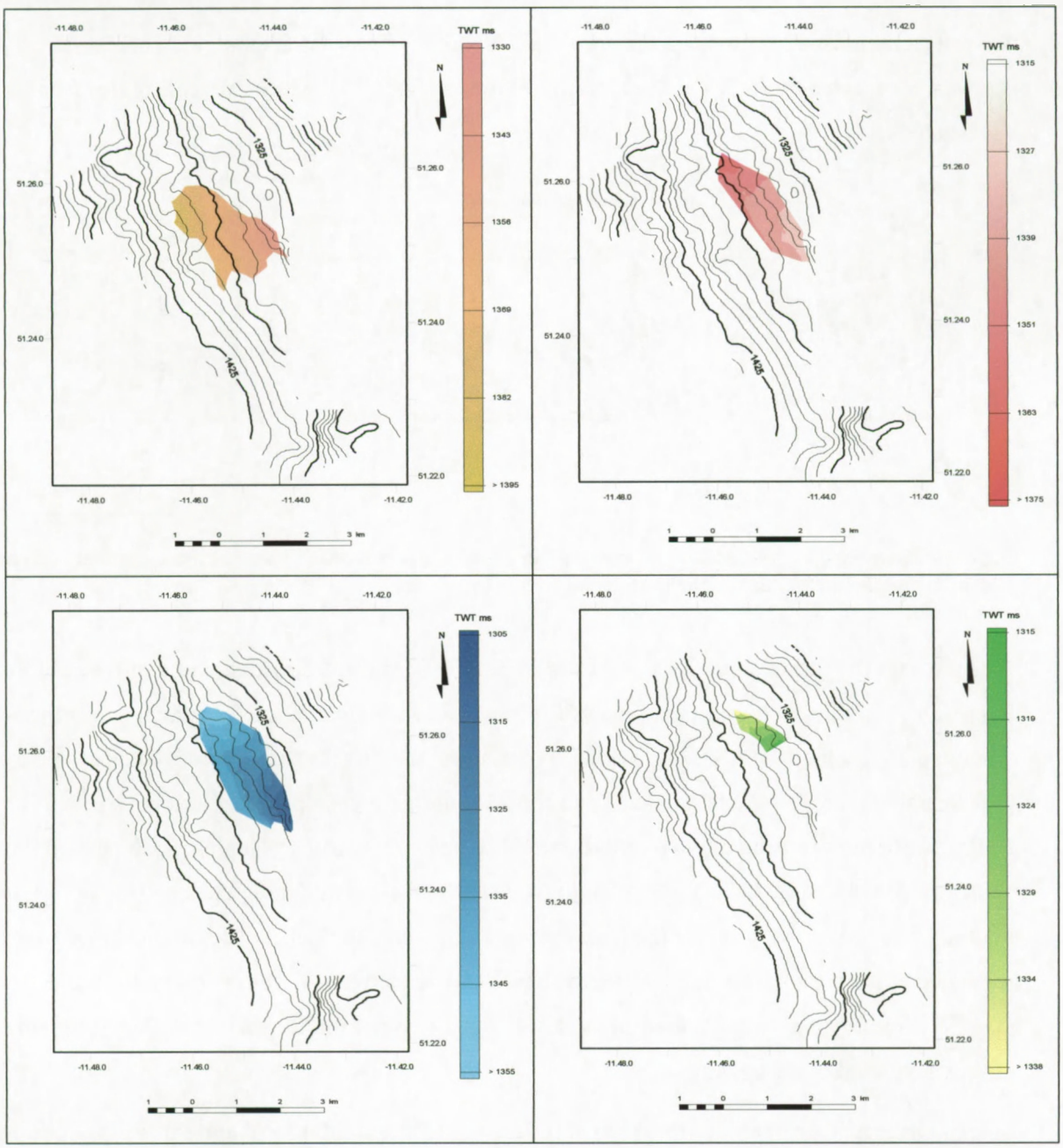

Fig. 4.33: Time structural maps of respectively reflectors B1, B2, B3, B4 as defined on profile P000644, plotted on top of the time structural map of R2. This set of time structural maps shows the upslope and northward migration of the sigmoidal bodies of facies Bb (Galanes-Alvarez, 2001).

4.4.2.3 Facies Bc

Facies Bc contains a second set of sigmoidal reflectors as observed on profile P010528 (Fig. 4.34). The facies shows an alternation of high and low amplitude reflectors with a high continuity. On the profiles crossing the upper part of the slope the upper 40ms of this facies have high amplitude reflectors just underneath facies Bd (P010517, P010521, P010528). This might indicate a dramatic change in lithology between the two facies. In the central part of the province the reflectors have a sigmoidal geometry on the NNE-SSW profiles (Fig. 4.28). These sigmoidal forms are truncated by R4, as seen on profile P010528 (Fig 4.34), which prevents to deduce their real shape.

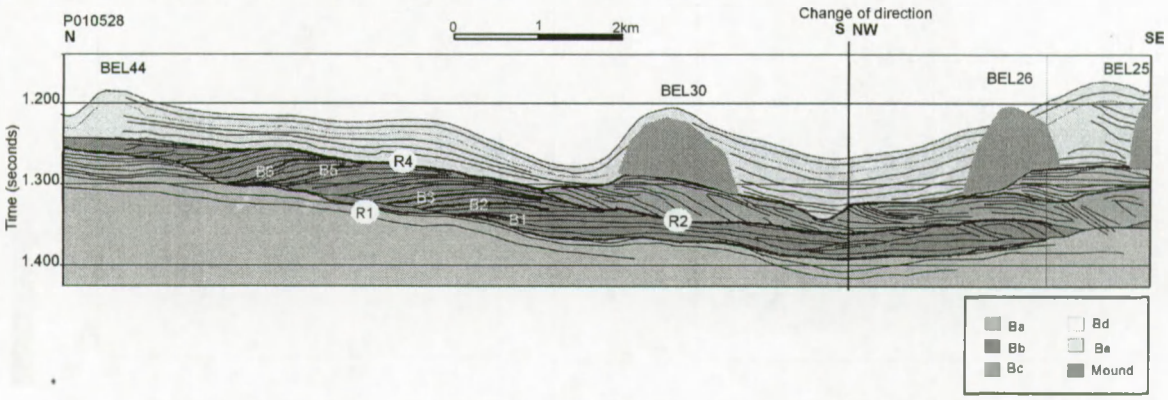

Fig.4.34: Interpreted high-resolution seismic profile P010528. This profile illustrates the sigmoidal units of Bb and Bc on the lower flank of the continental slope.

It seems that the forms climb locally on the slope in a northward direction and that they fill the incision within R2. At the steepest slopes of reflector R2 they are deposited on the EW profiles in a hummocky geometry (P980521). Higher on the slope and on less steep parts, this facies passes to subparallel high amplitude alternating reflectors, migrating upslope on reflector R2 (P010517, P010527). In the south the internal reflectors of this facies show a downlapping, upslope climbing geometry (P010528, P980521)(Fig. 4.28, Fig 4.34). The facies is thinning upslope (Fig. 4.35). In the southern part of the province the facies is more common and thicker. The extents of Bc to the north and to the west are limited by the erosional event related to R4. These observations indicate that the current energy was focused in the lower steep slope of the R2 surface with a SN regime during the period of deposition.

Lateral changes in geometry of the internal reflectors in Bc argue for local current regimes during the deposition. Local incisions and slope gradients may have enhanced the currents in this central part of the province, creating the sigmoidal forms. Outside the zone of enhanced currents, the geometry changes to subparallel reflections, indicating a calm current regime.

The real migration direction of these sigmoidal forms is not clear. The seismic grid did not allow mapping internal reflectors from the northern part of the province towards the south as seen on profile P980549 and P010528.

As seen on profile P980523, the facies might be correlated across the NS furrow CH created during the R4 event. On the western side of CH reflectors with approximately the same dip direction and angle as on the eastern side of the profile characterize this facies. Because this facies is hard to correlate with the present data set, it has been decided to leave this point open for interpretation.

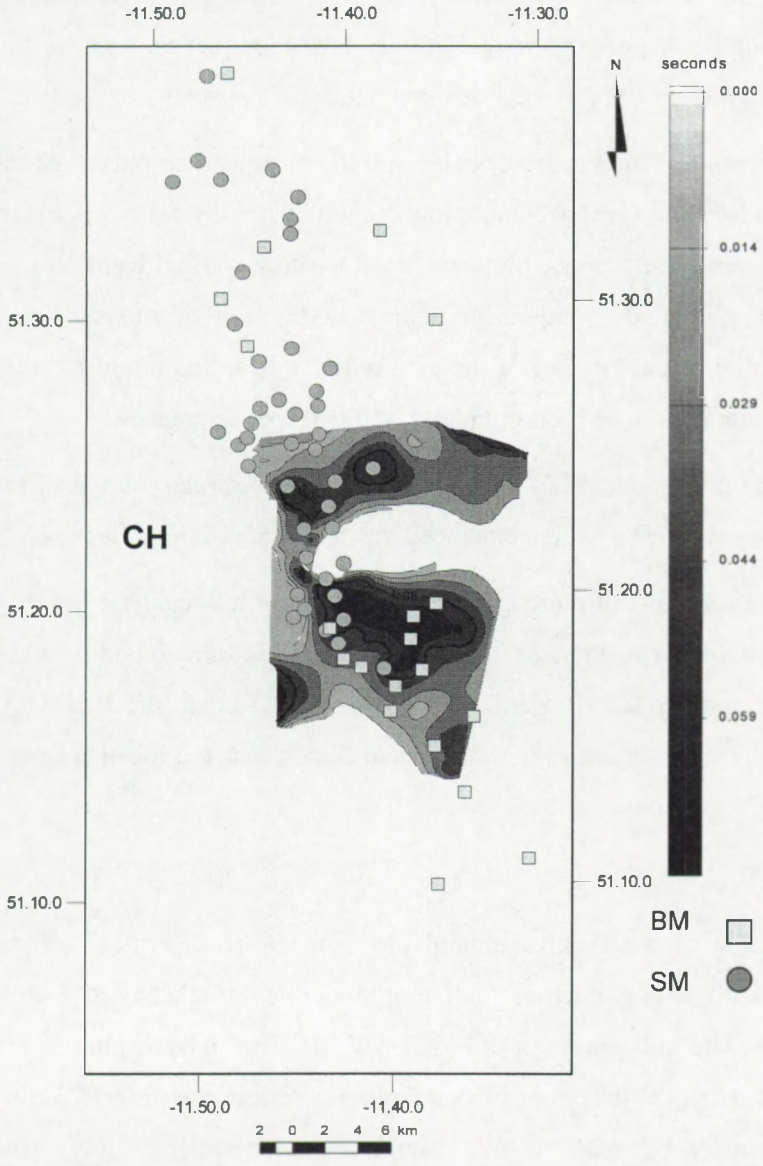

Fig. 4.35: Isopach map of sigmoidal facies of Bc with the mound distribution. The thickness is represented by the grey scale in ms TWT. No correlation is seen between the mound distribution and the facies occurrence. The facies is thinning upslope and became eroded in the NS furrow.

Indication for fluid accumulation

Remarkable in the facies Bb and Bc is the relative enhanced amplitude of the top part of the sigmoidal reflectors (P000644). A few of these enhanced amplitudes show a polarity inversion as seen on profiles P000644 (Appendix B). On the crossing line P010528, this polarity inversion has not been observed. Attribute analysis such as instantaneous frequency calculations show absorption of higher frequencies below this enhanced reflection (P000644). This might be an indirect indication of fluid accumulation in the top part of the sigmoidal shapes. To test this hypothesis Henriet et al. (2001a) performed a detailed study of profile P000658 (Appendix B), using seismic attributes to illustrate the phenomenon of the sigmoidal reflectors in Bc near the mound BEL26 (Challenger mound). A polarity inversion and lower frequencies below this reflector were evident. On the crossing profile P010523 this inversion was not seen.

The polarity inversions, the absorption of higher frequencies and the enhanced amplitude of the reflectors are indirect indications for fluid (gas) accumulation. Nevertheless, the reflectors below this enhanced reflector are not completely wiped out and do not show a significant loss of amplitude as should be expected if fluids were accumulating in the top of the sigmoidal structures. If fluids are accumulated in the top part of the sigmoidal bodies, this might be local because no indications for fluid migration have been found out of the deeper sequences.

An alternative explanation for the phenomenon is a contrast in lithology between the top of the sigmoidal bodies and the overlying sediments, which enhanced the amplitude of the reflection.

The top reflectors of this unit might consist of more compact sediments or a diagenetic cap may create higher amplitudes. During the deposition of these high-energy sediment bodies some organic matter could be trapped and produce biogenic gas that accumulated in the top of the sigmoidal forms. No correlation is seen between the mound distribution and the location of the enhanced reflectors.

4.4.2.4 Facies Bd

This facies is the most remarkable of the Belgica mound province. It has a typical, almost acoustic, transparent character with a few internal high amplitude low frequency reflectors (P010517, P010521, P980521). The reflectors on the NE-SW profiles have a basinward divergence with a subparallel character. On the NS profiles the internal reflections show a parallel configuration (Fig. 4.28). The upper boundary is the youngest erosive reflector (R4). The geographic extent of the facies is restricted by this erosional event (Fig. 4.36). For this reason the facies is restricted to the upper part of the slope.

This facies thins to the north and to the west till it disappears completely in the most northern and western part of the province (Fig. 4.36). The erosion of facies Bd has a terrace-like geometry on the EW profiles (P010517, P010521, P980521), which is seen in the bathymetry (see 4.1). The upper escarpment is located in the area between 11°34'/51°26' and 11°38'/51°22'. The maximum height of this structure is about 50 ms TWT. A second escarpment is located about 7 km more to the west and downslope between 11°38'/51°18' and 11°40'/51°22' with a height of 70 ms TWT. This escarpement is the western limit of facies Bd. Further to the west, a few patches of the facies Bd have been observed (P970536) and detached of the main sediment body. Mc Donnell related (2001) the scarps to the proximity of the shelf edge.

The lower boundary of the facies shows on the EW oriented profiles a smooth transition of high amplitude internal reflectors of facies Bc to the almost transparent facies Bd. On the NS profile the facies shows an infill aggradation of an irregular lower boundary and a thickening of the facies towards the south and upslope (Fig. 4.28).

The acoustically transparent facies might correspond with a similar seismic facies found in the south-western Rockall Trough (Jansen et al., 1996). This facies is related with the ODP LEG 162 site n° 980 nannofossil ooze dominated marine depositions of Pliocene age (Jansen et al., 1996). The higher amplitudes in the facies might represent a higher clay content.

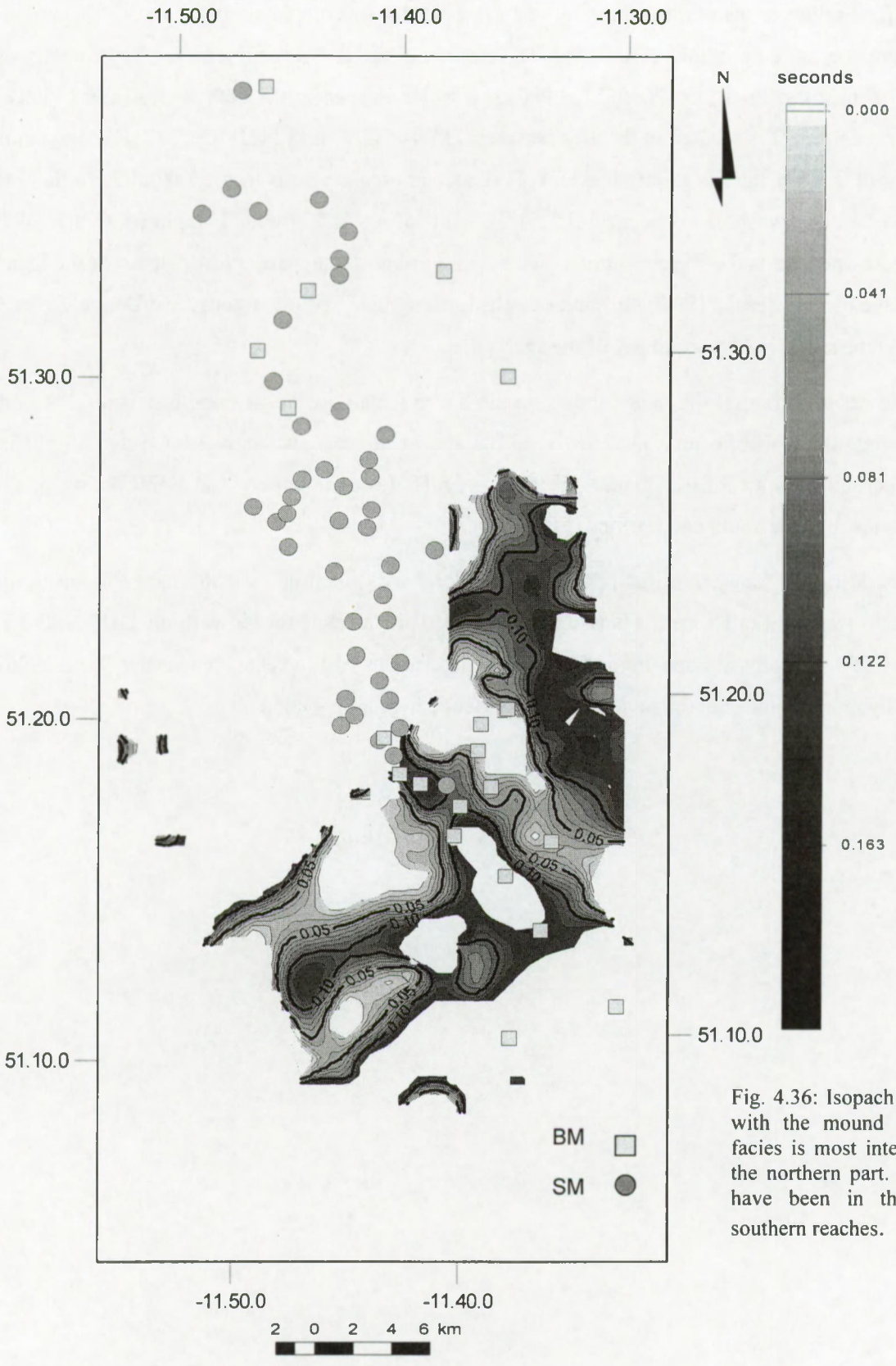

Fig. 4.36: Isopach map of facies Bd with the mound distribution. This facies is most intensively eroded in the northern part. Two escarpments have been in this facies in the southern reaches.

4.4.2.5 Mound substratum

A subcrop map is made along the R4 surface or mound base to illustrate the possible correlation between the distribution of the mounds and the substratum (Fig. 4.37). On this map it is clearly seen that the mounds have no preferential substratum. In the southern part facies Bd is most common, with buried and surface mounds on top. Most of the mounds are located on facies Bc and the most western mounds on Bb. Only a few mounds are located on the facies Ba.

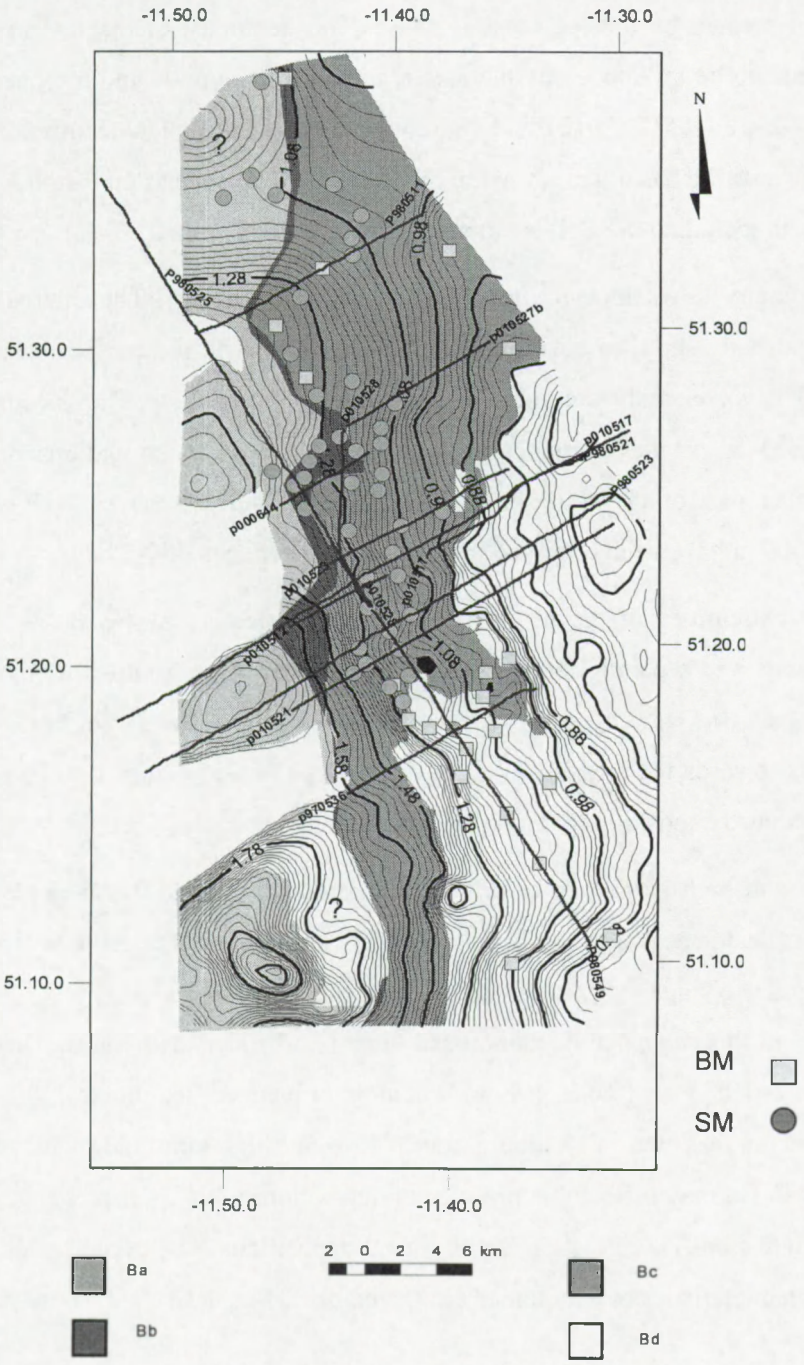

Fig. 4.37: Subcrop map along R4 or mound base. This map illustrates that no clear relation is seen between the mound substratum and the mound distribution. The seismic profiles have been illustrated in red in appendix B.

4.4.2.6 *Facies Be*

The upper sedimentary sequence in the area extends between the R4 reflector and the seabed reflector. This sequence covers the Pliocene to recent sediments (see R4). The seismic facies of this sequence is clearly different from the facies observed below the mound base (Appendix B).

This sequence is characterized by cycles of continuous reflections of variable amplitude with a low frequency. The reflectors are parallel to subparallel. The sediments of this sequence fill the youngest phase of channeling created by the R4 erosion phase. The geometry of the internal reflectors of the sequence seems to be influenced by the appearance of the mounds and by local incisions (e.g. P980525, P980523, P010512, P01017). This sequence has a basinwide occurrence and the thickness increases towards the basin margin, with a maximum of sediment deposition in the southeastern part of the basin including the Belgica mound province (Mc Donnell, 2001).

The seafloor has a wavy geometry downslope the mounds in the southern part. The internal reflectors in the wavy sediment body show an upslope migration onlapping on the erosive base R4 (Fig. 4.28, Appendix B). The wavelengths are quite large as seen on the profiles. They occur on the isopach map (Fig. 4.38) as patches, which are interpreted as local accumulations or sediment mounds. On the upper part of the slope on profile P010517, surface waves with a wavelength of approximately 500 m have been observed in water depths between 450-350 m.

To the northern and upslope extremities of the profiles the internal reflectors of Be show a thickening of the individual units and a parallel configuration. This observation argues that the sediment deposition in these areas was less energetic than in the steeper part of the slope. In the central part the sequence thins towards the NS furrow from an upslope direction and from the basin centre. This suggests a reduced deposition in the NS furrow due to enhanced currents.

This facies of alternating low and high amplitude reflectors contains in the thickest sequences several units of low and high reflector packages (Appendix B). This alternation of amplitudes is most probably related to a similar change in lithology as seen in the Feni drift (Jansens et al. 1996). The dominant lithology in this sequence is nannofossil ooze interbedded with clays. The shift from pre-glacial carbonate-rich ooze (facies Bd) to glacially influenced sediments (with varying degrees of clay content) is reflected in an alternation of low and high amplitude facies. The low-amplitude reflections in Bd may reflect this pre-glacial deposition, with a sharp change across R4 to the higher amplitude stratified reflection Be of glacial depositions. The upper facies shows on the isopach map all characteristics of a mounded elongated drift (Fig. 4.38).

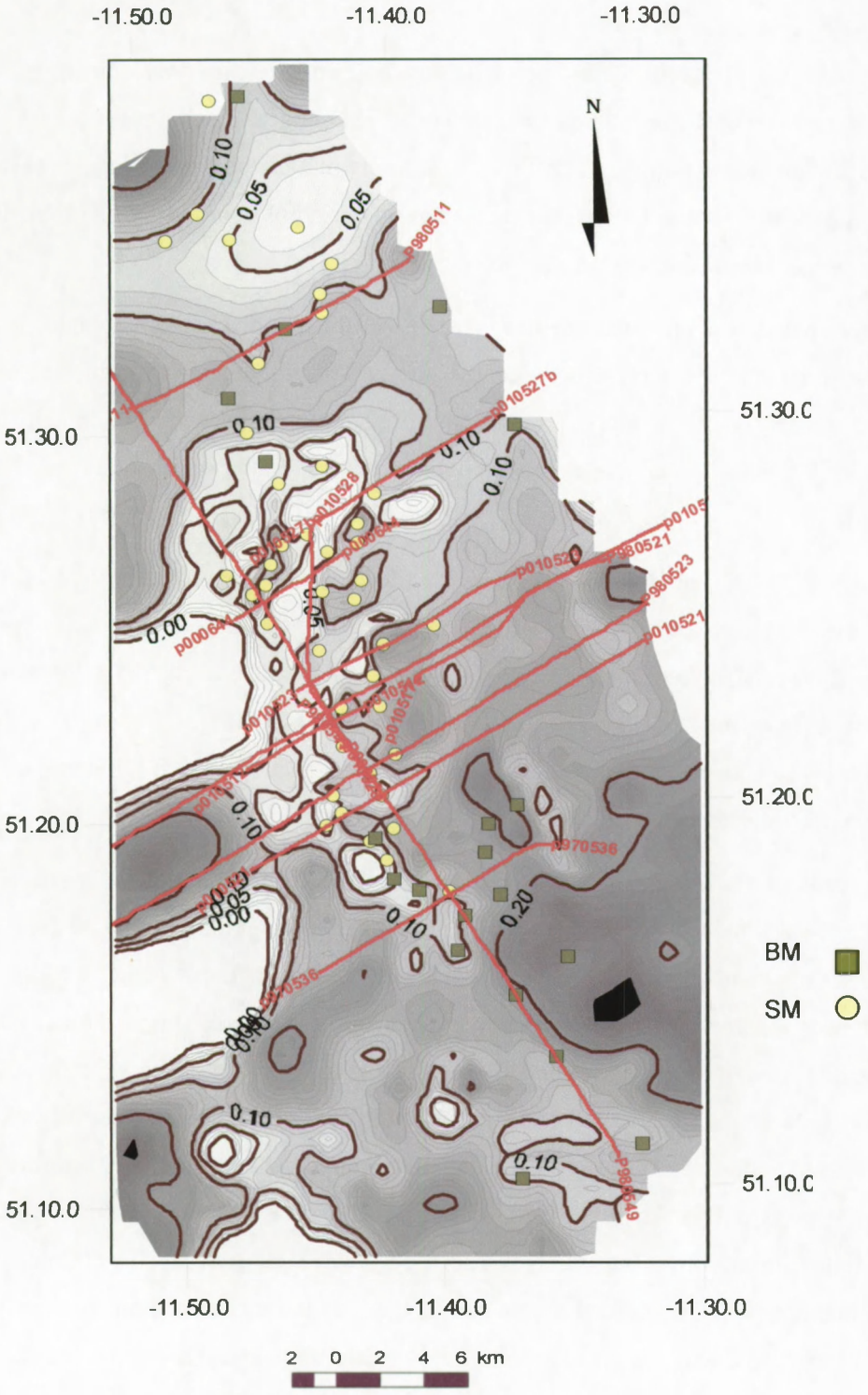

Fig. 4.38: Isopach map of facies Be. The mounds are closely related to the thinning of Be.

Mound-Be relation

The Belgica mounds are embedded in this facies Be and it seems that the development of the mounds steer the deposition of the sediments and vice versa. The reflectors endings have an onlap configuration on the mound, which suggests that the mounds had already a certain dimension during the deposition of this facies. This means that a certain period of non-deposition or erosion took place during the period in which the mound developed.

In the most southern part of the province, the upslope flank of the mounds is often completely or partly buried. The sediments are ponded between the margin and the mounds. In other cases a clear moat shape is seen on the upslope flank, suggesting turbulence around the mound. Its geometry shows infill structures and gets mostly smoothed upwards in the sedimentary sequence (e.g. P980521, P010521).

On the NS profiles P980525 and P980549 (Fig. 4.28) the mounds seem to be buried on the southern side of the mound, except BEL09, which is flanked by two local depressions. These channels can be followed further upslope and have been interpreted as turbidite channels, transporting sediment from the shelf to the rise (Van Rooij et al., accepted). On many locations the internal reflections converge to the mound, while the sediment sequences thin. This suggests a reduced deposition due to enhanced currents.

The downslope flank of the mounds, facing the NS furrow, remains mostly exposed. The sediment cover on the downslope side is relatively thin in comparison with the upslope flank of the mound. An isopach map of the facies has been made, based on the seismic profiles, to illustrate the sediment thickness and sedimentation pattern in the province (Fig. 4.38). On this figure a NS elongated zone of reduced sedimentation is seen at the location of the NS furrow CH in the bathymetry. Downslope, the mounds border a NS furrow, which lies in water depths of 1050-1500 m further southwards (see 4.1). A distinctive, rough seabed character within this topographic low suggests debris flows or slump deposits, which has probably been originated from upslope sediment instabilities, but this is not seen on the seismic profiles. The thinning of the sediments in this furrow is highlighted by the convergence of internal reflections to the west. This suggests a depositional and not an erosional origin of the thinning. This zone of reduced sedimentation during the development of the mounds argues for local and focused currents in the furrow, transporting sediments. This enhanced current regime in the furrow safeguards the downslope side of the mounds and, in general, the most northern mounds of the central mound province, from further burial.

The isopach map (Fig. 4.38) indicates that the sediment thickness increases to the east or upslope the mounds and that the mounds occur in zones with reduced sedimentation. The buried mounds are located in zones with more sediment pressure and probably calmer current regimes as on the lower flanks of the furrow. The same pattern of thickening of the sediments has been observed on the northern side of the province. In general, the smallest buried mounds appear in the zones with a thick sediment cover of facies Be (see 4.3). This observation suggests that sediment pressure limited the mound development. The mounds developed in active current zones with reduced sediment deposition. The deposition of the facies Be is also steered by the occurrence of the mounds, creating turbulence and reducing sedimentation around the mound.

- The geological units below the mound base indicate depositions in vigorous bottom currents, flowing to the north and migrating upslope. These facies have been interpreted as contourite deposits (Lekens, 2000; Mc Donnell, 2001; Van Rooij et al., accepted).
- A clearly change in drift sedimentation has been observed below and above the mound base, arguing for a major change in the hydrodynamic regime.
- The mound base is the last erosive event of Pliocene age.
- The mounds seem to be lined up along the contourite channel CH and along turbidite channels.
- The geometry of Be around the mounds inferred a rapid development of the mound during a period of non-deposition after a major erosional event.
- The largest surface mounds are located in the steepest zone of the mound base in a zone with reduced sedimentation of Be.
- Buried mounds have been observed in zones with a thicker sediment cover of Be.
- The development pattern of the mounds is influenced by the sedimentation rate. This suggests a biological origin of the mounds.
- The geometry of the youngest elongate-mounded drift (Be) indicates a focalized bottom current in the local NS furrow CH.
- No correlation has been observed between the underlying mapped seismic facies and the mound distribution.
- Indirect observations for subsurface migration of gas are weak and not directly linked to the mounds. These observations might only indicate some small-scale migration.

4.5 Seismic properties of the mounds

The mound structures appear on the seismic profiles as almost transparent dome shape structures. Inside the mound no internal reflectors have been recognized, which might indicate a uniform facies without any large impedance differences (Appendix B).

An important observation is that the reflectors underneath the mounds show reduced amplitudes although the reflectors are not completely wiped out. This argues for the fact that not all the energy is absorbed or dispersed in the mound facies.

These underlying reflectors show at most of the locations velocity pull-ups. On the profiles crossing the highest point of the mound structure, the pull-up is the most expressed and therefore useful to estimate the velocity difference between the surrounding sediment and the mound.

On two Belgica mounds a velocity analysis has been performed, with the aim to estimate the internal velocity of the mound facies (Fig. 4.39). The first mound, BEL27, is lying in the southern part of the Belgica mound province, which is partly buried on the eastern side. The velocity analysis is performed on the seismic profile P010516. The base of the mound is erosive, as seen in the abrupt termination of the underlying reflectors. Due to this erosion the general trend of the reflector is not visible. It has been estimated on a reflector around 1.2 s. The velocity pull-up is measured from this virtual base reflector. This trend and pull-up is shifted to the base of the mound. The time of the pull-up or the time between the actual time of arrival and the supposed time of arrival is symbolized by Tp. The travel time of the sonic wave through the mound is Tm, which is measured from the base till the top of the mound. This top of the mound is used as reference level for the other time measurements. The travel time in the sediment column is symbolized by Ts.

The internal sonic velocity of respectively the mound, water column and water is represented by Vm, Vs and Vw. The ratio of the average velocity inside the mound and outside the mound is given by:

$$V_m = \frac{T_m + T_p}{T_m}\left(\frac{T_w}{T_m + T_p}V_w + \frac{T_s + T_p}{T_m + T_p}V_s\right)$$

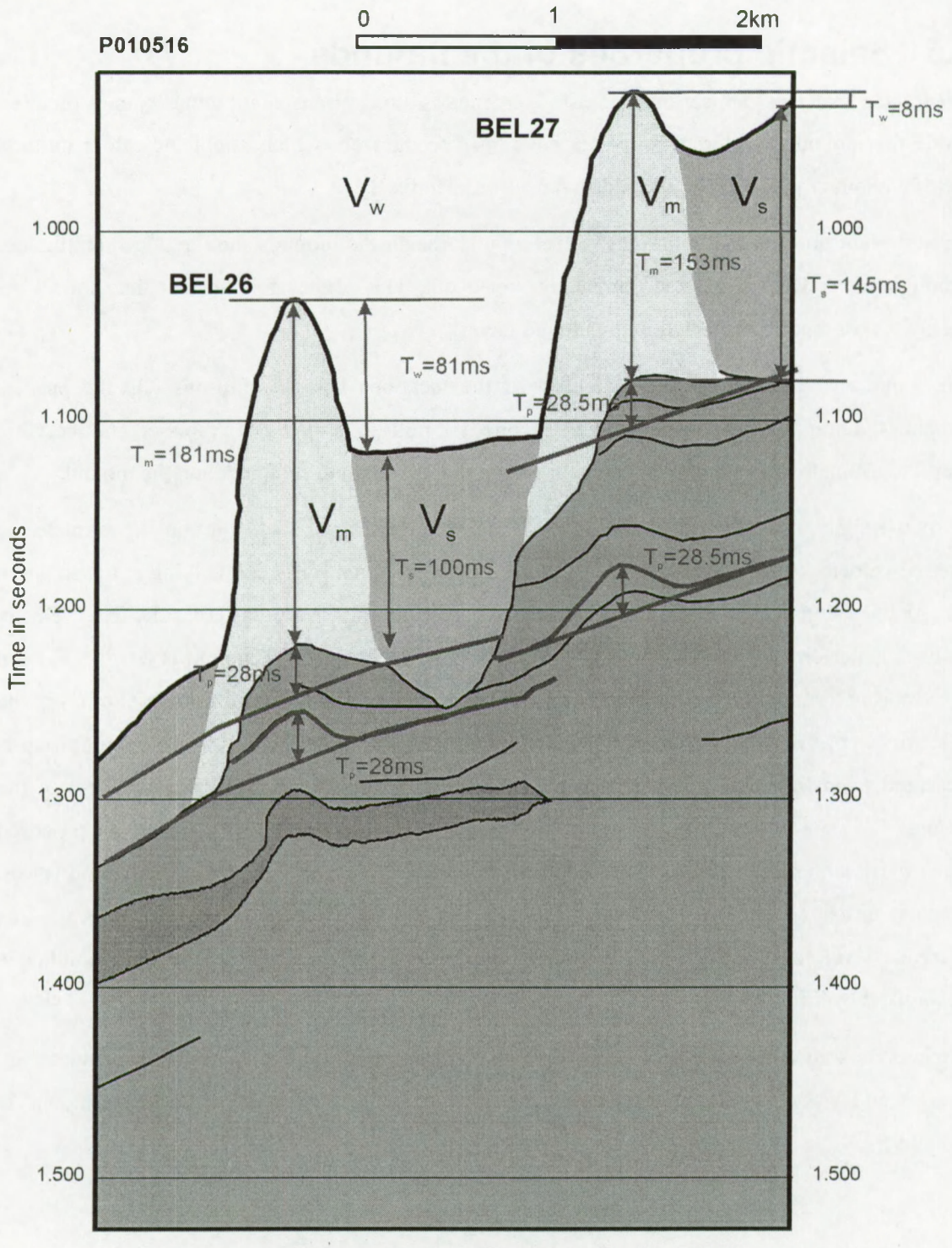

$$V_m = \frac{T_m + T_p}{T_m}\left(\frac{T_w}{T_m + T_p}V_w + \frac{T_s + T_p}{T_m + T_p}V_s\right)$$

Fig. 4.39: Model of the velocity calculation performed on profile P010516 for the mounds BEL26 and BEL27 (see text for explanation).

All factors in the formulae can be read on the seismic profiles except the velocities. The water velocity can be calculated from the salinity and the water temperature and is approximately 1500m/s. The velocity of the surrounding sediments is estimated to be 1600m/s, which is a common velocity for shallow fine-grained deep-sea sediments. With these factors the velocity can be calculated for the mound facies:

$$V_m = \frac{153ms + 28.5ms}{153ms}\left(\frac{8ms}{153ms + 28.5ms}1500m/s + \frac{145ms + 28.5ms}{153ms + 28.5ms}1600m/s\right) = 1893m/s$$

A similar exercise is done for the neighboring mound BEL26 on profile P010516:

$$V_m = \frac{181ms + 28ms}{181ms}\left(\frac{81ms}{181ms + 28ms}1500m/s + \frac{100ms + 28ms}{181ms + 28ms}1600m/s\right) = 1813m/s$$

This estimation of the velocity inside the mound suggests that the velocity is 1850 m/s ± 50 m/s. This enhanced velocity can be due to the amount of carbonate in the mounds. Theoretically, a large amount of carbonate can be suspected in the mounds if they are partly composed of carbonate rich sediments (foraminifera, coccoliths) (see 4.7).

Carbonates have generally an acoustic transparent character. Four main groups of parameters influence the seismic response in carbonate lithologies:

- petrophysical properties, such as porosity, pore compressibility, fluid saturation and fluid type,
- lithological parameters as mineralogy and shaliness or the degree of clay content in the sediment,
- physical conditions, such as effective stress, temperature and frequency,
- geometric factors such as bed thickness and anisotropy.

Porosity is the most important factor deterring the seismic response in carbonate rocks (Marion and Jizba, 1997).

The sonic velocity in unconsolidated carbonate mud to completely lithified limestones shows little correlation with depth of burial. Velocity inversions with increasing depth are thus common in such settings (Anselmetti and Eberli, 1997). The sonic velocity in carbonates is controlled by the combined effect of depositional lithology and diagenetic processes such as cementation and dissolution. The variations in velocity are due to the amount of porosity and the porosity type and

not to variations in mineralogy. Measured velocities generally show a positive correlation with density and an inverse correlation with the porosity, but departures from general trends can be as high as 2500 m/s affected by marine cementation.

If the mounds would consist completely of carbonates, the velocity should be around 2000 m/s or higher. This illustrates that the composition of the mound is a mixture between carbonate and siliciclastic sediments with a high porosity. Diagenesis in a mound might increase the speed. Nevertheless, real diagenetic banks should give a difference in impedance, which lead to a clear reflection inside the acoustic mound facies. This is not the case. The seismic facies reflect most probably a lithologic composition with a high percentage of carbonates related to the organism.

- The seismic velocity analysis of the mounds in the Belgica mound province results in an average velocity of 1850 m/s ± 50 m/s. This is about 15% higher than the surrounding sediments.
- The inferred composition suggests carbonate-rich sediment with intermixing of siliciclastic sediments.
- No indications for dramatic intern impedance changes have been found in the mound facies. This suggests a uniform composition under normal marine diagenetic processes.

4.6 Case studies

Two mound areas have been selected to discuss them in more details and to test the general observation made in 4.3. For this analysis two dense seismic grids have been used, covering BEL26 and the mound cluster BEL32, BEL35, BEL36, BEL38 and BEL39. These grids allow discussing the individual geometry, the mound base and the sedimentation around these mounds. BEL26 is situated in the southern part and all other mounds mentioned above are situated in the northern part of the central mound zone (Fig. 4.3). The interpretation of the seismic profiles has been presented in appendix B.2 and B.3.

4.6.1 BEL26, Challenger mound

4.6.1.1 Bathymetry

Challenger mound is located in the southern part of the central mound zone in a generally steep part of the continental slope (Fig 4.3). The mound is part of a NS trending ridge of surface mounds in narrow depth interval (Fig. 4.3, Fig. 4.40). Upslope of BEL26, BEL27 is almost perfectly located in line with BEL26 (Fig 4.3, Fig. 4.40).

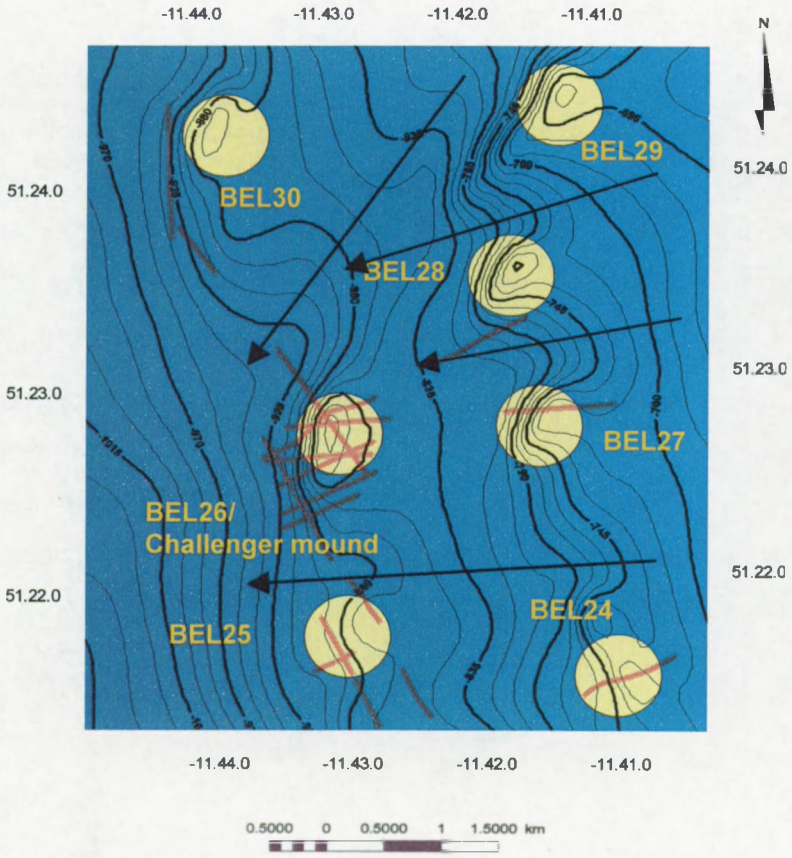

Fig. 4.40: Multi beam map of the area around Challenger mound. The mound facies mapped on the seismic profiles is indicated in red. The mounds are located near downslope channels (arrows) in the present seabed (source: AWI Bremerhaven).

The summit of BEL27 is about 100 m higher on the slope and 900 m more to the east. The area between the mounds is relatively gentle and argues for a certain sediment infill between the mounds. BEL26 has a steep western flank of which the slope decreases gradually to the base of the NS furrow CH (Fig 4.40).

BEL 26 is flanked by two EW incisions on the northern and southern flanks. These incisions are about 30 m deep, which separate the mound from the neighboring mounds at the same depth level (Fig. 4.40).

The incision on the southern flank between BEL25 and BEL26 lies in line with an incision along the southern flank of BEL27. A zone without any depression separates the two incisions in the seafloor. It shows a relatively low slope gradient and is about 400 min width. BEL25 lies about 900 m to the south of BEL26 at approximately the same water depth.

To the north, an incision of about 35 m depth and 650 m wide, with a NE-SW orientation, flank the mound. This channel can be followed higher up the slope, where it has a steep southern flank near the mounds and smooth northern slopes. Near BEL26 the southern flank of this channel is less steep than near mounds higher on the slope. The southern flank is less expressed in the bathymetry than the northern flank.

4.6.1.2 Geometry

The "real" mound geometry is based on the mapping of the seismic mound facies. The occurrences of the mound facies along the seismic profiles have been plotted on top of the bathymetric map in figure 4.40. This map illustrates that the mound facies extent is broader than seen on the bathymetric data. The multi beam map suggests a NS elongation of the mound. On the mound facies map a slight elongation in NE-SW direction is inferred of the real mound geometry (Fig. 4.41). The slopes of the mound are steep and well defined.

In total nine seismic profiles have been taken into consideration for the geometric analysis, six in EW direction and three in NS direction. The highest height of 200 ms has been observed on two NS-profiles (P000617, P000658), where the mound has a width of approximately 1 km (Fig. 4.42). In EW direction the measured widths are similar to the NS widths although they have been measured on a lower point of the mound.

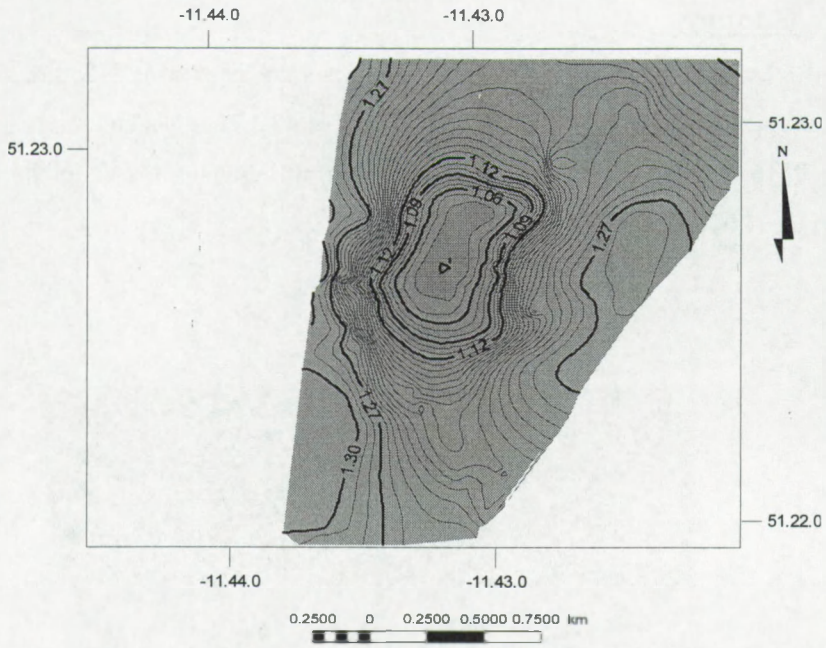

Fig. 4.41: Time structural map of Challenger mound superposed on the mound base surface.

The measured width and height shows a positive trend for the EW and NS directions (Fig. 4.42). This plot illustrates that the mound has a broad base of about 600 m and a low height, which suggests again that the development started first laterally. Later on the mounds developed vertically and less in width. In plan view the mound has an almost circular geometry with a dimension of 1 km across at the mound base. During the development of the mound, the shape seemed to be more elongated in NS direction. This is probably steered by external factors as currents.

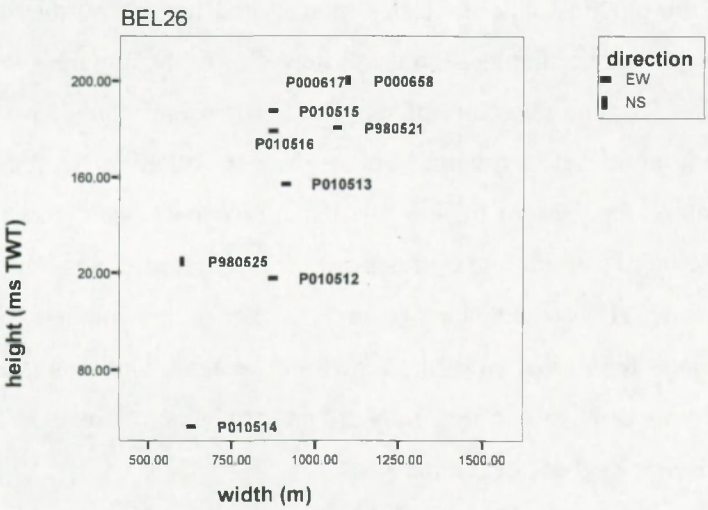

Fig. 4.42: Height-width measurements along the seismic lines for BEL26 (Challenger mound).

4.6.1.3 Geology

The mound base surface (R4) (Appendix B.2) shows an incision in NS direction on the eastern side of the mound between BEL27 and BEL26 (Fig. 4.43). This is also clearly seen on the seismic profile P010516 (Appendix B.2). The mounds are sitting on a break in the slope of the base mound surface (P010516, P010515).

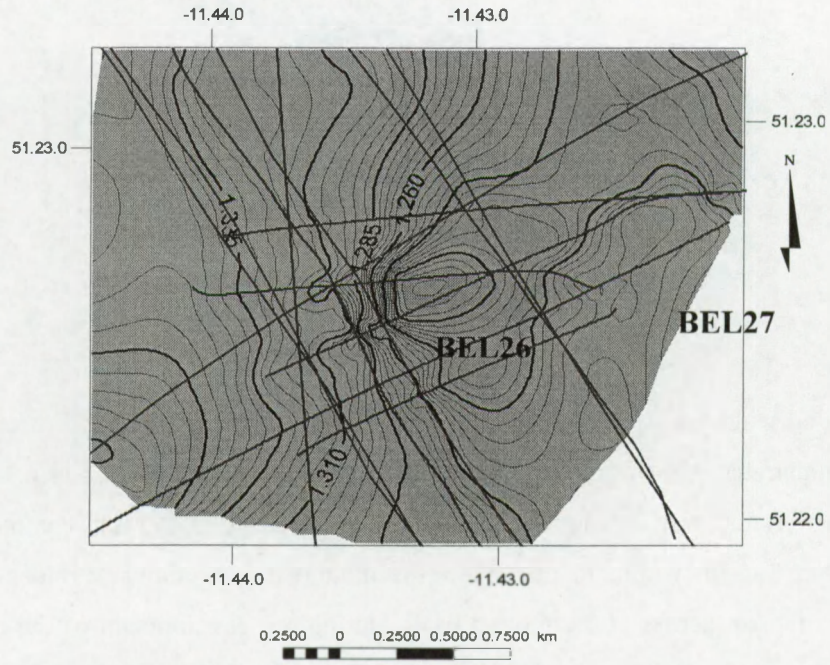

Fig. 4.43: Time structural map (in s TWT) of the mound base reflector R4, based on seismic profiles.

On the isopach map of facies Be, the mound shape is clearly imaged and limited by the zero contour (Fig. 4.44 and Fig. 4.45). Sediment accumulates on the eastern side of the mound, filling the incision between BEL26 and BEL27. The reflectors of this infill, onlap the mound, which suggests that the mound was already an elevated structure before the deposition of Be started (Appendix B.2). Sediment deposition on the western flank of the mound has only been observed on the lower part. This suggests enhanced current and non-deposition to reduced deposition on the western side, facing the NS furrow CH. The sediments cover is thicker on the southern side than on the northern side. This is due to the formation of the downslope channel on the northern side of the mound. The slope of the mound shows a more gently dip on the southern flank. On the northern flank the sediment cover forms a kind of tail geometry.

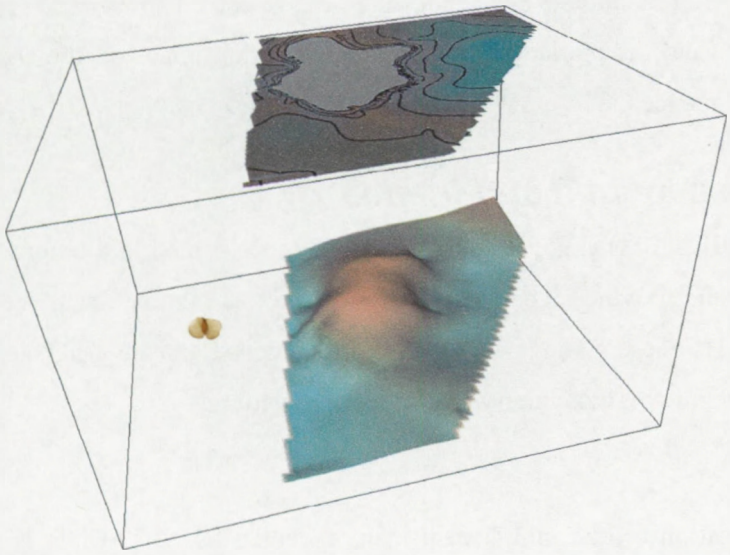

Fig. 4.44: 3D evocation of BEL26 where the sediments of Be are stripped. On top the isopach map of the surrounding sediment of Be.

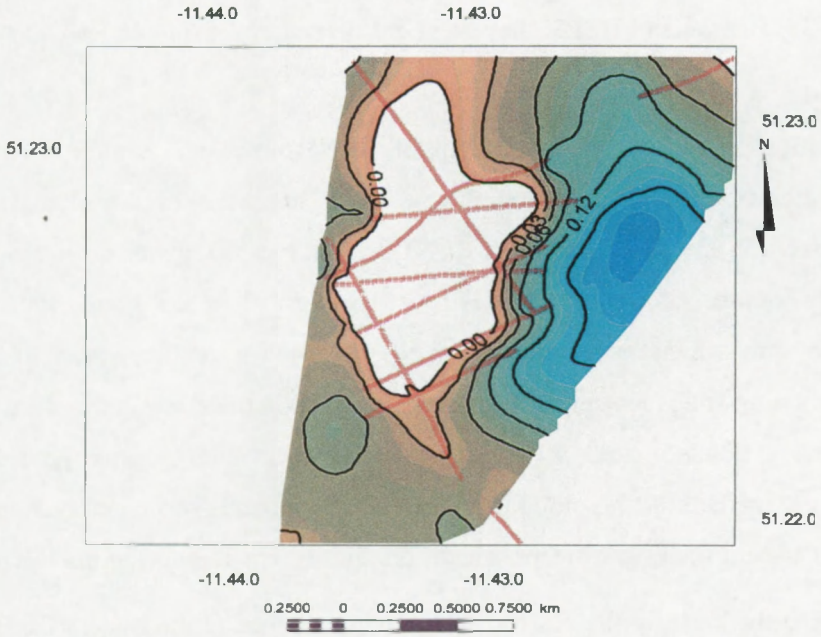

Fig. 4.45: Isopach map of Be around BEL26, Challenger mound. The red lines indicate the mound facies observed along the seismic lines. The zero contour illustrates the mound shape.

The mound geometry and the sediment distribution of Be suggest a bottom current along the western flank of the mound, focalized in the NS furrow CH. The infill of the incision in the mound base surface, on the eastern side of the mound shows a high-energy facies in the early stage and a draping in the final stage, which smoothes the erosional feature in the present bathymetry (Appendix B, P010516). This is seen in a thick sediment cover of Be on the eastern flank of the mound. This observation indicates that during the early phase of the mound development, the currents have been more vigorous but they slowed down during the development.

Facies Bc forms the substratum of the mound (Appendix B.2). As discussed above, no conclusive evidence has been found for fluid accumulation or migration near the mound in the sigmoidal reflectors of the underlying sequence.

4.6.2 BEL35 - Thérèse mound and friends

Thérèse mound, BEL35 and BEL32, BEL36, BEL38 and BEL39 are located in the north of the central part of the Belgica mound province. The mounds are located in a relative flat area close to the center of the NS furrow CH. These mounds are covered with a dense seismic grid (see 3) and allow a detailed study of the geometry, bathymetry and underlying geology.

4.6.2.1 Bathymetry

All mounds have a NS elongation on the multi beam map, excepted BEL36, which is almost circular (Fig. 4.46). Nevertheless, only BEL35 (Thérèse mound) has an almost perfect NS elongation. Mounds BEL38, BEL39 and BEL32 have a slight derivation of this direction to the east or the west.

BEL38 is located in a relative flat zone on the lower flank of the NS furrow and is more NW-SE oriented, parallel to the trend of the flank of the furrow CH. The shape of the mounds is symmetric with gentle flanks on the south and the west. BEL32 is located higher up the slope than BEL38, but they have both the same orientation (Fig 4.46). Nevertheless, the mound shows a clear asymmetry in shape with a high slope gradient on the west and a gentler eastern flank. BEL39 has a NW-SE orientation and is located at the highest position on the slope in this detailed grid. On the northern side it flanks a zone with small slope gradient and the greatest slope gradient is seen on the western flank of the mound. In general, the mounds show gently sloped flanks on the southern and eastern flanks and steeper slopes on the western and northern flank.

The mounds are bounded to the west by the NS furrow CH and between BEL35 and BEL32 a NE-SW orientated channel merges with the NS channel (Fig. 4.46). This channel has a more NS orientation upslope and separates the discussed mounds with mounds higher up the slope (Fig. 4.2). These channels indicate zones of reduced deposition and enhanced currents. The steep flanks of the mounds are oriented to the west and to the north or to the channels. In between neighboring mounds (BEL35, BEL36) the seafloor is smooth, arguing for sediment accumulation between the mounds (Fig. 4.46).

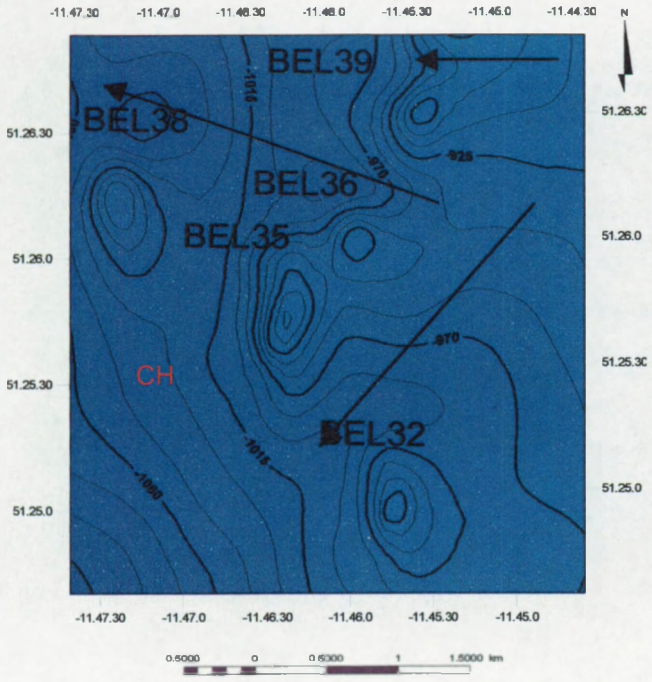

Fig. 4.46: Detailed bathymetric map of Thérèse mound (BEL35) and the surrounding mounds, based on multi beam data. Downslope channels (arrows) are observed in between the mounds (source: AWI Bremerhaven).

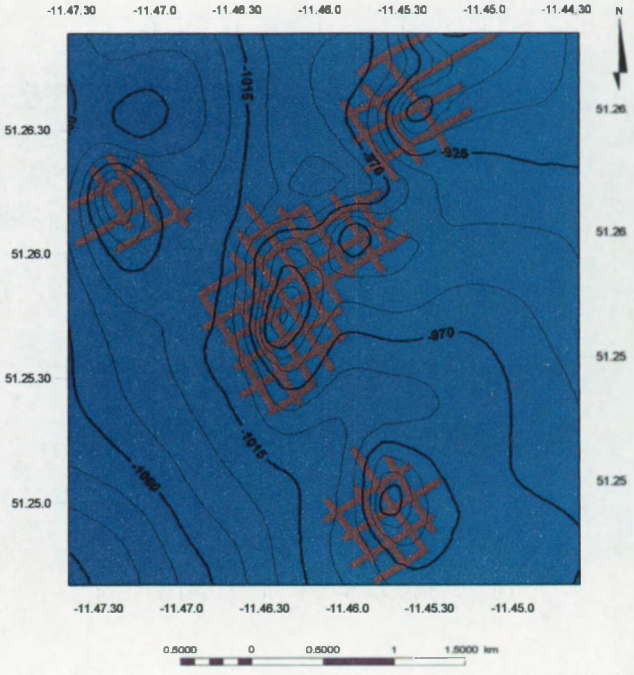

Fig. 4.47: Mound facies mapped on the seismic profile indicating the real mound shape without sediment cover.

4.6.2.2 Geometry

The seismic mound facies has been mapped on the profiles and plotted on top of the bathymetry recorded with multi beam (Fig. 4.47). This map shows the differences between the real extent and the surface expression of the mound. The mound facies is illustrated for each mound on seismic profiles in appendix B.3.

The width and height measured along the seismic profiles has been plotted for each mound in a height-width plot (Fig. 4.48). Three profiles of BEL35 with an EW orientation and two with a NS orientation display a maximum mound height of 210 ms TWT or 194 m. The related widths are smaller in the EW direction than in the NS direction and argue for a NS elongation of the mounds. The width varies with direction and from profile to profile, which indicates an irregular shape of the mound. The maximum width is approximately 1500 min NS direction and 1100 min EW direction or a NS/EW ratio of 1.4. In general, the width measured on the NS profiles is larger than on the EW for a similar height, which confirms the NS elongation. For smaller heights, the width does not decrease dramatically, which again argues for an early lateral development.

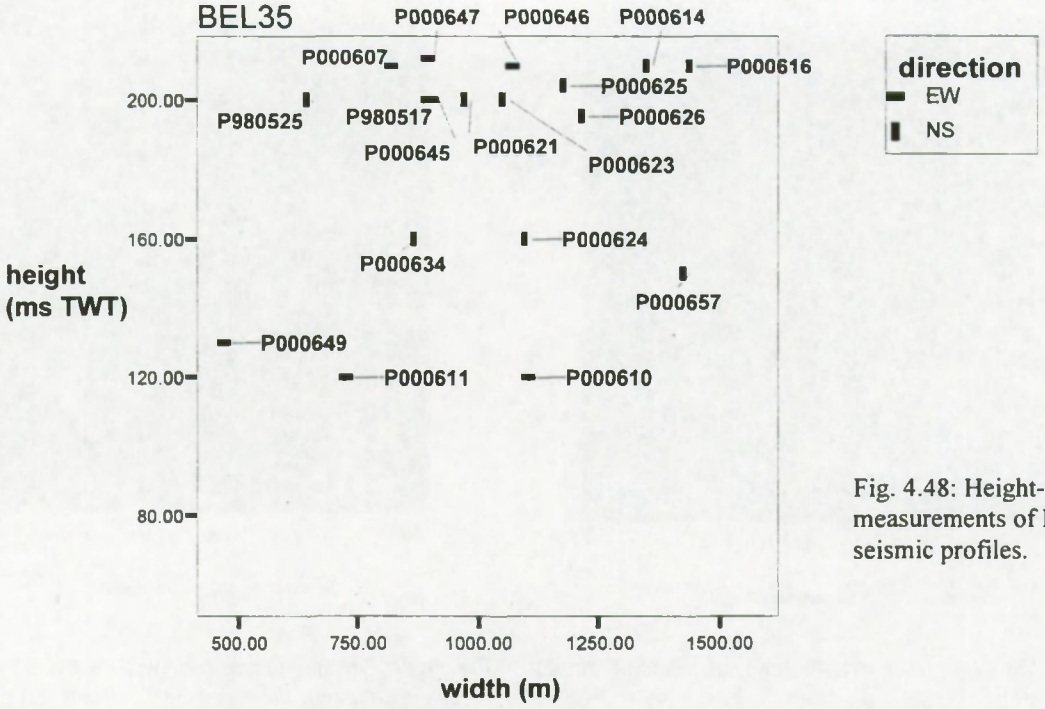

Fig. 4.48: Height-width measurements of BEL35 on the seismic profiles.

The mound geometry, based on the seismic profiles, yields the best approximation of the entire mound shape on the paleo-seafloor (Fig. 4.49, Fig. 4.49). The summit of BEL35 is relatively flat and the slope gradient increases towards lower flanks. The steepest flank is oriented towards the NS furrow CH (Fig. 4.49).

On the northeastern side, BEL35 is flanked by BEL36. This mound has an almost symmetric circular shape. The summit of the mound is relatively flat as seen in figure 4.49. The flanks of the mound are gentle towards BEL35 and have a more or less similar slope gradient on the other flanks. The mound has a height of about 170 ms TWT and is about 800 m across (Fig. 4.49).

BEL32 is the most southern mound in this area of interest. The mound has a slight elongation in NS direction. The top is relatively flat and the slopes have a more or less similar slope gradient. The width on the NS profiles is generally larger than on the EW profile for a similar height. The maximum height is 200 ms TWT and the width is about 1000 m. Again large widths have been measured on relatively low heights (Fig. 4.49, Fig. 4.50)

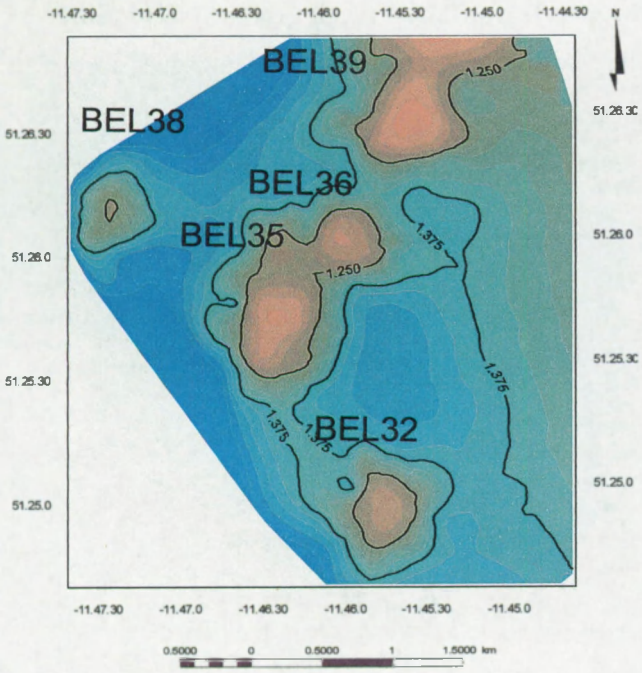

Fig. 4.49a: Time structural map of the mound base with the mounds superimposed.

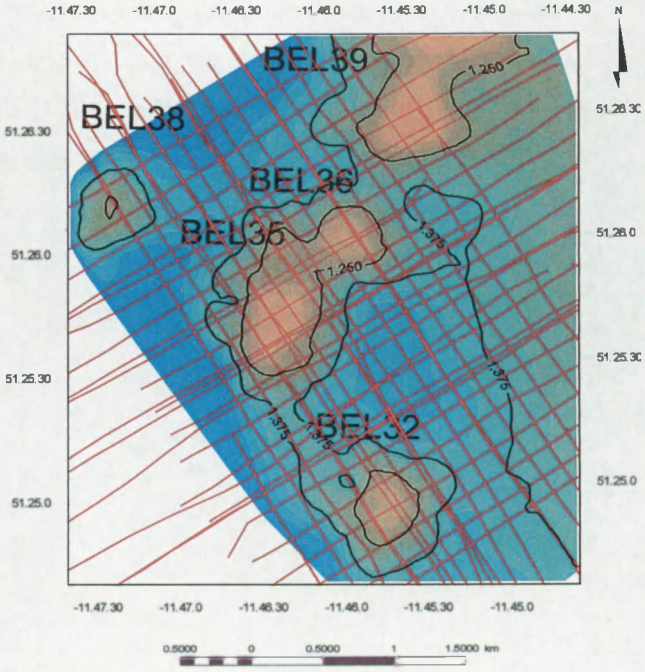

Fig. 4.49b: The seismic grid where the mapping is based upon.

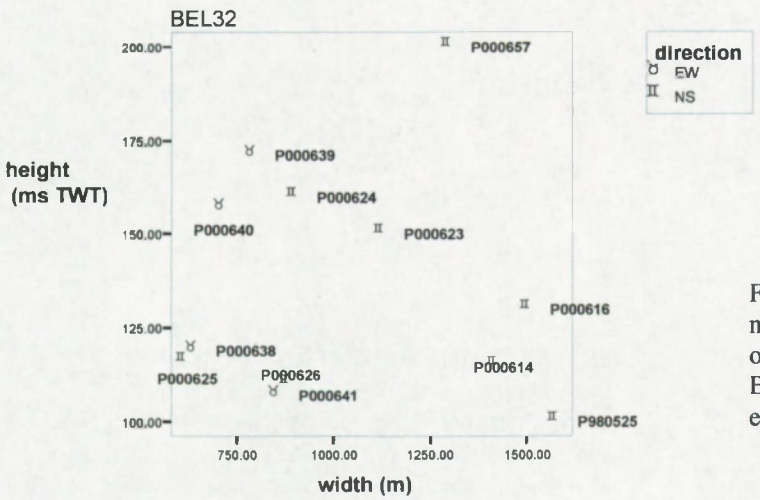

Fig. 4.50: Height-width measurements of BEL32 on the seismic profile. BEL32 has a NS elongation.

BEL38 has a conical shape with a narrow summit (Fig. 4.49). The shape is slightly elongated to the EW. The greatest width has been observed in connection with low heights on the NS profiles (Fig. 4.51). The highest height does not coincidence with the longest width, which argues for a wide base and narrow summit. The steepest flank is oriented to the west, facing the NS furrow. The height of the mound is 178 ms TWT and the length 800 m, with a maximum of about 1000 m in NS direction.

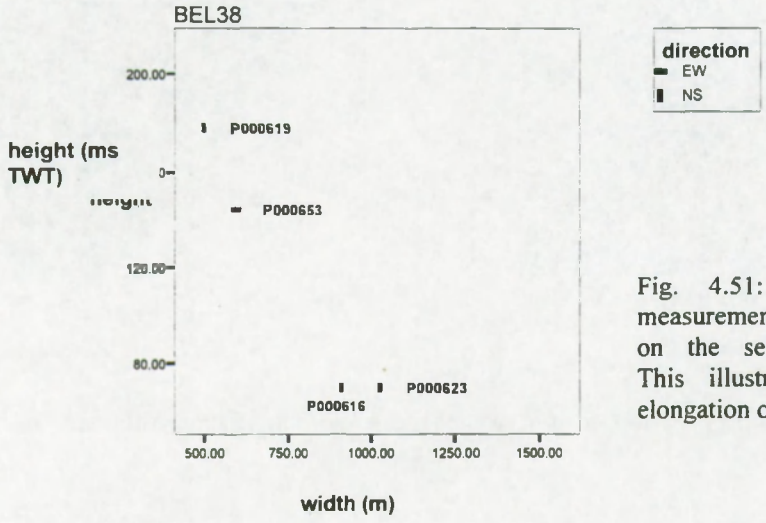

Fig. 4.51: Height-width measurements of BEL38 on the seismic profiles. This illustrates the EW elongation of the mound.

BEL39 shows a flat summit and a slight elongation to the EW (Fig. 4.49). The mound is about 180 ms high and has a width of about 900m, the greatest length has been observed on an EW profile and is generally larger than the NS widths (Fig. 4.52). The steepest flanks have been observed on the western and northern side of the mound.

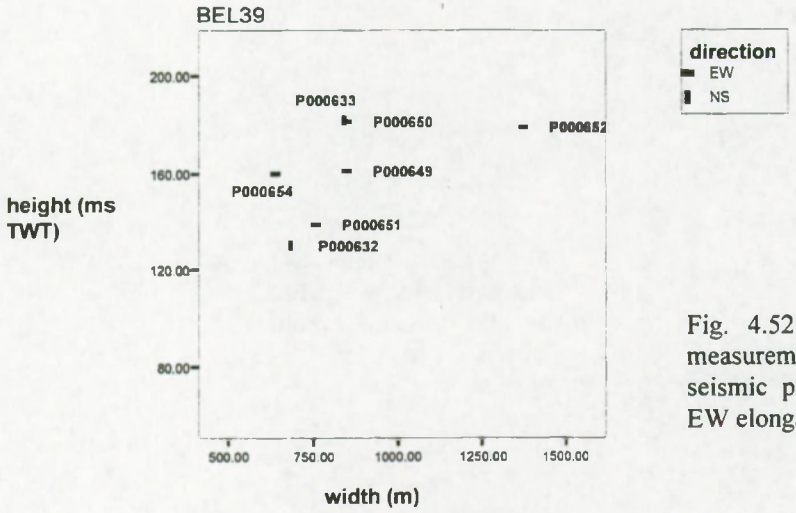

Fig. 4.52: Height (ms TWT)-width measurements of BEL39 on the seismic profiles. The mound has an EW elongation.

In general, the discussed mounds have all a similar height and horizontal dimension. The time structural map (Fig. 4.49) indicates that the mounds are flatted topped. The mounds flanks have a more or less similar slope gradient.

The elongation of the mound is not uniform even though they all have a more or less NS-elongation. The mounds are flanked by depressions in the mound base reflector and might indicate a development closely related to currents (Fig. 4.53). The elongation suggests a NS current in CH furrow with slight deviations along downslope channels.

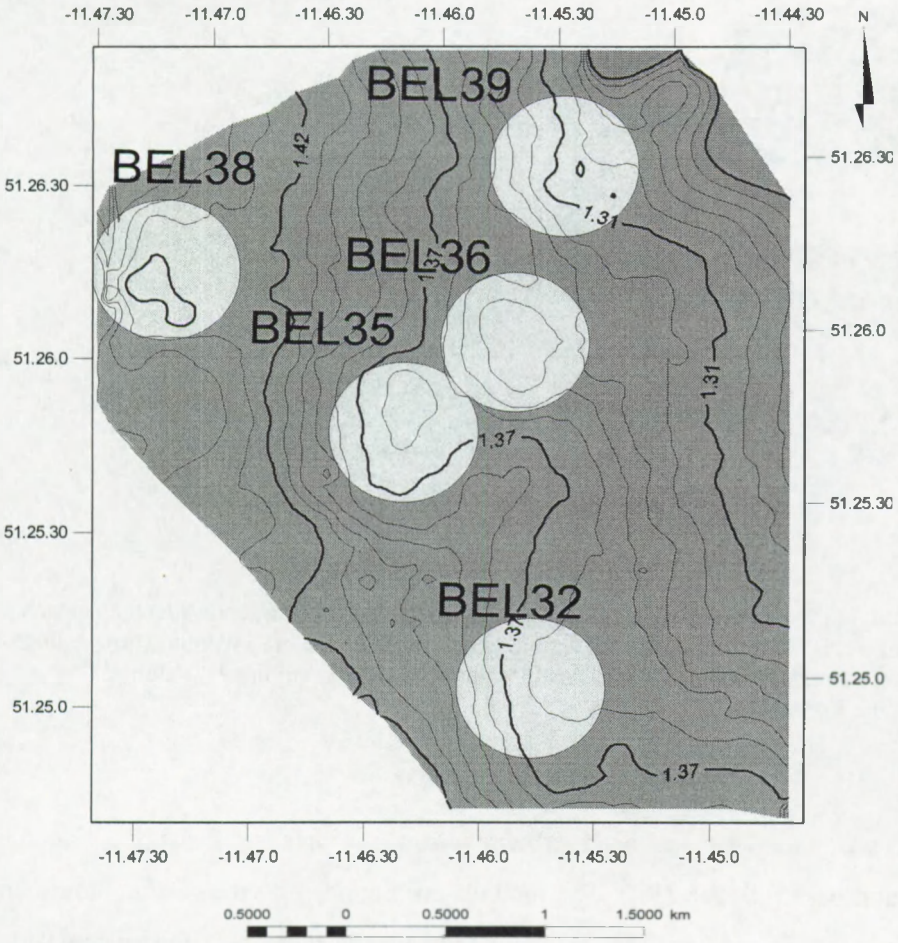

Fig. 4.53: Time structural map of R4, the mound base reflector. The mounds are located on the flank of a local channel in the mound base.

4.6.2.3 Geology

In this part the morphology of the mound base reflectors is compared to the mound location. A surface map has been made of the mound base reflector, R4, based on the seismic profiles (Fig. 4.53). The surface is dipping to the west towards the NS- furrow. In the western side of the area of interest, the slope gradient is smaller than in the upslope part. A downslope oriented channel has been observed between the mounds BEL32 and BEL35 and can be followed higher up the

slope, changing direction to a more NS direction as observed in the present-day bathymetry. On the western side of the mounds the surface has a greater slope gradient than on the eastern side. Due to the velocity pull-up, seen underneath the mounds, this slope can be slightly enhanced. Nevertheless on the seismic profile a real break in the base mound reflector has been observed on the western side of the mounds. The mounds are clearly lined up along the channel. BEL 38, sitting in a flatter zone, is the only exception.

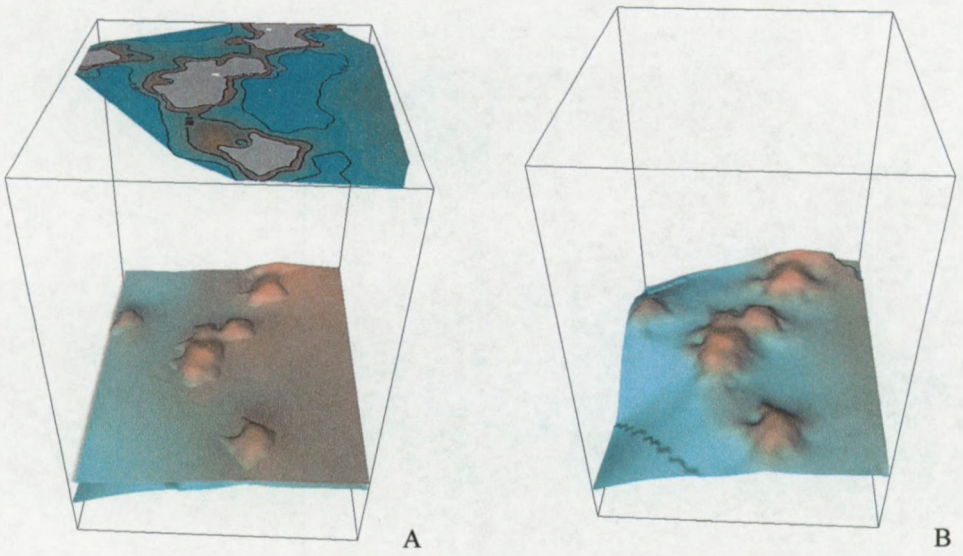

Fig. 4.54: A. 3D evocation of the mound base and the seafloor. The upper surface represents the isopach map of the sediments of Be. B. 3D evocation of the mound geometry from the base without surrounding sediments. This illustrates that the mounds are associated with a slope break and lined up along downslope channels in the R4 surface.

The sediment thickness of facies Be has been extracted from the data set by subtracting the seafloor from the mound base reflector (R4). The mounds are bounded by the zero contours on this isopach map (Fig. 4.54, Fig. 4.55). The sediment thickness is largest on the eastern side filling the downslope channel. On the eastern mound slope the isopach contours are close to each other. This indicates a thick package of surrounding sediments, thinning quickly on the eastern mound flank. On the western side the contour lines are more spread and indicate a smaller burial of the mound by the embedding sediments. The sediment thickness is reduced on the western side of the mounds. It seems that the sediments are accumulating to the eastern and northern side of the mounds.

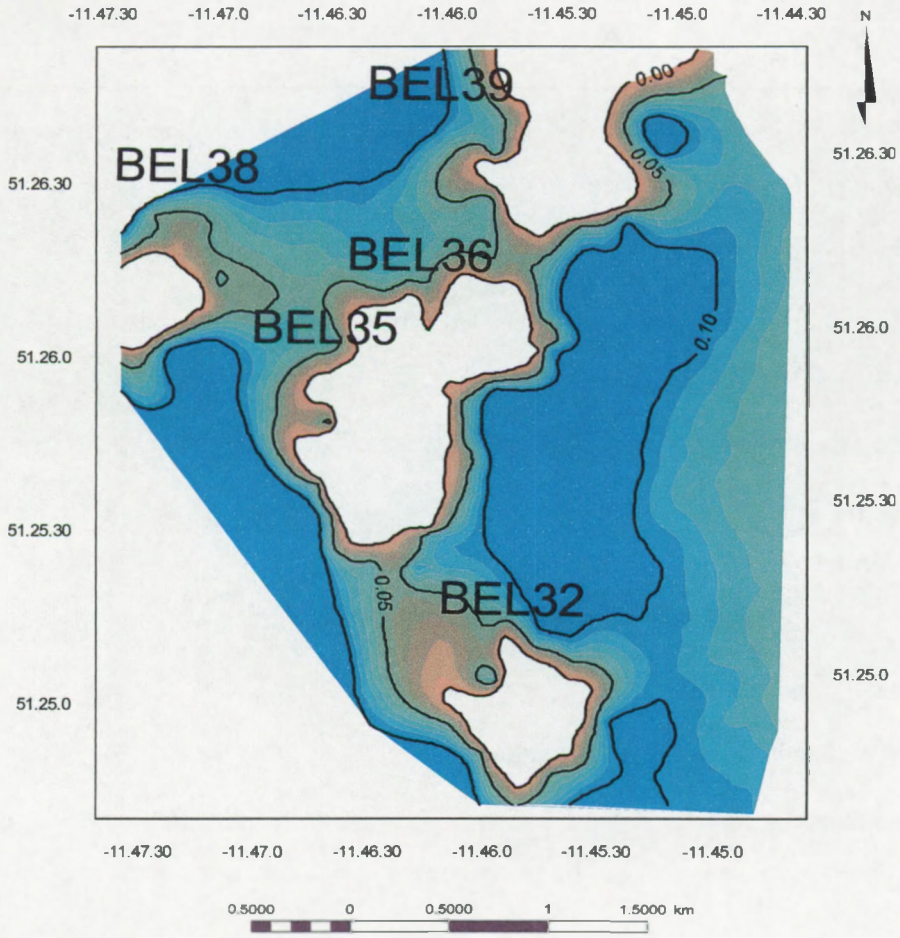

Fig. 4.55: Isopach map of Be which illustrates the sediment thickness burying the mounds. The zero contour represents the mound shape on the surface.

The substratum of BEL32, 35, 36 39 (excepted BEL38) is the Bb facies with sigmoidal reflectors (Appendix B.3). The mounds seem to be located at the extension of this facies, which creates the break in the slope. Nevertheless, it cannot be concluded that the mounds are exclusively rooted on this facies. BEL 38 roots on the Facies Ba. As discussed in the seismic facies section, the sigmoidal reflectors in this area seem to have enhanced amplitudes and inverted polarity near mound BEL35 and BEL36. Although these are indirect indications for fluid accumulation, no conclusive evidence is found.

- The mound geometry at the mound base is almost circular in plan view with a slight elongation in a NS direction.
- The summit of the mounds is flat.
- The initial mound development created a broad base. Afterwards the mound developed in a vertical direction.
- The final surface geometry of the mounds seems to be sculptured by NS currents.
- The mounds started to develop near erosive scarps of the R4/mound base reflector in an EW direction.
- The mounds line up along downslope channels with a NE-SW to EW orientation and along the large NS furrow CH.
- No preferential substratum is found.
- Sediments accumulated to the east, higher on the continental slope, because of a greater sedimentation rates induced by lower current speeds and a sediment source from higher up the shelf.
- The mounds had already a certain dimension before the installation of Be sedimentation and developed quickly in a period of non-deposition in an energetic current regime.

4.7 Sidescan sonar images

Beside the mound shape discussed in the geometry, four acoustic patterns have been recognized and mapped on the 2 NS sonographs (see 3). The sidescan sonar mosaic has been combined with the bathymetric data. The analysis of the data set provides some sedimentological and environmental information of the present-day situation in the Belgica mound province. It should be noted that the characteristics of each facies and seabed structure reflect the effect of the dominant current regime, long-term processes. The atypical processes, which infrequently affect the seafloor or short and weak events have not been recognized in the sonographs, because they do not leave a permanent mark on the seabed. The facies mapping and recognition have been based on the backscattering of the sidescan sonar signals. The backscattering recorded on the sonographs is a function of the density of the surface sediments, which is a function of the grain-size but also of the compaction or consolidation of the sediment (Blondel and Murton, 1997). Sandy patches in an active current form less compacted sediments with a weak backscattering. Fine sediments in a weak current regime can yield strong backscattering on the sonographs.

The sidescan sonar covered zone can be subdivided in two zones based on the general backscattering pattern: a relative weak pattern in the north and strong responses in the south (Fig. 4.56, Fig. 4.57).

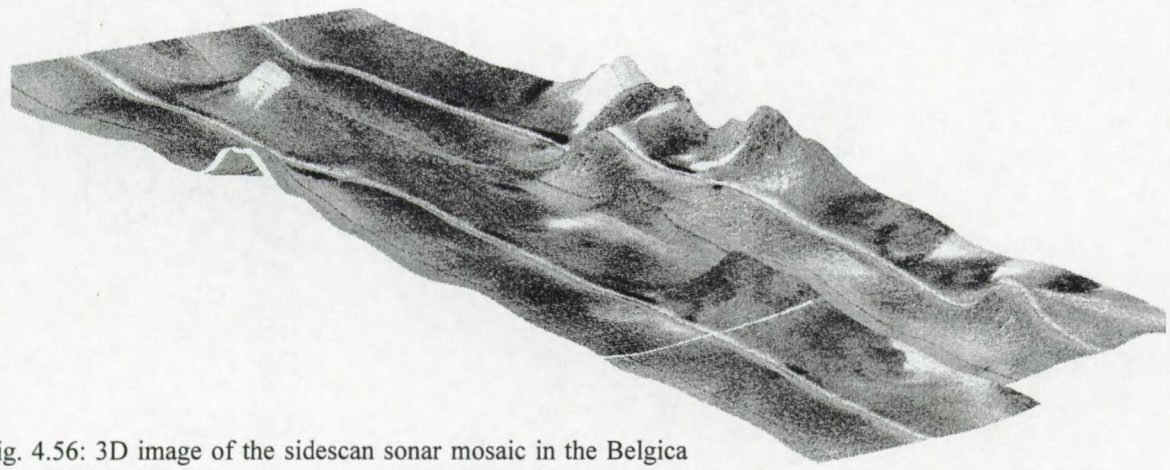

Fig. 4.56: 3D image of the sidescan sonar mosaic in the Belgica mound province. This figure combines the TTR7 sidescan sonar and multi beam bathymetry.

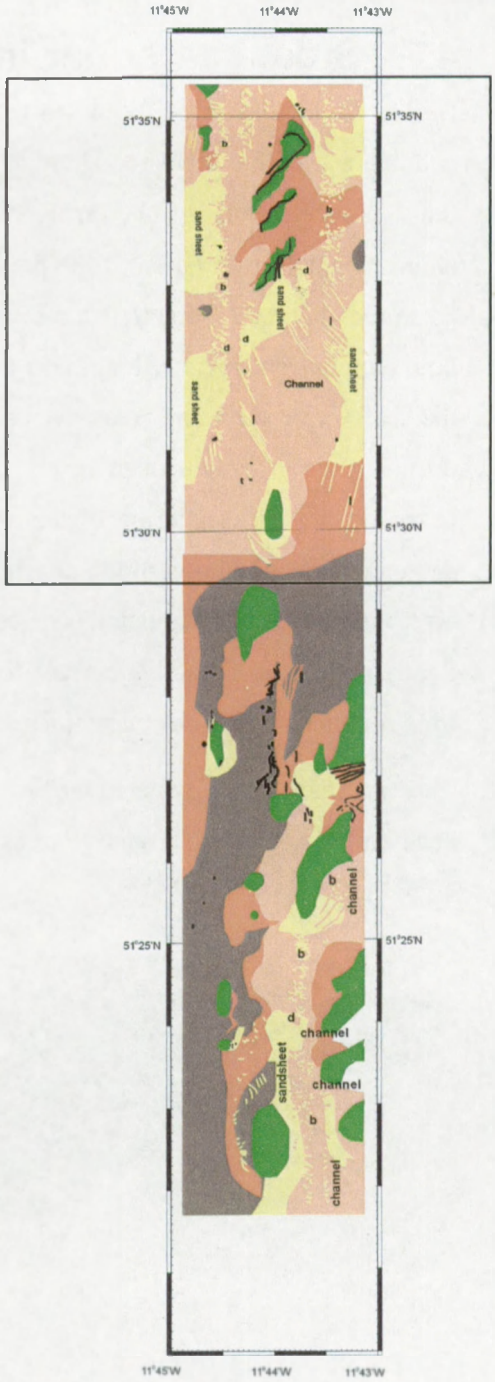

Fig.4.58

Legend

- positive structures, block, coral colonies
- weak backscattering, low compaction, sand
- moderate backscattering, coarse sediment
- moderate backscattering, more compacted, silt
- strong backscattering compacted fine sediment
- structural lineations
- d dune structure
- b barchanoid dunes
- l lineation
- t comet tails
- current direction
- mound facies

Fig. 4.57: The left panel represents the sidescan sonar mosaic with bathymetric contour lines, the right panel the sidescan sonar interpretation.

4.7.1 Northern zone

A moderate backscattering and large patches of weak backscattering dominate the northern zone. As observed in box core samples taken during TTR7, the sediments in areas of weak backscattering have a high sand content with a low degree of compaction (Kenyon et al., 1998). This facies represents patches of sand or sand sheets with a dimension of 1 to 2 km in NS direction and 0.5 to 1 km in an EW direction (Fig. 4.57, 4.58).

A second form of weak backscattering originates from ribbons up to 2 km long and up to 50 m width, associated with a sand sheet (4.58). These sand ribbons occur in a channel on the eastern side of the mosaic. In general, bottom currents are parallel to the trend of the sandy ribbons. For the northern side of the channel, more downslope, this direction is NE-SW and for the southern flank, NNW-SSE (Fig. 4.58). This might represent a change in direction of the current to the north after flow out the downslope channel for the NE-SW orientations (Fig. 4.58).

This suggests that two current directions might act in the area: one along the slope and another downslope current. The NNW-SSE orientations on the western flank of the channel represent current directions going north and entering the channel with a slight change in direction due to the local topography. These seabed structures formed in a high current regime, represent current speeds of 1 m/s or higher (Fig. 4.59). There are no shadowing effects on these structures, which suggest that they do not form elevated ridges but rather sand patches formed by scouring.

To the north of the downslope channel, dunes occur on the eastern and western side of the mounds and more downslope (to the west) in the channel (Fig. 4.58). In general, dunes are the simplest bed forms associated with sediment redistribution. They occur on non-cohesive surfaces (i.e. sands) as undulations, oriented transverse to the direction of the water flow. Two types of dune structures have been recognized: barchanoidal and transverse dunes (Fig. 4.58). Barchanoidal dunes have a wavelength of 100-300 m, with a spacing of about 100m that places them among large dunes according to the classification of Ashley (1990). The shape of the dunes mirrors the current direction.

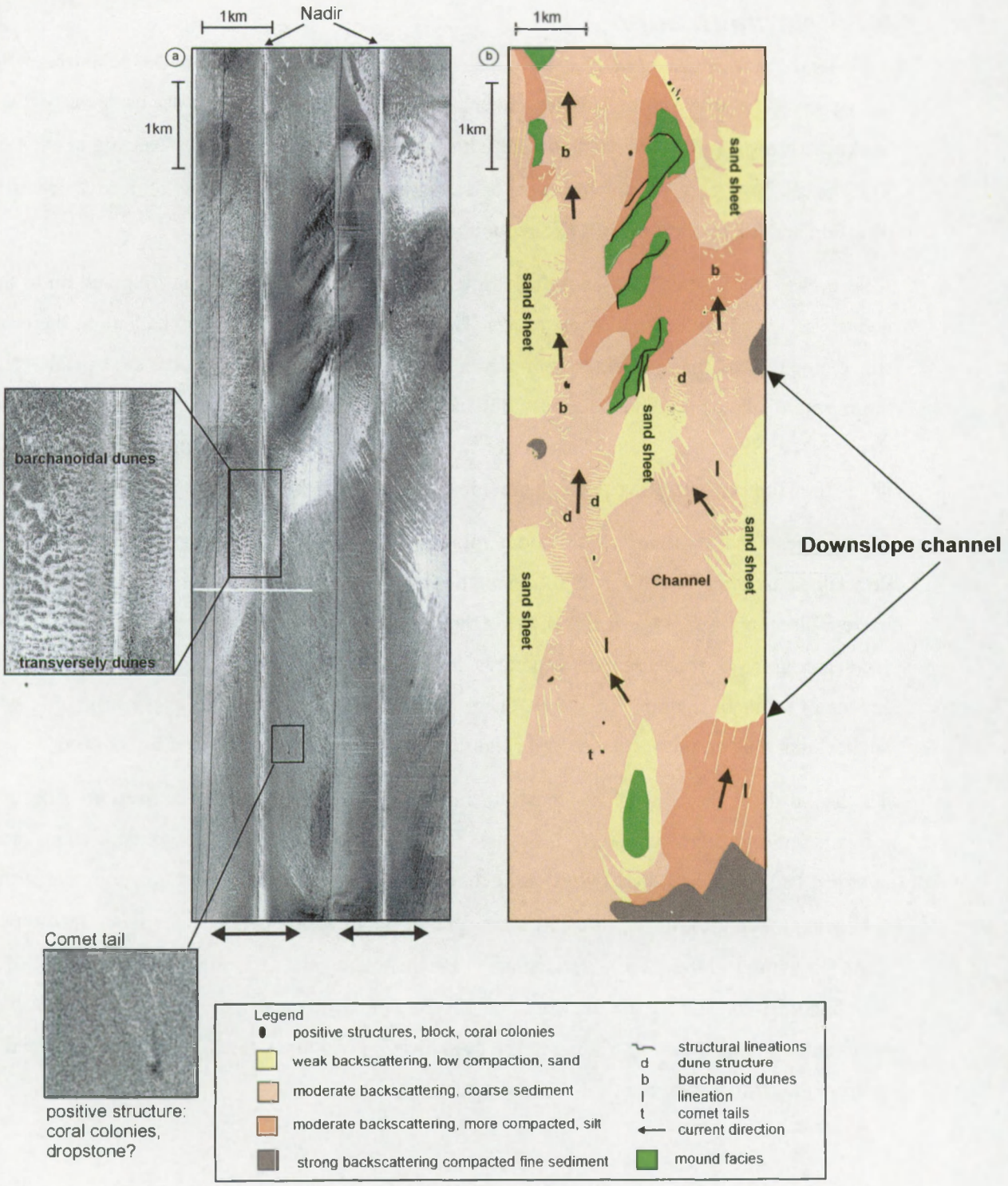

Fig. 4.58: The left panel represents the sidescan sonar mosaic of the northern part of the Belgica mound area, the right panel the interpretation of the sidescan sonar. Seabed features show a dominant northward flowing current and a downslope movement in the channels.

Most of the dunes point to the south, which indicate a northward flowing current. These structures still represent high current velocities, up to 1 m/s, but smaller values than at the ribbons (Fig. 4.59). Transverse dunes occur especially in the west of the mosaic and in some patches, in the north of the channel. Wave lengths range from 100-500 m, with a spacing of 500-1000 m, which classifies them as large dunes (Ashley, 1990). Current directions are perpendicular to the wave crest. Most of the dunes are EW oriented and suggest SN directed currents. Dunes occur in moderate background backscattering, mostly in the low to moderate backscattering facies near sand sheets. The formation of sandy dunes is not only a factor of current speed but also of supply of sediment (sand) (Van Lancker, pers comm.).

The sandy sediment is most probably provided by the downstream flow or scouring in the channels. This material is than reworked by vigorous currents at the end of the channels, in a northern direction. These zones are located near downslope channels or in narrow zones created by topography, where the currents are focussed. The weak backscattering in these zones can be explained by the low grade of compaction of the sediment due to reworking and (re)-suspension.

Zones with moderate backscattering are subdivided in two groups with relatively low and high backscattering. The low moderate backscattering represents low compacted coarse (medium sands) sediment and dominates the northern part of the mosaic. It appears in an active current regime with features as dunes and ribbons. The high-moderate backscattering zones are located in the vicinity of the mounds and in the south of the major channel. The facies is uniform with a few sand ribbons in the southern patch and dunes at the borders of the patches around the mounds (Fig. 4.58). They represent more compacted or consolidated, fine-grained sediment (fine sand-silt fraction). This facies near the mounds can be interpreted as a rougher seabed, which creates a stronger backscattering than structural features. Isolated strong circular backscattering zones in this facies show a positive relief and might represent coral colonies or clogged sediment in a coral framework (Fig. 4.58). The net long-term bottom current in the zone of the sand ribbons and dunes is dominantly to the north. This is indicated by the orientation of the EW orientation of the dunes and by the N orientation of ribbons behind obstacles. Local variations in the orientation are related to channels and suggest strong currents with downslope components.

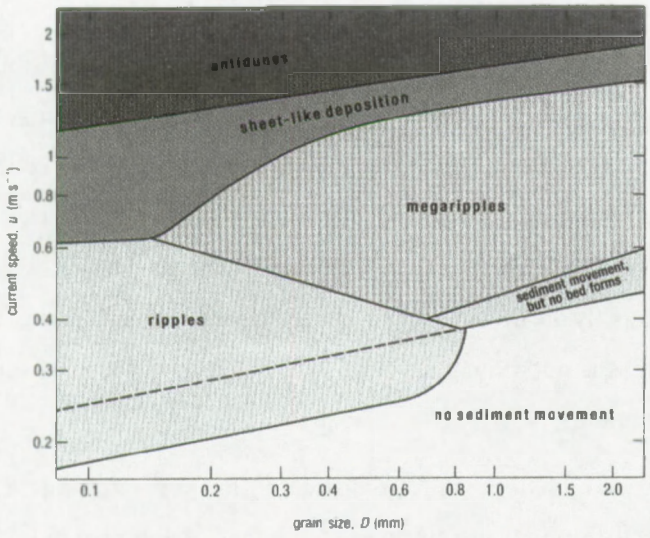

Fig. 4.59a: The relationship between the bed form, the mean current speed and the sediment grain-size based on experimental data [team, 1989 #459].

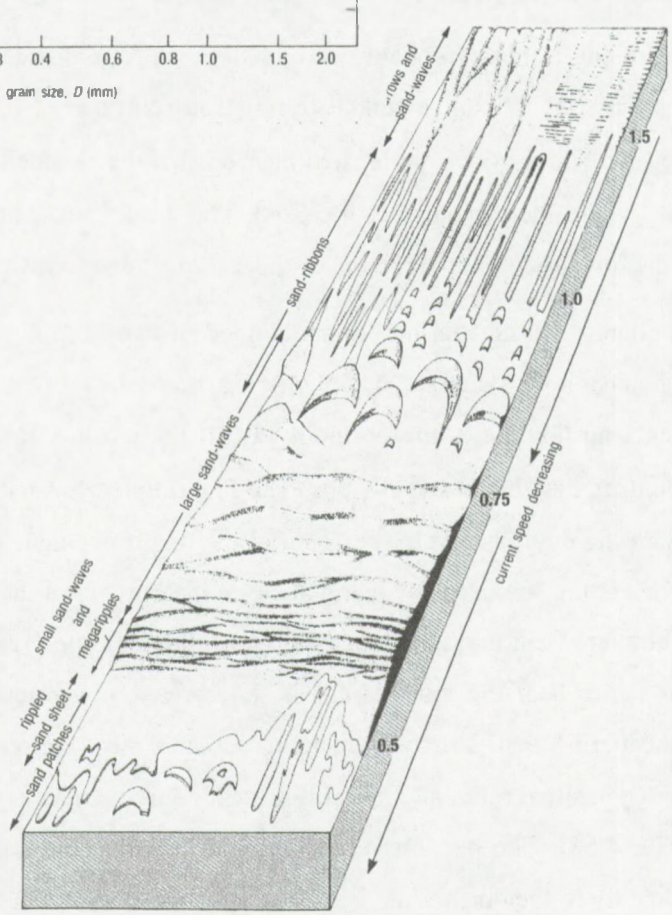

Fig. 4.59b: Block diagram show the development of t bed forms along a sedime transport path w decreasing current spee (m/s).

4.7.2 Southern part

The southern part of the mosaic is characterized by a general stronger backscattering than in the northern part (Fig. 4.56, Fig. 4.57). This can be interpreted as more consolidated sediment in a less vigorous current regime.

Moderate backscattering in the southern part of the mosaic appears in a narrow band between two mound ranges (Fig. 4.57, Fig. 4.60). In this zone a few downslope channels, located within the upper slope mound range, end in the relative flat area between the mound ridges. In this narrow zone low backscattering patterns occur as NS elongated patches, with a longest axis ranging between 1 to 4 km and a width of 0.3 to 1 km (Fig. 4.60). In the southern part, stripes of weak backscattering are plastered against the mounds and shift to the north in dune structures.

In the vicinity of the downslope channels (indicated with "channel" on figure 4.60) the weak backscattering forms become more extended in an EW direction, which might suggest a supply of sandy sediment by the channels. Barchanoid and transverse dunes appear in the low-moderate backscattering zones, between the weak backscattering patches. Occasionally, ribbons have been observed in the weak backscattering patches. Orientations of dunes and ribbons suggest a dominantly SN flowing current in this zone.

At the foot of the eastern mounds, bands of weak backscattering mark the relief lows. These ribbons of weak backscattering have their longest axis in a NS direction and become narrower to the north. Their geometry looks like a striated surface (Fig. 4.60, Fig. 4.59b). They are usually covered by small-scale ripple-like structures with an EW orientation. Due to their low backscattering and geometry they have been interpreted as sandy ribbons with sand ripples on top of it. In general, they occur at the foot of the mound, where the steep slope of the mound changes in a normal slope gradient. This backscattering pattern argues for a focalised vigorous current regime between the mound ridges, creating low compacted or low consolidated sandy sediment. Current speeds are probably 1m/s or higher (Fig. 4.59). The downlope channels have mostly a low-moderate backscattering.

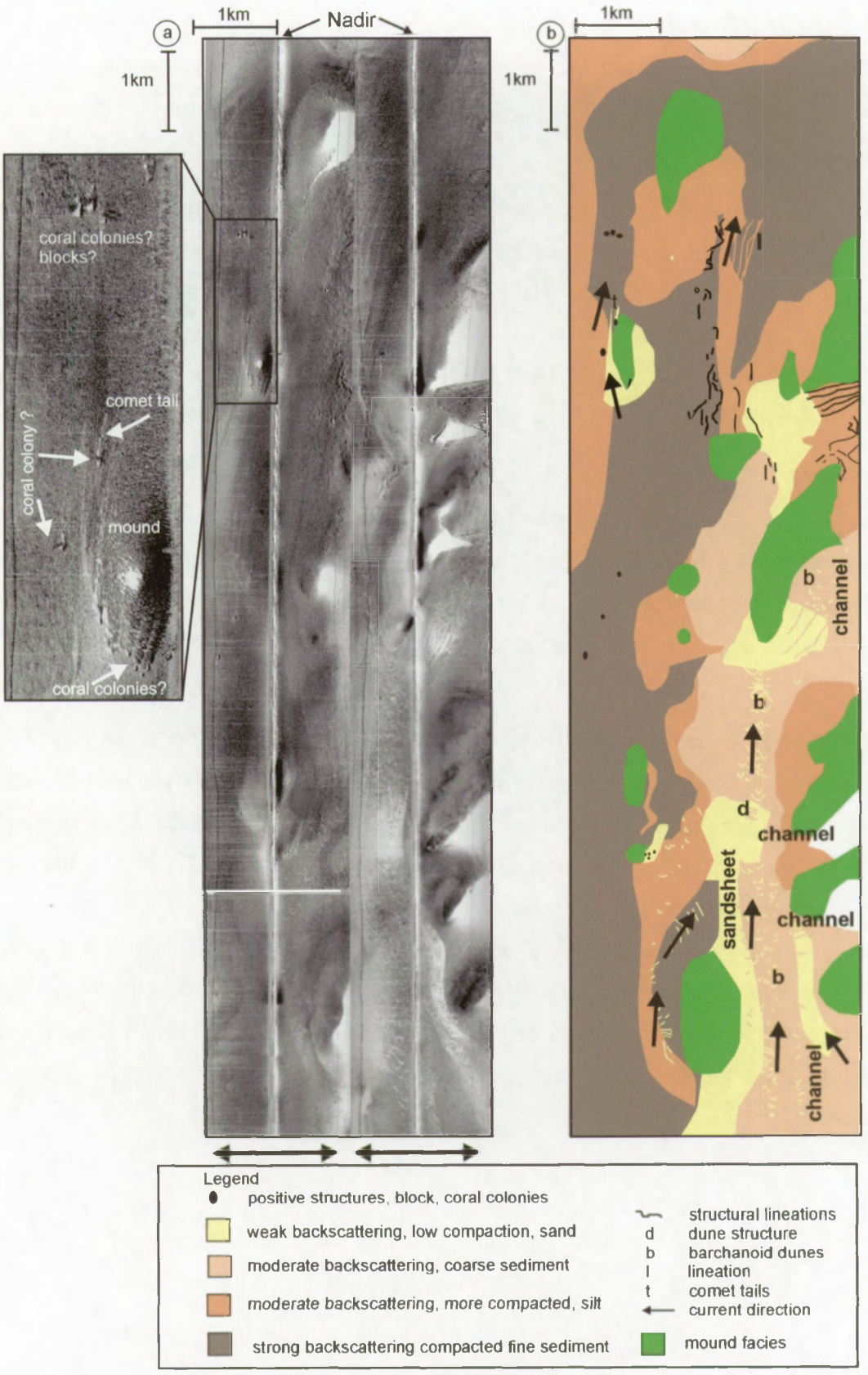

Fig. 4.60: Sidescan sonar interpretation of the southern mosaic, which indicates turbulence around the mounds in a dominant SN current.

The sediments on the northern side of the upslope mound range have high-moderate backscattering, which reflects a more consolidated sediment and less current activity.

To the west of the downslope mound ridge and in the northern part of this mosaic, where the mound density is less than in the south, strong backscattering dominates the sonograph image (Fig. 4.57, Fig. 4.60) To the west of the narrow low-moderate and weak backscattering zone in the south, high moderated backscattering zones occur, covered with some dune structures and form the transition to an area of uniform strong backscattering. The dune structures suggest a north flowing current but near a mound they show also a NE orientation, which indicate a current deflection caused by the mounds. The high backscattering zone is alternated with very strong backscattering due to elevated structures as mounds and isolated spots of blocks or coral colonies. On some of these elevated structures a ribbon of weaker backscattering occurs on the northern side, which has been interpreted as comet marks (or tails) created by a northern or northeastern flowing current.

The strong backscattering indicates compacted sediment, silty clay as found in different box cores around the mounds (see 4.8). High-moderate backscattering in this area has been found near the mounds and might indicate less consolidated sediments in zones with turbulence caused by the mounds. The weak backscattering zone near the mounds in the northern part might be elevated zones at the top of the mound.

The TTR8 sonograph in the westernmost part is characterized by a large variation of backscattering, but has a low average backscatter level. This pattern of variable scattering forms wave-like structures and show the characteristics of a dune field with EW oriented crests (Fig. 4.61). This pattern covers both flanks of a mound. The structure seems to occur on the flanks of the mounds but is not well expressed on the other sonographs.

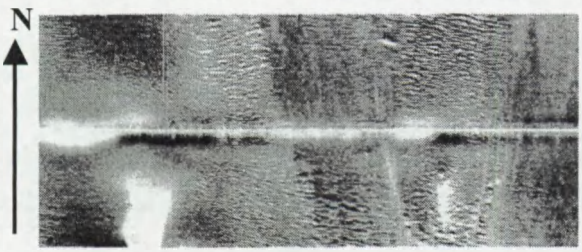

Fig. 4.61: Detail of TTR8-ORAT17 showing EW orientated ripples around a mound.

Near the top of the mound, this pattern fades out into a high backscattering on the mound. The orientation of the ripples seems to be related to the shape of the mound. Upslope the mound, the ripples are smaller and their frequency higher. They seem to be larger in the southern and western side in comparison with the northern and eastern side of the sonograph. This might argue for the fact that the currents, which created these structures, were reduced on the northern and eastern

side. The smaller size of the ripples in these zones reflects most probably the current pattern and turbulence around the mounds. The wavelength of the dunes is about 20-25 m in the upper slope zone. Wave heights decrease to the west with wavelengths of about 1-1.5 m. During the ROV Victor survey (2001) around Thérèse mound (BEL35), many small-scale ripples have been observed on the flanks of the mound (Huvenne, pers comm.).

In the most southern part of the Belgica mound province, sandy patches with moderate backscattering have been observed in the upper part and between the mounds. These patches are up to 200 m across and have a NE-SW orientation. On the easternmost side of this zone an irregular field of wavy, plane shaped transport routes with weak backscattering has been recorded and interpreted as sand sheets. Further downslope, this field transforms into discrete small (100 m) spots with low backscattering, which have no regular distribution and which are mostly accompanied by ripple marks (Wheeler et al., 1998).

- Active hydrodynamic conditions are present in the studied area on the eastern Porcupine margin.
- Bed form assemblages are formed due to vigorous bottom current activity with peaks of more than 1 m/s.
- The presence of different acoustic facies indicates variations in the flow regime steered by the local topography.
- Trains of dunes and comet tails, observed beyond obstacles indicate that the current is directed to the north.
- Small-scale dunes have been observed on the flanks of the mound.
- Possibly small coral colonies occur near the mounds.
- A clear downslope transport of sediments is seen in channels flanking the mounds.

4.8 Sedimentology

A selection of subsurface samples illustrates the lithology of the mound crests, flanks, moats and ripple shape structures observed on the sidescan sonar (Fig. 4.62, Table C.1). Box cores have been used to characterize the biology and the surface sediments of the mounds. These samples will be discussed in the biological description of the mounds (see 4.9). The subsurface samples taken on the flanks of the mounds all yielded corals (marked in grey in table C.1.) and associated benthic fauna. A map has been made to illustrate the coral yielding samples (Fig. 4.63). The samples taken on the western exposed side of the mounds contain more corals than those taken on the mostly buried eastern flanks (see 4.3). All the available data have been discussed, such as magnetic susceptibility, geochemistry, grain size, biostratigraphy and mineralogy, besides the visual description, to place the mounds in an age model and environment context. The samples have been discussed and described per target feature: background samples; ripple structure, channel, moats and mound (flank and crest). The lithocolumns and core descriptions have been illustrated in appendix C. The descriptions of the sediment samples of Lekens (2000) have been used for the ENAM samples and those of Swennen et al. (1998) for the TTR7 samples.

4.8.1 Off-mound sediment samples

4.8.1.1 Sandwaves field

TTR7-AT-36G (Appendix C.1, Fig. 4.62) is taken in a barchan shaped bed form field in between the two mound ridges, mapped by sidescan sonar (see 4.7). The gravity core comprises 3 cm coarse yellow-orange (2.5Y 4/4) oxidized sand. The rest (3-339 cm) of the core includes dark grey (2.5Y 4/2) silty clay, with some broken shells. At 308 cm a dropstone is found. Scattered foraminifera and shell debris become more common downcore. This observation confirms that the barchan structures are built of Holocene coarse-grained sediments and formed under a high current regime, as suggested in the sidescan sonar interpretation. The core missed the main dunes but it shows coarse sand on the seabed.

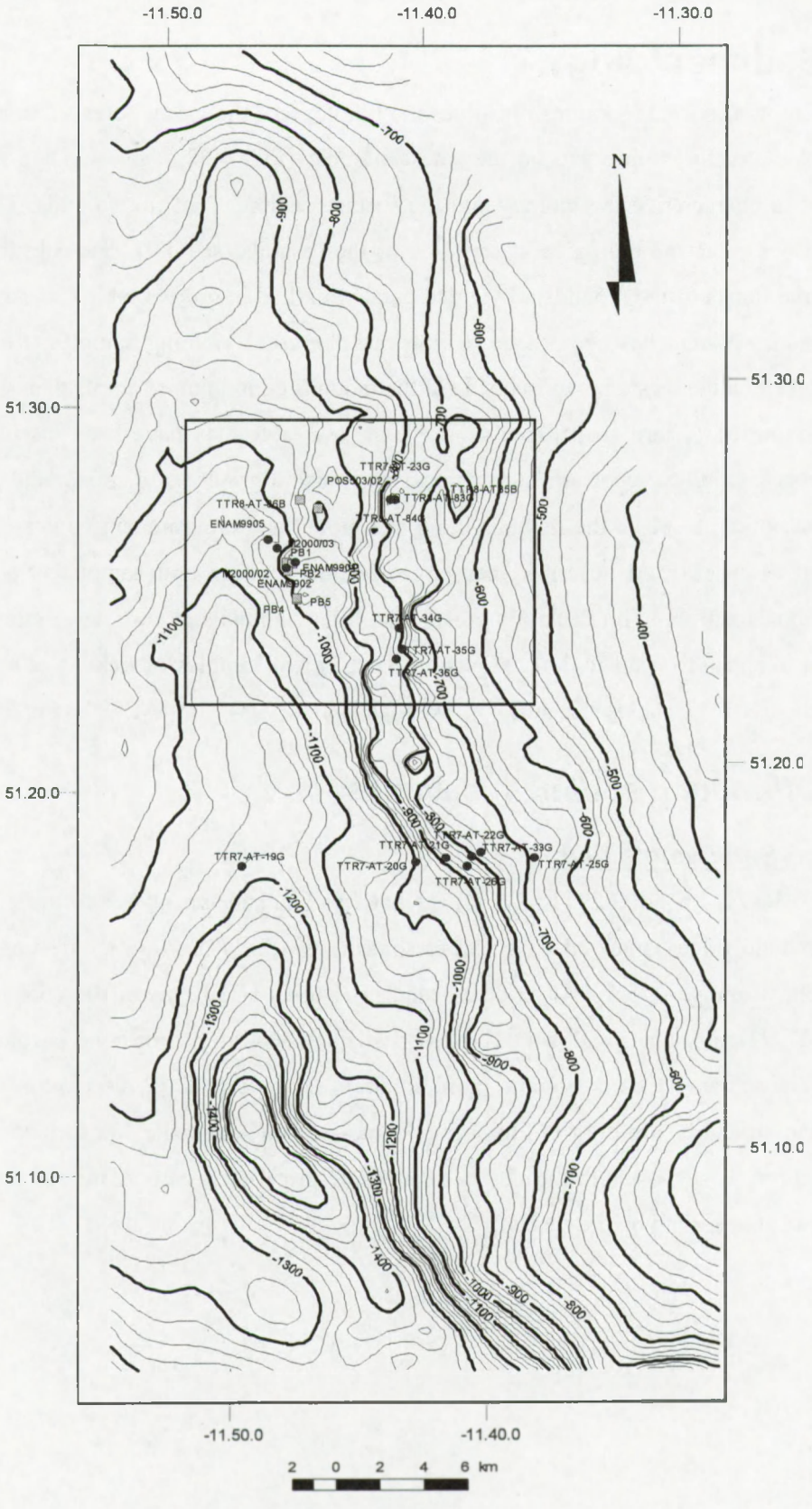

Fig. 4.62: Overview map of the core locations: squares indicate box cores, circles gravity cores.

4.8.1.1 NS channel

One gravity core, **TTR7-AT-19G** (Fig. 4.62, Table C.1, C.2) has been taken inside the NS oriented channel flanking the mounds. The core has penetrated a mounded sediment structure seen on the isopach map of facies Be (see 4.3). The gravity core has a recovery of 366 cm. The upper 5 cm of the core consist of foraminiferal silty sand. The rest of the core comprises fine-grained silty clay sediment, without any lamination or sediment structure. Reduction spots and pyrite are more common at the bottom of the core. Bioturbations are seen through the core, with horizontal bioturbation at a level between 120-150 m. The upper 1 m has been interpreted as Holocene sediments.

The upper sandy layer has been deposited in the active present current regime during the Holocene. The upper sediments correlate with the medium backscattering on the sidescan sonar and confirm the higher current regime in the channel. The intense bioturbation is an indication for slow sediment accumulation rates, where the infauna is able to keep pace with deposition or erosion.

4.8.2 Near-mound sediment samples

Two cores have been selected to illustrate the sediment at the foot of the mound, **TTR7-AT-20G** (275 cm) and **TTR7-AT-26G** (366 cm), respectively near BEL10 and BEL09. Both cores have been taken on the western side of the mounds (Fig. 4.62, Table C.1, C.2).

TTR7-AT-20G comprises in the upper 4 cm Holocene olive-brown (2.5Y 4/3) foraminiferal sandy silt. This lithofacies overlies the dark greyish brown (2.5Y 4/2) bioturbated silty clay (mud). Reduction spots and pyrite are common in the lower part of the core. Few rock and shell fragments have been observed in the section but they are more common at the bottom of the core.

TTR7-AT-26G is taken on the western side of the mound BEL09. The upper 3 cm comprise an olive-brown (2.5Y 4/3) sandy interval with foraminiferal and bioclastic fragments. The underlying sediments consist of dark greyish-brown (2.5 4/2) clays, which become siltier downcore. A shale fragment is found at 44 cm and at 214 cm quartz fragments. The bioturbation through the cores is intense and shell fragments are rare.

All cores described above have a similar lithology: a Holocene sandy upper 3-5 cm overlying Pleistocene bioturbated greyish silty clay with a few dropstone layers and biodebris. The coarsening upwards of the sediments illustrates the slight increase of current till the present-day after the last glacial maximum. The intensively bioturbated silty sediment is interpreted as a

deposit with a low sedimentation rate in a calm current regime (hemipelagic). The only observed lamination is a layer with a high concentration of rock fragments. These have been interpreted as dropstones transported by icebergs during the collapse of the ice sheets around the North Atlantic. Remarkable is the occurrence of rock fragments and coarse-grained layers around 210 cm.

4.8.3 On-mound sediment samples

Box cores taken on the western and upper flank of mounds BEL35, BEL36, BEL41 and BEL43 yielded an extensive biological life consisting of deep-water corals, sponges and other associated fauna (see 4.9). The sediments underlying the living cap is a dark greyish brown silty to sandy clay, consisting of carbonate fragments. These fragments in the sand fraction find their origin in shells and corals. In figure 4.63 an overview of the cores has been given.

Several attempts to sample the basinward flanks of the mounds with a gravity core were unsuccessful due to the dense coral cap. All recovered sediment cores are from the crest or landward side of the mounds. Gravity cores from the mounds generally yield a dark brown, silty to sandy, heavily bioturbated sediment (C.2). At the top few centimeters are composed of foraminifera-rich silty sand. This layer also generally contains a few pebbles, on which living and dead bryozoans and coral debris may be attached. Only two cores (TTR7-AT-23G and ENAM9905) contained some coral rubble deeper in the core (Fig. 4.62, Table C.1, C.2). The carbonate fraction of the sediments is largely composed of calcareous nannoplankton. The clay and silt particles are largely of terrigeneous origin.

4.8.3.1 Southern Belgica mound province

Several cores have been taken near mound BEL09 to illustrate the different sediment environments around the mounds (Fig. 4.62, Table C.1, C.2). TTR7-AT-26G has been taken on the western side of the mound. TTR7-AT-22G and TTR7-AT-33G have been taken respectively on the upper western slope and eastern flank of the mound. Additionally, the cores TTR7-AT-25G of the eastern buried flank of BEL08 and TTR7-AT-21G on the eastern flank of BEL10 illustrate the sedimentation of the mounds in the southern part of the Belgica mound province.

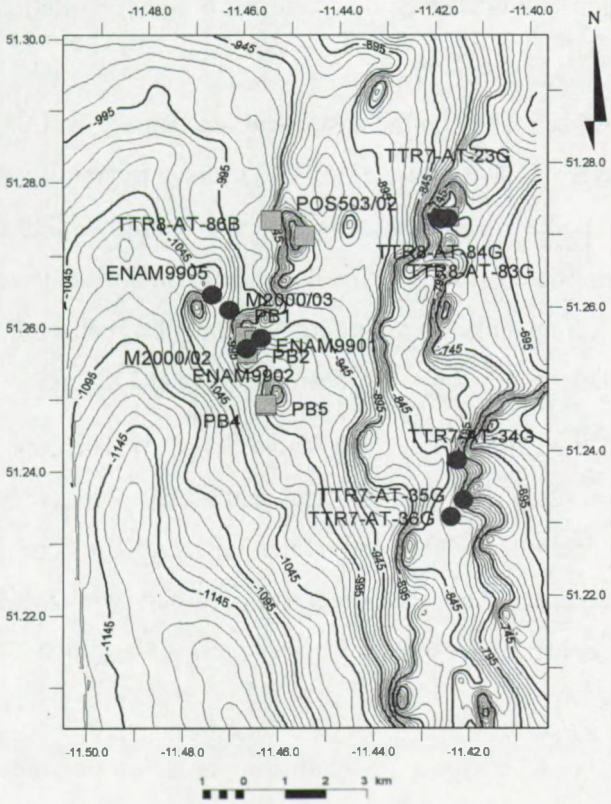

Fig. 4.63a: Overview map of the sampling stations in the central part of the Belgica mound province. Box cores are indicated with a square, gravity cores with a dot.

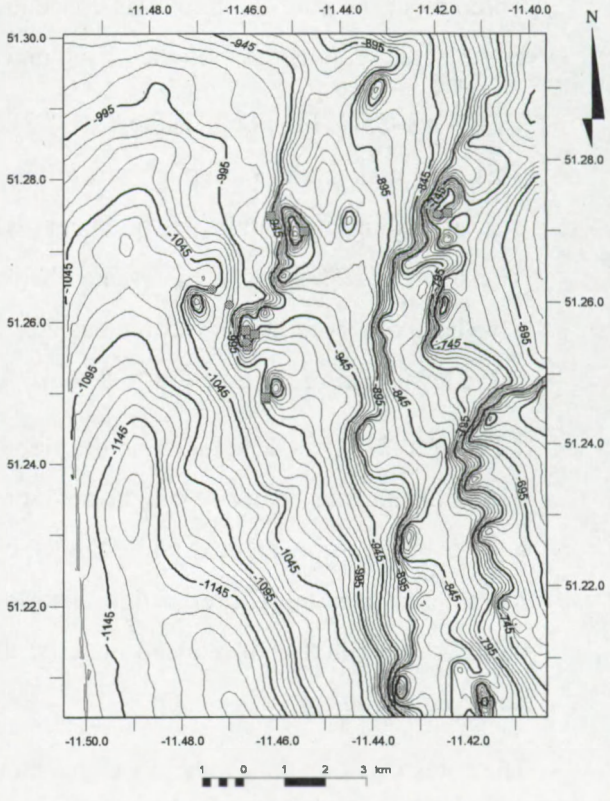

Fig. 4.63b: Overview map of the subsurface samples yielding corals.

Core **TTR7-AT-22G** consists of Holocene olive-brown (2.5 4/4) foraminiferal sand, similar to the off-mound samples in the upper 5 cm. The underlying bioturbated sediments are greyish brown (2.5Y 4/2) silty clay with reduction spots (349.5 cm). Rock fragments have been found at 168 cm and 250 cm. These layers have been interpreted as ice rafted debris (IRD). Below 250 cm coral fragments occur in a low concentration in the sediment. In the lower part almost no foraminifera have been observed in the sediments. The gravity core has the typical near mound facies with a higher concentration of shell and coral fragments than the background cores. The coral fragments seem to have fallen from locations higher on the mound flank.

Gravity core **TTR7-AT-33G** has been taken on the eastern flank of BEL09 (Fig. 4.62, Table C.1, C.2). This core comprises a thin (1-3 cm), brownish grey (2.5Y 4/3) coarse-grained foraminiferal sand. The Holocene upper sandy layer is coarser than in previous described cores. The underlying sediments comprise a slightly bioturbated light brownish (2.5Y/4/2) silty clay. The foraminifera concentration is relatively low. Between 160 cm and 238 cm rock fragments are common.

Throughout the core the biodebris concentration is low. The colour indicates a higher oxidation grade of the sediment than in the off-mound cores.

TTR7-AT-25G (Fig. 4.62, Table C.1, C.2) has been taken on the eastern buried flank of BEL08. This core contains in the upper part a thin layer of olive-brown (2.5Y 4/3) sandy foraminiferal ooze including lithic and shell fragments. The underlying sediment is light greyish brown (2.5Y 4/2) silty clay. This part is bioturbated between 160 cm-180 cm. Small and large shell fragments have been observed in this section, besides rock fragments. Foraminifera have only been observed in the lower part of the core (180-280 cm). A dark organic layer has been observed at 172 cm.

TTR7-AT-21G has been taken on the slope of the BEL10 (Fig. 4.62, Table C.1, C.2). The upper 13 cm of the core comprise a light olive-brown (2.5Y 5/3) foraminiferal sandy clay. This sandy layer overlies a greyish brown (2.5Y 4/2), bioturbated silty clay with reduction spots. The core is bioturbated over the entire section. The lower interval consists of grey marly clay with more burrows and filled with reduced material. Biodebris increase in the lower part. A dark layer is observed at 240 cm.

The cores taken on the southern Belgica mound province illustrate that the upper Holocene sandy layer becomes thicker higher on the continental slope. This observation indicates that sand is deposited in a high current regime, between the principal mound ranges as indicated on the sidescan sonar interpretation (see 4.7). Core TTR7-AT-21G with the thickest sandy layer is located at the upper flank of mound BEL10, at the level of the sandy facies seen on the sidescan sonar (see 4.7).

The lower section of the cores represents the glacial sedimentation in a calmer current environment. This observation argues for more vigorous currents during the Holocene than in the last glacial period. Rock fragments appear at similar depths for the western and eastern flank core of BEL09. Higher on the slope no concentrated rock fragments have been observed. This suggests that these rock fragments have been deposited during a regional event of ice rafted debris (IRD), which affected more the cores deeper in the basin than those higher on the slope.

The core on the western side of the mounds yield more coral fragments than on the eastern buried side. This suggests slope transport of coral fragments from the western flank of the mounds. The burial of the eastern flanks is more intensive than on the western flank. The sediment on the mound flanks and off-mound cores are similar, suggesting a similar source.

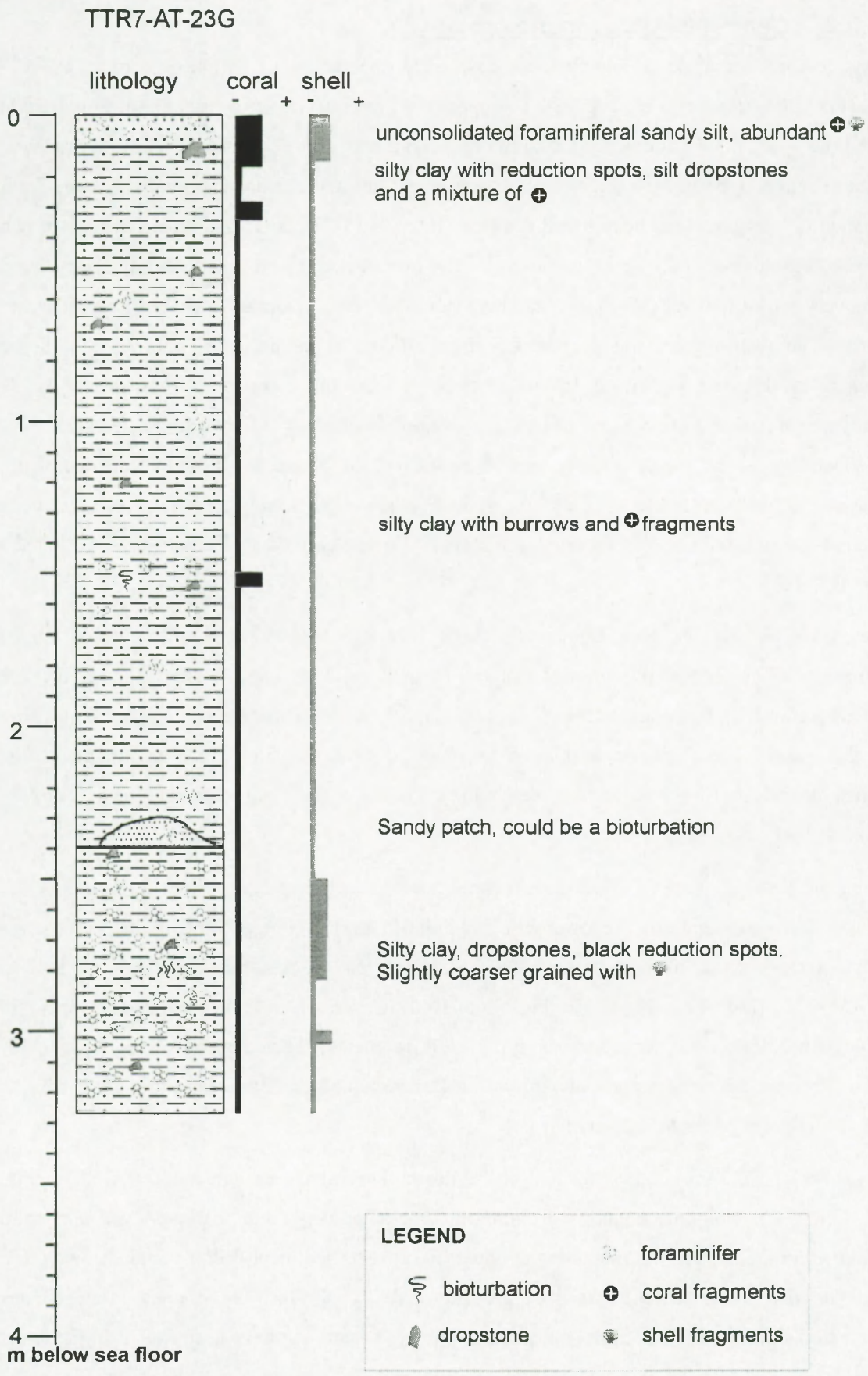

Fig. 4.64: Lithocolumn of TTR7-AT-23G.

4.8.3.2 Central Belgica mound province

A typical coral sediment sample from the basinward upper flank of BEL42 is core **TTR7-AT-23G** (Fig. 4.64) (Swennen et al. 1998). The upper 0-13 cm interval comprises foraminiferal, light olive-brown (2.5Y 5/3), soupy sand, rich in coral fragments. A well-rounded 1 cm rock fragment has been found at 10 cm, asa well as small shell fragments and echinoderm spines. A large 7 cm diameter rock fragment has been found at 13 cm. Interval 13-235 cm includes dark greyish-brown (2.5Y 4/2) to olive-grey silty marl, which is locally bioturbated. Coral fragments have been found at the very top of the unit (15-17 cm) and between 30-35 cm. A solitary coral head was found at 155 cm. There is a slight increase in the foraminiferal content and grain size below 35 cm. Some complete bivalves are present at 15 cm. Interval 235-239 cm comprises greyish-brown sandy marl. Interval 239-282 cm consists of dark greyish-brown (2.5Y 4/2) foraminiferal, biogenic silty clay. Two larger rock fragments have been observed at 239-282 cm and a smaller one at 310 cm. A gastropod has been found at 286.5 cm. Reduction spots and some burrowing have also been scattered through the section. Grain size increases from silty mud to medium sand within the interval 313-326 cm.

Cores taken during the R/V Marion Dufresne campaign MD123 contain up to 20 m of alternations of corals and fine-grained material (Van Rooij et al., 2002). This suggests that the mounds are built up by corals catching coarse-grained material in suspension or in traction within this framework. The corals are supported by other benthic-associated fauna as sponges in the Belgica mounds, to fill the holes and pores in the framework. The patchy character of the corals is similar to reef sediments in tropical reefs.

During the Pelagia cruise of 1999 (see 3) three piston cores have been taken in the vicinity of BEL35 (Thérèse mound): on the lower eastern flank of BEL35 (ENAM9901), on the northeastern partly exposed flank of BEL36 (ENAM99902) and on the southeastern flank of BEL35 (ENAM9905) (Fig. 4.62, Fig. 4.63, Fig. 4.65 Table C.1, C.2). All three cores are similar in lithology, besides the biodebris content (coral, shell fragments). The magnetic susceptibility (MS) of the cores has been measured onboard with a Bartington Mark. This additional information is used to recognize paleoclimatic markers.

ENAM 99-01 (635 cm) core is located at the lower flank of the eastern flank of BEL35 (Fig. 4.65, C.1, C.2). This core contains metamorphic rock fragments and coarse-grained silty sand with little coral and shell fragments in the upper 30 cm. The sediment is dull yellow brown (10Y 5/4). The rest of the core consists of greyish olive (7.5Y/ 4/2) fine-grained homogeneous bioturbated silt. In the fine section some intercalations of sandy silt have been found. In the lower

section, around 4 m, some black pebbles have been observed between 400-450 cm, creating a peak in the magnetic susceptibility (Appendix C.2).

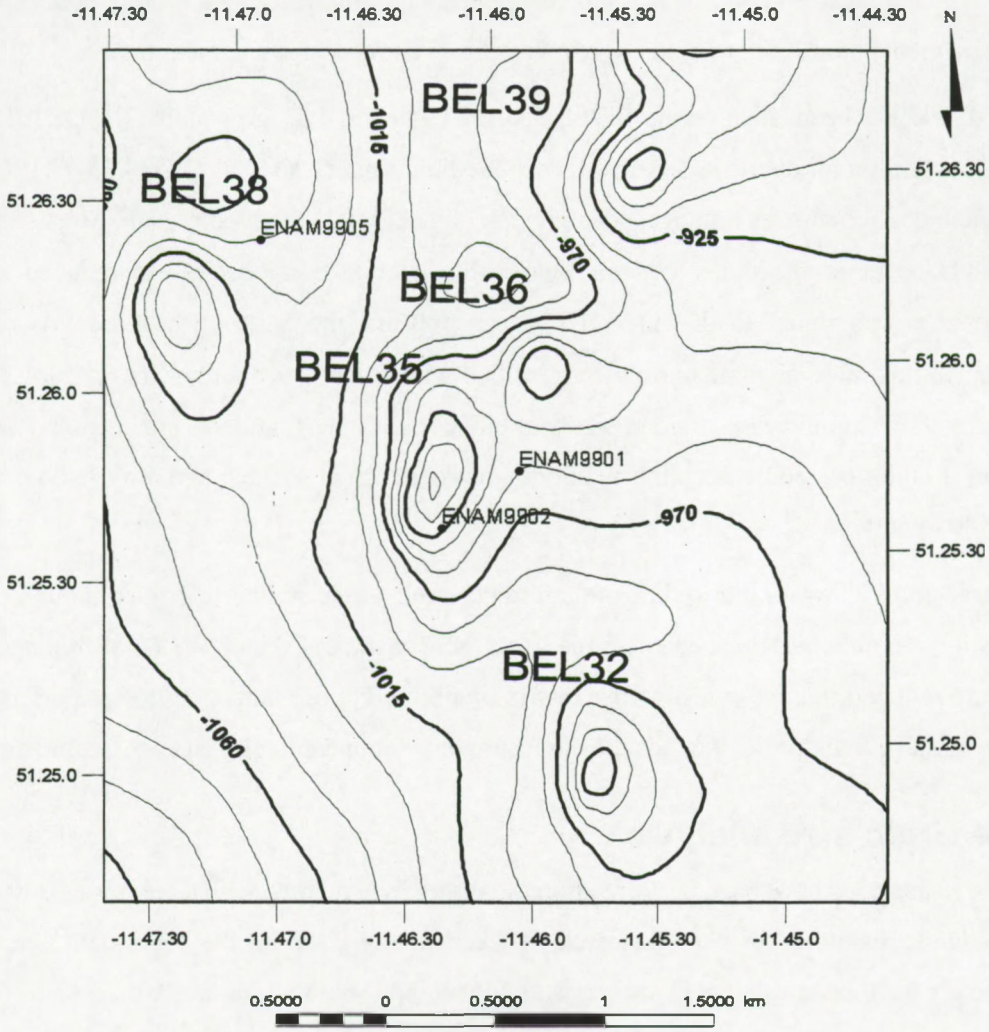

Fig. 4.65: Location of the ENAM core on the mound bathymetric map (source bathymetry: AWI Bremerhaven).

ENAM 9902 (675cm) has been taken on the southern upper flank of BEL36 (Fig. 4.65, Appendix C.1, C.2). The core contains coral fragments in a mainly silty sand matrix. The upper core section consists of yellowish brown (2.5Y5/3) fine to medium grained sand with coral debris and hydrozoans. Coral fragments up to 6 cm (at 300 cm) have been observed. Downcore the coral fragments get reduced and bioturbation is more intensive. The highest coral density is concentrated in the upper 300 cm. A zone with reduced coral occurrence has been observed between 400 cm and 625 cm. In the lower part a chunk of coral and shell debris has been observed in silty fine sand. In the coral-free zone, sandy lenses and burrows have been observed.

Around 4.5 m more pebbles have been seen, linked to a peak in the magnetic susceptibility. Nine sediment sequences have been recognized in the core (Appendix C.2). The sandy layer in the upper part is related to coral debris and fragments. The sediments with a large concentration of coral fragments have lighter colours (greyish-yellow) and a coarse sediment matrix.

ENAM9905 has been taken on the NE flank of BEL38 (Fig. 4.65, Appendix C.1, C.2). The upper 12 cm contains coral debris in an olive-brown medium sand (2.5Y 4/3) (Fig. 4.65, C.1, C.2). The rest of the core comprises homogeneous greyish olive (5Y4/2) sandy-silty clay. Most of the coral fragments occur in the upper 60 cm. Below this interval coral debris are reduced and shell fragments are common. In the interval between 360 cm and 560 cm the biodebris content is smaller. In this interval some burrows are infilled with more sandy sediments. The lower part of the cores shows an increase in grain size and biodebris. Lithic fragments are seen at 270 cm and 530 cm. In the magnetic susceptibility curve a peak is seen at 420 cm and a more complex peak from 500 to 560 cm.

The three cores show sandier sediment than in the cores of the southern Belgica mound province, suggesting a higher current speed near the lower NS furrow CH flank. The coral fragments in the cores are reduced in zones with a finer matrix and bioturbation, indicating lower current speeds. On the western flank of the mounds the corals are more abundant, with coarser sediments.

4.8.4 Grain size analysis

Grain size analyses have been performed on the three ENAM cores with a coulter LS230 at NIOZ (Netherlands Institute for Sea Research) (Lekens, 2000). From the total data set, specific parameters have been calculated such as sortable silt and the fraction larger than 150 μm (IRD), in order to propose an age model for the cores and an evaluation of the environment. The grain size analysis has only been performed on the siliciclastic part of the sediments. All parameters have been summarized in figure 4.66.

The results of the grain size analysis have been plotted as cumulative grain size curves as a function of depth in figure 4.66. Core **ENAM9901** (Fig. 4.66A) contains a homogeneous grain size in the silt fraction with only a coarser fraction at the upper centimetres and around 120 cm. The overall sediment is a poorly sorted silt. The log for **ENAM9905** (Fig. 4.66B) shows sandy sediment in the upper 50 cm, the rest of the core is silty with local variations to coarser grain sizes. At 600 cm a coarse layer has been observed. This coarse intercalation fits with higher contents of pebbles and biodebris in the lithological descriptions and has been interpreted as a

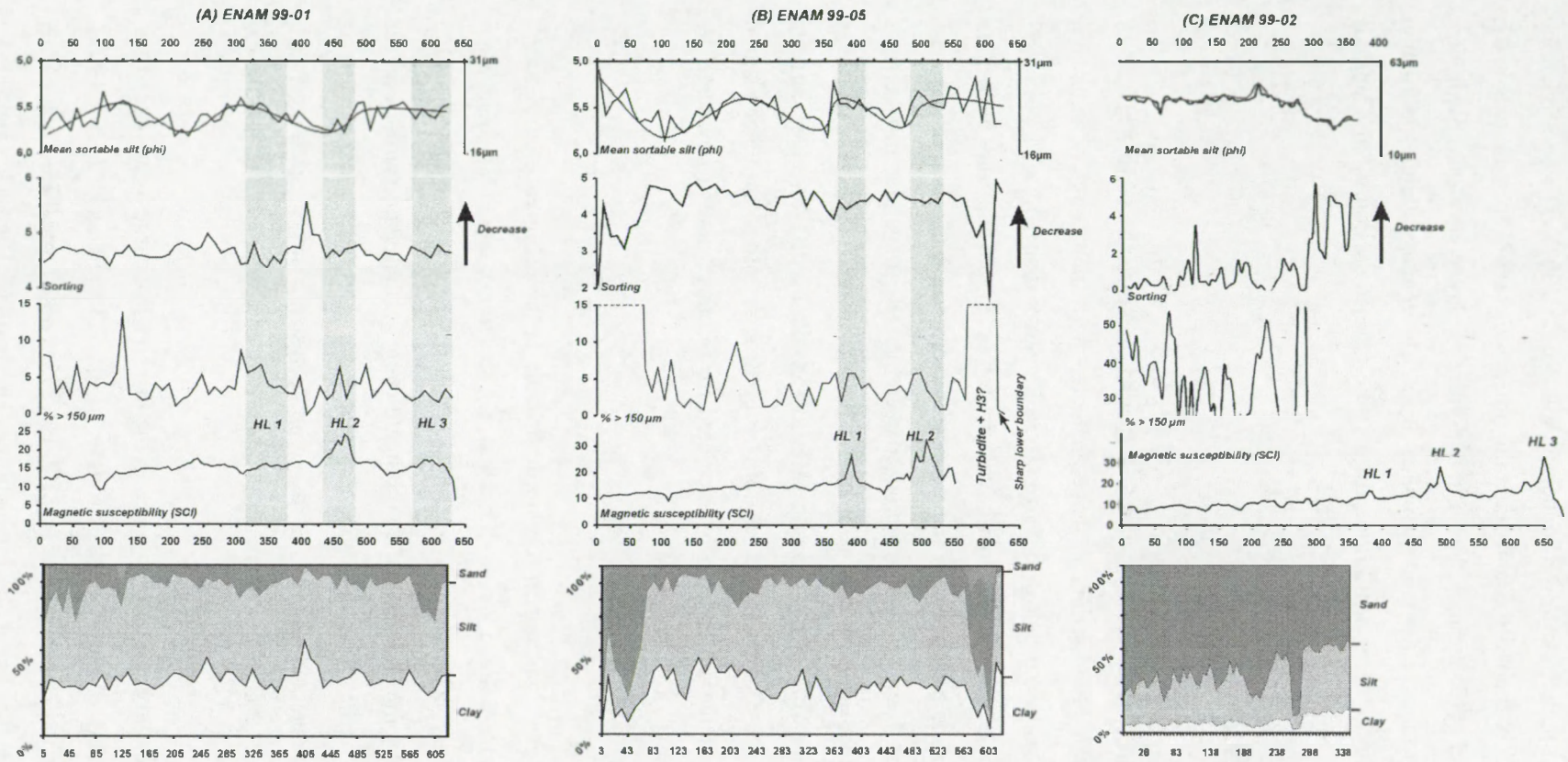

Fig. 4.66: Grain size analysis of ENAM 99 cores near Thérèse mound (BEL35). For each core the cumulative grain sizes, magnetic susceptibility, fraction greater than 150 µm, sorting and mean sortable silt have been represented, as well as an identification of potential Heinrich layers (HL) for A. ENAM 99-01 B. ENAM 99-05 modified after Van Rooij (2001) and C. ENAM 99-02 modified after the results of Lekens (2000).

turbidite because of the sharp upper and lower boundary (Van Rooij, 2001). The coral-yielding core **ENAM9902** (Fig. 4.66C) is generally coarser than the other two cores. The sediments in the upper part are mainly sand and grade around 280 cm in a mixture of clayey-silty-sand, with local variations. In the lower part of the core the sand dominates again. The coarser siliciclastic fraction has a positive correlation with the coral distribution. In the fine-grained section the biodebris is reduced or almost absent.

4.8.4.1 Paleoclimatology

Sortable silt

Distributions of grain size can provide relative current strengths owing to the sorting effects of currents (McCave et al., 1995a). Fine sediments have an increasingly non-cohesive behaviour above 10 μm and a cohesive behaviour below that size. The silt coarser than 10 μm (10 μm – 63 μm) responds largely as single particles to hydrodynamic forces in erosion and deposition processes because of the breakage of aggregates and is therefore sorted in size according to shear stress (McCave et al., 1995b). Deposition of material coarser than 10 μm under fast currents involves the suppression of deposition of finer sediments. The percentage of grains > 10 μm in the silt fraction is an indication for current strength (McCave et al., 1995b). Stronger currents yield coarser mean sizes of the non-cohesive silt fraction acting through both selective deposition and winnowing. The mean sortable silt fraction is calculated for the three cores to evaluate the current-coral relation (Fig. 4.66)

Heinrich layers

An important paleoclimatological indicator in the North Atlantic is the occurrence of Heinrich layers. Heinrich layers are coarse-grained layers with a high terrigeneous content deposited when melting icebergs unloaded their debris en masse (Snoeckx et al., 1999). The icebergs were released at the culmination of some (but not all) cold climate cycles called Dansgaard-Oeschger events, within the last glacial period. The underlying cause of those short-term climate cycles is still an important gap in the understanding of the Earth's climate system. The Heinrich layers are characterized by a peak in grain size greater than 150μm and are by nature ice rafted debris layers (IRD).

The originally defined Heinrich layers find their origin in the massive discharge of icebergs from the Laurentide ice sheet (Auffret et al., in press; Grousset et al., 2001; Snoeckx et al., 1999). These layers are called the typical Heinrich layer H1, H2, H4, H5. These typical Heinrich events show relatively high peaks in the magnetic susceptibility. The atypical Heinrich events have

generally lower IRD and higher carbonate fluxes than the other events and are interpreted to have a dominant European source (British, Fennoscandanavian, Icelandic ice sheets) (Auffret et al., in press; Grousset et al., 2001; Richter et al., 2001; Snoeckx et al., 1999). These events are seen as IRD layers with a relative small peak in the magnetic susceptibility. During a Heinrich event IRD deposition is not a continuous process but it reflects a time-transgressive multi source release of icebergs inducing an intermittent sedimentation. In the typical Heinrich layers, the IRD were first released by European ice sheets and followed by Laurentide (Grousset et al., 2001).

Parameters generally used to identify the Heinrich events as: magnetic susceptibility peaks, coarse lithic grain peaks (>150 μm), and/or bulk lithic accumulation increases, anomalies in $\delta^{18}O$ and anomalies in relative and absolute amounts of the planktonic foraminifer *Neogloboquadrina pachyderma sin* (Snoeckx et al., 1999). For the cores taken in the Belgica mound province, the magnetic susceptibility and grain size analysis have been used to identify Heinrich layers.

ENAM9901 and ENAM9905

The fine-grained cores on the eastern and northeastern lower mound flanks (ENAM9902 and ENAM9905) are most suitable for the analysis of the relative current speed and Heinrich event correlation. All paleoclimatological indicators as magnetic susceptibility, grain size fraction larger than 150 μm, sorting of the grains and the mean sortable silt are plotted in figure 4.66. (Lekens, 2000; Van Rooij, 2001).

Heinrich layers H1, H2 and H3 have been recognized (Fig. 4.66), throughout the comparison of the magnetic susceptibility curve of ENAM9901 and cores from adjacent areas (Auffret et al., in press; Richter et al., 2001). HL1 is not well expressed and yield a low content of IRD of the Laurentide ice sheet and a dominance of the European ice sheets. HL2 is characterized by a double peak. This suggests a two-step development of the IRD as explained above, with a European and Laurentide source. Both Heinrich events are defined as typical Heinrich layers with a large input of Laurentide IRD. The lower peak in magnetic susceptibility is interpreted as HL3, an atypical event with a large contribution of the European ice sheets.

The IRD or fraction >150 μm curve has a peak at the upper centimetres with a mixture of coarser grains sediments and corals. Two main peaks in IRD have been observed around HL1 and HL2 and a smaller around HL3, with a decrease in sorting (Fig. 4.66).

The mean sortable silt curve shows three cycles of weakening and increase of current speed. The Heinrich events are deposited in transitional periods between relatively high and low current speeds (Fig. 4.66). In the upper section of the core a general coarsening upwards is observed and

implies a general higher current speed. The mean sortable silt shows a low in the curve and relative low current speeds. This contrasting interpretation can be explained by the slumped material of the mound flank of BEL36 and the large sandy content of the sample.

The **ENAM9905** core is taken on the NE flank of BEL38 closer to the NS channel and higher currents speeds can be expected. The bulk top section (50 cm) of the core is coarse-grained with a relatively good sorting and contains coral fragments up to 5 cm. The dominance of coarse grains let suggest a higher current speed and slumping of coral fragments of the mound flanks. For this reason the upper part is not interpreted in terms of sortable silt due to the large error in slumping sediments. The magnetic susceptibility curve has a similar trend as **ENAM 9901**. The double peak is interpreted as HL2, the single peak as HL1. Other variation in the MS curve fits well with the curve of **ENAM9901**. At 600cm a peak in the IRD is observed at the location of HL3. In the lithological description this peak is interpreted as a turbidite. The mean sortable silt curve shows a similar trend as **ENAM9901** and the HL are deposited in periods of decreasing current speed.

The Heinrich layers are deposited at well known time periods, which allows estimating the sedimentation rates in the cores. The sedimentation rates have been calculated from the different markers and plotted in figure 4.67. HL1 peak is deposited at 14.74ky BP, HL2 at 21.1ky BP and HL3 at 27.48ky BP (Grousset et al., 2001). **ENAM9905** has an averaged sedimentation rate of 22.3 cm/ky and ENAM9901 22.9cm/ky. In the upper part of the cores (above HL1) the

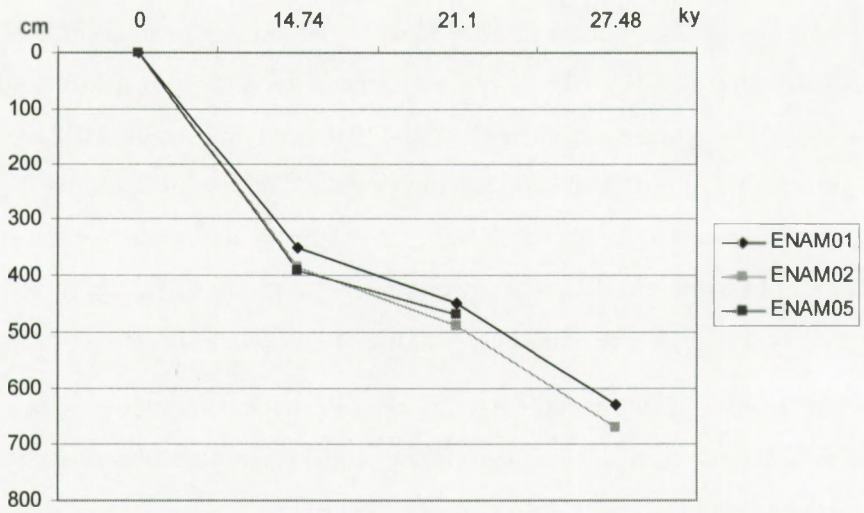

Fig. 4.67: Sedimentation rates calculated for the three ENAM cores based on the interpretation of Heinrich events. All cores have the same trend. The sedimentation rate increases in the Holocene, with higher current speeds.

sedimentation rate increases slightly in comparison with the glacial period. Each sample of the siliciclastic fraction of the cores has different peaks in the cumulative grain size diagram. These peaks represent different sediment populations and source areas of the sediment (Lekens, 2000). This distribution is comparable to sandy contourites for the upper section to muddy contourites for the lower part, as described by Arnishaw et al. (2000). The composition of the sediment encountered in the cores is clearly steered by changes in bottom currents and by different sediment sources. This contourite facies is interrupted by some gravitational deposition as material slumped from the mounds. Turbidites are located on the eastern flank of mound BEL35.

ENAM9902

The results of **ENAM9902,** the coral-yielding core, are compared with the contourite cores discussed above (Fig. 4.66, 4.67). In general, the core is coarser than the previously discussed cores and the majority of the sediment plots in the sand fraction. The coral-free zone has a high percentage of sortable silt and a well-sorted fine-grained composition. In the coral-rich zones the sediment is less sorted and the content of sortable silt in the coarse grain sediment is low. This indicates high current speeds in the coral-rich zone and the non-deposition or winnowing of fine sediments in the coral framework.

The magnetic susceptibility has a similar trend as the surrounding cores (Fig. 4.66). The double peak at 500 cm has been interpreted as HL2, the smaller peak just above the HL2 as HL1 and the complex double peak at the bottom as HL3. HL3 is probably more expressed than in the other cores due to the large amount of coarse grains and lithic compounds.

The mean sortable silt is only measured in the upper 350 cm and illustrates the high current speeds in the coral-rich zone. In comparison with the other core, the entire core shows a higher background current regime with similar variations.

The Cortex system (geochemical XRF results of core logger, NIOZ) has been used to plot the Ti/Ca and Fe/Ca ratio of the bulk sediment (Fig. 4.68). These parameters illustrate the relative part of biogenic sediments and terrigeneous input (Fe, Ti) (Arz et al., 1999). Both curves are parallel and illustrate the high terrigeneous input in coral-free zones and high biological carbonate production in the coral zones. The sharp peaks in the Fe and Ti content are identified as HL, on the base of MS and IRD. The Sr/Ca ratio mirrors the coral distribution in the core. The aragonite corals have a higher Sr/Ca value; hence this ratio illustrates the distribution of the corals in the core. This trend is negatively correlated with the terrigeneous input trend seen in the Fe/ Ti ratio.

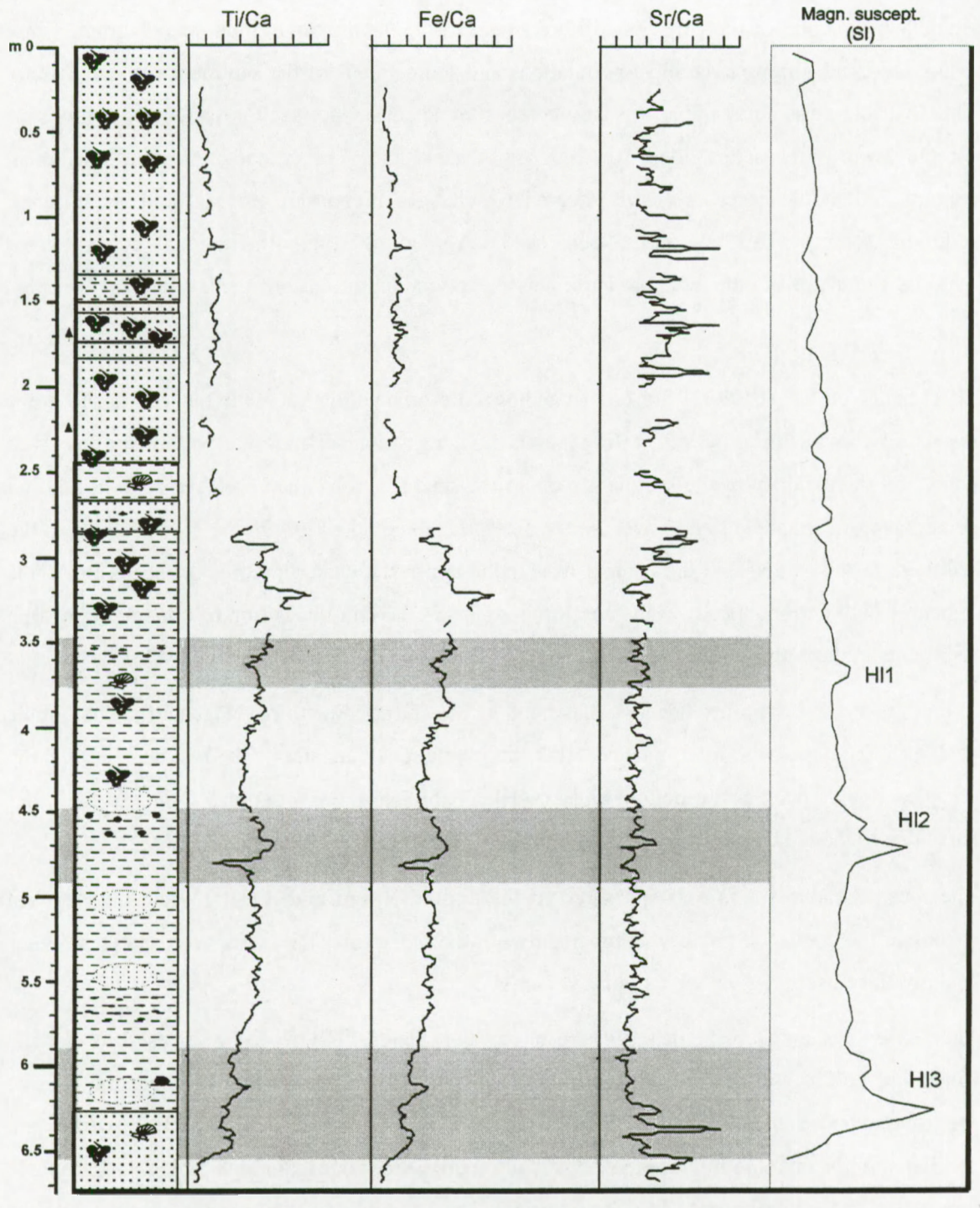

Fig. 4.68: Cortex results of ENAM9902. The ratio Fe/Ca and Ti/Ca shows the relative part of biogenic sediment and terrigeneous input. Peaks are seen near the Heinrich layers. The Sr/Ca ratio illustrates the amount of corals in the sediment.

For **ENAM9902** the sedimentation rate has also been calculated with the relative dating based on the Heinrich layers (Fig. 4.67). The coral core has a similar trend as **ENAM9901** and **ENAM9905** but with a slightly lower sedimentation rate. The average sedimentation rates for all cores is about 23 cm/ky.

The three cores illustrate the different sediment environments around the mounds. Core **ENAM9901** occurs in a calm current regime and the sedimentation did not change dramatically. **ENAM9905** is located in a more vigorous current regime and on a pathway of downslope transport. Core **ENAM9902** is facing the currents and has been influenced by the appearance of corals. The zones with corals have a relative high magnetic susceptibility background and argue for a higher current regime. This implies a high terrigeneous input in the sediments. Due to the stronger currents, fine carbonate sediments have been mixed with terrigeneous large grains that are baffled by the coral framework and transported by the currents. The relation between the MS and corals has also been demonstrated in a recent sampling with the R/V Marion Dufresne on top and on the flank of respectively BEL26 and BEL35 (Van Rooij et al., 2002).

Van Rooij (2000) performed a detailed study of drift sediment in core **MD9923237** (26.25 m), located in 651 m water depth outside the mound influence. A foraminifera-rich sandy facies is observed in the upper 10 cm (Holocene) and in the deepest part of the core between 15-26 m. In between the sandy layers a bioturbated silt clay is described, with a low IRD fraction containing the marine isotopic stages 2 till 4, covering the complete glacial period (10-71 ky BP.) The lower sandy unit has been interpreted as Eemian, between 71-91 ky. This results in an average sedimentation rate for the drift of 29 cm/ky (21.5 cm/ky in the glacial period and 55 cm/ky in the Eemian.

The sedimentation rates found in the ENAM core for the glacial period are similar. The high sedimentation rate for the Eemian is related to coarser sediment and higher current regimes. IRD layers and Heinrich events have not been observed in the MS and IRD fraction (Van Rooij, 2001). A possible explanation for the low MS is that the core has only been influenced by a source of IRD of the European ice sheets. The levels of inferred vigorous current regime are related with the occurrences of the benthic foram *U. mediterranea*. This species is associated with Mediterranean sea water. This suggests that the intensification of current occured during the introduction of MOW in the Holocene and in the Eemian.

4.8.5 Mineralogy

TTR8-AT-83 and **TTR8-AT-84G** have been taken at the same location on the eastern flank of mound BEL41 (Fig. 4.63, Appendix C.1, C.2). The cores have a similar sediment succession as the previously discussed cores on the eastern flank of the mounds **ENAM9905**. The upper 3 cm contains coarse Holocene sand. The section between 3-230 cm consists of olive grey to olive-brownish sandy-silty clay. In the lower part, from 230 cm to the end of the core, the sandy fraction consists of terrigeneous grains, foraminifera and biogenic carbonate debris. The very base of the core contains some rock fragments with a diameter up to 1 cm. Two peaks on the MS curve are seen and fit with the coarse rock fragments in core **TTR8-AT-83G** and **TTR8-AT-84G**. Bioturbation structures have been observed throughout the entire core, which argue for a relative low sedimentation.

Core **TTR8-AT-84G** has been scanned with a medical computerized X-ray tomographer at the University Clinic Gasthuisberg (K.U.Leuven) with a resolution of about 120 µm (Van Geet et al., 2000). Slices have been made every 5 cm to map lithological differences throughout the core. The X-ray images illustrate the density of the sediments in the core. Density contrasts have been observed between the low backscattering matrix and high backscattering of lithic pebbles and bioturbation, filled with coarser lithology. The core yielded a few dropstones at the level of 170 cm and 220 cm. Bioturbation filled with coarse-grained sediment has been observed at 250 cm and 280 cm. The identified zones of coarser material and higher input of siliciclastic material, as seen in the CT images, fit with higher peak in the MS curve. No lamination or sedimentation structures are found in the core.

The total geochemical analysis and XRD diffractograms have been run on the subsamples as indicated on the lithocolumn (Fig. 4.69). The interpretation of the XRD diffractograms has been combined with the total chemical analysis and the calculated parameters as the molecular ratio (Appendix C.3) to identify the minerals and to estimate the relative amount of the minerals throughout the core. The geochemical results are summarized in table C.3 in oxide percentage.

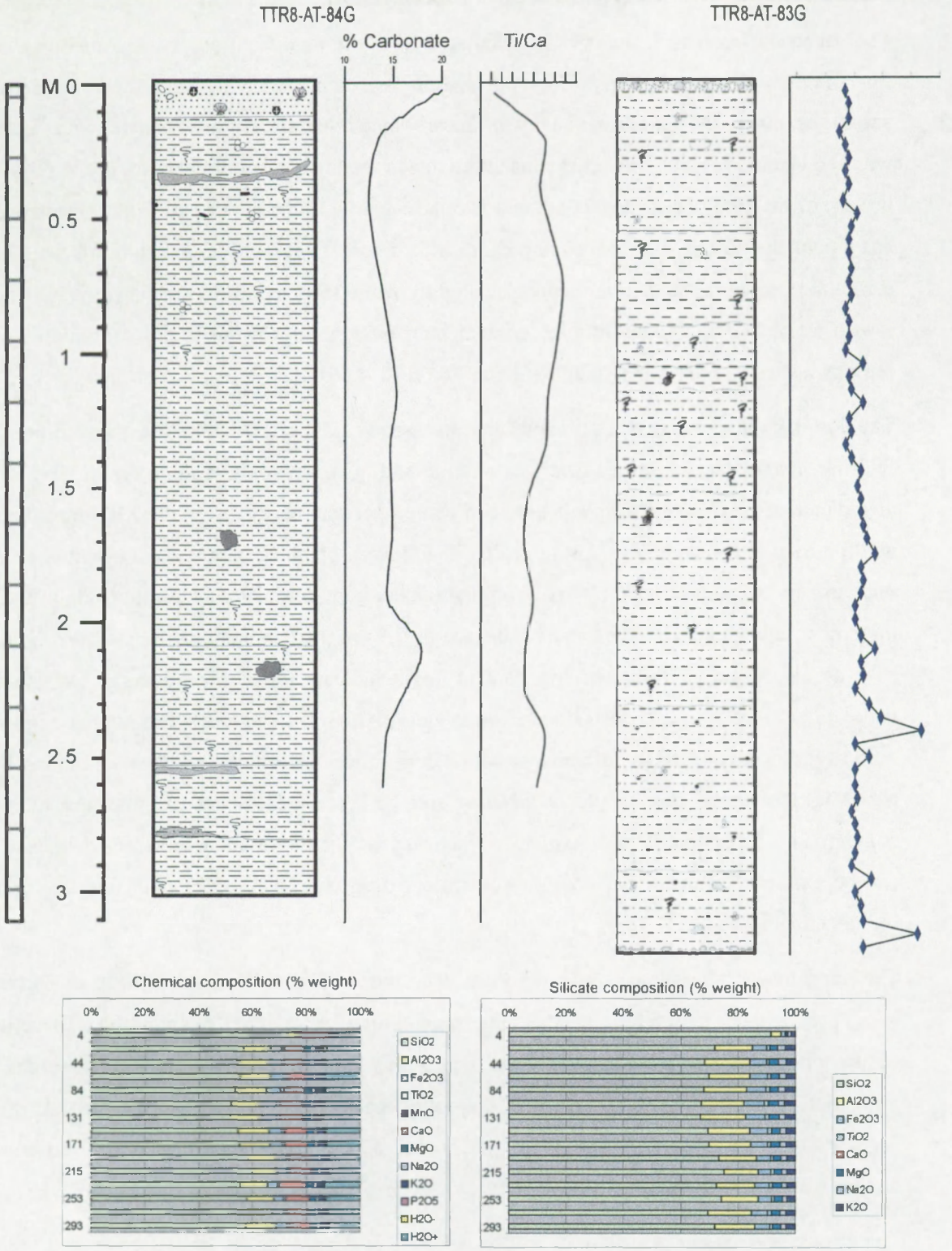

Fig. 4.69: Lithocolumn of core TTR8-AT-84 G and TTR8-AT-83G. The carbonate fraction and Ti/Ca illustrate the relative terrigeneous and biogenic input in the cores. The MS curve of TTR8-AT-83G has peaks related to high Ti, Fe content. The diagrams summarize the total chemical composition and the calculated siliciclastic composition in the core.

The carbonate content in the core is calculated from the total CaO percentage measured in the fine fraction (Appendix C.3). This calculation represents well the trend of the carbonate variations, due to the general high content in carbonate minerals. High carbonate values correlate with the levels with high biodebris concentrations, in the top section of the core (Fig. 4.69). At the bottom of the core, the carbonate content is relatively low to the upper part. The carbonate curve has a peak at 230 cm, just above the peak in MS of core **TTR8-AT-83G**. From this peak on the carbonate content is stable and decreases slightly from 150 cm till 50 cm where it reaches the lowest value (12%). The carbonate content increases rapidly in the upper centimetres to the present seabed and reaches a value of about 20% (Fig. 4.69).

The dominant minerals in the sediments are quartz and calcite (C.3). Other identified minerals are feldspar, mica, chlorite, mixed layers of chlorite and mica, aragonite and dolomite. The relative abundance of the different minerals has been plotted per sample, based on the XRD interpretation and the total chemical analysis in appendix C.3. Traces of mica, chlorite and possible chlorite-mica mixed layers have been observed throughout the core but they play a minor role in the total mineral composition. The mica shows absence of 0.5 nm peak indications for Fe-bearing mica's such as glauconite or illite. The Mg content might indicate for biotite minerals. The chemical content of the silicate fraction is dominated by quartz (high SiO_2 values). The relative high Al/Si ratio suggests the occurrence of feldspar with a dominance of the alkali feldspar containing K and Na. The glauconitic and biotite occurrence and Fe-bearing feldspars explains the high iron content. The Ti content is high, which is characteristic for biotite-glauconite and feldspars. Mg can be extracted from the high magnesium calcite-aragonite in the carbonate fraction, or from biotite and chlorite.

The trend in the mineralogical and chemical distribution subdivides the core in three parts. The lower part contains a high terrigeneous input seen in high levels of Fe, Ti and Al_2O_3. These levels decrease upwards to a minimum at 215 cm, with a maximum in carbonate content (Appendix C.3, Fig. 4.69). The XRD data reveal that the lower part is dominated by feldspar and quartz occurrences. The feldspar values might be related to the concentration of more terrigeneous minerals in the bioturbations.

The higher peak in the MS curve of **TTR8-AT-83G** at the end of the core is compared with the results of the ENAM cores and interpreted as HL1 (Fig. 4.69, Fig. 4.66). The above variations in the MS curve indicate some fluctuation of terrigeneous material but no real Heinrich layer. The higher content of terrigeneous minerals in the lower part of the core might represent the slightly decrease of the effect of terrigeneous input during HL1.

In the zone between 215 and 230 cm the feldspar content increases in comparison with the lower and upper part. In the upper centimetres the mineralogy is dominated by quartz, calcite with minor aragonite of shell and coral fragments in the matrix.

This distribution of the minerals reflects a high terrigeneous input under a steady regime in the middle part of the core and larger quartz grains with carbonate in the lower part near a Heinrich event and in the Holocene. Reworked material and *in situ* minerals argue for the influence of currents in the upper and lower part. The middle part is deposited by the high flux of terrigeneous material (icebergs or rivers) during the last glacial period.

The peaks in carbonate content around 1 m and 2.5 m might represent the European contribution to iceberg discharge. The Irish ice sheet margin retreated markedly form 21-18 ky (McCabe and Clark, 1998). As a consequence a new surface of glacial material has been exposed to erosion. The flux event recorded before HL1 results from the conjunction of a number of factors: an early phase of deglaciation, a very low sea level allowing the maximum seaward extension of the Celtic Sea deltas, the erosion of older delta deposits and ice rafted debris from European icebergs. The high percentage of terrigeneous grains including detrital carbonate and minor glauconite implies a shelf source for the contourites.

Rock fragments are dominantly clastic metasediments (claystone, sandstone, quartzite, micaschist, flintstone). XRD analysis in these levels shows enrichment in feldspar compared to the host rocks. The maximum IRD occurs prior to the main broad peaks of the MS. The fact that rock fragments are almost exclusively clastic (meta)sediments suggests that the major IRD input comes from the British/Irish ice sheet as put forward by Richter et al. (2001) for the Feni drift. Corresponding Palaeozoic sediments cover large parts of eastern Ireland. Rock fragments derived form other circum north Atlantic ice sheets should include granites and gneisses from Precambrium shields area of Canada and Greenland (Grousset et al., 2001).

4.8.6 Contourites

The sandy surface layer has been observed in the top section of all the cores taken in the province. It is mainly structureless, with a variable degree of bioturbation. This sandy layer has similarities with the surface layer observed in the Barra Fan (Armishaw et al., 2000) and has been interpreted as a Holocene sandy contourite. Deep-water sandy contourites are relatively rare, thin and highly bioturbated. They are mainly composed of mixed siliclastic-bioclastics and they have been associated with muddy/silty contourites (Viana et al., 1998).

The formation of such contourite drift requires the presence of a relatively strong-semi-permanent current flowing at intermediate depths along the margin. In the most active zone this current supplies sediment to these mid-depths. The sandy sheet drift is formed by a variety of sources, both internal and external, including bottom current erosion of the drift, shelf spill over pelagic and biogenic fallout and *in situ* winnowing.

The weak bottom currents deposited during the glacial periods fine-grained sediments in the non-coral cores. But these may fluctuate and therefore lead to the incorporation of sand and shelly lenses where current activity is strong enough to winnow away silt and clay size material. This homogeneous muddy to silty-moderated bioturbated facies has been interpreted as a muddy-silty contourite in analogy to the description of Armishaw et al. (2000). Poor sorting and occurrences of irregular coarse-grained sandy silt and biodetris concentrations represent fluctuations in the strength of the generally low current flow.

- All sediment samples have a similar lithology: a Holocene sandy layer overlying the Pleistocene bioturbated greyish silty clays. Biodebris and dropstone layers have been observed in these sediment successions.
- After the last glacial maximum the currents slightly increase till the present-day.
- The intensively bioturbated silty sediment of the glacial deposits is interpreted as a deposit with a low sedimentation rate in a calm current regime (hemipelagic).
- The only observed laminations are layers with a high concentration of rock fragments. These have been interpreted as dropstones transported by icebergs during the collapse of the ice sheets around the North Atlantic: Heinrich layers. The Heinrich events affect the deeper part of the province. The sediment source from the shelf influenced more the sedimentation on the eastern side of the mounds.
- The sediment samples located close to the NS furrow CH indicate local intensifications of the current speed in the central part of the province.
- The coral concentration is highest in the Holocene sediments and in warmer periods, related with intensification of current speed.
- On the western flank of the mounds the corals are more abundant. Fine carbonate sediments have been partly *in situ* produced and mixed with large terrigeneous grains baffled by the coral framework.
- The sediments are deposited in high energetic current regimes related to the MOW water masse in the Eemian and in the Holocene.
- The mineral distribution reflects a high terrigeneous input in the glacial period and coarse quartz grains with carbonate near the Heinrich event in the Holocene.
- The overall sediment succession in the sediment samples is interpreted as contourite deposits.

4.9 Biological results

The mounds house a rich fauna associated with deep-water corals. The biological zonation and diversity of the mounds reflect the present microhabitats and ecological-environmental conditions around and on the mound. These observations are not only important for the present-day setting and development but they also indicate a step in the evolution of the mounds, which might give a clue to the general development.

A video transect has been recorded during the TTR7- survey in the Belgica mound province with the aim to observe the biological zonation on and off-mound, around a few Belgica mounds. Additional box cores have been taken during several cruises (TTR8, Belgica 2000, Pelagia 2000 and Poseidon 2000) to analyze the biodiversity of the macrobenthos on the mounds. These results allow estimating the biological activity and diversity of the mound surface.

The biological surface samples have been analyzed in the department of Marine Biology at Ghent University in the MSc thesis of De Bergé (2000), focused on TV profiles and mega fauna distribution of box cores taken on BEL43 and in the MSc thesis of Van Gaever (2001), the biodiversity analysis of macrofauna of BEL32, BEL35 and BEL41. A bathymetric and geometric analysis of the mounds have been integrated to these studies. These studies have been combined with the bathymetric and geometric analysis of the mounds (See 4.1 and 4.2) to study the biozonation of the mounds.

4.9.1 Biological zonation

In the central part of the Belgica mound province a video line has been recorded in a NS direction during TTR7 (Kenyon et al., 1998). The TV-line crosses several mound flanks of the upslope located mound range (Fig. 4.70). Downslope channels with EW to ENE-WSW orientation separate the mounds.

The footage of the video transect has been interpreted in conformity with the detailed biozonation descriptions, based on submersible dives and intensive sampling of deepwater coral reefs offshore Norway (Freiwald and Henrich, 1997) (see 2.3.) The quality of the images of the TTR7 video does not allow to make a detailed analysis of the benthic communities as the study of the Norwegian reefs. Nevertheless, this video was a useful tool to map the occurrences of dead and living corals and sediment features in relation with geomorphological structures recognized on the multi beam map. Six biological zones have been distinguished along this track:

Two zones do not yield corals but characterize the surrounding seafloor:

- A zone of **sand waves** indicates a strong current regime related to a downslope channel. This zone fits with the sandwave descriptions of sidescan sonar images (see 4.7).

- A zone with normal fine-grained **bioturbated sediment** with dropstones on top represents a normal seafloor in the Porcupine Seabight. The main bioturbators in this soft sediment are Polychaeta (Scoffin and Bowes, 1988).

Four zones refer to the occurrences of deep-water corals (see 2.3):

- **Living coral zone** with red to white coloured corals can relatively easy be distinguished on the footage. In the mapping no difference is made between *Lophelia pertusa* and *Madrepora oculata* corals. The coral thickets in this zone, up to 50 cm high, are relatively dense. In the lower part dead coral framework functions as substratum for new settlements of corals and get filled with sediments.

- **Dying coral zone**.

- **Proximal coral rubble zone**.

- **Distal coral rubble zone**.

The recognized zones have been plotted on a profile along the video line and mapped on top of the multi beam map (Fig. 4.70).

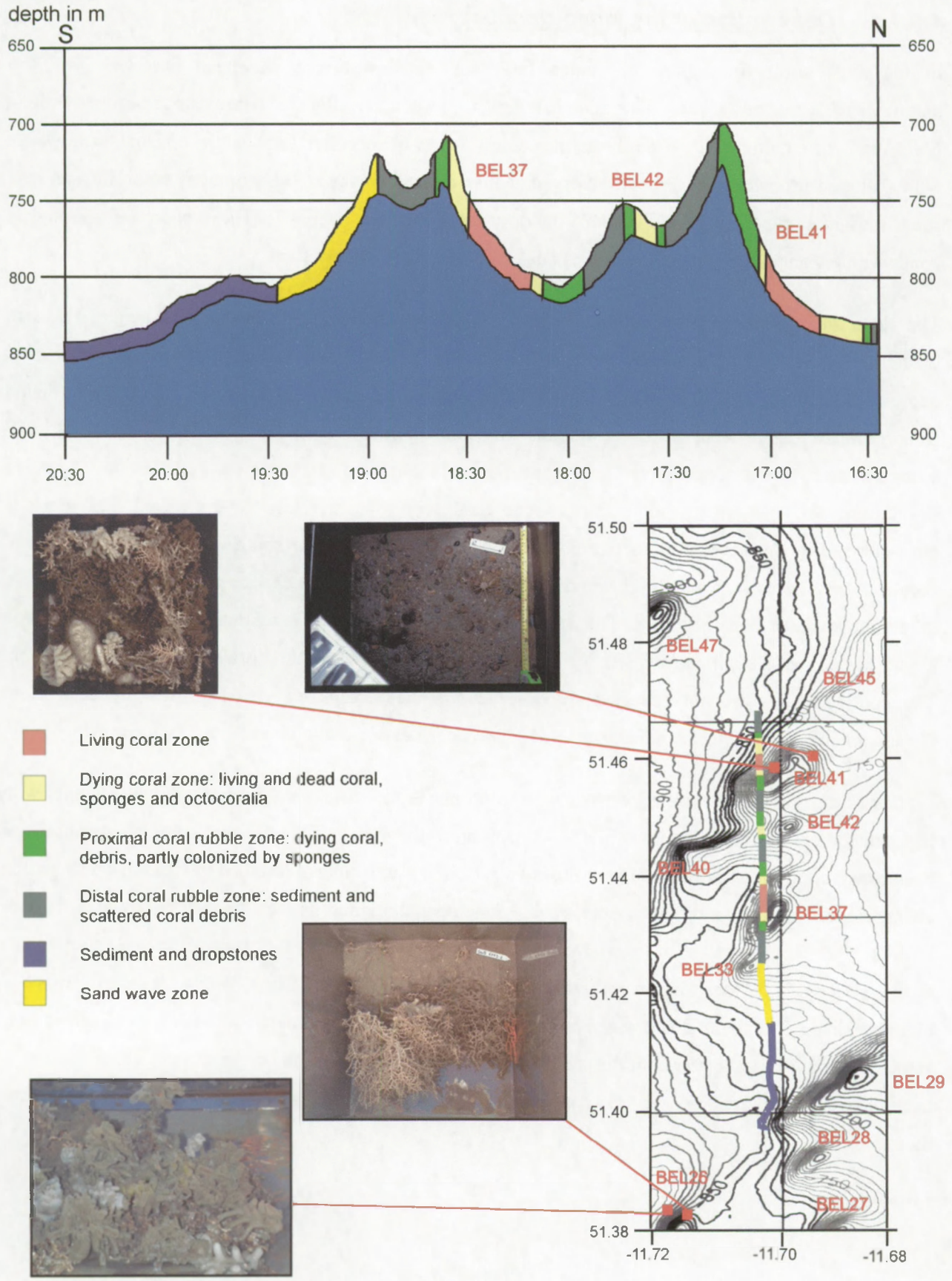

Fig. 4.70. Video profile interpretation plotted on the multi beam bathymetric map (source: AWI Bremerhaven) and zonation along the TV profile. The interpretation of the video track is tested with some box cores, illustrating the biological zonation on the seafloor.

4.9.1.1 Description of the video transect

In the most southern part of the video line bioturbated sediment has been observed, with no distinguishable seabed features. This zone is related to the southern flank of a downslope channel with an ENE-WSW orientation (Fig. 4.70). From the central part to the northern flank of the channel, sand waves with scattered dropstones have been observed. Zones of sand waves are also recognized on the sidescan sonar mosaic along the northern flank of the downslope channels (see 4.7). These observations indicate zones with enhanced currents in the downslope channel on the northern flank.

The video line crosses the eastern flank of BEL33, which is seen on the profile as a local height. This side of the mound is covered with bioturbated sediment. The video transect continues downslope into a local depression between BEL33 and BEL37 and reaches the lower flank of mound BEL37. In this depression some coral rubble is seen, which is probably transported from mound BEL37. BEL37 has a NE-SW elongated bathymetric appearance. The steepest flank of the mound is situated on the NW side. The video line crosses the southern to southeastern mound flank with a relative low slope gradient. This flank is characterized by an increase of coral rubble from the lower flank on the southeastern side to a proximal coral zone on the western side (highest point on the profile). In this zone *Octacorallia* and scattered living coral patches have been observed. The video track does not cross the real summit and goes downslope along the W-NW steep flank of BEL37. Living reddish *Lophelia pertusa* corals characterize this flank. The coral colonies are not continuously observed on the footage and are separated by dead coral framework and sediment. The red *Paragorgia arboreacolnies* occur also abundantly (*Octocorallia*).

Further north this living coral zone passes into a proximal and distal coral rubble zone the channel with EW orientation separating BEL37 of BEL42. On the northern side of the channel some coral rubble has been observed in the sediments. Most probably these coral fragments are slumped of BEL42. The zonation change form a distal to a proximal coral rubble zone once the video line approaches the western flank of BEL42. BEL42 is flanked to the north by a small incision, separating BEL42 from BEL41. The sediments on the flanks of this local depression contain some coral fragments. BEL41 has an explicit ENE-WSW elongate shape. This mound is crossed on its western spur. On the southern flank the mound shows only some coral fragments, scattered in the sediment. On the steep western and northern flank living coral have been observed. This living coral zone passes to a proximal and a distal coral rubble zones, away from the mound summit.

A more detailed VICTOR ROV survey has been carried out in the summer of 2001.The so called Caracole cruise gathered pictures, high quality video and a detailed bathymetric map of Thérèse mound (BEL35). The pictures show a rich faunal live on the upper flanks and on the summit of the mounds, which confirms the proposed biozonation. The footage of this cruise allows a much more detailed analysis of the biozonation and biodiversity.

4.9.2 Biodiversity on the mounds

In total six box cores from four different mounds in the Belgica mound province have been used in the biodiversity study (De Bergé, 2000; Van Gaever, 2001). During the Belgica 2000 survey, two samples have been taken on the southwestern flank of BEL35 (Thérèse mound) and two samples on the western flank of BEL32 (see Appendix C.1). One box core have been taken during the Poseidon cruise of 2000 on BEL43 (Van Gaever, 2001) and another one on the western flank of BEL41 (TTR8-AT-85B) (De Bergé, 2000) (Fig. 4.71). The number of samples and the spatial distribution do not allow to make a detailed biodiversity analysis of the mounds and their zonation. Nevertheless, the results have been used as an indication for the on-mound and off-mound biodiversity.

The Shannon-Wiener index of these samples has been calculated to estimate the biodiversity. The biodiversity is a parameter of a biological assemblage population that indicates its complexity. It characterized the interspecific relation and stability of a population. The diversity of a sample of a population can be calculated based on the amount of species and the distribution of individuals among these species. The most widely used biodiversity index for this study is the Shannon Wiener index. This diversity is a measurement of order (or disorder) within a particular system. This order can be characterized by the number of species and/or the number of individuals in each species within a sample. This number specifies the degree of diversity:

$$H' = \sum p_i (\log_2 p_i)$$

$p_i = N_i/N$ and Ni is the number of individuals of species (i) and N is the total number of individuals in the sample. This index is used to compare species richness between habitats from differently sized samples. Another advantage is that the method is sensitive to rare species, which are typically for deep-sea benthic fauna.

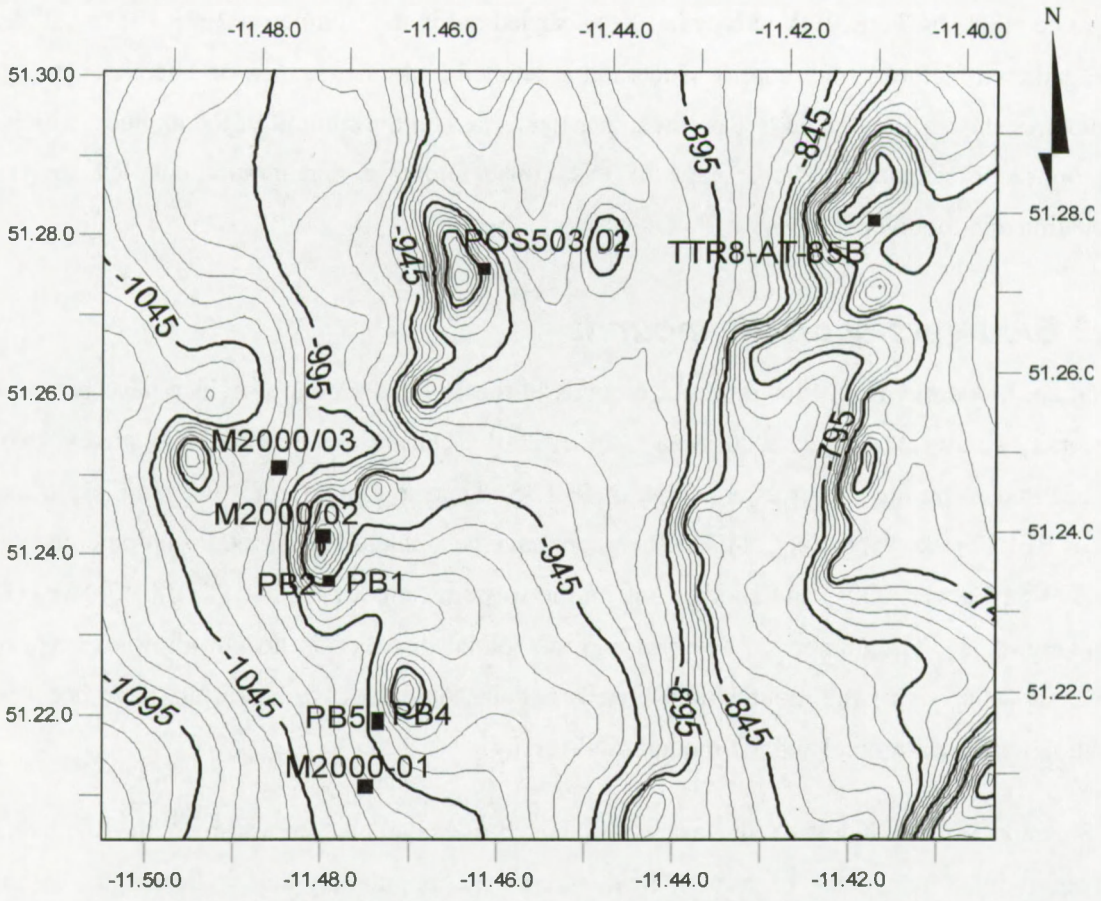

Fig. 4.71: Location map of the box cores taken in the Belgica mound province in the biodiversity study.

4.9.2.1 General observations

All box cores yielded coral fragments and fine to medium sands on the surface. The coarse-grained sediment consists dominantly of foraminifera and coral debris. About 80 % of the surface of the box cores is covered with corals, excepted the box core taken on BEL 32, which was covered for about 90% with sponges (Table 4.1, Appendix C.1). The samples on BEL32 have been taken on the lower steep western flank, which might be located in the dying coral zone. On BEL35 the samples have been taken on the gently sloping southern flank of the mound. The sediment stress on this flank is higher than on the sampled flank of BEL32 (see 4.6). The most probable biological zone a proximal or a dying coral zone with a small amount of living coral and more dead coral fragments than on the flank of BEL32. BEL41 has been sampled on the western steep upper flank of the mound. This sample might represent the transition zone of living to dying coral. *Hexactinellide* sponges are common in the samples and colonise the dead *Madrepora* and *Lophelia* corals. *Madrepora* and *Hexatinellid* sponges dominate the surface of the box core taken on BEL41. The coral colonies are up to 30 cm large.

In the associated fauna of the northeastern flank of BEL43, 728 individuals have been counted, of which 700 *Actiniaria*. 420 organisms have been counted in all the box cores on BEL32 and BEL35 (Table 4.1). In the samples of BEL32, BEL35 and BEL43, 94 different species have been observed, besides nematodes (>1 mm). The most important taxa found in the region are *Polychaeta*, *Crustacea* and *Nematoda*. These three taxa represent 59% of the total individuals in the region, followed by the *Cnidarian*, *Mollusca* and *Sipuncula*. In the box core on BEL41 a total 23 species have been observed, excluding the *Actiniaria*. The most abundant groups in this box core are *Polychaeta*, *Cnidaria*, *Crustacea* and *Mollusca*. The most abundant associated fauna observed in the Belgica mound province is the isopode *Janira maculosa*, with 60 individuals. Besides the echinoderms *Ophiactis abyssicola* and *Amphipholis squamata*, the bivalves *Delectopecten vitreus vitreus* and *Tetrarca tetragona tetragona* are common in all samples.

Sample	Mound	Volume of sediment (liter)	# organisms	Density per liter sediment	# species
PB1	BEL35	0.804	47	58.5	18
PB2	BEL35	1.608	51	31.7	25
PB4	BEL32	12.058	127	10.5	32
PB5	BEL32	12.058	77	6.4	37
POS503-02	BEL43	12.058	89	7.4	35
TTR8-AT-85B	BEL41		728	x	23

Table 4.1: Summarize of the biodiversity study of on-mound box core samples (Van Gaever, 2001).

To compare the biodiversity of the mounds with the surrounding sediments three samples have been taken during the Pelagia 2000 cruise (box cores labels starting with a M, Table C.1 and Fig. 4.71). The Shannon Wiener index of subsample with the same volume, taken from the box cores, has been calculated. The two subsamples, taken at location M2000/01 on the lower SW flank of BEL32, have an H' of 1 and 2.34 or an average of 1.67. The second sample, taken on the summit of BEL35, has an index of 1.56. A third sample is taken in a zone between the mounds as a reference. This sample yielded only one species, which did not allow calculating the index. The on-mound samples indicate a higher diversity than the off-mound samples.

The Shannon-Wiener index of the different box cores per mound location is quite variable. The highest calculated index has been found on the upper western flank of BEL41, with a value of 3.87 (without the *Actinairia*, otherwise the index is 0.45) (De Bergé, 2000). This sample yielded living coral and plenty of sponges. On the southern flank of BEL35 an index of 2.61 and 1.89 with an average of 2.25 has been found. These samples were largely composed of dead coral fragments. The samples of the western steep flank of BEL32 resulted in an index of 3.26 and 1.93 with an average of 2.60 (Van Gaever, 2001). The lowest value for the index is found in the samples with the living *Lophelia* coral. Nevertheless, the variation of the calculated index in the different sampling sites is quite large.

4.9.2.2 Microhabitats

Van Gaever (2001) subdivided the samples of BEL32 and BEL35 in seven microhabitats to evaluate the biodiversity. Three microhabitats are related to deep-water corals: living coral, dead coral and coral debris. Two microhabitats relate to the occurrence of sponges: sponges and sponges debris. Two habitats refer to the sediment, which consists largely of biological debris such as mixed debris and sediment with less *in situ* biological components.

The most species-rich microhabitat is sediment, with 72 species (*Nematoda* are considered as 1 species). Coral and sponge debris are relatively poor in species diversity with respectively 19 and 24 species. On the dead coral branches and sponges, respectively 34 and 43 macrofaunal species have been counted. Five species are common in all microhabitats (dead coral, coral debris, sponges, sponge debris and sediment): *Amphipholis squamata, Janira maculosa, Ophiactis abyssicola, Delectopecten vitreus vitreus* and *Typosyllis variegata.* The sediment microhabitat has the most species in common with the other microhabitats.

The *Crustacea* and *Annelidea* are the most abundant groups in all microhabitats. The Nematoda are most common in the sediment and are absent on the dead corals and in coral debris. Brachiopods and Pycnogoniden are common in sediments but less in the other microhabitats. The taxa *Mollusca*, *Ophiuroidea* and *Cnidaria* are abundant in all microhabitats excepted in the sediment microhabitat.

- Corals are concentrated on the mounds.
- The mounds show a laterally and vertically biozonation.
- A living coral zone has been observed at the steep exposed flank of the mounds, facing the NS furrow CH on the west or local channels.
- In the upper flanks the coral framework is less filled with sediment than in the lower flank.
- *Lophelia* and *Madrepora* are the dominant coral framework builders.
- *Hexactinellide* sponges are common in the samples.
- The fauna observed on the mounds is common in the deep-sea.
- The biodiversity on the mounds is higher than in the surrounding sediments.
- The highest biodiversity has been observed in the sediment microhabitat.
- The biodiversity in the dead coral zone and in the sponge microhabitats is higher than in the living counterparts.

4.10 Oceanography

In addition to the previous oceanographic description (see 2.4), additional CTD and current measurements have been performed in the framework of the EC 5th Framework projects ECOMOUND and ACES.

CTD profiles in the Belgica mound province have been listed in table 4.2 and plotted as Depth-Temperature, Depth-Salinity plots and Temperature-Salinity plots (Fig. 4.72). Additionally, a virtual profile has been made with the available data downslope the continental margin (Fig. 4.72). These plots allow analyzing the characteristics of the water masses and their upslope distribution.

CTD	Date	Latitude N	Longitude W	Maximum depth (m)	Cruise or reference
1	28/09/1980	51°01.98	11°52.20	1520	Rice et al. (1991)
2	12/06/2000	51°04.80	11°43.02	1388	R/V Polarstern ANT17/4
3	28/09/1980	51°10.98	11°40.98	984	Rice et al. (1991)
4	28/09/1980	51°16.02	11°34.02	520	Rice et al. (1991)

Table 4.2: CTD measurements taken in the Belgica mound province.

The physical characteristics of the water masses follow a similar trend at all the CTD sites. A break in the temperature curve has been found around 50 m, which illustrates the seasonal thermocline (Fig. 4.72). This line caps a core of highly saline water interpreted as the results of the **shelf edge current** (SEC) (White, 2001).

Below the seasonal thermocline, the slope of the temperature profile decreases gradually till a water depth of 600-700 m (Fig. 4.72). At this depth level a slight change in the temperature gradient has been observed, associated with a salinity decrease, which goes to a minimum around a water depth of 600 m. These characteristics of the water masses are similar to the ENAW water masses (see 2.4) (van Aken, 2000). From this point on, the salinity increases to salinity maximum at about 900 m water depth. The S-T graph of all CTD profiles illustrates that this water mass with a high salinity, plots in the area of Mediterranean Water as defined in van Aken (2000) (Fig.

4.72). Below the salinity maximum, the salinity decreases with a larger gradient to the minimum value recorded in the profiles.

Around 50 m and 900 m water depth, the salinity and temperature lines show a larger scattering, which might indicate vertical mixing (internal tides?). It is important to note that the CTD-profiles have been recorded during different periods and that the scattering might illustrate seasonal variation in the oceanography at these levels. Especially the data points in the vicinity of 700 m water depth show a larger range in the salinity plots.

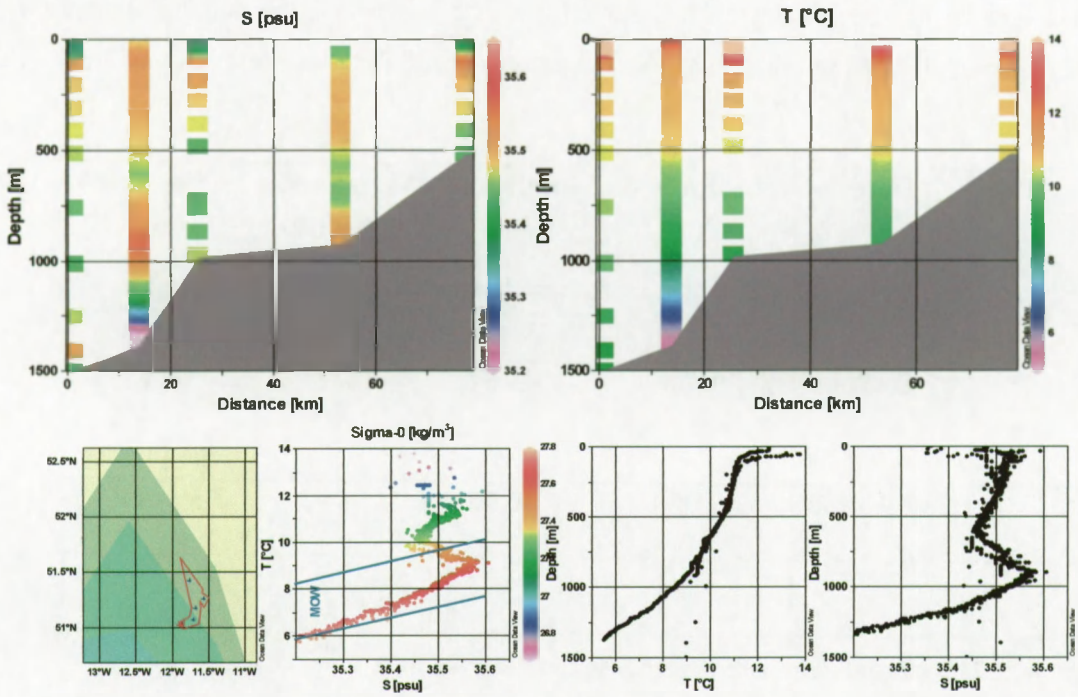

Fig. 4.72: Oceanographic plots near the Belgica mound province. In the upper panel virtual profiles of salinity (psu) and temperature (°C) have been plotted. In the lower part a Salinity-Temperature-Density plot shows the characteristics of the water masses. The variation of the temperature and the salinity of all CTD measurements indicate the water masses in the province. The lower water mass is identified as MOW.

In the upslope profile the salinity maximum seems to climb slightly upslope (Fig. 4.72). This makes the range of the salinity maximum band wider and might indicate the interaction between the water masses and the seabed. In the most eastern CTD profile (upslope), the salinity maximum has not been recorded. It seems that the more saline water mass climbs a bit upslope near the seabed but this is restricted in its extent.

As described in the geometry of the mounds (see 4.1 and 4.2), the bathymetric range of the mounds is between 500 and 1000 m water depth, with a mean of 800 m. The highest density of outcropping mounds occurs in a narrower band between 750-1000 m. This bathymetric zone fits

with the oceanographic transition zone from the ENAW to the MOW water with a maximum salinity core near 900 m in the CTD curves.

The mean current in the Porcupine Seabight at the depth of the Belgica mounds is oriented to the north (Pingree and LeCann, 1990). Currents near the seabed are generally stronger, persistent and directed more along-slope, as one might expect from a topographic steering of currents (White, 2001) (see 4.7). In summer the currents are weaker than in the winter (Pingree and LeCann, 1990). Anyhow, White (2001) reported a very stable northward current (98%) in a mooring on the western side of the mound province, in a water depth of 1000 m. 35.8 % of the currents measured exceed 20 cm/s and 11.10% more than 30 cm/s (Table 2.2, see 2.4). An adjacent mooring more to the south is less consistent in direction and speed (2.20% exceed 20cm/s and 0.10% 30cm/s). The difference between these two locations is not only the depth but also the slope of the seabed. The slope angle at the first location is greater than the latter.

The enhanced current regime in the area can be explained by reflection and breaking of internal waves, as postulated by Rice et al. (1990). To verify this hypothesis, the critical slope angle for breaking of internal waves is calculated as explained in 2.4. The needed parameters are calculated from the CTD data of CTD-2 (Table 4.2), Fig 4.72). The density gradient and density have been calculated for the water masses near the coral banks and included in the formulae (see. 2.4). The density gradient is taken for an interval from 570 m (10.31° C and 35.46 psu) to 900 m (9.13° C, 35.58psu) and the calculation is performed for 760 m with a density of 1030.8 kg/m^3. The Coriolis frequency for that latitude is $1.138*10^{-4}$ s^{-1} and the semidiurnal frequency is $1.405*10^{-4}$ s^{-1}. The theoretical critical slope for this depth interval and region is **2.8°** or a slope gradient of 0.046.

Sites in the bathymetric map exceeding this critical slope are potential sites for breaking of internal waves. The slope angle is calculated for the seabed topography based on a general map of GEBCO data (IOC et al., 1997). In this way a smoother and more general map is obtained without local anomalies as the mounds and small downslope channels. The zones exceeding 3°-slope angle have been marked in grey (Fig. 4.73). This grey string start at the south of the Belgica mound province in a wide depth range (500-1250 m). In this southern area no mounds have been observed. The steep slope is related to a downslope channel.

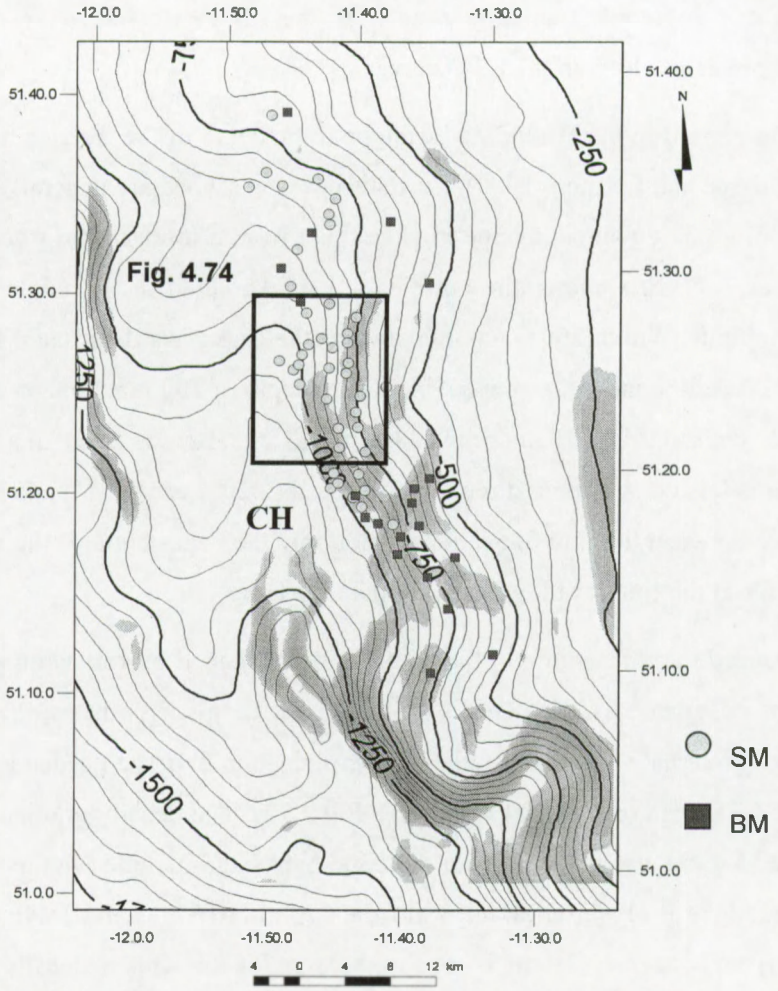

Fig. 4.73: General bathymetric map of the Belgica mound province. The grey shaded zone indicates slope angles over 3°. This band indicates potential sites for breaking of internal waves. A close relation is seen between the mounds and these sites.

A narrow grey band goes north along the local steeper part of the slope, which is part of the major NS furrow CH further to the west. In the northern part of the Belgica mound province the zone exceeding 3° fades out. In this zone much smaller and more buried mounds appear compared to the central part. The central part, where the highest density of mounds and the largest outcropping mounds occur, fits well with zone exceeding 3°-slope angle. The mounds partly shape the slope gradient due to their influence on the sedimentation and cause a steeper slope to the western side of the mound ridge.

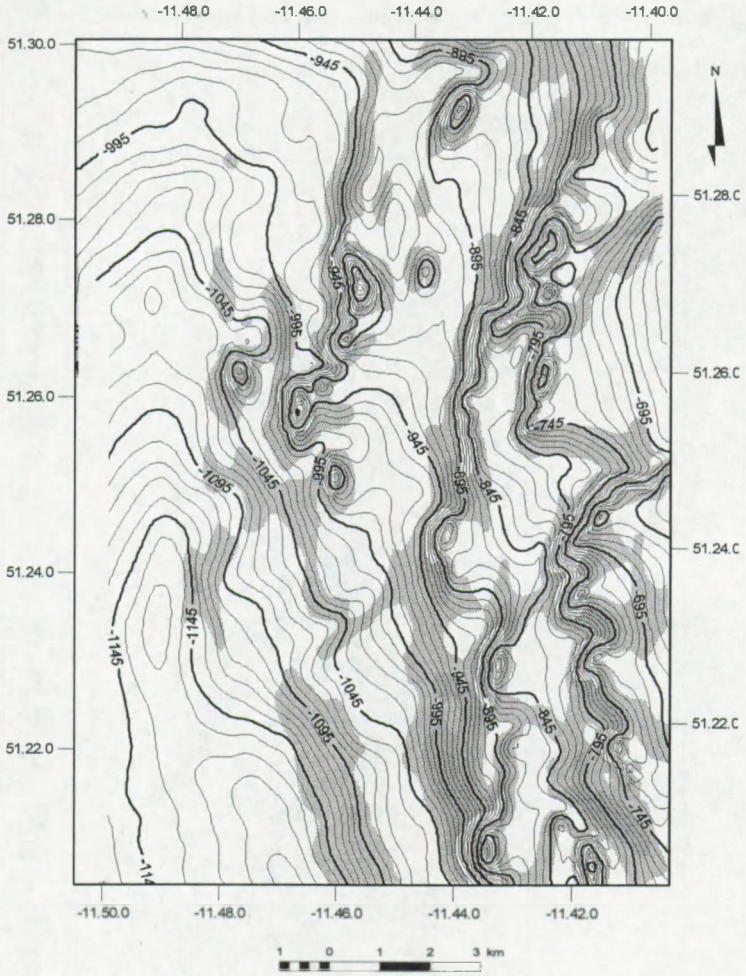

Fig. 4.74: Detailed bathymetric multi beam map (source: AWI Bremerhaven) as indicated in Fig.4.73. The grey zones indicate slope angles exceeding 3°. These potential sites for internal waves breaking relate closely to the mounds.

In the central part of the Belgica mound province a similar exercise has been done on the multi beam map recorded by A.W.I. Bremerhaven in the framework of the GEOMOUND project. All slopes exceeding 3° have been marked in grey and slopes larger than 10° have been excluded because these are mound related. In this way, a general overview from the slope topography is obtained without the influence of the mounds. Two narrow trails of the potential internal wave-breaking zone fits with the occurrence of the mounds, which appear also in two zones. These zones are well consistent with the mound but fade out to the north. The upper trail follows the contour of 800 m and the lower one the contour of 1000 m. Note that not all the mounds are located in the zone of the critical slope.

These mapped zones are similar to the zones marked by Rice et al. (1990) as potential areas of enhanced currents, due to breaking internal waves.

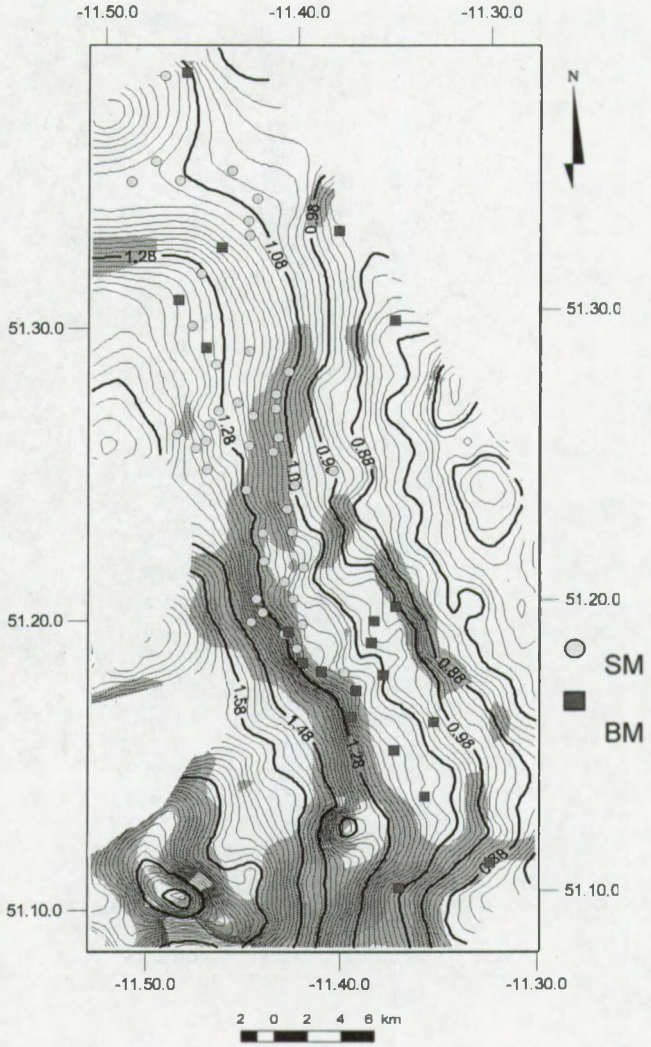

Fig. 4.75: Mound base map with indications of the slopes exceeding 3°. The mounds correlate closely to the potential site for reflection of internal waves generated by the density difference in the water mass.

The zones exceed 3° along the highest dip have also been marked on a map of the base of the mounds (Fig. 4.75). This map gives an estimation of the paleo-potential zone for internal wave-breaking if the oceanographic conditions were similar as in the present-day. These potential zones are concentrated on the lower eastern flank of NS furrow CH and at the erosional scars in faceis Bd (see 4.3). The central and southern mound zones are all situated in this potential zone or inside the flatter zone of the CH, related to vigorous current. To the north the relation between the mound and breaking of internal waves is hard to evaluate because of the large spacing of the seismic profiles (see 3.1).

- In the present oceanographic conditions the mounds are related to vigorous northward flowing currents at the boundary between ENAW and MOW.
- The currents are locally enhanced probably due to density effects and reflection of internal waves.
- Mounds are located in potential sites for reflection of internal waves generated by the density difference between the ENAW and MOW.
- The mound base surface indicate steep slopes in the vicinity of the mounds, which are potential sites for reflection of internal waves, if similar oceanographic condition were present during the initiation of the mounds.

5. Hovland mound province 207

5.1 Mapping of the Hovland-Magellan mounds 209
5.1.1 General bathymetry in the Hovland-Magellan mound province 213
5.1.2 Distribution of the mounds in the Hovland mound province 215
5.1.2.1 General depth analysis 215
5.2 Geometry of the Hovland mounds 217
5.2.1 General mound geometry 217
5.2.1.1 Width 217
5.2.1.2 Height 219
5.2.1.3 Development of the mound 221
5.2.1.4 Detailed mound geometry 224
5.2.2 Magellan mounds 232
5.2.2.1 General observations 232
5.2.2.2 Mound geometry 234
5.3 Geological record 237
5.3.1 Unconformities 238
5.3.1.2 Facies Ha 244
5.3.1.3 Facies Hb 245
5.3.1.4 Facies Hc 246
5.3.1.5 Facies Hd 251
5.3.1.6 Facies He 252
5.3.1.7 Mound facies 256
5.3.2 Mound / facies relation 257
5.3.3 Mound / faults relation 258
5.3.4 Pockmarks and migration structures 260
5.4 Sedimentology 265
5.4.1 Off-mound samples 265
5.4.1.1 Magellan mound province 265
5.4.1.2 Hovland mound province 268
5.4.2 Moats 268
5.4.3 On-mound cores 269
5.4.3.1 Magellan mound 269
5.4.3.2 Cores on HOV02 271
5.4.3.3 Cores on HOV03 275
5.4.3.4 Cores on HOV04 275
5.4.3.5 Cores on HOV05 277
5.4.4 Sediment characterization 279
5.4.4.1 Clay mineralogical analysis 279
5.4.4.2 Binocular analysis 283
5.4.4.3 Scanning electron microscopy 284
5.4.4.4 Cathodoluminescence microscopy 285
5.4.4.5 Petrographic microscopy 285
5.4.5 Isotopic analysis 287
5.4.5.1 Isotopic analysis of TTR7-AT-16G 288
5.4.5.2 Isotopes of corals 290
5.4.6 Gas analysis 293
5.4.6.1 Headspace gas 293
5.4.6.2 Occluded gas 295
5.4.6.3 Gas isotopes 295
5.4.6.4 Gas chromatography - Mass spectrometry 297
5.4.6.5 Carbonate isotopic values 298
5.4.6.6 Summary 298
5.5 Biological results 301
5.5.1 Biological zonation 301

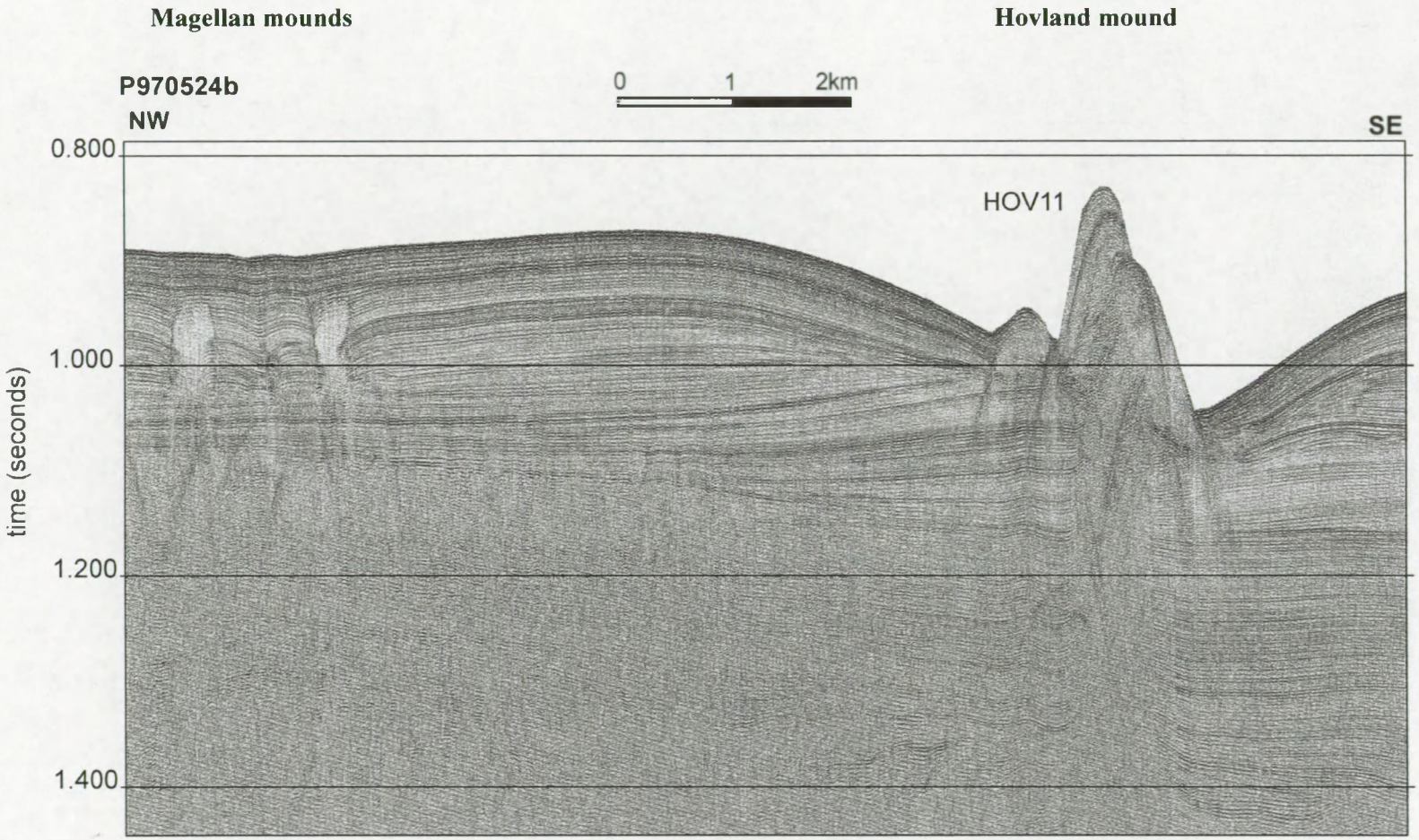

Fig. 5.1: 2D high-resolution seismic profiles illustrating the seismic facies of the Hovland mounds and Magellan mounds (R/V Belgica surveys).

Hovland-Magellan mound province
Geometry 301
5.5.1.1 Introduction 302
5.5.1.2 Results 304
5.5.1.3 Biological zonation based on boxcore samples. 309
5.6 Oceanography

5.1 Mapping of the Hovland-Magellan mounds

The **Hovland mound province**, named after the author who first described these mounds in the Porcupine Basin (Hovland et al., 1994), is situated on a slope break in the central part of the basin between 52°06'-52°22'N and 11°53'-12°45'W in water depths ranging between 400-1100 m. The original paper of Hovland et al. (1994) reports 31 surface mounds in the area. During the surveys of the RV Belgica 25 buried mounds and 14 outcropping mounds (Fig. 5.1) have been imaged in this area. The mound province in this thesis comprises 27 buried and surface mounds in the eastern part of the province and 12 outcropping mounds in the central part. The central outcropping mounds are located closely to a rough NS trending amphitheatre-like seafloor depression (Fig. 5.2, Fig. 5.3).

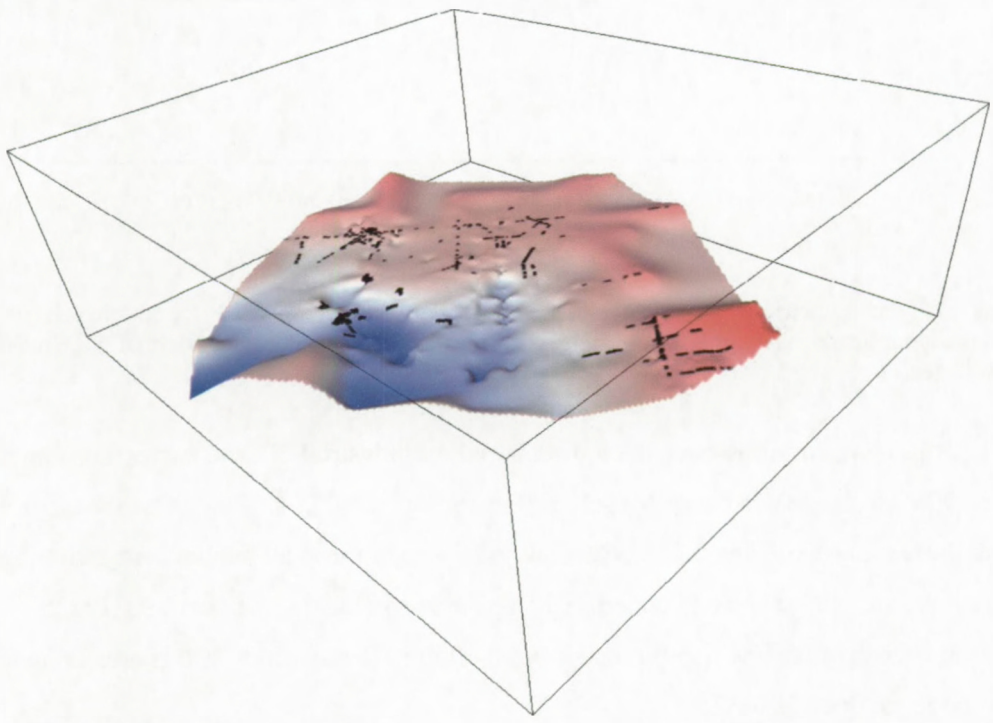

Fig. 5.2: 3D bathymetric model and mound occurrence in the Hovland-Magellan mound province (based on the 2D seismic data acquired in the Belgica surveys).

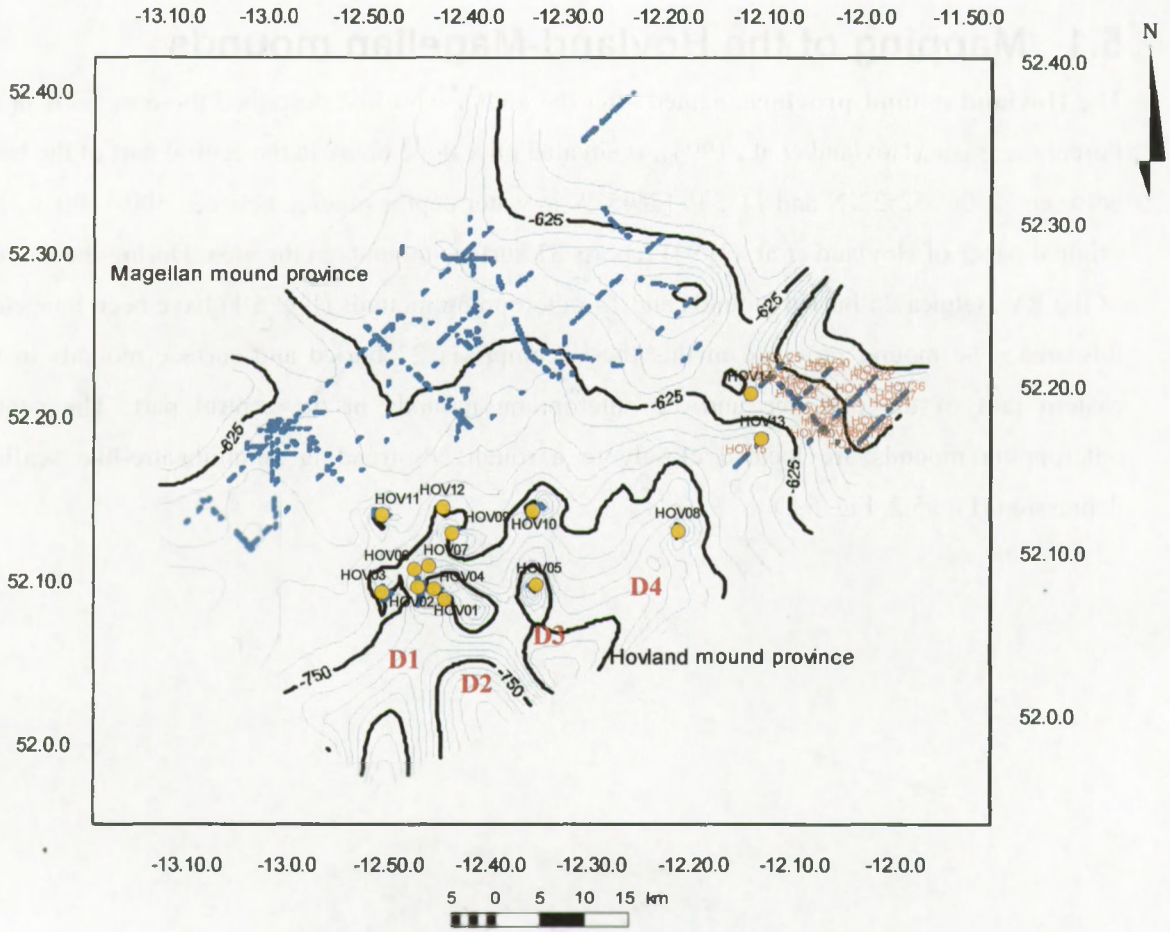

Fig. 5.3: Bathymetric map of the Hovland-Magellan mound province based on seismic profiles. The Magellan mounds, as mapped in the Belgica surveys, and the database numbers of the Hovland mounds are indicated.

The **Magellan mounds** have been discovered on industrial 2D site survey seismic data, obtained in 1996 by the MV Svitzer Magellan (Britsurvey, 1997). The mounds appear in a large well-delineated cluster (Fig. 5.3). With only few exceptions, all mounds in the Magellan mound province are buried and embedded in the upper seismic facies He (see 5.3) (Fig. 5.1). The mounds are located in a narrow depth range around 600 m. The seafloor in this area is gentle and shows no large seafloor features.

These buried mounds form a kind of sickle around the central part of the Hovland mound on the northern and northwestern flanks of the province (Fig. 5.2). The buried Hovland mounds are located approximately in the same depth range as the Magellan mounds close the sickle to the east of the central Hovland mound province. These buried mounds are generally larger and appear on a steeper slope than the Magellan mounds. A mound-free zone of 10 km in the east and 6-8 km in the northwest to north has been observed between the central Hovland mounds and the buried

Hovland and Magellan mounds. This distance is similar to the distance between neighboring surface mounds (HOV03-HOV11 or HOV10-HOV12). This observation only illustrates that the mounds in the central Hovland mound province are more separated and that the mounds in the Magellan mound province are denser and more numerous.

In total 255 Magellan mounds have been observed on the 2D high-resolution seismic grid (1080 km^2) (R/V Belgica surveys), 306 on a seismic 3D block (350 km^2) (Huvenne et al., submitted) northwest of the 2D grid and about 80 on an industrial 2D data set of 72 km^2 (8x9 km) (Britsurvey, 1997). This results in a minimum of 641 mounds over a total area of about 1500 km^2. This estimation of the mound population is underestimated because the 2D seismic grid is not dense enough to cover all the mounds in the area. The density of the mounds, observed on the 3D and pseudo 3D seismic blocks of about 1 mound per km^2 (Britsurvey, 1997, Huvenne et al., 2002 Huvenne et al., submitted) is extrapolated for the total area. A total number of 1500 mounds might be a realistic estimation.

The shape of the mounds is hard to deduce from the 2D seismic data. Most of the mounds are only crossed by one seismic profile (Fig. 5.1). For this reason no geometric measurements have been made of the Magellan mounds on the 2D data set. The geometry of the buried mounds is deduced from the 3D studies [Britsurvey, 1997 #454; Huvenne, 2002 #455] and a qualitative description of the 2D seismic grid.

The Hovland mounds have been mapped, based on the mound facies seen on the seismic high-resolution profiles (Fig. 5.1). All the recognized mounds have been numbered from west to east and from south to north (HOVX) (Fig. 5.3, Appendix D, Table D.1). The geometry information deduced out of the seismic profiles has been summarized in table D.1. This table includes the identification of the seismic profiles, orientation of the profile, height, width, slope of the flanks and moat depth. The highest point observed on the profiles is taken as the central point of the mound structure. Figure 5.4 shows the available acoustic data: sidescan sonar data and high-resolution seismic lines in the mound province together with the distribution of the mounds.

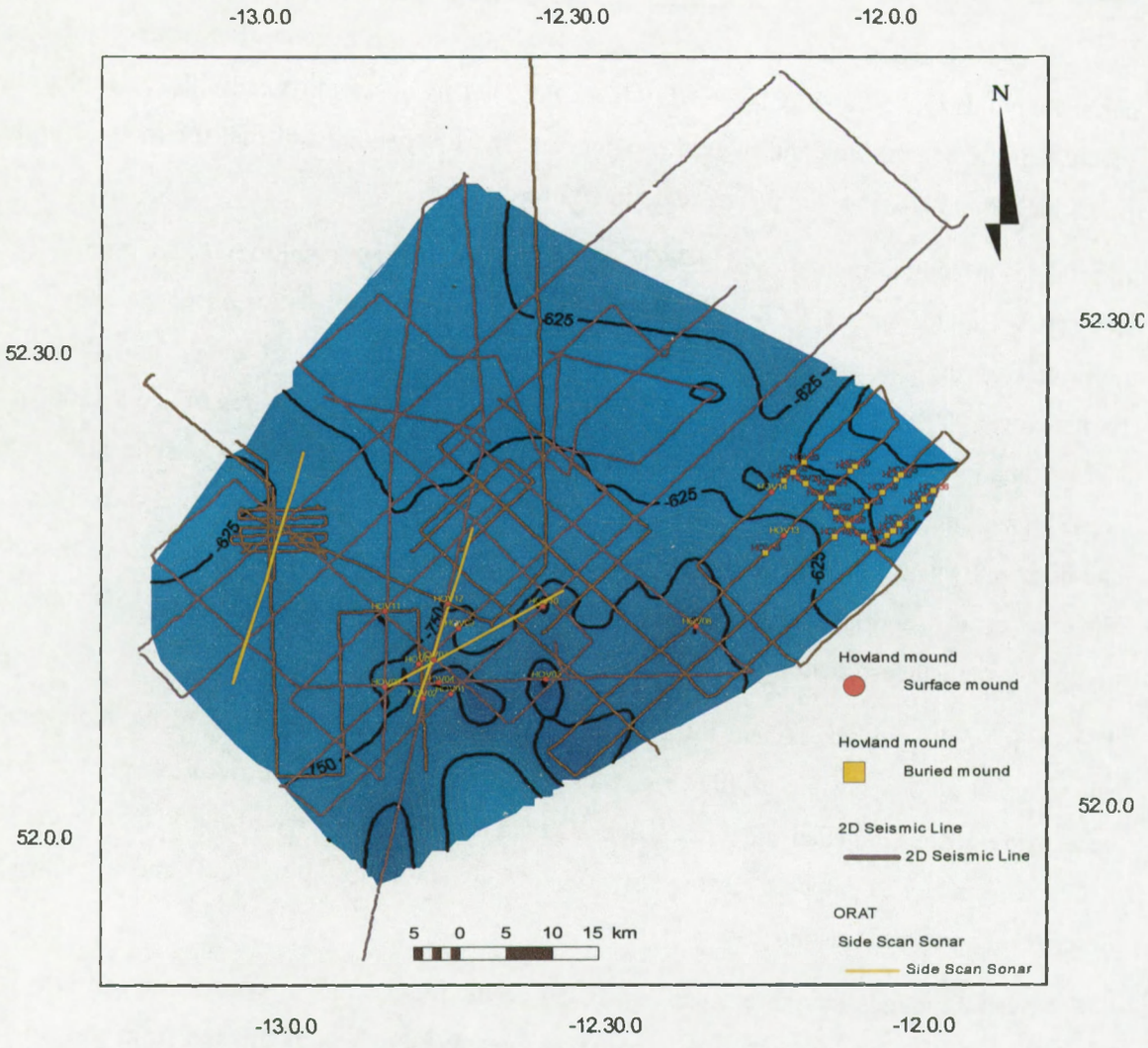

Fig. 5.4: Acoustic data of the 2D Belgica seismic lines and sidescan sonar sonographs.

Hovland et al. (1994) made a detailed bathymetric map of the central part of the province and observed additionally a few smaller mounds. These mounds, however, have not been included in the database because they have not been recorded on the high-resolution seismic grid presented in this thesis. The numerous mounds in the eastern part of the Hovland mound province have only partly been imaged on the seismic profiles. The mound facies of these mounds has been mapped but it was not possible to correlate it from one profile to another. This does not exclude that large mounds can exist in this part, but with the available data only one large mound could be mapped over more than one profile (HOV19). The apparent line up of the Magellan and buried Hovland mounds is an artefact of the mapping technique based on seismic lines.

5.1.1 General bathymetry in the Hovland-Magellan mound province

The bathymetric map of the province is based on the high-resolution seismic profiles (Fig. 5.2, Fig. 5.3). The bathymetric range is between 475-1100 m. The seafloor in the area is dipping to the south with a slope angle of about 0.5-1° in the north (Magellan province) interrupted by a relative steep amphitheatre shape depression in the central part of the Hovland province. This depression consists of four NS oriented branches, which merge in a local depression in the south (Fig. 5.2, Fig. 5.3, Fig. 5.5). The bathymetric map based on the own data is used in combination with the detailed bathymetric map of the central Hovland mound province of Hovland et al. (1994) (Fig. 5.5).

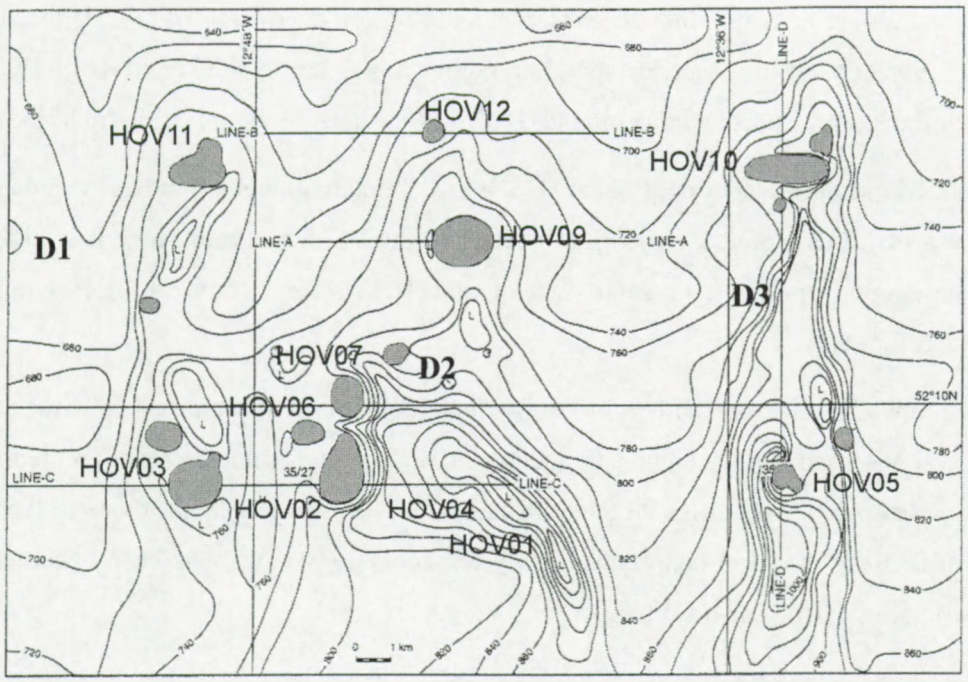

Fig 5.5: Bathymetric map of Hovland et al. (1994) in combination with the mound occurrences of the high-resolution seismic (modified after Hovland et al. (1994).

The most western branch D1 is located in water depths between 700-750 m over a length of approximately 10 km. Inside the large depression an array of several smaller depressions, related to two large outcropping mounds (HOV03 and HOV11) has been observed.

The deepest western branch D2 has a NS orientation in the south, in water depths between 860-960 m and changes direction around 52° 07'N in the NW-SE. Towards the north, the depression fades out and continues in a normal seafloor trend at the 840 m contour. To the east, the depression ends with steep slopes at about 12°45'W. The depression is 4 km long in a NS

direction and 5km in a NE-SW direction. Along the western flank of D2 several mounds are located. HOV01 and HOV04 are located in the bend of the depression. Both mounds flank the depression on the NE to SE sides. HOV02 and HOV07 are located at the western end of the depression. HOV06 is not directly linked to a large depression and is located on the western side of HOV02 and HOV07. Hovland et al. (1994) found one additional mound at the northern tip of the depression. To the most northern extend of D2, two mounds are located: HOV09 and HOV12. On the map the mounds show steeper slopes on the northern than on the southern flank (Fig. 5.3, Fig. 5.5).

To the east of D2 a clear 20 km long NS trending depression (D3) has been observed. The flanks of D3 boarder to the south and finally merge with D4. The depth varies between 750 and 1100 m. Two mounds are related to this depression. On the eastern deep flank HOV05 is located. Hovland et al. (1994) observed a second mound approximately 1 km to the northeast of HOV05 on the eastern flank. In the north a large mound (HOV10) has been observed in the tip of the depression.

About 17 km to the east of depression D3 a NE-SW trending depression has been mapped. In the northern part, the depression changes direction to the NS. The depth range is similar to D3 and both depressions merge in the south. One mound (HOV08) is located on the eastern flank of D3 (Fig. 5.2, Fig. 5.3).

All the mounds of the central part of the Hovland mound province are related to depressions with a general NS trend. Most mounds are located on the northern slope break of the depressions. For the western part of the province they are located at the western flank, more to the east on the eastern flank of the local depressions. Only one mound (HOV05) has been observed inside the deepest parts of depression D3 (Fig. 5.5).

The observed depression has its strongest expression between 1000-840 m. Shallower than 600 m (Magellan mound province) the seafloor features (channels, depression, scouring) are limited on the gentle southward dipping seafloor. Hovland et al (1994) suggested a current controlled scouring or seepage of fluids to explain the origin of these depressions. Due to the dimension and the fading of the effect to the north, the most realistic explanation is the scouring by currents. This suggested a NS trending current regime. Around the mounds local depression have been observed in the seafloor. These have been explained by scouring of turbulence currents around the mounds and interpreted as moats (Fig. 5.3, Fig. 5.5).

In the east of the Hovland province a cluster of buried mounds and two surface mounds are located in water depths between 450-675 m. HOV15 (BM) and HOV13 (SM) are located in the

eastern end of the D4 depression with a NW-SE trend. Both mounds are located near the most northern extent of the depression. A surface mound, HOV14 is located on the western limits of the buried mound area. A local depression has been observed on the north-to-north western flank of the mound. This might be a local moat structure created around the mound (Fig. 5.2, Fig. 5.3). The buried Hovland mounds are located closely to a slight enhanced slope between depths of 450-600 m. (Fig. 5.2, 5.3) No seabed features are observed, which might be related to the mounds. Only slight undulations of the seafloor, related to buried mounds, have been observed on the lower slope of this eastern part. These undulations are seen on the seismic profiles as surface expressions of buried mounds.

In the Magellan mound province only small undulations of the seafloor, related to buried mounds, but no large seabed features, have been observed.

5.1.2 Distribution of the mounds in the Hovland mound province

5.1.2.1 General depth analysis

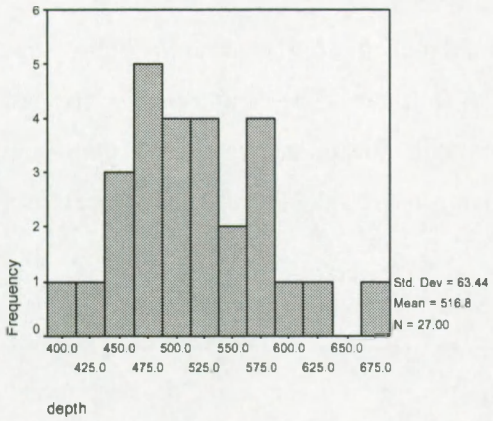

Fig. 5.6: Depth distribution of the mounds in the eastern part of the Hovland mound province.

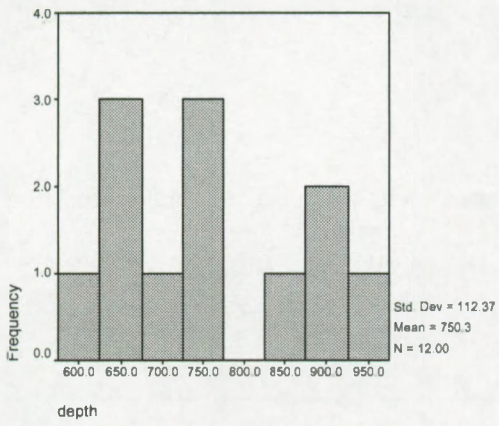

Fig. 5.7: Depth distribution of the Hovland mounds in the central part of the province the mounds cluster in two zones: around 700m and around 900m.

The measured depth of the mounds, listed in table D.1, has been statistically analyzed to show the general depth distribution of the mounds. The water depth of the mound has been measured from the highest point observed on the seismic profiles.

The eastern buried mounds are all located in a narrow depth range between 400 and 675 m (HOV15 is the deepest located mound). The mean depth is 517±12 m with a standard deviation of 63m (Fig. D.2.1). The distribution of the depth is normal with a few extremes to shallower and deeper water depths (Fig. 5.6).

The mean depth of the central surface mound is 750±32 m in a 95% confidence zone between 679 and 822 m (Table D.2.2, Fig. 5.7). This illustrates that the mounds appear in a narrow depth range. The mounds located around the central depression can be subdivided in two

clusters based on their depth distribution. Eight mounds (HOV01, HOV02, HOV03, HOV06, HOV07, HOV10, HOV11 and HOV12) cluster around 700 m and four mounds (HOV04, HOV05, HOV08 and HOV09) around 900 m (Fig. 5.7). The first cluster around 700 m contains mounds related to the northern flank of the depression D1 and D2. The second cluster contains mounds located in the depressions that are isolated (HOV05, HOV08) (Fig. 5.3).

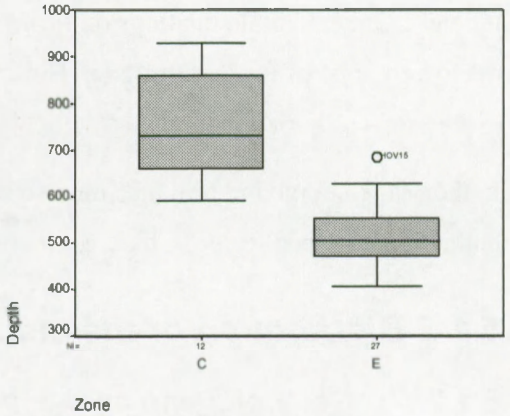

Fig. 5.8: Depth distribution for the two parts in the Hovland mound province. The eastern (E) part of the province is located in a shallower part and shows a narrow depth zone. The central mounds (C) show a broader depth range due to the clustering in two narrow depth ranges.

The buried mounds in the eastern part and the north (Magellan) are located in a shallow part of the province and the surface mounds in the deeper part (Fig. 5.8). The depth range of the eastern and northern mounds is narrow while the surface mounds cluster in two narrow depth ranges around 700 and 900m (Fig. 5.7), thus displaying a large overall depth range in the central part (Fig. 5.8).

- Two types of mounds appear in the central part of the Porcupine Basin: buried Magellan mounds and outcropping Hovland mounds.
- All surface Hovland mounds (17) are related to current scoured depressions, which fade out to the north.
- Moats are formed around the surface mounds.
- The surface mounds cluster in two depth zones around: 700 m and around 900 m.
- Buried mounds are numerous (1500) and closely spaced (1 mound/km^2).
- Buried mounds appear in a large area around 600 m water depth.

5.2 Geometry of the Hovland mounds

5.2.1 General mound geometry

The width and height of each Hovland mound has been measured on the seismic profiles (Appendix D). These measurements depend on the place where the mound has been crossed by the seismic profile. Nevertheless, this analysis allows calculating the average dimension of the mounds. If the mound is crossed by more than one profile, the width is related to the height and the orientation of the profiles, to obtain a more detailed geometry. Additionally, the sidescan sonar data and echo-sounding grid covering HOV02 and HOV07 has been used to describe the surface expression of the mounds. The geometric parameters are divided in two mound categories: the surface (SM) and buried mounds (BM).

5.2.1.1 Width

The mound width has been measured along the seismic profiles and listed per mound, per profile and per orientation in table D.1. For each mound the maximum width has been analyzed. The results are subdivided in two categories: the buried mounds (25) and the surface mounds (14) (Fig. 5.9a and b)

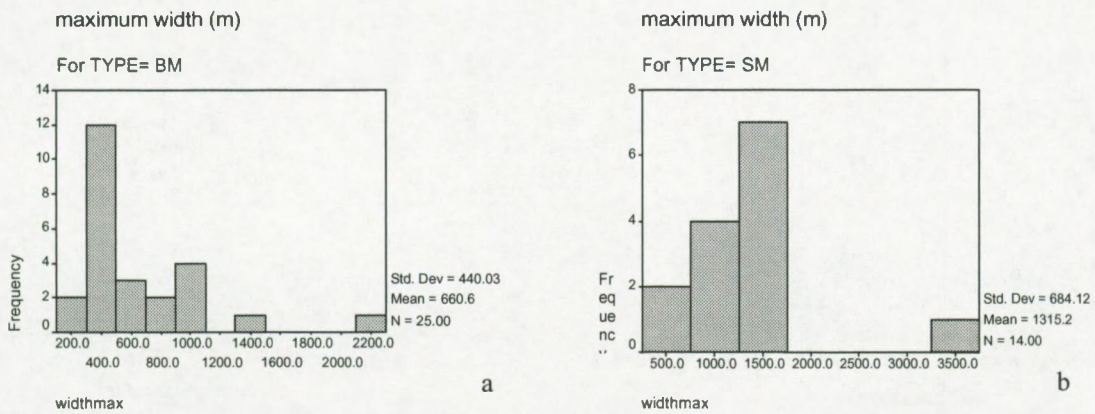

Fig. 5.9: Maximum width distribution for the buried (a) and surface (b) mounds in the Hovland mound province.

The mean of the maximum width for the buried mounds is 661m±88m with a 95% confidence zone of 463-608 m (Table D.3.1). One extreme value, a width of 2172 m, has been recorded for HOV19. This is the only mound where the mound facies could be correlated over more than one seismic profile. The statistic parameters for the maximum width (Table D.3.1) indicate an asymmetry to lower values and a long tail to higher values. This suggests that the width in the

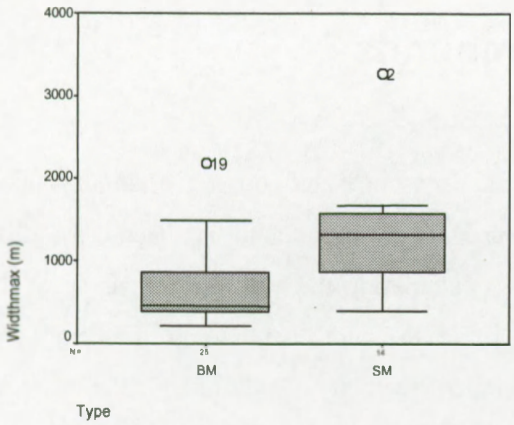

Fig. 5.10: Comparison between the maximum width of the SM and BM. The numbers of the extremities refer to the mound number HOV19 and HOV02.

population of the buried mounds is small and that they cluster around the median of 463 m (Fig. 5.9).

The surface mounds have a similar distribution as the buried mounds. The mean width is 1315±183 m in a wide zone of 95% confidence. 920-1710 m. The statistic parameters (Table D.3.1) illustrate that the mounds cluster around one value, with one extreme of the complex mound HOV02, creating the asymmetry in the distribution.

In general, the maximum width of the BM is smaller and they appear in a narrower range than the width of the SM (Fig. 5. 10).

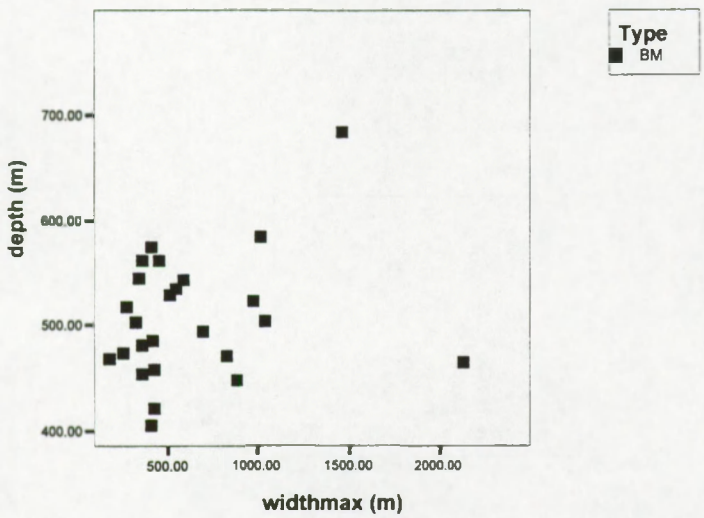

Fig. 5.11a: Width-depth correlation for the buried mounds.

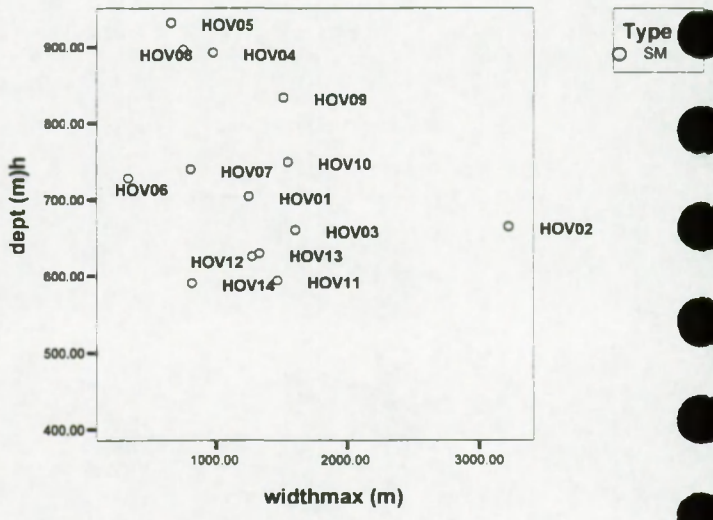

Fig. 5. 11b: Width-depth correlation for the surface mounds.

The width is plotted against the depth of occurrences to identify possible environmental factors controlling the mound growth. (Fig. 5.11). The smallest buried mounds are not restricted to any depth range. The larger buried mounds are located in the deepest part, close to the depth range of the surface mounds (Fig. 5.11a). The largest surface mounds appear in a depth zone between 800

and 650 m with a mean of 700 m. The mound size decreases to greater (HOV05, HOV04 and HOV08) and shallower depths (HOV12, HOV14) (Fig. 5.11b).

5.2.1.2 Height

The height of the mounds has been measured on the seismic profiles from the mound base reflector to the highest point of the mound facies (top of the diffraction hyperbola) (Table D.1). The data have been listed in milliseconds two way travel time (Table D.3.2). No depth conversion has been applied to stay faithful to the data and because no exact velocity measurement is gathered in the area.

The buried mounds have a mean height of 73±6 ms TWT in a 95% confidence zone range between 60 ms-85 ms TWT (Table D.3.2). The median is 67 ms TWT. The distribution of the height is asymmetric to smaller mounds (40-50 ms TWT) (Fig. 5.12). Only seven mounds are higher than 100 ms. The data range for the height is broad but the highest frequency is around 50 ms. This suggests that only a few mounds developed to a larger size and that the majority stopped to develop at a similar development stage.

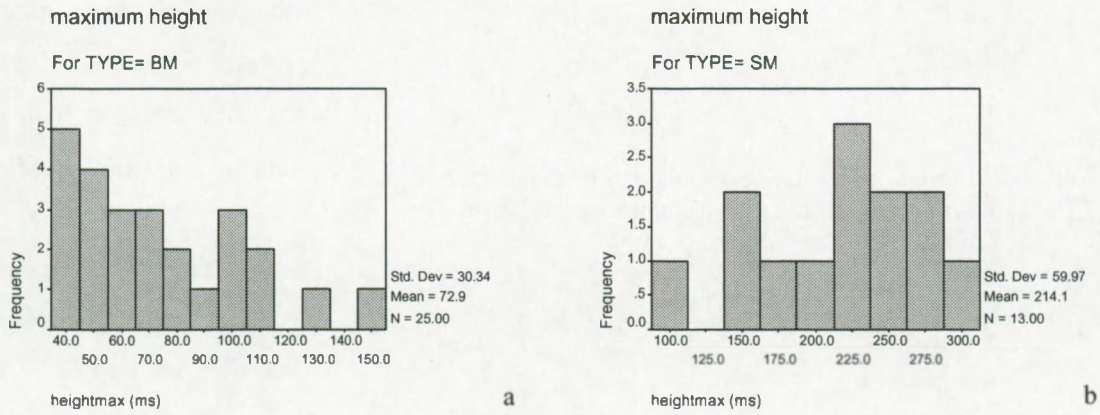

Fig. 5. 12: Maximum height distribution of the buried (a) and surface mounds (b) in the Hovland mound province.

The surface mounds are much higher than the buried mounds. The mean height is 214±17 ms TWT in a relative narrow zone of 95% confidence between 178-250 ms TWT. Most of the measurements cluster around 250 ms TWT. The negative skewness and kurtosis indicate the non-normal distribution with a tail to smaller values (Fig. 5.12). None of the mounds is smaller than 100 ms and only one is higher than 300 ms TWT (HOV02) (Fig. 5.12b, Table D3.2.2). The relative narrow range of height distribution indicates that the surface mounds are in a similar stage of development.

These observations suggest that the mounds could develop larger around the central seafloor depressions than on the eastern slope. To quantify this observation, the height and width are compared with the water depth (Fig. 5.13).

The height-depth correlation of the surface mounds shows that the highest mounds appear in water depth around 700 m. HOV01, HOV02, HOV03, HOV10, HOV11, HOV12 have approximately the same height and depth values (Fig. 5.13). These mounds are freestanding and located at the flanks of the depressions (Fig. 5.1, Fig. 5.3). The smaller mounds HOV05 and HOV08 are located in a deeper part of the province. HOV06 is the smallest mound that is located behind other mounds and which is not related to any seafloor structure. The relative small mounds HOV14 and HOV13 are located in the east of the province in shallower water depth.

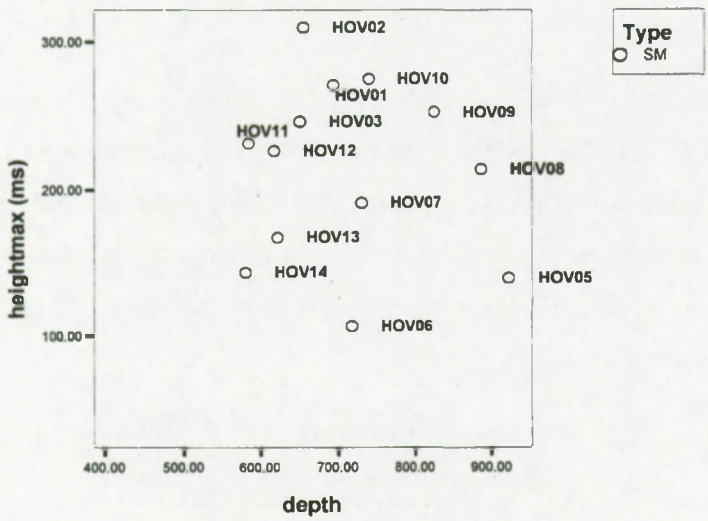

Fig. 5.13: Depth-maximum height relation of the surface mounds. The highest mounds cluster around 700m water depth.

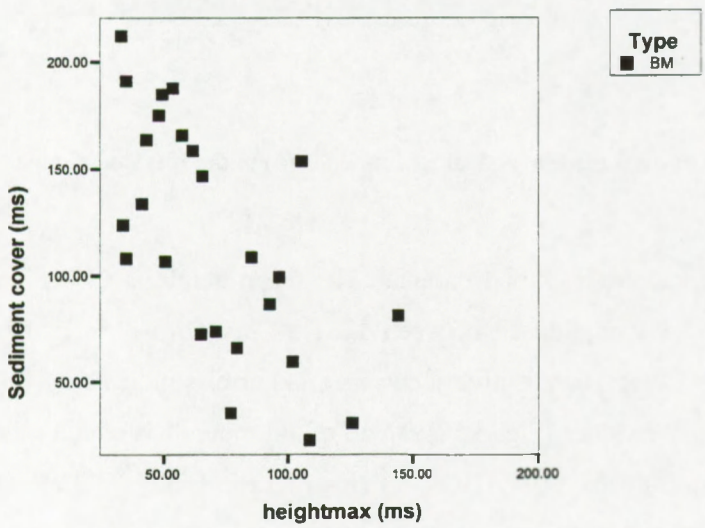

Fig. 5.14: Scatterplot with the maximum height and sediment cover of the buried Hovland mounds. This graph shows a negative relation. The highest mounds have a smaller sediment cover than the smaller mounds.

The relation between the embedding sediment thickness and the height of the buried Hovland mounds has been analyzed (Fig. 5.14). A negative correlation has been observed between the

two parameters. The highest mounds are embedded in the thinnest sediment cover. This suggests that the sediment stress limited the development of the mounds.

These observations suggest that the conditions on the flanks of the depression in a certain depth range were favourable for the mounds to develop. The largest mounds are related to features of current scouring. In a certain depth range these conditions might favoured the nutrient support for the framework builders and thus created a protection against sediment stress. In recent times, the sediment stress at the buried mound locations is higher than in the central part of the province.

5.2.1.3 *Development of the mound*

If the buried mounds can be considered as a frozen earlier stage of mound development of the surface mounds, the geometry difference might indicate development patterns.

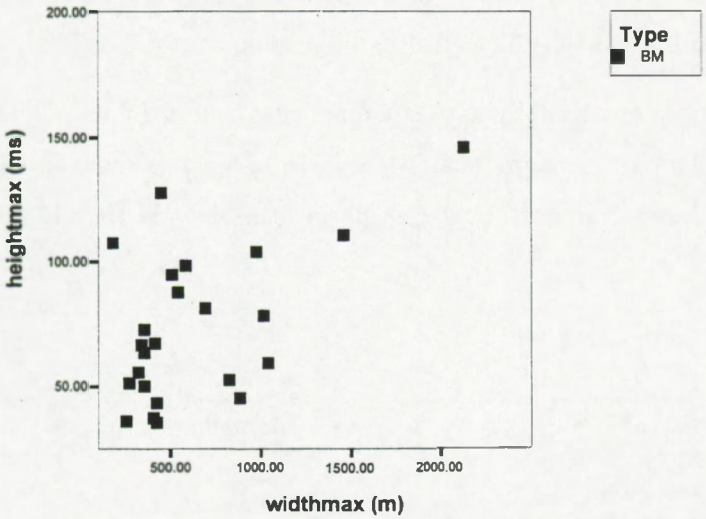

Figure 5.15. Height-width correlation for the buried mounds. The highest mounds have the largest width but no positive correlation is seen. Many mounds show a similar width with a different height.

The maximum measured width is plotted against the height of both mound types to compare the geometry (Fig. 5.15, Fig. 5.16). The buried mounds cluster at a similar width with variable heights (Fig. 5.15). Nevertheless, the tallest mound has the broadest base. This suggests that the mounds formed a broad base and that they started to develop in a vertical direction afterwards. In the next stage, the horizontal extension is in pace with the vertical mound development.

A positive correlation has been observed between the height and the width of the surface mounds (Fig. 5.16). The highest mound has also the broadest base. The mean height of the surface mounds is about three times higher and the width two times longer than the buried mounds. These observations confirm the hypothesis that the mounds developed first in a horizontal and later in a vertical direction.

Plan shape of the mounds

The height-width correlation of the surface mounds has been plotted for all seismic profiles covering the mounds with their specific orientation (Appendix D.3, Fig. 5.16). The mounds crossed by more than one profile, with a different profile orientation at a similar point on the structure (same height), have been used to evaluate the mound elongation.

Nine mounds, two buried mounds (HOV27 and HOV32) and seven surface mounds are crossed by more than one profile, which allows to make a geometric estimation (Fig 5.16, Fig. D.3.1, D.3.2, D.3.3, D.3.4). HOV02 is the highest and largest mound observed in the province. The highest values for both parameters have been measured on NS orientated profiles, suggesting a NS elongation of the mound. HOV03 have also a NS elongated shape. The mounds are located at a similar depth on the eastern flank of depression D2 (HOV02) and depression D1 (HOV03). HOV11 has a clear EW elongation (Fig. 5.4). A slight NW-SE elongated mound shape is deduced from the plots for HOV06, HOV12, HOV10 and HV07. For the buried mounds no real trend is seen. HOV27 shows a NW-SE elongation and HOV32 a NE-SW elongation.

This analysis illustrates that the mounds are steered by local environmental factors. In general, the mound elongation is parallel to the flank of the depression. More isolated mounds show an EW development as HOV10 and HOV11 or an almost circular shape in plan view as HOV12 and HOV09.

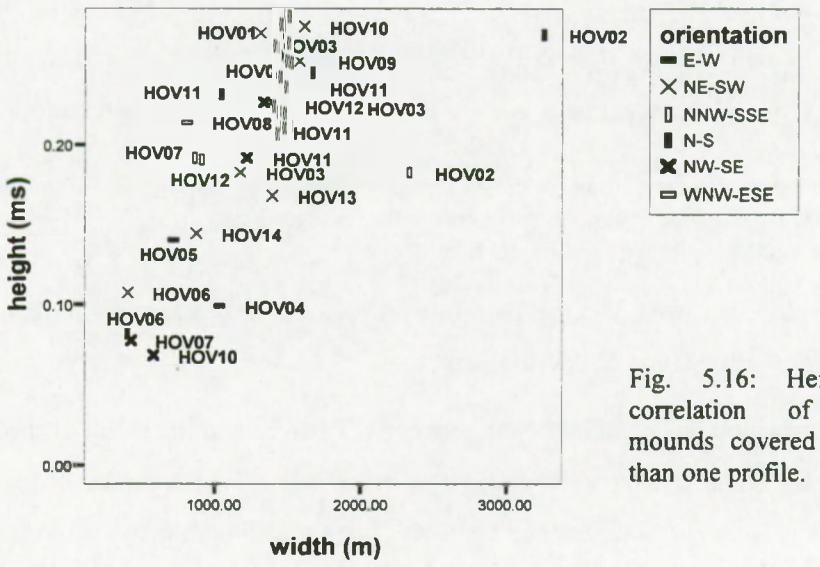

Fig. 5.16: Height-width correlation of surface mounds covered by more than one profile.

Mound flank

The slope angle of the mound flanks is calculated from the edge of the mound facies to the highest point on the seismic profiles (Fig. 5.1). Table 5.1 summarizes the measurement of the SM and BM for each flank orientation specific (Fig. D.3.8). This exercise allows to estimate the average steepness of the mound slopes.

The overall average slope is 12° (Table D.1). The slope of the surface mounds is steeper than this of the buried mounds. The median slope of the flanks on the SM and the BM is respectively 15° and 10°. The flanks of the BM are gentle with a few extreme values (up to 27°). The slope angles of the SM appear in a narrow zone around the median, which indicates for a certain averaging of the flanks during the development. If the orientation of the slopes is taken into account (Table 5.1, Fig. D.3.8) it seems that the northern flanks are generally steepest.

Orientation	SM			BM		
	Number	Median	Maximum	Number	Median	Maximum
W	4	18	22	/	/	/
NW	4	10	21.5	3	13	23.5
NNW	2	20.5	22	/	/	/
N	4	16.5	22	/	/	/
NE	8	14	20	21	10	27
E	4	13	16	/		
SE	4	15	20	3	4.4	5
S	4	15	21.5	/	/	/
SSE	2	14	16	/	/	/
SW	8	14	19	19	8	22

Table 5.1: Average slope angle of the flanks of the surface and buried mounds based on the seismic profiles.

The slope of nine mounds covered with more than one profile has been plotted against the orientation of each mound (Fig. D.3.8). If the location of these mounds is taken into account, it seems that the steepest flanks are facing away the depressions they are flanking. This observation will be explained in 5.2.1.4.

5.2.1.4 Detailed mound geometry

HOV02 or Propeller mound

A NS elongation of HOV02 is inferred based on the geometric measurements on the seismic profiles (see 5.2.1.3, Fig. 5.17, Fig. 5.18). The longest observed width is 3272 m in a NS direction and 1459 m in an EW direction. The maximum height is 310 ms TWT. The average slope angle of the flanks is 12°. The steepest slope has been observed on the western flank, away from the depression D2.

The depth of the moat surrounding the mound is measured on the different profiles (Table D1, Fig. D.3.9, Fig. 5.18). The deepest moat has been observed on the southern flank and towards D2. In between the HOV07 and HOV02 a reduced sedimentation has been observed, which creates also a moat on the NNE flank of the mound. On the seismic profiles (Fig. 5.17, Fig. 5.18) the mounds are clearly sitting on slope breaks of the mound base surface.

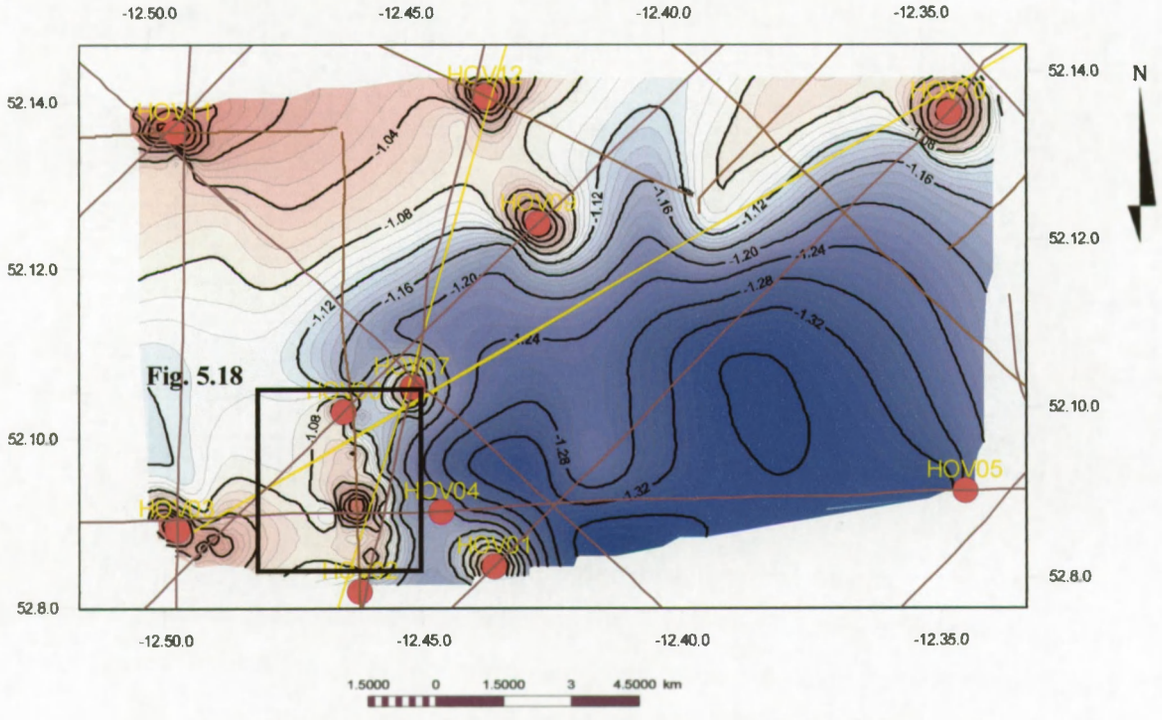

Fig. 5.17: Time structural map (in seconds) of the central part of the Hovland mound province based on seismic profiles (indicated in brown). The mounds are integrated in the mound base reflector (R4) to illustrate the "real" mound shape. The sonographs lines have been indicated in yellow.

Additionally, a dense grid of echo-sounding profiles has been sailed during the Poseidon 265 cruise, with a spacing of 200 m in either direction (EW and NS) (Freiwald et al., 2000). This allowed to make a more detailed surface mapping of the mound. The time profile has been

converted to a depth map with a velocity of 1500 m/s (average velocity calculated from the salinity, temperature and depth of the CTD profiles, see 5.6). For a better interpretation of the surface expression the seismic mound facies has been indicated on the bathymetric map (Fig. 5.19) The facies distribution illustrate that sediments accumulated in between two mounds (Fig. 5.18, Fig. 5.19).

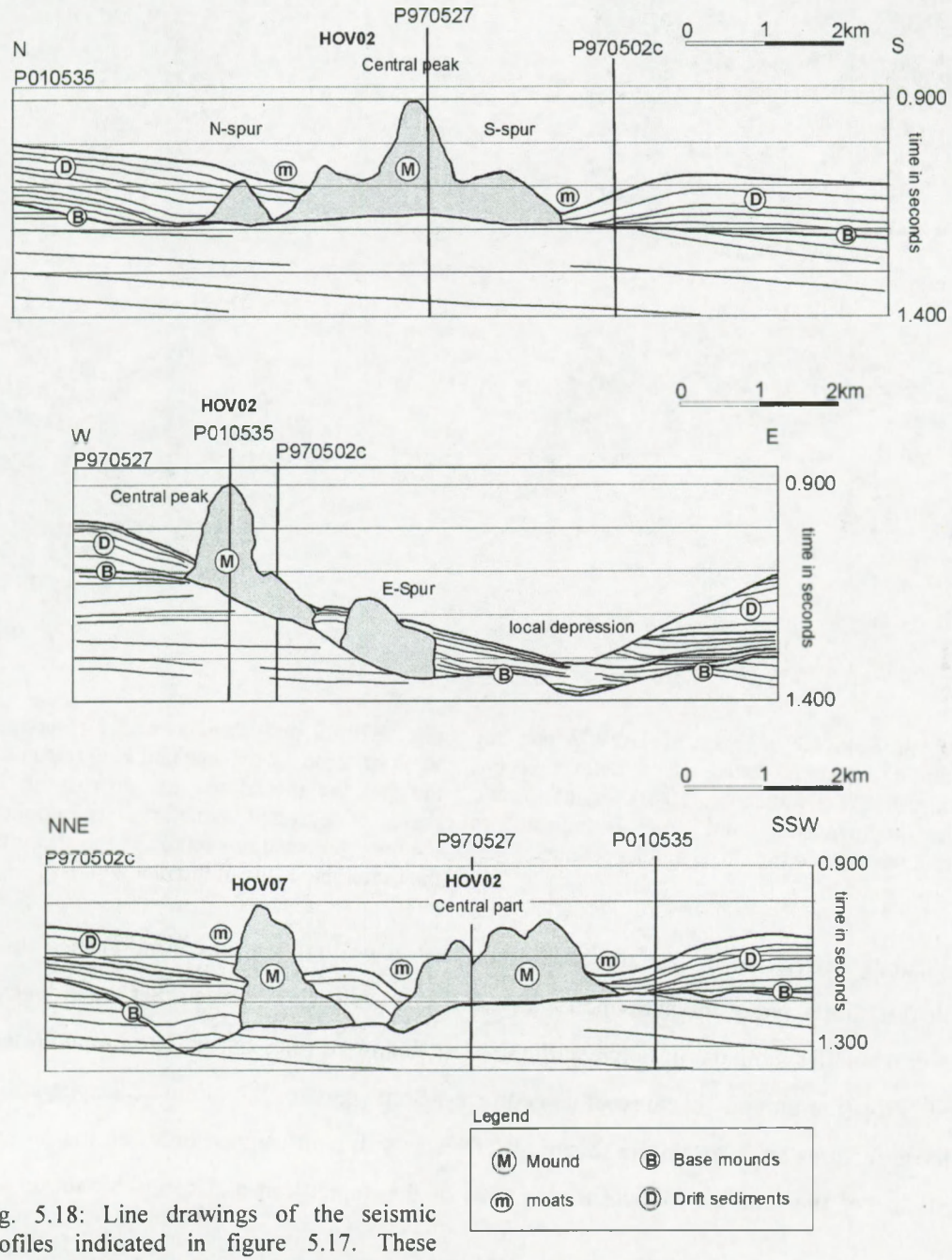

Fig. 5.18: Line drawings of the seismic profiles indicated in figure 5.17. These profiles illustrate the mound geometry and interpretation of the bathymetric map.

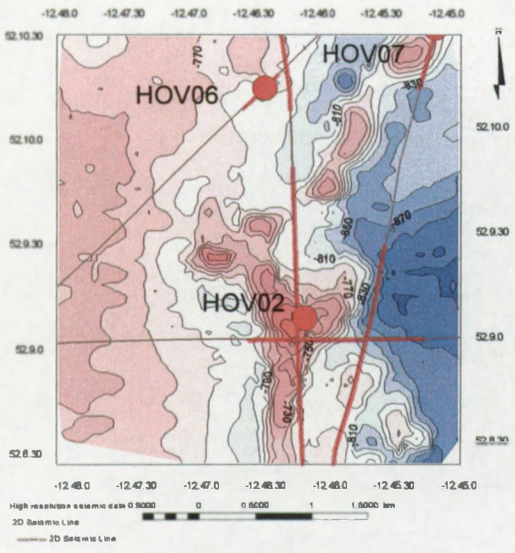

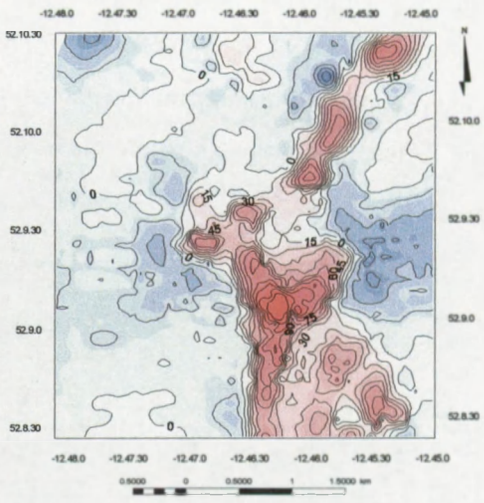

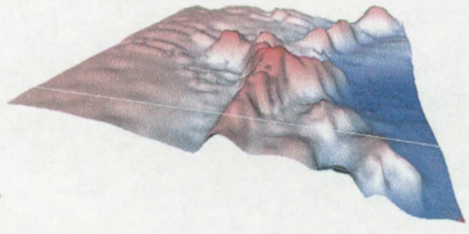

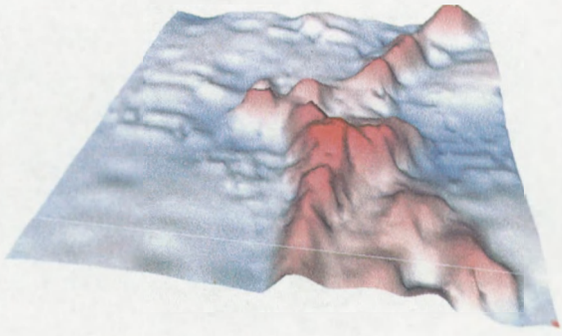

Fig. 5.19: Bathymetric map of HOV02 and the surrounding mounds based on a detailed echo-sounding grid (Freiwald et al., 2000). On the seismic profiles the mapped mound facies is indicated to illustrate the real mound shape and its extents.

Fig. 5.20: Trend map created by subtracting the normal seafloor trend of the mapped bathymetry. The blue colours indicate the moats and the depressions. The red colours represent elevated structures as mounds and sediment mounds. The contours represent the elevation above or below the virtual base line of the mound.

To illustrate better the mound and moat geometry, a normal seafloor trend (based on seismic profiles) is subtracted of the bathymetry (Fig. 5.20). It is clearly observed that the mounds consist of several smaller mounds. In between the mound, sediment piles occur. The mound (HOV02) is called "Propeller mound" because of its geometry. Some parts of the mound are apparently linked but these features are seen on the seismic profiles as sediment trapped between the mounds. The orientation of the mounds follows the contour of the depression and forms moats on the other sides.

The major spur is NS oriented and extents to the north in a sediment mound with a NW-SE orientation towards HOV07. A second short minor spur with an EW orientation has been

observed on the eastern side of the central peak. The facies indicates that the mound is broad in the south and becomes narrower to the north. The mound developed with a gentle slope into the depression on the eastern side. The extension of the mound is sharply bounded with steep flanks to the west. The mound covers an area of 3 km^2, and is about 150 m high. The length in NS direction is about 800 m on the western flank and 900 m on the eastern flank. The width measured on the surface is about 600 m in the central part and becomes broader to the south, 1000 m. The mound has an asymmetric shape, as illustrated on the seismic profiles (Fig. 5.18), with a steep and high western flank and broad, gentle dipping eastern flank.

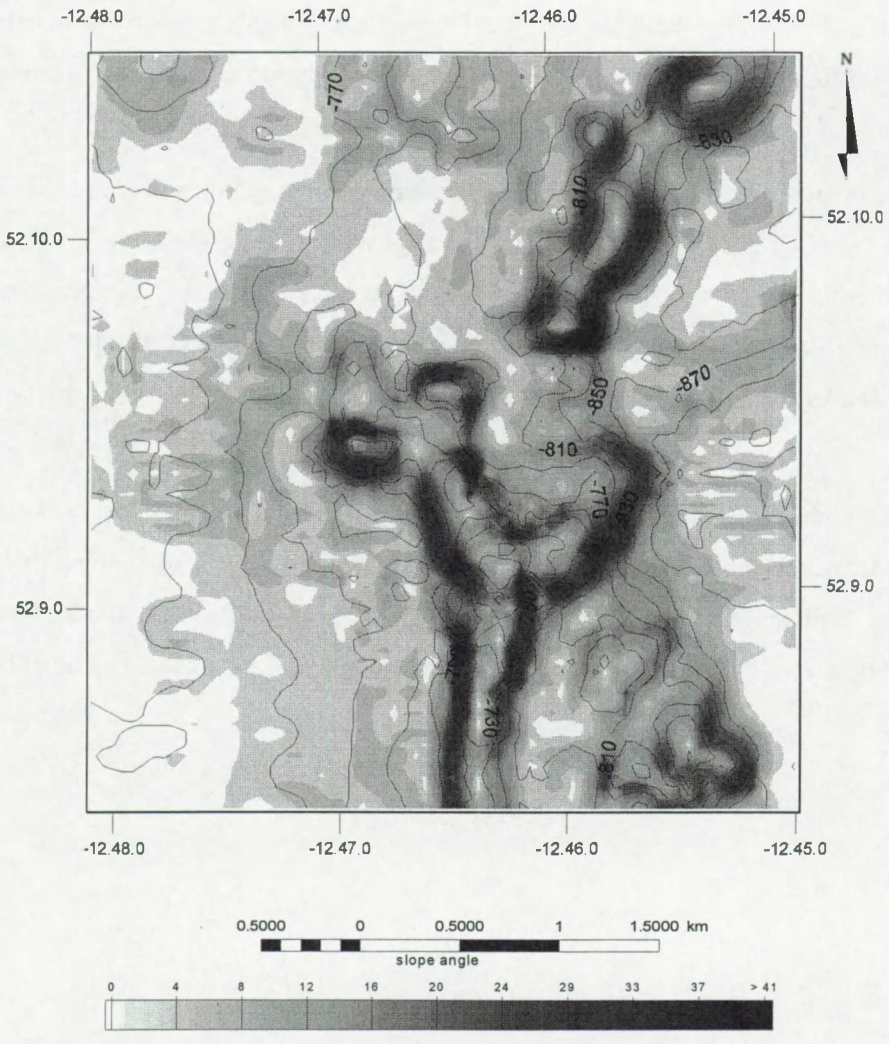

Fig. 5.21: Dip map on top of the bathymetric echo-sounding map of HOV02 and the surrounding mounds. The upper flanks of the mound have the steepest slopes. The mounds are flatted topped.

A slope gradient map has been made, based on the surface grid of the echo-sounding data (Fig. 5.21). The slopes are the steepest in the upper flanks of the mound with a slope angle of more than 35°. The top of the mound is flat. Gentle slopes have been observed in the lower eastern flank. Sediment accumulated on the lower flanks, which smoothes the slope observed on the seafloor (Fig. 5.18). It is clearly observed on the seismic profiles that the mound developed into the depression D2. It seem that on the western flank of the mound, the mound developed in a vertical direction due to the sediment pressure to keep-up with the sediment. On the eastern flanks, the sediment pressure is lower and the mound could extent more horizontally. The extension of the mounds inside the depression and the forced vertical development on the flanks because of the high sediment pressure, might explain the steep average flanks away from the depression (see 5.2.1.3.). Nevertheless, locally the flanks facing the depressions are steeper than the opposite flanks. This is probably due to the accumulation of a living epifauna layer on the upper flanks of the stoss side of the mounds.

The southern and eastern spurs of the HOV02 have been imaged on sidescan sonar line ORAT 01 and ORAT-3 (Fig. 5.21). Three summits have been recognized on the NE-SW branch, in the north of the map and a smaller summit on the SW branch. The main structures have an elevated zone on the SE and on the E. On the eastern side of the mound, the flanks are the steepest, facing the large depression D2. To the west of the NW branch the moat is deeper than on the northern side.

The moats around the mounds have a higher backscattering on the sidescan sonographs. The deepest part of the moat has been observed on the upslope side of the general depression (Fig. 5.20). The turbulence created by the mound in the current flow on flanks with the highest sedimentation rates will create deeper moats than around flanks with slow sedimentation rates.

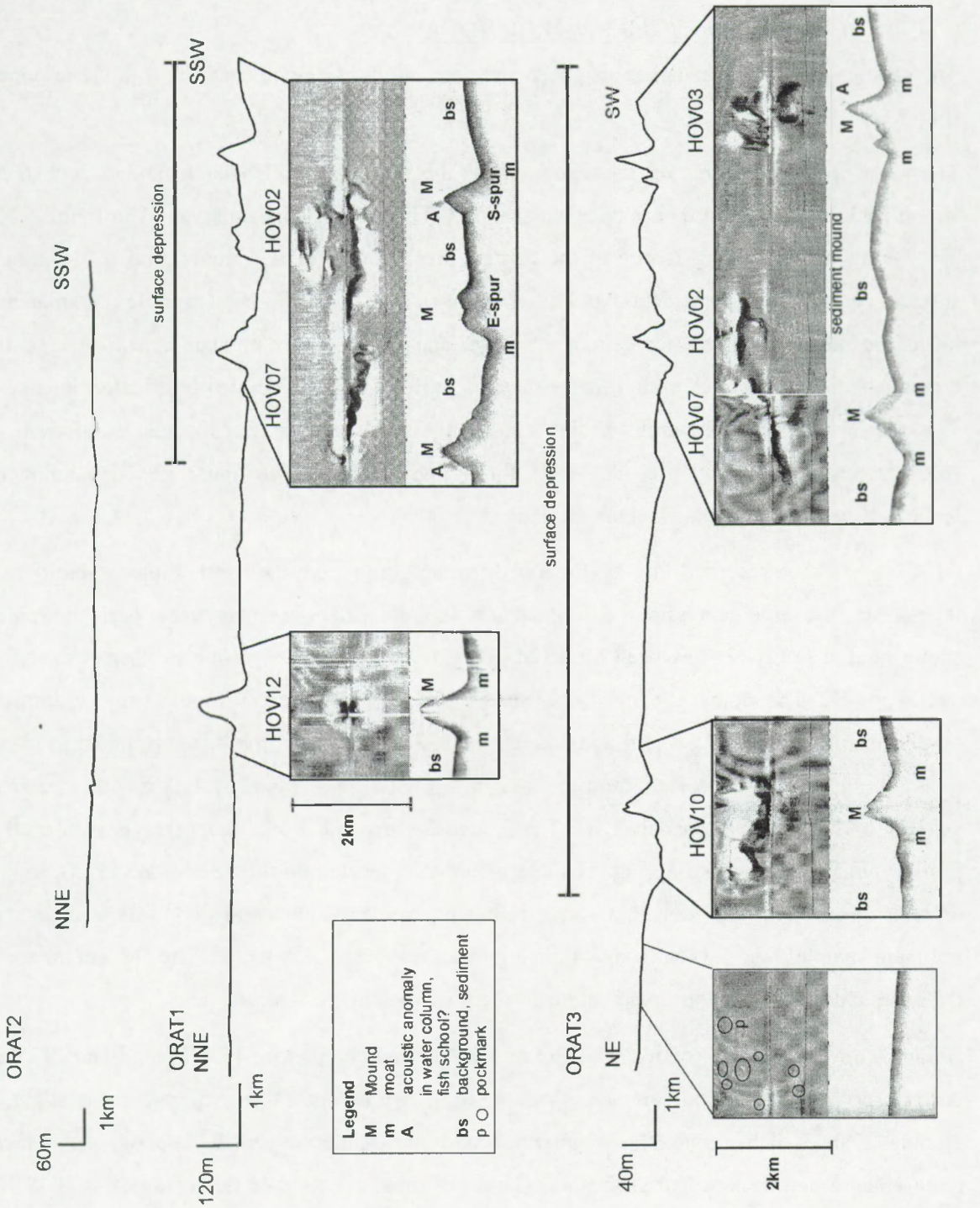

Fig. 5.22: Sidescan sonar lines in the Hovland mound province (see general map).

Sidescan sonar HOV07, HOV10, HOV12

The geometry of the mounds has also been analyzed on two sidescan sonar lines in the province (Fig. 5.22).

The most obvious features on these sonographs are the complex Hovland mounds with their strong backscattering and their associated shadows. This facies is indicated as **M** in figure 5.22. The strong backscattering is due to the relative steep flanks of the mound and to the rough surface, composed of coral debris and coral colonies (see 5.4). The most complex mounds are located at the flank of the depressions. Smaller and less complex mounds appear in a gentle dipping seafloor. The background facies shows a uniform high-moderated backscatter intensity. This facies represents fine-grained, silty clay of the pelagic or drift sediments as inferred by subsurface samples (Kenyon et al., 1998), this is indicated as **bs** in figure 5.21. No sediment features have been recognized on the seafloor.

ORAT-1 has been recorded in a NNE-SSW direction going from the gentle dipping seafloor in the north to the large depression D2 in the south. In the northern zone an almost perfect circular single mound (HOV12) has been observed. This mound is located in the northern tip of the depression D2. The mound is conical and has a diameter of 1 km (the maximum length measured on the seismic profiles is 1.3 km) and a height of 150 m measured from the surrounding seabed (maximum height on the seismic profiles is 227 ms TWT from the base or 210 m with a internal velocity of 1850 m/s) (Appendix D.1). The mound is surrounded by a moat (**m**) as seen on the profiler with a high backscattering. The deepest moat is located on the SSW side (15 m), in the dipping direction of the seabed. Coarser sediments and possible coral debris as seen in the sediment samples (see 5.4) can explain the high backscattering in the moat. The deepest moat on the seismic data has been observed on the northern side facing the depression.

About 3 km more to the south of the HOV12 the mound complex of HOV02 and HOV07 has been observed. This mound complex is composed of two mound ridges separated by a slight S dipping seabed. This zone shows intermediated backscattering on the sonograph, which represents normal background sediments. The northernmost mound of this complex is HOV07. HOV07 forms a narrow sinusoidal ridge with a general NS orientation. The length is about 2 km and covers an area of about 1km^2. The maximum height of the mound observed on the profiler is 120 m (190 ms TWT from the base of the mound, Appendix D.1).

ORAT-3 covers in a NE-SW direction the northern flank of D3 and the central part of the D2. The bathymetry seen on the echo-sounding profiler decreases from the north to the south and enters the local depression D3 just before the northernmost mound (HOV10). The deepest moats

of the mounds are oriented to the north (Fig. 5.18) towards the flank of the depression. In between the mounds, the seabed sediments form an elevated dome shape but with gentler slopes than the mound flanks.

The northernmost mound (HOV10) has a sinuous shape going from a NS crest over to an EW to again a NS orientation. The length of the crest is about 2.2 km with a width of 1km. The height of the mound below the profiler is about 70 m. On the seismic profiles this mound has a height from the base of 275 ms (255 m) and a length of 1.6 km (Appendix D.1). This mound shows an elongation following the bathymetric contour. Nine kilometers to the SW, along the sonograph a mound complex of 2 mounds has observed, which is also recorded on ORAT-1. HOV07 is the most northern mound of this complex and HOV02 is lying to the south. As observed on ORAT-1, HOV07 has a sinusoidal shape with a longest axe in a NS direction. The length of the mound, along his longest axis is about 1.7 km with an estimated area of 1 km^2 and a height of 60 m higher above the surrounding moat on the profiler. HOV02 is lying on the eastern side of the sonograph and is only partly recorded. The mound on this image shows a 1 km long curving SW-NE ridge and a moat on the western flank.

The background facies on the sonographs is uniform, with an intermediate backscattering. Only in the northern part of ORAT-3 circular features have been recognized. These spots of high backscattering have been interpreted as depressions (Wheeler et al., 1998), because the shadow (white) is the closest to the beam (or nadir line) and the highest backscattering behind. These possible pockmarks in the seabed, also observed on the seismic profiles, are up to 100 m in diameter (see 5.3).

Furthermore, some acoustic anomalies have been observed on ORAT1: on the NNE side of HOV07, near the summit of HOV02, and on the SW flank of HOV03. These acoustic anomalies can represent gas seeping or fish schools. Schools of fish are visible on high frequency sidescan sonar images because of the large acoustic contrasts of their gas-filled swim bladders (Blondel and Murton, 1997). They appear as clusters of strong backscattering points as seen on the profiler and the sonograph. Sizeable heterogeneities of the water column can be produced by the presence of gas bubbles. The sonar data become partially scattered and partially reflected before they reach the seafloor, creating data gaps. This is not the case and no evidence of active seepage is found. For this reason the acoustic anomalies have been interpreted as fish schools.

5.2.2 Magellan mounds

As already mention above, the Magellan mounds are too numerous for a detailed description. Some general trends and observations can be made by the analysis of the 2D profiles (Appendix E). More qualitative analysis will be done on the 3D seismic block (Huvenne et al., submitted) and extrapolated on the 2D seismic.

5.2.2.1 General observations

The mounds are up to 100 ms TWT high and 300-800 m width. Some mounds are quite small, 10-20 ms high reflection-free hummocks (Appendix E, P970505, P970514). The small mounds appear closely to the mound base, as a layer. At the other end of the spectrum, some mounds develop tall and at least three of the tallest mounds pierce the seafloor (Appendix E, P970524b). The mounds appear to be larger in the southern part of the Magellan province and become smaller to the northeast of the 2D grid (Appendix E, P970505, P970522). At least three mounds in the Magellan mound province reach the present-day seafloor; others are buried by sediment up to 100 ms TWT. The average sediment cover is 60 ms.

In contrast to the conical Hovland mounds, the Magellan mounds are predominantly vertical, stock-like features with a convex, and often wider, top. Some mounds show a narrow base and get a broader structure to the top, other have a more conical shape. The mounds occur closely to eachother suggesting a high mound density. On the 2D line different configurations of the mound facies have been observed in figure 5.23. Some occur in symmetric (Fig. 5.23B) and some in asymmetric (Fig. 5.23D) twin patterns, which suggest sections through ring structures (Henriet et al., 2001; Henriet et al., 1998) or profiles through adjacent mounds. The different shapes of the mounds observed on the seismic profiles (twin mounds, symmetric and asymmetric mounds) are artefacts of crossings the 3D structures at different positions. The analysis of a dense 2D grid (Britsurvey, 1997; Mc Donnell, 2001) or a 3D seismic block does not show a geometry ring shape structure of the mounds (Huvenne et al., submitted). The mounds show an elongated geometry with smooth slopes. The profiles crossed several mounds at different locations because they are very densely distributed.

The mounds are outlined by abrupt reflection terminations of the embedding horizons (Fig. 5.1, Fig. 5.23, Appendix E e.g. P970505). Such horizons progressively onlap the higher parts of the mounds and finally mould the convex top. Some differential compaction has been observed around the mounds in the onlapping reflectors.

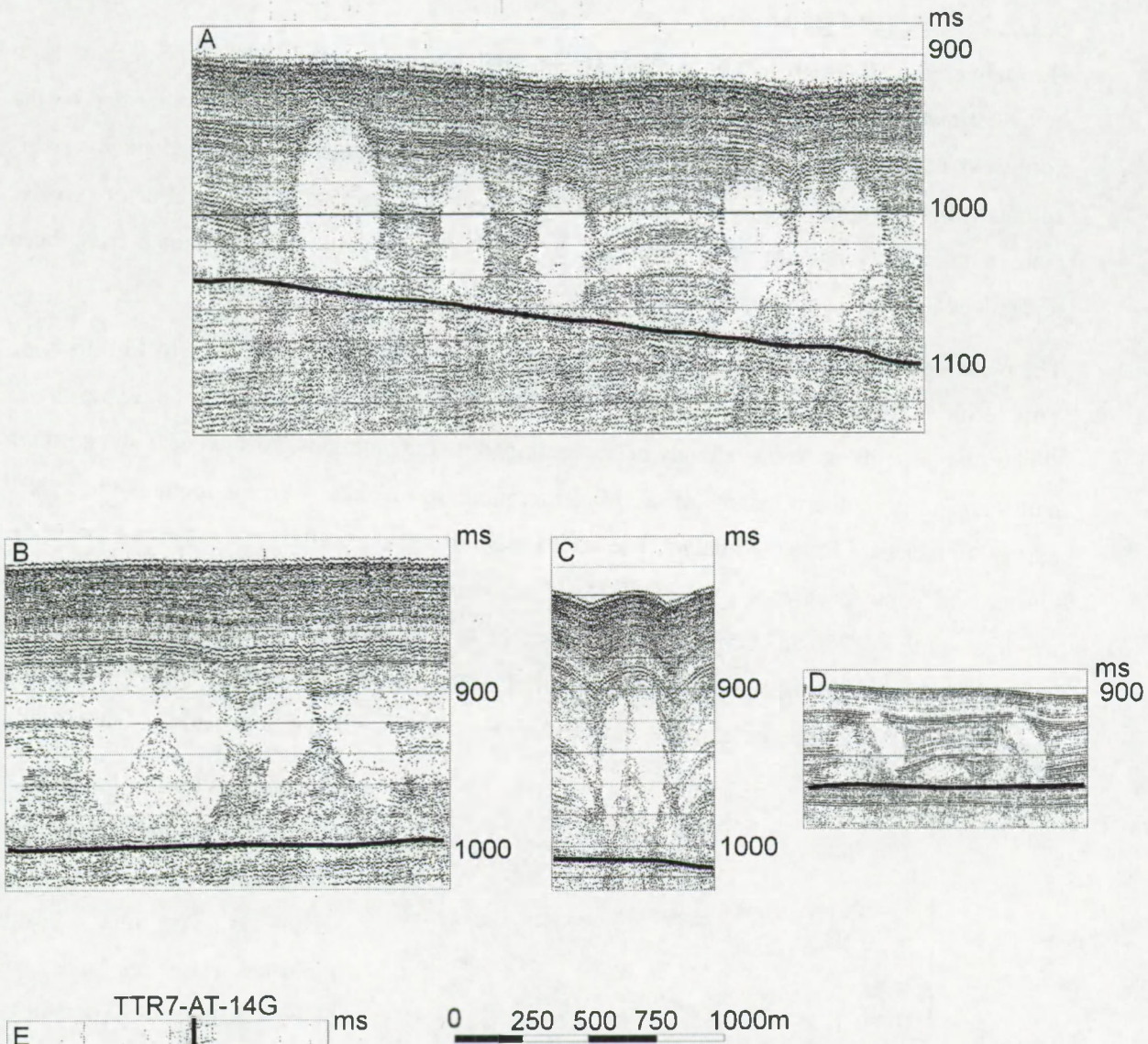

Fig. 5.23: Examples of the morphological variations of the Magellan mounds. All examples have an identical vertical and horizontal scale. The erosional surface at the base of the mounds is marked in black.

A. Three independent single mounds with associated moats.

B. Two pairs of symmetric twins, one pair is closing to the crest and the other is opening.

C. Twin mounds.

D. Asymmetric twin mounds

E. Location of core TTR7-AT-14G at a mound piercing the seafloor flanked by smaller buried mounds.

5.2.2.2 *Mound geometry*

Huvenne et al. (submitted) study the Magellan mounds on a 3D seismic block, which provides a better estimation of the geometry of the mounds and the moats. This 3D block is located on the northwest of the 2D seismic grid. The geometric analysis of the mounds is done by semi-automatically mapping on a isopach map of a mound shape and mound base reflector (see for more details Huvennne et al., submitted). In total 306 mounds and 172 moats have been recognized in the 3D seismic block.

The mean height of the mounds in the 3D blocks is 80 ms while the tallest is up to 174 ms high. This result is comparable to the analysis of the 2D seismic even the average in the 2D grid was slightly larger, 100 ms. It has already been mentioned that the mounds are smaller in the northern part than in the southern extents of the Magellan mound provicne. Even the mounds in the NW part (3D block) are little bit smaller. The tallest mounds appear on the southwestern edge of the cluster and some even reach the seafloor (Huvenne et al., submitted). The mounds have an average width of 250 m, while the mean area of the mounds is 0.05 km^2 (Huvenne et al., submitted). The width of the Magellan mounds observed on the 2D grid is larger. The height distribution shows similar values. The mounds show a NS elongation (Huvenne et al., submitted).

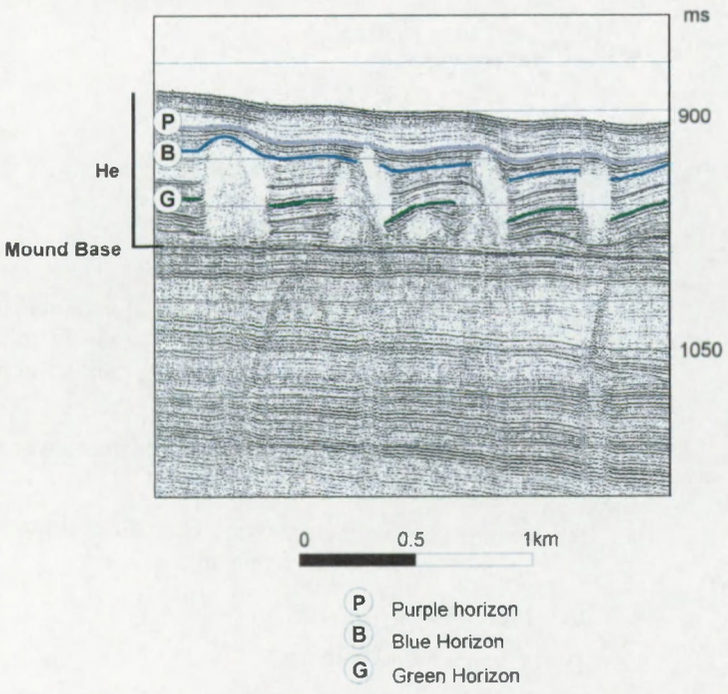

The dimension of the mounds has been compared with the thickness of the overlying sediments. For this analysis three key reflectors have been picked in the area: P, B and G, as indicated in figure 5.24. These reflectors represent three time intervals of the mound development. This is compared with the thickness of the sediment, embedding the mounds between the seafloor and the mound base (Fig. 5.24).

Fig. 5.24: Zoom of the Magellan mounds of P970502c (Appendix E). On the seismic section, the erosional surface at the base of the mounds and the three marker horizons P, B and G are indicated. Configurations of the horizons illustrate the effect of currents on the sedimentation around the mounds during their individual evolution.

A colour scale has been used to map the different sizes of the mounds (Fig.5.25). The largest mounds appear on the southern edge of the area of interest. In these zones the thickness of the sediment cover is relatively thinner than in the other areas. A central thin sediment cover is observed where local the largest mounds appear. More to the north and the east, the sediment cover becomes thicker and the mounds are smaller. About 50% of the mounds in this area stopped in an early phase to develop before the first G reflector. 70% of the remaining mounds stopped accreting between B and P. The largest mounds are situated on the margins of the province and in zones with less sediment pressure.

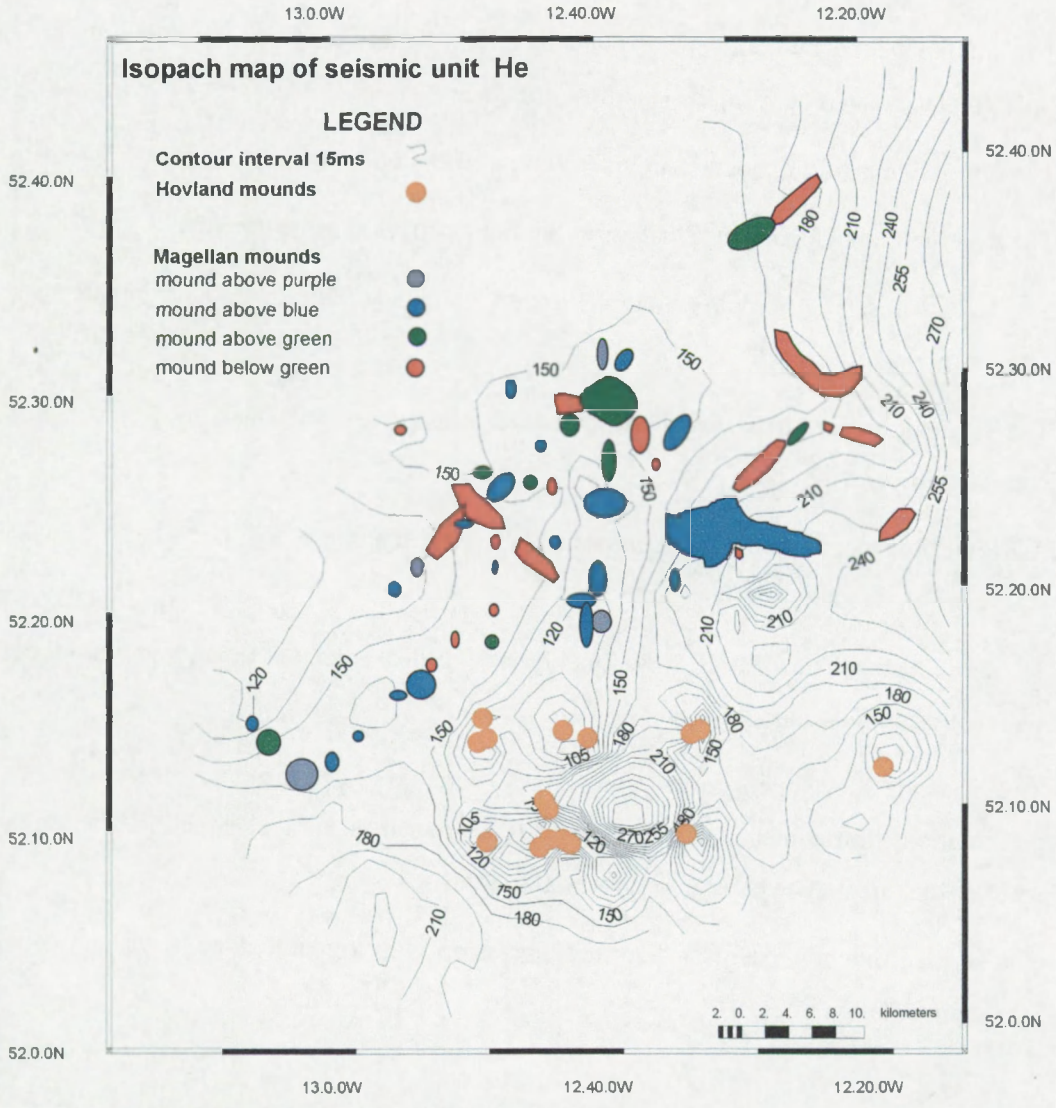

Fig. 5.25: Interval isochron map of unit He in ms TWT with the distribution of the Magellan mounds in relation to the highest marker horizon they reach.

- Buried Hovland mounds have a mean width of 460 m and a height of 74 ms TWT.
- The largest buried Hovland mounds appear in zones with reduced sedimentation and in greater depth than the average mound appearance.
- Surface mounds have a mean width of 1300 m and a height of 215 ms TWT.
- The tallest surface mounds appear around the current scoured depression around 700m water depth. The mounds become smaller in shallower en greater depths.
- The mound geometry follows the contour of the depression they are flanking. In isolated places the mound shape is almost circular.
- The upper flanks of the mounds are the steepest. The mounds are flat topped.
- The average flank slope is the steepest in the flanks covered by sediments.
- The largest observed complex mound (Propeller mound) seem to be amalgamate by smaller mounds.
- The vertical stocked-like Magellan mounds are numerous and small in comparison with the Hovland mounds.
- A NS current regime seems to be responsible for the shaping of the Magellan mounds (Huvenne et al., submitted).
- The buried Magellan mounds grow quickly in a vertical direction to keep-up with the sediment accumulation.
- The mounds developed largely in zones with low sedimentation rates, in a preferentially horizontal plane. The mounds accrete in a vertical direction, creating steep flanks in zones with high sedimentation rates.
- The surface mounds extents inside the depression with a gentle slope to places with low sedimentation rates.

5.3 Geological record

The geological record imaged on the high-resolution seismic profiles is limited to the sediments of upper Megasequence 2 in the seismostratigraphy of Mc Donnell (2001) (see 4.3). In agreement with the seismostratigraphic work of Mc Donnell (2001), the sediments have an estimated age of Miocene to recent. In the North Atlantic this period is generally characterized by drift deposition (Faugères et al., 1999; Faugères et al., 1993; Stoker, 1998; Stoker et al., 2002) as seen in the Belgica mound area (see 4.3.). Also in the Hovland-Magellan mound province, the sedimentary sequences in the deeper part show the characteristics of a drift deposition. Along the shallower eastern slope of the province, cut and infill depositions have been observed in local depressions (Fig. 5.26). The substratum is intensely eroded in this province, compared to the more southern part of the basin. In the northern part of the province (Magellan mounds) the erosion is less intense and a calmer sedimentary regime is induced. These observations argue for erosion concentrated on the eastern flank of the province and some local erosion in the central part of the province. In the upper sequences a typical drift sequence has been deposited approximately during the period of the mound development.

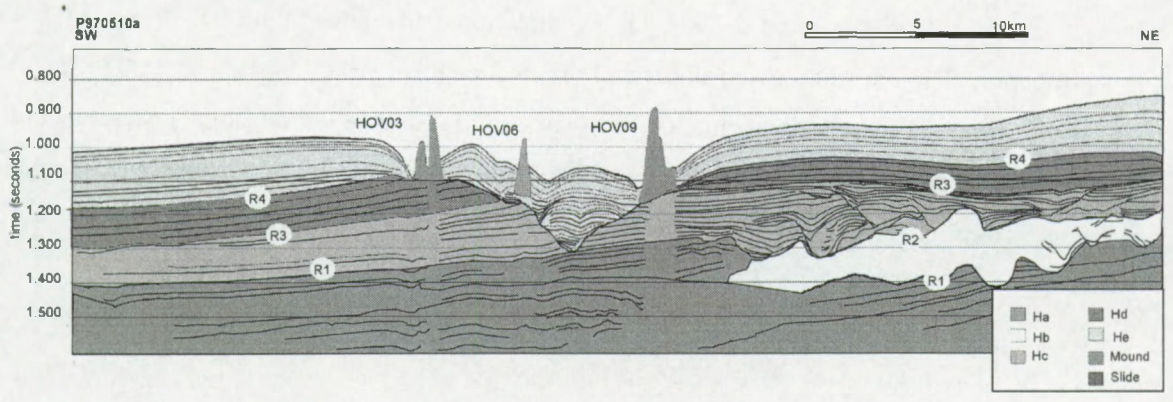

Fig. 5.26: Interpretation of the high-resolution seismic profile P970510a in the Hovland mound province. In the eastern part of the province the erosion was more intensive and high-energy infill argues for higher current regimes than in the western part of the province.

These geological sequences have been analyzed in order to find a relation between the substratum and the mounds and to estimate the environmental changes between the conditions before the mound initiation and during the mound evolution. Many geological features have been recognized in this area as possible pockmarks, erosional features, moats, faults and slumps in relation to the mounds.

5.3.1 Unconformities

In total five different seismic facies have been recognized on the high-resolution seismic profiles. The facies of the Hovland-Magellan mound province have been indicated with an H and from the base to the top with a, b, c, d, e. In addition, the seismic characteristics of a slide inside Hc and of the mounds have been indicated by separate symbols.

The bounding reflectors of the facies have been indicated with a letter on the seismic profiles (Fig. 5.26). An overview of several profiles crossing the mounds is presented in appendix E. A short description of each bounding unconformity is given:

- The high-amplitude unconformity **R1** truncates the lowermost high amplitude reflectors (Ha) seen on the profiles. This reflector is clearly observed in the eastern shallowest part of the province and to the north in the Magellan province (Appendix E, P980528, P970505 P970510a, P970512, P980533-43). The erosive surface is irregular and dips to the west and to the south (Fig. 5.27). In the eastern part of the province this erosional event forms a large incision with a steep flank in the north of the depression, in addition to incisions and gullies in the underlying facies Ha (Fig. 5.27). The incision on the lower eastern slope has a dimension of minimum 30 km in NS direction and a maximum of 15 km in EW direction. The incision is well illustrated on profiles P970510a, P980533 and P980528. A time structural map has been made of this surface to illustrate the erosional character (Fig. 5.27.). In the age model of Mc Donnell (2001) this reflector corresponds to erosional unconformity C20, of Mid Miocene age.

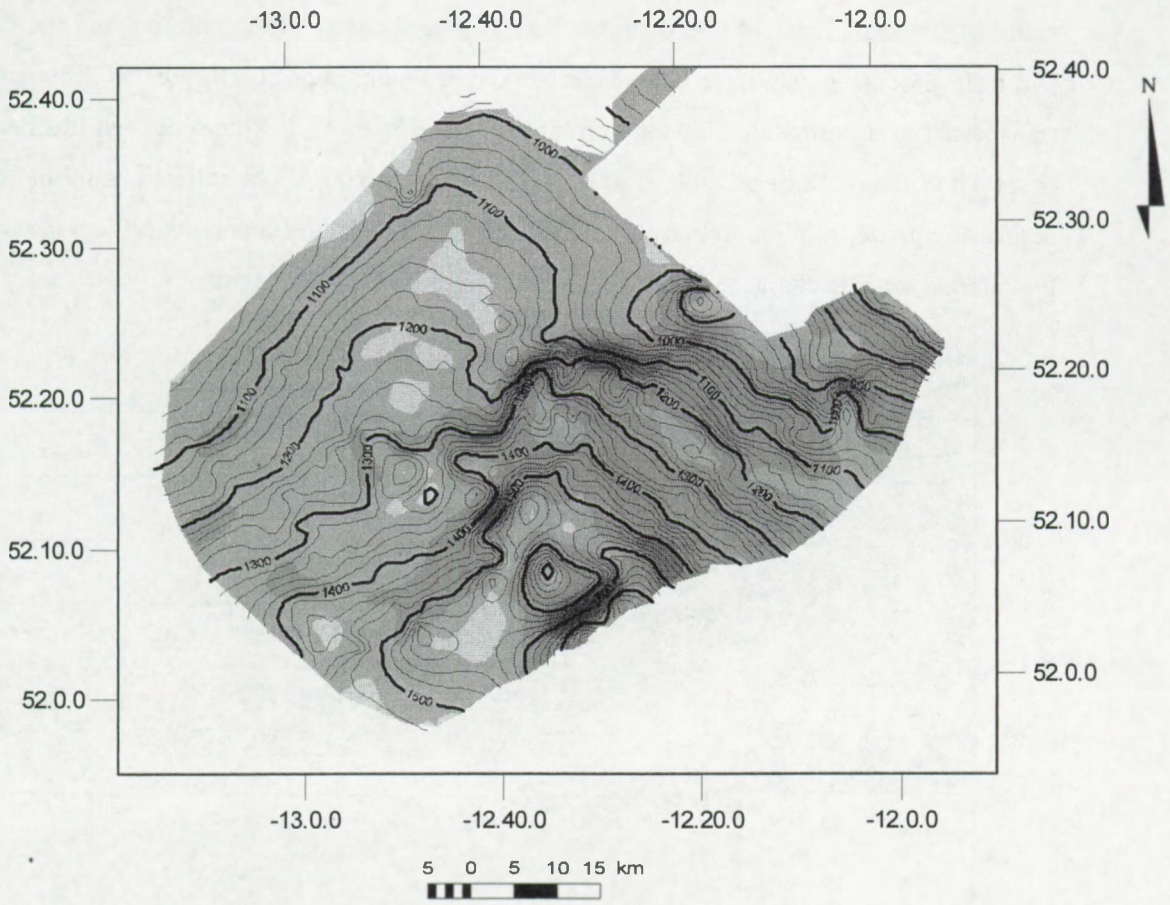

Fig. 5.27 Time structural map in TWT (seconds) of the R1 reflector as indicated in appendix E. The grey shading represents the dip of the gridded surface of R1. This map shows the steep slope in the east and in the north, and the formation of an incision along the eastern margin.

The incised valley could not be traced in the northern part of the province and stops abruptly halfway to the north (Fig. 5.27, 5.29). This excludes a generation of the incision from shelf valleys. It seems that during the formation of the depression the current regime was erosive in the deeper part of the province and calmer on the shelf. These channels have similar morphological characteristic to channels formed in the sediment drift on the Gabon continental margin by upslope prograding currents (upwelling) (Séranne and Nzé Abeigne, 1999). The morphological structures can be explained by an upslope current along the eastern slope, prograding upslope (Fig. 5.27). The sediments in this context might essentially be contourites (Mc Donnell, 2001).

Henriet et al. (2001) suggest gravitational processes such as slides for the formation of the depression. The steep slopes bounding the channel in the north can be interpreted as a slide scar with a length of approximately 20 km, and 200 m high (Fig. 5.26, Fig. 5.27). This slide may have transported the sediment in a downslope direction and deposited to the

south of the scar. Later on the depression may have focused strong currents and the cut and infill processes may have built the reworked sediment deposits from basin sediments transported in a northward flowing current regime. However, no slump deposit has been observed to the south of possible slide scar (Mc Donnell, 2001). The reflections filling the depression grade from hummocky, discontinuous events to flat, subparallel reflections and the internal seismic character is too consistent to represent mass failure.

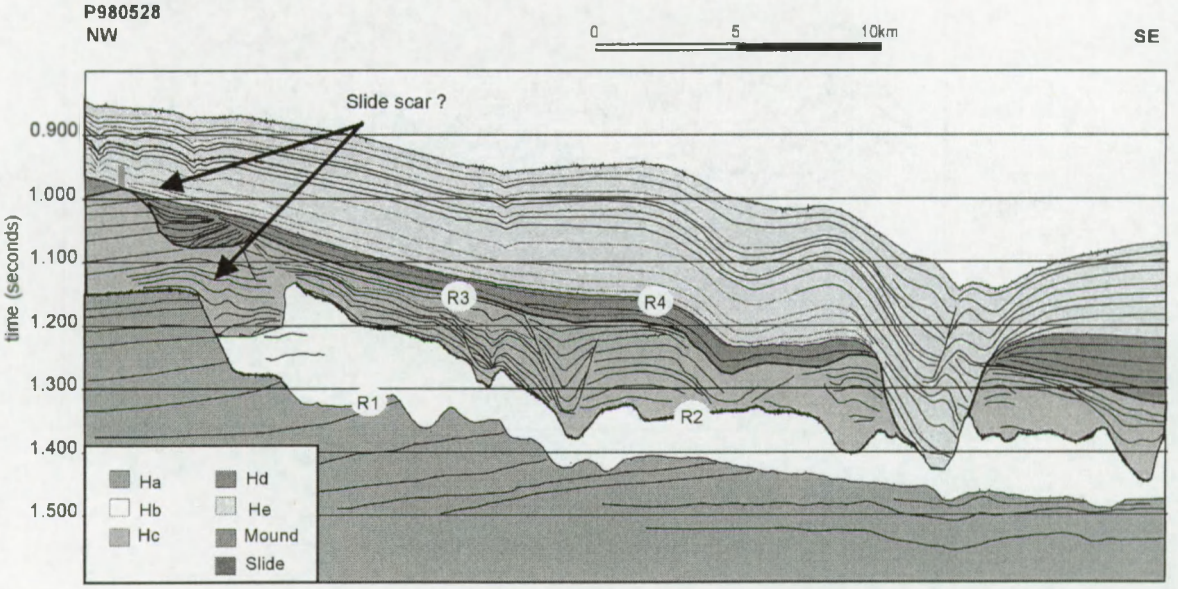

Fig. 5.28: Interpretation of high-resolution seismic profile P980528. This profile illustrates the strong erosional effect in the eastern part of the province. The slope breaks on the NW side of the profile might be interpreted as slide scars or channel walls of upslope prograding contourite currents.

- **R2** has an irregular erosive character in the eastern part of the province. The reflector forms incised gullies in the facies Hb. More to the central part of the province, the reflector dips to the west. This unconformity was difficult to map on base of amplitudes and has been mapped on the phase attribute profiles. The reflector is the upper boundary of Hb and lower boundary of Hc. The extension of the reflector illustrates the location of Hb and is limited to the eastern part of the province.

- Unconformity **R3** is the upper boundary of facies Hc. This reflector is characterized by a high amplitude. R3 has an erosive character in the eastern part of the province, forming incisions in the underlying facies Hb and Hc (Fig. 5.26 and 5.28). The facies above R3 (Hd and He) and below this unconformity (Ha, Hb, Hc) are different in seismic response. The lower lying facies shows a hummocky, wavy or cut and infill configuration. Above

R3 the facies has a more parallel to subparallel configuration, with only local cut and infill around a central depression. In the eastern part the R3 surface has a steep flank parallel to the steep erosional surface of R1. A time structural map of R3 (Fig. 5.29) illustrates the NS trending depression with a steep flank in the north and on the eastern flank. This depression shows two branches: one in the very east and one more central on the map. Profiles P980528 and P970527 (appendix E) illustrate the deposits in the depression. A second depression has been mapped in the south of the central Hovland mounds. In general, the distribution of the buried mounds is limited by the steep slope of reflector R3 in the south. In analogy to R1, this depression is interpreted as the results of scouring by contour currents on the eastern flank of the province.

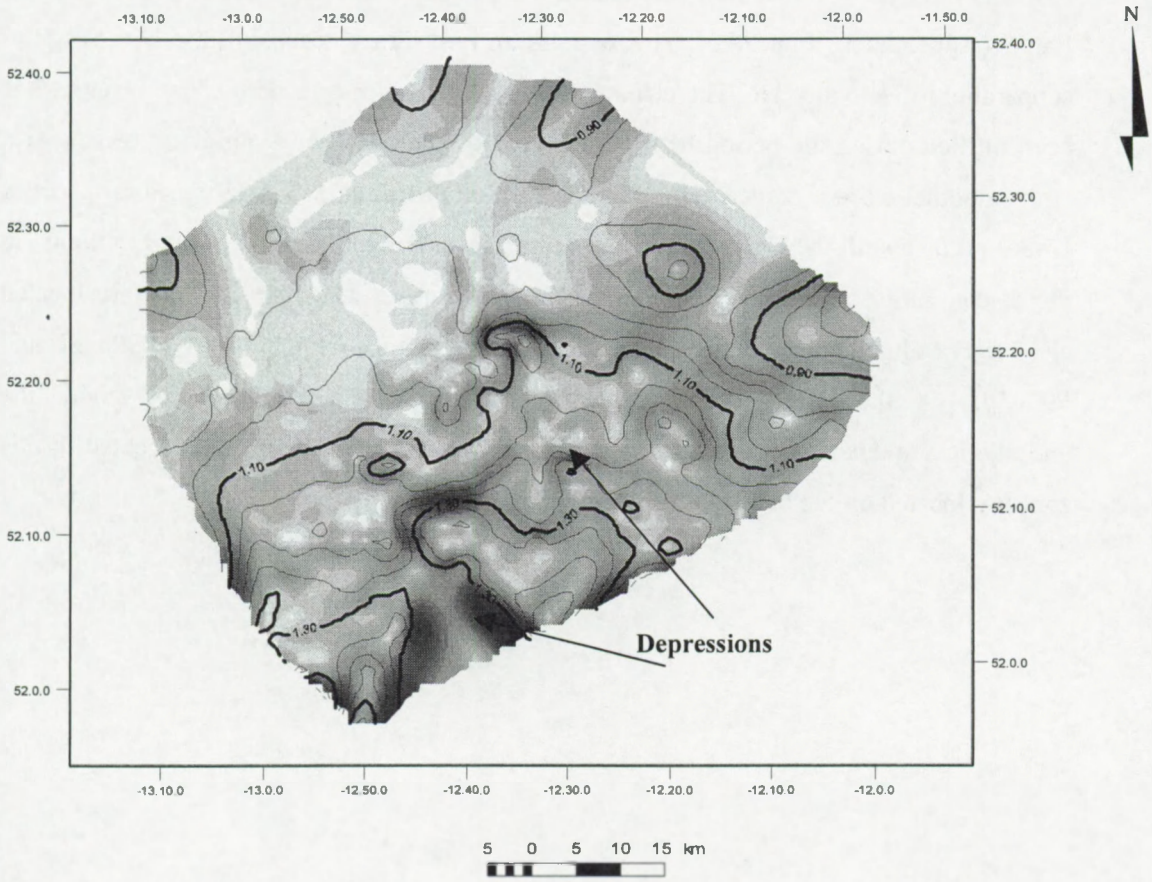

Fig. 5.29: Time structural map in TWT (seconds) of R3. The greyscale indicates the dip angle of the surface. This illustrates steep flanks in the north and the west formed by channels.

- **R4** is the last regional erosive event in the province. The Hovland and Magellan mounds root on this unconformity. The reflector R4 is marked by a high-amplitude reflection of variable continuity, with above reflectors onlapping to the north. It truncates underlying reflectors of Hd, which argues for its erosional character. This unconformity cuts a deep incision in the underlying facies in the central part of the province (Fig. 5.26). This created a depression of 12-18 km in width, with steep flanks to the north, the west and the east (Appendix E, P970502c, P970510a, P970512, P970527). To the south the depression slightly fades out. The depth of the depression is about 100 ms compared to the surrounding trend of the surface. The depression is deepest below the NS to NW-SE channel-like depressions (Appendix D.2, see 5.1) in the present-day topography. The Hovland mounds in the central part cluster around this depression and are located at the flanks (Appendix E, Fig. 5.29). This depression has been cut and infilled with wavy to subparallel reflectors of He. The channel observed on the eastern part of the province has been infilled during the period between R3 and R4 and has only a minor expression left, with smoother slopes. A local depression is seen on profile P980528 to the eastern part, it erodes all facies till the Ha. To the north in the Magellan mound province and to the west, the discontinuity shows no erosive character. The largest Magellan mounds are located also near a slight break in the slope as seen in appendix F on profiles P970524c and P970505. On the eastern flank of the province the mound base reflector eroded the underlying sequences till facies Ha on the upper most slope. The mounds located in this zone are located on the breaks of the slope (Fig. 5.30).

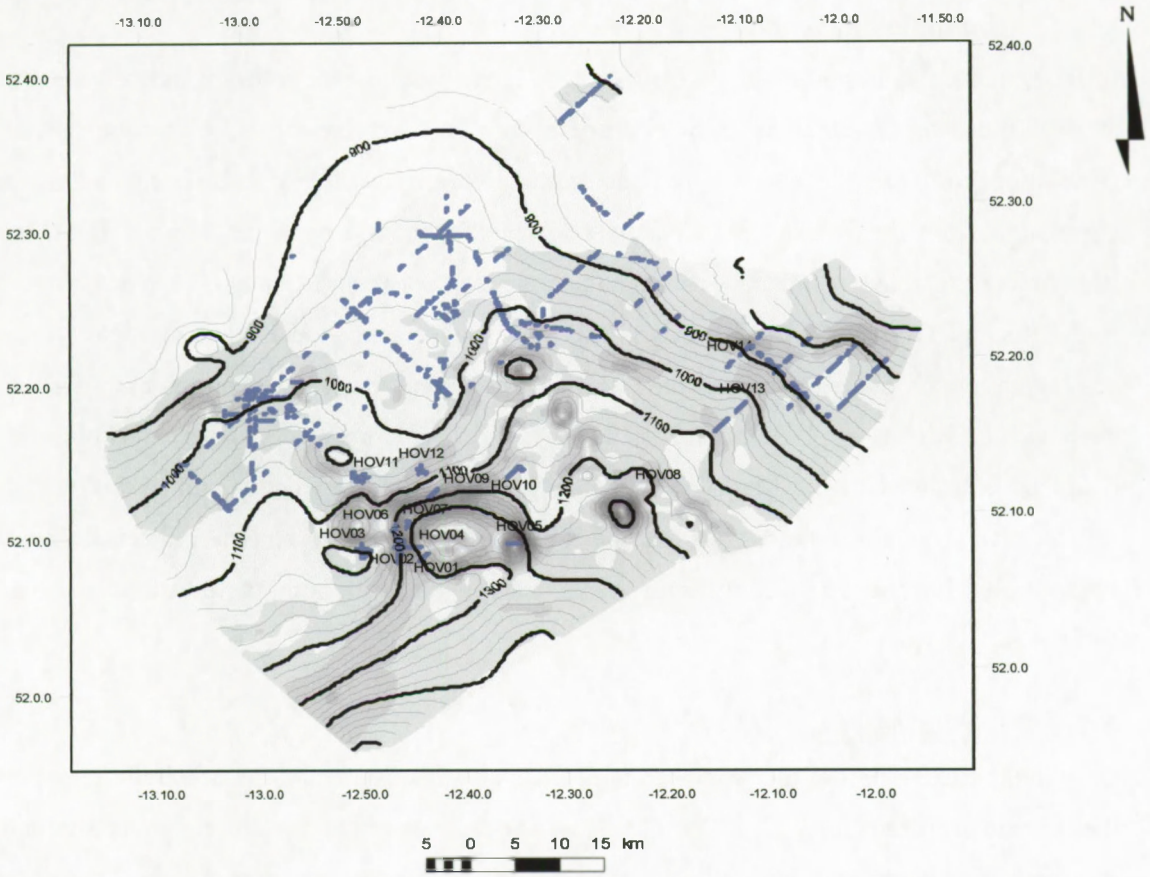

Fig. 5.30: Time structural map of reflector R4, mound base in TWT (seconds). The greyscale represents the dip angle calculated on the grid. The dark zone illustrates steep flanks in the surface. A central and eastern depression has been observed. The mounds are located around the depressions.

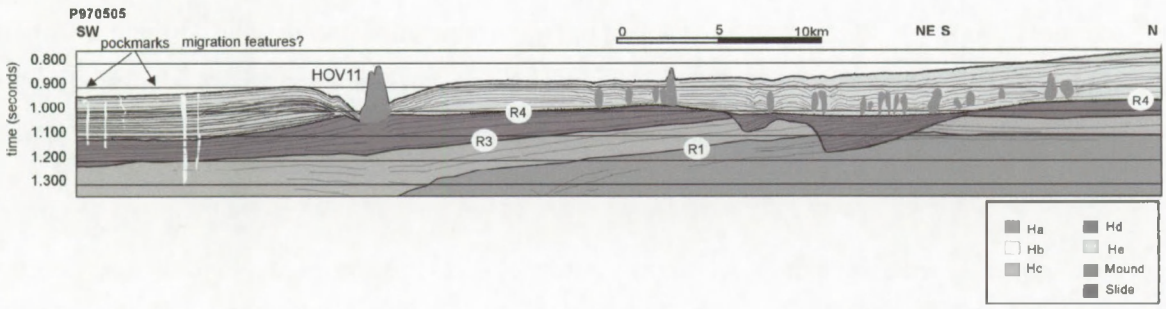

Fig. 5.31: Interpretation of high-resolution seismic profile P970505. The largest mounds appear on the slope breaks of reflector R4.

Dating of the mound base

In the sequence stratigraphy of Mc Donnell (2001) the mound base reflector has been identified as C10 and dated as an Intra Early Pliocene event. This was based on facies comparison and correlation with seismic data of the last erosional event in the Rockall Trough. The facies correlation from the Rockall to the Hovland-Magellan mound province mounds is not clear. Many more erosional events appear in the upper section between C20 and C10, much more than in the Rockall Trough. On the other hand two industrial seismic studies have been carried out in the region, which place the mound base at a near quaternary age, based on the extrapolation of deep wells (Britsurvey, 1997; Games, 2001). The reflector mapped on these seismic surveys could be correlated to the Magellan mound province and fits perfectly with the mound base reflector R4. This allows to suggest that the R4 event took place in the Late Pliocene rather than in the Early Pliocene. The C20 reflector seems in agreement with both interpretations to be at the level of R1.

5.3.1.2 Facies Ha

Only in the eastern part of the province facies Ha is clearly observed in the penetration window of the seismic profiles (Fig. 5.31, 5.32). The facies is characterized by parallel rhythmic alternations of continuous high and low amplitude reflections. Towards the eastern slope the internal reflectors are pinching out. The internal reflections are parallel to subparallel and show a break in their dip in the orientation seen on profiles P980533-43 P970510a, P980528 (Fig. 5.26, Fig. 5.31 and Fig. 5.32). These reflections show an aggradational trend. Facies Ha can be interpreted as a basinward stepping advance of the successive units of sediments prograding on the eastern and northern slope (P980528 and P980533-43). The progradation trend is in northern and eastern direction (Mc Donnell, 2001). This progradation can be explained by an alongslope current flowing from the south along the eastern slope. The current eroded older sediments and deposited the reworked sediments along the northern flank.

The upper erosive boundary R1 shows a terrace-like erosion in a NS direction on profile P980528. The erosion was more intensive in the central and deeper parts of the province. Mc Donnell (2001) suggests an early Miocene age for the sequence but no well data is available for an exact dating. The facies is mapped based on the upper reflector R1 and presented in figure 5.27.

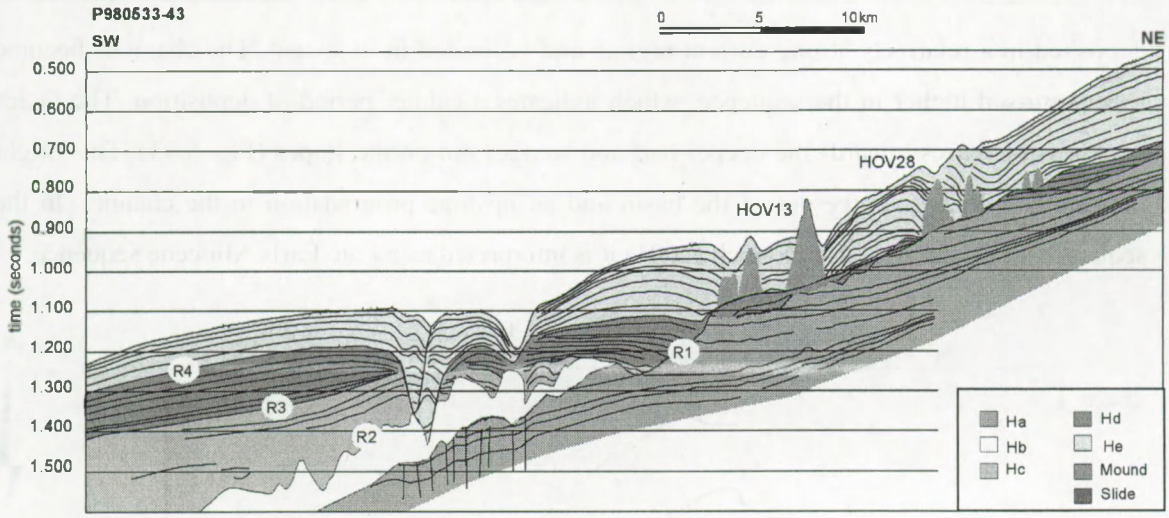

Fig. 5.32: Interpretation of high-resolution seismic profile P980533-43. This profile illustrates the occurrences of buried mounds on the eastern slope of the Hovland mound province. The erosion of R1 was focalized near the slope break and in a later phase has been continuously eroded till the present day by along slope currents

5.3.1.3 Facies Hb

Facies Hb fills the incisions formed by R1 on the eastern flank of the province and is on its turn eroded by R2. This facies is limited inside the NS depression along the eastern margin. Facies Hb is characterized by an almost transparent acoustic facies on the sparker profiles, with a few internal reflectors. The internal reflections have a cut and infill geometry, arguing for deposition during a strong current regime. The acoustic transparent character may indicate a chaotic infill and disordered depositions of coarse-grained sediments.

On the upper part of the eastern slope this facies has completely been eroded by R2 or later erosional events (Fig 5.32). The mapping of Hb has been performed by subtraction of the R2 and R1 grids. This isopach map has been plotted on top of the time structural map of R1 and the mound occurrences (Fig. 5.33). The facies is thinning to the flanks and thickening in the deepest parts of the depressions eroded by R1 (Fig 5.33, Fig 5.28). The upper boundary is truncated by R2 or R3 (Fig 5.26, Fig. 5.33). The facies ends abruptly on the eastern flank of the depression limited by R1 (Fig. 5.32). The upper boundary R2 is a high amplitude event onlapping on R1 and truncated by R3 with an angular unconformity.

The channels and gullies formed inside this facies show no preferential progradation which could be deduced from this data set (P980528, P980510a, P970512). The cut and fill channel deposits are comparable to the geometry and facies architecture of infills in fluvial systems or delta systems (Harris, 1994; Thomas and Anderson, 1994). This illustrates that the infill has been

deposited in a relatively strong current regime and is limited in its extent. The channels become less expressed higher in the sequence, which indicates a calmer period of deposition. The facies thickness increases towards the deeper part and wedges out on the slopes (Fig. 5.33). This might indicate a sediment source out of the basin and an upslope progradation in the channel. In the sequence stratigraphy of Mc Donnell (2001) it is interpreted as a Late Early Miocene sequence.

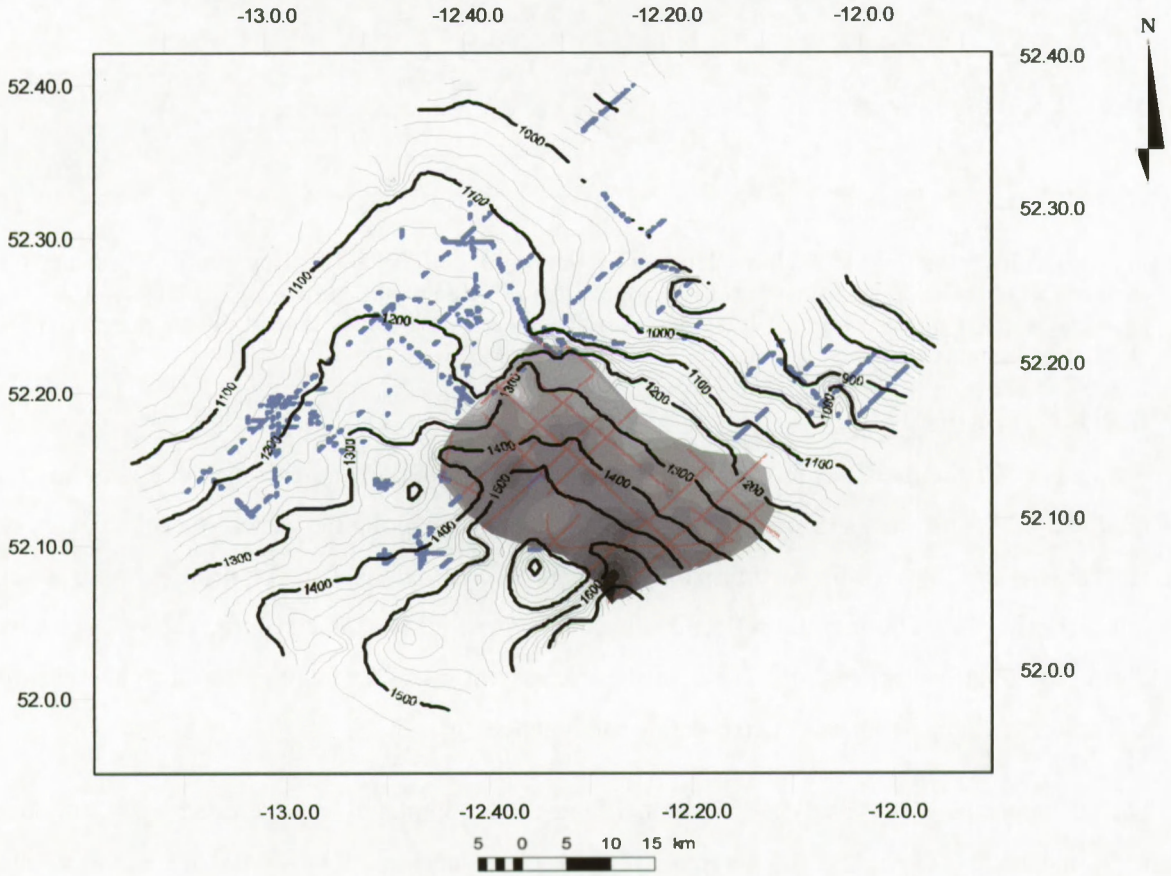

Fig. 5.33: Isopach map of facies Hb (greyscale, dark indicates thicker) plotted on the time structural map of R1. The facies extent on the seismic profiles is plotted in red and the mound occurrence in purple. Hb fills the depression created by R1. No mounds appear on top of Hb.

5.3.1.4 Facies Hc

Facies Hc fills topographic lows created by earlier margin progradation in the eastern part of the province (Fig 5.26, 5.28, 5.31, 5.32). Its lower boundary R2 was difficult to map because it shows no clear contrast between the facies Hb and Hc. The internal reflections of Hc have small scale hummocky configurations. More to the center these grade to concordant continuous parallel reflections with a high amplitude. Hc has a less chaotic infill than Hb. The cut and infill geometry

is restricted to the depression formed by R1 on the eastern margin (Fig. 5.31, Fig. 5.32). In this eastern part the facies has been truncated by R3 or R4 forming deep irregular incisions (Fig. 5.32, 5.33). The facies characteristics suggest a gradient transition from high energetic cut and infills (Hb) over less energetic cut and fill to wavy and subparallel reflectors in a calm regime (Hc). This might be related to a continuous sea level rise. The facies invades the depression and forms a parallel to subparallel deposition arguing for a calm marine environment. The facies thins toward the basin margin.

Stoker (1998) observed a similar facies in the Rockall Trough, with paleo-erosional gullies ranging from a few tens of meters to about 70 m in depth and 2-3 km width. These incisions are interpreted as paleo-scour zones formed by strong bottom currents. Internal reflections within the infilled gullies display typical lateral progradation, with both western and eastern infilled directions noted, arguing for an upslope prograding sequence. The author interpreted this facies as contourite fans inside a contourite channel. Contourite fans are characterized by channels and moats with an elongated mound or drift development primarily along one flank of the basin (Faugères et al., 1999). The seismic expression is often similar to submarine fan systems with chaotic to strong impenetrable reflectors in the channel or moat and parallel to wavy reflectors on the lèvee or mound. The contourite deposits migrate according to four principal factors: the flow direction, the Coriolis effect, the morphological context, and any interaction with other currents (Faugères et al., 1999).

This general description fits well with the facies Hb, Hc. First, the contourite deposits tend to migrate downstream. Second, the moats are located to the east implying a northward flowing current enhanced on the right. Furthermore, deposits are influenced by the morphological factors, as margin steepness and trend. The local morphology of the base reflector has initiated drift construction with lateral variation in the depositional environment. The eastern flank of the basin can be described as an overlapping or interdigitating fan/drift system. Mc Donnell (2001) interpreted this facies as a contourite deposit of Middle to Late Miocene age.

Slide

Inside facies Hc a chaotic acoustic facies has been encountered in the Magellan mound province. This facies ends abruptly laterally in the more stratified facies of Hc (P990524, P970514, P970524c, P99024, Fig 5.34). The upper boundary of this facies shows some irregular dipping reflectors and some minor faults (Appendix E).

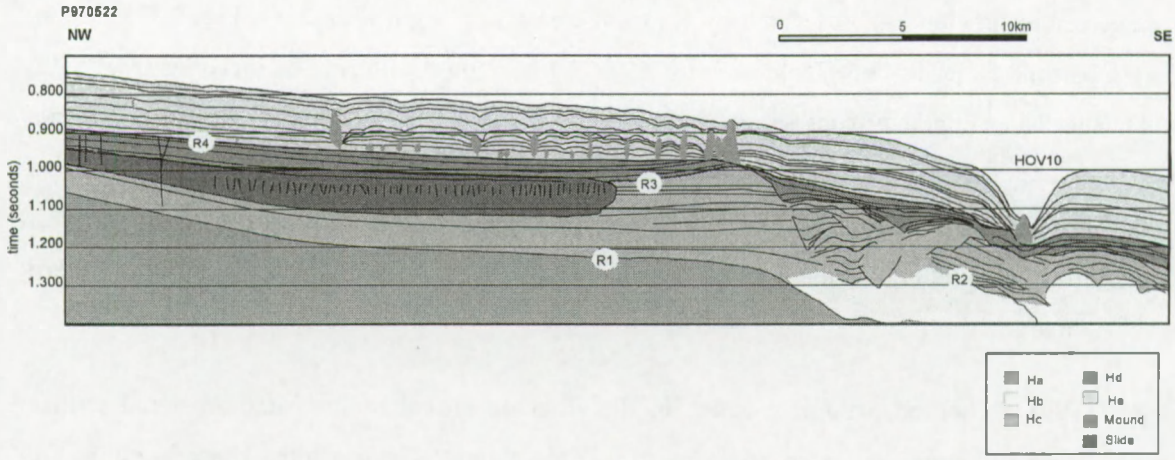

Fig. 5.34: The interpreted high-resolution seismic profile P970522 illustrates well the abrupt ending of a chaotic facies interpreted as slide. The facies is faulted. No convincing correlation is observed between the mounds and the slide facies.

The base reflector is a clear high amplitude continuous reflector, dipping to the S-SE with a normal slope gradient for this area, less than 1°. Both reflectors have been mapped and subtracted to create an isopach map (Fig. 5.35). The internal reflectors show small faulted blocks with internal reflectors in a chaotic mass. This facies ends abruptly at its thickest part (about 110 ms TWT) in the south and wedges out in the other directions. The facies covers an area of 1135 km^2, with a longest length in NE SW direction and a minimum width of 30 km (WNW-ESE). The northern edge is not observed on the 2D grid discussed in this thesis.

Further to the northwest, this facies has been mapped in a 3D seismic block (Huvenne et al., 2002). The facies wedges out upslope and ends in the north in a small scarp of maximum 25 m seen in the top reflector R2. This headwall extends over a min length of 19 km with a NE-SW strike. This facies is found about 30 km downslope of the headwall in the 3D block. This brings the overall length in combination with the 2D data to about 60km in a downslope direction and 60 km along the headwall orientation. Based on the geometry and facies characteristic this facies is interpreted as a slide (Huvenne et al., 2002). The estimated area of the slide is in total 3600 km^2.

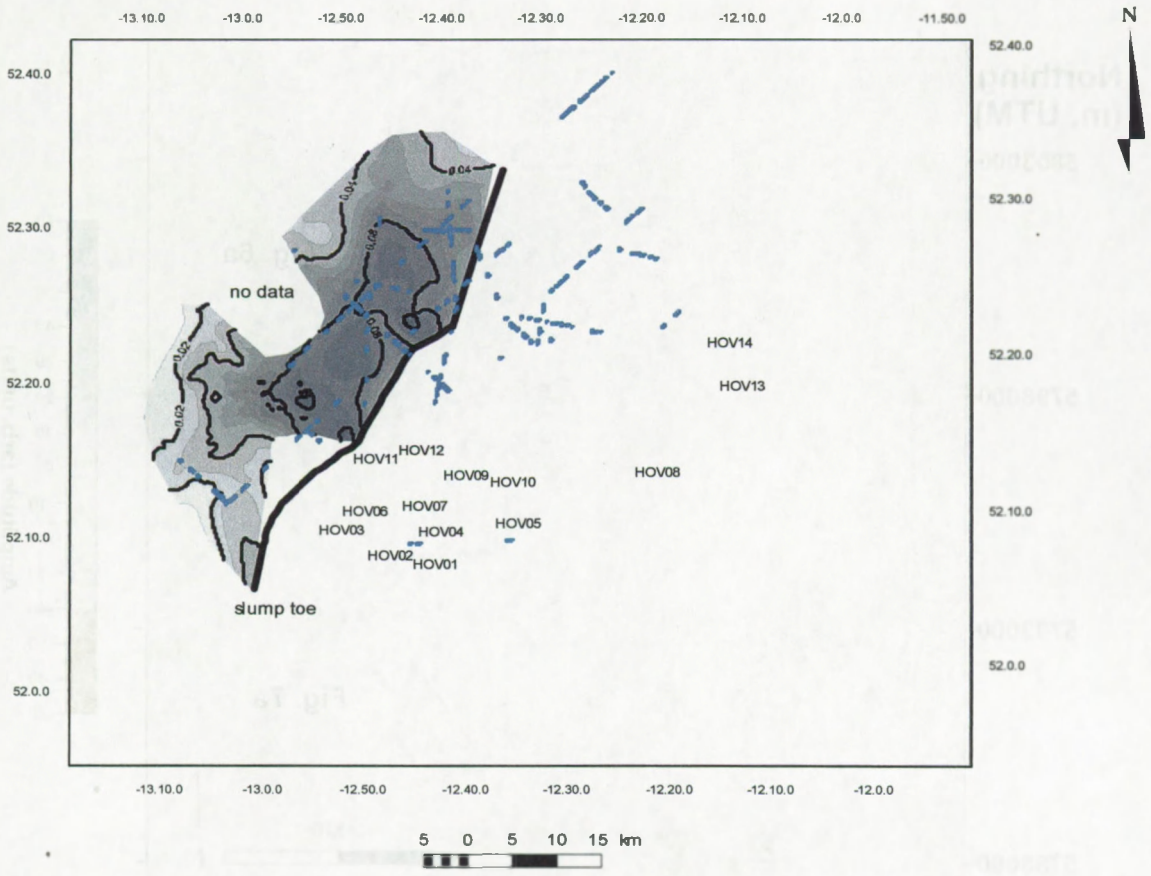

Fig. 5.35: Isopach map of the slump facies in Hc based on the Belgica surveys. The mounds are indicated in purple. The slump facies thickens to the slump toe. No correlation between the mounds and the slide facies is evident.

Inside the 3D data block an amplitude map of the upper boundary, shifted over 43 ms of this facies has been prepared. This map shows a blocky pattern, with blocks of an average diameter of 200 m (Fig. 5.36). The blocks are irregular in plan view and become more elongated near the toe. In the vertical dimensions the blocks have a trapezoid shape and did not loose their original stratification (P990524) (Huvenne et al., 2002). The structures show some compressional features at the southern extent of the facies (Huvenne et al., 2002).

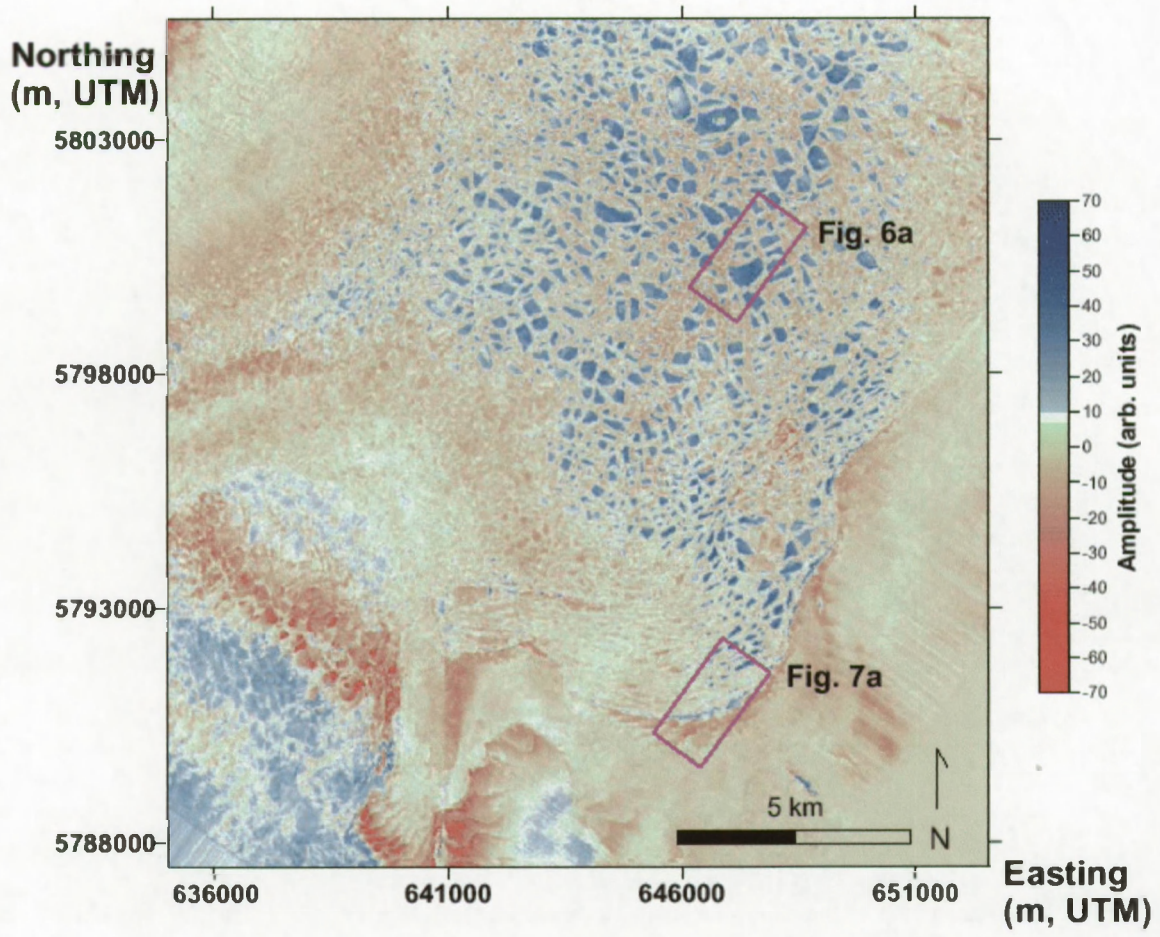

Fig. 5.36: Amplitude map of an artifical surface created by downward shifting of the top slide reflector R3 over 43 ms TWT. Detail showing toe and blocky part of the slope failure (Huvenne et al., 2002).

Huvenne et al. (2002) suggest that the well-stratified layers overlaid an overpressured weaker layer. Once the failure was triggered along the headwall scarp, the stratified layers broke apart by tension cracks causing the blocky pattern. The overpressure was released through the cracks by partial liquification of the weaker layers. A small downward flow probably occurred, which stopped rapidly. At the toe of the facies, the blocks piled up and got compressed, showing their elongated sides and building compressional ridges. Once the pressure dropped by the expulsion of the fluids along the tension cracks, the sediments became more consolidated and the shear strength increased, which slowed down the downward movement. The termination of the displacement of the sediment has probably been caused by a combination of the low slope angle and the increase in shear strength. The slide has been frozen in the initial phase of failure. No expulsion of fluids is seen in the later sediment depositions.

Henriet et al. (2001) suggest a possible triggering of the slope failure by the decay of gas hydrates during glacial and interglacial times. Mc Donnell (2001) dates this facies as Miocene. In such frame a glacially influenced hydrate destabilization event is not possible. Nevertheless, no evidence is found for any trigger mechanism of the slide.

5.3.1.5 *Facies Hd*

Facies Hd fills the erosional depression formed by R3 in the lower facies in the Magellan mound zone and eastern part of the Hovland province. The thickness of Hd increases in the center and thins to the eastern margin (Fig. 5.38). R4 is the upper boundary of facies Hd. The erosional event during R4 erodes Hd almost completely in the center part of the province (Fig. 5.38). The facies is characterized by an alternation of low to moderate amplitude subparallel reflections. The aggradational set thins to the eastern slope and to the north (Fig. 5.31, Fig. 5.38). Near the eastern flank the facies shows a cut and infill geometry, but less intensive than the previous facies. This suggests a decrease in current strength during the period of deposition of Hd in comparison with the previous period. The NS trend along the eastern margin, suggests again a north flowing current in a contourite drift system.

Other characteristics of drifts have been observed in local cut and infill in subunits. Internal channeling and scouring at the base of internal units highlight erosion alternating with deposition. Deposits are manifest in the onlapping reflections accreting upslope onto the eastern basin flank. The geometry of the sediment body implies a drift influenced by a SN current. The age of this facies is estimated to be Pliocene.

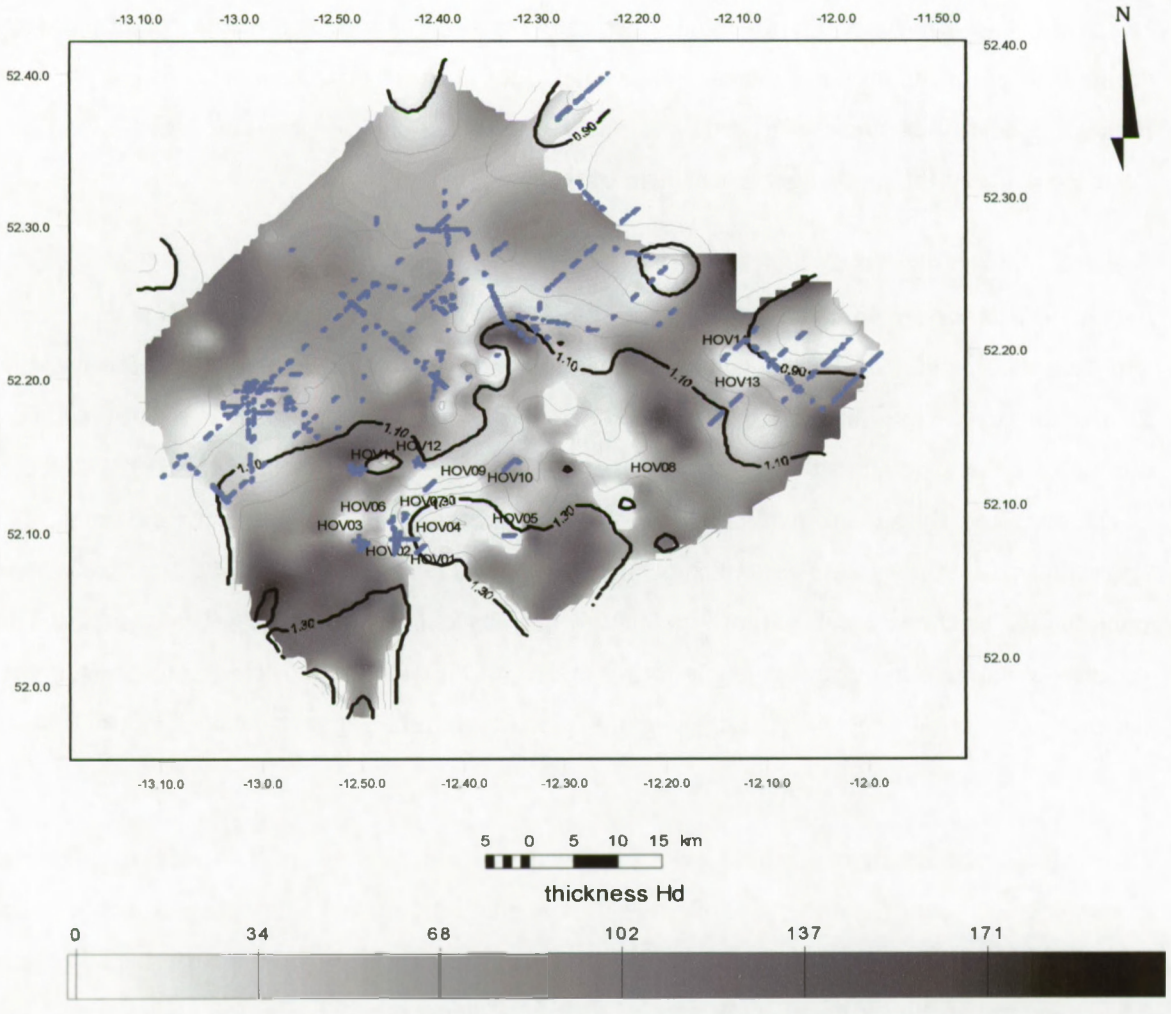

Fig. 5.38: Isopach map of Hd on top of its base boundary R3. Facies Hd fills the depressions formed by R3 and has been eroded in the central part by the erosion during R4. The map shows the erosion of R4 in light colours and the infill of the R3 erosional event in dark colours. The mound distribution appears in light colours, or in zones of erosion of R4.

5.3.1.6 Facies He

Facies He consists of high amplitude low frequency events of variable continuity. The reflection varies from parallel to subparallel configurations. In the central part of the Hovland mound province a local depression is eroded by R4, which is still visible in the bathymetry (see 5.1). This depression is infilled by sequences with parallel reflectors (Appendix E). On an isopach map between the seabed and R4, the depression with the infill is clearly seen as a depocenter (Fig. 5.38). The wavy character of the sediment package is seen as a local variation in the sediment thickness. The facies thickens to the east, towards the Irish continental shelf. The minimal thickness occurs in a 10 km wide zone stretching northwards from the Hovland mound cluster (Fig. 5.38). The fill in the center of the erosional incision creates a local depocenter. The mounds

are embedded in this facies. Near the mounds, the reflectors are convergent towards the mound and form an erosive moat. The moats are illustrated in the isopach map by lighter colours (white on the map).

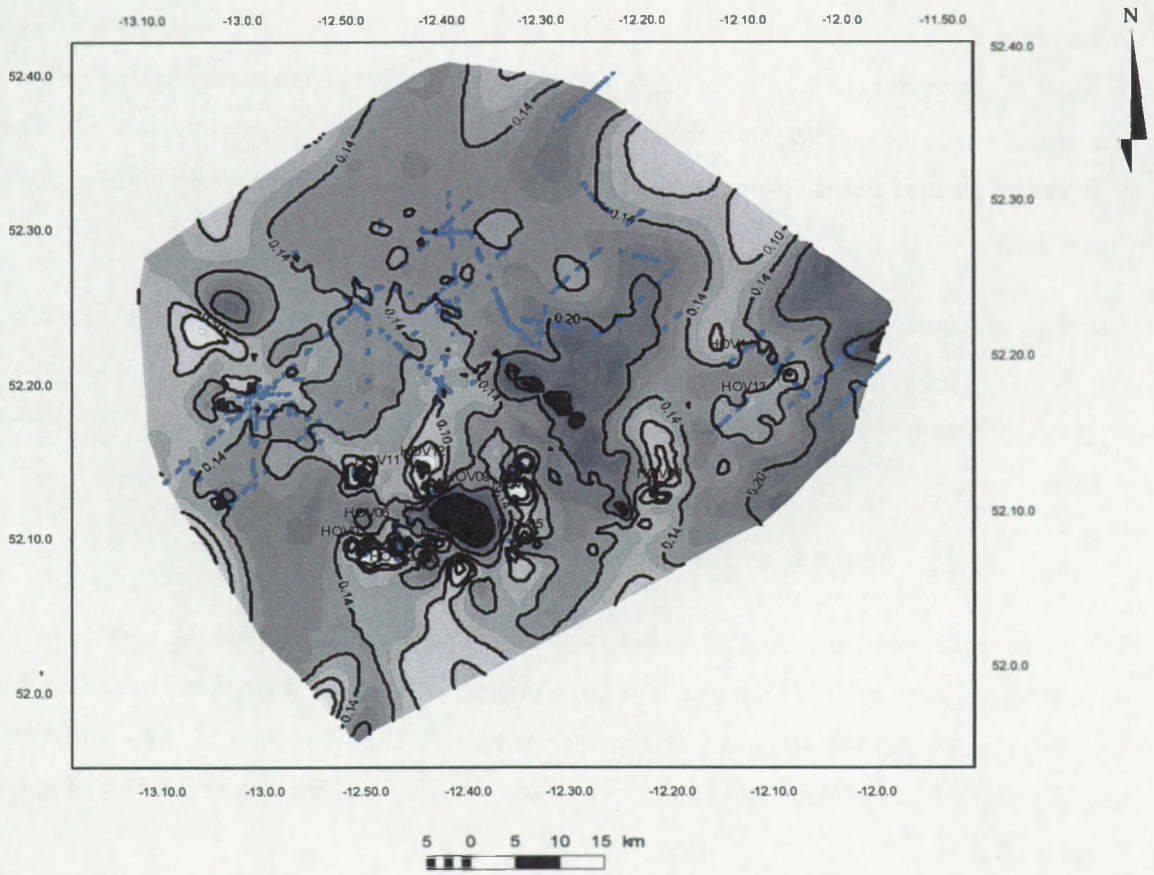

Fig. 5.38: Isopach map of facies He. Light colours indicate the reduced deposition zone of He. White indicates moat structures in the mound vicinity. A thin zone is trending NS suggesting SN currents. Local depocenters are seen in the depression eroded during the R4 event in the central part of the Hovland mound province.

The largest Hovland and Magellan mounds appear in zones with reduced sediment thickness. This infers that the mounds preferred sites with lower sedimentation rates during their development or that sediment stress limited the development of the mounds. The largest surface mounds appear on the flanks of the central depression or local smaller depression (Appendix E, Fig 5.26, 5.31, 5.32, 5.34). The largest Magellan mounds appear on local slope breaks or perturbations in the base reflector R4. In addition, the largest Magellan mounds are located in zones where the thickness of He is reduced. The deposits of He, clearly steered by bottom currents with a NS trend, are interpreted as drift of Quaternary age The alternation of high and

low amplitude reflection packages probably reflects the sediment response of glacial and interglacial cycles. This is not proven.

Moats in He

In the discussion of the general bathymetry it is already mentioned that some mounds are flanked by local depressions (see 5.2). Near most of the Magellan and Hovland mounds, the reflectors converge towards the mound and form a moat. This is observed on all sites of the mounds. These depressions are interpreted as moat structures formed by turbulence of scouring currents around the mounds.

The observed moats have no preferential orientation (P970505, P970514) on the seismic data. In the Magellan mound province the moats are apparently deepest between neighboring mounds. In some cases the moats merge to larger structures as seen on the isopach map of He for the Hovland mounds.

Moats of the Hovland mounds

The depth of the moats is measured on the seismic profiles in ms TWT from the normal seafloor trend to the deepest point in the moat. The large depression flanking the mounds (see 5.1) is not considered as a moat but as a channel. For each moat orientation in table 5.2 the median depth and maximum depth of the moat is listed in milliseconds TWT. These results are plotted in table D.1, Fig. D.3.9).

HOV10 has a deep moat on the northeastern flank. HOV12 and HOV07 have the deepest moat on the western flank. HOV06 has a moat on the eastern flank, which is connected to the moat of HOV07. HOV03 shows a moat on the southern and southeastern side but also on the northern flank. HOV11 shows only a clear depression on the southern part. HOV05 is surrounded on the southern, western and northern side by the depression and shows no clear moat structure. This illustrates the variation of the moats, related to the location of the mound.

The maximum depth of the moats is generally observed on the western and eastern flank. These moats are related to the depressions flanking the mounds, which focalized currents. The measured depths of the mound on the northern and southern flanks are almost equal.

The moats on the southern flank of the mounds are slightly deeper than the northern, but no significant difference is observed. The only observed relation is that the highest mounds are

related to the deepest moats (Fig. D.3.9). For the buried Hovland mounds the moats are less deep, which suggests a less strong current activity in the region (Table 5.2)

Orientation	SM			BM		
	Number	Median	Maximum	Number	Median	Maximum
W	4	146	240		/	/
NW	5	108	130	1	5	5
NNW	2	54	80		/	/
N	3	82	90		/	/
NE	7	85	140	2		
E	2	170	270			
SE	5	103	150	1	23	23
S	3	89	100	/	/	/
SSE	2	14	20	/	/	/
SW	7	64	110	8	18	40

Table 5.2: Moat depth listed in relation to their orientation, for surface and buried mounds.

Moats occur on all sides of the mounds but they are not always symmetrical. The seismic profiles document in most cases large differences in depth, onset of erosion and timing of maximum activity in moats on different sides of the mounds. However, no clear trend can be identified. Such differences may indicate variations in the current pattern but also migration of moats in time, possibly in pace with the development of the mound.

Moats of the Magellan mounds

Magellan mounds are often associated with moats, similar but smaller than those in the Hovland province. Typical moats have a depth up to 40 ms TWT referred to the normal paleoseafloor depth. The infill of the moats indicates differences in timing, magnitude and duration of erosion on opposite sides of a mound. Although most moats and mounds are buried, sometimes the morphology is reflected at the present-day seafloor (Appendix E, e.g. P970505).

The average moat depth observed in the 2D grid is 30 ms TWT. In the 3D block an average depth of 40ms has been observed (Huvenne et al., submitted). The moat analysis has been performed on the 3D picked isopach map between a mound shaped reflector and the mound base (see 5.2.). A high variability in the moat depths has been deduced from the 2D and 3D data set. The area of the individual moats is on average an order of magnitude larger than the mounds, partly due to the fact that some of them have blended into large moats. The moats are elongated in a NS direction

like the mounds (see 5.2). The elongation ratio of the mounds is 1.44 and for the moats 2.30 in NS direction. This suggests a strong NS directed influence in a rather flat area (Huvenne et al., submitted)

In the early phase of deposition of He the moats have been created around the mounds by turbulence in the current flow. The close spacing of the mounds enhanced the turbulence between the mounds and formed larger and deeper moats. In less vigorous current periods the moats have been infilled. The degree of infill of the moats depends on the amount of the available sediment and on the strength of the scouring current. This results in asymmetric moat infills. At some period the moat erosion has been reactivated on all flanks but finally they all have been filled with sediments. Once the moats are completely filled, the sediment onlaps the mound structures. In a final evolutional step, the He sediment has draped the mound structures in the Magellan mound province.

5.3.1.7 Mound facies

The mound facies is characterized by an acoustic transparency without internal reflections, similar to the facies discussed for the Belgica mounds. This suggests a homogeneous composition of the mound without internal stratification. No clear velocity pull-ups are seen underneath the mounds on the high-resolution data. Velocity pull-ups measured on profiles presented in Hovland et al (1994) have values of 50-60 ms underneath a mound of 250 ms (HOV03). The only velocity pull-ups have been observed on the high-resolution profile P970502c for mound HOV02 and HOV03.

The time of the pull-up or the time between the actual time of arrival and the supposed time of arrival is symbolized by Tp. The time that the sonic wave travels through the mound is Tm, which is measured from the base till the top of the mound. This top of the mound is used as reference level for the other time measurements. The travel time till the seafloor is the time required by the sonic ray to travel through the water column, Tw. The sediment column is symbolized by Ts. The internal sonic velocity of respectively the mound, the water column and water is represented by Vm, Vs and Vw. The ratio of the average velocity inside the mound and outside the mound is given by:

$$V_m = \left(\frac{T_w V_w + T_s V_s}{T_w + T_s - T_p} \right)$$

The velocity of the surrounding sediments is estimated to be 1600 m/s, which is a common velocity for shallow fine-grained deep-sea mud alternated with more sandy sediments. With these factors the velocity of the mound facies can be calculated.

For HOV03 a velocity pull-up of 20 ms on a total height of 278 ms is measured. The surrounding water column is 100 ms and the sediment cover is 67 ms thick. This results in an internal velocity of 1700 m/s. On the industrial seismics a velocity pull-up of 60 ms is observed for a mound height of 220 ms besides a water column of 150 ms and sediment cover of 70 ms. This results in an internal velocity of 2100 m/s. Hovland et al. (1994) did the same calculation and found a velocity of 2035 m/s without taking the water column into account. This is in contrast with the result of the high-resolution seismic profile. It must be noted that these calculations are performed on migrated industrial seismic profiles. For HOV02 a velocity pull-up of 21 m is observed for a mound facies of 174ms, which corresponds with a water column of 124 ms and 52 ms sediments. The internal velocity is 1760 m/s.

No clear pull-ups are seen under the Magellan mounds, which suggest that the velocity in the mounds is approximately the same as in the surrounding sediment. Estimation is made using the average sound velocity in the sediments of 1800 m/s (average value for mud and sand in a medium compaction), which is also the internal velocity of the mounds. This fits with the internal velocity estimation of the Belgica mounds and the Hovland mounds on the high-resolution seismic.

5.3.2 Mound / facies relation

The mound distribution is plotted on top of the slide facies inside Hc (Fig. 5.35). No relation has been observed between the slide deposition and the location of the mounds. A large part of the Magellan mounds is located on top of the slide but not the entire province (e.g. P970522, P990524, P8970505).

The other, not province-wide facies is the cut and infill of facies Hb and Hc (Fig. 5.33, Fig. 5.38). This shows clearly a negative relation with the mounds. No mounds are seen on top of the cut and infill facies.

The only observed relation is that the Hovland mounds appear at enhanced slope gradients on the flank of the depression (darker colours) on the R4 time structural map (Fig. 5.26, Fig. 5.31, Fig.

5.30). The eastern Hovland mounds appear also on relative steep slopes on the flank of the NS gully, but they were limited in their extension due to the sediment pressure (Fig 5.32).

The Magellan mounds appear in a relative flat zone and the highest mounds are located on local heights, with enhanced erosional slopes of R4 (Fig. 5.31, 5.34, Appendix E). The largest mounds appear in zones with the thinnest sediment cover of He, illustrating the preferential site of reduced sedimentation during the mound development.

5.3.3 Mound / faults relation

Hovland et al. (1994) suggested a close relation between faults and the appearance of the mounds. On some of the profiles presented in this work apparently faults have been observed in the reflections under the mounds (Fig. 5.39). The mound structures however occult the underlying reflection at some stage. In the lower part the reflections bend upward at the edge of the disturbance of the mounds and are interpreted as faults. Nevertheless, faults are difficult to distinguish from migration artefacts created by the elevated structures with a higher internal velocity. These structures are not taken into account during the migration of the seismic profiles and forming a artificial bending in the reflectors.

Only one faults presented in the paper of Hovland et al. (1994) could be found in the high-resolution seismic profiles. The other faults presented by Hovland et al. (1994) are interpreted in this work as processing artefacts. On the high resolution seismic one fault has been observed near mound HOV03 on profile P970527, which is also reported by Hovland et al. (1994) and McCann et al. (1995) (Fig. 5.39, Fig. 5.42, P970527). At least no clear relation is seen between faults in the subsurface and the mounds.

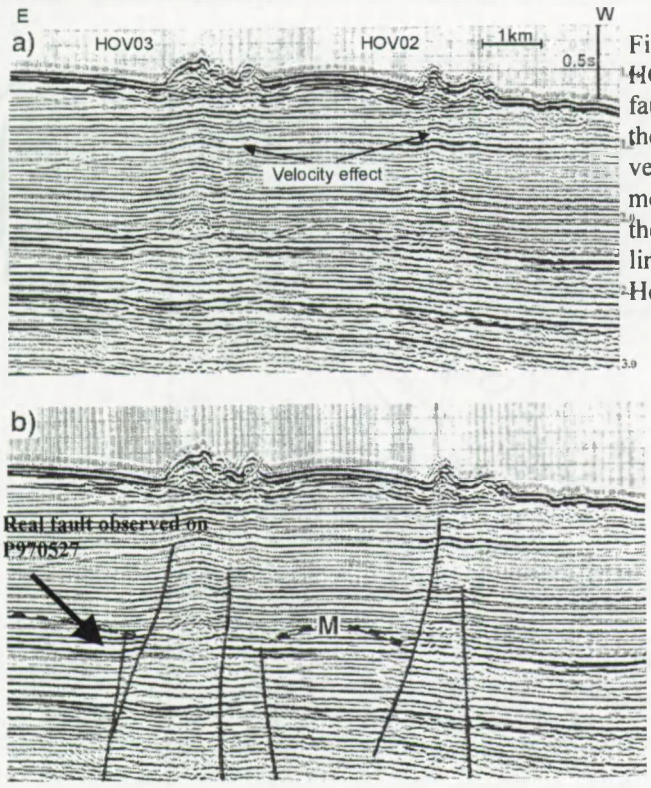

Fig. 5.39: a) EW industrial profile of mound HOV03 and HOV02 b) Interpretation of faults by Hovland et al. (1994). Compared to the surrounding sediment, these faults are a velocity effect due to the higher internal mound velocity. The faults perfectly bound the velocity effects. This line is parallel with line P970527 (Appendix E) (modified after Hovland et al., 1994).

To show the relation between the deeper fault structures and the mounds, the faults have been digitized from the paper of McCann et al (1995a and b) and plotted together with the mound elongation near the faults. Most of the large faults do not extend to the seafloor and show no clear indications so far for vertical fluid migration pathways neither on industrial seismic data nor on the interpreted high-resolution seismic data. In figure 5.15, the orientation of the coral banks has been plotted for each province against the strike of deeper lying faults, as compiled by McCann et al. (1995a) and McCann et al. (1995b). Additionally, a map has been made of all available data on faults in Oligocene and Miocene sequences and mounds. This illustrates that no clear evidence is seen in the fault-mound relationship (Fig 5.41).

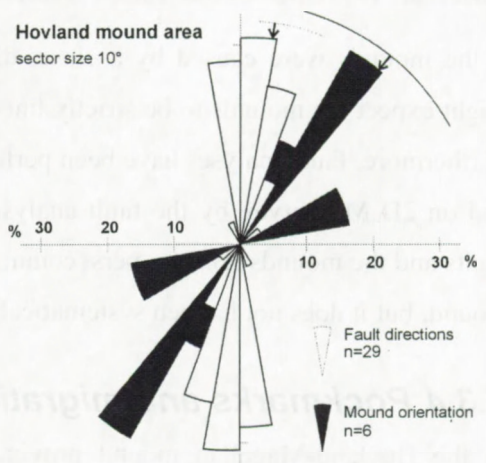

Fig. 5.40: Rose diagram of the orientation of elongated mounds and strike of deeper faults in the Hovland mound province.

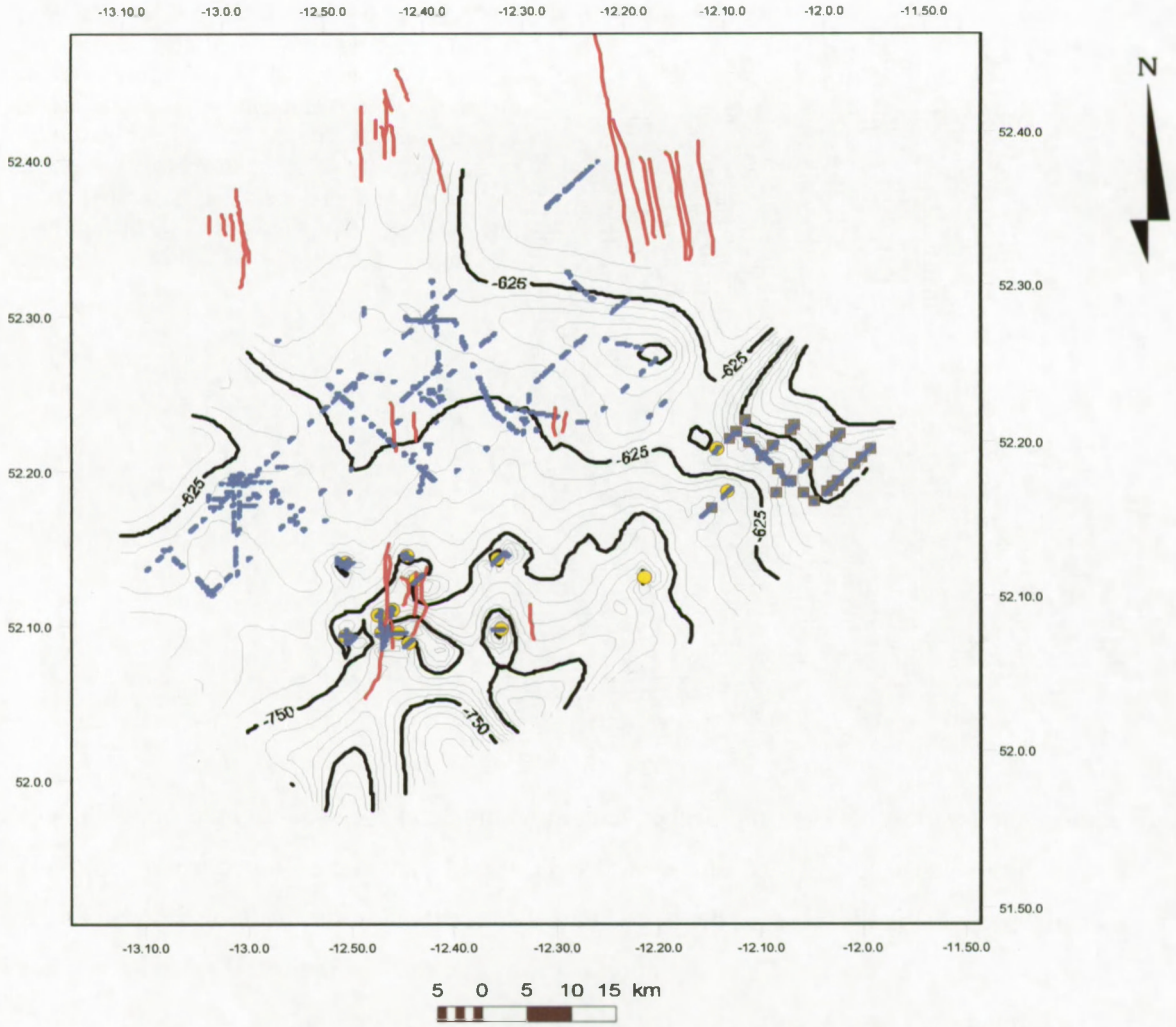

Fig. 5.41: Oligocene and Miocene faults (red) distribution in the Hovland-Magellan mound province (Mc Cann et al., 1995). No obvious relation is observed between the mound and the fault distribution.

If the mounds were caused by a close, direct link with hydrocarbon seepage along faults, we might expect the mounds to be strictly lined up along the faults, which is apparently not the case. Furthermore, fault analyses have been performed on the 3D seismic block in the Magellan mound and on 2D MS-survey by the fault analysis group of UCD and no relation is seen between the faults and the mounds (Bailey, pers. comm.). This does not exclude that some faults appear near a mound, but it does not happen systematically.

5.3.4 Pockmarks and migration structures

In the Hovland-Magellan mound province 16 pockmarks have been observed on the high-resolution seismic profiles and sidescan sonar data (Fig. 5.23). They appear as depressions and show some enhancement of amplitudes below (Fig. 5.42). This is probably due to the focalization

of the side diffractions. The enhanced amplitudes occur typically around 10-20 ms below the depression. The width, depth and depth of influence of the pockmarks are measured along the seismic profiles (Appendix E). No pockmark is crossed by more than one profile, which did not allow a systematic analysis. The location of the pockmarks is indicated with the coordinates of the deepest point in the profile. These values in TWT are converted in meter with an internal speed of 1600 m/s in the sediment and 1500 m/s in the water column. The maximum width observed on the seismic profiles is 250 m, while the minimum is 38 m, which results in an average of 117 m. The depth of the pockmarks varies between 5 and 1.5 m with an average of 2.6 m. These values are very large in comparison with other pockmarks described in literature (see 2.3).

Hovland (1983) describes an elongated large pockmark structure of 2-4 m depth and 100-220 m width in soft clays offshore Norway. This depression is at least 2.5 km in length. Due to the conspicuous disturbance of the fine layers in the clays beneath the depression, it is interpreted as having been formed by escaping gas having lifted fine-grained particles into suspension, in much the same way as pockmark formation. On the seismic record presented in the paper, indications have been given of such as acoustic disturbance, which suggests vertical migration of fluids. This argues for a shallow gas formation of these structures, reshaped by currents that merged the pockmarks. This might also be the case for the pockmarks observed in the area. The influence of the structures is limited to the shallow part of the sediments. Only two pockmarks show an indication for deeper formation (45 m) but they are still limited to the subsurface sediments.The seismic characterization of the pockmarks is illustrated in figure 5.42 (P970527).

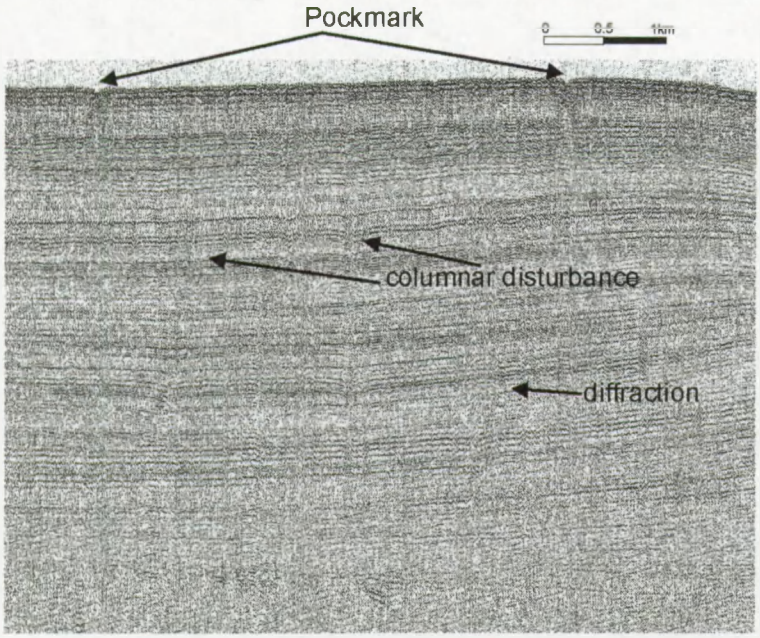

Fig. 5.42: Part of line P970527 (Appendix E). Pockmarks and columnar disturbances are indicators for possible fluid escape to the seafloor.

Furthermore, columnar disturbances have been observed on P970527 near the pockmarks, indicating potential migration paths for fluids. They are seen as a local shift in the reflectors that might indicate buried pockmarks and local masking of the reflectors. These features are seen in the vicinity of the pockmarks, which might suggest a formation of the pockmarks by fluid escape. The acoustic indication for fluid escape is seen over the entire record on the seismic profile but still suggesting a shallow origin.

The pockmarks are plotted on a map (Fig. 5.43) to evaluate the link between pockmarks and indication for gas seepage with the mound occurrences. No correlation is observed between the pockmarks and the mounds. This might be due to the available data set, but also due to the large disturbance of diffracting reflections near the mound, it will be hard to recognize these features. The density of the observed pockmarks is low.

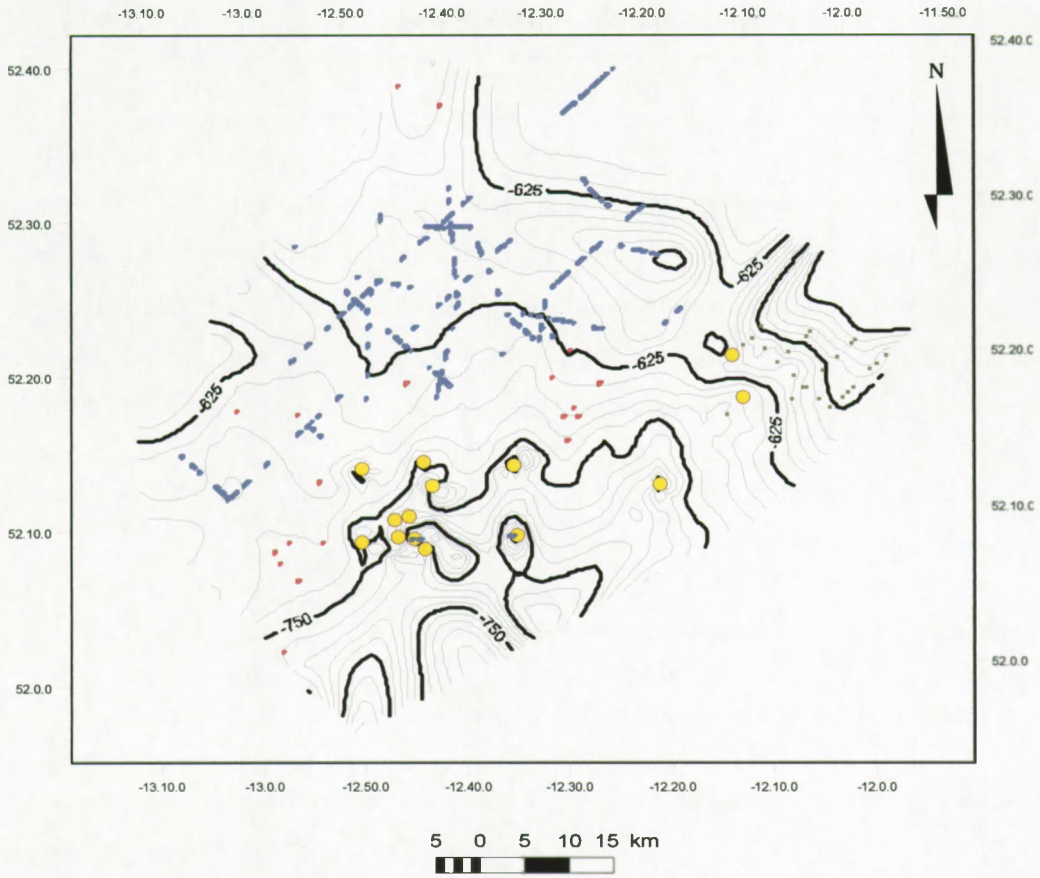

Fig. 5.43: Pockmark (red) and mound distribution in the Hovland-Magellan mound province.

In the Connemara Field about 70 km more to the north many gas escape structures have been related to the gas-oil accumulation in Block 26/28. In that area many pockmarks have been observed with a high density (100/km^2) and a dimension between 120 m, with a depth of a few centimeters to 2 m. It is suggested that the pockmarks have been formed by the escape of fluids in that area (Games, 2001). Even though in the Connemara field large evidence is seen for gas escape and migration, the pockmarks are numerous but relative small compared to the depression seen in the mound province. This might suggest that currents enhanced the original depressions formed by the gas escape. It is worth to note that no active pockmarks have been observed.

- The regional unconformities in the area are related to major oceanographic changes.
- The entire sediment sequence can be interpreted as the deposition of a drift. An upslope progradation from the sequences, observed on industrial data, is suggested. Submarine currents have eroded gullies along the eastern margin and in the central part. These are filled by reworked sediments in a SN regime during calmer periods. The gullies did not migrate significantly in time and suggest that similar processes were active in the entire time period of the deposition.
- The mound base is dated to be the last erosional event in a drift contourite sequence of Late Pliocene-Quaternary age.
- The mounds are largest in zones with reduced sedimentation.
- The mounds appear preferentially at breaks in the slope or small perturbations of R4.
- Moats are formed during the early phase of deposition of He in the Magellan mound province. In the Hovland mound province the moats are still erosive. In the Magellan mound province the moats have a clear NS trend.
- No relation is observed between the mounds and the underlying geological facies, faults and pockmarks.

5.4 Sedimentology

The subsurface sampling in the Hovland-Magellan province has been focused on the characterization of on-mound sediments. Off-mound samples in the surrounding drift sediments are only used for comparison or for geochemical gas sampling. The on-mound cores have sampled the flanks, the crest and the moats of the mounds HOV02, HOV03, HOV04, HOV05, HOV08, HOV10, HOV12, HOV15 and of an outcropping Magellan mound (Fig. 5.23). Most of the on-mound cores yielded corals in the core as indicated in table F.1. Mineralogical and chemical analyses have been performed on a selection of on-mound cores to characterize the sediment and a possible diagenesis (TTR8-AT-89G, PAD18, PAD25, PAD81, PAD83). One core **TTR7-AT-16G** on HOV03 has been studied in more detail by binocular, petrographic, cathodoluminiscence and scanning electron microscopy, clay mineralogy, isotopic $\delta^{13}C$ and $\delta^{18}O$ analysis of the carbonate fraction and coral fragments.

Several gravity cores have been taken during an industrial geochemical survey (Statoil *Report No 6096/7)* to evaluate the potential for hydrocarbon seepage near the mounds and pockmarks. The results of this survey have briefly discussed in combination with the published data of Hovland et al. (1994).

5.4.1 Off-mound samples

The off-mound samples are TTR7-AT-07G in the Hovland mound province and TTR7-AT-12G, TTR8-AT-93B, TTR8-AT-94B, TTR8-AT-95B, TTR8-AT-96B, TTR8-AT-97B, TTR8-AT-98B, TTR8-AT-99B and TTR8-AT-110B in the Magellan mound province (Table F.1). The lithologs have been presented in appendix F.2.

5.4.1.1 Magellan mound province

In the Magellan mound province, the off-mound box cores consist of a homogeneous succession of olive-grey (2.5Y 4/2) silty clay containing foraminifera and some biogenic carbonate debris. Burrows have been found throughout the entire core. The upper centimeters (2-6 cm) of the cores comprise a sandier facies of oxidized (yellowish, 5Y 5/3) sandy silty clay with a high water content (soupy). The sand is composed of large foraminifera. In the lower part of the core, the lithology is a compact olive-grey (5Y 5/2) sandy clay containing some foraminifera and shell debris.

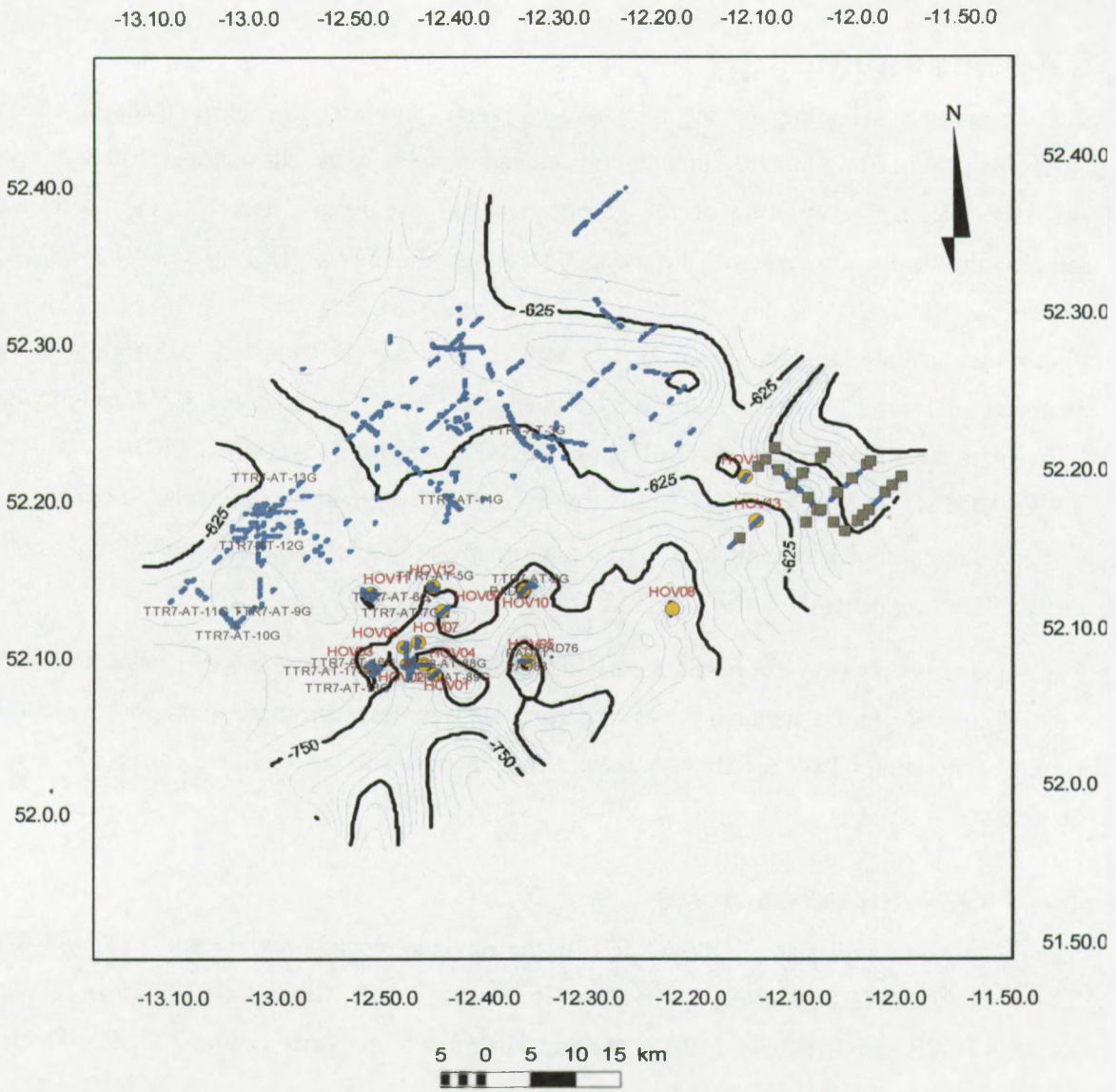

Fig. 5.44: Location map of the sediment cores taken in the Hovland-Magellan mound province. The mound structures are indicated in purple.

The sediments in core **TTR7-AT-12G** are greyish-brown (2.5Y/5/3 to 2.5Y 4/2), massive bioturbated marls with occasional rock fragments and bioclastic material. The core becomes coarse downcore, with more bioclastic material. The upper centimeters comprise water-rich marls with high concentrations of foraminifers. An intact polychaete tube has been found at the surface, which confirms the intensive surface bioturbation by worms in the area, as seen on the video track (see 5.5) and in the box cores. Between 28-80 cm an intense bioturbated interval has been observed. The bioturbations are filled with a mixture of silt and clay or bioclastic material. Below

the intensive bioturbated zone an interval of dark silty clay is present. In this zone a large rock fragment has been observed at 88 cm. The lower part of the core (between 218-403.5 cm) contains silty marl with shell fragments, small rock fragments and occasionally gastropods. One patch of extremely intensive bioturbation has been seen around 310 cm.

The core illustrates the intensive bioturbation in the Magellan mound province for the off-mound sediments. In several cores a higher concentration of rock fragments and bioturbations has been observed in the intervals around 1 m and 3 m (Swennen et al., 1998), suggesting a deposition during colder periods with ice rafting. Near the sample location TTR7-AT-12G, a sample (ST108) has been taken (Table F.1) for geochemical analysis (see 5.4.6).

The entire seafloor is intensively bioturbated, with two distinct sizes of circular holes in the sediment surface. The larger holes are up to 5 cm in diameter, the smaller ones, approximately 1-2 cm. Two underwater TV-tracks have been made across the Magellan mound province during the TTR8 cruise (De Mol et al., 1999). These tracks show an intensive bioturbation of the low relief. It is suspected that deep mixing in the core is caused by the presence of large echiuran or sipunculid worms observed in the box cores (Sumida and Kennedy, 1998). These large worm species live at depth in the sediment in a burrow, feed at the surface and excrete at depth. This intensive bioturbation argues for a zone, where the bioturbating animals can survive under the present conditions.

The upper sediment cover is a homogeneous yellowish brown mud with an unconsolidated, water-saturated upper layer. The sandy sheet on the top argues for peak current regimes depositing sandy material and winnowing fine material The sandy layer on top of the cores contains more fine material than in the Belgica mound province, suggesting lower current activities.

The cores TTR7-AT-9G, TTR7-AT-10G and TTR7-AT-13G have been taken on the flank of buried Magellan mounds. These cores comprise a similar sediment succession as other off-mound cores. From bottom to top, the sediments have a fining upwards sequence arguing for a decrease in current speed. In the lower part of the cores bioclastics are common, in particular gastropods, bivalves and foraminifera.

5.4.1.2 Hovland mound province

Core TTR7-AT-7G (Appendix F.2), comprises olive greyish brown, silty, structureless, foraminiferal marl. Locally very strong bioturbations have mixed lithic fragments, shell fragments and other coarser material. Reduction spots are scattered throughout the section. The most intensive bioturbations are seen at a level between 300-306 cm. This argues for periods with intense benthic life. A rock fragment is found at 16 cm. The sediment at the surface is sandier than in the underlying sediments and in the Magellan mound province. This argues for a higher current activity in the Hovland mound province than in the Magellan mound province.

5.4.2 Moats

Two cores have been taken in the moat features (see 5.2 and 5.3), one around mound HOV10 (TTR7-AT-3G) and another one around HOV12 (TTR7-AT-6G) (F2). Both cores contain relatively high concentrations of bioclastic material such as shell and coral fragments compared to the off-mound cores. Rock fragments - up to 7 cm - are also more common in the moat sediments (TTR7-AT-6G). Rock fragments and bioclasts are concentrated in the upper 1.5 m in core TTR7-AT-3G and between 70-130 cm in TTR7-AT-6G (Appendix F.2). The sediment in the cores shows a general fining upward sequence.

The sediment of the lower unit is a structureless olive-grey mud (2.5 Y 5/2). Core TTR7-AT-3G contains typically massive mud between 296-369 cm apart from thin bioclastic and foraminiferal layers (at some specific locations with intact corals and bivalves (326 cm, 347 cm, 352 cm) (Appendix F.2). The upper boundary of this unit ends with the deposition of the coarse-grained layers, around 150 cm (175 cm for TTR7-AT-3G and 130 cm for TTR7-AT- 6G).

The upper sediment unit consists of olive-grey (5 Y6/3) foraminiferal sands and marls, fining downcore to more silty foraminiferal marls. Large burrows filled with coarse material have been found between 143-174 cm (5Y 5/3) in core TTR7-AT-3G. Lenses of finer marl material occur (65-86 cm). Shell fragments have been observed as well as several coral fragments. Core TTR7-AT-6G comprises interbedded grey marl sand with thin sandy foraminiferal and bioclastic debris layers. The marls vary in colour form olive-grey to olive-green to greyish-brown. They are commonly strongly bioturbated but otherwise structureless. Polymictic rock fragments (schists, granites, sandstones, metamorphic rocks, etc.) have been found scattered in the core.

The fine-grained sediments have been interpreted as deposits in periods of reduced current activity. The coarse sediments with the bioturbation and rock fragments mark the end of the last cold period and the intensification of current. The coral fragments are not *in situ* and transported by gravitational processes to the moat.

5.4.3 On-mound cores

Several cores have been taken on the flank or crest of the Hovland mounds: TTR7-AT-2G, TTR7-AT-5G, TTR7-AT-16G, TTR8-AT88G and TTR8-AT-89G TTR7-AT-18G, PAD18, PAD25, PAD81, PAD83. Only three cores hit the mound facies of a Magellan mound: TTR7-AT-11G, TTR7-AT-14G and ST166. Core ST166 has been used for the chemical characterization and no detailed lithological description is available (Table F.1). Besides the lithological description, several mineralogical and petrographic techniques have been applied to characterize the on-mound sediment. The carbonate content in the samples is calculated from the entire CaO content measured in the chemical analysis and measured with a calcimeter. The variation in the values between the different techniques is due to the difference in sample content of bioclasts.

These analyses are supported by petrographic and cathodoluminescence microscopy studies of thin sections. Stubs of the sediment have been studied by scanning electron microscopy for more detailed cement and chemical or texture analysis. 21 samples of the sediment and the coral fragments have been taken at several depths for isotopic δ13C and δ18O analysis to find the origin of the carbonate at these levels. Additional mineralogical and chemical analyses have been performed on core PAD18, PAD25, PAD81, PAD83 and TTR8-AT-89G.

5.4.3.1 Magellan mound

Core **TTR7-AT-14G** (Fig. 5.45) has been taken at the crest of an outcropping Magellan mound at 52°18.88'N, 12°40.70'W in 642m water depth (Fig 5.23). The core consists of bands of dead coral interbedded with olive-grey (5Y 5/2) silty foraminiferal mud with coral fragments. The upper 80 cm consists of about 80% of branching corals with some silt and coral fragments. A dropstone of 2 cm in diameter occurs at 21 cm. Silty foraminiferal marl with occasional coral fragments has been found between 80-90 cm. A second band consisting of 80% of coral branches in a clay-silt matrix has been observed between 90-93 cm. Interval 93-105 cm comprises silty foraminiferal marl with occasional coral fragments and interval 105-112 cm contains up to 80% coral fragments in a silty clay matrix. Interval 112-120 cm comprises silty foraminiferal clay, while interval 120-145 cm consists of olive-grey (5Y 4/2) clay and 50% of corals

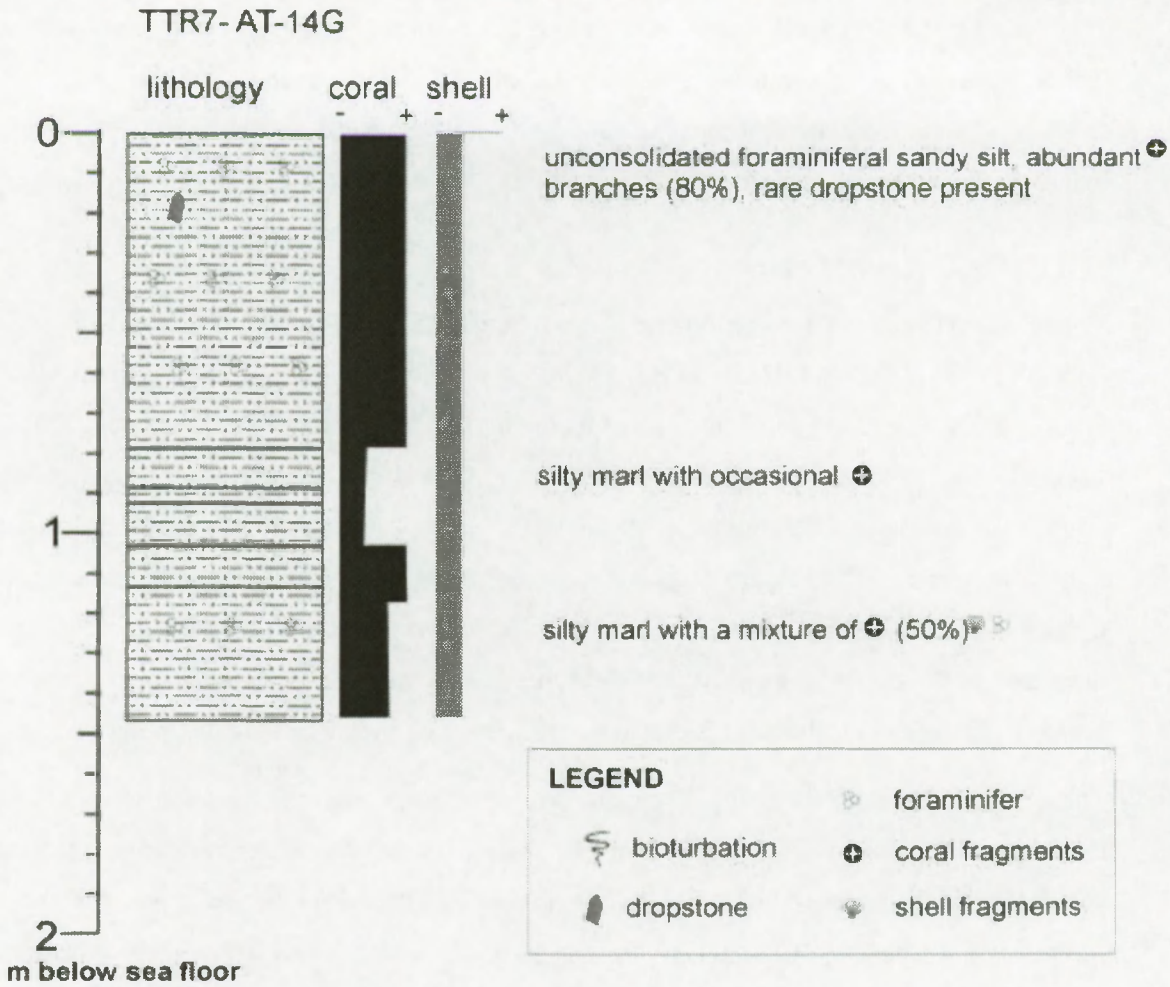

Fig.5.45: Lithocolumn of core TTR7-AT-14G.

5.4.3.2 Cores on HOV02

TTR8-AT-88G and TTR8-AT-89G

Cores TTR8-AT-88G and TTR8-AT-89G have been taken at approximately the same location at the crest of HOV02 (Propeller mound). The cores consist of a relative dark and light olive-green to brown silty marl containing irregular distributions of coral debris with a maximum size of 6 cm. The oxidized top of the core (0-13 cm) has a light olive-brown colour. The coral distribution and the relative concentrations of the coral species *Madrepora* and *Lophelia* have been mapped based on computer tomography images of core TTR8-AT-89G (Fig. 4.47, 4.48, 4.49). Besides the corals, lithic fragments are clearly imaged on the CT-scans.

Fig. 5.46: CT images of core TTR8-89G.

The upper scan illustrates the occurrences of broken coral fragments.

The calyx formation has been observed in areas with *Lophelia* corals.

Madrepora corals have no calyx formation.

The lower scan illustrates a reconstruction of the core.

The density contrast between the lithic pebbles, corals and the matrix was large enough for a good imaging. Shell fragments have been recognized by their shape and slightly higher density on the scans. Figure 5.46 shows the CT scan quality throughout the core and the interpretation key for the different species is presented in figure 5.47.

Two major units have been recognized in the coral distribution throughout the core (Fig. 5.48). The lower part (130-200 cm) has a high concentration of corals. A low but variable coral content has been observed between 50 cm and 130 cm. In the upper part of the core the coral content increases again quickly and stays stable but relatively low in comparison with the lower part. Several zones have been observed where only one coral species dominates (Fig. 5.48). The transitions show smaller coral fragments. *Madrepora* dominate zones with relative low coral concentrations. *Lophelia* appear to be dominant in zones of transition between high and low coral

concentrations. The coral framework is completely filled with sediments. The low coral content at several levels might reflect periods of minor coral occurrences, or migration of coral patches on the mound.

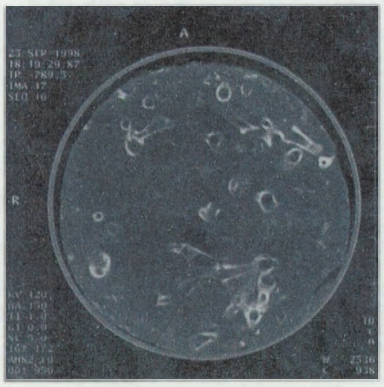

Fig. 5.47a: A CT-scan of TTR8-AT-89G with the distribution of *Lophelia* corals.

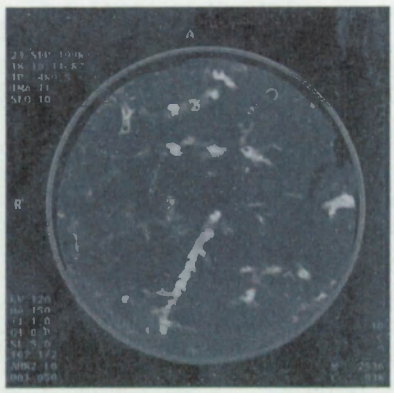

Fig. 5.47b: A CT-scan of TTR8-AT-89G with the distribution of *Madrepora* corals.

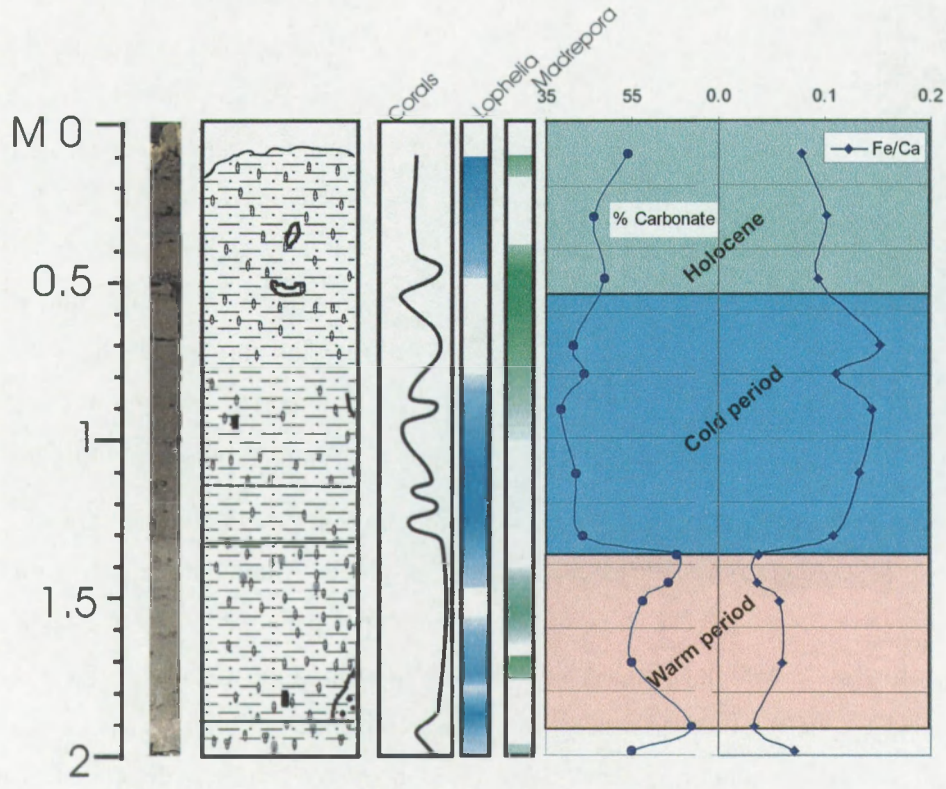

Fig. 5.48: Lithocolumn of TTR8-At-89G. The additional columns represent the coral distribution and the relative distribution of *Lophelia* and *Madrepora*. The chemical parameters indicate the carbonate % and the ratio for Fe/Ca. These observations fit well with the inferred paleoecological interpretation of De Mol et al. (1999).

The matrix sediment is a silty clay with a high carbonate content, consisting of fine-grained bioclastic fragments. The light grey colour of the sediments in the lower part is due to the high carbonate content. Sections with lower carbonate content show a more brownish colour.

The variation in coral distribution parallels the mineralogical composition of the matrix in the core (Table F.3.5, Fig. F3.5). The calcite content is low in the zone with low coral content. Quartz and feldspar mineral distributions have relatively high values between 130 and 90 cm. Peaks of aragonite have been found at levels with high densities of coral debris. Dolomite peaks are related to peaks in feldspar and quartz, suggesting a detrital origin rather than *in situ* formation. Pyrite is more common in the muddy section, indicating more reducing environments than in the dense coral layers. Chlorite is not variable in the core and increases in the upper 50 cm. The main components of the fine fraction of the sediments are calcite, quartz and minor feldspar (K-feldspar), mica's, chlorite and mixed layers. This composition is slightly different from the off-mound cores in terms of the higher carbonate content and variation in aragonite content.

The magnetic susceptibility curve of core TTR8-AT-88G is compared with the mineralogical and chemical distribution of core TTR8-AT-89G (Fig. 5.49). This curve reflects well the siliciclastic minerals. The curve trend is similar to the trend in the Belgica mound province but the HL1 is not reached in the core. The only possible marker is Younger Dryas at 70 cm (Fig. 5.49)

The samples taken on mound HOV02 contain all a large concentration of corals, forming a framework, which has been filled with sediments of similar composition as the surrounding sediment samples. The baffled sediment is coarser than in the off-mound cores. The carbonate content in the samples found its source in the bioclasts related to the corals and associated fauna.

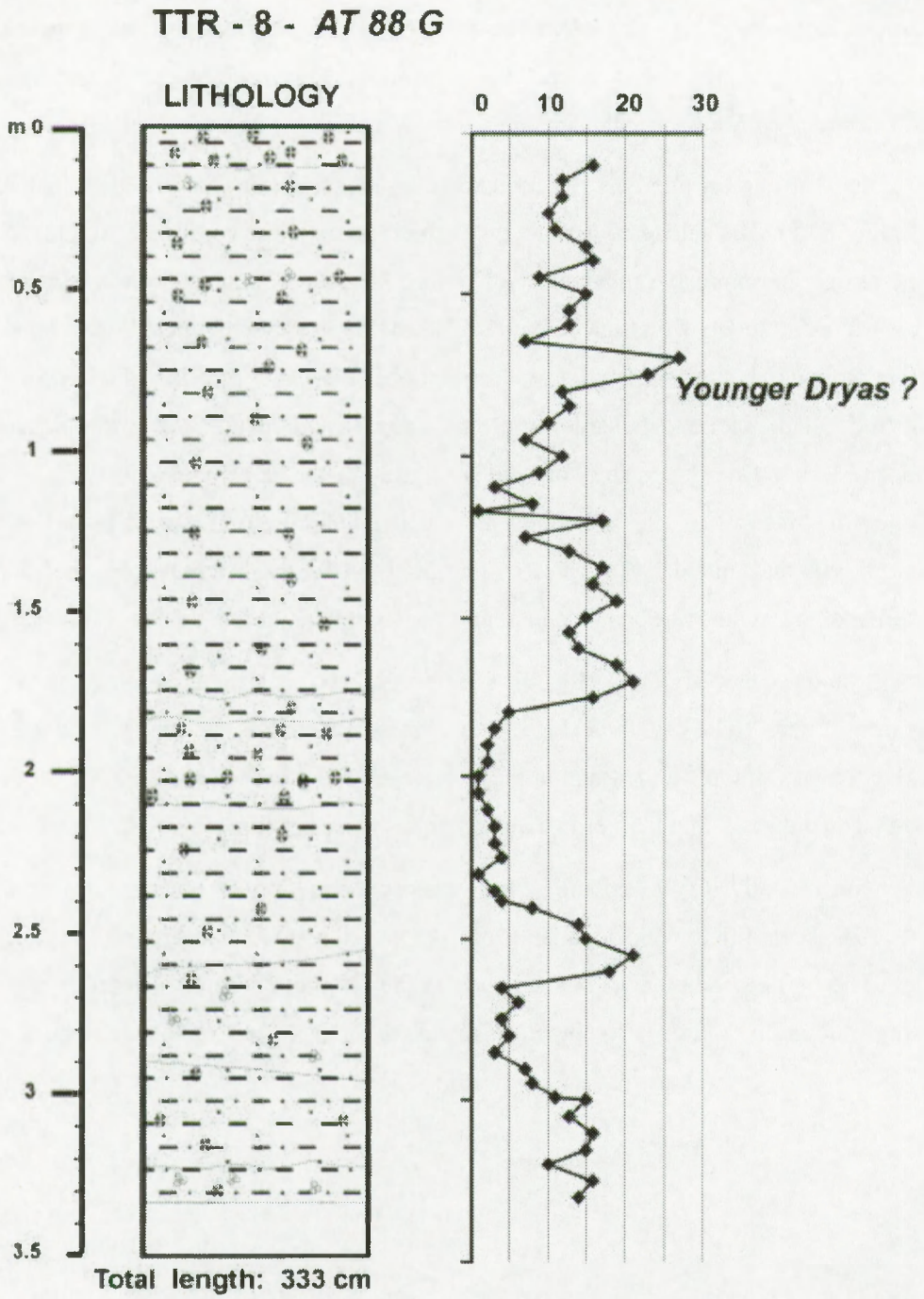

Fig. 5.49: Lithocolumn of TTR8-AT-88G and magnetic susceptibility curve. The only possible marker in the curve is the Younger Dryas (De Mol et al., 1999).

5.4.3.3 Cores on HOV03

The flank facies of HOV03 has been sampled in core **TTR7-AT-17G** (126 cm). The core comprises alternating light grey (2.5 7/0) and grey (5Y 6/1) foraminiferal marls with interbedded coral fragments (Appendix F.2). The upper interval (0-11 cm) contains coarse foraminiferal sandy silt (2.5Y 5/3) with coral fragments, up to 5 cm. Interval 11-42.5 cm consists of light grey marls with lower shell and broken coral fragments concentrations than in the upper interval. Interval 42.5-66 cm includes grey clays without bioclasts. Interval 66-94 cm consists of grey sitly foraminiferal marls with a coral density of about 40% of the total sediment. Interval 94-108 cm comprises grey silty foraminiferal marl with a coral density of about 20%. In the lower part the coral density increases again to about 40%.

A second core sampled on the flank of HOV03 has a different lithology than TTR7-AT-17G. In general, the core is composed of a fine-grained matrix with coral fragments with a yellow staining. Interval 0-11 cm comprises a large amount of bioclastic debris in a dark greyish-brown (2.5 Y 4/2), medium grained, foraminiferal sand. Pebbles up to 1 cm are found in this interval. Interval 11-24 cm is made of dark greyish–brown (2.5Y 4/2) silty mud, which fines downwards to clay. This level contains dark coloured rock fragments up of 2 cm. Shell and coral fragments have been found at the base. Interval 24-58 cm cm is intensively bioturbated and full of coarse-grained sediment. Bivalves of 1.5 cm in diameter have been found, scattered through this interval. Interval 58-198 cm comprises bioturbated silty marls without shell fragments in the upper part, and both shell fragments and echinoderm spines come in at 154 cm.

The paleoecological study of the cores indicates a sharp marker between the Holocene and the last glacial maximum sediments at about 50 cm (Swennen et al., 1998). The end of the glacial period is followed by a period of intensive bioturbation, filled by coarse-grained sediment. The Pleistocene sediments are fine-grained and suggest a slaggy current regime during the colder period. Biodebris is relatively low in these periods probably due the decrease in production on the mound. In Core TTR7-AT-17G no difference can be seen between the Holocene and Pleistocene sediments in the nannofossil distribution. This indicates that reworked sediments are baffled in the framework of the corals.

5.4.3.4 Cores on HOV04

PAD18 and **PAD25** have been taken on the flank of HOV04. In appendix F2, the coral distribution of the cores is represented in a curve next to the lithocolumn. In the coral core **PAD18** the upper 5 cm comprises brownish silty clay with scattered lumps of coral. Corals at the top of the core show reddish colours of bioerosion by Fe and Mn bacteria (see 2.1). Downcore the

coral fragments have a light whitish colour and no visible bioerosion. The upper part of the core has a relatively high amount of coral fragments, with a local low at 100 cm. From this level on the coral concentration increases again with a maximum at 170 cm. Between 170-200 cm, the coral concentration is low. In the lower part of the core the coral fragments increase again, together with other bioclastic material. The matrix sediments have high concentrations of carbonate with a chalky texture. The bioclastic material consists of corals, shells and echinoderm needles.

The mineralogical distribution in core PAD18 (Table F.3.1, Fig. F.3.1, Fig. F.2.1) is dominated by carbonate. The highest carbonate content has been found in the section below 100 cm. A coral-rich zone is characterized by a higher content in aragonite in the sediment. The dolomite distribution, observed in most of the samples, is not related to the coral distribution. The surface of the core is rich in quartz and feldspar. Peaks of quartz and feldspar (at 60 and 100 cm) fit with layers with only a few corals. These minerals, deposited in the matrix, are omnipresent in the samples. Pyrite is present just below and above high peaks of carbonate and bioclasts at 100 cm and around 170 cm. Probably formed during in the sulphate reduction zone by the decay of organics matter. Mica and chlorite have peak values around 200 cm and 100 cm. Kaolinite has been observed in the upper samples above 100cm. These higher values in Kaolinite might indicate a source area with a warmer climate in the upper 100 cm. High values in TOC correlated with levels of high bioclastic material (Table F.3.1).

The bottom of this core has been dated by dinocyst as Bølling-Allerød (15-13ky) at 2 m (Coles et al., 1996)

PAD25 comprises in the upper part an olive-green sandy-clay with high concentrations of coral fragments of a few centimetres (Appendix F.2). Bioclasts are common throughout the core. The sediment below this upper layer is silty clay, rich in carbonate. The coral concentration is high in the upper layer. Between 50 cm and 100 cm the coral concentration is low and starts to increase downcore. The coral fragments are well preserved and have a light coloured skeleton in the lower section of the core. This might imply that the bioerosion is limited and that the cores only a short period stayed exposed at the surface. Between 100-150 cm the skeletons are more altered by bioerosion and show Fe-Mn staining with a reddish colour. This might implies a lower sedimentation rate in this part of the core so that the bacterial community could work on the coral during the period it was exposed at the seabed.

In the mineralogical composition (Fig. F.3.2, Fig. F.2.2, Table F.3.2), quartz is dominant in the levels with reduced bioclasts. The feldspar, chlorite and mica have a trend that is parallel with quartz. Aragonite and calcite correlate positively with the coral distribution. Dolomite is

uniformly present in the core. Pyrite values are high in zones with plenty of bioclasts. Mixed layers are common in the lower and upper samples but they have not clearly been observed in the middle part. Kaolinite has been observed in the upper 100 cm of the core, indicating a change in source or an additional source of sediments.

The flank core of mound HOV04 contains a larger concentration of coral and biodebris. Both cores show a variation in the coral density. Reduced concentrations of corals are seen at 100 cm and around 170 cm in both cores. The 1m level is also characterized by a change in mineralogy and the introduction of kaolinite. In coherence with the other core, this has been interpreted as the end of the last glacial period. The 170 cm level might correspond to a short warmer period in the last glacial period.

The sediments in the coral-rich zones are generally coarser than in the off-mound cores. Bioclast concentrations increase slightly above the normal trend just before a low in the coral distribution curve occurs. Quartz and minor K-feldspar dominate the siliciclastic minerals. Mica's are dominating by iron bearing mica as glauconite and illite, due to the absence of the odd peaks in the XRD profiles.

5.4.3.5 Cores on HOV05

Cores **PAD81** and **PAD83** have been taken on the flanks of HOV05. Core **PAD81** (Appendix F.2) yield in the upper centimetres (10 cm) a high concentration of shells and coral fragments in a grey yellowish sandy sediment. The interval between 10-35 cm contains low concentrations in bioclasts. Between 35 cm and 1m a zone with high coral concentrations has been observed in the upper part. The coral fragment content increases slightly to the base of the interval. Below 120 cm no coral fragments have been observed. At about 75 cm a quartz rock fragment has been found in a zone with a relative low coral concentration. Between 110 cm and 170 cm the bioclasts material consist mostly of shells and foraminifera. The lower section of the core contains no bioclasts.

The mineralogical composition of the upper coral-rich part consists dominantly of calcite and aragonite (Fig. F.3.3, F.2.3, Table F.3.3) Dolomite, present in most samples, has no clear relation with the coral distribution. The quartz distribution in the core shows no variations and is relatively dominant in the sediment. Mica and chlorite decrease in the section below 100 cm.

Core **PAD83** (Appendix F.2) consists in the upper 14 cm of dull yellow (2.5Y 6/3) homogeneous silt. The lower boundary of this unit is sharp. Between 14 cm and 100 cm homogeneous silty clay has been observed with a dull yellow (2.5Y 6/3) colour. Lighter thin layers are rich in coral and

shell fragments. A rock fragment has been found around 70 cm and 145 cm. Downcore the bioclasts decrease parallel with an increase in finer sediments. Bioturbations are filled with yellowish sandy material at 100 cm. The underlying sediments show greyish bioturbated silty clay with a few bioclastic fragments.

This core has been scanned before opening with CT tomography. The CT medical tomographer allows recognizing dropstones (Fig. 5.50) and coral fragments in the core. The images of the CT tomography show homogeneous sitly clay with a backscattering of carbonate-rich sediments.

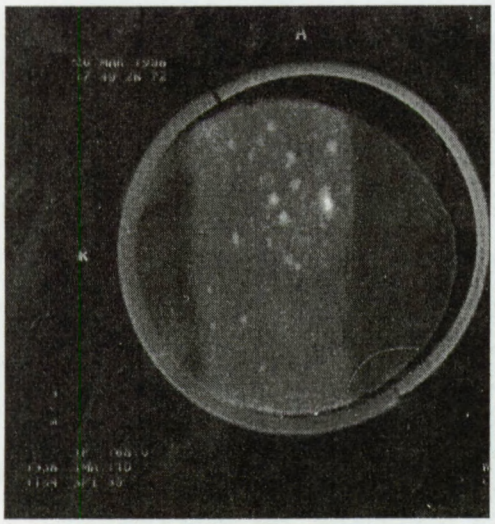

Fig. 5.50a: Bioturbation seen in CT-scan with lithic fragments.

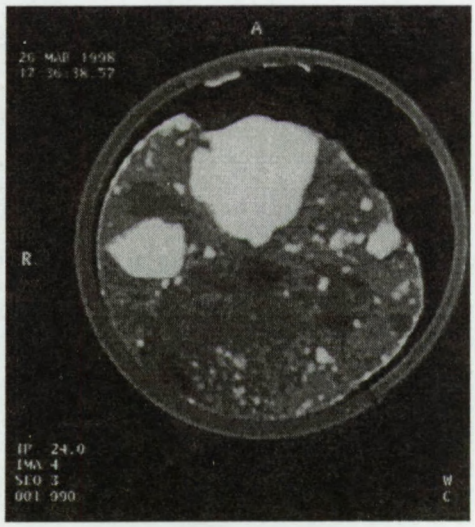

Fig. 5.50b: Lithic fragments dominating certain levels.

The mineralogical composition (Appendix F.2.4, Fig. F.3.4, Table F.3.4) of the core is uniform and is dominated by quartz and feldspars. Quartz has in the distribution curve lower values between 75-180 cm. The feldspar curve shows peaks around 100 cm and 140 cm. Aragonite has only been observed in the upper section of the core (110 cm). Chlorite, mica and kaolinite and mixed layers show no variation through the core.

The coral concentration in the cores on HOV05 is less than in the previous cores. The corals concentrated at the levels between 30-100 cm for PAD83 and in two zones between 35-60 cm and 80-95 cm for PAD81. The rock fragments in core PAD83 suggest cold periods with input of dropstones at the levels of 70, 90 and 140 cm. Just below these levels dense concentration of corals have been found. This might indicate that more coral debris have been produced in the transition zones between the warm and colder period. The matrix sediments are very similar to the off-mound cores.

5.4.4 Sediment characterization

A detailed study has been performed on core TTR7-AT-16G, located on the flank of HOV03. Core TTR7-AT-16G (Fig. 5.51) with a recovery of 389 cm is located on the upper flank of HOV02. The upper 111 cm of the core consists of light olive-brown (2.5Y 6/3- 5/3) silty clay with coarse, angular, grey to greyish-brown, clast-supported sand intervals. Numerous angular corals and other bioclastic fragments occur between 15 cm-30 cm and 89 cm-111 cm. One large (1 cm in diameter) coral has been located at 106 cm. The interval between 111-205 cm comprises a strongly bioturbated marl with foraminifera, shells and coral fragments. It is associated with a colour change (5Y 5/3 –2.5Y 6/2), mottling and strong burrowing. Some of the burrows are filled with a grey, soupy mud. The deepest interval (206-389 cm) is composed of greyish-brown to dark and light grey (2.5Y 7/0) marls, which coarsen downwards to silty foraminiferal marls. Scattered black (reduction) spots, coral fragments and shells have been found in this interval. Age estimations based on calcareous nannofossil (coccolithophores, foraminifera) biostratigraphy of core TTR7-AT-16G (Saoutkin, 1998) provide an approximate age of 72ky at 340 cm sediment depth. Figure 8 summarizes the age model of Saoutkin (1998). This implies an average sedimentation of about 5 cm/ky.

5.4.4.1 Clay mineralogical analysis

On core TTR7-AT-16G, the mineralogical and clay mineralogical analyses have been performed in the laboratory for soil science at the University of Ghent (Van Ranst).

Table 5.3 provides an overview of the relative abundance of the most important minerals observated in the core. The dominant minerals are quartz, calcite, feldspar, mica and chlorite. Levels with high coral concentrations match with the appearance of aragonite at 25 cm and 162 cm. Calcite has also peaks in zones with corals. Dolomite has been found around 230 cm and in the upper 130 cm in levels with a low coral concentration. Siliciclastic minerals occur in low levels in the coral-rich zones.

Saoutkin (1998) has performed a paleoenvironmental analysis of the coccoliths and foraminifera, supported by absolute C^{14} dating of species in the core. This interpretation is compared with the mineralogical variation in the core (Table 5.3). Corals appear in large quantities in warmer periods. At the boundary of the warm periods the coral abundance decrease. Cold periods are characterized by a decrease in the carbonate content and an increase of quartz and feldspar mineral. The dolomite content is relatively higher in the cold zones

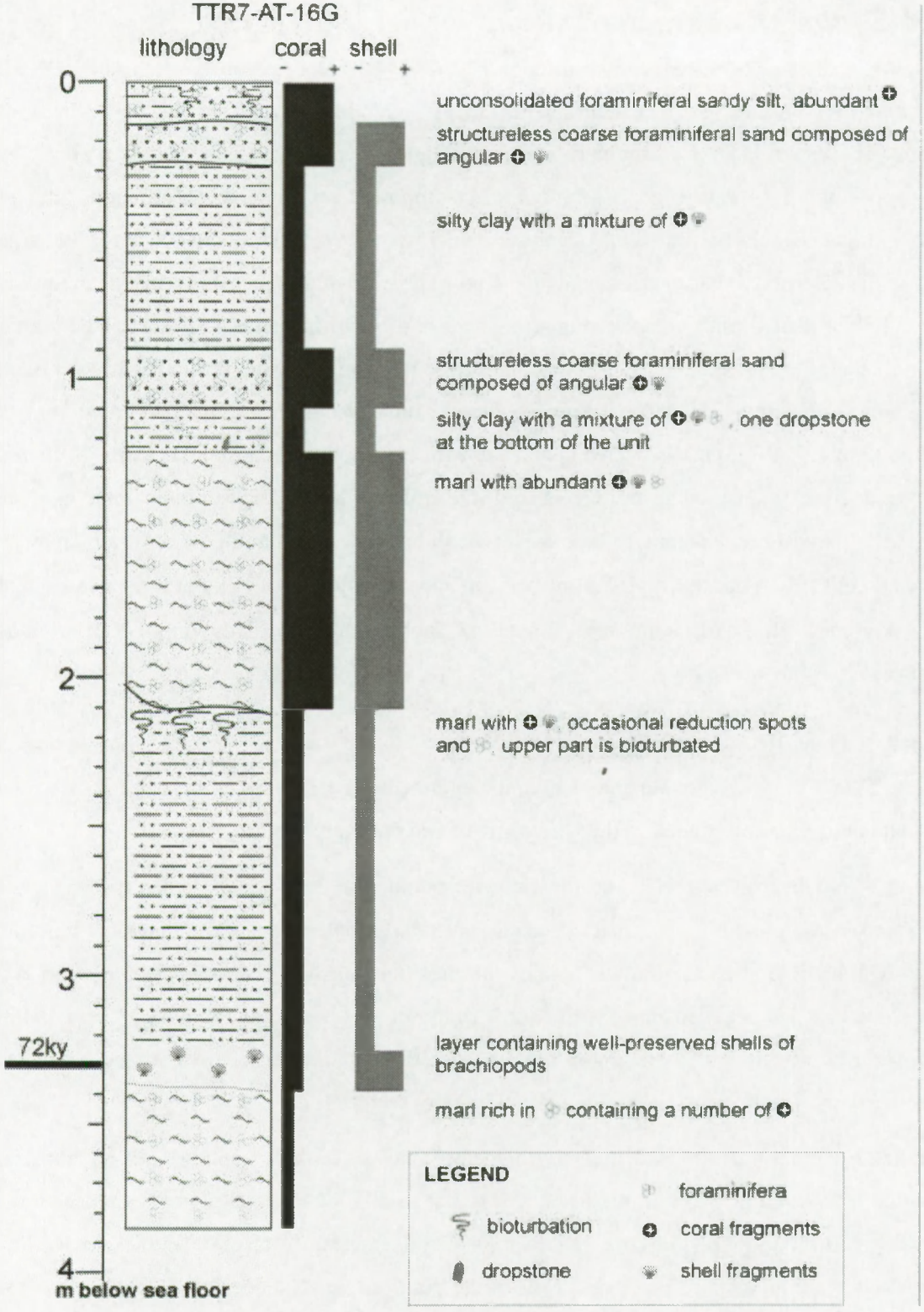

Fig. 5.50: Lithocolumn of core TTR7-AT-16G.

Smectite is more common in colder periods recognized in the core.. Vermiculite has only been observed in the transition zone and in the last cold period. The trioctahedral chlorite and dioctahedral mica decrease from the bottom to the top of the core. The highest values of these minerals have been observed in colder periods and in the transition zones. Mixed layers of chlorite have only been observed in the warmer periods and mixed layer of mica in the colder.

DEPTH (CM)	TRIOCT. CHLORITE	MICA (DIOCT.)	KAOLINITE	QUARTZ	FELDSPAR	ARAGONITE	CALCITE	DOLOMITE	SMECTITE	VERMICULITE	IRREGULAR MIXED LAYERS
25	(+)	+	+	+++ +	++	++	++++	+	(+)	+	
31	+	+	+	+++	++		++++	+(+)	++	(+)	+
86	+	++	++	+++	+(+)		++++	+(+)		+	++
118	**++**	**++**	**+**	**+++**	**+(+)**		**+++**	**+(+)**	**+**	**+**	**+**
162.5	**+(+)**	**+(+)**	**+**	**++**	**+**	**++**	**++++**	**(+)**	**++**		**+**
216.8	**+(+)**	**+(+)**	**+**	**+++**	**+(+)**		**++++**	**+(+)**			**+**
253.2	+(+)	++	+	++	+(+)		+++	+	++		+
302.2 .	++	++	+	+++ +	+		+++(+)	+	++		(+)
336.2	++	++	+	++	+		+++(+)	+(+)	++		+

Table 5.3: Mineralogical composition based on XRD and geochemical analysis of TTR7-16G. The crosses indicate the relative amount of the minerals throughout the core. The bold crosses evoke the warm period (Saoutkin, 1998).

The chemical composition of the carbonate fine fraction is measured with an AAS. Figure 5.51 shows the basic elements in % or in ppm depending of the relatively amount. Mg, Ca and Fe are the most common elements. Ca correlates with coral concentrations and has a peak in the warm period. Fe, Mg, K have an opposite trend as Ca and are related to clay minerals, indicated by traces of Zn and Pb. Strontium is abundant in the coral-rich zones and is clearly related to the aragonite content.

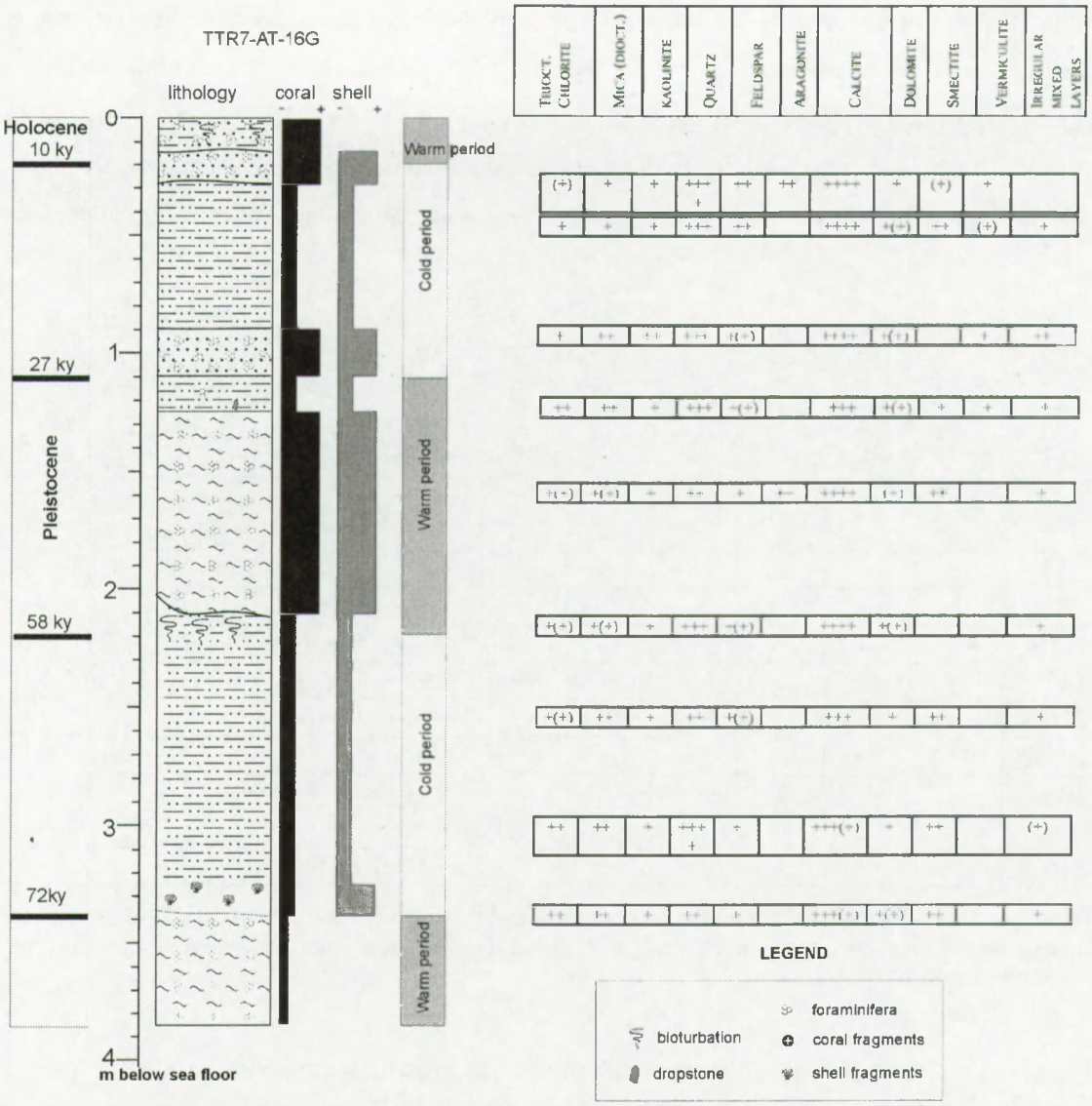

Fig. 5.51: Mineralogical distribution in TTR7-AT-16G compared with the age and paleo environment model of Saoutkin (1998).

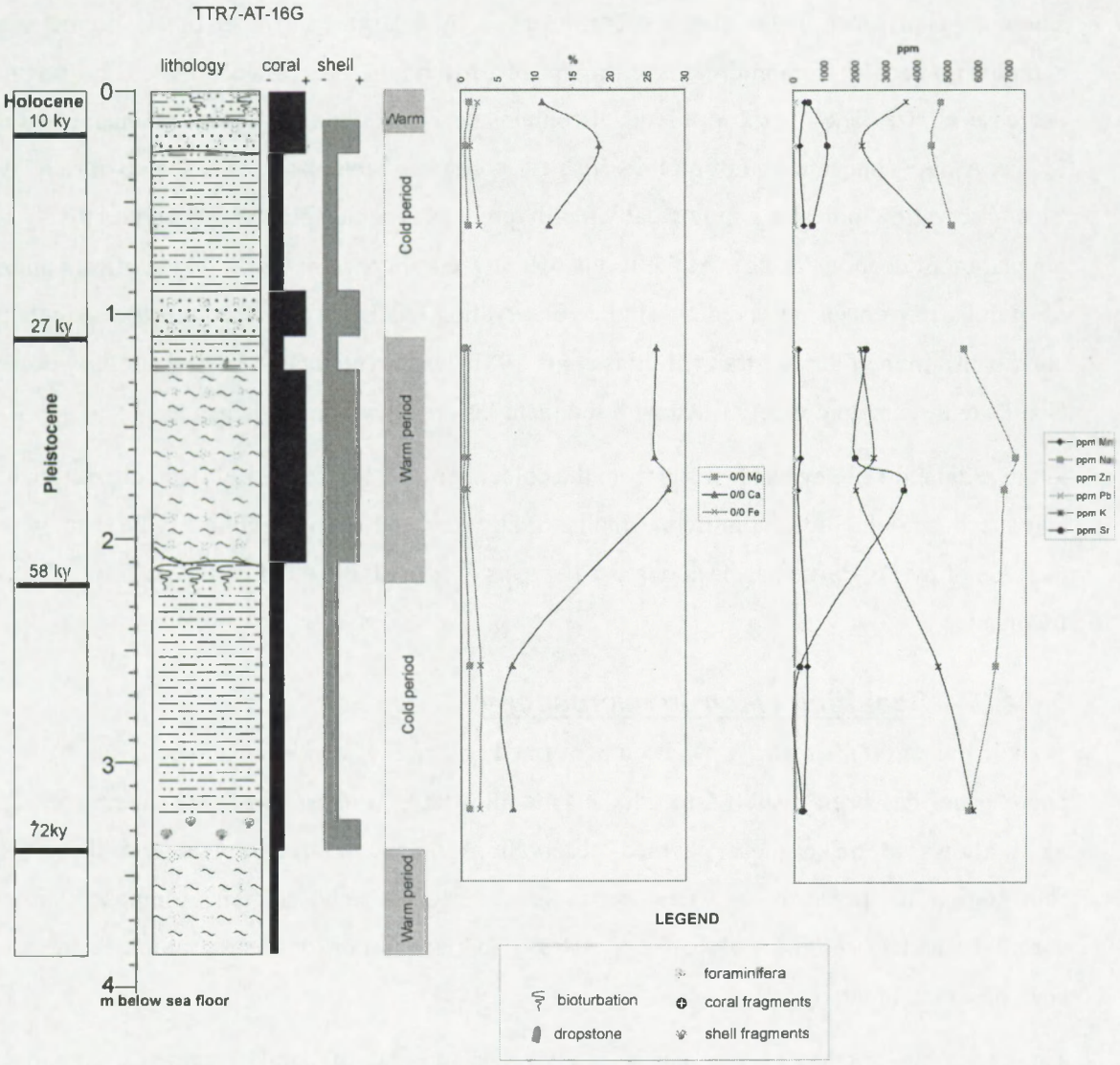

Fig. 5.52: Chemical distribution in TTR7-AT-16G compared with the age and paleo environment model of Saoutkin (1998). The main elements are expressed in %, the trace elements in ppm.

5.4.4.2 Binocular analysis

A first optical analysis of the sediment compounds has been performed by binocular investigation of smearslides. The upper centimeters of the core are composed of coral fragments and quartz grains. A large amount of foraminifera have been observed in these samples of the upper part. Remarkable is the high content of coral fragments in the upper centimeters. Historically, the Porcupine Seabight was a dumpsite of cider during the age of steamers, which explains the high content of coal in the surface layers.

The coral-rich zones in the core are characterized by a large content of bioclastic material as echinoderm needles, foraminifera, shell fragments, fish bones, etc. Downcore the coral fragments decrease in size. The matrix at this level contains coarse-grained large angular quartz and mica grains. A high concentration of otoliths (fish ear bone) has been observed in the coral rich layers. This observation indicates a biologically highly productive area, able to support a relatively large population of deep-water fish. At the levels with low coral concentrations, no significant amounts of otoliths have been observed. A similar observation has been described for the sediments of coral banks in the Florida Strait (Mullins et al., 1981) but has not been reported at other locations. Coral cavities are completely filled with sediment inside the broken branches.

In the sediment-rich levels, deposits from the colder periods (Saoutkin, 1998) are characterized by a reduced amount of foraminifera, smaller grain size and more common reduction, with an increase of pyrite. Pyrite has been observed in tests of foraminifera and in the cavities of the coral fragments.

5.4.4.3 Scanning electron microscopy

Scanning electron microscopy has been performed on stubs, in coral-rich and coral-poor zones. A photo panel has been made (Appendix F.4) to illustrate the most important observations. The SEM allows to make more detailed observations of the matrix content and the possible cementation in the sediment. The matrix is a carbonate-rich sediment composed of many coccoliths and foraminifera (Fig. F.4.1, F.4.8). No cementation or clear solution features have been observed in the matrix.

The carbonate fraction of the matrix is largely composed of corals fragments, foraminifera (benthic and pelagic) and coccoliths. The matrix can be classified as a coccoliths ooze. The most common coccoliths are Emiliana huxley and *Coccolithus pelagicus*. Bundles of aragonite needles have been observed in the matrix (Fig F.4.5). The different needles have a banding in the backscattering indicating growth stadia. The aragonite has been related to the occurrences of corals and is probably a bioerosional product of boring fauna. Approximately 1 μm sized spheres with high backscattering have been observed on the needles (Fig. F.4.3, F.4.4). These spheres are related to the occurrence of bacteria. These bacteria might represent heterotrophic bacteria or might be the Fe-Mn bacteria responsible for the alteration the corals, but this is not investigated.

Around the foraminifera tests and coral fragments some micritic carbonate cement is formed (Fig F4.1.). Dolomite crystals with an euhedral shape of detrital origin (Fig F.4.2, F.4.3). Besides the carbonate and angular quartz mineral, high backscattering and heavy minerals have been observed in the matrix.

5.4.4.4 Cathodoluminescence microscopy

Cathodoluminescence microscopy allows imaging the mineralogical distribution of the sediment and different chemical compositions of carbonate minerals. The microscope used in this study is a Technosyn model 8200 Mk II at ± 20kV with an electron beam of 400 µA. The aim of this study was to find indications for carbonate diagenesis and different phases of precipitation. The luminescence character of the carbonate minerals is depending on the ratio of the luminescence activator Mn^{2+} and the quencher Fe^{2+}. This is on its turn an indication for the environment of carbonate formation.

The carbonates in the thin sections have all a similar brown yellow dull luminescence. The colour is indicative for a high ratio for Fe^{2+}/Mn^{2+} in the carbonate structure. The orange colour of the luminescence indicates a low Mg-carbonate. Dolomites have been observed as reddish luminescence spots in the dull matrix. The dolomite minerals are scattered in the matrix. The carbonates observed on the thin sections are precipitation in marine conditions. Bioclasts have a brighter orange colour than high Mg, low Fe content of aragonite (Fig. F.5.3.G). These observations confirm the marine precipitation of the carbonates. Neither significant diagenetic overprint has been observed nor any indication for *in situ* precipitation of cement. The feldspars are blue in luminescence and suggest a high Ti^{4+} activator of K-feldspars (Fig. F.5.3.H).

5.4.4.5 Petrographic microscopy

Thin sections have been studied with a petrographic microscope in core TTR7-AT-16G and other on-mound and off-mound samples in the area (TTR7-AT-16G 23-24 cm, TTR7-AT-16G-162.5 cm, TTR7-AT-16G 303 cm, ST16, ST38A, ST43A, ST43B, ST44B, ST78B, ST110A, ST116B, ST130B, ST133A, ST134B, ST138A, ST143A, ST166A, ST166B, ST192A, ST196A) (Appendix F.5).

The matrix is composed of micrite-sized carbonates, clay minerals, quartz, mica and feldspars (Fig. F.5.1). This composition is similar in all samples. As observed in the SEM images, the matrix is mainly composed of coccolithoporids. Foraminifera such as pelagic small robust shapes and large benthic foraminifera, are common in the matrix in the coral-rich zones and in the upper

centimeters of the cores. The only difference observed between the samples is the amount of bioclastic carbonate and coarse-grained siliciclastic minerals embedded in the matrix.

Carbonate

The carbonate content of the sediments is subdivided in skeleton carbonates of corals, shell and echinoderm fragments (bioclasts) and non-biological carbonate minerals (Fig. F.5.1). These non-skeleton carbonate grains are dolomite minerals and reworked carbonate sediments or rocks. Dolomite minerals have been observed in all samples. The highest concentrations of dolomite relate to levels with a high siliciclastic content, arguing for an external source.

Skeleton grains as coral and shell fragments are present in the on-mound cores and dominate the coral-rich zones (Fig. F.5.1). Gastropods, and benthic foraminifera are more dominant in layers without large coral fragments. The large coral fragments are bioeroded by boring fauna, which created small holes in the calyx and stem (Fig. F.5.3.C). The rim of the calyx of the corals is characterized by black spots (Fig. 5.3. A, B, E). These black spots inside the carbonate skeletons have been interpreted as bioerosion by encapsulations of Fe and Mn reducing bacteria in the corals (see 2.1).

Authigenic minerals

Inside the coral cavities large clusters of framboidal pyrite have been formed (Appendix F.5.3 A-F). Pyrite has also been observed in the lower parts of the cores, which suggests the formation of authigenic pyrite under sulphate reducing environments, triggered by the available organic matter. Pyrite is more common in samples of the Magellan mound province than in those of the Hovland mound province. Inside bioclasts clusters of framboidal pyrite have been observed in association with carbonate precipitation.

Glauconite has presumably two sources in the sediments (Fig. 5.1H, 5.2 E, F). Authigenic precipitation is inferred inside bioclasts and individual glauconite minerals occur in the matrix of detrital origin. The authigenic glauconitic minerals are formed in reducing environments just below the seafloor under relative slow sedimentation rates. These requirements are fulfilled inside bioclasts and in fine-grained sediments with a high reduction potential.

Reworked siliciclastic minerals

The detrital minerals are angular to subangular quartz and feldspar minerals, heavy minerals and mica's. Most quartz grains are 0.1-0.3 mm in diameter (Fig. F5.2A, B, C). Rock fragments have been observed in several samples, with major minerals as plagioclase, quartz and mica's. These

have been interpreted as rock fragments of metasediments (Appendix F.5.2.D). In the coral-rich zones the siliciclastic minerals are larger than in the fine-grained mud. Bioturbations have clearly been observed in the samples as accumulations of large quartz and feldspar grains.

Summary

Carbonate sediments presently accumulate on the mounds, mixing with quartz and lithic pebbles and cobbles. The non-carbonate mud fraction consists of quartz and in smaller amounts feldspar, mica, kaolonite, pyrite, dolomite, heavy minerals, glauconite and clay minerals. The environment and faunal assemblage of nannofossils largely control the carbonate mineralogy of sediments. The biota found in the carbonate fraction are dominated by planktonic foraminifera, calcareous nannofossils (coccoliths, low magnesium calcite), fine coral fragments (aragonite), gastropods and molluscs, which provided the skeleton carbonate. Corals seem to be the only source of aragonite. It is obvious that three major sediment sources are involved: pelagic, detritic and authigenic sedimentation. The siliciclastic sediments dominate in colder periods. In the transition zones between cold and warm periods, the skeleton fragments increase. The matrix in the coral-rich zones is coarser and the aragonite and calcite content is higher. The sediments are baffled in the coral framework. The coarse reworked sediment implies higher bottom currents winnowing the fine fractions in the framework.

The depositional texture of the sediment, with original components is not bound during the deposition and is mud-supported. This description fits with the definition of wackstone and with that of packstone in more coral-rich layers, in the classification of Dunham's (Tucker and Wright, 1990).

5.4.5 Isotopic analysis

To test the hypothesis proposed by Hovland et al. (1994) for the Hovland mounds (see 2.2.1), several data have been collected to evaluate the potential methane occurrence or the effect of methane on the sediments and organisms (see 2.2). Bacteria feeding on the hydrocarbon energy supply produce carbon dioxide as a metabolite, which can be subsequently precipitate as $CaCO_3$ in the presence of seawater (see 2.2). The authigenic carbonate produced by methane metabolising bacteria carries the $\delta^{13}C$ signature of the petroleum energy source. This will typically be isotopically depleted to normal marine carbonate precipitation with values lower than -25 $^0/_0$ (see 2.2). The first data set is the stable isotopic analysis of core TTR7-AT-16G and the embedded deep-water corals.

5.4.5.1 Isotopic analysis of TTR7-AT-16G

Isotopic $\delta^{13}C$ and $\delta^{18}O$ analyses of 21 bulk carbonate samples through core TTR7-AT-16G have been performed at the laboratory of isotopic geology of the Vrije Universiteit Brussel (Keppens) (Table F.6.1, Fig. 5.53). In the core coral and shell fragments have been sampled at discrete levels. The non-bioclastic samples have been plotted downcore to illustrate the variation in time. A $\delta^{18}O$- $\delta^{13}C$ plot shows the position of the samples in comparison with the normal marine signature in carbonates.

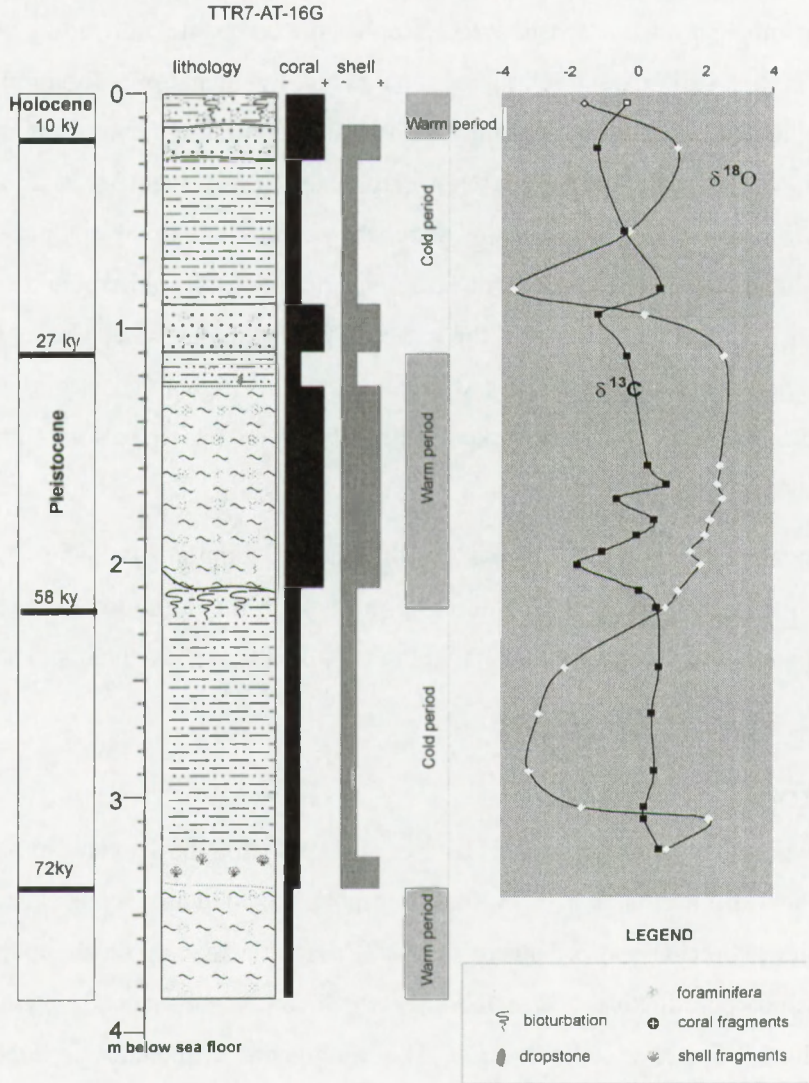

Fig. 5.53: Stable isotopic values of carbonates in the sediment in core TTR7-AT-16G. The variation of δ13C is narrow and positively correlated to the coral distribution. Coral-rich zones are characterized by positive values for δ18O and negative values for δ13C. This illustrates the relative amount of aragonite in the sediment matrix.

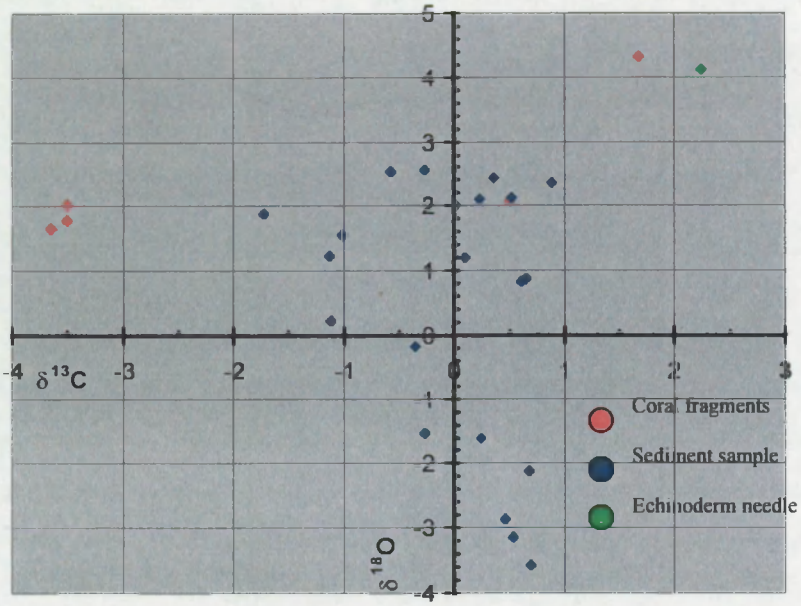

Fig. 5.54. Stable isotope measurements in core TTR7-AT-16G. The sediment samples plotted in a narrow zone for δ13C have a typical marine realm. The positive values for δ18O are a contamination of the aragonite component in the sediment.

The bulk carbonate samples have a relatively large variation in $\delta^{18}O$ (-3.6 to 2.6‰ PDB) and rather stable $\delta^{13}C$ values (mean values of -0.02 ‰ σ 0.73 ‰ PDB). $\delta^{13}C$ values plotted in the marine isotopic signature without indications for methane oxidized carbonate formations.

Variations in $\delta^{13}C$ downcore are due to different contributions in carbonate faunal assemblage in the sediment. The values are more depleted in ^{13}C in coral-rich zones. The coral aragonite is depleted in ^{13}C (Adkins et al., 2001; Blamart et al., 2001; Land et al., 1977; Mikkelsen et al., 1982; Mortensen et al., 2001; Mortensen and Rapp, 1998; Swart, 1983) and appears in the matrix as fine-grained bundles (see appendix F4). This leads to a mixed signature between carbonates with a marine signature (e.g. coccoliths, foraminifera) and a depleted source of aragonite of the corals.

The fluctuations in $\delta^{18}O$ are large in a zone of 4‰. This variation can be due to changes in temperature through time and the composition of the carbonates in the sediment. The isotopic curve of the samples is placed in the age model of Saoutkin (1998) (Fig. 5.53). Warmer periods are characterized by positive $\delta^{18}O$ values. A close correlation could be observed between levels with accumulation of corals and isotopically heavier stages. It is well known that the ahermatipical corals are enriched in ^{18}O relative to equilibrium precipitators of calcium carbonate from seawater (e.a. Land and Lang., 1977). The positive overprint in $\delta^{18}O$ and negative in $\delta^{13}C$ can be explained by the contamination of aragonitic coral fragments in the matrix. A diverse fauna, consisting of forams, coccoliths, shells and corals downcore, indicates a variation in source

of marine water. Therefore the $\delta^{18}O$ values are probably related to the combined effect of water temperature, composition and presence of coral fragments and carbonate clasts.

Five coral branches and one shell fragment have been sampled in the core. The shell fragment at 140.5 cm has a positive $\delta^{13}C$ and positive $\delta^{18}O$. The surrounding sediments are less positive for both parameters. The $\delta^{18}O$ values for the coral fragments are similar for all samples and have a positive value around 2 $^{0}/_{00}$. An exception is formed by the *Madrepora* samples at 67.5 cm, which have similar isotopic composition as the shell fragment. Three samples (97.5, 162.5 and 192.8 cm) have a $\delta^{18}O$ value around -3.5 $^{0}/_{00}$. In zones with coral fragment the $\delta^{18}O$ values in the sediment are similar to the values of the corals. This suggests a control of aragonitic components in the matrix for the $\delta^{18}O$ values. This effect is not seen for the $\delta^{13}C$-values, which might imply that the carbonates in the matrix, mostly coccoliths and foraminifera, precipitated carbonate with a similar fractionation for oxygen isotopes as the corals, but with a different fractionation for carbon. The sediment in the colder period contains less authigenic carbonates and is more dominated by detrital carbonates with depleted values for oxygen. The negative values appear in the transition zones between warm and colder periods where a greater influx of detrital carbonate is expected.

5.4.5.2 Isotopes of corals

Stable isotope analyses have been carried out on ahermatypic corals collected by TV-grab TTR7-24GR in the Belgica mound province (BEL42) and gravity core TTR7-AT-16G, at HOV03. Detailed sampling of the separated coral compounds (polyps, stem, polychaete tubes, surface layers and encrusted bryozoa) was carried out on 14 *Madrepora oculata* (1 living species) and 4 *Lophelia pertusa* corals, 2 shells and 1 echinoderm needle (as reference) for carbon and oxygen stable isotope investigation (Table F.6.2, Fig. 5.55).

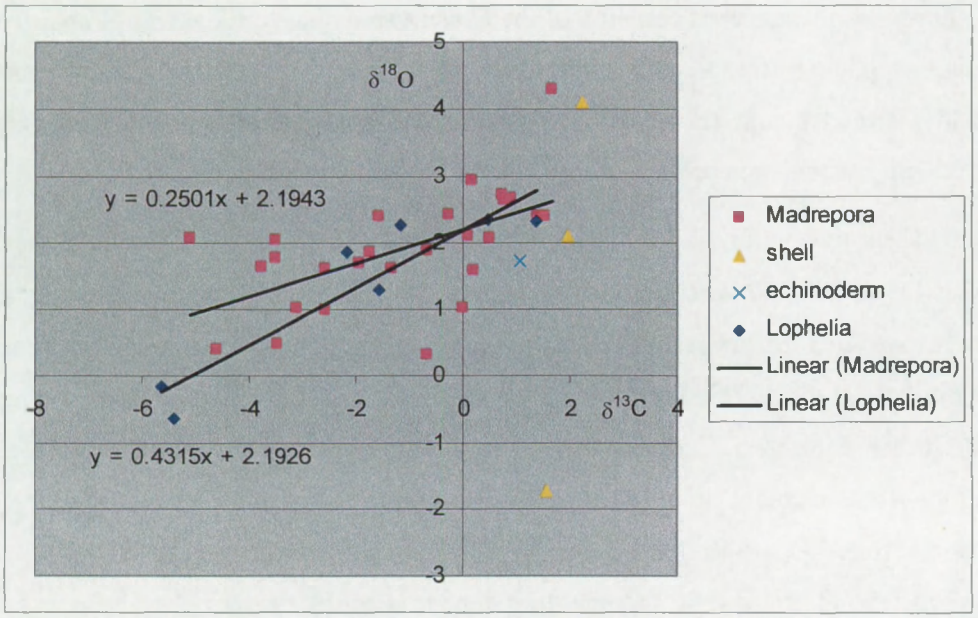

Fig. 5.55: Stable isotopic composition of bioclasts. The linear correlation of the *Madrepora* and *Lophelia* corals has been calculated based on all available data. Other authors also observed the linear connection with a same slope.

Bulk skeleton $\delta^{13}C$ values vary between +1.7 and -5.4‰ (PDB) and values of $\delta^{18}O$ vary between +4.3 and -0.6 ‰(PDB). In comparison with the isotope data of shells and the echinoderm needle, the corals are characterized by higher concentrations of lighter isotopes. The $\delta^{13}C$ and $\delta^{18}O$ values of skeletons show an excellent positive correlation over a 4‰ range for $\delta^{18}O$ and 8‰ range for $\delta^{13}C$. The *Madrepora oculata* measurements show a linear correlation $\delta^{18}O=0.25\ \delta^{13}C+2.19$. The *Lophelia pertusa* samples have a linear correlation $\delta^{18}O=0.43\ \delta^{13}C+2.19$. The positive linear correlation between $\delta^{18}O$ and $\delta^{13}C$ found is in agreement with previous studies on the isotopic composition of *Lophelia* skeleton (Freiwald and Henrich, 1997; Mikkelsen et al., 1982; Mortensen and Rapp, 1998; Swart, 1983; Weber and Woodhead, 1972). This linear correlation $\delta^{18}O=0.43\delta^{13}C+2.91$ is remarkably similar to the results on *Lophelia* corals in the Rockall Trough (Blamart et al., 2001). The isotopic composition of the corals is controlled by the temperature, as normal equilibrium fractionation processes affect the $\delta^{18}O$ values in the skeleton (Swart, 1983; Weber and Woodhead, 1972). Variation in seawater salinity has an affect on the $\delta^{18}O$ value of coral skeletons because the $\delta^{18}O$ of seawater largely depends on the salinity. However, the observed variation cannot be explained by these mechanisms. Mikkelsen et al. (1982) put forward that the slope of the C and O ratio varies with the geographic origin of the specimen and may reflect differences in the organisms' growth response to various types of oceanic conditions.

Swart (1983) attributes the apparent coupling of the C and O isotopes to the effect of absence of photosynthesis, as photosynthesis only affects the O isotopes. In the ahermatypic corals, respiration and thermodynamic fractionation are the only processes affecting C and O and therefore the overall fractionation of the isotopes will be positively correlated.

Within individual specimens large differences in the isotopic composition of separate skeletal elements occur. In general, the variation in $\delta^{18}O$ is less than that in $\delta^{13}C$. Intraskeleton isotopic heterogeneity is explained by differences related to variations in growth rate during the life span of the coral (Emiliani et al., 1978). Those isotopic variations presumably reflect also changes in food supply. The variation in $\delta^{13}C$ (between +1 and -10 $^{0}/_{00}$) in the data set are explained by assuming that the isotopic composition of the skeleton is controlled by mixing between inorganic CO_2 (-7$^{0}/_{00}$) and respired CO_2 (-13.5 to -19.45 $^{0}/_{00}$). The relative contribution of C and O from inorganic and metabolic sources is thought to be controlled by factors that influence the efficiency of metabolic CO_2 removal via diffusion through coral tissues to the ambient seawater (Swart, 1983). An alternative explanation of the offset and large coherent variation in $\delta^{18}O$ and $\delta^{13}C$ from the skeletons of modern deep-sea corals is proposed by Adkins et al. (2001). Their study is based on high-resolution isotopic measurements of recent deep-water corals and proposes a creation of the offset by a mechanism that relies on the thermodynamic response to a biologically mediated pH gradient, across the calcifying membrane. In this case the metabolic fractionation (food) and the kinematic fractionation are minor to this process. This results on microscale in banding of the coral aragonite, with different isotopic values.

The presence of the polychaete *Eunice sp.* seems to stimulate the coral to secrete a surplus of aragonite around the parchment tube of the worm (Fig. F.6.1). These aragonite crossing tubes between coral stems have the same composition of the coral stems and indicate that the mucus is responsible for the formation of aragonite of the tubes (see 1.3). $\delta^{18}O$ values of these crossing tubes are close to equilibrium; $\delta^{13}C$ values show a larger variation. This can be interpreted as a vital effect stimulated by changes in the environment. Parts of the living coral that are not protected by mucus, and dead corals are encrusted by bryozoa. The honeycomb-like bryozoa sheets attached on *Madrepora oculata* and *Lophelia* species show characteristic isotopic values of $\delta^{13}C$ between +1.36 and +1.56$^{0}/_{00}$ and of $\delta^{18}O$ between +2.4 and +2.33 $^{0}/_{00}$. These bryozoa are not affected by the mucus and show a marine signature.

The isotopic analysis for both sediment and organism shows no indication for any relation of methane alteration.

5.4.6 Gas analysis

Two chemical industrial subsurface sampling surveys have been undertaken in the region of the Hovland-Magellan mound province to test the potential seepage of hydrocarbon. In this paragraph the results of the surveys will be summarized and reinterpreted. The results of Hovland et al. (1994) have been summarized in combination with the results of the survey performed by Statoil (Geochemical operations limited, *Statoil (UL) Ltd., Seabed Coring, Porcupine Licence 8/95, Offshore Ireland, 1996, Report No 6096/7)*. During the latter survey a site-specific approach was used in choosing core locations: locations were chosen on the basis of strong indications of gas (wipe-out zone and bright spots) or indications of actual seepage (gas bubbles) on the reflection seismic records. In the area some indications for acoustic anomalies and surface craters have been found but no actual bubble trace are observed. This indicates that passive seepage might occur. A list of geochemical results of both surveys is listed in table F.7.1. From all available data a selection of samples has been made, which have a positive indication for any gas occurrences.

5.4.6.1 Headspace gas

The headspace gas technique analysis has been applied for testing the presence of free hydrocarbon gases in the surface sediments at the time of sampling. This is a useful technique to identify the presence of active gas seeps of relatively large magnitude (see 2.2). The results have been listed in table F.7.1.

The concentrations in all samples are very low and no anomalous samples occur. The range of the lowest methane content is a factor of 2 between the mean and the maximum. Greater differences exist for the propane and ethane: Eight times the mean, but the absolute concentrations are low. Only these samples have been selected for isotopic gas characterization because the concentration of the others was too low.

The Hovland paper reports 20 off-mound, 20 inter-mound and 37 on-mound samples analyzed for gas content. The non-mound areas have a mean value of headspace methane of **6.8** ppm v/v (5-9) and the on-mound value **7** ppm v/v although these values are very variable (2.1-21.9 ppm) (Table F.7.1). The values are all relatively low. The data shows that higher values of methane and other hydrocarbons do not appear to be associated with the higher Total Organic Carbon content (**TOC**).

There is no correlation between the sand content, the methane content and the TOC. No geographic clustering has been reported. The fact that there are no anomalies is not so surprising. Large-scale gas seepages in NW Europe seem to be a rare phenomenon. Microseepage is more

common but more difficult to detect. 90 samples of 266 of the Statoil survey, comprising those with the highest levels of hydrocarbons other than methane, have been submitted to occluded gas analysis in an attempt to identify microseepage.

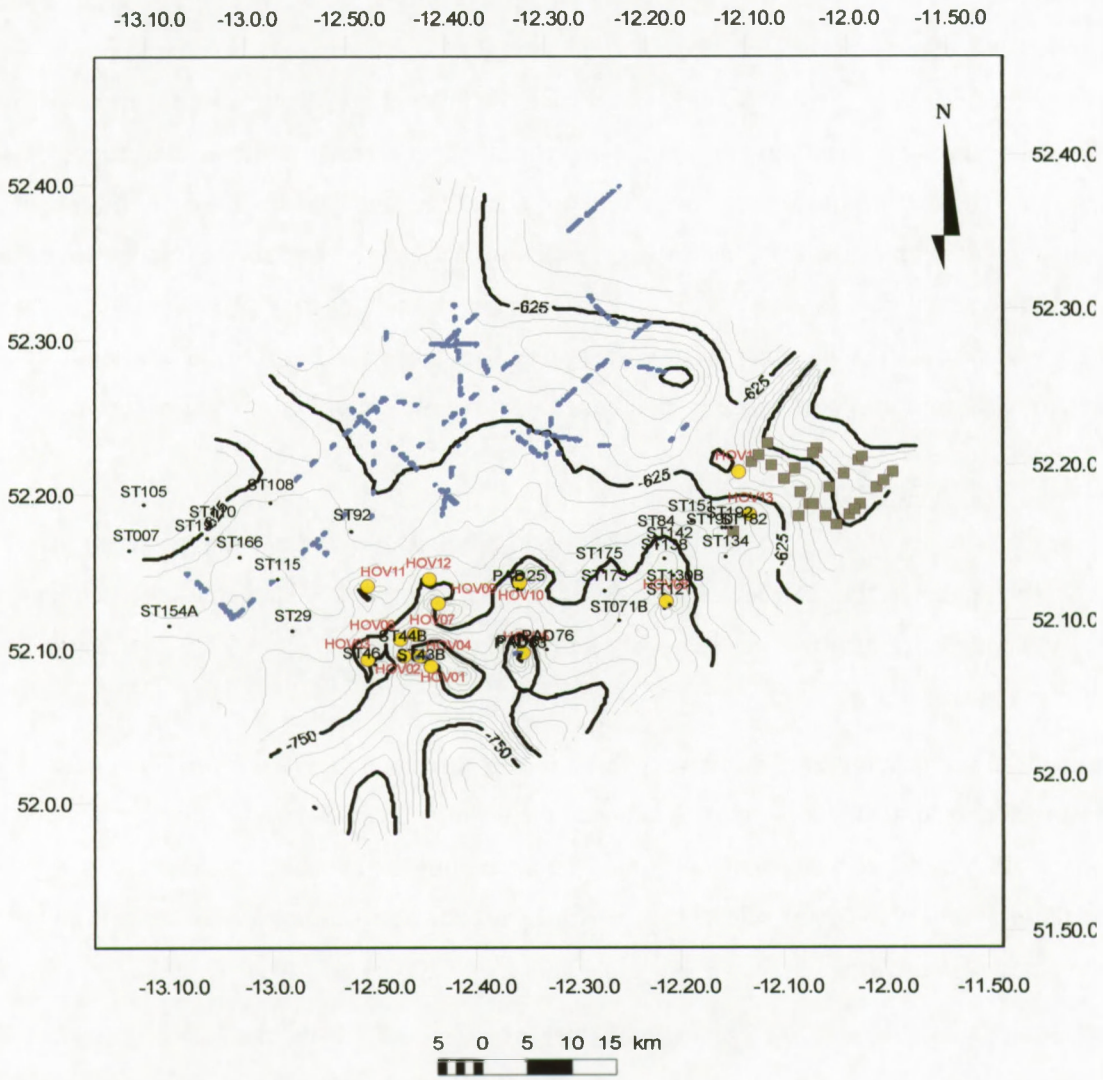

Fig. 5.56: Sample locations of the gas-survey.

5.4.6.2 Occluded gas

This technique takes a known weight of the sediment and liberates gasses trapped in pore spaces by grinding with water in a gas-tight ball mill. The gases so liberated have been sampled and analyzed by capillary gas chromotography. With this technique is it possible to identify small-scale seepage over an extended period of time. This technique is more sensitive than the headspace gas, which detects petroleum rather than biogenic gas seepage. The sum of acyclic saturated compounds from ethane to hexane [Sum sats], the sum of the cyclic compounds cyclopentane methylcyclopentane [Sum cycs] and the sum of cyclohexane [Sum enes] have also been derived from the results. These results are compared with the published data of Hovland et al. (1994) for occluded gas (Table F.7.1)

No obvious anomalies have been detected and the mean values are quite to extremely low. In most of the samples no cyclic compounds have been detected. The highest values of gas content do not cluster in one area and show a random distribution. The highest values of methane have been found in ST139, ST142, ST143, which appear near mound HOV08. In general, the mounds do not show any significant hydrocarbon concentration anomalies.

The results of Hovland et al. (1994) indicate that the propane in the occluded gas of on-mound and non-mound sediment is 0.10 ppm v/v. The methane content of on-mound sediments is 4-5 ppm v/v and in the non-mound 6-7 ppm v/v. Further there was no significant vertical variation in the geochemistry of the cores and no systematic trend in the distribution of the values. These values illustrate the low level of methane and propane in the on-mound samples and the slightly higher values in the off-mound samples. From these results it is clear that the mounds do not show any consistent elevated hydrocarbon concentrations and thus they are not considered to be areas of active seepage.

5.4.6.3 Gas isotopes

The data of Hovland et al. (1994) contains subsamples of three off-mound samples, five inter-mound and four on-mound samples for isotopic measurements. Six samples comprising the highest gas occurrence have been selected for gas isotopic analysis in the Statoil survey.

Prospecting for hydrocarbons, it is often assumed that the carbon isotopic composition can provide information on the origin of gas. This assumption may not be valid for methane carbon isotopes extracted from surface marine sediments because of

- the mixing of gases with multiple origins and
- the alteration resulting form secondary processes.

Examination of a relative large data set by Abrams (1996b) reveals a correlation of methane concentrations with carbon isotopic compositions. Three groups have been defined based on a comparison of molecular concentrations to methane carbon isotopes:

- Type I - small concentrations (<200 ppb) of methane with heavy isotopic (heavier than -45 $^{0}/_{00}$) compositions most likely represent methane that has been altered by bacterial oxidation. The extent, to which the oxidation proceeds, depends on the sulphate-reducing activity.
- Type II - large concentrations of methane (> 1000 ppb) with very light isotopic compositions (lighter than -55 0/00) indicative of biogenic gas represent gas that has been derived either exclusively from a biological process or from a mixture of predominant biogenic gas that has isotopically overwhelmed the presence of migrated thermogenic gas. It would be difficult to determine if thermogenic hydrocarbons are present in these samples.
- Type A - average concentrations of methane with intermediate isotopic compositions may represent migrated thermogenic hydrocarbons. Examination of significant concentrations of higher molecular weight hydrocarbons, can confirm the evidence for thermogenic seepage.

Core number	$\delta^{13}C_1$ $^{0}/_{00}$	Comments
18	-33.6	On-mound samples with wet gas characteristics
25	-34.8	
41	-35.5	
83	-37.7	
12	-37.3	Absorbed gas anomaly samples
13	-37.5	
60	-37.1	Biogenic mix
75	-36.9	
68	-36.9	
2	-37.8	Background samples
88	-37.0	
90	-36.9	

Table 5.4: Carbon isotopic values of gas published in Hovland et al. (1994) for on- and off-mound subsamples. No significant difference is measured between the samples.

The methane concentration of only six occluded gas samples was high enough for additional measurements. The attempts to make isotopic measurements on the heavier hydrocarbon gases were unsuccessful due to low concentrations. Two samples have a definitive biogenic methane signature (142B and 182 A). The four other samples may indicate either exclusively thermogenic gases or mixes with some biogenic contribution (44B, 71B, 142A, 175B). The carbon isotopic

result of methane in the cores presented by Hovland et al. (1994) are -37 $^{0}/_{00}$ for off-mound and inter-mound sample and -34 $^{0}/_{00}$ for the on-mound samples (Table F.7.1). It is worth to notice that these samples were not frozen but corrected for biological activity with 1 $^{0}/_{00}$. This means that the samples can be categorized as type I samples and no conclusion can be drawn out of the results about active hydrocarbon seepage. The results only indicate the occurrence of low methane gas in the cores of biogenic nature. This is quite evident due to the large amount of organic matter in and around the mound.

While this may give some encouragement for the presence of petroleum seepage, it should be borne in mind that the concentrations of gases, on which these measurements were made, were extremely low. Low levels of hydrocarbon gases in shallow subsurface may be derived from a variety of sources and may be affected by a number of alteration processes. These factors may significantly alter the isotopic ratio of C present in the methane to an extent where the differentiation between bio- and thermo-sources becomes unclear.

The samples fit all in type I and a few in type II, indicating biogenic gas. The lack of large concentrations of gasoline-range and higher molecular weight hydrocarbons in the surface sediments reduce the change that thermogenic hydrocarbon migration and leakage is active in this area.

5.4.6.4 Gas chromatography - Mass spectrometry

This technique has been applied to recognize and to identify biomarkers. Most of the samples show evidences of the presence of phenanthrene (m/z 178) and methyl-substituted phenanthrenes (m/ 192). However, these are comparatively simple molecules and does not necessarily indicate petroleum

Therefore the molecules have not been considered to be a reliable evidence of seepage. The substituted nophtalenses are simple and only detected in two samples (121-190) and hence cannot be considered diagnostic. Triterpanes, dibenzothiophenes, sterones and their aromatized derivatives indicate petroleum origin in the samples ST7A, 19B, 29A, 46A, 84A, 92A, 105A, 108B, 115A, 121B, 138A, 142B, 142A, 151A, 166A, 173B, 175B, 190A, 192A.

In addition to the presence of these biomarker species, it is usually expected that the ratios of peak sensitive to thermal processes will indicate the presence of mature, migrated petroleum rather than immature organic precursors. This is often difficult with surface sediments since there is inevitably an immature overprint from the presence of recent organic matter (levels are very

low). The samples with a few indications for possible thermogenic hydrocarbons show no clustering in a geographical way.

5.4.6.5 Carbonate isotopic values

Additionally to the already discussed samples of isotopic values (see 5.4.5), samples have been analyzed with promising seepage results in the geochemistry. Unfortunately, these $\delta^{13}C$ values are common within normal marine carbonates, with no evidence of isotopically light authigenic carbonate.

5.4.6.6 Summary

The observations can be summarized as follows:

- The level of hydrocarbon is extremely low.
- Encountered concentrations of hydrocarbons are quite small. This should be borne in mind when considering the evidence of possible seeps.
- There is no evidence for petroleum seepage on any scale. The absence of visible oil staining or headspace gas anomalies precludes macroseepages.
- Some microseepage evidence has been found in somewhat elevated levels of the higher hydrocarbon gasses.
- The most encouraging samples are subdivided in weak evidence, possible evidence and probably evidence of microseepage. The samples have been plotted on a map with the mound locations (Fig. 5.57). Some of these samples are close to a mound or even on mounds. But most of the samples are lying outside the mound area.

Certainly seepage is not a major phenomenon in this area. The sample density was quite high and well focused on possible conduits to surface. However, if large-scale seepage is an ongoing process in this area, it should have been detected. Microseepage is a more difficult process to confirm. The quantities of petroleum seeping are much smaller, the aerial extent of their influence is much smaller and a number of alteration processes may be active which will disguise or alter the geochemical signatures.

The absence of convincing seepage evidence in this area may be due to a number of factors, including the absence of a petroleum system below the province, the presence of an effective regional seal or unsuitable present-day environmental conditions for the preservation of seepage signatures. The samples were taken on a grid survey with maximum recoveries of 4m. Thus, all

samples have been collected within the aerobic sulphate-reduction zone. This is reflected in the large number of type I samples. It seems that the seepage is not active enough to overcome *in situ* bacterial alteration if active seepage would take place.

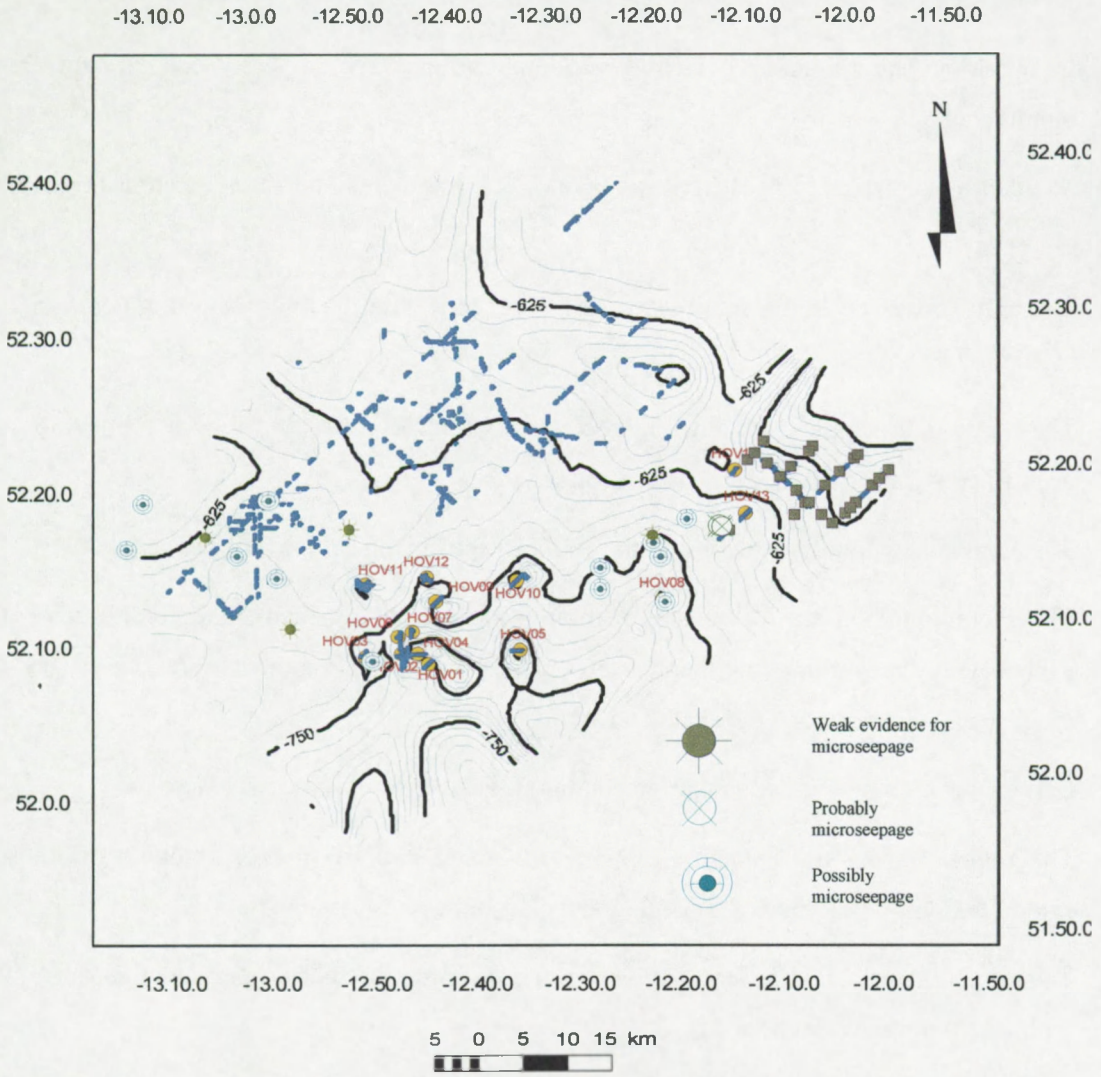

Fig. 5.57: Location map of possible migration sites based on the geochemical survey in the area. No macroseepage is active in the present setting. Only potential sites have been observed. These spots appear sometimes at near mounds but no convincing relation has been observed.

- The off-mound sediment samples contain a Holocene sandy layer overlying Pleistocene bioturbated greyish silty clay with a few dropstone layers and biodebris.
- In the Magellan mound province the sediments have a high water content and are intensely bioturbated.
- Moats are characterized by coarser sediment, rock fragments and slumped coral fragments near the seabed.
- The only observed sedimentary structures are concentrations of rock fragments and levels of bioturbation.
- The on-mound samples contain a large concentration of corals, forming a framework, which has been filled with carbonate-rich coarse sediments.
- The coral concentration is highest in the Holocene sediments and in warmer periods.
- The biota found in the carbonate fraction is dominated by planktonic foraminifera, calcareous nannofossils (coccoliths, low magnesium calcite), fine coral fragments (aragonite), gastropods and molluscs, which provided the skeleton carbonate.
- Carbonates are precipitated in marine conditions (isotopic analysis, microscopy).
- The non-carbonate mud fraction consists of quartz and in smaller amounts of feldspar, mica, kaolonite, pyrite, dolomite, heavy minerals, glauconite and clay minerals.
- The mineral distribution reflects a high terrigeneous input in the cold period and coarse quartz grains with carbonate in warm periods.
- Three major sediment sources are recognised: pelagic (coccolith ooze), reworked sediment from the basin and a low amount of authigenic mineral precipitation (pyrite, glauconitic, carbonate).
- Seepage is currently not a major phenomenon in this area.

5.5 Biological results

In the Hovland mound province the biological zonation of HOV02 (Propeller) mound has been investigated with a video transect, recorded during the TTR7 cruise, and box cores, collected during TTR7, TTR8 and Poseidon 265 cruises. Two dredge hauls, performed on HOV10 and HOV12, have been studied onboard by biologists (Sumida and Kennedy, 1998). The biological descriptions of these samples have been used in this discussion.

5.5.1 Biological zonation

5.5.1.1 Introduction

The TTR8 video line has been sailed in a general NE-SW direction in the central part of the Hovland mound province crossing HOV02 in the south and HOV07 in the north. These mounds are located on the western side of the central depression.

The footage of the interpreted video transect confirms the detailed biozonation descriptions of the deep-water coral reefs offshore Norway (Freiwald and Henrich, 1997). The quality of the images does not allow detailed analysis of the benthic communities in the different zonations on the mounds. Nevertheless, this video has been used to map the occurrences of dead and living corals, and sediment features in relation to geomorphological structures recognized on the seafloor map. Four zones have been distinguished along the track and mapped in Fig.5.58.

- Normal fine-grained **bioturbated sediment** with dropstones on top. This zone represents the common seafloor in the Porcupine Seabight. Mainly polychaetes are responsible for the bioturbation of the seafloor (Scoffin and Bowes, 1988). Remarkable is the high density of echinoderms on the seafloor between the mounds. Occasional fish have been observed in these sections of the TV-profile.

Three zones refer to the occurrences of deep-water corals:

- **Living coral zone**: This zone is characterized by living coral colonies of *Lophelia pertusa, Madrepora oculata* and *Desmophillum cristagalli* corals. The coral thickets in these zones are up to 50 cm high and are relatively dense. The observation of the colour of the corals from box core and dredge samples in the area suggest that *Madrepora* is orange-red and

Lophelia pale rose. *Madrepora* corals dominate on the footage. In the lower part dead corals were seen, that function as a substratum for later settled corals and, which gets filled with sediments.

- **Dying coral zone**: this zone is characterized by dead coral constructions, observed on the seafloor. This dead framework is partly buried and infilled with sediment. The faunal assemblage attached to these degraded and dying framework comprises corals, *Octocoralia* and a few sponges as far as can be inferred from the video.

- **Coral rubble zone**: dead coral largely filled and buried with sediments characterizes this zone. No obvious macrofauna life besides some Echinoderms and coral fragments is observed.

The recognized zones have been plotted on a profile along the video line and mapped on top of the bathymetric map (Fig. 5.58 Fig. 5.59).

5.5.1.2 Results

In the southwestern part of the video line, bioturbated sediment has been observed, with no other seabed features. Echinoderms, sea pens, shrimps and fish have commonly been observed. Further to the north, this facies grades into a moat structure on the eastern flank of the southern spur of HOV02, without any change in the biozonation. In the moat, more dropstones appear.

The transect climbs on the southwestern flank of the southern spur of HOV02, which is characterized by a lot of sediment-filled coral fragments. The transect continues on the southeastern flank of the southern spur and changes in a downslope direction over a dying coral zone to living a coral zone, again to bioturbated sediment at the foot of the mound. The living coral zone has only been observed over a short distance on the eastern upper slope. The boundaries between the different coral zonations are sharp . *Octocorallia* have frequently been observed in the dying coral zone.

The bioturbated sediment connects the southern spur with the central summit of HOV02 along the transect. The profile climbs steeply on the eastern flank to the central summit of HOV02. On the upper part of the southeastern flank the profile crosses coral rubble and a dying coral zones. Near the summit, the profile changes direction. Sediment is observed on the summit. This suggests that the mounds have only a living coral cover on the upper flanks. The profile descends on the

southern flank of the eastern spur of HOV02. On this flank a symmetric pattern of coral rubble, dying coral zone and coral rubble has been observed along the upper part. The dying coral zones is relatively large. This suggests that corals densely colonized this flank. On the lower flank the sediment dominates and the profile continues in the surrounding sediments.

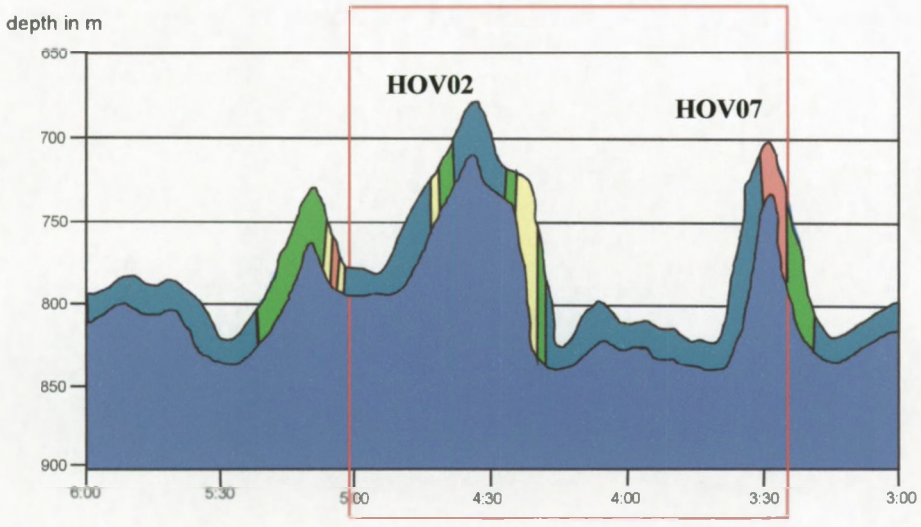

Fig. 5.58: Footage of the different zonations mapped on the profile along the video transects. The red square indicates the detailed bathymetric map of Fig.5.59.

Normal sediment separates HOV02 and HOV07 in the north of the video transect. The profile climbs on the southern flank of the mound before crossing a small moat with dropstones on the surface.

HOV07 is crossed by the profile on the southern flank, which changes direction near the upper flank to the northeast. Remarkable is the sharp boundary between sediment and the living coral zone at the southern side. The living coral cap appears on the summit, which gently dips to the north and the upper slope of the northeastern flank of the mound. In the middle slope the living zone changes into a dying zone. On the lower flank and a moat normal sediment facies appears.

5.5.1.3 Biological zonation based on boxcore samples.

Many subsurface cores have been taken around HOV02 (Fig. 5.59). To the author's knowledge, no biodiversity analysis has been performed on the samples of the Hovland mound province. The samples have been interpreted by coral occurrences and the onboard biological analysis of the associated fauna. The subsurface samples are indicating corals living or dead (Table 5.4, Fig. 5.59).

The box cores and dredges taken during the TTR7 cruise on mound HOV 10 and HOV12 yield many dead coral fragments and living corals beside echinoderms, like sea urchins. The dead coral was extremely colonised by bryozoa, Porifera, hydroids, octocorals Ascidiacea, serpulide, zoanthids, crionoids and bivalves (Sumida and Kennedy, 1998). Most of the reported species are suspension feeders. These organisms may take advantage of the higher settlement and currents sweeping around the mounds. In general, in these samples the amount of *Madrepora* is larger than that of *Lophelia*.

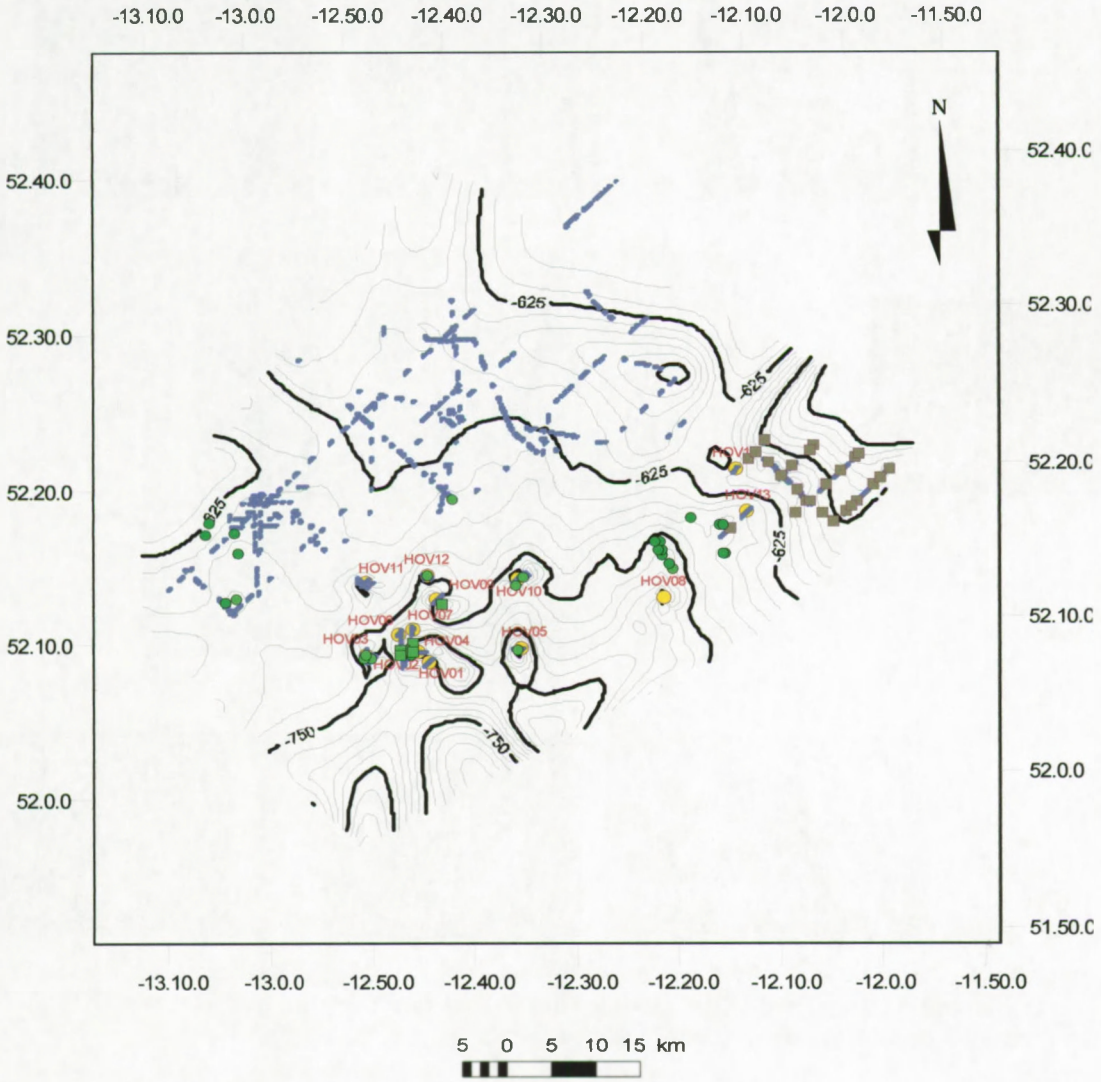

Fig. 5.59: Bathymetric map of the Hovland-Magellan mound province indicating the mound facies (purple) and the surface and buried Hovland mounds. The green squares (box cores) and dots (gravity cores) represent subsurface samples yielding corals.

During the Poseidon cruise 265 seven box core samples have been taken on HOV02 to illustrate the observed biozonation on the video track. A reference core is taken in the eastern part of the area of interest and confirms that the sediment is fine-grained and bioturbated by *Polychaeta* and *Crustacea* (Freiwald et al., 2000). Some polymictic dropstones have been found on the surface of these box cores. Five cores have been taken on the mound; the exact location has been plotted together with the video line interpretation on the bathymetry of the region (Fig. 5.60). Two box cores have been taken on the summit of the mound which yielded dead coral, clogged in sediment.

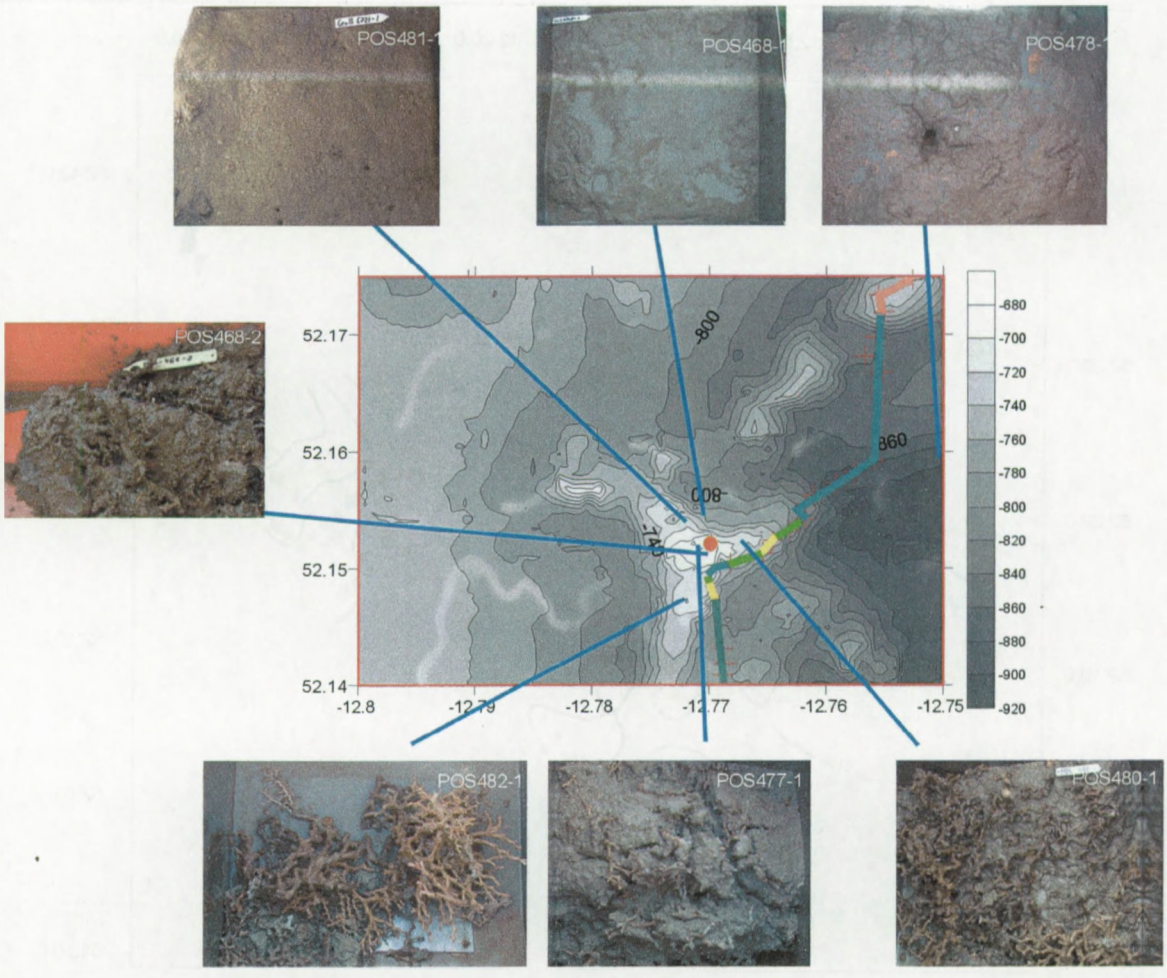

Fig. 5.60: Biozonation interpreted on the TV-video line plotted on the detailed bathymetry of HOV02. The box core samples confirm the observations of the video line.

Only a few living polyps have been observed on the summit of the spurs of HOV02. *Madrepora* is more abundant than *Lophelia*. These box cores have the characteristic of the dying coral zone compared to the biozonation descriptions. On each spur of the mound box cores have been taken to test the general distribution of the biozones. The box core on the most southern spur recovered living *Lophelia* and *Madrepora* species. No sediment was recovered, which confirm the presence of living coral zones as observed in the video transect. On the eastern flank a large dense dead and living coral framework was sampled in sediments. On the northern flank only sediments have been recovered in the box cores. On the seismic profiles, it has been observed (Fig. 5.18) that the northern flank got partly buried by sediment. One of the box cores on the northern flank hit the moat of the mound and yielded dropstones and a sandier upper layer. The dominance of sediment on the northern flank suggests a high sediment pressure on the western and northern side of the mound, as observed in the seismic profiles.

Freiwald et al. (2000) identified four species of Scleractinia corals and one calcifying hydrocoral in the samples: *Desmophyllum cristagalli, Flabellum macandrewi, Lophelia pertusa* and *Madrepora oculata.* The only calcifying coral *Stylaster gemmascenss* is found on the summit of HOV02. On a neighboring mound HOV10, in a dredge haul, one individual of a fifth coral species, belonging to the family of *Caryophyllidae,* has been observed. In the same dredge also *Flabellum* has been observed besides the most common corals *Madrepora* and *Lophelia.*

Additionally, three dredge hauls have been taken on the three spurs during the Poseidon cruise (Freiwald et al., 2000). Most of the corals are recovered on the southern spurs in accordance to results of the video transect and the box cores. No sediment has been recovered in these samples, which suggests a dense coral framework.

In the two dredges taken on the summits of HOV10 and HOV12 a similar fauna, living coral and large dead coral frameworks have been observed (Kenyon et al., 1998).

In the transition zone in between the mounds bioturbated sediment has been observed. Apparently the bioturbation is performed by echiurans, Ceriantharia and caridean or thalassinean shrimps, which have been observed in the surface sediments (Sumida and Kennedy, 1998). Sea pens are frequently observed organisms on the seafloor. Other visible epifauna included echinoids and holothurians. In general, all these species are common in deep-sea sediment environments.

Near the mound, cobbles and boulders appear on the sediment surface. These have been observed in the depression just in front of the mound and have been interpreted as moats, scoured by currents. These dropstones are used by juvenile coral as substratum as observed in a dredge sample during the TTR7 cruise AT8D on HOV12 (Kenyon et al., 1998).

In general, the amount of living coral increases towards the upper flank of the mound. On the video line, living coral zones have been observed on the eastern upper flank on the northern spur of HOV02 and on the summit of HOV07. These flanks face a local depression, while on the opposite site the mound is more buried with sediments. This suggests that the healthy corals are located on the steep flank facing the local depression, with less sedimentation stress than on the other flanks.

The coral thickets on the mounds show a patchy distribution, separated by dead coral and sediment. Large amounts of dead coral and only few patches of living healthy coral have been recovered in the box cores. In the lower slope of the mound HOV02 and in many samples of

other locations dead coral framework is observed filled with sediments. The cavities of the coral framework are filled with silty clay, as the surrounding sediments. The baffling and trapping of sediments by the coral framework will strengthen the build-up. In zones where the sediment supply is high enough to fill completely the coral framework, the slope become gentle due to baffling and draping of sediments. If the currents are strong enough to keep the sediment in suspension or when the sediment supply is reduced, the coral framework stays exposed or grows in pace with the trapping and baffling of sediments in the framework. Such flanks of stacked coral colonies create steep slopes on the upper mound flank. The dominant framework builders are *Madrepora* and *Lophelia*. Besides these common deep-water corals some rare coral species are found, which are not important for the construction of the buildup (*Desmophyllum* and *Stenocyathus vermiformis*).

The summit of the HOV02 consists mostly of sediment and dead coral fragments. It seems that a kind of rim of living corals is formed on the upper slope. A few new settled juvenile corals have been observed of the dead coral structures on the summit.

- Living corals have been observed on the upper slopes of the mounds. They form a living rim on the upper slope.
- Mound flanks facing depressions and stoss sides are more densely colonized by living corals. The leeward sides of the mounds are dominated by sediment.
- The sediments in the lower part of the mounds fill the coral framework.
- The main framework builders are *Madrepora* and *Lophelia.*
- All observed species are common in the deep-sea.

5.6 Oceanography

In the framework of the EC 5th Framework projects, ECOMOUND and ACES, 12 CTD profiles have been recorded in the Hovland mound province around HOV02 (Propeller mound) and one mooring has been deployed in the vicinity (Freiwald et al., 2000).

CTD	Date	Latitude	Longitude	Maximum depth	Cruise or reference
1	17/09/2000	52°12.019	12°41.895	815	Poseidon265
2	17/09/2000	52°08.357	12°46.257	786	Poseidon265
3	17/09/2000	52°08.370	12°46.576	796	Poseidon265
4	17/09/2000	52°08.432	12°46.684	805	Poseidon265
5	18/09/2000	52°08.315	12°46.185	802	Poseidon265
6	18/09/2000	52°08.186	12°46.031	849	Poseidon265
7	18/09/2000	52°08.091	12°46.605	833	Poseidon265
8	24/09/2000	52°08.436	12°45.454	884	Poseidon265
9	24/09/2000	52°09.436	12°45.674	853	Poseidon265
10	24/09/2000	52°09.192	12°48.037	737	Poseidon265
11	24/09/2000	52°08.886	12°46.119	772	Poseidon265
12	24/09/2000	52°08.793	12°46.612	799	Poseidon265
13	25/09/2000	52°08.973	12°46.704	794	Poseidon265

Table 5.4: CTD profiles taken in the Hovland mound province

The location of the CTD profiles is listed in table 5.4 and plotted on the bathymetric map (Fig. G.1). The oceanographic characteristics have been illustrated in Depth-Temperature, Depth-Salinity and Temperature-Salinity plots (Fig. 5.61). The density of the water mass has been calculated from the temperature, depth and salinity measurements. This calculated density is plotted together with the salinity and temperature to identify the different water masses (Fig. 5.61). In addition, virtual profiles have been made with the available CTD data crossing HOV02 in NW-SE, NE-SW direction (Fig. G.2, G.3) and a profile containing all CTD profiles (Fig. 5.61). These profiles illustrate the vertical and lateral distribution of the water masses around the mound. Temperature and salinity maps have been gridded through depth (Fig. G4, G.5). In this way, the horizontal and vertical distribution of the temperature and salinity around mound HOV02 has been illustrated.

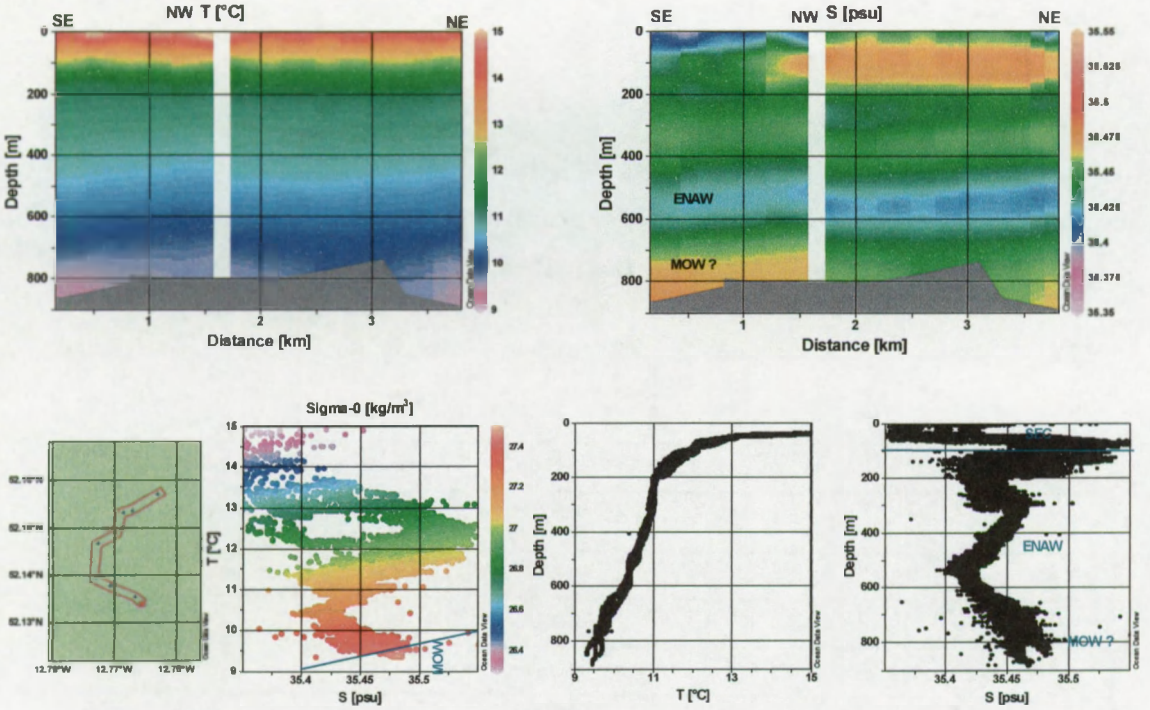

Fig. 5.61 CTD plots and water masses characterization of all available data around HOV02. Temperature and salinity profiles are gridded to show the variations around the mound. Salinity-Temperature-Density plots and an overall scatterplot of temperature (t) and salinity (s) indicate the variation in the data and the water mass characteristics.

The temperature and salinity trend with depth is similar for all CTD stations but varies in absolute values (Fig. 5.61). Because all CTD profiles have been recorded with the same equipment in a time frame of seven days, it seems unlikely that the drift of the sondes influenced the data in that way (see 3).

The temperature-depth curve decreases with a large gradient from the surface temperature to the seasonal thermocline at about 50 m. Below the thermocline the temperature curve decreases slightly to the bottom temperature of 9° C. Around 600 m water depth, another break in the temperature curve has been observed. The temperature range of these values is larger than in the water depths above.

The salinity curve has a more complex course. In the upper 100 m of the water column the Salinity-Depth plot shows a large variety probably due to the mixing of water masses near the sea level. Around 100 m the salinity reaches a first maximum in a wide value range. Below 100 m the salinity decreases till 150 m to increase again to a local maximum around 300 m. From this point onwards the range of values are narrower and the salinity decreases till 550 m, where the

minimum values are recorded. Around 550 m water depth the curve shows a sharp break and increases again in a wider values range.

The upper 50 m is interpreted as the SEC (see 2.4) due to the large variation of the values in salinity and high temperature. Blow the SEC the water mass has the characteristic of ENAW (high salinity and lower temperatures, see 2.4) down till the salinity minimum around 500-550 m. At this depth level the salinity increases and the temperature decreases slowly. Most probably this effect is due to the presence of the MOW, which creates a higher salinity. Nevertheless, in the Salinity-Temperature-Density plot the lower datapoints reach the MOW characteristic values nearly (Fig. 5.61, G2, G3). This observation might suggest that the salinity increase is a boundary effect between the MOW and ENAW. The variation in temperature and salinity at this depth might be due to mixing of these two water masses.

The profiles crossing the mounds show the distribution of temperature and salinity on different flanks of the mound (Fig. F.2 and F.3). On the profiles it is clearly observed that a second salinity core occurs below 180 m water depth in the northern side of the mounds. The first core is related to the SEC and the second only appears on the northern side of the mound. On the southern side of the mound, the bottom water mass has a higher salinity and a slight increase in temperature compared to the northern side of the mounds. In the knowledge that the currents are flowing northwards at these levels (see 2.4) it seems that the more saline water masses arrived at the southern side of the mound and are not observable anymore on the northern side. The source for the second salinity core is unknown, but it may be an indication of an interaction between two separate shelf edge currents on either side of the Seabight (Freiwald et al., 2000).

From the data set, temperature and salinity surfaces have been gridded on several depth levels (100, 250, 500, 600, 700 and 800 m) to illustrate the vertical and horizontal distribution of the temperature and salinity. The variation in the upper layer is due to wave movements and mixing. At 100 m water depth a clear difference has been observed in the salinity values between the northern and southern side of the mounds. At 250 m this effect is still visible but less expressed than at 100 m. A second variation between the two flanks of the mound is observed at 700 and at 800 m water depth. The southern side is more saline and has a higher temperature than the northern flank. This indicates warmer and more saline water at the southern side of the mound. This might be induced by the interaction between ENAW and MOW. It seems that the influence of the MOW is greater on the southern side than on the northern side of the mound. This oceanographic depth level fits with the depth range of the largest mounds (see 5.2).

To evaluate the possible influence of enhanced currents by internal wave breaking, the critical slope is calculated from the parameters of the CTD (see 2.4.3.1). The calculations have been performed for a depth of 700 m, which is the average depth of the mounds and the level of the salinity anomalies. In this depth range also slope breaks and channels have been observed on the bathymetric map. The needed parameters have been calculated from the CTD data. The density gradient and the density has been calculated for the water mass near the coral banks and included in the formulae (see 2.4.3.1). The density gradient is taken for an interval from 600 m (10.15° C and 35.43 psu) till 800 m (9.3° C, 35.46 psu (practical salinity units) and the calculation has been performed for a 700 m water depth with a density of 1029.7 kg/m^3. Coriolis frequency for that latitude is 1.115*10^{-4} s-1 and the semidiurnal frequency is 1.405*10^{-4} s^{-1}. The theoretical critical slope for this depth interval and region is **3.1°** or a slope gradient of 0.0536.

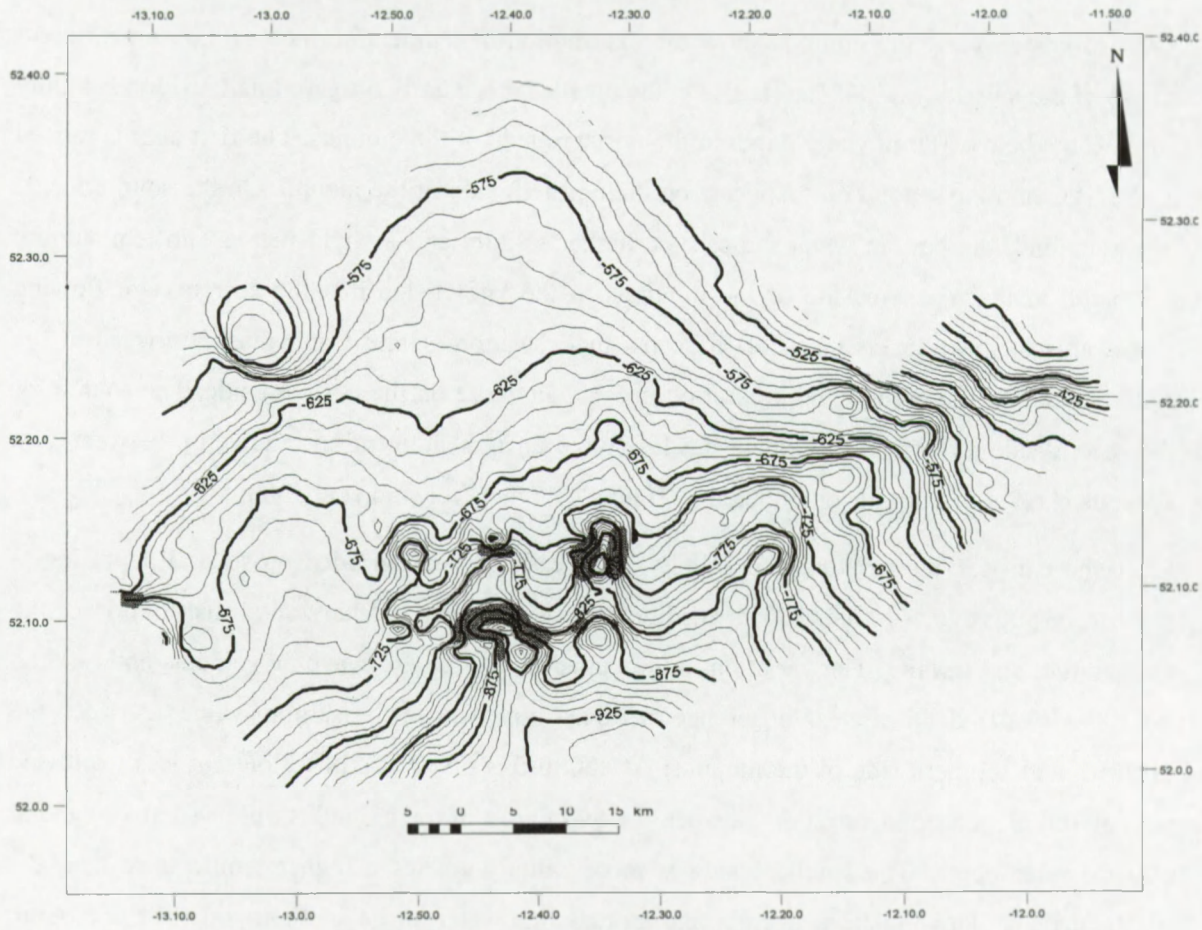

Fig. 5.62: Seafloor map with slope angles exceeding 3°, or potential sites for internal wave breaking, created by the density inversion.

This critical value is marked on the seabed map based on the seismic profiles (Fig. 5.62). The zone exceeding 3° is marked in grey. These zones might be theoretical potential sites for breaking of internal waves. Because these zones are isolated and small, the change is rather small that it is a still ongoing process. No real indications for enhanced currents could be deduced from the sidescan sonar images (see 5.2).

The same exercise is applied to the erosional surface or base of the mounds with the same parameters. In this map the zone exceeding 3° is larger and fits with the channels, filled with cut and infill sediment related to high current regimes.

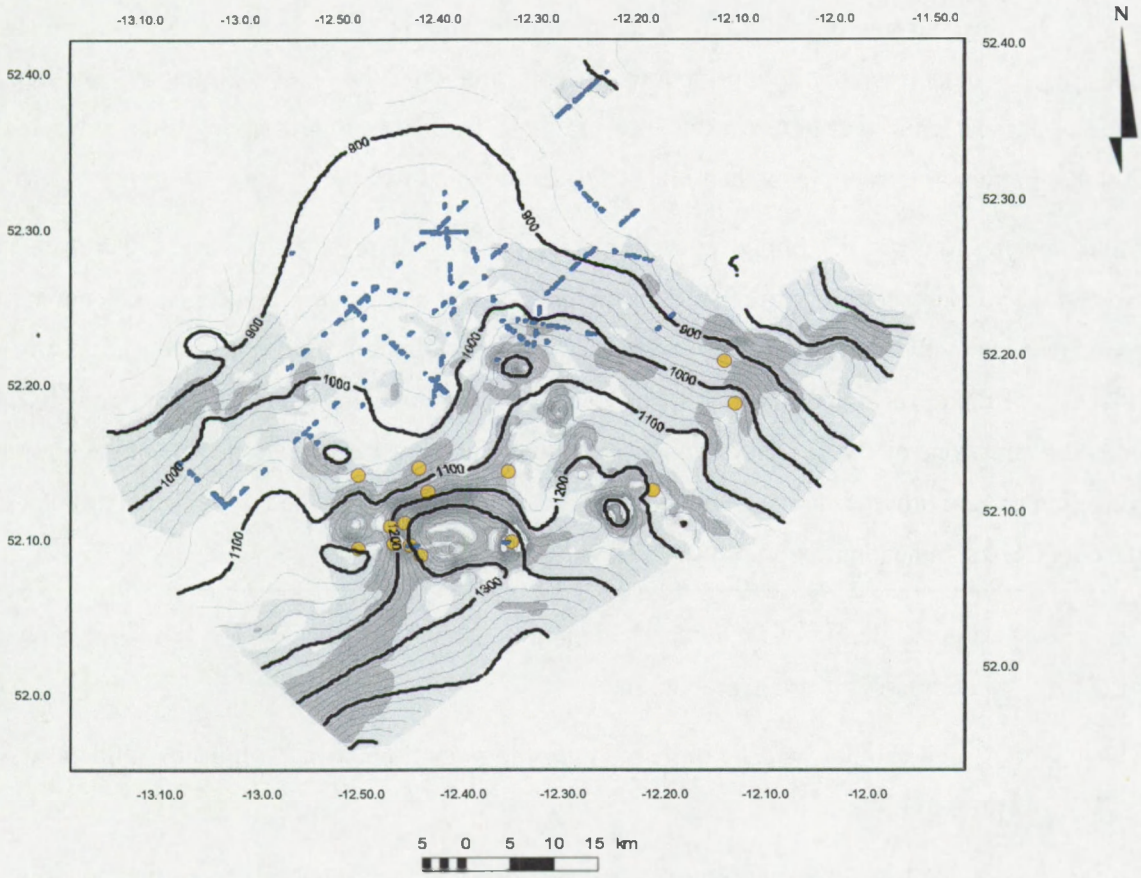

Fig. 5.63: Time structural map of reflector R4. The mound base with slope angles exceeding 3° is indicated in grey. These sites are potential sites for internal wave breaking (the most northern Magellan mound is lying outside this potential zone). The mound distribution is plotted on top of this map.

In the Hovland mound province NS trending channels have been observed without upslope extension on the eastern flank nor in the central part (see 5.1, 5.3). These channels are less expressed in the bathymetry than the alongslope channel in the Belgica mound province. The shape and geometry of the channels argue for a northward, upslope current scouring. A second argument for bottom currents is the well-developed moats located around the coral banks. Inside the moats local coarse-grained sediment and dropstones have been observed, indicating stronger current speeds than those in the surrounding fine muddy sediments. The moats have no preferential deep side. Current measurements (New et al., 2001; Rice et al., 1991; White, 2001) and textural analysis of sidescan sonar images (Huvenne et al., in prep) indicate that the currents are less stable in direction and speed than in the Belgica mound province. Rice et al. (1991) suggest for this reason a turning of the mean northward current to the south-southwest alternated with periods of northward flowing bottom currents following the local topography. The depth level of current induced features in the Hovland mound province ranges approximately between 700-900 m, the same depth level than in the Belgica mound province.

More upslope towards the buried coral banks of the Magellan mound province there are no indications for any bottom current regime in the present bathymetry. The only indication for present current activity in the central part of the Magellan mound province is a reduced sediment thickness of the upper unit and a slight bathymetric depression. This feature lays in line with the central depressions of the Hovland mound province. The coral banks piercing the surface in the Magellan mound province are surrounded with moats with a deeper side on the southern flank of the coral banks, indicating for a northward flowing current.

- Large scattering of the temperature and the salinity might indicate vertical mixing of water masses near the seabottom.
- A high salinity layer is observed near the seabottom, which might be influenced by the MOW.
- The high salinity water mass is best expressed on the southern flank of the mound.
- At the present seafloor the potential sites for internal wave breaking are restricted to the steep slope of the seabed depressions.
- Potential sites for reflection of internal waves at the mound base have a broader extension and might influence the entire mound province.
- Inferred current directions are variable in time and direction and suggest a tidal influence.

6 Discussion 317

6.1 Present setting 317
6.1.1 Coral bank distribution 317
6.1.1.1 Surface coral banks 317
6.1.1.2 Buried coral banks 318
6.1.2 Coral bank geometry 318
6.1.2.1 Circular banks 318
6.1.2.2 Elongated banks 319
6.1.2.3 Sediment pressure 319
6.1.3 Framework builders 319
6.1.3.1 Associated fauna 320
6.1.3.2 Site specific associated fauna 320
6.1.3.3 Microhabitat 321
6.1.3.4 Sponges 321
6.1.3.5 Bioeroders 321
6.1.3.6 Distribution of living corals 322
6.1.3.7 Baffling of sediment 322
6.1.3.8 Zonation 323
6.1.4 Oceanographic environment 323
6.1.4.1 Origin of MOW 324
6.1.4.2 Nutrients 325
6.1.4.3 Model of the present 326
6.2 Initial coral bank development and triggering 327
6.2.1 Paleo-environment before the coral bank initiation 327
6.2.1.1 Contourites 328
6.2.2 Coral bank base 329
6.2.2.1 Dating 329
6.2.2.2 Origin of the erosion 329
6.2.2.3 MOW in the past 330
6.2.3 Internal structure of the coral bank 330
6.2.4 Coral bank triggering 331
6.2.5 Coral bank development 332
6.2.5.1 Start-up 332
6.2.5.2 Catch-up 335
6.2.5.3 Keep-up 336
6.2.5.4 Give-up 336
6.2.5.5 Evolutional Stadia 336
6.3 Are coral banks related to seeps? 338
6.3.1 Critical evaluation of the models 340

6 Discussion

In the previous chapters the setting, morphology, sedimentology, biology and oceanography of the large coral banks in the Porcupine Seabight have been described. The description is comparable to the definition of other coral banks in the North Atlantic Ocean (Cairns and Stanley, 1981; Hovland et al., 1998; Pratje, 1924; Reed, 1992; Stetson et al., 1962; Teichert, 1958) (see 2.1). As described in literature, azooxanthellate coral banks (Table 2.1) consist mostly of a coral framework supported by sponges (Freiwald et al., 1999), with biogenic material and terrigeneous mud infill. In this case, this definition is applicable to the upper meters of the structure. The core nor the base of the coral banks has been sampled and hence the internal build-up of the corals banks could not be retrieved. Nevertheless, indirect indications argue for a biological build-up of the mounds in analogy to the other coral banks in the North Atlantic Ocean.

In the following paragraphs the present-day setting and environmental controls of the development of the coral banks will be discussed. This will be combined with the observations and indications for the paleoenvironment in the initial period of development of the coral banks, to end up in a model for the genesis and development of the coral banks in the Porcupine Seabight. In a third part the existing models of hydrocabon linkage and the coral bank development are discussed in view of the newly acquired data.

6.1 Present setting

6.1.1 Coral bank distribution

The coral banks occur in two restricted geographical provinces: the Belgica mound province, located along the eastern slope, and the Hovland-Magellan mound province, located more to the north in the central part of the Porcupine Basin. These two areas are characterized by local strong bottom erosion (See 4.1, 4.7, 4.10, 5.1, 5.6). Contour currents created in the Hovland mound province NS channels, merging in an amphitheatre-like depression.

6.1.1.1 Surface coral banks

In general, the surface coral banks are located along steep channel flanks, in zones with reduced sedimentation. The reduction of the sediment around the coral banks is probably a combined effect of the presence of the mound, creating turbulence in the water column, of slope gradients in the underlying structures, and vigorous currents in the channels.

The depth distribution of the largest coral banks indicates that the coral banks have a preferable depth range between 700-900 m in both provinces. The height distribution illustrates that most of the coral banks have a similar height at a certain location, arguing for a local controlling factor in the mound development.

The most favourable locations in the Belgica mound province are situated on the steepest slope in the central part of the province and in the Hovland mound province at the northern tip of the NS channel D2.

6.1.1.2 Buried coral banks

The buried coral banks appear on a gentle seafloor morphology without clear surface expression in the present bathymetry. These coral banks are located in zones with a high sedimentation rates, of the embedding sediment (Be and He). The buried mounds are located further away from the seafloor channels and depressions.

The buried Belgica mounds have a broader depth occurrence and are more abundant in shallower depths around 600 m. The buried coral banks of the Magellan and Hovland mound province form continuous aureole around the central, deeper located surface coral banks of the Hovland mound province. The distribution of the surface and the buried mounds can best be compared to an open air Greek amphitheatre, where the Hovland mounds represent the players and the Magellan mounds the audience.

The mound distribution indicates that in the recent past the conditions for mound development were more favourable in the Belgica mound province than in the Hovland-Magellan mound province. Nevertheless, the high number of coral banks in the Hovland-Magellan mound province argues that the conditions during the start-up phase have been very favourable for the formation of coral banks.

6.1.2 Coral bank geometry

6.1.2.1 Circular banks

The circular coral banks are located at protected sides surrounded by other coral banks in the Belgica mound province. Circular coral banks are more isolated in the Hovland mounds. It seems that in the most ideal conditions (available space, reduced sedimentation, good balance of currents), the coral banks developed a circular shape in plan view.

In the surface expression this circular shape changes to a more or less NS elongated shape due to the accumulation of sediments on the flanks in the NS current regime. In some cases the sediment

accumulation forms a bridge between the coral banks, which creates a complex structure with several mound summits.

6.1.2.2 Elongated banks

The elongated coral banks are located at the edge of the channels and are formed parallel to the channel flank in the Belgica and Hovland mound provinces. The channels steer the mound development direction. Most of the Magellan mounds have a NS elongation, which suggests that they have been shaped by NS currents [Huvenne et al, submitted].

6.1.2.3 Sediment pressure

The development direction of the coral banks is inferred from the height and width ratio of the surface and buried coral banks in the Belgica mound province. The surface coral banks are about 3.5 times higher than the buried coral banks. The width is only 1.5 times longer. This suggests that the coral banks formed a broad base in the early phase of development and later started to develop in a vertical direction. In a later stage, the horizontal extension is in pace with the vertical mound development. Such a broad base is also observed in the Hovland mound province, suggesting a similar development as in the Belgica mound province.

The height of the buried coral banks has a negative correlation with the embedding sediment thickness. This indicates that sediment stress is an important factor, limiting the development of the coral banks.

In areas with high sediment pressure, as the Magellan mound province, the coral banks start to develop quickly after the initiation in a vertical direction.

In the Hovland mounds it seems that the Propeller mound consists of multiple summits. These observations suggest that the mound is composed of several smaller coral banks, which merged during their development.

6.1.3 Framework builders

One of the most important observations is the intense colonization by a benthic community on the surface coral banks. The present-day biozonation of the epibenthic life and the surface sediment fauna sheds a light on the sediment processes ongoing on the flanks of the mound. These processes are used as a key to the past in the development of the mound.

6.1.3.1 *Associated fauna*

The associated fauna of the dominant framework builders *Madrepora* en *Lophelia* consists mainly of suspension feeders as porifera, hydrozoa, polychaeta, hexacorallia, bryozoans, brachiopods, asteroids, ophiuroids and ascidiaceans.

Polychaeta are the most common group of associated fauna of deep-water corals. Crustacea, *Nematoda* and *Ophiuroidea* are common in all samples in agreement with the observations of Jensen and Frederiksen (1992) and Mortensen et al. (1995) for other locations in the Northeast Atlantic. *Crustaceae* are the most important predators in the build-ups.

The presence of a complex coral framework located above the seabed is particularly favourable for these organisms. This observation supports the view that the coral banks are located in areas of considerable water movement and abundant material in suspension, which provides nutrients to the corals and associated fauna. The high concentration of suspension feeders attracts on their turn predators, bioeroders etc., which create a rich faunal niche.

6.1.3.2 *Site specific associated fauna*

The species found have a wide distribution and depth range (De Bergé, 2000; Van Gaever, 2001), which suggests that the deep-water coral build-ups have no specific associated fauna (Burdon-Jones and Tambs-Lyche, 1960; Jensen and Frederiksen, 1992; Mortensen et al., 1995). Many juvenile individuals have been observed in the studied samples, which confirms the observation of Jensen and Frederiksen (1992). They suggest that the coral construction might act as a temporary site of protection until they reach a certain size. The fauna consists of facultative inhabitants representing the fauna present in the region. The reason why the coral framework supports diverse communities is complex and reflects a combination of factors. The coral banks have a relative stable environment with moderated fluctuations in physical parameters and a predictable supply of food. A situation, which is parallel to that of the shallow reefs.

The diversity of macrobenthos species associated with the deep-water coral structures is similar to that of some tropical reefs (Jensen and Frederiksen, 1992; Rogers, 1999). The main difference between the deep-water coral build-ups and tropical reefs is the absence of algae, which increase the habitat complexity of the reefs. Algae are important food for many fish and echinoderm species. The high diversity of azooxanthellate corals is a second difference in the biodiversity between tropical and deep-water reefs. If these differences are taken into account, the indexes calculated for the deep-water coral build-ups are similar to those of tropical reefs.

6.1.3.3 Microhabitat

The microhabitat analysis of Van Gaever (2001) indicates that sediment is the richest microhabitat of all, with a Shannon-Wiener index of 3.17, although it has the lowest density. This habitat has also most species in common with the other considered microhabitats: 79% with sponge debris and 58% with sponges. Van Gaever (2001) suggests that many species migrate from the sediment to the other microhabitats. The coral debris and framework are the richest biological habitats for colonizing fauna. This is also observed in the Norwegian reefs [Mortensen, 1995 #70.

6.1.3.4 Sponges

A remarkable observation is the large volume of sponges found in the samples of the Belgica mound province and the total absence of large sponges in the Hovland mound province. The sponge volume consists mostly of the *Hexactinellide* sponge *Aphrocallistes beatrix* in association with the corals. The sponges colonized the dead coral framework and are later filled with sediment, which strengthens the entire framework.

Rice et al. (1990) reported dense aggregations of the hexactinellid sponge, *Pheronema carpenteri* in the area of the Belgica mounds. These sponges have been observed in a restricted bathymetric depth between 750 and 1200 m. The authors related the dense occurrence of the sponges to local hydrographic conditions supplying the fauna with food. This condition does not imply an enhanced organic input but more organic particles remain available in the watercolumn, which favour the conditions for suspension feeders.

In the samples of the Hovland mound province large sponges have not been observed. This indicates a different biological setting: probably currents were less favourable for the settlement of the species. The biodiversity of macrofauna in the Hovland mounds is smaller than in the Belgica mound province. This can be due to the higher sediment input and weaker currents. This illustrates the site-specific fauna of the mounds, depending on the local ecological conditions.

6.1.3.5 Bioeroders

Another important group is the bioeroding fauna. This group consists for about 1/3 of the *Polychaeta* observed in the samples. The bioeroding *Polychaeta*, *Cirratulidae*, *Sabellidae*, *Spionidae* and *Paraonidae* are common in the dead coral zone. Further, the most important bioeroding organisms encrusting sponges (Freiwald and Wilson, 1998), which have not been studied in the Belgica mound province. The bioerosion of the coral skeletons weakens the entire framework and reduces the aragonitic skeleton to grains inside the sediment. Similar to tropical

reef settings, the coral debris is used in the sediments filling caves inside the framework. Several observations indicated that the bioeroding fauna increase the biodiversity in the dead coral zone (Freiwald and Wilson, 1998; Jensen and Frederiksen, 1992; Mortensen, 2000).

6.1.3.6 Distribution of living corals

The results of the biozonation of the coral banks illustrates that living corals and associated fauna are localized on the steep flanks facing local depressions or at the stoss side of the coral banks. At the foot of the steep flanks, where the slope gradient decreases, less living fauna is observed due to the high sediment stress. The living coral zone is narrow and appears only at the upper slope where sediments accumulate on the flanks.

Isolated coral banks with a low sediment pressure, in the deepest part of the mound province -e.g. Thérèse mound (BEL35)- have more intensely colonized steep flanks. This is confirmed by a recent cruise with video footage of ROV Victor (Huvennne, pers. comm.). Coral banks that are partly buried on the leeward flank or landward side, suffer a large sediment pressure on the benthic community, which partly dies (e.g. Propeller mound HOV02, Challenger mound BEL26). These coral banks probably stopped developing and have slightly been buried with sediment. Only the exposed steep flanks contain a rich benthic life. The extents of the living coral zone are controlled by the steepness of the flanks and the current speed, controlling the sedimentation on the flanks.

6.1.3.7 Baffling of sediment

A dead coral zone is observed just below the living coral zone as a coral framework colonized by a new benthic community. Further in a downward direction the coral framework gets progressively filled with sediment and the macrobiotic fauna reduces quickly in the lower part of the flanks. The baffling of sediments by the coral framework supports the framework and strengthens the construction. In zones where the sediment supply is high enough to fill completely the coral framework, a smoothed flank with a gentle slope is encountered. If the currents are strong enough to keep the sediment in suspension or when the sediment supply is reduced, the coral framework stays exposed or grows in pace with the baffling of sediments in the framework. Such flanks of stacked coral colonies create steep slopes on the upper mound flanks.

The sediment observed in the framework is mostly coarse-grained, which suggests that strong currents washed out the fine fraction. Finally, the framework is initially covered with coarse-grained sediments. The small cavities in the framework get later completely filled with finer sediment.

6.1.3.8 Zonation

The vertical zonation of the mounds is not sharply bounded as described for the Norwegian reefs (Freiwald and Henrich, 1997). The different zones seem to overlap strongly. It suggests that the zones migrated slowly along the mound structure during its evolution. The lower part of coral rubble shifts slowly upward and the upper flanks and summit of the mounds develop in a vertical direction by new settlements.

6.1.4 Oceanographic environment

Several observations argue that the surface coral banks are closely related to high current regimes in a certain period:

- the present-day measurements of periodic vigorous northward flowing currents in the Belgica mound province
- the formation of NS trending contourite channels
- the presence of sand ripples, sand sheets, ribbons in the Belgica mound province
- sediment structures indicating for changes in the current direction near the mounds
- moat formation around the coral banks
- a reduced sedimentation thickness
- colonization of benthic suspension feeders
- biozonation of the coral banks

An explanation for this typical mean northward flowing bottom current regime is found in the water mass distribution at these levels. The coral banks occur in a water depth zone related to the interface between the ENAW and MOW. The interaction with the MOW-ENAW boundary water mass and the seabed morphology can cause local changes in the current patterns due to breaking of internal waves. The density ranges of these water masses show considerable overlap, which allows both diapycnal and isopycnal mixing. The presence of breaks in the slope may enhance the diapycnal mixing (Garrett, 1991) and force the circulation near the margin to be aligned with the topography (see 2.4). The MOW is an important player in the coral bank evolution in the present-day. For this reason some more details and related processes have been discussed.

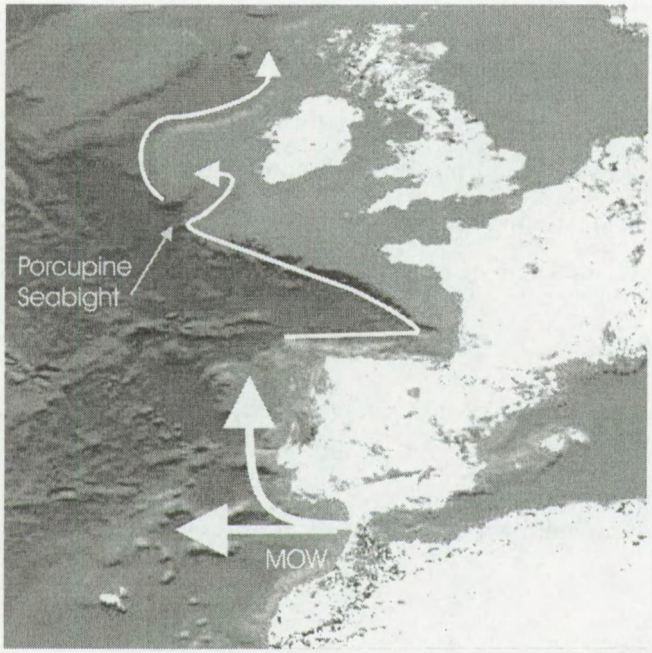

Fig. 6.1. Flow pattern of the MOW along the southern part of the North East Atlantic margin. (after New et al., 2001 and van Aken and Becker, 1996)

6.1.4.1 Origin of MOW

The Mediterranean Outflow Water (MOW) is formed by the density driven overflow of saline water from the Mediterranean Sea over the shallow sill near Gibraltar, and subsequent entrainment of less dense water from the thermocline when it passes through the Gulf of Cadiz (O'Niel Barringer and Price, 1999) (Fig. 6.1). Even close to the Gibraltar sill in the Gulf of Cadiz, two different cores of MOW have been observed at different levels, which following different paths along the topography (van Aken, 2000). Both MOW cores enter the North Atlantic through a gateway south west of Cape St Vincent and flow northwards, forced by a combination of Coriolis effect and gravity force (Nelson et al., 1993), along the east Iberian ocean margin off Portugal (O'Niel Barringer and Price, 1999). The main MOW core, characterized by a clear salinity maximum, spreads northward in a deep boundary current or Mediterranean under current along the European ocean margins till the Porcupine bank (53°N) (New et al., 2001; van Aken and Becker, 1996) (Fig. 6.1).

This high salinity of the water is due to the arid climate in the Mediterranean causing large evaporation and the reduced fresh water inflow in the Mediterranean Sea. Nearly all intermediate salinity maxima related to the MOW core have been found between 700-1500 m with a main core around 1000 m (Mauritzen et al., 2001; van Aken, 2000) in the northeast Atlantic.

6.1.4.2 *Nutrients*

The core of the MOW is not only characterized by a salinity maximum in the Porcupine Seabight but also by a low level in Apparent Oxygen Utilization (AOU, $\sigma_0 = 27.20$ kg/m^3 at the isopycnal 31.85) (van Aken, 2000). The AOU value is calculated by subtracting the measured value from the saturation value computed at the potential temperature of water and 1 atm total pressure. In this way, the AOU represents the biochemical utilisation of oxygen in the water mass. Low values indicate a high activity of living organisms.

At the upper edge of the oxygen minimum zones, generally a higher activity of biogeochemical processes has been observed (Mullins et al., 1985). This can lead to a high activity in macrobenthos and production of nutrient-rich water at the edge of water masses. In the Porcupine Seabight this upper level fits approximately with the inferred boundary between ENAW and MOW, and with the coral bank level (Fig. 6.2).

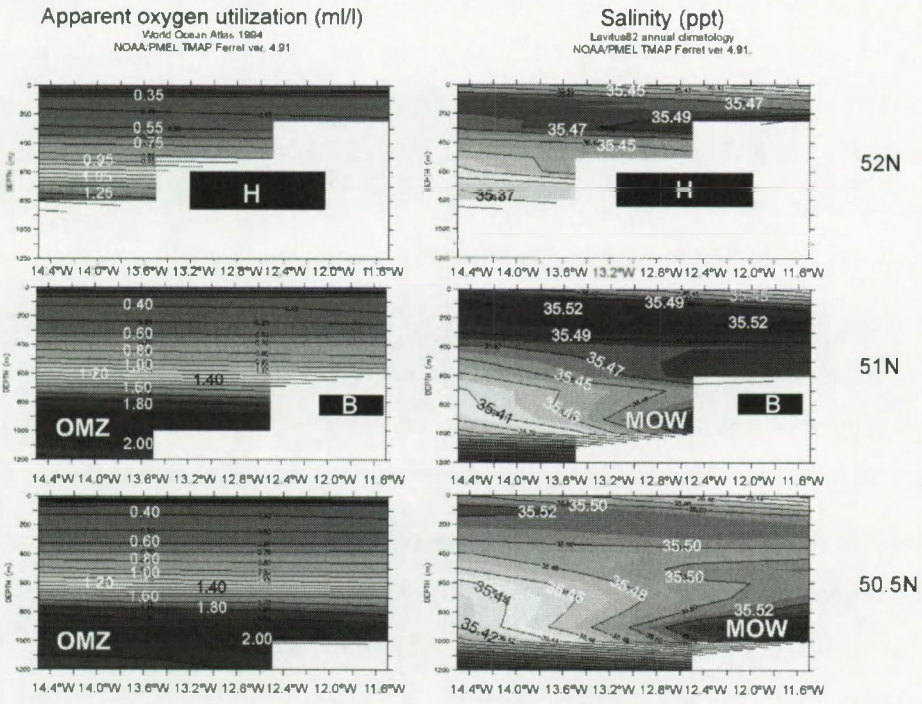

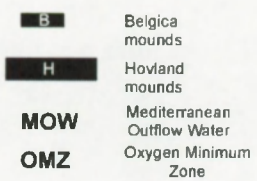

Fig. 6.2: Position of mound provinces in relation to ocean water stratification in terms of apparent oxygen utilisation and water salinity. The Oxygen Minimum Zone (OMZ) is indicated as maximum apparent oxygen utilisation; the Mediterranean Outflow Water (MOW) is characterized by a higher salinity in intermediate depths on the salinity plots.

Where the MOW is flowing out of the Mediterranean Sea it is poor in nutrients (Grousset et al., 1998). The core of the Antarctic Intermediate Water appears to contribute to the formation of the MOW since it becomes entrained into the overflow near Gibraltar. This entrainment gives rise to an enhanced concentration of the nutrients in the Mediterranean water in the North Atlantic (van Aken, 2000). An extra enrichment in nutrients of the MOW water mass is probably due to mixing at the interface between the MOW and ENAW and winter cascading of the Irish shelf [van Aken, 2000].

6.1.4.3 Model of the present

The interaction between the density gradient between MOW and ENAW and the local seabed morphology can explain the enhanced northward currents in a restricted water depth and a nutrient enrichment at the coral bank levels.

Most of the benthic life consists of suspension feeders, which prefer locations with high current speeds transporting nutrients. Deep-sea corals need a balance in the dynamical regime so that currents are strong enough to keep hard substrate clear of sediment and to keep organic material in suspension. Nevertheless, too strong currents can topple or break the corals. This effect explains the localized living cap on the coral banks but implies that the system is very sensitive for changes in the oceanography. Changes in the MOW flow in the basin will affect the current velocity, nutrient supply and may affect the biozonation on the coral banks.

The lower range of the Belgica mounds are seated at the eastern flank of the NS oriented contour channel associated with vigorous northward flowing currents. The coral banks in the upper coral bank range, flanking downslope channels, take probably advantage of the nutrient-rich cascading water. The latter coral bank level act as a kind of barrier for downslope sediment transport.

The currents in the Hovland-Magellan mound province are less strong than in the Belgica mound province. Current measurements result in a variable current direction and speed arguing for internal waves with a tidal signature. It appears that the bank accretion cannot keep pace with sediment accumulation. Only few coral banks flanking the central depressions are safeguarded from burial. The flanks facing the depression have the largest living cap of benthic life.

Off shore the Faroer (Frederiksen et al., 1992) and in the Rockall Trough (Kenyon et al., accepted) the link between enhanced focalized currents with a tidal signature, and the occurrences of deep-water corals is also proposed.

6.2 Initial coral bank development and triggering

The present setting and processes of the mound development have been discussed in the previous section. The indication for the paleo-environment during the mound development and the mound initiation is mainly based on the geological interpretation of the seismic profiles.

The geological observation of the two provinces can be summarized as follows:

- the mound base is a basinwide last erosive event of Late Pliocene age
- sediment units below and above the base are steered by bottom currents and downslope turbidity transport
- characteristics of high intensification of bottom currents are locally observed in the Hovland and the Belgica mound province
- moats surround the surface coral banks
- buried coral banks are associated with moat structures in the initial phase but later they got progressively filled
- the erosional structures and current related sediment structures are not well developed in the buried mound zones, which indicates weaker currents with a tidal influence
- the coral banks are located at local heights, steep slopes and channel flanks at the mound base reflectors
- no special relation is found between the mapped seismic facies of the substratum and the mound distribution
- no significant relation could be found between faults and coral banks
- indications for subsurface fluid migration are weak and only account for possible small-scale migration. No large seepage and migration features are observed in the seismic sections in this part of the Porcupine Basin

6.2.1 Paleo-environment before the coral bank initiation

All seismic facies below the mound base are characteristic for bottom-controlled sedimentation, in particular for drift sediments, as characterized by Faugères et al. (1999) on seismic profiles:

- major discontinuities in the drift sequence can be traced across the whole drift and represent time lines corresponding to hydrological events

- lenticular, convex upward depositional units with a variable geometry (Belgica mound province)
- specific style of progradation-aggradation of these units shows the interaction of the bottom current with Coriolis force and seabed morphology

6.2.1.1 Contourites

The different facies are interpreted as phases in a slope parallel drift under changing oceanographic conditions. The build-up of a drift body implies both erosion and deposition. Erosional features are seen as local discontinuities, channels, and scouring of the slope, creating local and more regional incisions in the underlying units.

Belgica mound province

From the geometry of the drift and the sigmoidal units of facies Bb and Bc in the Belgica mound Province, a NS along slope bottom current is inferred (see 4.3). The Coriolis effect deflects the flow to the right, effectively constraining the flow against the slope. Being so constrained, the flow intensifies, erosion occurs and a channel develops with a drift, tending to migrate upslope. Lower velocities to the west of the flow favour deposition and drift levee construction. These currents seem to be dominant since the onset of the drift sequence in the Miocene (Mc Donnell, 2001), with intervals of vigorous pulses, creating erosion and slowdown of the currents with a local reorientation of the currents (see 4.3). The driving current seems to be focalized near the lower end of the slope as bottom currents, similar to the present-day situation but probably more vigorous.

Hovland-Magellan mound province

Contourite channels have been observed since the Miocene on the eastern boundary of the Hovland mound province (see 5.3). These channels shift in time to a more central location. These channels have similar morphological characteristics as channels formed in the sediment drift on the Gabon continental margin by upslope prograding currents (upwelling) (Séranne and Nzé Abeigne, 1999).

An alternative explanation for the formation of the steep channels without upslope extension is that they represent slide scars (Henriet et al., 2001), which act in the later period as preferential site for current funneling. Nevertheless, no slide or slump deposit is found in the deeper part of the basin (Mc Donnell, 2001).

The central depression in the Hovland mound province is filled by a contourite fan cut and infill system (see 5.3). This illustrates the locally high current regime at these locations. Outside the channels, the facies have the characteristics of a hemi-pelagic set with parallel reflectors, prograding upslope to the north and east. The eastern alongslope channel shows several stages of infill, illustrating variability in the current activity trough time.

6.2.2 Coral bank base

The last major erosion formed the unconformity of the mound base, corresponding to a great instability and/or to a drastic change in the current regime. After this erosional event, a new depositional phase started, which did not significantly change till recent times.

6.2.2.1 Dating

By extrapolation of sedimentation rates from shallow cores (core MD9923237 (Van Rooij, 2001), TTR7-AT-16G (Saoutkin, 1998), EANAM9902, ENAM9905, ENAM9901) the mound base is estimated to be Late Pliocene-Quaternary for both provinces. This age is also proposed by seismic investigations in the basin (Britsurvey, 1997; Games, 2001).

6.2.2.2 Origin of the erosion

The origin of this large erosional event is linked to the oceanographic changes in the Late Pliocene. The evolution of oceanic gateways within the Neogene and Quaternary had a strong impact on the global ocean circulation pattern. The closure of the Isthmus of Panama that started 4.6 Ma ago (Haug and Tiedemann, 1998) deviated huge water masses from the tropical region of the Atlantic towards the north. They still control the present-day surface water conditions of the NE Atlantic. Supposedly northern hemisphere glaciation started as a result of this transport of latent heat, which increased the advection of deep water. In combination the MOW resumed after the Late Miocene-Early Pliocene Messinian salinity crisis in the Mediterranean Sea (Maldonado and Nelson, 1999). A regional Late Pliocene hiatus is found in the Rockall-Goban Spur transect and is interpreted in terms of the reintroduction of MOW in the NE Atlantic (Pearson and Jenkins, 1986). Based on microfaunal associations in deep cores of the North Atlantic (west of Rockall bank and at the Western Approaches), Schnitker (1986) suggests that the present-day water stratification in the North Atlantic Deep Water only established at the onset of modern glacial conditions about 2-2.5 Ma ago.

6.2.2.3 *MOW in the past*

The introduction of the MOW in the NE Atlantic is recorded in terrigeneous drift in the Gulf of Cadiz (Maldonado and Nelson, 1999). Sedimentological and biostratigraphic studies of the drift of Late Pliocene and Quaternary age in the Gulf of Cadiz (Caralp, 1988; Heileman, 2000; Nelson et al., 1993; Nelson et al., 1999; Seirro et al., 1999) revealed a periodic intensification of the MOW related to periods of sea level rise. It was found that MOW flow strength alters in glacial-interglacial and with short-term climatic changes as the Bølling-Allerød and younger Dryas events (Schönfeld and Zahn, 2000).

During the glacial periods the outflow of MOW was reduced (Grousset et al., 1998). More restricted inflow-outflow conditions during glacial sea level low-stands promoted salt build-up in the Mediterranean, thereby potentially enhancing MOW density (Schönfeld and Zahn, 2000). This affects the outflow because the MOW is heavier and thus needs more energy to pass the sill of Gibraltar. Short-lived phases of enhanced MOW flow occurred during Bølling-Allerød (14-11ky) and at the end of the Younger Dryas Since 3 ky a new intensification of the MOW has been observed (Heileman, 2000; Seirro et al., 1999).

There is evidence that the MOW entered the Porcupine Seabight (New et al., 2001; Rice et al., 1991; van Aken, 2000). Mediterranean benthic foraminifera and ostracodes have been recognized in 3m gravity cores in the Hovland mound province (Coles et al., 1996). Van Rooij (2001) observed a change in faunal assemblages during the intensification of the current regime with occurrence of the benthic foram *U. mediteranea* in the Belgica mound province. This suggests that intensifications of currents occurred during the introduction of MOW in the Holocene and in the Eemian (Van Rooij, 2001). Intensification of the currents is observed during interglacial periods and short-term climatic events.

6.2.3 *Internal structure of the coral bank*

The internal structure of the coral banks is derived from the observation of shallow cores (up to 20 m) (Van Rooij et al., 2002) and seismic velocity analyses. The seismic facies of the coral banks is homogeneous and transparent with an estimate internal velocity between 1850-2000 m/s depending of the mound location. This velocity suggests carbonate-rich sediment (with a velocity of 2300 m/s) and intermixing of terrigeneous material (1700 m/s).

On-mound sediments are intensely bioturbated and are dominated by terrigeneous components. They contain a large amount of bio-detritic material; azooxanthellate corals (dominating species

are *Madrepora* and *Lophelia*) and shells. The carbonate in the terrigeneous mud is covered by coccolithophores, foraminifera, spicules of octocorals, gastropods, crustaceans and coral rubble. In the short cores it seems that coral growth was more intensive during interglacial or short warm periods than in glacial periods. In these periods also higher current have been suggested.

Beside the autochtoneous sedimentation allochtoneous sediment is observed in the form of terrigeneous sediment trapped in the coral-sponge framework.

6.2.4 Coral bank triggering

Lophelia and *Madrepora* corals require a hard substratum, an adequate nutrient supply and a protection against burial to grow (see 2.1). Concentrations of *Lophelia* corals are found where strong currents (upwellings, internal waves between stratified water masses, etc.) prevent deposition of fine-grained sediment and supply large quantities of food (Cairns and Stanley, 1981; Freiwald, 1998) (see table 2.1). In these favourable areas, azooxanthellate corals might form patches or banks on top of topographic elevations, for example on moraine ridges where they attach to dropstones (Freiwald et al., 1999), on seamounts (Zibrowius and Gili, 1990), on carbonate-cemented rocks (Neumann et al., 1977; Messing et al., 1990), in hydrocarbon seep areas (Hovland, 1990; 1992; Hovland et al., 1994; 1998; Hovland and Thomsen, 1997), on outcropping hardrock (Stetson et al., 1962) or even on submarine pipelines (Hovland pers. comm.) and oil rigs (Roberts pers. comm.). Topographic irregularities in areas with strong currents cause local current accelerations, which increase food supply and protect the corals from sediment settling. When environmental conditions are favourable, the corals can produce extensive frameworks that trap sediments and provide niches for other benthic life (e.g. sponges, fish, etc.) (Rogers, 1999).

The oldest fossil record of *Lophelia* and *Madrepora* in the North Atlantic territory is reported in the Mediterranean Sea where they occur since the Early Pliocene (Chevalier, 1961; Cairns and Stanley, 1981; Esteban, 1996; Pérès, 1985). Deep-water corals, banks or patches occur all along the European shelf margin from Gibraltar up to Norway (Freiwald, 1998). It is therefore possible that larvae of azooxanthellate corals got introduced in the North East Atlantic water together with the MOW, which took advantage of the currents created by the intrusion of the high-density water mass in the North Atlantic to colonize the continental slopes. The MOW, however, only extends north up to the Porcupine Bank or the Rockall Basin (New et al., 2001; van Aken, 2000). Larvae may have been carried further northwards by other polewards flowing currents related to the

NAC (Freiwald et al., 1999). In this scenario, different development events could be related to major phases of MOW input and withdrawal in the Porcupine Seabight (Fig. 6.3).

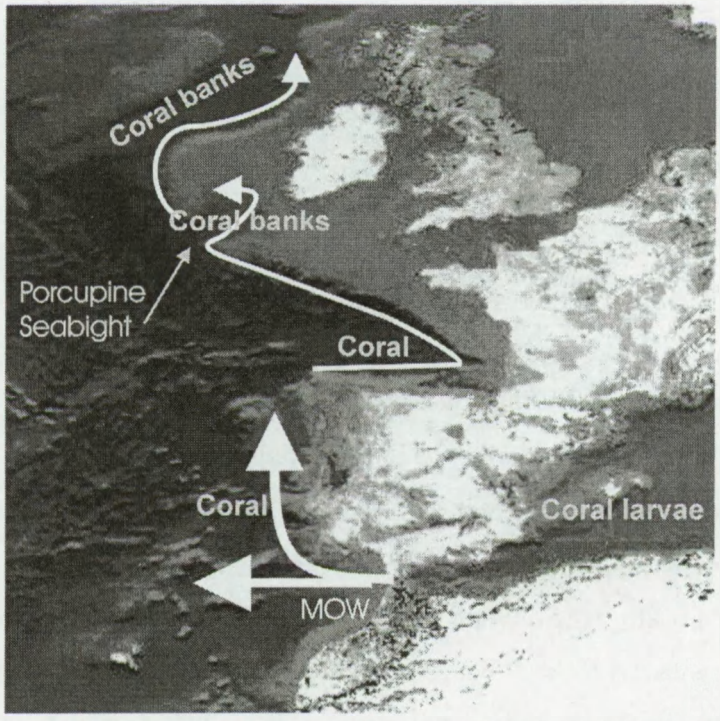

Fig. 6.3: It is possible that the deep-water coral larvae are introduced together with the MOW flow in the southern part of the NE Atlantic. Deep-water corals occur all along the pathway of the MOW, but only in the Porcupine Seabight and in the Rockall Trough coral banks have been formed.

6.2.5 Coral bank development

The coral banks may have undergone a multi-stage evolution from colony to thickets to coppice to banks as proposed by Squires (1965) (see 2.1). This evolution is accomplished through the *in situ* contribution of skeletal material along with the baffling and trapping of nannofossil ooze and terrigeneous sediment winnowed from adjacent areas by bottom currents. In analogy with shallow reef evolution, the different stages of the coral bank development are called start-up, catch-up, keep-up and give-up (Neumann and Macintyre, 1985).

6.2.5.1 Start-up

Various observations argue for a brief moment of rapid initial growth of the coral banks after the creation of the erosional surface in Porcupine Basin:

- the coral banks are rooted on one unconformity suggesting one start-up phase
- the start-up phase occurred after an erosional event, during a period of non-deposition

- the mound initiation is restricted to well-delineated areas, the presently defined mound provinces
- the Belgica mounds have apparently developed to their full size before the drift sediments draped their flanks
- moat formation by turbulence around the coral banks is observed at the base of the Magellan mounds and in the full sequence of the drift around the Hovland mounds. These observations argue for a certain dimension of the coral banks before the initiation of the drift depositional phase
- Belgica mounds and Hovland mounds are associated with dominant northward current flows
- the scouring around the Magellan mounds indicate a current with a tidal influence (Huvenne et al., submitted)

The period of non-deposition, after the intensive erosional event seems to have been favourable for framework builders, creating the coral banks. In analogy to other locations the nucleation of the coral bank begins with colonization of a seafloor hard substratum (Fig. 6.5 a) (Mullins et al., 1981; Neumann et al., 1977; Squires, 1965). This might be an allochtoneous block, an eroded feature or lag deposits. Currents will provide the framework builders with nutrients at location where the current balance is most favourable to transport the nutrients and will safeguard the framework constructors of sedimentation, without toggling the corals. These places occur at the flanks of the main current core.

The erosional features in the Belgica and Hovland mound province argue for more intensive northward current regimes than in the present setting. The powerful erosion related to the re-introduction of the MOW (see above) in the basin can explain the northward scouring in the Belgica and Hovland mound province (Fig. 6.3).

The possible reflection of the density driven internal wave created at the boundary of the MOW at the enhanced slopes of the amphitheatre shape depression in the Hovland mounds probably resulted in an aureole of nutrient-rich and slightly enhanced currents in the Magellan area (Fig. 6.4). Due to the fact that the conditions in the entire Magellan mound province are similar - gentle seafloor, no depth differences, hard substratum of lag deposition - the coral framework builders could settle over a large area in a zone of favourable current influence. This coral settlement and concentration in the basin formed "gardens" of corals and associated fauna on the seafloor. As

discussed in the biology section the fauna associated with the corals migrated from surrounding habitats to take advantage of the more favourable locations, associated with the corals.

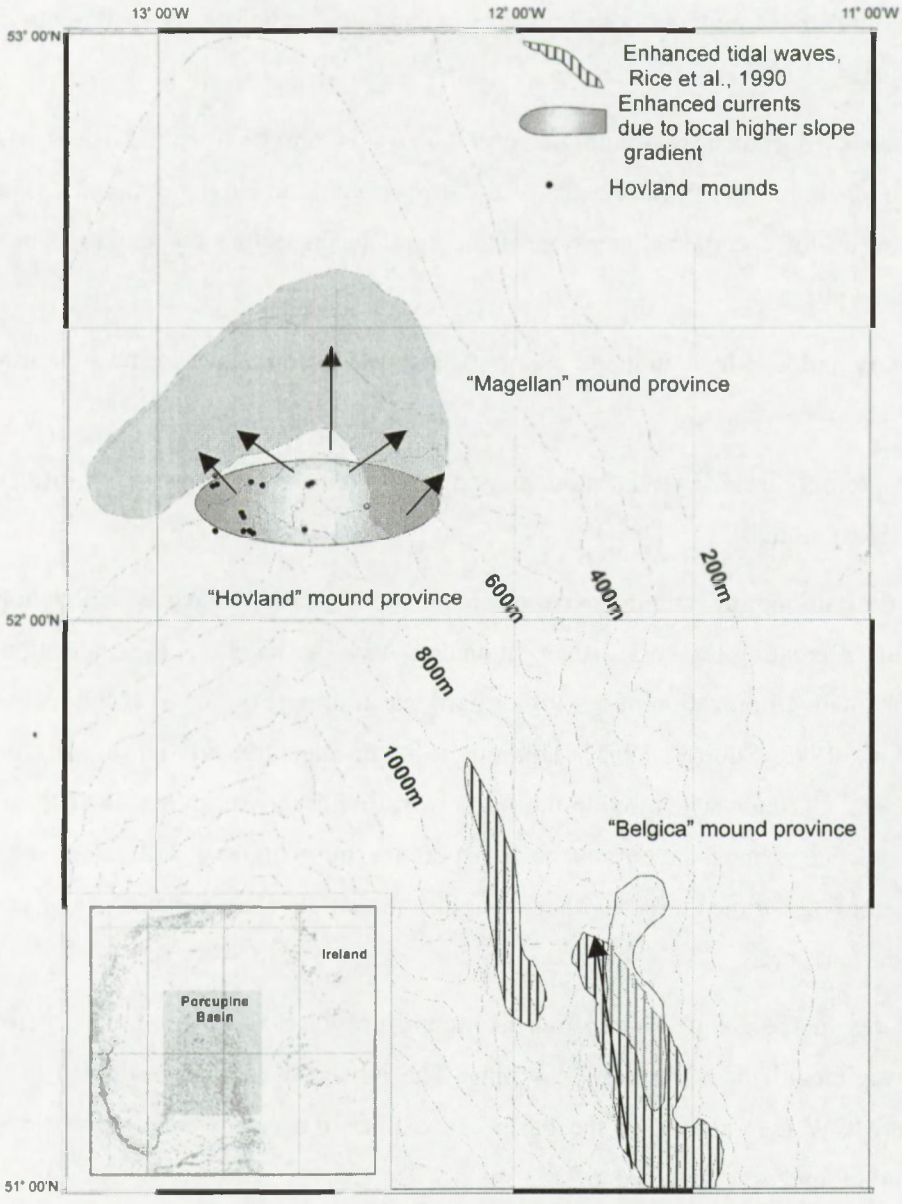

Fig. 6.4. Coral bank distribution in relation to zones where current enhancement at the top of the MOW may occur (Rice et al. 1990). The Belgica mounds are located within a zone of current enhancement as predicted by Rice et al. (1990). The overall slope gradient in the Hovland mound province is below the critical angle but current enhancement may occur locally. The breaking of the internal waves in the Hovland mound province might influence the Magellan mounds.

Once the coral settlements started to cluster for a longer period at a certain place they formed a coral debris layer, which served as a hard substratum for a new settlement (Fig. 6.5 b). These can be induced either by bioerosion or by breakage caused by overloading.

Wilson (1979) proposed that rings of living colonies that surround an area of dead coral accomplished the development. Under relatively quite and uniform conditions this build-up may have resulted in circular structures (Fig. 6.b). The growth of the coral banks is an interplay

between growth and destruction. During the initial phase "gardens" of corals developed and their disintegrated skeletal remains accumulated to form matrix-poor packstones (Fig. 6.d).

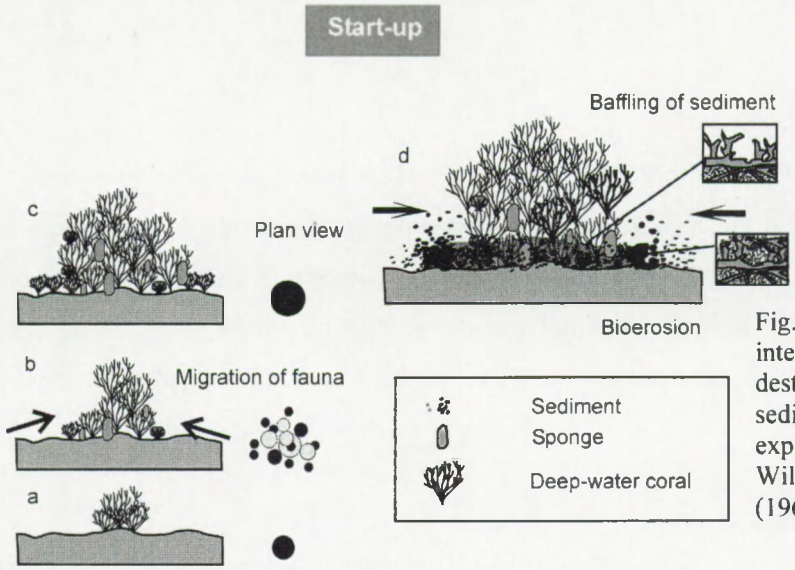

Fig. 65. Start-up phase is an interplay between growth, destruction and baffling of sediments. See 6.2.5.1 for explanation Partly based on Wilson (1979), Squires (1964),Mullins et al. (1981).

In some restricted areas that eventually were more exposed to nutrient supply than others, corals started to accrete by trapping mud (Fig. 6.4 d). Rapid *in situ* accretion of framework builders and accumulation of sediment, created the first generation of coral build-ups (Fig. 6.6 a, b).

6.2.5.2 Catch-up

As inferred in the present-day geometry the coral banks started to accrete first in a horizontal plane (Fig. 6.6 c, d). This suggests that in the Belgica and Hovland mound province some of the initial coral build-ups continued growing and coalesced with adjacent clusters into multiple structures (Fig. 6.6 d). Continuous growth of closely spaced coral banks may have caused lateral amalgamation along channels in any phase of development (Fig. 66. d, f). Others coalesced in an early phase to form circular structures (Fig. 6.6 d).

However, local currents greatly alter this simplified development scheme, and produces coral structures that are elongated, parallel to current directions, in the Magellan mound province or along -turbidite or contour- channels in the Hovland and Belgica mound province (Fig. 6.6 e, f).

From this stage on, the banks modify the bottom currents by acting as a structural high. In this way the coral banks protect themselves against burial and create moats in environments with a high sedimentation rate (Fig. 6.6 c, e). During periods in the development of the coral banks, the currents decreased resulting in a higher lateral sediment stress, which may have forced the banks to grow in a vertical direction (Fig. 6.6.c-e). The sedimentation rate is generally higher in the Magellan mound province than in the Belgica and Hovland mound province (Fig. 6.6c-d). The

lateral sediment stress forced the coral banks to grow in a vertical direction, quickly after their intation (Fig. 6.6.c-d. This development pattern results in a large number of vertical stacked coral banks.

6.2.5.3 Keep-up

The moat structures in the Magellan mounds indicate a period of non-scouring and progressively infill (Fig. 6.6 g). In a few moats a second phase of scouring is observed, probably induced by a new period of MOW inflow in the basin. Finally the sediments drape the coral bank. Sediment stress pushes the living benthic cap to the summit of the coral banks and sediments fill the cavities in the framework on the flanks. In this phase the vertical accretion dominates (Fig. 6.6 g h).

6.2.5.4 Give-up

Finally the vertical sediment accretion is higher than the accumulation of the framework builders. In this phase the framework get completely filled and no new settlements of framework builders will be established (Fig. 6.6. I).

6.2.5.5 Evolutional Stadia

Several steps of this evolution still occur simultaneously in the Porcupine Basin.

- ***Start-up?***

  Little "Moira mounds"(thickets) have been observed during a recent sidescan survey as small nuclei of coral generating on sand ripples near Thérèse mound (Wheeler, pers. comm.).

- ***Catch-up?***

  Thérèse mound (BEL35) represents a mature "living" coral bank.

- ***Keep-up***

  Coral banks with a limited living biological cap and partly draped by sediment are observed in the upper range of the Belgica and Hovland mounds (Propeller mound and Challenger mound) and in a few Magellan mounds (mound Perseverance).

- ***Give-up***

  The rest of the Magellan mounds represent the dead population of the once wealthy and beautiful garden of coral banks.

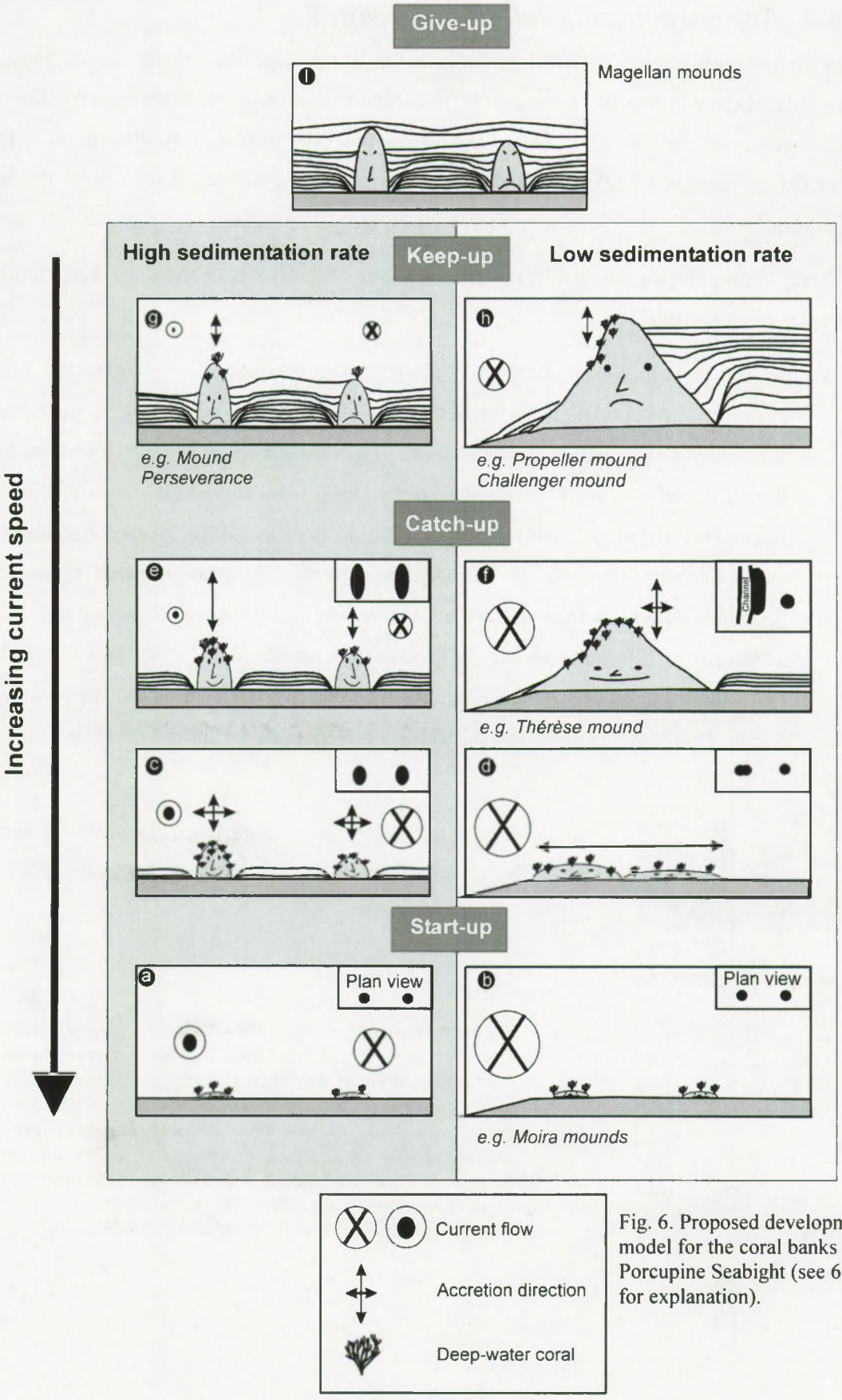

Fig. 6. Proposed development model for the coral banks in the Porcupine Seabight (see 6.2.5 for explanation).

6.3 Are coral banks related to seeps?

In the previous section the coral banks genesis, distribution, development and dying history is postulated to be in a close relation with the current evolution of the basin and possibly related to occurrences of the MOW. In literature however the coral banks in the Porcupine Seabight are related to seepage of hydrocarbons. These hypotheses have been discussed in the following paragraphs.

Three models proposed an evolution and triggering of the Hovland and the Magellan mounds by hydrocarbon seepage:

- A first model is proposed by Hovland (1990), Hovland et al. (1994) and (1998) that suggests a causal relationship between hydrocarbon seeps and deep-water coral banks (Fig. 6.7). Deep-water coral banks could form as a consequence of local fertilization that results from focused hydrocarbon seepage. In the case of the Hovland mounds in the Porcupine Basin, Hovland et al. (1994) interpreted that the coral banks are located immediately above major faults, which could be hydrocarbon migration pathways. Seeped hydrocarbons are thought to provide a food source for bacteria, fertilizing the waters around the seepage. An additional effect is the formation of carbonate crusts at the seep location, by methane oxidating bacteria, providing preferential sites for colonization by the framework building corals. This model explains the focalized occurrences of the surface coral banks.

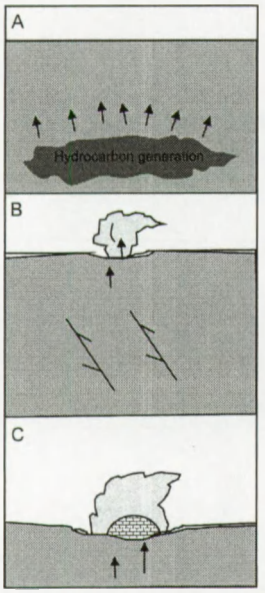

Fig. 6.7: Hovland et al. (1994) suggest a close relation between hydrocarbon seeps and coral bank formation. According to their model, the first condition is that hydrocarbons are generated at depth (A) and that some of them find their way to the surface in a focused manner, through faults and fissures (B). The seabed is here locally eroded by seepage and the local seawater is provided with nourishment on which bacteria and microorganisms depend. Over time, organisms and their skeletal remains accumulate, whereas authigenic carbonates precipitate locally, and cement the sediment and skeletal debris (C).

- The potential role of methane in triggering mound growth in the Magellan province has further been evoked by Henriet et al. (1998; 2001) in a model developed to unravel possible causal relationships between methane migration, slope destabilization and mound growth (Fig. 6.8). Such model also implies a possible phase of hydrate build-up and decay, in an environment, which has experienced extreme variations in bottom water temperatures in the recent suite of glacial and interglacial periods. This model provides a process for focused seeps around which the coral bank develop, hence forming ring-shaped coral banks in the Magellan province. During Quaternary times, with repeated fluctuations from polar (in front of an Irish ice-sheet) to temperate conditions, extreme variations in bottom water temperatures (up to 11° C) may have translated into cycles of local growth and decay of gas hydrates, fuelled by methane from deeper hydrocarbon reservoirs. The authors suggest that the Magellan mound province fully coincides with an underlying slope failure, where hydrates may have played a role.

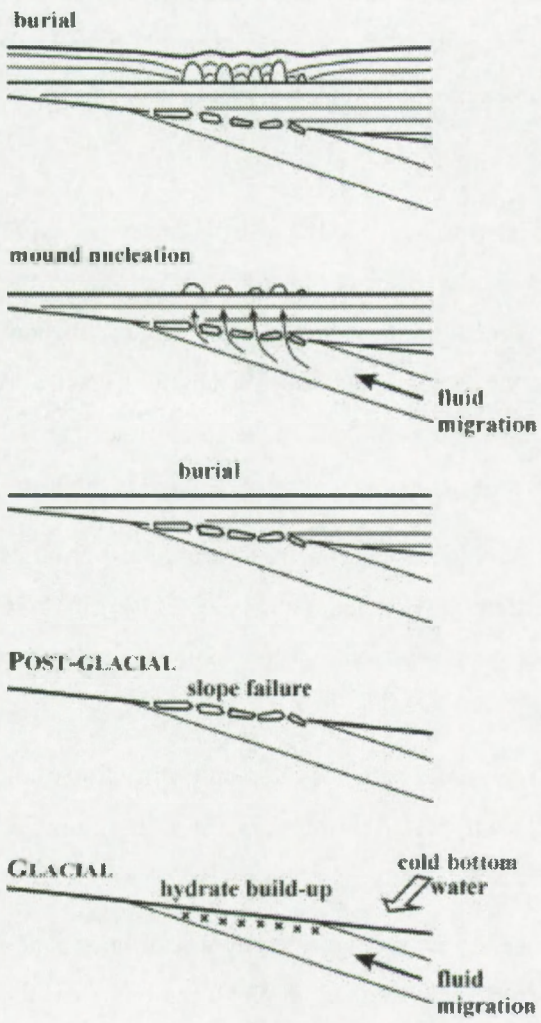

Fig. 6.8: Henriet et al. (2001) proposed a model for the genesis of the Magellan mounds on a site of episodic fluid migration, under strong varying bottom water temperatures. Under glacial conditions, a horizon of gas hydrates could built up in regions of prolific (even transient) methane flux. Decay of the hydrated horizons could generate slope failure. In renewed methane flux conditions, in warm waters, the disrupted horizon funneled the migrating fluids to the seabed, possibly contributing to venting and mound nucleation.

- A third model is proposed by Mc Donnell (2001) based on the coincidence between coral banks and the relation of underlying Oligocene and Miocene contourite deposits. The underlying contourites may have played a role as fluid migration pathway. But no evidence of migration neither of hydrocarbon accumulation are reported in the work of Mc Donnell (2001).

Seepage of thermogenic hydrocarbons at the seafloor does occur at the present in the northern part of the Porcupine Basin, in the non-commercial Connemara field about 65 km north of the Magellan mound province. These seeps appear clearly on industrial seismic data and high-resolution seismic sections as high-amplitude patches along reflections, vertical disruption of seismic reflections or vertical zones of chaotic facies ("gas chimneys") (Games, 2001). In the Magellan, Hovland or Belgica mound provinces however there are no such features. Most large faults do not extent to the seafloor and there are no clear indications so far for vertical fluid migration pathways neither on industrial seismic data (Mc Donnell, 2001) nor on the interpreted high-resolution seismic data. Pockmarks in the region of the coral banks are not active structures but might have been active in the recent past. Till now no paleo pockmarks horizons have been observed in the data set, which can link the mound development to the coral bank evolution.

6.3.1 Critical evaluation of the models

The major point in the seepage models is the causal relation between the distribution of the coral banks and structures identified as potential seepage site. Henriet et al. (2001) have related the buried Magellan mounds to the occurrence of the polygonal faults observed in the slide sequences (Hc), Hovland et al. (1994) related the coral banks to deeper faults and Mc Donnell (2001) to Oligocene contourite deposits in the Magellan-Hovland mounds. This made to assume that the start-up phase of the coral banks are preferentially located at sites where fluid seepage is highest.

- Venting could have facilitated the formation of authigenic carbonate, forming hard grounds on which ambient benthic fauna could have settled on (Henriet et al., 1998, 2001; Hovland et al., 1994). The formation of local hard grounds by venting can explain the spatial distribution of the coral banks.

- Hovland et al. (1994) assume that the shape of the coral banks is the result of hydrocarbon seepage distribution. Henriet et al. (1998, 2001) interpreted a ring shape of a large number of Magellan mounds, which may argue for a focused venting.

  If deep-water coral banks were caused by a close, direct link between hydrocarbon seepage along faults, we might expect the coral banks to be strictly lined up along the faults, which

is apparently not the case as discussed in 5.3. In the detailed 3D and 2D studies of the Magellan mound province (Britsurvey, 1997; Huvenne et al., submitted; Mc Donnell, 2001) no ring structures has been observed as interpreted by Henriet et al. (1998; 2001) The elongated shape indicates the current direction. These observations argue for an external control of the coral bank development.

- In the present-day setting no indications are seen to relate the occurrence of coral banks to seepage of hydrocarbons. There are no indications for high hydrocarbon concentrations near the seafloor. Even out of the geochemical analysis of the sediments (see 5.4) no large-scale seepage can be inferred for at least the last 100 ky.
- To the authors knowledge no proven hydrocarbon systems are located in the underlying sequences of the coral banks. Even underneath the Magellan mounds a very promising hydrocarbon site was reported based on geophysical data (G. Haarr, pers comm.). Nevertheless, an exploration well drilled in the area was dry and no indication for gas or petroleum system was proven (Peter Crocker , pers. comm.).

In the Belgica mound province some local enhanced reflectors are observed in the top of the sigmoidal units. This might indicate a very local and small accumulation of some fluids as gas. But these amount of gas and the very local distribution cannot explain the initiation of the coral banks, neither the feeding of the coral banks as proposed by Hovland et al (1994). Nevertheless, the gas content in the samples taken on the Thérèse mound, overlying these structures, is low and in the order of atmospheric values (J. Naeth, pers comm.). During the Marion Dufresne coring campaign MD123 of 2001 (Van Rooij et al., 2002) a H_2S smell has been reported for one core located on Thérèse mound, but the occurrences of H_2S is not confirmed by chemical analysis (J. Naeth, pers. comm.).

No conclusive evidence is seen in the present between methane seeps and coral bank formation as observed in the Atlantic Ocean (Table 2.1), which suggest an important external control for the present development. Nevertheless all genetic models -external and internal control- do not provide conclusive evidence regarding the origin of the coral banks because they are based on spare data of the internal structure and the mound base. Only scientific drilling will provide such conclusive evidence.

7 Conclusion and perspectives 345

7.1 Conclusion 345
7.2 Perspectives 346
7.2.1 EU 5th Framework projects 346
7.2.2 IODP 347

7 Conclusion and perspectives

7.1 Conclusion

This multidisciplinary study describes the morphology, seismic facies, sedimentology, biology and oceanography of large deep-water coral banks and their geological setting in the Porcupine Seabight offshore Ireland. Coral banks in the Porcupine Seabight are larger than most of their North Atlantic counterparts. They are about 1 km wide, can be up to 3 km long and attain heights of almost 200 m above the seafloor. The banks are mound-shaped elevations hosting living deep-water coral and associated fauna on their upper flanks. This biologically active layer covers a dead assemblage of corals, filled with terrigeneous mud similar to the surrounding seabed. The coral banks in the Porcupine Seabight occur in two geographical zones, each characterized by a typical coral bank shape: surface banks in the Hovland mound province, partly buried banks in the Belgica mound province and a large numbers of smaller buried coral banks in the Magellan mound province.

All coral banks, buried or outcropping, occur in association with current-induced features such as moats, sediment tails and sediment waves indicating their location in regions of strong currents. Only few coral banks are still outcropping today, which suggests that environmental conditions in the past were more favourable for the development of coral banks. The depth range of these outcropping coral banks coincides with the top of the dense Mediterranean Outflow Water, where current enhancement through internal tidal waves could control coral growth (Start-up). Coral bank growth started simultaneously, probably since the Late Pliocene after a period of erosion and non-deposition. Various phases of mound development in the past few millions years may have occurred and can be related to important fluctuations in oceanographic conditions, where the MOW can play a major role.

Sediment stress steered by currents plays an important factor in the mound development. Coral banks accrete by active baffling of sediment by the biological framework and extension of the biological cap (Catch-up). Once this fragile system between sedimentation and biological growth is out of balance, the framework will progressively be filled with sediment (Keep-up) with only a few living patches. Once the sediment dominates the structure, the coral banks get buried and draped by sediment (Give-up).

The start-up event suggests drastic environmental changes that favoured coral growth at a certain period. Such changes may have been triggered by changes in the oceanographic circulation

patterns, with the inflow of Mediterranean Outflow Water into the Porcupine Basin. No link is found between hydrocarbon seeping and the mound occurrences.

Carbonate mounds are known as hydrocarbon reservoirs. The discovery of potential modern counterparts on the present seabed might open a new field of reservoir model studies. These may permit insight into the sedimentological context, depositional environment, the relationship to embedding sediments and fluid migration paths, the internal structure and compartmentation of such reservoirs to reservoir modelling.

7.2 Perspectives

A few points in this work are uncertain and need more investigation to be conclusive in the possible triggering of the mound start-up phase

- What is the exact age of the mound base reflector?
- What is the composition of the internal structure of the mounds?
- Can paleo indicators of the MOW fluxes be found in the deeper sedimentary record
- Have the corals along the southern part of the northeast Atlantic the same genetic pool ?
- Is their indication for paleo seepage at the mound base?
- Is hardground formation due to seepage at the mound base possible?

7.2.1 EU 5th Framework projects

This study is not an isolated project and contributes as a case study in three large research projects on mound genesis studying several mound/coral bank locations along the European margin. The main question to be solved in this cluster of project outlines:

- **GEOMOUND** project, which focuses on the geological evolution of the mounds and the internal controls relations between the geosphere and the biosphere as fluid fluxes in the start-up phase of the coral banks, along the North Atlantic European margins.
- **ECOMOUND** focuses on the exogenic (environmental: i.e.: oceanographic and biological) controls of mound development.
- **ACES** project (Atlantic Coral Ecosystem Studies) is a focussed research efforts on deep-water corals along the eastern slope of Porcupine Basin and the Norwegian area around

Sula Ridge, where azooxanthellate corals are the major mound builders, in association with their respective "reef" dwellers. These corals will serve as indicators and recorders of environmental boundary conditions.

This work contributed to these projects. An inventory of recorded coral banks in the Porcupine Seabight has been made, documenting geometry, spatial patterns, bathymetric structures, geological associations, chemical analysis, biological patterns and oceanographic environment The new results achieved in this project cluster will be reported in 2003.

7.2.2 IODP

With the newly achieved subsurface data, the existing mound genesis hypotheses will be tested. The present available data scratch only the upper surface of the structures and the information about the start-up phase of the mounds is limited. Drilling is the only tool that can provide the lacking information on the coral bank genesis in the Porcupine Seabight.

The site surveys, largely presented in this work laid the base for the IOPD Porcupine Drilling proposal 573-FULL. This proposal is supported by the team of the above mentioned EU 5th Framework mound related projects as well as the **DEEP-BUG** project, which aims to the development and assessment of new techniques and approaches for detecting deep sub-seafloor bacteria and their interaction with Geosphere processes.

The proposed hypotheses will be tested by drilling at 13 sites (Fig. 7.1.):

- the role of gas seeps as a prime trigger for mound genesis,
- the role of bacteria as main mound builders,
- the role of reef-forming corals as major part of the mound community and their environmental record potential,
- the significance of mound "events" in a palaeoenvironmental plot,
- the identification of prominent erosional surfaces as product of global oceanic turn-overs,
- the potential of mounds as high-resolution palaeoenvironmental recorders,
- the value of the Porcupine-Rockall mounds as present-day analogs for Phanerozoic reef mounds and carbonate mud mounds,
- and the potential role of fluid flow as common source of both slope failures and mound growth.

Correlation of the Porcupine drift record with other drilling sites (DSDP, ODP) along the Atlantic margin opens perspectives of cross-basin comparisons. Corals within the drill cores might provide information on the palaeoceanographic conditions. The variations in terrigeneous content and organic matter in drift sediments should allow to trace terrestrial sources and shelf-to-slope sediment pathways. These mounds thus should provide palaeoenvironmental information, in an otherwise ersosive setting - the deep continental slope environment.

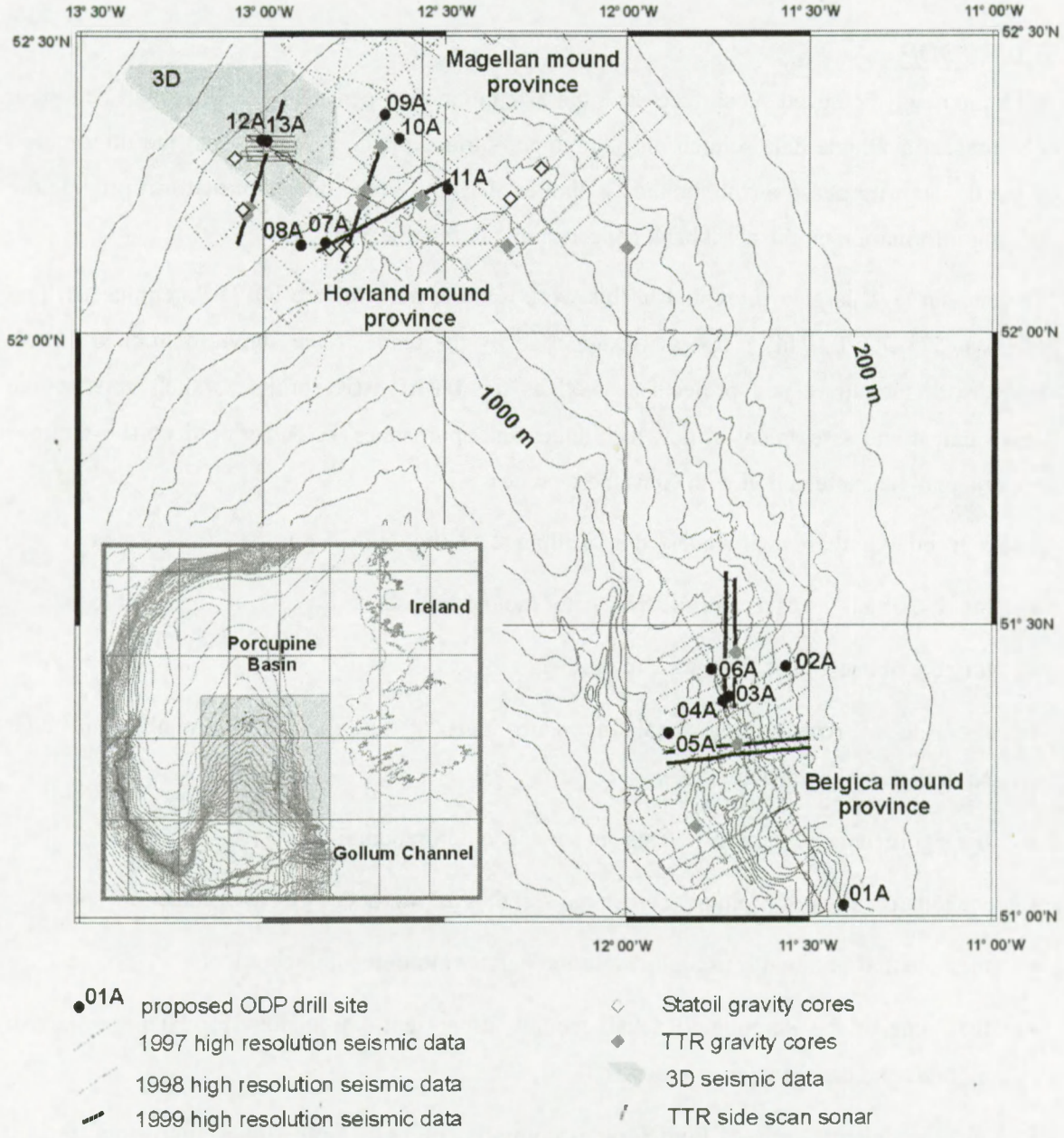

Fig. 7.1: Location map of the proposed IODP sites and available data.

References

Abrams, M.A., 1996a, Distribution of Subsurface Hydrocarbon Seepage in Near-Surface Marine Sediments. In: Schumacher, D. and Abrams, M.A., eds., Hydrocarbon migration and its near-surface expression: AAPG Memeoir 66: AAPG, p. 1-14.

Abrams, M.A., 1996b, Interpretation of Methane Carbon Isotopes Extracted from Surficial Marine Sediments for Detection of Subsurface Hydrocarbons. In: Schumacher, D. and Abrams, M.A., eds., Hydrocarbon migratio and its near-surface expression: AAPG Memeoir 66: AAPG, p. 309-318.

Adkins, J., Boyle, E. and Curry, W., 2001, STABLE ISOTOPE "VITAL EFFECTS" IN DEEP-SEA CORALS: Geophysical Research Abstracts, p. 9319.

Albert, D.B., Martens, C.S. and Alperin, M.J., 1998, Biogeochemical processes controlling methane in gassy coastal sediments-Part 2: groundwater flow control of acoustic turbidity in Eckernförde Bay Sediments: Continental Shelf Research, v. 18, p. 1771-1793.

Alexandersson, T., 1974, Carbonate Cementation in Coralline Algal Nodules in the Skagerrak North Sea: Biochemical Precipitation in Undersaturated Waters: Journal of Sedimentary Petrology, v. 44, p. 7-26.

Anderson, A.L. and Bryant, W.R., 1990, Gassy Sediment Occurrence and Properties: Northern Gulf of Mexico: Geo-Marine Letters, v. 10, p. 209-220.

Anderson, A.L. and Hampton, L.D., 1980, Acoustic of gas-bearing sediments I. Background.: Journal of the Acoustical Society of America, v. 67, p. 1865-1889.

Anselmetti, F.S. and Eberli, G.P., 1997, Sonic Velocity in Carbonate Sediments and Rocks. In: Palaz, I. and Marfurt, K.J., eds., Carbonate Seismology: Geophysical Developments Series: Society of Exploration Geophysicists, p. 53-74.

Armishaw, J.E., Holmes, R.W. and Stow, D.A.V., 2000, The Barra Fan: A bottom-current reworked, glacially-fed submarine fan system: Marine and Petroleum Geology, v. 17, p. 219-238.

Arz, H.W., Pätzold, J. and Wefer, G., 1999, Climatic changes during the last deglaciation recorded in sediment cores from the northeastern Brazilian Continental Margin: Geo-Marine Letters, v. 19, p. 209-218.

Ashley, G.M., 1990, Classification of large-scale subaqueous bedforms: a new look at an old problem: Journal of Sedimentary Petrology, v. 60, p. 160-172.

Auffret, G., Zaragosi, S., Dennielou, B., Cortijo, E., Van Rooij, D., Grousset, F., Pujol, C., Eynaud, F. and Siegert, M., in press, Terrigenous fluxes at the Celtic Margin during the last galcial cycle: Marine Geology.

Bates, R.L. and Jackson, J.A., 1980, Glossary of Geology: Falls Churchee, Virginia, American Geological Institut, 751 p.

Belderson, R.H., Kenyon, N.H. and Wilson, J.B., 1973, Iceberg Plough Marks in the Northeast Atlantic: Palaeogeography, Palaeoclimatology, Palaeoecology, v. 13, p. 215-224.

Bell, N. and Smith, J., 1999. Coral growing on North Sea oil rings. Nature, 402, 6762, 601

Berner, R.A., 1968, Calcium Carbonate Concentrations Formed by the Decomposition of Organic Matter: Science, v. 159, p. 195-197.

Blamart, D., van Weering, T.C.E., Ayliffe, L., Labeyrie, L., Lutringer, A., Vonhof, H.B. and Ganssen, G., 2001, Modern NE Atlantic Ocean Cold Water Coral Characteristics: Geophysical Research Abstracts, v. 3, p. 9320.

Blondel, P. and Murton, B.J., 1997, Handbook of Seafloor Sonar Imagery: Wiley-Praxis Series in Remote Sensing: Chichester, John Wiley & sons, Praxis Publishing.

Bohrmann, G., Greinert, J., Suess, E. and Torres, M., 1998, Authigenic carbonates from the Cascadia subduction zone and their relation to gas hydrate stability: Geology, v. 26, p. 647-650.

Boulvain, F., 2001, Facies architecture and diagenesis of Belgian Late Frasnian carbonate mounds (Petit-Mont Member): Sedimentary Geology, v. in press.

Britsurvey, 1997, Total Oil Marine plc, site survey Irish Block 35/17-1,14/11/96-13/12/96, final report: Report released by Petroleum Affairs Division, Dublin.

Burdon-Jones, C. and Tambs-Lyche, H., 1960, Observations on the fauna of the North Brattholmen Stone-coral Reef near Bergen. In: Brattsröm, H., ed., Publications from the Biological Station, Espegrend: Acta universitatis Bergensis. Series Mathematica Rerumque Naturalium: Bergen, Norwegian Universities Press, p. 1-24.

Cairns, S.D. and Stanley, G.D.J., 1981, Ahermatypic Coral Banks: Living and Fossil counterparts: Fourth International Coral Reef Symposium, p. 611-618.

Caralp, M.-H., 1988. Late Glacial to Recent Deep-sea Benthic Foraminifera from the Northeastern Atlantic (Cadiz Gulf) and western Mediterranean (Alboran Sea): Paleooceanographic Results. Marine Micropaleontology, 13: 265-289.

Cavanga, S., Clari, P. and Martire, L., 1999, The role of bacteria in the formation of cold seep carbonates: geological evidence from Montferrato (Tertiary, NW Italy): Sedimentary Geology, v. 126, p. 253-270.

Chevalier, J.P., 1961. Recherches sur les Madreporaires et les formations rècifales miocënes de la Mèditèrranèe occidentale. Mèmoires de la Societè Gèologique de France (NS), 40(93): 1-562.

Claypool, G.E. and Kaplan, I.R., 1974, The Origin and Distribution of Methane in Marine Sediments. In: Kaplan, I.R., ed., NATURAL GASES IN MARINE SEDIMENTS: New York - London, Plenum Press.

Clayton, C.J., 1994, Microbial and organic processes. In: Parker, A. and Sellwood, B.W., eds., Quantitative Diagenesis: Recent Developments and Applications to Reservoir Geology: Netherlands, Kluwer Acadamic Publishers, p. 125-160.

Coleman, M.L. and Raiswell, R., 1981, Carbon, oxygen and sulphur isotope variations in concretions from the Upper Lias of N.E. England: Geochimica et Cosmochimica Acta, v. 45, p. 329-340.

Coles, G.P., Ainsworth, N.R., Whatley, R.C. and Jones, R.W., 1996. Foraminifera and Ostracoda from Quaternary Carbonate Mud Mounds associated with Gas Seepage in the Porcupine Basin, Offshore Western Ireland. Revista Espanola de Micropaleontologia, XXVIII(2): 113-151.

Colpaert, A., 2000. 3D-seismische interpretatie, toegespitst op migratie van fluida, in het Connemara Field, Porcupine Bekken, Offshore Ierland. MSc thesis, Ghent, University of Ghent. (in Dutch)

Conti, S. and Fontana, D., 1999, Miocene Chemoherms of the northern Apennines, Italy: Geology, v. 27, p. 927-930.

Cremer, M. and Faugères, J.-C., 1993. Late Quaternary sediment flux on sedimentary drifts in the Northeast Atlantic. In: Stow, D.A.V. and Faugères, J.-C. (Eds.), Contourites and bottom Currents. Sedimentary Geology, pp. 89-101.

Croker, P.F. and Shannon, P.M., 1987. The Evolution and Hydrocarbon Prospectivity of the Porcupine Basin, Offshore Ireland. In: Brooks, J. and Glennie, K.W. (Eds.), Petroleum Geology of North West Europe. Graham & Trotman, pp. 633-642.

Croker, P.F., 1995, The Clare Basin: a geological and geophysical outline. In: Croker, P.F. and Shannon, P.M., eds., The Petroleum Geology of Ireland's Offshore Basins: London, Geological Society Special Publication, p. 327-339.

Croker, P.F. and Shannon, P.M., 1995, The petroleum geology of Ireland's basins: introduction. In: Croker, P.F. and Shannon, P.M., eds., The Petroleum Geology of Ireland's Offshore Basins: London, Geological Society Special Publication, p. 1-8.

De Bergé, B., 2000, Epi- en endofauna geassocieerd met koudwaterkoralen in de NO Atlantische Oceaan [unpublished Licentiaatsthesis thesis]: Universiteit Ghent, Ghent, 133 p.

de Haas, H., Grehan, A., White, M. and Shipboard scientific crew, 2000, Cold water corals in the Porcupine Bight and along the Porucpine and Rockall Bank margins Texel-Thorshavn: Texel, Netherlands Institute for Sea Research.

De Mol, B., 1998, Geosphere-biosphere coupling: Carbonate Mud Mounds and Cold Water Reefs: Workshop Report No. 143, v. 143, UNESCO, 60 p.

De Mol, B., Friend, P., Akhmetzhanov, A., Ivanonv, M., de Haas, H., Belenkaya, I. and Stadnitskaya, A., 1999, Porcupine Seabight: Short Visit. In: Kenyon, N.H., Ivanov, M.K. and Akhmetzhanov, A.M., eds., Geological Processes on the Northeast Atlantic Margin: UNESCO, p. 34-47.

De Mol, B., Van Rensbergen, P., Pillen, S., Van Herreweghe, K., Van Rooij, D., McDonnell, A., Huvenne, V., Ivanov, M., Swennen, R. and Henriet, J.P., in press, Large deep-water coral banks in the Porcupine Basin, southwest of Ireland: Marine Geology.

Dickson, R.R. and McCave, I.N., 1986, Nepheloid layers on the continental slope west of Porcupine Bank: Deep-Sea Research, v. 33, p. 791-818.

Dickson, R.R., Gould, W.J., Muller, T.J. and Maillard, C., 1985, Estimates of the mean circulation in the deep (>2000m) layer of the eastern north Atlantic: Progress in Oceanography, v. 14, p. 103-127.

Dons, C., 1935. Die Verbreitung von Steinkorallen in West-Finnmark. Zoologische Notizen XXIX Det Kongelige Norske Videnskabers Selskab, VIII(18): 57-60.

Dons, C., 1944, Zoologische Notizen XXV. Über die nördlichsten Korallenriffen der Welt: Det Kongelige Norske Videnskabers Selskab, v. VI, p. 206-209.

Druon, J.N., Langlois, G. and Le Fèvre, J., 2001, Simulating vertical mixing in a shelf-break region: addition of a shear instability model, accounting for the overall effect of internal tides, on top of a one-dimensional turbulence closure mixed layer model: Continental Shelf Research, v. 21, p. 423-454.

Ehrlich, H.L., 1996, Geomicrobiology: New York, Marcel Dekker, Inc., 719 p.

Ellet, D.J., Edwards, A. and Bowers, R., 1986, The hydrography of the Rockall Channel - an overview: Proceedings of the Royal Society of Edinburgh (B), v. 88B, p. 61-81.

Eriksen, C.C., 1982, Observations of internal wave reflection of sloping boundaries: Journal of Physical Oceanography, v. 87, p. 525-538.

Esteban, M., 1996. A review of Miocene reefs from Mediterranean areas: general trends and facies models. SEPM Concepts in Sedimentology and Paleontology, 5: 3-53.

Fannin, N.G.T., 1980, The use of regional geological surveys in the North Sea and adjacent areas in the recognition of offshore hazards. In: Ardus, D.A., ed., Offshore site investigation: London, Graham and Trotman, p. 5-21.

Faugères, J.C., Mèzerais, M.L. and Stow, D.A.V., 1993, Contourite drift types and their distribution in the North and South Atlantic Ocean basins: Sedimentary Geology, v. 82, p. 189-203.

Faugères, J.C., Imbert, P., Mézerais, M.L. and Crémer, M., 1999, Seimic patterns of a muddy contourite fan (Vema Channel, South Brazilian Basin) and a sandy distal turbidite deep-sea fan (Cap Ferret system, Bay of Biscay): a comparison: Sedimentary Geology, v. 115, p. 81-110.

Floodgate, G.D. and Judd, A.G., 1992, The origins of shallow gas: Continental Shelf Research, v. 12, p. 1145-1156.

Frederiksen, R., Jensen, A. and Westerberg, H., 1992. The Distribution of the Scleractinian Coral Lophelia Pertusa around the Faeroe Islands and the Relation to Internal Tidal Mixing. Sarsia: 77, 157-167.

Freiwald, A., 1998, Geobiology of Lophelia Pertusa (Scleractinina) Reefs in the North Atlantic [unpublished Habilationsschrift zur Erlangung der venia legendi am Fachbereich Geowissenschaften der Universitat Bremen thesis]: Universitat Bremen, Bremen, 110 p.

Freiwald, A. and Henrich, R., 1997, Anatomy of a Deep-water Coral Reef Mound From St Jernsund West Finnmark, Northern Norway: SEPM Special Publication, v. 56, 440 p.

Freiwald, A. and Wilson, J.B., 1998. Taphonomy of Modern Deep, Cold Temperate Water Coral Reefs. Historical Biology, 13: 37-52.

Freiwald, A., Wilson, J.B. and Henrich, R., 1999, Grounding Pleistocene icebergs shape recent deep-water coral reefs: Sedimentary Geology, v. 125, p. 1-8.

Freiwald, A., Dullo, W.C. and Shipboard Party, 2000, RV Poseidon Cruise 265 - Thorshavn - Galway - Kiel: cruise report.

Galanes-Alvarez, H., 2001, A pseudo 3D very high resolution seismic study of the Therese mound, Porcupine Basin, offshore SW Ireland [unpublished MSc-Thesis thesis]: University of Wales, Bangor, 114 p.

Games, K.P., 2001, Evidence of shallow gas above the Connemara oil accumulation, Block 26/28, Porcupine Basin.. In: Shannon, P.M., Haughton, P.D.W. and Corcoran, D.V., eds., The Petroleum Exploration of Ireland's Offshore BAsins: London, Geological Society, p. 361-373.

Garrett, C., 1991. Marginal Mixing Theories: Atmosphere-Ocean, v. 29, p. 313-339.

Gilbert, D. and Garrett, C., 1989, Implications for ocean mixing of internal wave scattering off irregular topography: Journal of Physical Oceanography, v. 19, p. 1716-1729.

Graham, C.C. and Straw, A., 1992, Quaternary. In: Cope, J.C.W., Ingham, J.K. and Rawson, P.F., eds., Atlas of Palaeogeography and Lithofacies: London, Geological Society, p. 149-153.

Grousset, F.E., Joron, J.L., Latouche, C., Treuil, M., Maillet, N., Faurgères, J.C. and Gonthier, E., 1998, Mediterranean Outflow through the Strait of Gibraltar since 18,000 Years B.P.: Mineralogical and Geochemical Arguments: Geo-Marine Letters, v. 8, p. 25-34.

Grousset, F.E., Cortijo, E., Huon, S., Hervé, L., Richter, T., Burdloff, D., Duprat, J. and Weber, O., 2001, Zooming in on Heinrich layers: Paleoceanography, v. 16, p. 240-259.

Gunnerus, J.E., 1768, Om nogle Norske coraller: Kongelige Norske Videnskabers Selkabs Skrifter, v. 4, p. 38-73.

Hargreaves, P.M., 1984, The distribution of Decapoda (Crustacea) in Open Ocean and NearBottom Over an Adjacent Slope in the Northern North-east Atlantic Ocean During Autumn 1979: Journal of Marine Biology Association of United Kingdom, v. 64, p. 829-857.

Harris, P.T., 1994, Incised valleys and backstepping deltaic depositis in a foreland-basin setting, Torres Strait and Gulf of Papua, Australia. In: Dalrymple, R.W., Boyd, R. and Zaitlin, B.A., eds., Incised-valley systems: origin and seimentary sequences: SEPM Special Pubication No. 51, p. 97-108.

Haug, G.H. and Tiedemann, R., 1998, Effect of the formation of the Isthmus of Pananma on Atlantic thermohaline circulation: Nature, v. 393, p. 673-676.

Heileman, K., 2000, Hydrodynamische änderungen des Mittelmeerausstromwassers und deren Abbilding in den Sedimenten des Iberischen Kontinentalhangs[unpublished PhD thesis]: GEOMAR, Kiel, p88

Henrich, R., Freiwald, A., Wehrmann, A., Schäfer, P., Samtleben, C. and Zankl, H., 1996, Nordic Cold-water Carbonates: Occurences and Controls. In: Reitner, J., Neuweiler, F. and Gunkel, F. (Eds.), Global and Regional Controls on Biogenic Sedimentation. I. Reef Evolution. Research Reports, Volume SB2: Göttingen, Göttinger Arb. Geol. Paläont, p. 35-52.

Henriet, J.-P., De Mol, B., Pillen, S., Vanneste, M., Van Rooij, D., Versteeg, W., Croker, P.F., Shannon, P.M., Unnithan, V., Bouriak, S., Chachkine, P. and Party, T.P.-B.S., 1998, Gas hydrate crystals may help build reefs: Nature, v. 391, p. 648-649.

Henriet, J.P., De Mol, B., Vanneste, M., Huvenne, V., Van Rooij, D. and The "Porcupine-Belgica" 97, 98 and 99 shipboard parties., 2001, Carbonate mounds and slope failures in the Porcupine Basin: a development model involving past fluid venting.. In: Shannon, P.M., Haughton, P. and Corcoran, D., eds., Petroleum Exploration of Irelands's Offshore Basins: London, Special Publication Geological Society of London, p. 375-383.

Holloway, P.E., 1985, A comparison of semi-diurnal internal tides form different bathymetric locations on the Australian North West Shelf: Journal of Physical Oceanography, v. 15, p. 240-251.

Holt, J.T. and Thorpe, S.A., 1997, The propagation of high frequency internal waves in the Celtic Sea: Deep-Sea Research, v. 44, p. 2087-2116.

Hovland, M., 1982, Pockmarks and the recent geology of the central section of the Norwegian Trench: Marine Geology, v. 47, p. 283-301.

Hovland, M., 1983. Elongated depressions associated with pockmarks in the Western slope of the Norwegian Trench. Marine Geology, 51: 35-46.

Hovland, M., 1990. Do Carbonate Reefs form due to Fluid Seepage? Terra Nova, 2: 8-18.

Hovland, M., 1992, Hydrocarbon seeps in Northern Marine waters - Their occurrence and effects: Palaios, v. 7, p. 376-382.

Hovland, M. and Judd, A.G., 1988, Seabed Pockmarks and Seepages: London, Graham and Trotman Limited, 293 p.

Hovland, M. and Mortensen, P.B., 1999, Norske korallrev og prosesser i havbunnen, John Grieg Forlag, Bergen, 155 p.

Hovland, M. and Thomsen, E., 1997, Cold-water Corals - Are they hydrocarbon Seep related?: Marine Geology, v. 137, p. 159-164.

Hovland, M., Croker, P.F. and Martin, M., 1994, Fault-associated Seabed Mounds (Carbonate Knolls?) off Western Ireland and North-west Australia: Marine and Petroleum Geology, v. 11, p. 232-246.

Hovland, M., Mortensen, P.B., Brattegard, T., Strass, P. and Rokoengen, K., 1998. Ahermatypic Coral Banks off Mid-Norway: Evidence for a Link with Seepage of Light Hydrocarbons. Palaios, 13: 189-200.

Huthnance, J.M., 1989, Internal tides and waves near the continental shelf edge: Geophysical Fluid Dynamics, v. 48, p. 81-106.

Huthnance, J.M. and Gould, W.J., 1989, On the northeast Atlantic slope current. In: Neshyba, S.J. (Ed.), Poleward flows along eastern ocean boundaries. Coastal and Estuarine Studies, pp. 76-81.

Huthnance, J.M., Coelho, H., Griffiths, C., Knight, P.J., Rees, A.P., Sinha, B., Vangriesheim, A., White, M. and Chatwin, P., G, 2001, Physical structures, advection and mixing in the region of Goban spur: Deep-Sea Research II, v. 48, p. 2979-3021.

Huvenne, V.A.I., Croker, P.F. and Henriet, J.-P., 2002, A refreshing 3D view of an ancient sediment collapse and slope failure: Terra Nova, v. 14, p. 33-40.

Huvenne, V., Blondel, P. and Van Rensbergen, P., submitted, BOTTOM CURRENTS AND MOUNDS IN THE PORCUPINE SEABIGHT: RESULTS FROM SIDESCAN SONAR ANALYSES: Marine Geology.

Huvenne, V.A.I., De Mol, B. and Henriet, J.P., submitted, A 3D seismic study of the morphology and spatial distribution of buried mounds in the Porcupine Basin: Marine Geology.

IOC, IHO and BODC, 1997, GEBCO-1997: The 1997 Edition of the GEBCO Digital Atlas: Birkenhead, British Oceanographic Data Centre.

Irwin, H. and Curtis, C., 1977, Isotopic evidence for source of diagenetic carbonates formed during burial of organci-rich sediments: Nature, v. 269, p. 209-213.

Jansen, E., Raymon, M.E. and Blum, P., 1996, Proceedings of the Ocean Drilling Progam Initial reports North Atlantic-Artic Gateways II: Initial Reports, 162: Washington, US Govt. Printing Office.

Jensen, A. and Frederiksen, R., 1992, The Fauna associated with the Bank-forming Deepwater Coral Lophelia Pertusa (Scleractinaria) on the Faroe Shelf: Sarsia, p. 53-63.

Judd, A.G. and Hovland, M., 1992, The evidence of shallow gas in marine sediments: Continental Shelf Research, v. 12, p. 1081-1095.

Kelly, S.R.A., Ditchfield, p.W., Doubleday, P.A. and Marshall, J.D., 1995, An Upper Jurassic Methane-seep Limestone from the Fossil Bluff Group Forearc Basin of Alexander Island, Antarctica: Journal of Sedimentary Research, v. A65, p. 274-282.

Kenyon, N.H., Ivanov, M.K. and Akmetzhanov, A.M. (Eds), 1998. Cold water carbonate mounds and sediment transport on the Northeast Atlantic margin. IOC Technical Series, 52. UNESCO, 178 pp.

Kenyon, N., Akhmetzhanov, A.M., Wheeler, A.J., van Weering, T.C.E., de Haas, H. and Ivanov, M.K., accepted, Giant Carboante Mud Mound in the Souther Rockall Trough: Marine Geology.

King, L.H. and MacLean, B., 1970, Pockmarks on the Scotian shelf: Geological Society of America Bulletin, v. 81, p. 3141-3148.

Krumbein, W.E., 1983, Stromatolites-the challenge of a term in space and time: Precambrian Res., v. 20, p. 493-531.

Land, L.S., Lang, J.C. and Barnes, D.J., 1977, On Stable Carbon and Oxygen isotopic composition of some shallow water, ahermatypic, Scleractinia coral skeletons: Geochimica et Cosmochimica Acta, v. 41, p. 169-172.

Le Danois, E., 1948, Les profondeurs de la mer: Paris, Payot, 303 p.

Lekens, W., 2000, Een studie van de driftsedimentatie in het Porcupine bekken [unpublished MSc thesis]: University Ghent, Ghent, 93 p.

Levitus, S., Burgett, R. and Boyer, T.P., 1994a. World Ocean atlas 1994. NOAA Atlas NESDIS 3, 3: Salinity. U.S. Department of Commerce, Washington DC, 99 pp.

Levitus, S., Burgett, R. and Boyer, T.P., 1994b. World Ocean atlas 1994. NOAA Atlas NESDIS4, 4: Temperature. U.S. Department of Commerce, Washington DC, 117 pp.

Link, W.K., 1952, Significance of oil and gas seeps in world oil exploration: American Association of Petroleum Geologists Bulletin, v. 36, p. 1505-1541.

Maas, L., R. M. and Lam, F.-P., A., 1995, Geometric focusing of internal waves: Journal of Fluid Mechanics, v. 300.

MacDonald, H., Allan, P.M. and Lovell, J.P.B., 1987, Geology of Oil accumulation in Block 26/28, Porcupine Basin, Offshore Ireland.. In: Brooks, J. and Glennie, K., eds., Petroleum Geology of North West Europe: Graham & Trotman, p. 643-651.

Maldonado, A. and Nelson, C.H., 1999. Interaction of tectonic and depositional processes that control the evolution of the Iberian Gulf of Cadiz margin. Marine Geology, 155: 217-242.

Marion, D. and Jizba, D., 1997, Acoustic Properties of Carbonate Rocks: Use in Quantitative Interpretation of Sonic and Seismic Measurements. In: Palaz, I. and Marfurt, K.J., eds., Carbonate Seismology: Geophysical Developments Series: Society of Exploration Geophysicists, p. 75-95.

Masson, D.G. and Miles, P.R., 1986, Structure and development of Porcupine Seabight sedimentary basin, offshore southwest Ireland: The American Association of Petroleum Geologists bulletin, v. 70, p. 536-548.

Mattews, M.D., 1996, Migration-A View from the Top. In: Schumacher, D. and Abrams, A., eds., Hydrocarbon migration and its near-surface expression: AAPG Memoir 66, p. 139-155.

Mauritzen, C., Morel, Y. and Paillet, J., 2001, On the influence of Mediterranean Water on the Central Waters of the North Atlantic Ocean: Deep-Sea Research I, v. 48, p. 347-381.

Max, M.D., 1987, The three-phase development of the Porcupine Seabight: basin formation and the structurally-dependent sedimentary pattern: Journal of petroleum geology, v. 10, p. 59-72.

Mc Donnell, A., 2001, Comparitive Tertiary basin Development in the Porcupine and Rockall Basins [unpublished PhD-thesis thesis]: National University of Ireland, Dublin.

McCabe, M. and Clark, P.U., 1998, Ice sheet variability around the North Atlantic Ocean during the last deglaciation: Nature, v. 392, p. 373-377.

McCann, T., Shannon, P.M. and Moore, J.G., 1995a. Fault patterns in the Cretaceous and Tertiary (end syn-rift, thermal subsidence) succession of the Porcupine Basin, offshore Ireland. Journal of Structural Geology, 17(2): 201-214.

McCann, T., Shannon, P.M. and Moore, J.G., 1995b. Fault styles in the Porcupine Basin, offshore Ireland: tectonic and sedimentary controls. In: Croker, P.F. and Shannon, P.M. (Eds.), The petroleum geology of Ireland's offshore basins. Geological Society Special Publication, 93, pp. 371-383.

McCave, I.N., Manighetti, B. and Beveridge, N.A.S., 1995a, Circulation in the glacial North Atlantic inferred from grain-size measurements: Nature, v. 374, p. 149-152.

McCave, I.N., Manighetti, B. and Robinson, S.G., 1995b, Sortable silt and fine sediment size/composition slicing: Paramters for palaeocurrent speed and palaeoceanography: Paleoceanography, v. 10, p. 593-610.

Messing, C.G., Neumann, C.A. and Lang, J.C., 1990, Biozonation of Deep-Water Lithoherms and Associated Hardgrounds in the Northeastern Straits of Florida: Palaios, v. 5, p. 15-33.

Mikkelsen, N., Erlenkeuser, H., Killingley, J.S. and Berger, W.H., 1982, Norwegian corals: radiocarbon and stable isotopes in Lophelia pertusa: Boreas, v. 11, p. 163-171.

Monty, C.L.V., Bosence, D.W.J., Bridges, P.H. and Pratt, B.R., 1995, Carbonate Mud-Mounds Their Origin and Evolution: Special Publication, v. 23: Paris, Blackwell science, 537 p.

Moore, D.R. and Bullis, H.R., 1960, A deep-water coral reef in the Gulf of Mexico: Bulletin of Marine Science of the Gulf and Caribbean, v. 10, p. 125-128.

Moore, J.G., 1992, A syn-rift to post-rift transition sequence in the Main Porcupine Basin, offshore western Ireland. In: Parnell, J., ed., Basins on the Atlantic Seabord: petroleum sedimentology and basin evolution: Geological Society special publications, p. 333-349.

Moore, J.G. and Shannon, P.M., 1991, Slump Structures in the Late Tertiary of The Porcupine Basin, Offshore Ireland: Marine and Petroleum Geology, v. 8, p. 184-197.

Moore, J.G. and Shannon, P.M., 1992, Palaeocene-Eocene deltaic sedimentation, Porcupine Basin, offshore Ireland-a sequence stratigraphic approach: First Break, v. 10, p. 461-469.

Moore, J.G. and Shannon, P.M., 1995, The Cretaceous Succession in the Porcupine Basin, Offshore Ireland: Facies Distribution and Hydrocarbon Potential. In: Croker, P.F. and Shannon, P.M., eds., The Petroleum Geology of Ireland's Offshore Basin: p. 345-370.

Mortensen, P.B., 2000. Lophelia pertusa (Scleractinia) in Norwegian waters. Distribution, growth and associated fauna. PhD Thesis, University of Bergen, Bergen.

Mortensen, P.B. and Rapp, H.T., 1998, Oxygen- and carbon isotope ratios related to growth line patterns in skeletons of Lophelia Pertusa (L) (Anthozoa: Scleractinia): Implications for determination of Lineas extension rates: Sarsia, v. 83, p. 433-446.

Mortensen, P.B., Hovland, M., Brattegard, T. and Farestveit, R., 1995. Deep Water Bioherms of the Scleractinian Coral Lophelia Pertusa (L.) at 64 N on the Norwegian Shelf: Structure and Associated Megafauna. Sarsia: 145-158.

Mortensen, P.B., Hovland, M., Fosså, J.H. and Furevik, D., 2001, Distribution, abundance and size of Lophelia pertusa coral reefs in mid-Norway in relation to seabed characteristics: Journal of the Marine Biological Association of the United Kingdom, v. 84, p. 581-597.

Mudge, T.D. and Lueck, R.G., 1994, Mixing around a shallow seamount: EOS, v. 75, p. 120.

Mullins, H.T., Newton, C.R., Kathryn, H. and Van Buren, H.M., 1981. Modern Deep-water Coral Mounds North of Little Bahama Bank: Criteria for Recognition of Deep-water Coral Bioherms in the Rock Record. Journal of Sedimentary Petrology, 51(3): 999-1013.

Mullins, H.T., Thompson, J.B., McDougall, K. and Vercoutere, T.L., 1985, Oxygen-minimum zone edge effects: Evidence from the central California coastal upwelling system: Geology, v. 13, p. 491-494.

Naylor, D. and Shannon, P., 1982, The geology of offshore Ireland and West Britain: London, Graham & Trotman.

Nelson, C.H., Baraza, J. and Maldonado, A., 1993. Mediterranean undercurrent sandy contourites, Gulf of Cadiz, Spain. Sedimentary Geology, 82: 103-131.

Nelson, C.H., Baraza, J., Maldonado, A., Rodero, J., Escutia, C. and Barber Jr., J.H., 1999, Influence of the Atlantic inflow and Mediterranean outflow currents on Late Quaternary sedimentary facies of the Gulf of Cadiz continental margin: Marine Geology, v. 155, p. 99-129.

Neumann, A.C. and Macintyre, I.G., 1985, Reef response to sea level rise: keep-up, catch-up or give-up: Proceedings of the Fifth International Coral Reef Congress, p. 105-110.

Neumann, A.C. and Paull, C.K., 1998. Lithoherms in Blake-Bahama Region: Controlled by Bottom Currents not Methane Seepage. In: De Mol, B. (Ed.), Geosphere-Biosphere coupling: Carbonate Mud Mounds and Cold Water Reefs. UNESCO, Ghent, pp. 39.

Neumann, A.C., Kofoed, J.W. and Keller, G.H., 1977. Lithoherms in the Straits of Florida. Geology, 5: 4-10.

New, A.L., 1987, Internal Tidal Currents in the Bay of Biscay: Advances in Underwater Technology, Ocean Science and Offshore Engineering, v. 12, p. 279-291.

New, A.L., Barnard, S., Herrmann, P. and Molines, J.-M., 2001, On the origin and pathway of the saline Inflow to the Nordic Seas: insight from models: Progress in Oceanography, v. 48, p. 255-287.

Oehler, D.Z. and Sternberg, B.K., 1984, Seepage-induced anomalies, "false" anomalies and implications for electrical prospecting: American Association of Petroleum Geologists Bulletin, v. 68, p. 1121-1145.

O'Niel Barringer, M. and Price, J.F., 1999, A review of the physical oceanography of the Mediterranean outflow: Marine Geology, v. 155, p. 63-82.

Paull, C.K., Chanton, J.P., Neumann, A.C., Coston, J.A. and Martens, C.S., 1992, Indicators of Methane-derived Carbonates and Chemosynthetic Organic Carbon Deposits: Examples from the Florida Escarpment: Palaios, v. 7.

Paull, C.K., Neumann, A.C., am Ende, B.A., Ussler III, W. and Rodriguez, N.M., 2000. Lithoherms on the Florida-Hatteras slope. Marine Geology, 166: 83-101.

Pearson, I. and Jenkins, D.G., 1986, Unconformities in the Cenozoic of the North-East Atlantic. In: Summerhayes, C.P. and Shackleton, N.J. (Eds.), North Atlantic Palaeoceanography, Geological Society Special Publication, 21, p. 79-86.

Peckman, J., Theil, V., Michaelis, W., Clari, P., Gaillard, C., Martire, L. and Reitner, J., 1999, Cold seep deposits of Beauvoisin (Oxfordian; southeastern France) and Marmorito (Miocene; northern Italy): microbially induced authigenic carbonates: Int Journ Earth Sciences, v. 88, p. 60-75.

Pérès, J.M., 1985, History of the Mediterranean biota and the colonization of the depths. In: Margaleff, R., ed., Western Mediterranean: Oxford, Pergamon Press., p. 198-232.

Pingree, R.D. and Morrison, G.K., 1973. The relation between stability and source waters for a section in the Northeast Atlantic. Journal of Physical Oceanography, 3(280-285).

Pingree, R.D. and LeCann, B., 1989. Celtic and Armorican slope and shelf residual currents. Progress in Oceanography, 23: 303-338.

Pingree, R.D. and LeCann, B., 1990, Structure, strength and seasonality of the slope currents in the Bay of Biscay region: Journal of Marine Biology, Association of United Kingdom, v. 70, p. 857-885.

Pollard, R.T., Griffiths, M.J., Cunningham, S.A., Read, J.F., Pérez, F.F. and Ríos, A.F., 1996, Vivaldi 1991-a study of the formation, circulation and ventilation of Eastern North Atlantic Central Water: Progress in Oceanography, v. 37, p. 167-192.

Pratje, O., 1924, Korallenbänke in tiefem und kühlen Wasser: Zentralblatt für Mineralogie, p. 410-415.

Rasch, H.H., 1836, Naturhistorike notitser fra en reise, foretagen i sommeren 1833: Magazin for Naturvidenskaberne, v. R. II.

Reed, J.K., 1992, Submersible studies of deep-water Oculina and Lophelia coral banks off southeastern U.S.A.. In: Cahoon, L.B., ed., Diving for Science: Wilmington, University of North Carolina, p. 143-151.

Reston, T.J., Pennell, J., Stubenrauch, A., Walker, I. and Perez-Gussinye, M., 2001, Detachment faulting, mantle serpentinization and serpentinite-mud volcanism beneath the Porcupine Basin, southwest of Ireland: Geology, v. 29, p. 587-590.

Ribbe, J. and Holloway, P., E., 2001, A model of suspended sediment transport by internal tides: Continental Shelf Research, v. 21, p. 395-422

Rice, A.L., Thurston, M.J. and New, A.L., 1990, Dense aggregations of a hexactinellid sponge, Pheronema carpenteri. In: the Porcupine Seabight (northeast Atlantic Ocean) and possible causes: Prog. Oceanog, v. 24, p. 179-196.

Rice, A.L., Billett, D.S.M., Thurston, M.H. and Lampitt, R.S., 1991. The Institute of Oceanographic sciences Biology Programme in the Porcupine Seabight: Background and General Introduction. J. Mar. Biol. Ass. U.K., 71: 281-310.

Richter, T.O., Lassen, S., van Weering, T.C.E. and de Haas, H., 2001, Magnetic susceptibility patterns and provenance of ice-rafted material at Feni Drift, Rockall Trough: implications for the history of the British-Irisch ice sheet: Marine Geology, v. 173, p. 37-54.

Roberts, D.G., Masson, D.G., Montadert, L. and Charpal, O.d., 1981, Continental Margin from the Porcupine Seabight to the Armorican Marginal Basin. In: Illing, L.V. and Hobson, G.D., ed., Petroleum Geology of the Continental shelf of North-West Europe: London, Institute of Petroleum, p. 455-473.

Roberts, H.H. and Aharon, P., 1994, Hydro-carbon-derived carbonate buildups of the norther Gulf of Mexico continental slope: a review of submersible investigations: Geo-Marine Letters, v. 14, p. 135-148.

Roberts, J. M., 2000. Coral colonies make a home on North Sea oil rigs. Reef Encounter 27: 17-18.

Rogers, A.D., 1999, The biology of Lophelia pertusa (Linnaeus 1758) and Other Deep-Water Reef-Forming Corals and Impacts from Human Activities.: International Revue der gesamten Hydrobiologie, v. 84, p. 315-406.

Saoutkin, A., 1998, Calcareous nannoplankton from upper Quarternary deep water coral banks in Porcupine Basin (North Atlantic) implications to environmetal growth conditions of the coral banks [unpublished MSc thesis]: Moscow State University, Moscow, 60 p. (in Russian)

Sars, M., 1865, Om de i Norge forekommende fossile dyrelevinger fra Quartaerperioden: Christiania, Universitetsprogram for forste halvaar, v. 1864, p. 1-164.

Sassen, R., McCabe, C.M., Kyle, J.R. and Chinn, E.W., 1989, Deposition of magnetic pyrrhotite during alteration of crude oil and reduction of sulfate: Organic Geochemistry, v. 14, p. 381-392.

Schlitzer, R., 2001, Ocean Data View: http://www.awi-bremerhaven.de/GEO/ODV.

Schnitker, D., 1986, North-east Atlantic Neogene benthic foraminiferal faunas: tracers of deep-water palaeoceanography. In: Summerhayes, C.P. and Shackleton, N.J., eds., North Atlantic Palaeoceanography: London, Geological Society Special Publication, p. 191-203.

Schönfeld, J. and Zahn, R., 2000, Late Glacial to Holocene history of the Mediterranean Outflow. Evidence from benthic foraminiferal assemblages and stable isotopes at the Portuguese margin: Palaeogeography, Palaeoclimatology, Palaeoecology, v. 159, p. 85-111.

Schumacher, D., 1996, Hydrocarbon-Induced Alteration of Soils and Sediments. In: Schumacher, D. and Abrams, M.A., eds., Hydrocarbon migration and its near-surface expression: AAPG Memoir 66. p. 71-89.

Scoffin, T.P. and Bowes, G.E., 1988, The Facies Distribution of Carbonate Sediments on Porcupine Bank, Northeast Atlantic: Sedimentary Geology, v. 60, p. 125-134.

Scoffin, T.P., Alexandersson, T.E., Bowes, G.E., J., C.J., Farrow, G.E. and Milliman, J.D., 1980, Recent, temperate, sub-photic, carbonate sedimentation: Rockall Bank, northeast Atlantic: Journal of sedimentary petrology, v. 50, p. 331-356.

Seirro, F.J., Flores, J.A. and Baraza, J., 1999, Late Glacial to recent paleoenvironmental changes in the Gulf of Cadiz and formation of sandy contourite layers: Marine Geology, v. 155, p. 157-172.

Séranne, M. and Nzé Abeigne, C.-R., 1999, Oligocene to holocene sediment drifts and bottom currents on the slope of Gabon continental margin (west Africa) Consequences for sedimentation and southeast Atlantic upwelling: Sedimentary Geology, v. 128, p. 179-199.

Shannon, P.M., 1991. The development of Irish offshore sedimentary basins. Journal of the Geological Society, London, 148: 181-189.

Shannon, P.M., 1992, Early Tertiary Submarine Fan Deposits in the Porcupine Basin, Offshore Ireland. In: Parnell, J., ed., Basins on the Atlantic Seaboard: Petroleum Geology, Sedimentology and Basin Evolution: p. 351-373.

Shannon, P.M., Williams, B.P. and Sinclair, I.K., 1995, Tectonic Controls on Upper Jurassic to Lower Cretaceous Reservoir Architecture in the Jeanne D'Arc Basin, with some Comparisons from the Porcupine and Moray Fith Basins. In: Croker, P.F. and Shannon, P.M., eds., The Petroleum Geology of Ireland 's Offshore Basins: Geological Society Special Publication, p. 467-490.

Sherwin, T.J. and Taylor, N.K., 1987. Modelling Internal Tide Processes Around the North-west European Shelf Edge. Advances in Underwater Technology, Ocean Science and Offshore Engineering, 12: 263-278.

Sinclair, I.K., 1995, Sequence stratigraphic response to Aptian-Albian rifting in conjugate margin basins: a comparison of the Jeane d'Arc Basin, offshore Newfoundland and the Porcupine Basin, offshore Ireland. In: Scrutton, R.A., Stoker, M.S., Shimmield, G.B. and Tudhope, A.W., eds., The Tectonics, Sedimentation and Palaeoceanography of the North Atlantic Region: London, Geological Society Special Publication, p. 29-49.

Sinclair, I.K., Shannon, P.M., Williams, B.P.J., Harker, S.D. and Moore, J.G., 1994, Tectonic controls on sedimentary evolution of three North Atlantic borderland Mesozoic basins: Basin Research, p. 193-217.

Smith, R., 1989, Poleward flows along eastern boundaries: An introduction and historical reviews. In: Neshyba, S.J., Mooers, C.N.K., Smith, R.L. and Barber, R.T., eds., Poleward flows along the eastern ocean boundaries: Berlin, Springer-Verlag, p. 17-25.

Snoeckx, H., Grousset, F., Revel, M. and Boelaert, A., 1999, European contribution of ice-rafted sand to Heinrich layers H3 and H4: Marine Geology, v. 158, p. 197-208.

Squires, D.F., 1965, Deep-water coral structure on the Campbell Plateau, New Zealand: Deep-Sea Research, v. 12, p. 785-788.

Stanley, G.D. and Cairns, S.D., 1988, Constructional azooxanthellate coral communities: an overview with implications for the fossil record: Palaios, v. 3, p. 233-242.

Stetson, T.R., Squires, D.F. and Pratt, R.M., 1962, Coral Banks occurring in Deep Water on the Blake Plateau: Novitates, v. 2114.

Stoker, M.S., 1998, Sediment-drift development on the continental margin off NW Britain. In: Stoker, M.S., Evans, D. and Cramp, A., eds., Geological Processes on Continental Margins: Sedimentation, Mass-Wasting and Stability: Special Publications: London, Geological Society Special Publications, p. 229-254.

Stoker, M.S., van Weering, T.C.E. and Svaerdborg, T., 2002, A Mid- to Late Cenozoic Tectonostratigraphic framework for the Rockall Trough. In: Shannon, P.M., Haughton, P.D.W. and Corcoran, D.V., eds., The Petroleum Exploration of Ireland's Offshore Basins: London, The Geological Society.

Strömgren, T., 1971. Vertical and horizontal distribution of Lophelia pertusa (Linnè) in Trondheimsfjorden on the west coast of Norway. Kongelig Norske Videnskabers Selskabs Skrifter, 6: 1-9.

Sumida, P. and Kennedy, R., 1998, Porcupine Seabight. - Biological Data. In: Kenyon, N.H., Ivanov, M.K. and Akhmetzhanov, A.M., eds., Cold water carbonate mounds and sediment transport on the Northeast Atlantic margin: UNESCO, p. 102-106.

Swart, P.K., 1983, Carbon and Oxygen Isotope Fractionation in Scleractinian Corlas: a Review: Earth-Science Reviews, v. 19, p. 51-80.

Swennen, R., Cronin, B., Ivanov, M., Kozlova, E., Wheeler, A., Akhmetzhanov, A., Saoutkin, A., Van Rooij, D., Zaragosi, S., Mazurenko, L., Degryse, C., Sumida, P., Satur, N., Kennedy, R., Akhmanov, G., Belen`kaya, I., Pillen, S., Yu Naumov, A., Stadnitskaya, A., De Mol, B., Balashova, A. and Saprykina, A., 1998, Porcupine Seabight. Bottom Sampling Results. In: Kenyon, N.H., Ivanov, M.K. and Akhmetzhanov, A.M. (Eds.), Cold water carbonate mounds and sediment transport on the Northeast Atlantic margin,, UNESCO IOC, 52, p. 59-97.

Tate, M.P., 1993, Structural framework and tectono-stratigraphic evolution of the Porcupine Seabight Basin, offshore western Ireland: Marine and Petroleum Geology, v. 10, p. 95-123.

Tate, M., White, N. and Conroy, J.-J., 1993, Lithospheric Extension and Magmatism in the Porcupine Basin West of Ireland: Journal of Geophysical Research, v. 96, p. 13905-13923.

Teichert, C., 1958, Cold- and deep-water coral banks: The Bulletin of the American Association of Petroleum Geologists, v. 42, p. 1064-1082.

Theil, V., Peckmann, J., Seifert, R., Wehrung, P., Reitner, J. and Michaelis, W., 1999, High isotopically deplited isoprenoids: Molecular markers for ancient methane venting: Geochimica et Cosmochimica Acta, v. 63, p. 3959-3966.

Thomas, M.A. and Anderson, J.B., 1994, Sea-level controls on the faceis architectrue of the Trinity/Sabine incised-valley system, Texas continental shelf. In: Dalrymple, R.W., Boyd, R. and Zaitlin, B.A., eds., Incised-valley systems: origin and sedimentary sequences: SEPM Special Pubication No. 51, p. 63-82.

Thomson, C.W., 1873. The depths of the Sea. MacMillan, London, 527 pp.

Thorpe, S.A., 1989, The distortion of short internal wave produced by a long wave with application to ocean boundary mixing: Journal of Fluid Mechanics, v. 178, p. 279-302.

Thorpe, S.A., 1992, The generation of internal waves by flow over the rough topography of a continental slope, Proceedings of the Royal Society of London: p. 115-130.

Thorpe, S.A. and White, M., 1988, A deep intermediate nepheloid layer: Deep-Sea Research, v. 35, p. 1665-1671.

Toole, J.M., Polzin, K.L. and Schmitt, R.W., 1994, New estimates of diapycnal mixing in the abyssal ocean: Science, v. 264, p. 1120-1123.

Tucker, M.E. and Wright, P.V., 1990, Carbonate sedimentology: London, Blackwell Science Ltd., 481 p.

Tudhope, A.W. and Scoffin, T.P., 1995, Processes of sedimentation in Gollum Channel, Porcupine Seabight: submersible observations and sedimentation analyses: Transactions of the Royal Society of Edinburgh: Earth Sciences, v. 86, p. 49-55.

Urick, R.J., 1982, Sound propagation in the sea: New York, McGraw-Hill, 423 p

van Aken, H.M., 2000, The hydrography of the mid-latitude Northeast Atlantic Ocean II: The intermediate water masses: Deep-Sea Research I, v. 47, p. 789-824.

van Aken, H.M. and Becker, G., 1996, Hydrography and through-flow in the north-eastern North Atlantic Ocean: the NANSEN project: Progress in Oceanography, v. 38, p. 297-346.

Van Gaever, S., 2001, Gemeenschapsanalyse van macrofauna geassocieerd met koudwaterkoraalriffen in de NO Atlantisische Oceaan [unpublished MSc thesis thesis]: University of Ghent, Ghent, 110 p.

Van Geet, M., Swennen, R. and Wevers, M., 2000, Quantitative analysis of reservoir rocks by microfocus X-ray computerised tomography: Sedimentary Geology, v. 132, p. 25-36.

Van Rooij, D., 1998, Sequentie-stratigrafie met hoog-resolutie-sesimiek aan de rand van de Keltische zee en het Porcupine bekken, ten zuidwesten van Ierland [unpublished Licentiaatsverhandeling thesis]: IWT report Universiteit Gent, Ghent, 103 p.

Van Rooij, D., 2001, Laat-Cenozoische evolutie van het Zuidelijk Porcupine bekken, ten zuidwesten van Ierland: sesmostratigrafie en sedimentaire dynamiek van een passieve periglaciale rand: Ghent, RCMG.

Van Rooij, D., Blamart, D. and Unnithan, V., 2002, Cruise Report MD123-Gescineces: LEG2, part GEOMOUND Porcupine Basin and Rockall Trough, off Western Ireland September 7-11, 2001: Ghent, RCMG.

Van Rooij, D., De Mol, B., Huvenne, V., Ivanov, M. and Henriet, J.P., accepted, Seismic evidence of current-controlled sedimentatiion in the Belgica mound provicne, southwest of Ireland: Marine Geology.

Vangriesheim, A., 1985. Hydrologie et circulation profonde. In: Laubier, L. and Monniot, C. (Eds.), Peuplements profonds du Golfe de Gascogne. IFREMER, Brest, pp. 43-70.

Viana, A.R., Faugères, J.-C. and Stow, D.A.V., 1998, Bottom-current-controlled sand deposits-a review of modern shallow-to deep-water environments: Sedimentary Geology, v. 114, p. 53-80.

Wallace, H.E., Thomson, J., Wilson, T.R.S., Weaver, P.P.E., Higgs, N.C. and Hydes, D.J., 1988. Active diagenetic formation of metal-rich layers in N.E. Atlantic sediments. Geochimica et Cosmochimica Acta, 52, 1557-1569.

Weber, J.N. and Woodhead, P.M.J., 1972, Temperature dependence of Oxygen-18 concentration of Reef Coral Carbonates: Journal of Geophysical Research, v. 77, p. 463-473.

Wheeler, A., Degryse, C., Limonov, A. and Kenyon, N., 1998. Porcupine Seabight. ORETech Sidescan Sonar Data The Northern Porcupine Seabight. In: Kenyon, N.H., Ivanov, M.K. and Akhmetzhanov, A.M. (Eds), Cold water carbonate mounds and sediment transport on the Northeast Atlantic margin., UNESCO IOC 52, 40-54.

Wheeler, A., Zaragosi, S. and Sautkin, A., 1998, Interpretation of Cores form Middle Gollum Channel. In: Kenyon, N.H., Ivanov, M.K. and Akhmetzhanov, A.M., eds., Cold water carbonate mounds and sediment transport on the Northeast Atlantic margin: UNESCO IOC 52, p. 98-100.

White, M., 2001, Hydrography and physical dynamics at the NE Atlantic margin that influence the deep water cold coral reef ecosystem: Galway, Department of Oceanography, NUI.

White, M. and Bowyer, P., 1997, The shelf-edge current north-west of Ireland: Annales Geophysicae, v. 15, p. 1076-1083.

White, N., Tate, M. and Conroy, J.-J., 1992, Lithospheric stretching in the Porcupine Basin, west of Ireland. In: Parnell, J., ed., Basins on the Atlantic Seabord: petroleum geology, sedimentology and basin evolution: Geological Society special publication, p. 327-331.

Whiticar, M. and Werner, F., 1981, Pockmarks: submarine vents of natural gas or freshwater seeps?: Geo-Marine Letters, v. 1, p. 193-199.

Wilber, R.J. and Neumann, A.C., 1993, Effect of Submarine Cementation on Microfacies and Physical, Properties of Carbonate Slope Deposits, Northern Bahamas. In: Rezak, R. and Lavoie, D.L., eds., Carbonate Microfabrics: Frontiers in Sedimentary Geology: New York, Springer-Verlag, p. 79-94.

Wilkins, R.H. and Richardson, M.D., 1998, The influence of gas bubbles on sediment acoustic properties: in situ, laboratory and theoritical results form Eckernförde Bay, Baltic sea: Continental Shelf Research, v. 18, p. 1859-1892.

Wilson, J.B., 1975, The Distribution of the Coral Caryophyllia Smithii S. & B. on the Scottish Continetal Shelf: Journal of Marine Biology Association of United Kingdom, v. 55, p. 611-625.

Wilson, J.B., 1979a. The distribution of the coral Lophelia Pertusa (L.) [L. prolifera (Pallas)] in the North-east Atlantic. Journal of Marine Biology Association of United Kingdom, 59: 149-164.

Wilson, J.B., 1979b, The first recorded specimens of the deep-water coral Lophelia pertusa (Linnaeus, 1758) from British waters: Bull. Br. Mus. Nat. Hist. (Zool.), v. 36, p. 209-215.

Wilson, J.B., 1979c, "Patch" Development of the deep-water coral Lophelia pertusa (L.) on Rockall Bank: Journal of Marine Biology, Association of United Kingdom, v. 59, p. 165-177.

Wunsch, C., 1975, Internal tides in the ocean: Reviews of Geophysics and Space Physics, v. 13, p. 167-182.

Zibrowius, H., 1980, Les Scléractiniaires de la Méditerranée et de l'Atlantique nord-oriental: Memoires de l'Institut Oceanographique, Monaco, v. 11, p. 1-227.

Zibrowius, H. and Gili, J.-M., 1990. Deep-water Scleractinia (Cnidaria: Anthozoa) from Namibia, South Africa and Walvis Ridge, southeastern Atlantic. Scientia Marina, 54: 19-46.

1051-B

UNIVERSITEIT GENT

Faculteit Wetenschappen
Vakgroep Geologie en Bodemkunde
Academiejaar 2001 - 2002

Development of coral banks in Porcupine Seabight (SW Ireland) A multidisciplinary approach

Ontwikkeling van koraalbanken in de Porcupine Seabight (SW Ierland) Een multidisciplinaire studie

Ben De Mol

Appendix

Promotor: Prof. Dr. J.-P. Henriet
Co-promotor: Prof. Dr. R. Swennen

Proefschrift ingediend bij de Faculteit Wetenschappen van de Universiteit Gent voor het verkrijgen van de graad van Doctor in de Wetenschappen

UNIVERSITEIT GENT

Faculteit Wetenschappen
Vakgroep Geologie en Bodemkunde
Academiejaar 2001 - 2002

UNIVERSITEIT GENT
RCMG-Seismostratigrafie
inventarisnummer : .....
1051 (B)

Development of coral banks in Porcupine Seabight (SW Ireland) A multidisciplinary approach

Ontwikkeling van koraalbanken in de Porcupine Seabight (SW Ierland) Een multidisciplinaire studie

Ben De Mol

Appendix

Promotor: Prof. Dr. J.-P. Henriet
Co-promotor: Prof. Dr. R. Swennen

Proefschrift ingediend bij de Faculteit Wetenschappen van de Universiteit Gent voor het verkrijgen van de graad van Doctor in de Wetenschappen

Table of content

Appendix A: Geometry Belgica mound province 1

1. Mound location and geometric database 2
2. Depth distribution: statistical parameters 20
3. Geometry: statistical parameters 25

Appendix B: Geology Belgica mound province 31

1. Seismic profiles 32
2. Case study of BEL26, Challenger mound 52
3. Case study of Thérèse mound and friends 56

Appendix C: Sedimentology Belgica mound province 63

1. Table of sample locations 64
2. Lithologs 66
3. Mineralogical and chemical data 79

Appendix D: Geometry Hovland mound province 81

1. Mound location and geometric database 82
2. Depth distribution: statistical parameters 94
3. Geometry: statistical parameters 96

Appendix E: Geology Hovland-Magellan mound province 104

Seismic profiles 105

Appendix F: Sedimentology Hovland-Magellan mound province 124

1. Table of sample locations 125
2. Lithologs 131
3. Mineralogical and chemical data 150
4. Scanning electron microscopy 159
5. Petrographic and cathodoluminescent microscopy 162
6. Isotopic analysis 168
7. Gas analysis 171

Appendix G: Oceanography Hovland-Magellan mound province 172

Appendix A: Geometry Belgica mound province

1. Mound location and geometric database

Grey shaded profiles have a NNW-SSE orientation, the other ones a ENE-WSW

2. Depth distribution: statistical parameters

3. Geometry: statistical parameters

Abbreviations:

SM: Surface mounds
BM: Buried mounds
HR: High-resolution seismic profiles
MP: Mid point
SP: Seismic profile

Database			HR		Shotpoints zone 28N WGS84				MP or highest point			
number	Type	Multibeam	profile	shot	Northing	Easting	Lat	Long	Northing	Easting	Lat	Long
BEL01	BM		P980548	230	5676204.6	742292.9	51.186	-11.533	5676064.8	742092.6	51.185	-11.536
				310	5675925.0	741892.3	51.183	-11.539				
BEL02	BM		P98054B	600	5674629.3	736945.9	51.174	-11.610	5674414.8	736642.4	51.172	-11.615
				760	5674200.3	736338.9	51.170	-11.619				
BEL03	BM		P980549	700	5679955.3	738384.7	51.221	-11.586	5680293.7	738185.4	51.224	-11.589
				800	5680632.0	737986.0	51.227	-11.591				
BEL04	BM		P980549	1160	5682981.1	736510.0	51.249	-11.611	5683263.1	736367.7	51.252	-11.613
				1250	5683545.0	736225.3	51.254	-11.615				
BEL05	BM		P980547B	200	5685223.7	738670.7	51.268	-11.578	5685105.2	738732.2	51.267	-11.578
				240	5684986.6	738793.6	51.266	-11.577				
BEL06	BM		P970541	1900	5685576.4	734005.9	51.273	-11.645	5685419.4	733737.8	51.272	-11.649
				1750	5685262.3	733469.6	51.271	-11.653				
BEL07	BM		P970543	1400	5687231.5	734338.8	51.288	-11.639	5687043.6	734029.6	51.287	-11.644
				1520	5686855.6	733720.3	51.285	-11.648				
BEL08	BM		P970543	1050	5688381.2	736083.8	51.298	-11.613	5688102.3	735651.8	51.295	-11.620
				1220	5687823.3	735219.7	51.293	-11.626				
BEL09	SM	X	P970536	1150	5687684.0	732759.8	51.293	-11.661	5688199.8	733340.6	51.297	-11.653
				920	5688301.1	733733.9	51.298	-11.647				
			P980549	2000	5687805.7	733596.6	51.294	-11.649	5688264.0	733276.1	51.298	-11.654
				2175	5688722.3	732955.5	51.302	-11.658				
BEL10	BM		P970539	1800	5688355.9	732101.4	51.299	-11.670	5688266.4	731982.9	51.298	-11.672
				1850	5688176.9	731864.4	51.298	-11.674				
BEL11	BM		P970539	1150	5690394.4	735386.9	51.316	-11.622	5690120.7	734957.9	51.314	-11.628
				1320	5689847.0	734528.9	51.312	-11.635				
BEL12	BM		P970538	1100	5688733.3	730668.1	51.303	-11.691	5688835.2	730864.3	51.304	-11.688
				1200	5688937.0	731060.4	51.305	-11.685				
BEL13	SM	X							5689775.2	730553.6	51.313	-11.692
BEL14	BM		P970538	2160	5691238.4	734674.5	51.324	-11.632	5691528.1	735099.5	51.326	-11.625
				2400	5691817.8	735524.4	51.329	-11.619				
BEL15	BM		P970538	2600	5692306.6	736266.1	51.333	-11.608	5692414.6	736444.3	51.334	-11.606
				2700	5692522.5	736622.5	51.335	-11.603				
BEL16	SM	X	P980509	3230	5690395.2	729404.3	51.319	-11.708	5690649.6	729797.0	51.321	-11.702
				3375	5690904.0	730189.7	51.323	-11.696				

Database number	Type	HR profile	Width along SP	Height TWT ms	Buried TWT ms	Seafloor m	Max width	Surface km^2	Ratio NS/EW
BEL01	BM	P980548		75	55	579		0.22	
			489			565	489		
BEL02	BM	P98054B		50	20	770			
			743				743	0.50	
BEL03	BM	P980549		50	80	718			
			785			734	785	0.42	
BEL04	BM	P980549		50	110	728			
			632			721	632	0.27	
BEL05	BM	P980547B		50	190	580			
			267				267	0.05	
BEL06	BM	P970541		30	5	820			
			622			888	622	0.35	
BEL07	BM	P970543		30	80	773			
			724			807	724	0.47	
BEL08	BM	P970543		130	25	666			
			1029			738	1029	0.96	
BEL09	SM	P970536		150		809			
			1153			733	1153	1.01	0.97
		P980549		160		800			
			1119			737	1119		
BEL10	BM	P970539		15	10	825			
			297			832	297	0.08	
BEL11	BM	P970539		50	5	638			
			1018			688	1018	0.94	
BEL12	BM	P970538		55	10	912			
			442			853	442	0.18	
BEL13	SM					860			
BEL14	BM	P970538		160	40	666			
			1029			626	1029	0.96	
BEL15	BM	P970538				592			
			417			605	417	0.16	
BEL16	SM	P980509		100	5	991			
			936			854	936	0.79	

Database			HR		Shotpoints zone 28N WGS84				MP or highest point			
number	Type	Multibeam	profile	shot	Northing	Easting	Lat	Long	Northing	Easting	Lat	Long
BEL17	SM	X	P980509	3410	5691012.1	730388.7	51.324	-11.693	5691305.3	730862.3	51.326	-11.686
				3580	5691598.5	731335.8	51.329	-11.679				
			P980549	2675	5691409.8	731349.9	51.327	-11.679	5691941.2	731005.9	51.332	-11.684
				2870	5692472.6	730661.9	51.337	-11.688				
BEL18	SM		P980551	350	5691735.4	727688.9	51.331	-11.731	5691461.5	727829.2	51.329	-11.730
				450	5691187.6	727969.4	51.326	-11.728				
BEL19	SM	X							5692004.3	728514.6	51.333	-11.719
			P010521	2995	5692054.0	728875.0	51.334	-11.714				
				3178	5691531.0	728034.0	51.329	-11.727				
BEL20	BM		P980509	3300	5690625.5	729769.5	51.320	-11.702	5690803.5	730049.4	51.322	-11.698
				3400	5690981.5	730329.3	51.323	-11.694				
BEL21	SM	X	P980549	2900	5692626.2	730536.3	51.338	-11.690	5692858.9	730317.5	51.340	-11.693
				3075	5693534.9	729987.4	51.346	-11.697				
			P010521	2589	5693173.0	730691.0	51.343	-11.687				
				2827	5692504.0	729645.0	51.337	-11.703				
BEL22	SM	X	P980523	2489	5692893.0	727855.0	51.342	-11.728	5692913.4	728086.3	51.342	-11.725
				2684	5693581.0	728634.0	51.347	-11.717				
BEL23	SM	X	P980523	2812	5693880.0	729215.0	51.350	-11.708	5693917.9	729785.3	51.350	-11.700
				2926	5694161.0	729741.0	51.352	-11.700				
			P980549	3125	5693812.3	729790.1	51.349	-11.700				
				3200	5694232.4	729521.4	51.353	-11.704				
BEL24	SM	X	P980523	3119	5694713.0	730582.0	51.357	-11.688	5694896.7	730903.6	51.358	-11.683
				3285	5695083.0	731398.0	51.350	-11.676				
			P980549	3300	5694800.9	729108.8	51.358	-11.709				
				3250	5694489.5	729316.7	51.355	-11.706				
BEL25	SM	X	P980525	1	5695376.9	728836.1	51.363	-11.713	5695255.4	728562.8	51.363	-11.717
				100	5695808.9	728534.3	51.367	-11.717				
			P000660	1280	5695353.5	728363.6	51.363	-11.719				
				1410	5694880.0	728612.2	51.359	-11.716				
			P000660	1410	5694880.0	728612.2	51.359	-11.716				
				1520	5694490.2	728811.7	51.356	-11.714				
			P000616	3570	5694961.8	728720.8	51.360	-11.715				
				3700	5694575.1	728942.5	51.356	-11.712				

Database number	Type	HR profile	Width along SP	Height TWT ms	Buried TWT ms	Seafloor m	Max width	Surface km^2	Ratio NS/EW
BEL17	SM	P980509		230		853		1,11	
			1114			785	1114		
		P980549		170		783			1,14
			1266			811	1266		
BEL18	SM	P980551		70		1052			
			615			1017	615	0,26	
BEL19	SM					900			
		P010521		169		855			
			990				990	0,67	
BEL20	BM	P980509		60	110	892			
			663			853	663	0,40	
BEL21	SM	P980549		210		806		1,04	0,85
			1062			818	1062		
		P010521				716			
			1242	222			1242		
BEL22	SM	P980523		196		975	1039	0,98	
			1039			864			
BEL23	SM	P980523		62		863			0,84
			596			787	596	0,23	
		P980549		110		817			
			499			858	499		
BEL24	SM	P980523		166		700	896	0,73	
			896			727			
		P980549		40	40	747			0,42
			374			847	374		
BEL25	SM	P980525		150		850			
			527			885	973	0,19	
S1		P000660		110	70	878			
			535						
S2		P000660		65					
			438						
		P000616			115	758			
			446						

Database			HR		Shotpoints zone 28N WGS84				MP or highest point			
number	Type	Multibeam	profile	shot	Northing	Easting	Lat	Long	Northing	Easting	Lat	Long
			P010528	3719	5695690.0	728441.0	51.366	-11.718				
				3848	5695338.0	728660.0	51.363	-11.715				
BEL26	SM	X	P980525	225	5696473.2	728144.8	51.374	-11.722	5697108.3	728479.8	51.379	-11.717
Challenger mound				325	5697015.0	727855.6	51.379	-11.726				
			P980521	1770	5697463.5	728817.0	51.382	-11.712				
				1940	5696923.7	727882.7	51.378	-11.725				
			P000617(D)	1500	5697265.0	728438.4	51.381	-11.717				
				1830	5698234.1	727891.7	51.390	-11.724				
			P000658	580	5696917.8	728596.1	51.377	-11.715				
				1000	5697836.7	727970.8	51.386	-11.724				
			P010516	259	5697249.0	728893.0	51.380	-11.711				
				193	5697214.0	728467.0	51.380	-11.717				
				119	5697170.0	728008.0	51.380	-11.723				
			P010512	959	5696759.0	728792.0	51.376	-11.712				
				896	5696608.0	728464.0	51.375	-11.717				
				803	5696378.0	727991.0	51.373	-11.724				
			P010513	129	5697041.0	728789.0	51.378	-11.712				
				206	5696804.0	728293.0	51.377	-11.720				
				260	5696638.0	727958.0	51.375	-11.724				
			P010514	199	5696553.0	728651.0	51.374	-11.715				
				150	5696434.0	728384.0	51.373	-11.718				
				90	5696281.0	728070.0	51.372	-11.723				
			P010515	46	5696922.0	728756.0	51.377	-11.713				
				123	5696899.0	728271.0	51.377	-11.720				
				182	5696861.0	727871.0	51.377	-11.726				
			P010528	3146	5696925.0	727788.0	51.378	-11.727				
				3438	5696244.0	728100.0	51.372	-11.723				
BEL27	SM	X							5697186.5	730219.0	51.379	-11.692
			P010516	582	5697394.0	730889.0	51.381	-11.682				
				508	5697354.0	730424.0	51.381	-11.689				
				432	5697320.0	729947.0	51.380	-11.695				
BEL28	SM	X	P980521	1525	5698271.8	730240.9	51.389	-11.691	5698567.4	729963.1	51.392	-11.694
side of mound				1700	5697740.4	729201.9	51.385	-11.706				

Database number	Type	HR profile	Width along SP	Height TWT ms	Buried TWT ms	Seafloor m	Max width	Surface km^2	Ratio NS/EW
		P010528		113		887			
			415						
BEL26	SM	P980525		125		866			
Challenger mound			614			918			
		P980521		180		842		0,54	
			1079			900	1079		1,03
		P000617(D)		200					
			1113				1113		
		P000658		200					
			1111						
		P010516				838			
				179		780			
			889			920			
		P010512				837			
				118		829			
			887			921			
		P010513				837			
				157		780			
			924			915	924		
		P010514				832			
				57	24	853			
			642			909			
		P010515		157		835			
						776			
			887			922			
		P010528		109		888			
			726						
BEL27	SM								
		P010516				718			
				151		694			
			945			832	945		
BEL28	SM	P980521		120	5	737			
			1167			833	1167	1,23	

Database			HR		Shotpoints zone 28N WGS84				MP or highest point			
number	Type	Multibeam	profile	shot	Northing	Easting	Lat	Long	Northing	Easting	Lat	Long
BEL29	SM	X	P980547	3950	5699717,4	730429,9	51,402	-11,687	5700133,3	730376,2	51,406	-11,688
				4150	5698580,6	731108,6	51,391	-11,678				
			P010523	855	5700392,0	731107,0	51,408	-11,677				
				534	5699583,0	729487,0	51,401	-11,701				
BEL30	SM	X	P980519	2090	5700009,0	727001,4	51,406	-11,736	5699848,7	727486,0	51,404	-11,729
				2250	5700468,9	727770,9	51,410	-11,725				
			P000658	1350	5698522,0	727453,0	51,392	-11,730				
				1700	5699166,7	726948,3	51,398	-11,737				
			P000617(ch1)	2100	5699019,9	727428,0	51,397	-11,731				
				2310	5699615,1	727062,1	51,402	-11,735				
				2310	5699615,1	727062,1	51,402	-11,735				
				2550	5700283,6	726639,4	51,408	-11,741				
			P010530	2350	5698910,0	727012,0	51,396	-11,737				
				1941	5700128,0	726980,0	51,407	-11,736				
BEL30b			P010517	263	5699266,0	733010,0	51,397	-11,650	5699614,0	733621,0		
				507	5700044,0	734331,0	51,403	-11,631				
BEL31	SM	X							5701010,7	732658,6	51,413	-11,654
			P010523	1150	5701290,0	732559,0	51,415	-11,655				
				901	5700540,0	731331,0	51,409	-11,674				
BEL32	SM	X	P980525	1000	5700645,4	725783,2	51,412	-11,753	5701135,3	725106,8	51,417	-11,763
				1260	5702026,3	725020,0	51,425	-11,763				
			P000614	1020	5702080,6	724938,9	51,425	-11,764				
				600	5700839,2	725631,2	51,414	-11,755				
			P000616	1410	5701152,6	724883,8	51,417	-11,766				
				1850	5699887,7	725701,9	51,405	-11,755				
			P000623	1200	5701474,7	724711,5	51,420	-11,768				
				1600	5700512,7	725301,5	51,411	-11,760				
			P000624	410	5701435,0	724896,0	51,419	-11,765				
				231	5700681,0	725392,0	51,412	-11,759				
			P000626	400	5701008,4	725526,8	51,415	-11,757				
				700	5701779,0	725095,0	51,422	-11,762				
			P000657	1800	5701667,6	724817,9	51,422	-11,766				
				2300	5700567,8	725515,0	51,411	-11,757				

Database number	Type	HR profile	Width along SP	Height TWT ms	Buried TWT ms	Seafloor m	Max width	Surface km^2	Ratio NS/EW
BEL29	SM	P980547		150	50	635			
			1324				1324	2,17	
		P010523				643			
			1811	130			1811		
BEL30	SM	P980519		110		921			
			896			890	896	0,86	
		P000658		20	100	908			1,36
			819						
		P000617(ch1)			95	720			
			699						
					90	731			
			791				791		
		P010528		73			1218		
			1218						
BEL30b	SM	P010517							
			1533	130	14	592	1533		
BEL31	SM					631			
		P010523		134	5	610	1439	1,63	
			1439						
BEL32	SM	P980525		100		940			1,27
			1578			947	1578		
		P000614		115				2,25	
			1421						
		P000616		130					
			1506						
		P000623		150		953			
			1129			952			
		P000624		160		950			
			903			977			
		P000626		110					
			883						
		P000657		200					
			1302						

Database			HR		Shotpoints zone 28N WGS84				MP or highest point			
number	Type	Multibeam	profile	shot	Northing	Easting	Lat	Long	Northing	Easting	Lat	Long
BEL32	SM		P000638	677	5700927,0	725431,0	51,415	-11,758				
				905	5700577,0	724892,0	51,412	-11,766				
			P000639	270	5700781,0	724836,0	51,414	-11,767				
				583	5701205,0	725506,0	51,417	-11,757				
			P000640	1073	5700917,0	724702,0	51,415	-11,768				
				748	5701317,0	725292,0	51,418	-11,760				
			P000641	302	5701213,0	724716,0	51,418	-11,768				
				598	5701656,0	725448,0	51,421	-11,757				
			P000625	921	5701376,0	725134,0	51,419	-11,762				
				1089	5700840,0	725444,0	51,414	-11,758				
BEL33	SM	X							5702242,7	729120,1	51,425	-11,704
BEL34	SM	X							5702640,9	727651,4	51,429	-11,725
BEL35	SM	X	P980525	919	5701381,0	725129,0			5702499,4	724466,2	51,429	-11,771
				1098	5700814,0	725459,0						
			P980517	1940	5702443,6	724683,4	51,429	-11,768	5702161,7	724327,5	51,426	-11,773
Thérèse mound				2060	5701879,8	723971,5	51,424	-11,778				
			P000607	1935	5702798,3	725173,2	51,432	-11,760				
				1680	5702330,1	724483,0	51,428	-11,771				
			P000610	2400	5702950,2	726210,2	51,433	-11,746				
				2075	5702441,5	725215,5	51,428	-11,760				
			P000611	2375	5702631,0	724234,3	51,430	-11,774				
				2625	5702261,9	723593,3	51,427	-11,784				
			P000614	1530	5703530,2	724038,1	51,439	-11,776				
				1120	5702367,4	724748,7	51,428	-11,767				
			P000616	1000	5702405,7	724151,7	51,428	-11,775				
				1410	5701152,6	724883,8	51,417	-11,766				
			P000621	841	5702596,0	723830,0	51,430	-11,780				
				520	5701747,0	724332,0	51,422	-11,773				
			P000623	697	5702698,0	723993,0	51,315	-21,129				
				1067	5701776,0	724522,0	51,423	-11,770				
			P000624	780	5702890,0	724053,0	51,433	-11,777				
				534	5701927,0	724608,0	51,424	-11,769				
			P000625	377	5703039,0	724115,0	51,434	-11,776				
				708	5702030,0	724744,0	51,425	-11,767				

Database number	Type	HR profile	Width along SP	Height TWT ms	Buried TWT ms	Seafloor m	Max width	Surface km^2	Ratio NS/EW
BEL32		P000638		119		931			
			643						
		P000639		171		888			
			793						
		P000640		157		900			
			713						
		P000641		107		942			
			856				856		
		P000625		116		924			
			619						
BEL33	SM					735			
BEL34	SM					820			
BEL35	SM	P980525		200		892			
			656			997			
		P980517		200		927			1,30
Thérèse mound			908			1003		1,27	
		P000607		210					
			834						
		P000610		120					
			1117				1117		
		P000611		120					
			740						
		P000614		210					
			1363						
		P000616		210					
			1451				1451		
		P000621				1015			
			986			978			
		P000623		200		985			
			1063			963			
		P000624		160					
			1111						
		P000625		204		987			
			1189			964			

Database			HR		Shotpoints zone 28N WGS84				MP or highest point			
number	Type	Multibeam	profile	shot	Northing	Easting	Lat	Long	Northing	Easting	Lat	Long
BEL35			P000626	1300	5703332.9	724111.5	51.437	-11.775				
				900	5702303.2	724783.6	51.427	-11.766				
			P000634	354	5702802.0	724597.0	51.432	-11.769				
				644	5702347.0	723845.0	51.428	-11.780				
			P000645	200	5701845.1	724118.6	51.423	-11.776				
				500	5702329.4	724896.6	51.427	-11.765				
			P000646	660	5702484.0	724811.0	51.429	-11.766				
				1005	5701934.5	723873.7	51.424	-11.780				
			P000647	241	5702235.0	724015.0	51.427	-11.777				
				557	5702734.0	724776.0	51.431	-11.766				
			P000649	771	5703001.0	724159.0	51.434	-11.775				
				979	5703249.0	724571.0	51.436	-11.769				
			P000657	1800	5701667.6	724817.9	51.422	-11.766				
				1200	5702888.2	724055.9	51.433	-11.776				
BEL36	SM	X							5702988.2	725024.9	51.433	-11.762
			P000611	2180	5702947.0	724730.8	51.433	-11.767				
				2375	5702631.0	724234.3	51.430	-11.774				
			P000634	137	5703162.0	725168.0	51.435	-11.760				
				354	5702802.0	724597.0	51.432	-11.769				
			P000629	430	5703398.3	724710.8	51.437	-11.767				
				675	5702696.9	725145.7	51.431	-11.761				
			P000647	755	5703034.0	725277.0	51.434	-11.759				
				557	5702734.0	724776.0	51.431	-11.766				
			P000649	1190	5703525.0	724996.0	51.438	-11.763				
				1520	5703946.2	725689.0	51.442	-11.752				
			P000630	797	5702922.0	725161.0	51.433	-11.761				
				932	5703312.0	724926.0	51.436	-11.764				
BEL37	SM	X							5703182.1	729367.9	51.433	-11.700
BEL38	SM	X							5703374.9	723267.3	51.438	-11.788
			P000623	200	5703867.1	723290.2	51.442	-11.787				
				580	5702968.1	723820.5	51.434	-11.780				
			P000616	650	5703422.5	723489.4	51.438	-11.784				
				910	5702647.3	723997.6	51.431	-11.777				
			P000619	260	5703093.0	723336.0	51.435	-11.787				
				107	5703533.0	723075.0	51.439	-11.790				

Database number	Type	HR profile	Width along SP	Height TWT ms	Buried TWT ms	Seafloor m	Max width	Surface km²	Ratio NS/EW
BEL35		P000626		195		998			
			1230			965			
		P000634		160		940			
			879			1011			
		P000645		200		999			
			916			956			
		P000646		210		950			
			1086			1002			
		P000647		212		998			
			910			953			
		P000649		130		968			
			481			995			
		P000657		150					
			1439						
BEL36	SM								
		P000611		120				0,53	
			589						
		P000634		160		949			
			675						
		P0006029		150					
			825				825		1,02
		P000647				938			
			584						
		P000649		170		957			
			811			899	811		
		P000630		104		915			
			455						
BEL37	SM					730			
BEL38	SM								
		P000623		70		920			
			1044				1044	0,47	1,59
		P000616		70					
			927						
		P000619		178		926			
			512			977			

Database			HR		Shotpoints zone 28N WGS84				MP or highest point			
number	Type	Multibeam	profile	shot	Northing	Easting	Lat	Long	Northing	Easting	Lat	Long
BEL38	SM		P000621	1242	5703625.0	723197.0	51.440	-11.788				
				1033	5703085.0	723528.0	51.435	-11.784				
			P000652	1197	5703317.0	723519.0	51.437	-11.784				
				1434	5702972.0	722961.0	51.434	-11.792				
			P000653	521	5703255.0	722910.0	51.437	-11.793				
				758	5703576.0	723430.0	51.439	-11.785				
BEL39	SM	X							5703927.4	725273.4	51.442	-11.758
			P000633	347	5704387.0	725115.0	51.446	-11.760				
				647	5703654.0	725553.0	51.439	-11.754				
			P000649	1536	5703969.0	725722.0	51.442	-11.752				
					5703520.0	724987.0	51.438	-11.763				
			P000650	143	5704163.0	725662.0	51.444	-11.753				
				417	5703741.0	724912.0	51.440	-11.764				
			P000651	1017	5703956.0	724893.0	51.442	-11.764				
				1364	5704344.0	725559.0	51.445	-11.754				
			P000652	173	5704927.0	726153.0	51.450	-11.745				
				605	5704262.0	724936.0	51.445	-11.763				
			P000654	519	5704117.0	725005.0	51.443	-11.762				
				789	5703574.0	725365.0	51.438	-11.757				
			P000632	1054	5704044.0	724821.0	51.443	-11.765				
				859	5703454.0	725194.0	51.437	-11.760				
BEL40	SM		P980517	1380	5704713.8	728136.4	51.448	-11.717	5704545.8	727905.5	51.446	-11.720
				1460	5704377.8	727674.6	51.445	-11.724				
BEL41	SM	X	P980517	1100	5705803.3	729844.7	51.457	-11.691	5705961.4	729242.6	51.458	-11.700
				1350	5704844.3	728315.0	51.449	-11.714				
			P000608	850	5706174.4	729255.9	51.460	-11.700				
				1100	5705775.9	728494.5	51.457	-11.711				
BEL42	SM	X							5705035.0	729284.4	51.450	-11.700
			P000607	1950	5702827.9	725213.0	51.432	-11.760				
				1850	5702635.5	724943.0	51.430	-11.764				
			P000610	3400	5704993.4	729571.6	51.450	-11.696				
				3550	5705325.6	730069.6	51.452	-11.689				
			P000652	117	5704995.0	726358.0	51.451	-11.742				
				604	5704263.0	724941.0	51.445	-11.763				
BEL43	SM	X							5704879.5	725811.2	51.450	-11.750

Database		HR	Width	Height	Buried	Seafloor	Max	Surface	Ratio
number	Type	profile	along SP	TWT ms	TWT ms	m	width	km²	NS/EW
BEL38	SM	P000621				1018			
			633			1005			
		P000652				1014			
			656			1077	656		
		P000653		144		1035			
			611			1028			
BEL39	SM								
		P000633		182		938			
			854			913	854	0,00	#DIV/0!
		P000649		161		899			
			861			967			
		P000650		181		891			
			861			947			
		P000651		139		962			
			771			895			
		P000652		179					
			1387			825	1387		
		P000654		160					
			651			863			
		P000632		130					
			698			808			
BEL40	SM	P980517		80		873			
			571			897	571	0,29	
BEL41	SM	P980517		170		742			
			1805			868	1805	2,94	
		P000608							
			859	100					
BEL42	SM					700			
		P000607						1,74	
			332						
		P000610		80					
			599						
		P000652		181		917			
			1595			965	1595		
BEL43	SM					825			

Database			HR		Shotpoints zone 28N WGS84				MP or highest point			
number	Type	Multibeam	profile	shot	Northing	Easting	Lat	Long	Northing	Easting	Lat	Long
BEL44	SM	X							5705394.3	726948.2	51.454	-11.733
			P010528	206	5705312.0	727149.0	51.5	-11.7				
				70	5705690.0	727164.0	51.5	-11.7				
BEL45	SM	X							5707390.3	730047.8	51.471	-11.688
			P010527	1005	5707956.0	730320.0	51.476	-11.683				
				1286	5707073.0	729016.0	51.468	-11.703				
BEL46	SM		P980547	2420	5708439.6	725333.1	51.482	-11.755	5707834.9	725686.9	51.477	-11.750
				2620	5707230.1	726040.7	51.471	-11.745				
BEL47	SM	X							5708675.7	727671.1	51.483	-11.721
BEL48	BM		P980547	2288	5709185.0	724785.4	51.489	-11.762	5708879.5	725042.4	51.486	-11.759
				2400	5708574.0	725299.3	51.483	-11.755				
BEL49	BM		P980516	200	5710973.5	736230.1	51.500	-11.596	5710628.7	736363.0	51.497	-11.595
				300	5710319.5	736540.1	51.494	-11.592				
BEL50	SM		P980547	2100	5710288.6	724249.9	51.499	-11.769	5710288.6	724249.9	51.499	-11.769
				2200	5709713.9	724553.4	51.494	-11.765				
BEL51	BM		P980547	1800	5712133.0	723334.4	51.516	-11.781	5711995.6	723375.2	51.515	-11.781
				1850	5711858.1	723416.0	51.514	-11.780				
BEL52	SM	X							5713650.8	724746.0	51.529	-11.760
BEL53	BM		P980511	1150	5715037.1	725526.5	51.541	-11.748	5715305.1	725978.9	51.544	-11.737
outliers				1300	5715573.1	726431.3	51.546	-11.734				
BEL54	SM	X							5716100.1	727627.5	51.550	-11.717
BEL55	SM	X	P980511	1480	5716179.3	727481.4	51.551	-11.719	5717026.6	727585.9	51.558	-11.717
outliers				1790	5717257.0	729318.2	51.560	-11.692				
BEL56	SM	X							5718442.2	728100.8	51.571	-11.708
BEL57	BM		P980512	300	5716729.1	732838.8	51.554	-11.641	5716371.2	732989.7	51.550	-11.639
				400	5716013.3	733140.5	51.547	-11.637				
BEL58	SM	X							5719499.3	720534.9	51.583	-11.817
BEL59	SM	X							5719625.9	723420.8	51.583	-11.775

Appendix A
Geometry Belgica mound province

Database		HR	Width	Height	Buried	Seafloor	Max	Surface	Ratio
number	Type	profile	along SP	TWT ms	TWT ms	m	width	km^2	NS/EW
BEL44	SM					880			
		P010528		58		890	378		
			378						
BEL45	SM					745			
		P010527	103	1575		756	1575		
								1,69	
BEL46	SM	P980547		170		900		1,34	
			1401				1401		
BEL47	SM					825			
BEL48	BM	P980547		30	15	960		0,43	
			798				798		
BEL49	BM	P980516		5	20	556		0,47	
			724			522	724		
BEL50	SM	P980547		175		940		0,38	
			650				650		
BEL51	BM	P980547		40	30	940		0,07	
			287				287		
BEL52	SM					900			
BEL53	BM	P980511		50	30	824		1,00	
outliers			1052			775	1052		
BEL54	SM								
BEL55	SM	P980511		80	20	760		4,10	
Outliers			2130			722	2130		
BEL56	SM					750			
BEL57	BM	P980512		50	60	592		0,54	
			777			578	777		
BEL58	SM					880			
BEL59	SM					920			

Database			HR		Shotpoints zone 28N WGS84				MP or highest point			
number	Type	Multibeam	profile	shot	Northing	Easting	Lat	Long	Northing	Easting	Lat	Long
BEL60	SM	X							5720230.3	726574.5	51.588	-11.729
BEL61	SM	X							5720801.9	722019.8	51.594	-11.794
BEL62	SM	X	P980546	1165	5725901.1	722708.4	51.640	-11.781	5726240.1	722551.1	51.643	-11.783
				1249	5725601.3	722223.2	51.637	-11.788				
BEL63	BM		P980546	1057	5726205.3	723341.6	51.642	-11.772	5726468.3	723820.3	51.645	-11.765
				893	5726731.2	724298.9	51.647	-11.758				

Database number	Type	HR profile	Width along SP	Height TWT ms	Buried TWT ms	Seafloor m	Max width	Surface km^2	Ratio NS/EW
BEL60	SM					900			
BEL61	SM					950			
BEL62	SM	P980546		100		752		0,29	
			570			763	570		
BEL63	BM	P980546		50	50	766		1,08	
			1092			729	1092		

		Total Province
TOTAL	40,25	430,00

Area ratio mound/province
0,093613

2. Depth distribution: statistical parameters

Case Processing Summary

	Cases					
	Valid		Missing		Total	
	N	Percent	N	Percent	N	Percent
SEAFLOOR	63	100.0%	0	.0%	63	100.0%

Descriptives

			Statistic	Std. Error
SEAFLOOR	Mean		790.7143	14.1554
	95% Confidence Interval for Mean	Lower Bound	762.4181	
		Upper Bound	819.0104	
	5% Trimmed Mean		793.1305	
	Median		787.0000	
	Variance		12623.562	
	Std. Deviation		112.3546	
	Minimum		522.00	
	Maximum		1017.00	
	Range		495.00	
	Interquartile Range		158.0000	
	Skewness		-.324	.302
	Kurtosis		-.450	.595

Table A.2.1: Depth distribution of the Belgica mounds imaged on seismic profiles (N=46) of which 39 have a depth annotation.

Case Processing Summary

		Cases					
		Valid		Missing		Total	
	Type	N	Percent	N	Percent	N	Percent
SEAFLOOR	BM	20	100.0%	0	.0%	20	100.0%
	SM	43	100.0%	0	.0%	43	100.0%

Descriptives

	Type			Statistic	Std. Error
SEAFLOOR	BM	Mean		725.8500	28.3230
		95% Confidence Interval for Mean	Lower Bound	666.5693	
			Upper Bound	785.1307	
		5% Trimmed Mean		724.1667	
		Median		725.0000	
		Variance		16043.818	
		Std. Deviation		126.6642	
		Minimum		522.00	
		Maximum		960.00	
		Range		438.00	
		Interquartile Range		213.5000	
		Skewness		.180	.512
		Kurtosis		-.864	.992
	SM	Mean		820.8837	14.0112
		95% Confidence Interval for Mean	Lower Bound	792.6080	
			Upper Bound	849.1595	
		5% Trimmed Mean		821.5866	
		Median		825.0000	
		Variance		8441.486	
		Std. Deviation		91.8776	
		Minimum		631.00	
		Maximum		1017.00	
		Range		386.00	
		Interquartile Range		157.0000	
		Skewness		-.077	.361
		Kurtosis		-.691	.709

Table A.2.2: Descriptive statistics for the depth-mound type relation.

Case Processing Summary

		Cases					
		Valid		Missing		Total	
	ZONE	N	Percent	N	Percent	N	Percent
SEAFLOOR	C	43	100.0%	0	.0%	43	100.0%
	N	15	100.0%	0	.0%	15	100.0%
	S	5	100.0%	0	.0%	5	100.0%

Descriptives

ZONE				Statistic	Std. Error
SEAFLOOR	C	Mean		803.3256	15.4824
		95% Confidence Interval for Mean	Lower Bound	772.0809	
			Upper Bound	834.5703	
		5% Trimmed Mean		803.1873	
		Median		820.0000	
		Variance		10307.272	
		Std. Deviation		101.5247	
		Minimum		605.00	
		Maximum		1017.00	
		Range		412.00	
		Interquartile Range		147.0000	
		Skewness		-.182	.361
		Kurtosis		-.604	.709
	N	Mean		794.5333	33.5782
		95% Confidence Interval for Mean	Lower Bound	722.5153	
			Upper Bound	866.5514	
		5% Trimmed Mean		801.0370	
		Median		775.0000	
		Variance		16912.410	
		Std. Deviation		130.0477	
		Minimum		522.00	
		Maximum		950.00	
		Range		428.00	
		Interquartile Range		191.0000	
		Skewness		-.659	.580
		Kurtosis		-.052	1.121
	S	Mean		670.8000	41.2473
		95% Confidence Interval for Mean	Lower Bound	556.2791	
			Upper Bound	785.3209	
		5% Trimmed Mean		671.1667	
		Median		718.0000	
		Variance		8506.700	
		Std. Deviation		92.2318	
		Minimum		565.00	
		Maximum		770.00	
		Range		205.00	
		Interquartile Range		173.0000	
		Skewness		-.385	.913
		Kurtosis		-2.793	2.000

Table A.2.3: Depth distribution in the 3 sub zones of the Belgica mound province.

Case Processing Summary

		Cases					
		Valid		Missing		Total	
	Type	N	Percent	N	Percent	N	Percent
SEAFLOOR	BM	10	100.0%	0	.0%	10	100.0%
	SM	33	100.0%	0	.0%	33	100.0%

Descriptives

	Type			Statistic	Std. Error
SEAFLOOR	BM	Mean		761.9000	38.1455
		95% Confidence Interval for Mean	Lower Bound	675.6090	
			Upper Bound	848.1910	
		5% Trimmed Mean		759.6111	
		Median		796.5000	
		Variance		14550.767	
		Std. Deviation		120.6266	
		Minimum		605.00	
		Maximum		960.00	
		Range		355.00	
		Interquartile Range		218.0000	
		Skewness		.046	.687
		Kurtosis		-1.275	1.334
	SM	Mean		815.8788	16.2715
		95% Confidence Interval for Mean	Lower Bound	782.7349	
			Upper Bound	849.0227	
		5% Trimmed Mean		815.8519	
		Median		825.0000	
		Variance		8737.110	
		Std. Deviation		93.4725	
		Minimum		631.00	
		Maximum		1017.00	
		Range		386.00	
		Interquartile Range		155.5000	
		Skewness		-.074	.409
		Kurtosis		-.480	.798

Table A.2.4: Depth distribution of the different mound types in the central zone.

Case Processing Summary

		Cases					
		Valid		Missing		Total	
	Type	N	Percent	N	Percent	N	Percent
SEAFLOOR	BM	5	100.0%	0	.0%	5	100.0%
	SM	10	100.0%	0	.0%	10	100.0%

Descriptives

	Type			Statistic	Std. Error
SEAFLOOR	BM	Mean		708.8000	74.2451
		95% Confidence Interval for Mean	Lower Bound	502.6625	
			Upper Bound	914.9375	
		5% Trimmed Mean		706.3333	
		Median		729.0000	
		Variance		27561.700	
		Std. Deviation		166.0172	
		Minimum		522.00	
		Maximum		940.00	
		Range		418.00	
		Interquartile Range		307.5000	
		Skewness		.355	.913
		Kurtosis		-.781	2.000
	SM	Mean		837.4000	28.1663
		95% Confidence Interval for Mean	Lower Bound	773.6835	
			Upper Bound	901.1165	
		5% Trimmed Mean		837.5556	
		Median		840.0000	
		Variance		7933.378	
		Std. Deviation		89.0695	
		Minimum		722.00	
		Maximum		950.00	
		Range		228.00	
		Interquartile Range		173.5000	
		Skewness		.010	.687
		Kurtosis		-2.038	1.334

Table A.2.5: Depth distribution of the different mound types in the northern zone.

3. Geometry: statistical parameters

Case Processing Summary

		Cases					
		Valid		Missing		Total	
	Type	N	Percent	N	Percent	N	Percent
max width	BM	19	95.0%	1	5.0%	20	100.0%
	SM	26	60.5%	17	39.5%	43	100.0%
max height	BM	19	95.0%	1	5.0%	20	100.0%
	SM	26	60.5%	17	39.5%	43	100.0%

Descriptives

	Type			Statistic	Std. Error
max width	BM	Mean		694.3500	59.4716
		95% Confidence Interval for Mean	Lower Bound	569.8744	
			Upper Bound	818.8256	
		5% Trimmed Mean		696.0000	
		Median		724.0000	
		Variance		70737.503	
		Std. Deviation		265.9652	
		Minimum		267.00	
		Maximum		1092.00	
		Range		825.00	
		Interquartile Range		509.2500	
		Skewness		-.109	.512
		Kurtosis		-1.009	.992
	SM	Mean		1114.9231	77.3971
		95% Confidence Interval for Mean	Lower Bound	955.5207	
			Upper Bound	1274.3254	
		5% Trimmed Mean		1092.9573	
		Median		1053.0000	
		Variance		155748.2	
		Std. Deviation		394.6494	
		Minimum		570.00	
		Maximum		2130.00	
		Range		1560.00	
		Interquartile Range		512.2500	
		Skewness		.656	.456
		Kurtosis		.349	.887

Table A.3.1: Descriptive statistic parameters for the maximum measured length for the buried mound and the surface mound population.

Descriptives

	Type			Statistic	Std. Error
max height	BM	Mean		54.2105	8.2829
		95% Confidence Interval for Mean	Lower Bound	36.8089	
			Upper Bound	71.6122	
		5% Trimmed Mean		51.0673	
		Median		50.0000	
		Variance		1303.509	
		Std. Deviation		36.1041	
		Minimum		5.00	
		Maximum		160.00	
		Range		155.00	
		Interquartile Range		25.0000	
		Skewness		1.851	.524
		Kurtosis		4.088	1.014
	SM	Mean		153.0385	8.6226
		95% Confidence Interval for Mean	Lower Bound	135.2799	
			Upper Bound	170.7970	
		5% Trimmed Mean		153.5043	
		Median		163.0000	
		Variance		1933.078	
		Std. Deviation		43.9668	
		Minimum		70.00	
		Maximum		230.00	
		Range		160.00	
		Interquartile Range		71.2500	
		Skewness		-.381	.456
		Kurtosis		-.743	.887

Table A.3.2: Descriptive statistic parameters for the maximum measured height for the buried mound and surface mound population.

Case Processing Summary

		Cases					
		Valid		Missing		Total	
	Type	N	Percent	N	Percent	N	Percent
max width EW	BM	15	75.0%	5	25.0%	20	100.0%
	SM	21	48.8%	22	51.2%	43	100.0%

Descriptives

	Type			Statistic	Std. Error
max width EW	BM	Mean		741.2000	66.8929
		95% Confidence Interval for Mean	Lower Bound	597.7290	
			Upper Bound	884.6710	
		5% Trimmed Mean		746.3889	
		Median		724.0000	
		Variance		67119.886	
		Std. Deviation		259.0751	
		Minimum		297.00	
		Maximum		1092.00	
		Range		795.00	
		Interquartile Range		540.0000	
		Skewness		-.117	.580
		Kurtosis		-1.175	1.121
	SM	Mean		1030.8095	86.4923
		95% Confidence Interval for Mean	Lower Bound	850.3898	
			Upper Bound	1211.2293	
		5% Trimmed Mean		996.2011	
		Median		945.0000	
		Variance		157099.3	
		Std. Deviation		396.3575	
		Minimum		570.00	
		Maximum		2130.00	
		Range		1560.00	
		Interquartile Range		426.5000	
		Skewness		1.274	.501
		Kurtosis		2.039	.972

Table A.3.3: Descriptive statistic parameters of the maximum width on EW profile for the different mound types.

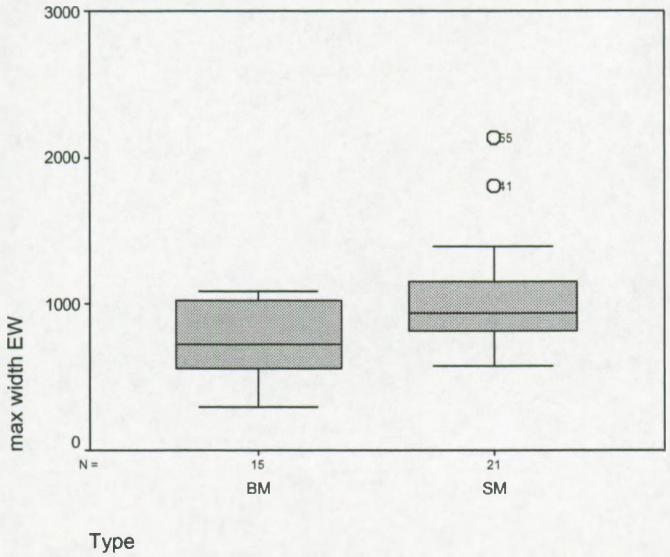

Fig. A.3.1: Stem-Leaf plot of the width on the EW-profile for the buried and surface mounds.

Case Processing Summary

		Cases					
		Valid		Missing		Total	
	Type	N	Percent	N	Percent	N	Percent
max width NS	BM	5	25.0%	15	75.0%	20	100.0%
	SM	16	37.2%	27	62.8%	43	100.0%

Descriptives

	Type			Statistic	Std. Error
max width NS	BM	Mean		553.8000	116.7559
		95% Confidence Interval for Mean	Lower Bound	229.6337	
			Upper Bound	877.9663	
		5% Trimmed Mean		556.1667	
		Median		632.0000	
		Variance		68159.700	
		Std. Deviation		261.0741	
		Minimum		267.00	
		Maximum		798.00	
		Range		531.00	
		Interquartile Range		514.5000	
		Skewness		-.356	.913
		Kurtosis		-3.081	2.000
	SM	Mean		970.1875	87.6642
		95% Confidence Interval for Mean	Lower Bound	783.3356	
			Upper Bound	1157.0394	
		5% Trimmed Mean		969.5417	
		Median		1008.5000	
		Variance		122960.3	
		Std. Deviation		350.6569	
		Minimum		374.00	
		Maximum		1578.00	
		Range		1204.00	
		Interquartile Range		567.0000	
		Skewness		.053	.564
		Kurtosis		-.802	1.091

Table A.3.4: Descriptive statistic parameters for the maximum width on NS profile for the different mound types.

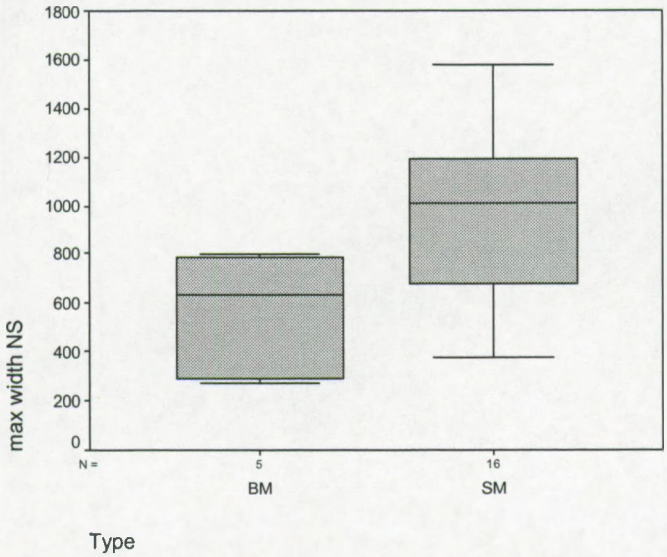

Fig. A.3.2: Stem-Leaf plot of the width on the NS-profile for the buried and surface mounds.

Appendix B: Geology Belgica mound province

1. Seismic profiles

- Bathymetric map with profile locations
- P970536
- P980511
- P980521
- P980523
- P980525
- P980549
- P980525-49
- P000644
- Seismic attributes of P000644
- P010512
- P010517
- P010521
- P010523
- P010527
- P010528
- Time structural map of the Base of facies Bb R1

2. Case study of BEL26, Challenger mound

- Bathymetric map with profile locations
- P000658, seismic profile, interpretation, real scale 1:1
- P010515
- P010516

3. Case study of Thérèse mound and friends

- Bathymetric map with profile locations
- P000624, seismic profile, interpretation, real scale 1:1
- P000629
- P000633
- P000639
- P000647
- P000652

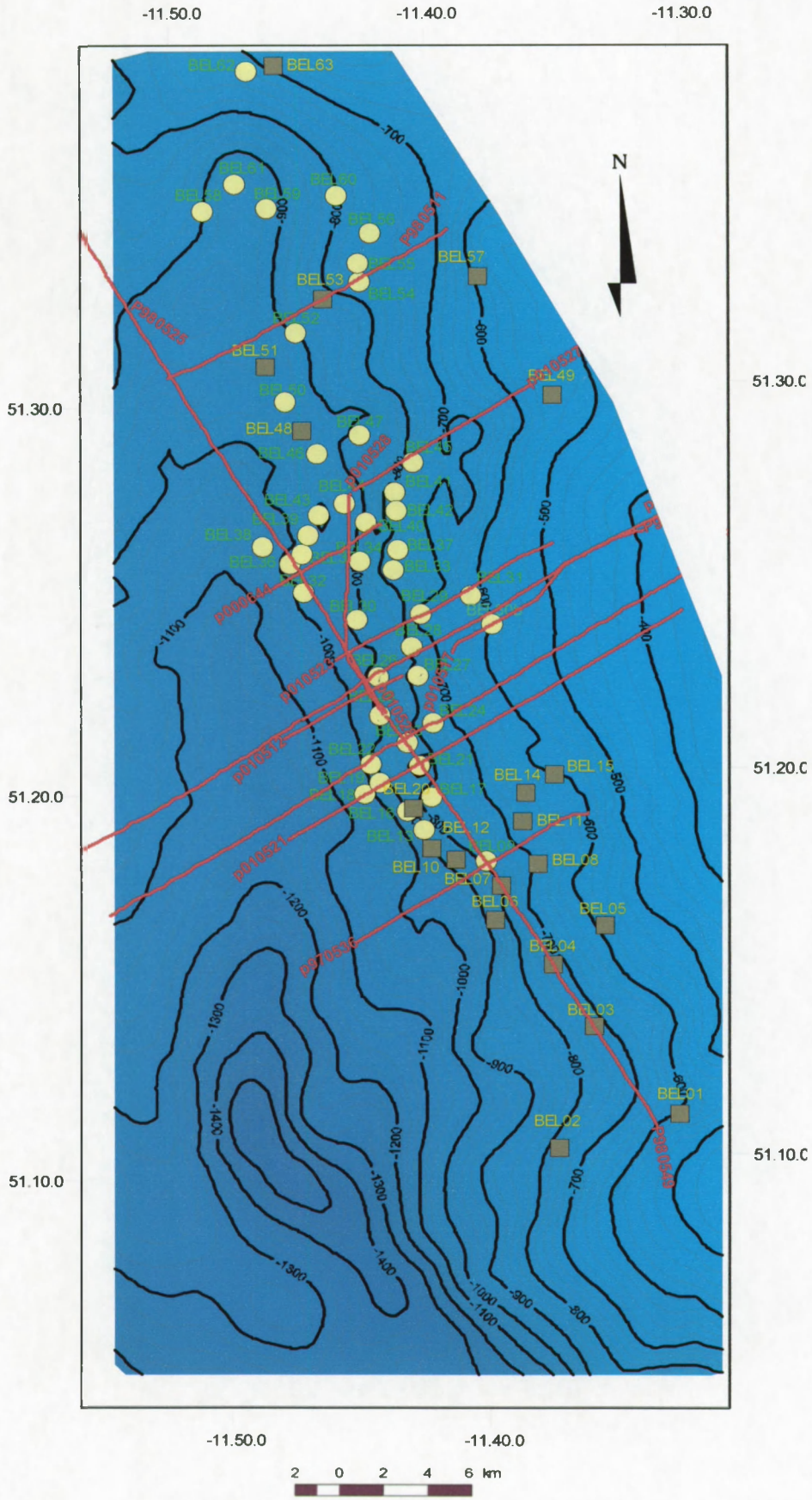
-11.50.0
-11.40.0
-11.30.0
51.30.0
51.20.0
51.10.0
N
BEL63
BEL57
BEL53
BEL51
BEL49
BEL48
BEL15
BEL14
BEL12
BEL11
BEL10
BEL08
BEL07
BEL06
BEL05
BEL04
BEL03
BEL02
BEL01
2 0 2 4 6 km

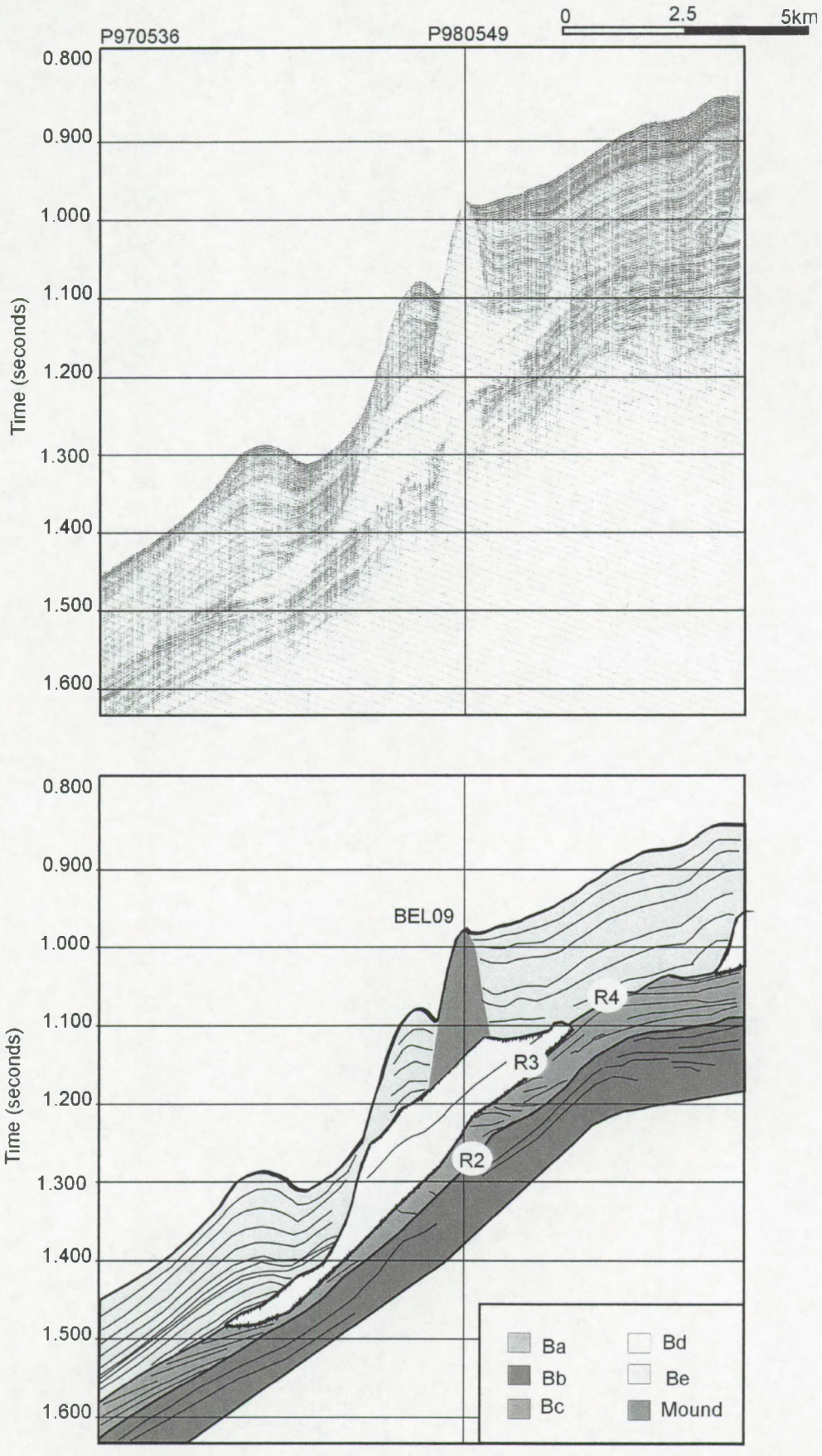
0
2.5
5km
P970536
P980549
0.800
0.900
1.000
1.100
1.200
1.300
1.400
1.500
1.600
Time (seconds)
BEL09
R4
R3
R2
Ba
Bb
Bc
Bd
Be
Mound

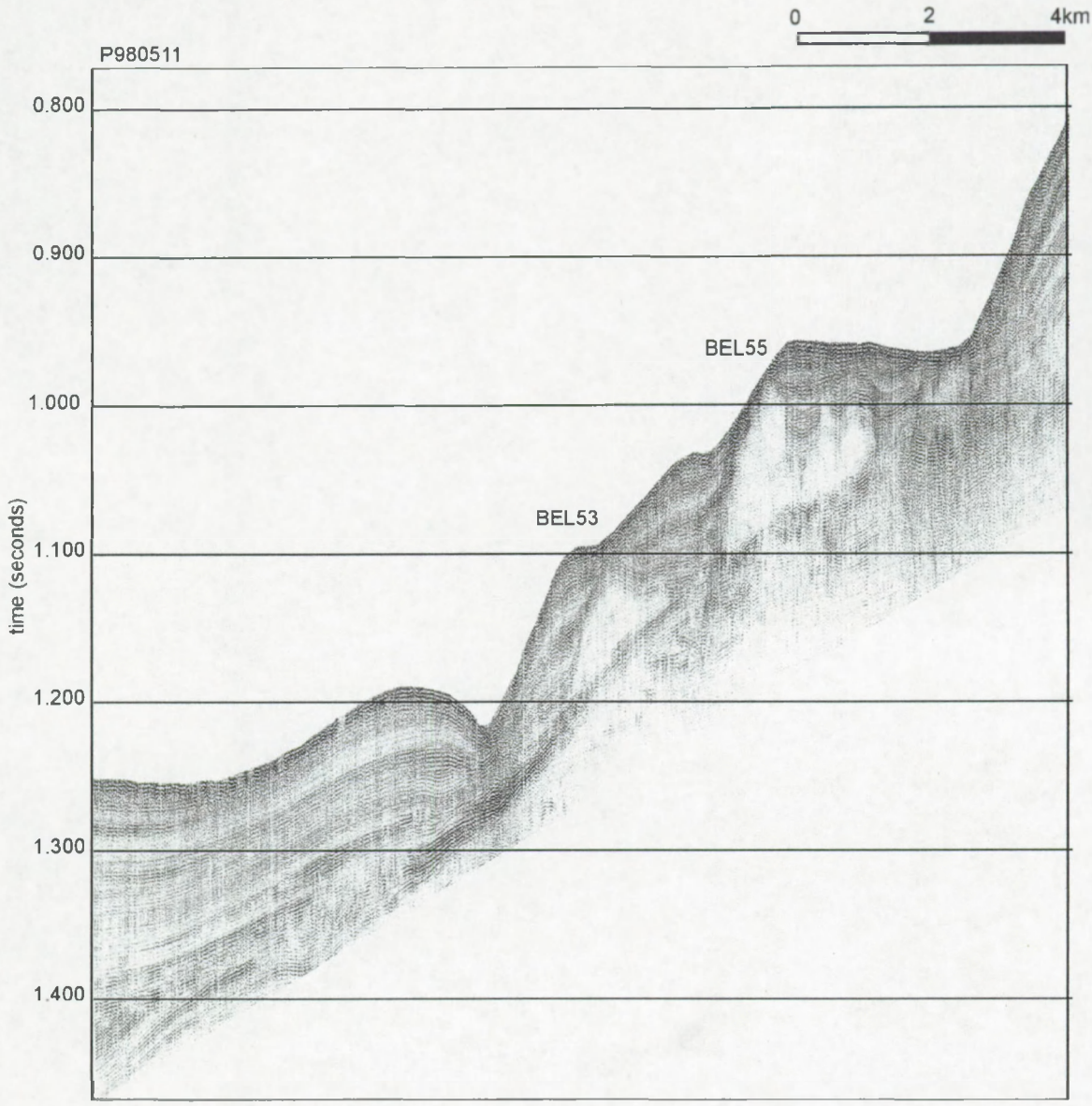
0
2
4km
P980511
0.800
0.900
1.000
1.100
1.200
1.300
1.400
time (seconds)
BEL55
BEL53

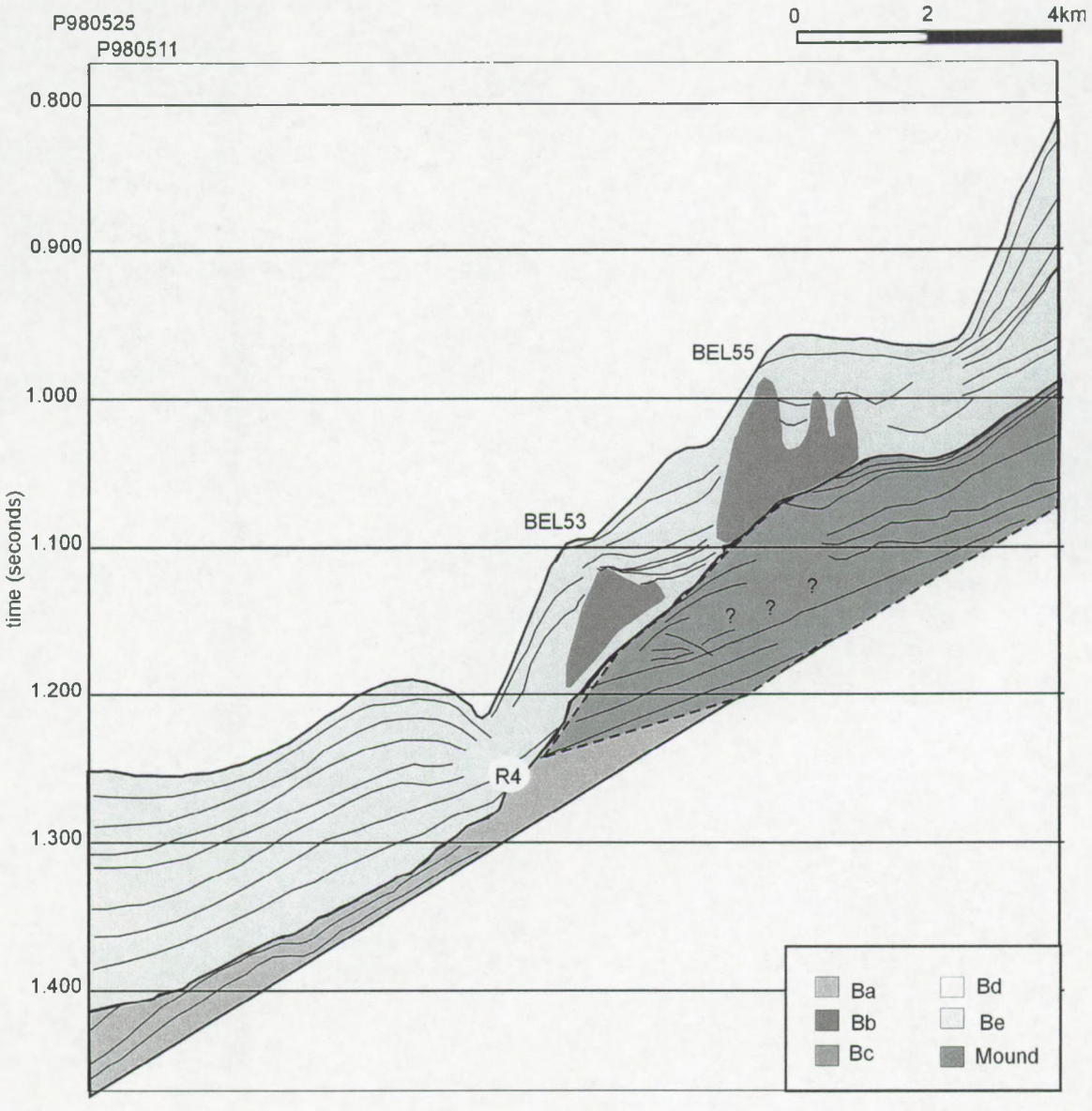
P980525
P980511
0
2
4km
0.800
0.900
1.000
1.100
1.200
1.300
1.400
time (seconds)
BEL55
BEL53
R4
?
?
?
Ba
Bb
Bc
Bd
Be
Mound

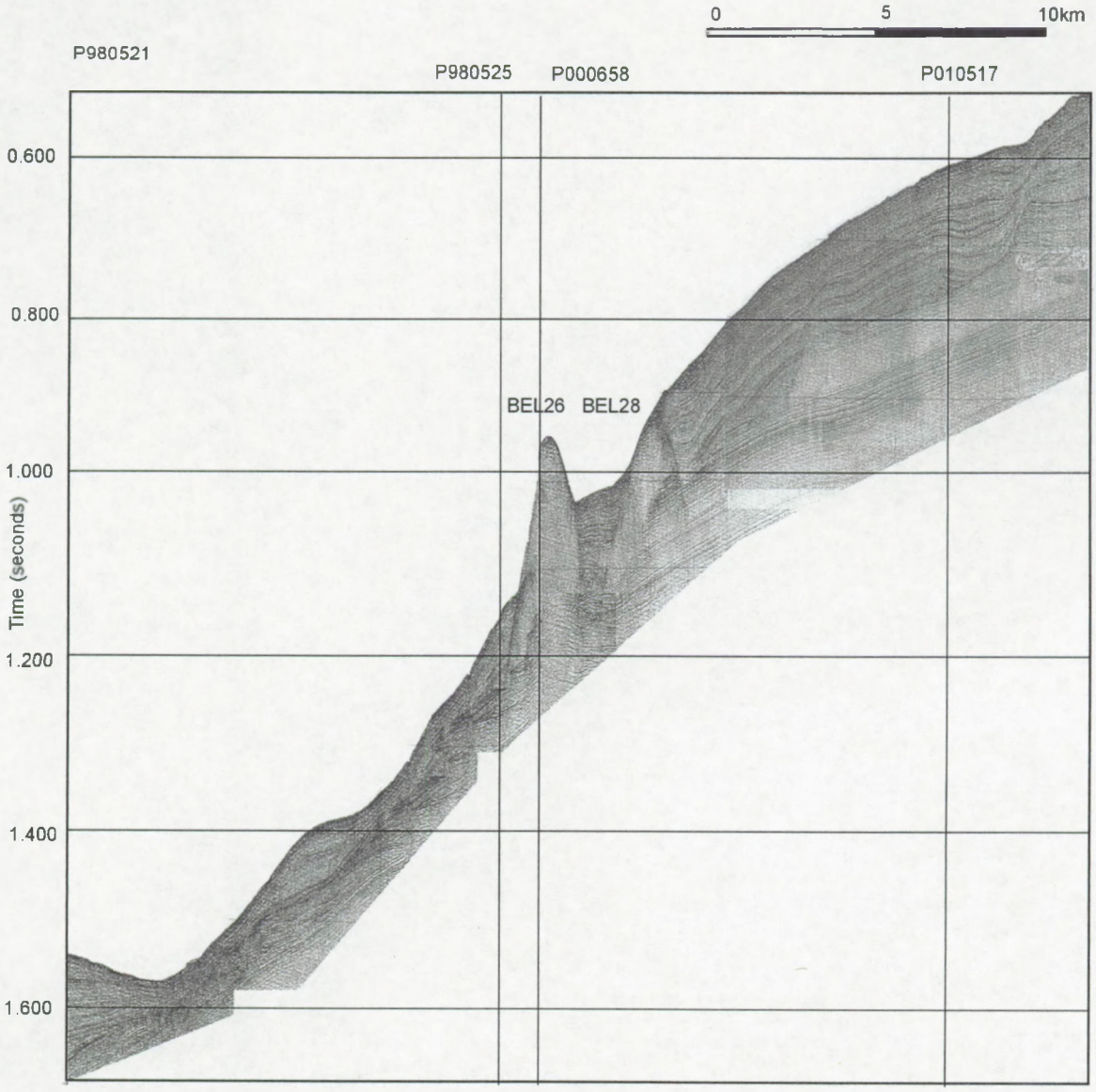
0
5
10km
P980521
P980525
P000658
P010517
0.600
0.800
1.000
1.200
1.400
1.600
Time (seconds)
BEL26
BEL28

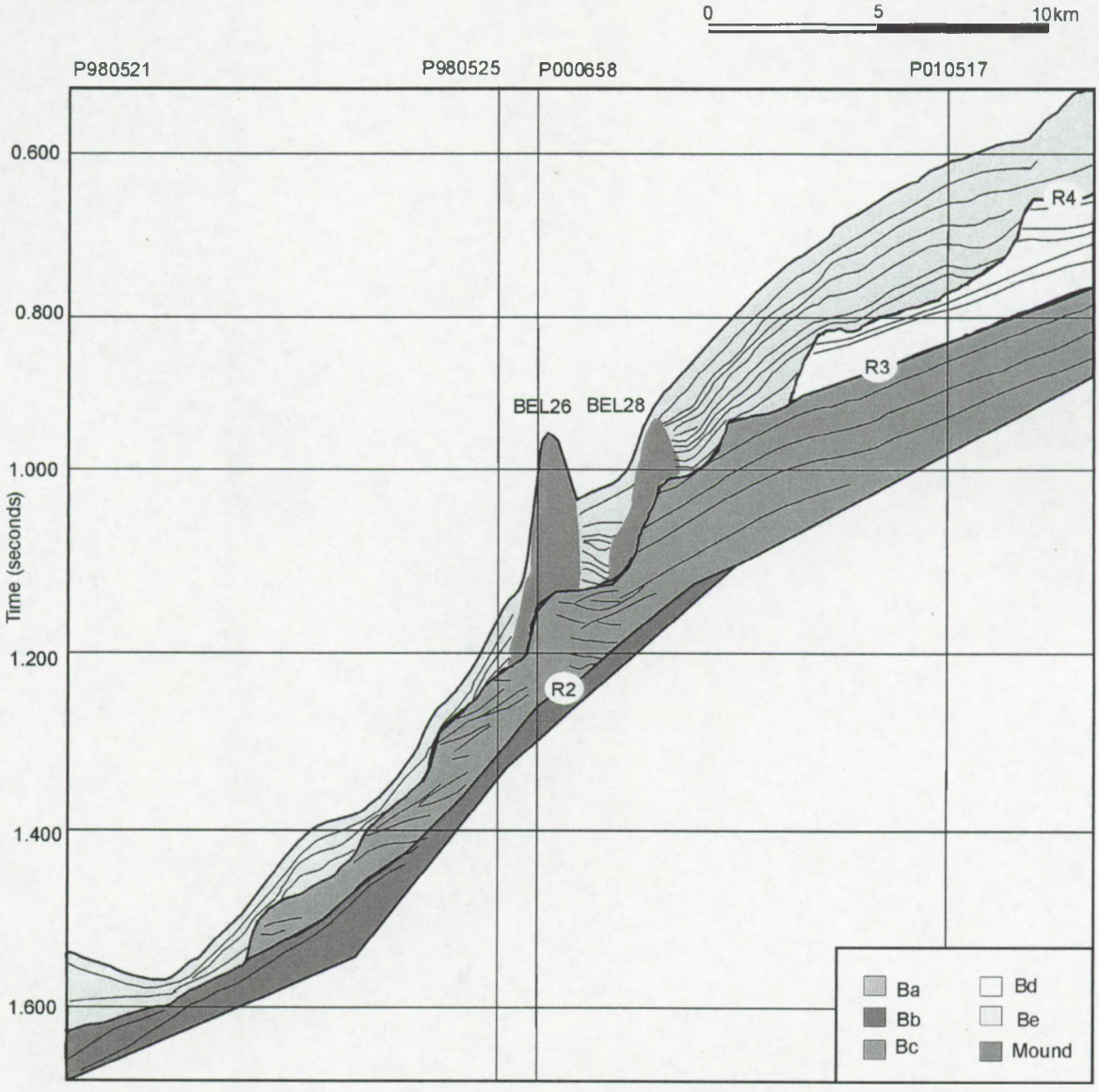
0
5
10km
P980521
P980525
P000658
P010517
0.600
0.800
1.000
1.200
1.400
1.600
Time (seconds)
R4
R3
R2
BEL26
BEL28
Ba
Bb
Bc
Bd
Be
Mound

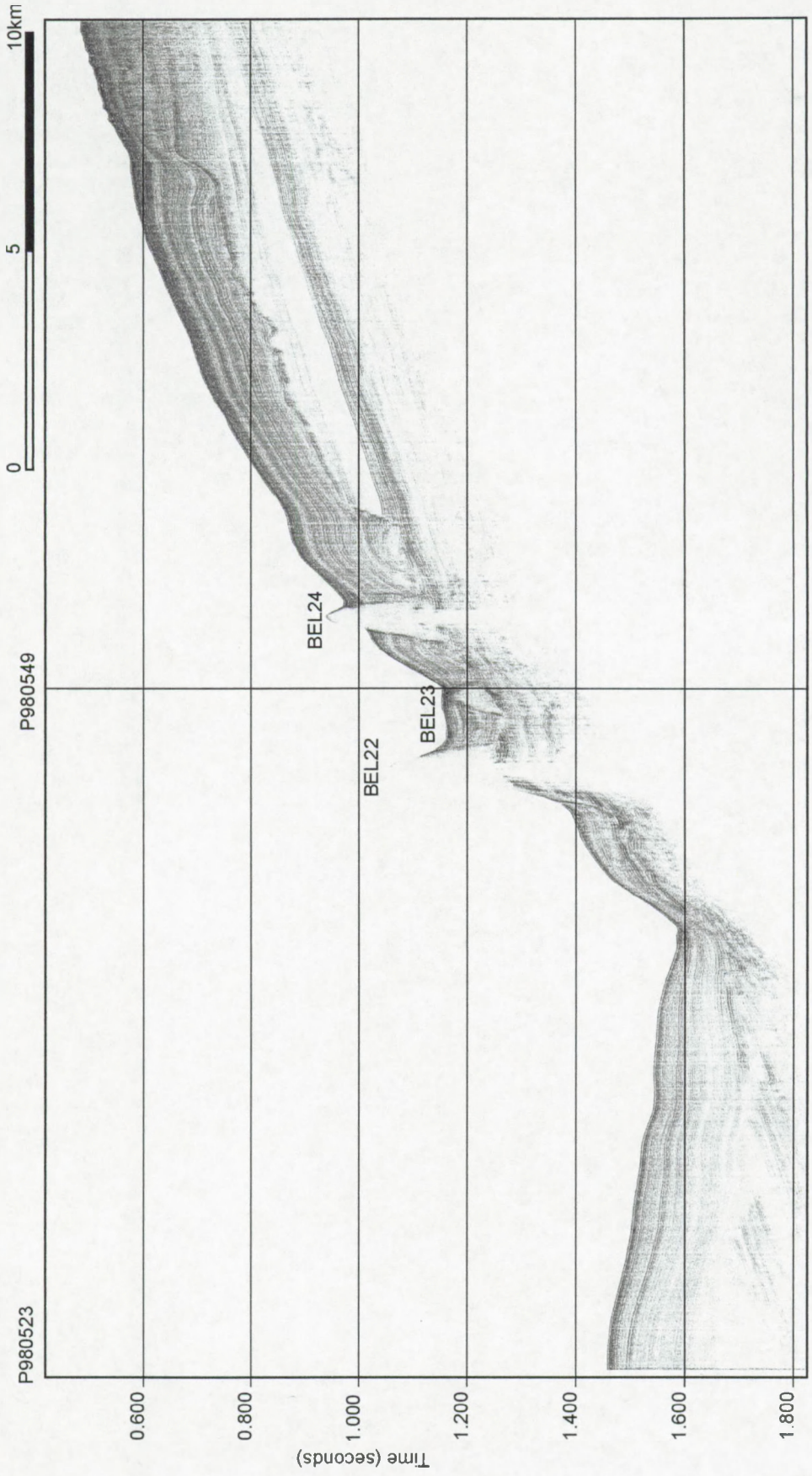
P980523
P980549
0
5
10km
BEL24
BEL23
BEL22
0.600
0.800
1.000
1.200
1.400
1.600
1.800
Time (seconds)

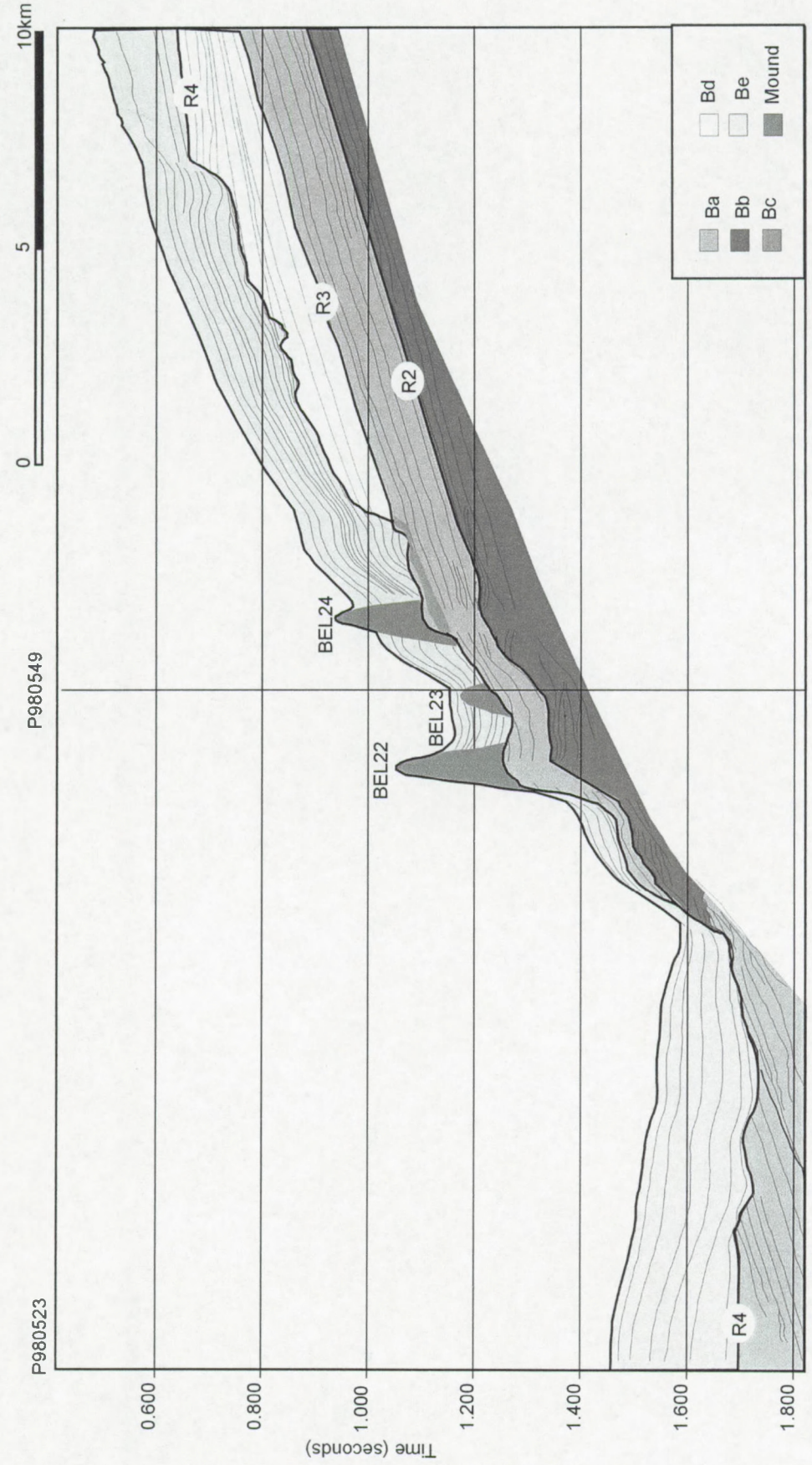
P980523
P980549
0
5
10km
R4
R3
R2
BEL24
BEL23
BEL22
R4
Ba
Bb
Bc
Bd
Be
Mound
0.600
0.800
1.000
1.200
1.400
1.600
1.800
Time (seconds)

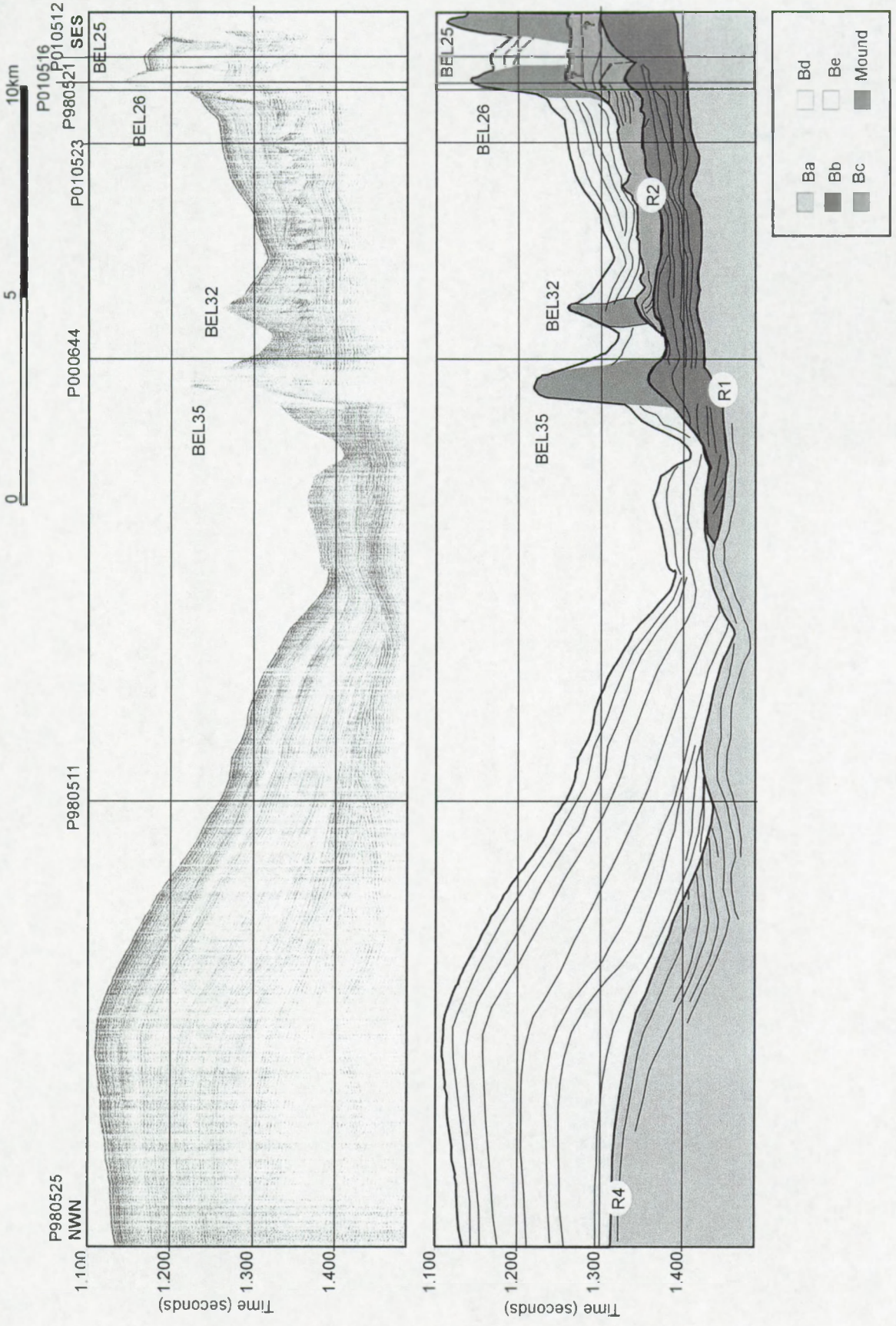
P980525
NWN
P980511
P000644
P010523
P980521
P010516
P010512
SES
0
5
10km
BEL25
BEL26
BEL32
BEL35
R1
R2
R4
Time (seconds)
1.100
1.200
1.300
1.400
Ba
Bb
Bc
Bd
Be
Mound

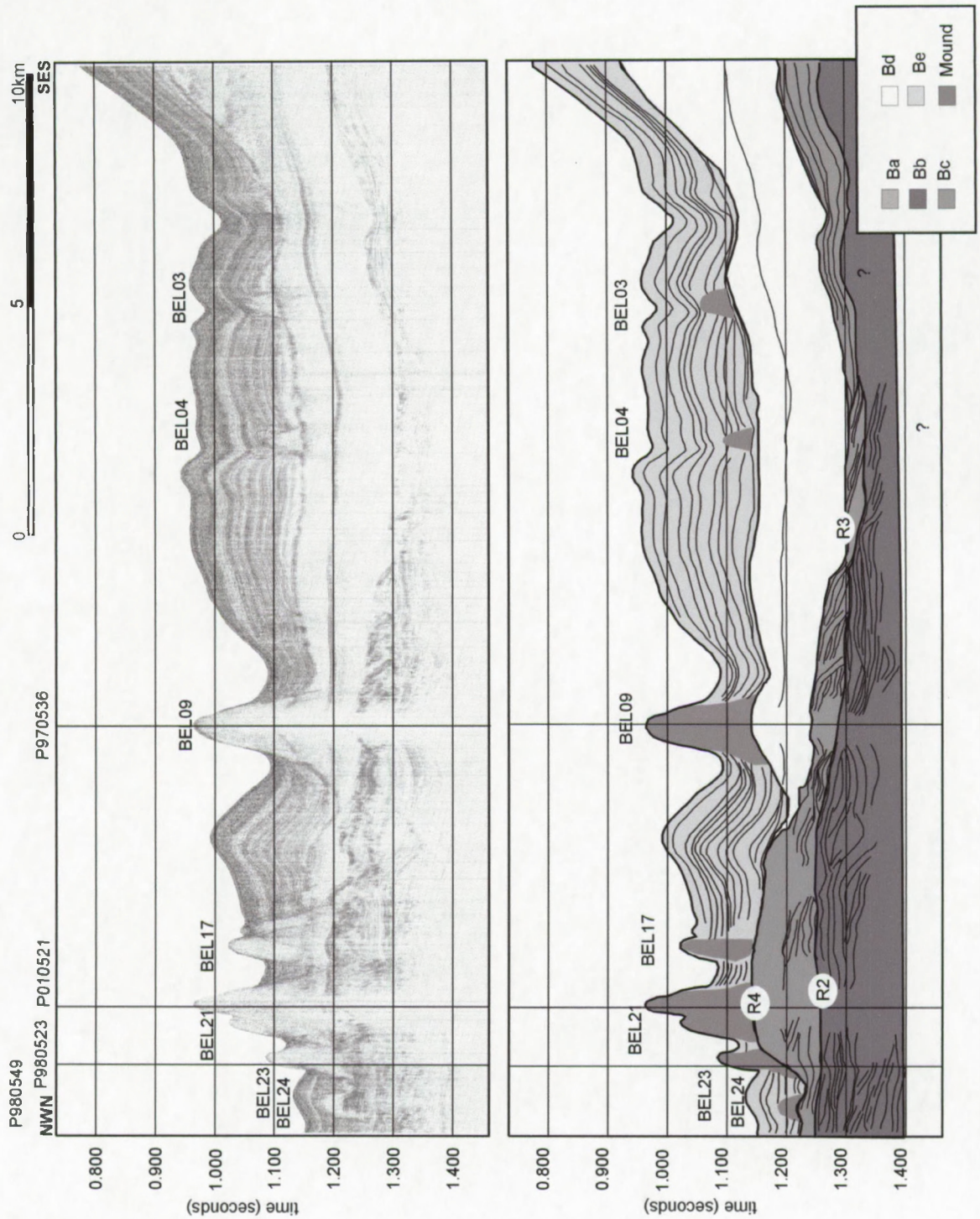
P980549
NWN
P980523
P010521
P970536
0
5
10km
SES
BEL03
BEL04
BEL09
BEL17
BEL21
BEL23
BEL24
R2
R3
R4
?
Ba
Bb
Bc
Bd
Be
Mound
time (seconds)
0.800
0.900
1.000
1.100
1.200
1.300
1.400

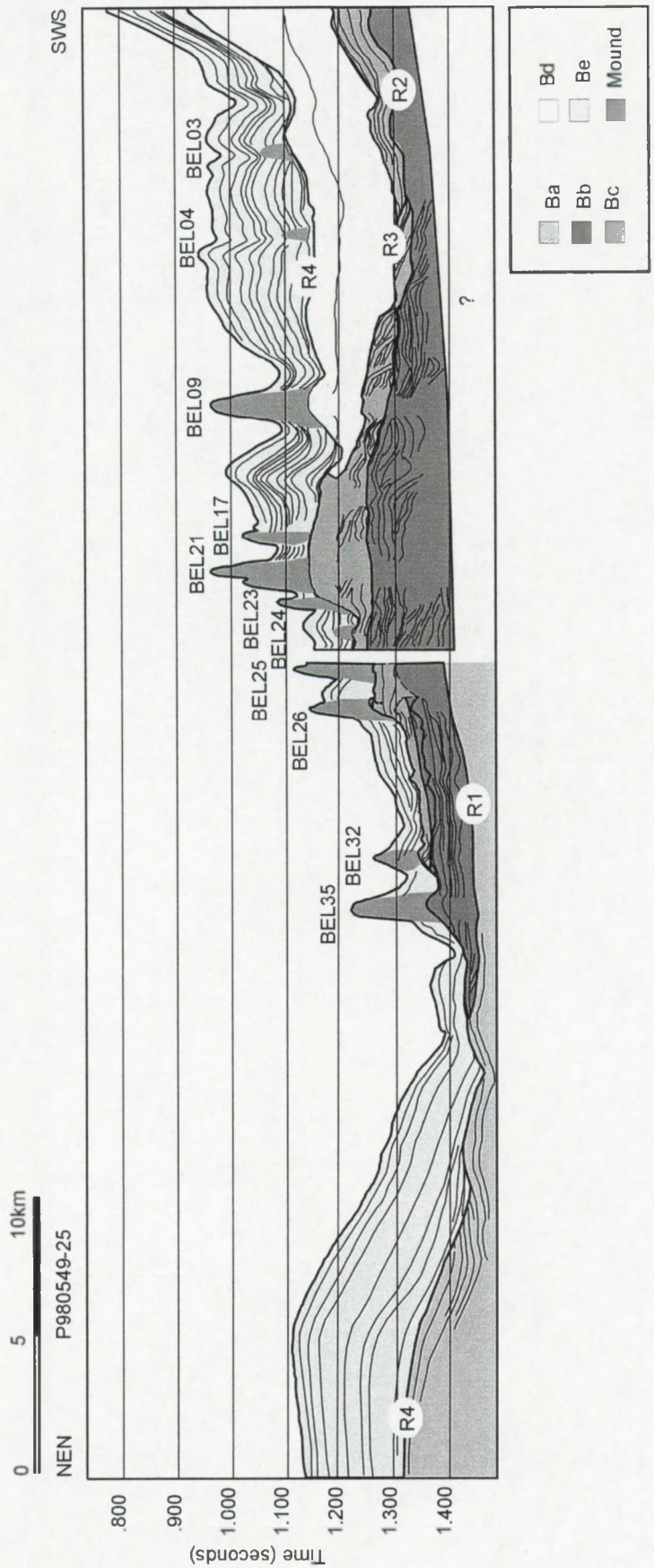
SWS
NEN
P980549-25
0
5
10km
Time (seconds)
800
900
1.000
1.100
1.200
1.300
1.400
BEL03
BEL04
BEL09
BEL17
BEL21
BEL23
BEL24
BEL25
BEL26
BEL32
BEL35
R1
R2
R3
R4
R4
?
Ba
Bb
Bc
Bd
Be
Mound

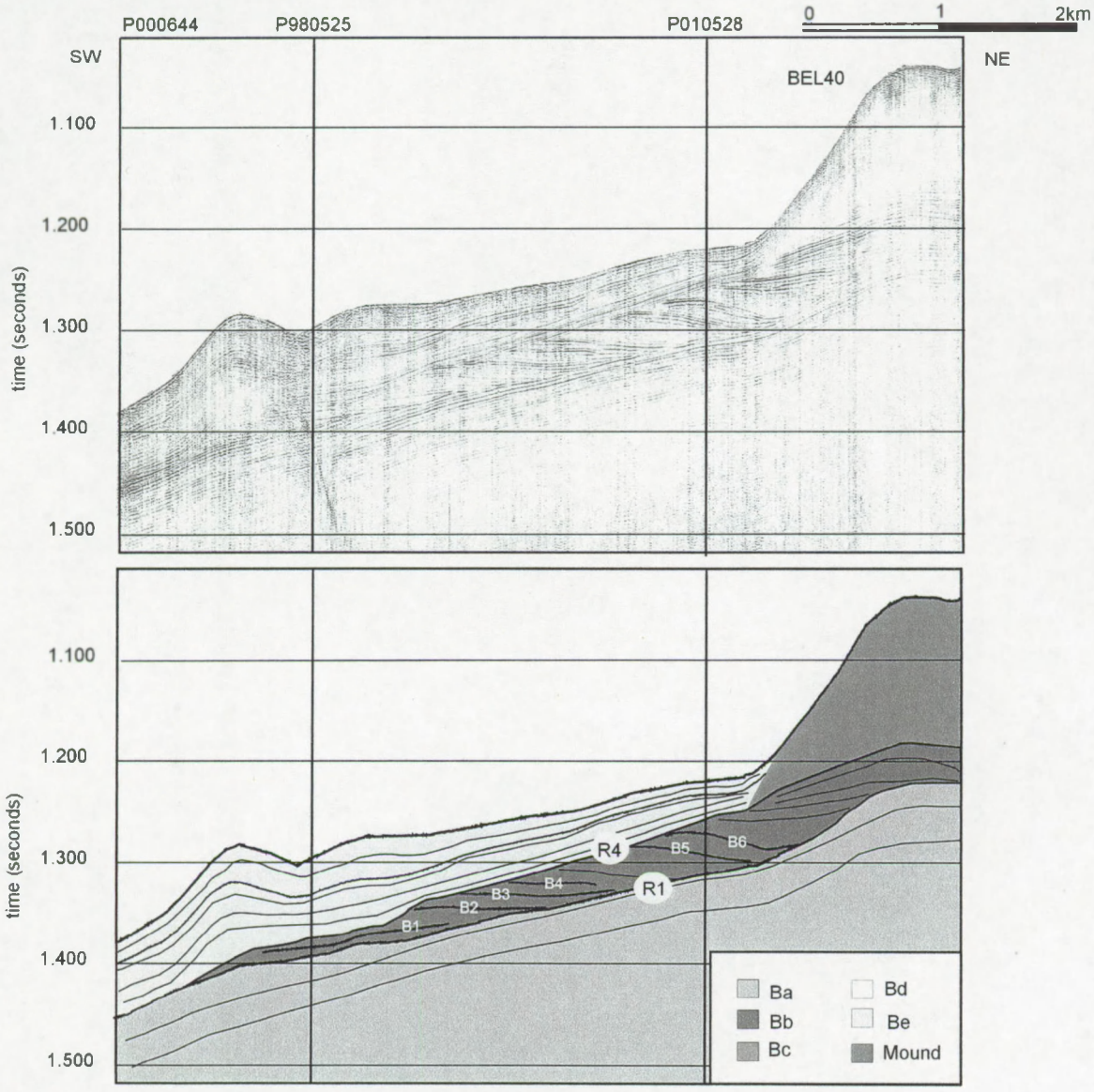
P000644
P980525
P010528
0
1
2km
SW
NE
BEL40
1.100
1.200
1.300
1.400
1.500
time (seconds)
R4
R1
B1
B2
B3
B4
B5
B6
Ba
Bb
Bc
Bd
Be
Mound

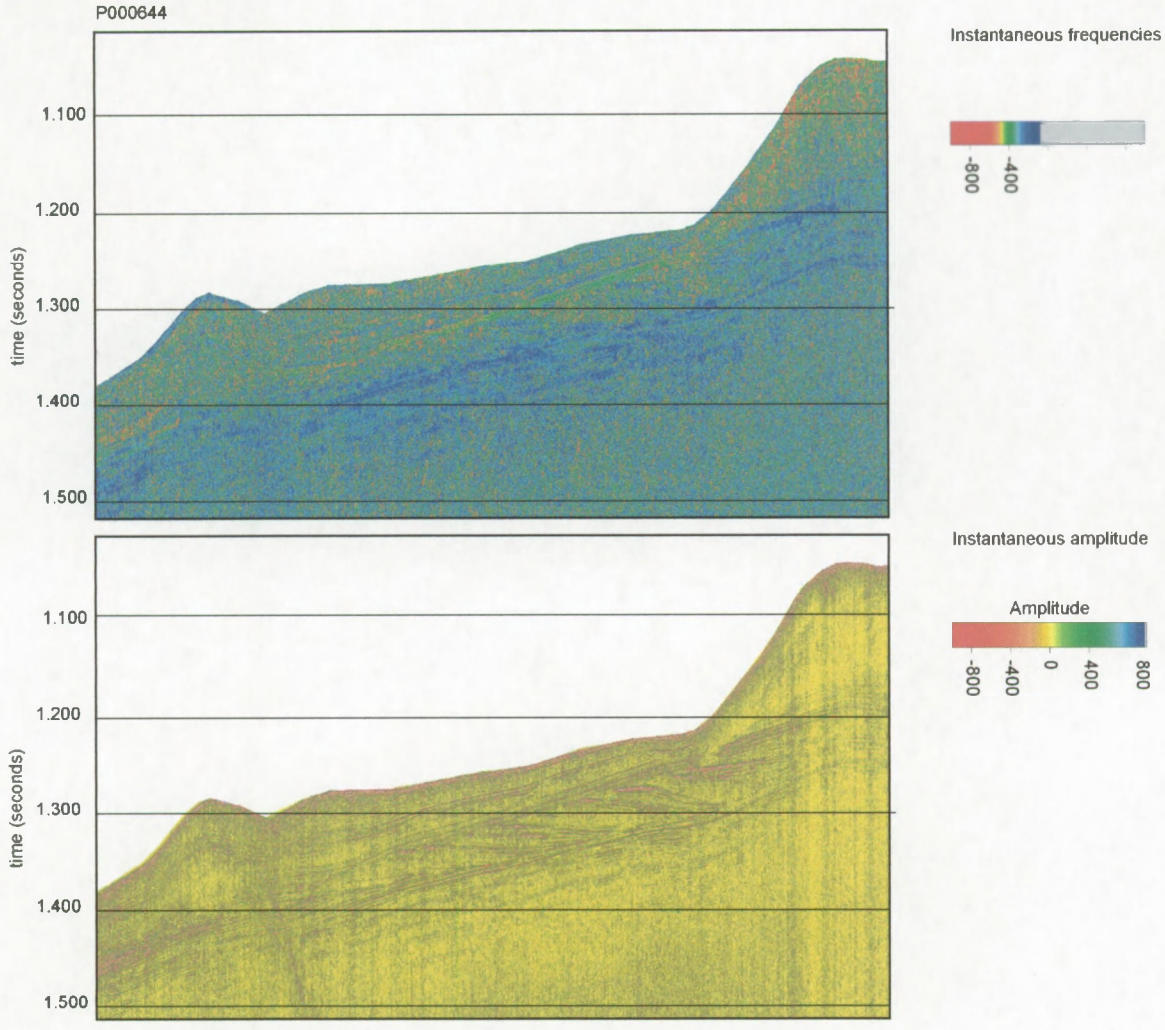
P000644
1.100
1.200
1.300
1.400
1.500
time (seconds)
Instantaneous frequencies
-800
-400
1.100
1.200
1.300
1.400
1.500
time (seconds)
Instantaneous amplitude
Amplitude
-800
-400
0
400
800

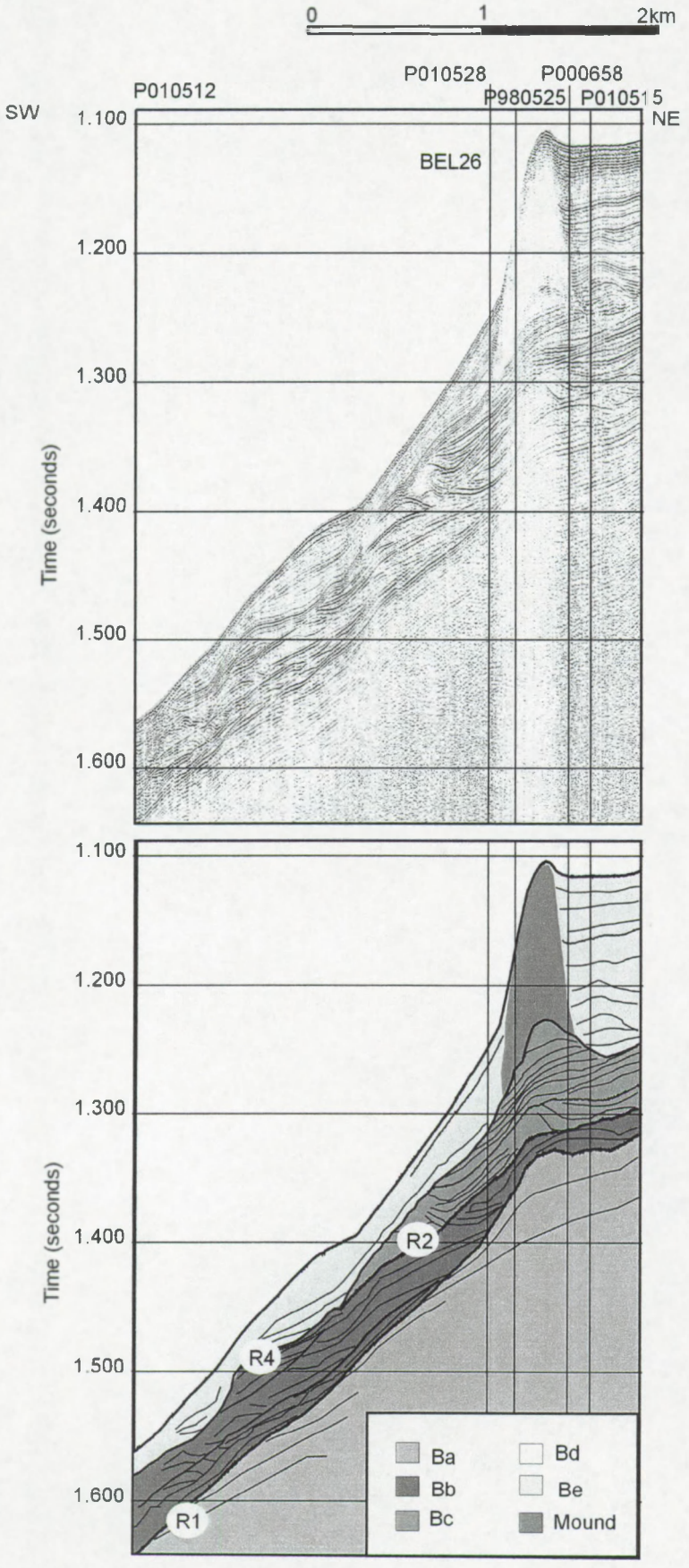
0
1
2km
P010512
P010528
P000658
P980525
P010515
SW
NE
BEL26
1.100
1.200
1.300
1.400
1.500
1.600
Time (seconds)
R1
R2
R4
Ba
Bb
Bc
Bd
Be
Mound

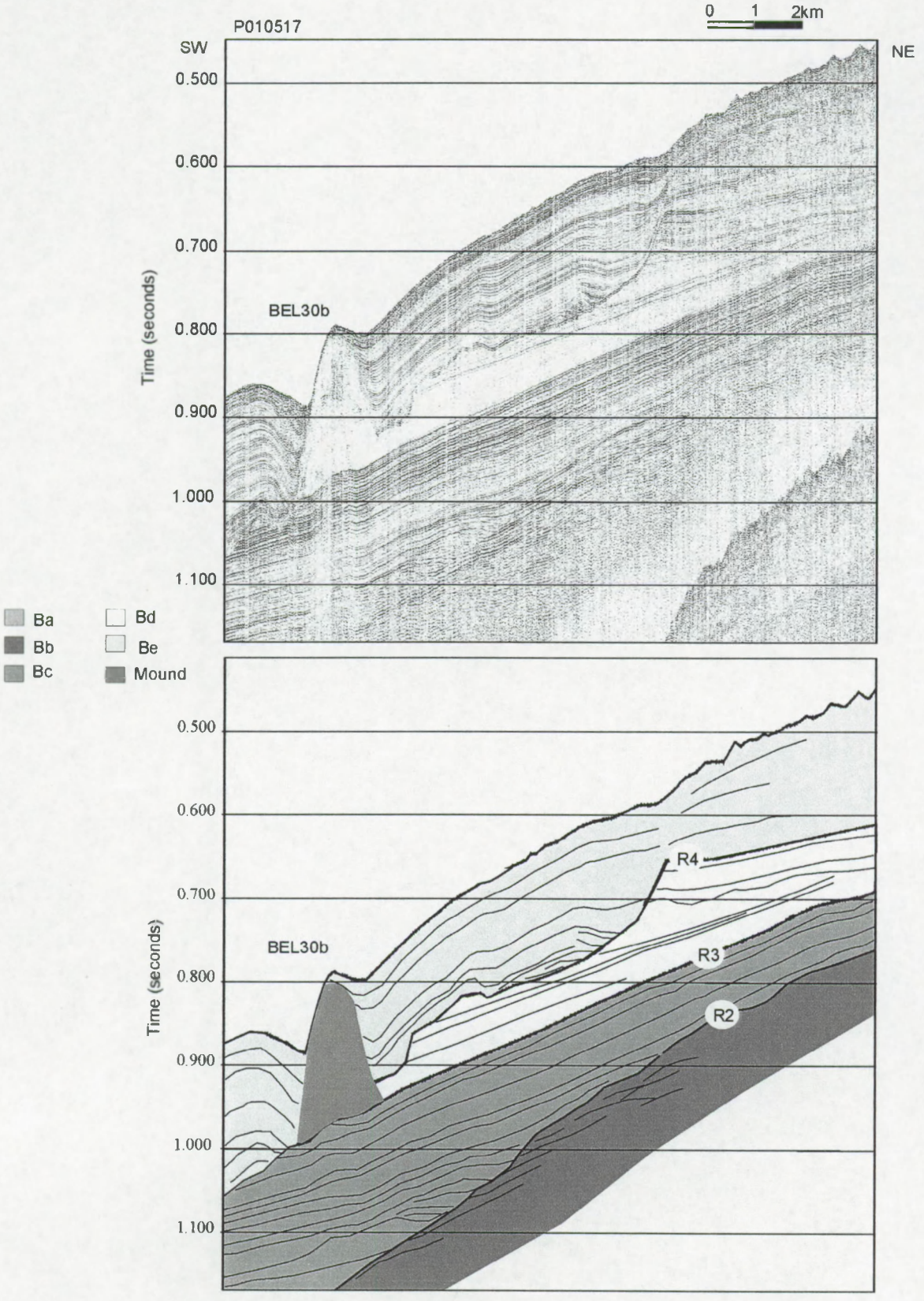
P010517
0 1 2km
SW
NE
0.500
0.600
0.700
0.800
0.900
1.000
1.100
Time (seconds)
BEL30b
Ba
Bb
Bc
Bd
Be
Mound
R4
R3
R2

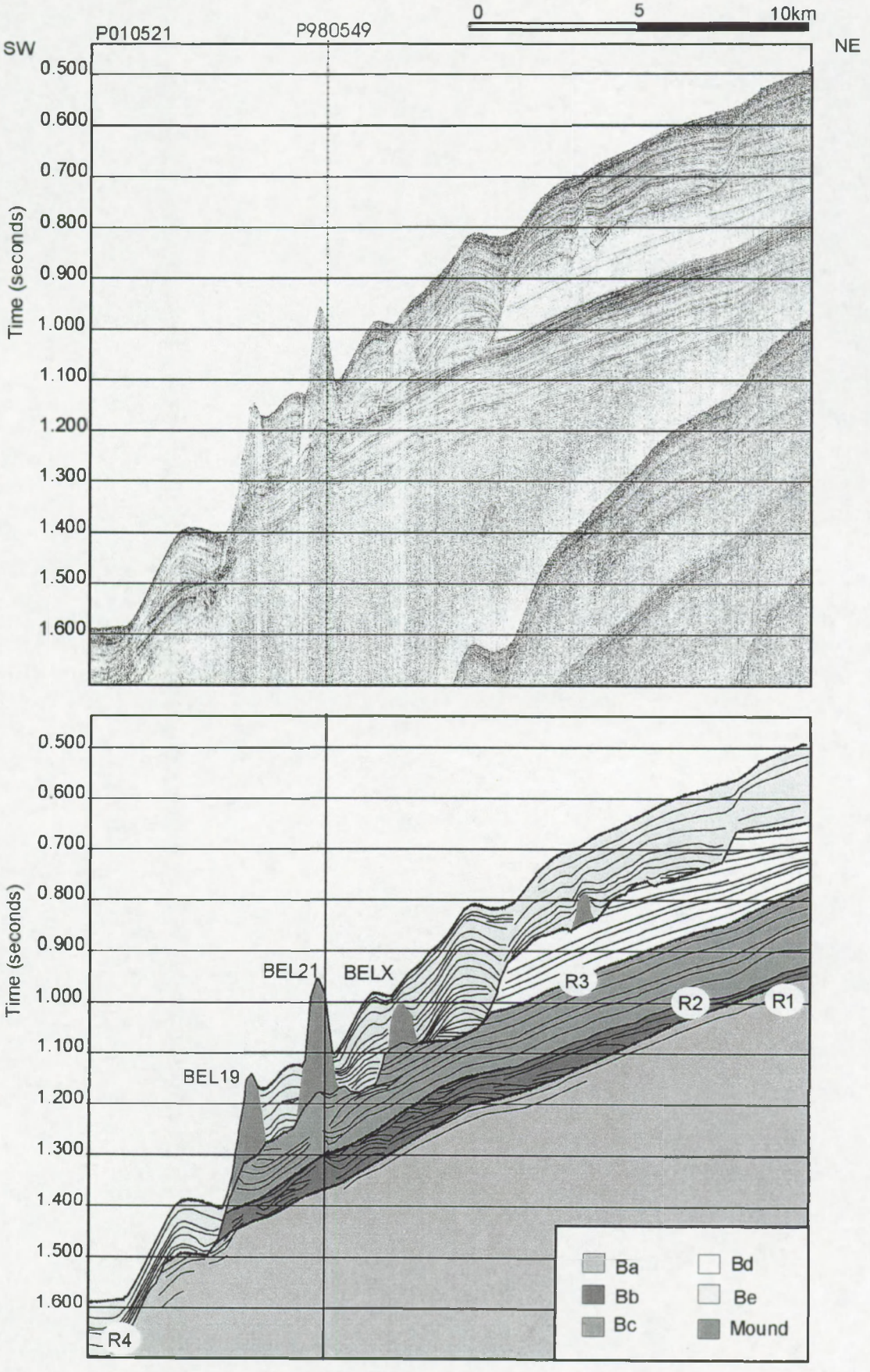
0
5
10km
P010521
P980549
SW
NE
Time (seconds)
0.500
0.600
0.700
0.800
0.900
1.000
1.100
1.200
1.300
1.400
1.500
1.600
BEL21
BELX
BEL19
R1
R2
R3
R4
Ba
Bb
Bc
Bd
Be
Mound

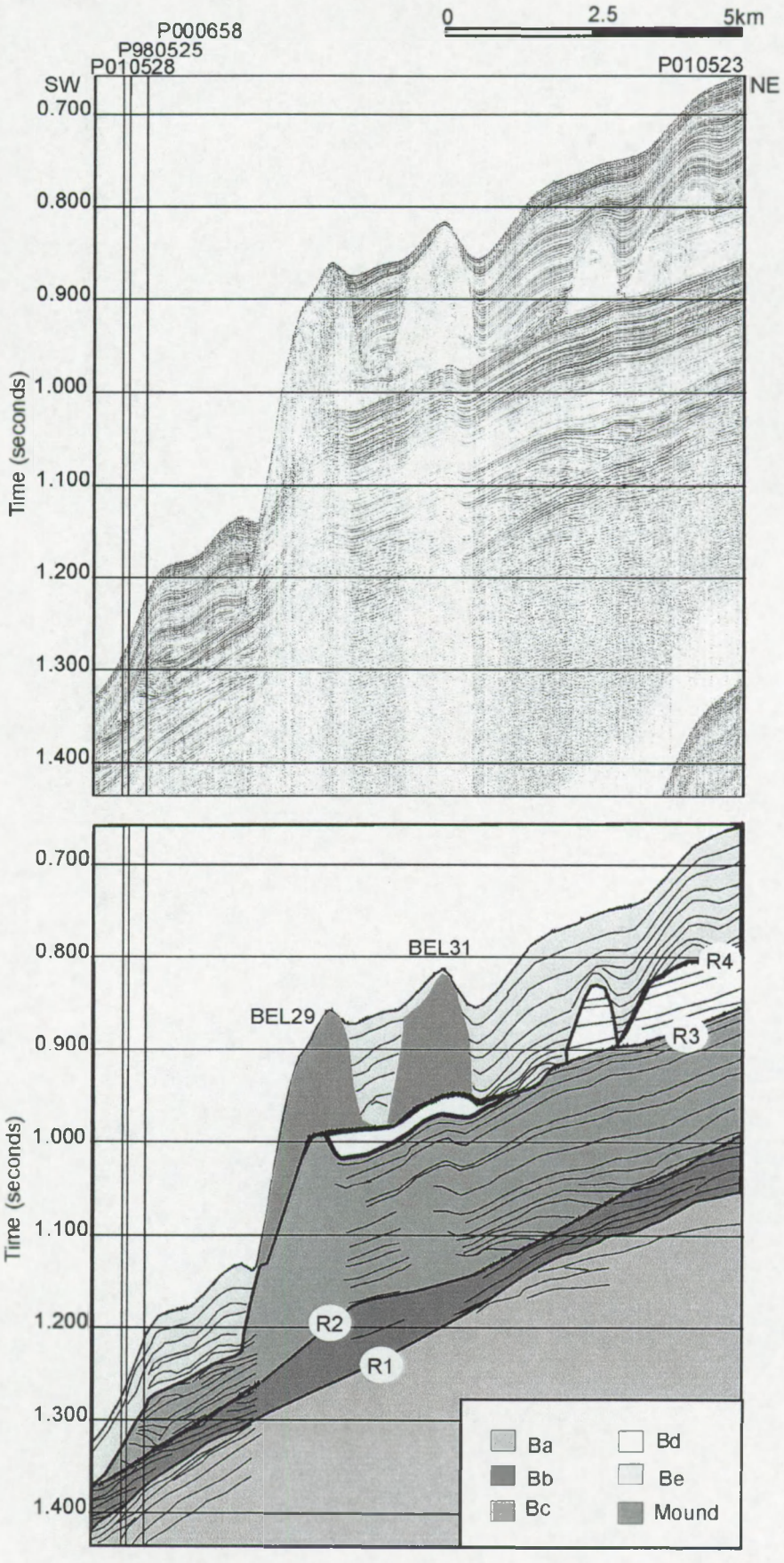
0
2.5
5km
P000658
P980525
P010528
P010523
SW
NE
0.700
0.800
0.900
1.000
1.100
1.200
1.300
1.400
Time (seconds)
BEL31
BEL29
R4
R3
R2
R1
Ba
Bb
Bc
Bd
Be
Mound

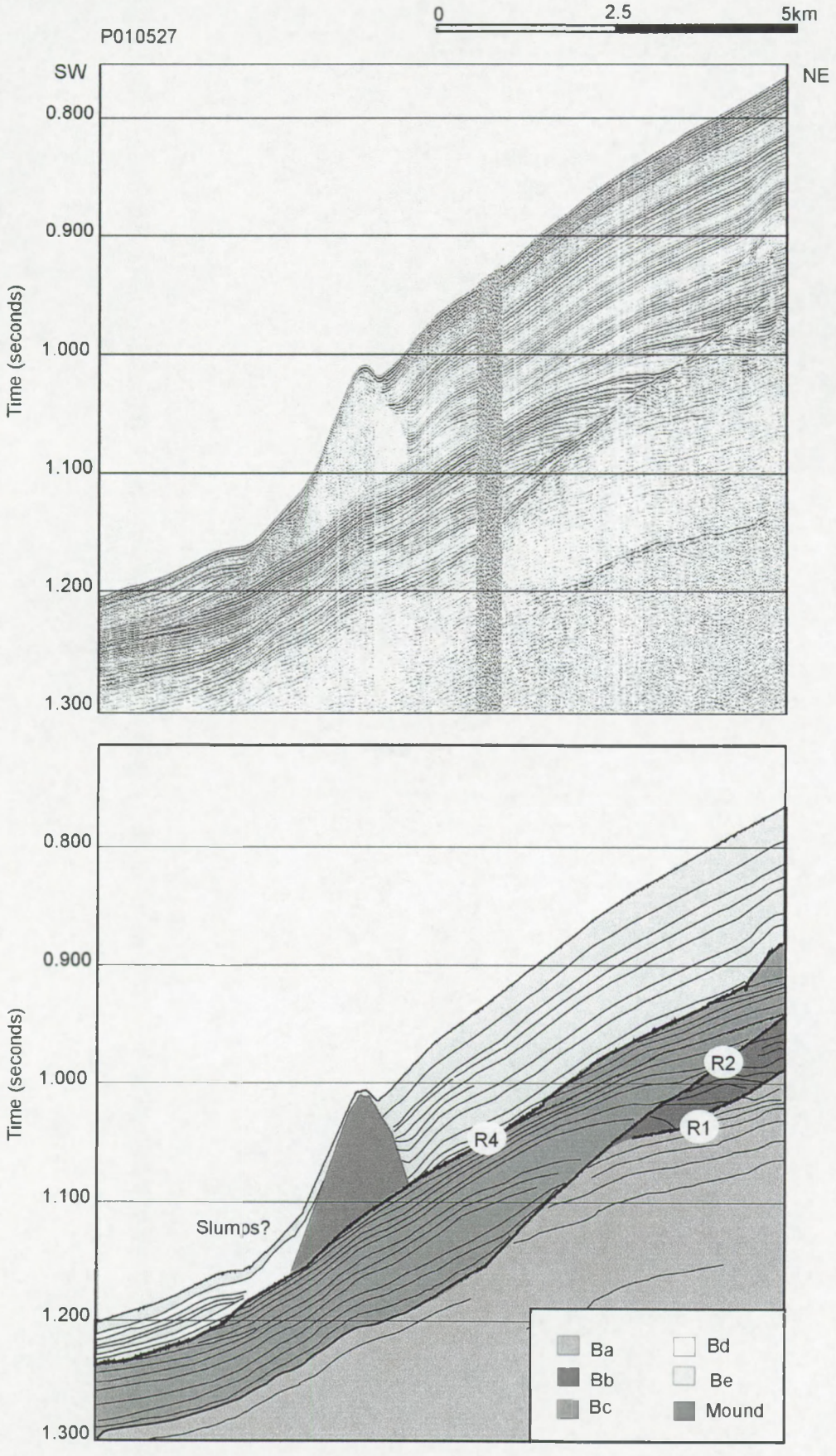
0
2.5
5km
P010527
SW
NE
0.800
0.900
1.000
1.100
1.200
1.300
Time (seconds)
R2
R1
R4
Slumps?
Ba
Bb
Bc
Bd
Be
Mound

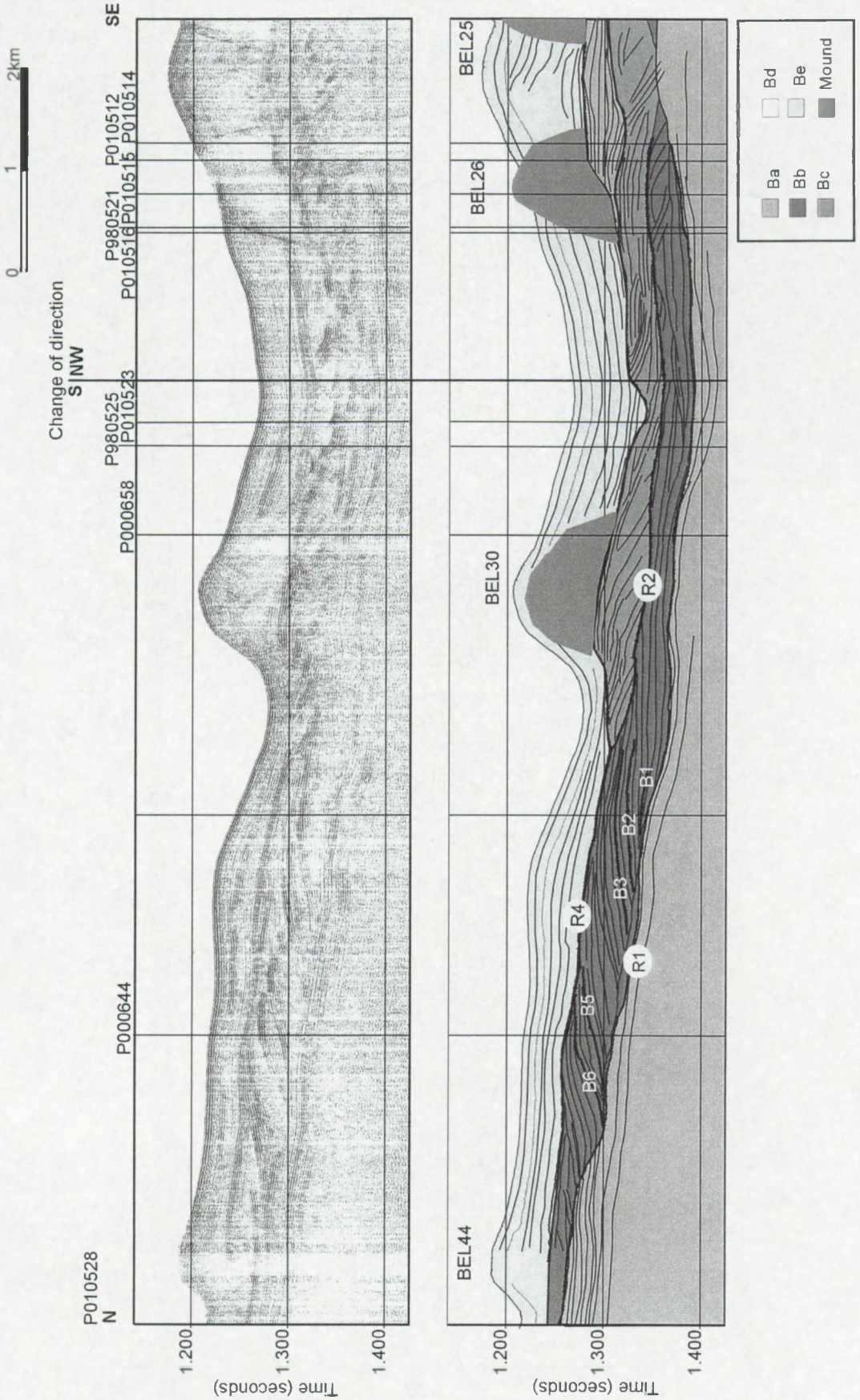
0
1
2km
Change of direction
S NW
P010528
N
P000644
P000658
P980525
P010523
P980521
P010516
P010515
P010512
P010514
SE
BEL44
BEL30
BEL26
BEL25
R1
R2
R4
B1
B2
B3
B5
B6
Time (seconds)
1.200
1.300
1.400
Ba
Bb
Bc
Bd
Be
Mound

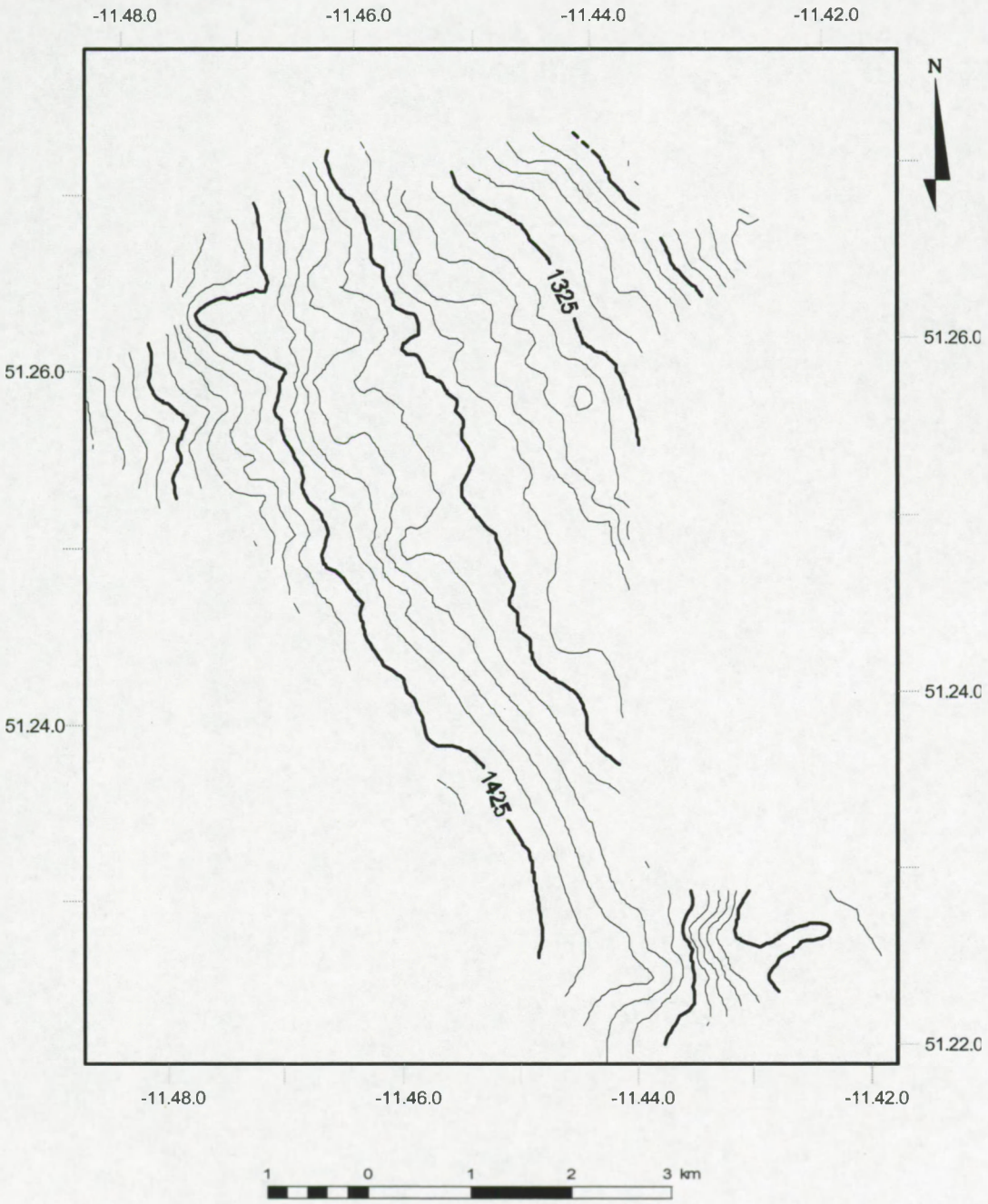
-11.48.0
-11.46.0
-11.44.0
-11.42.0
N
1325
1425
51.26.0
51.24.0
51.22.0
1 0 1 2 3 km

2. Case study of BEL26, Challenger mound

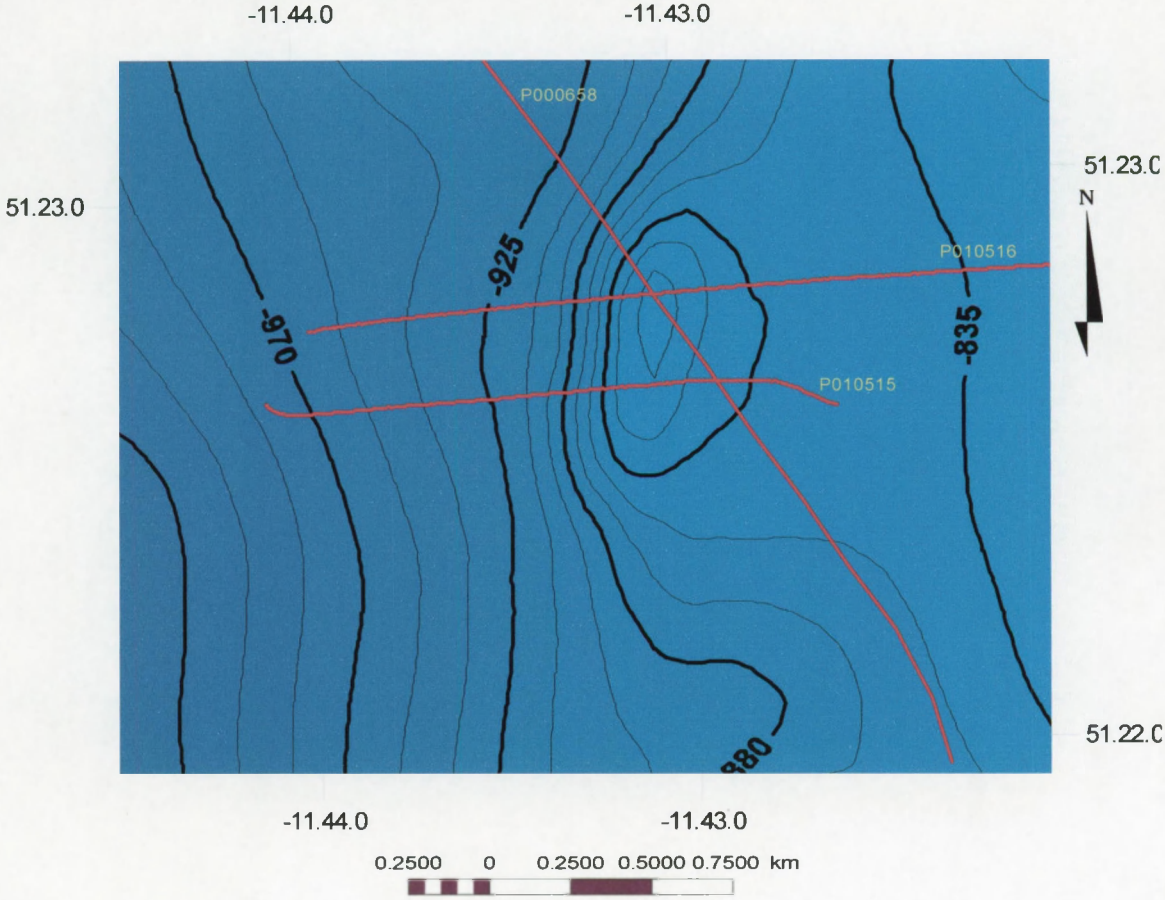

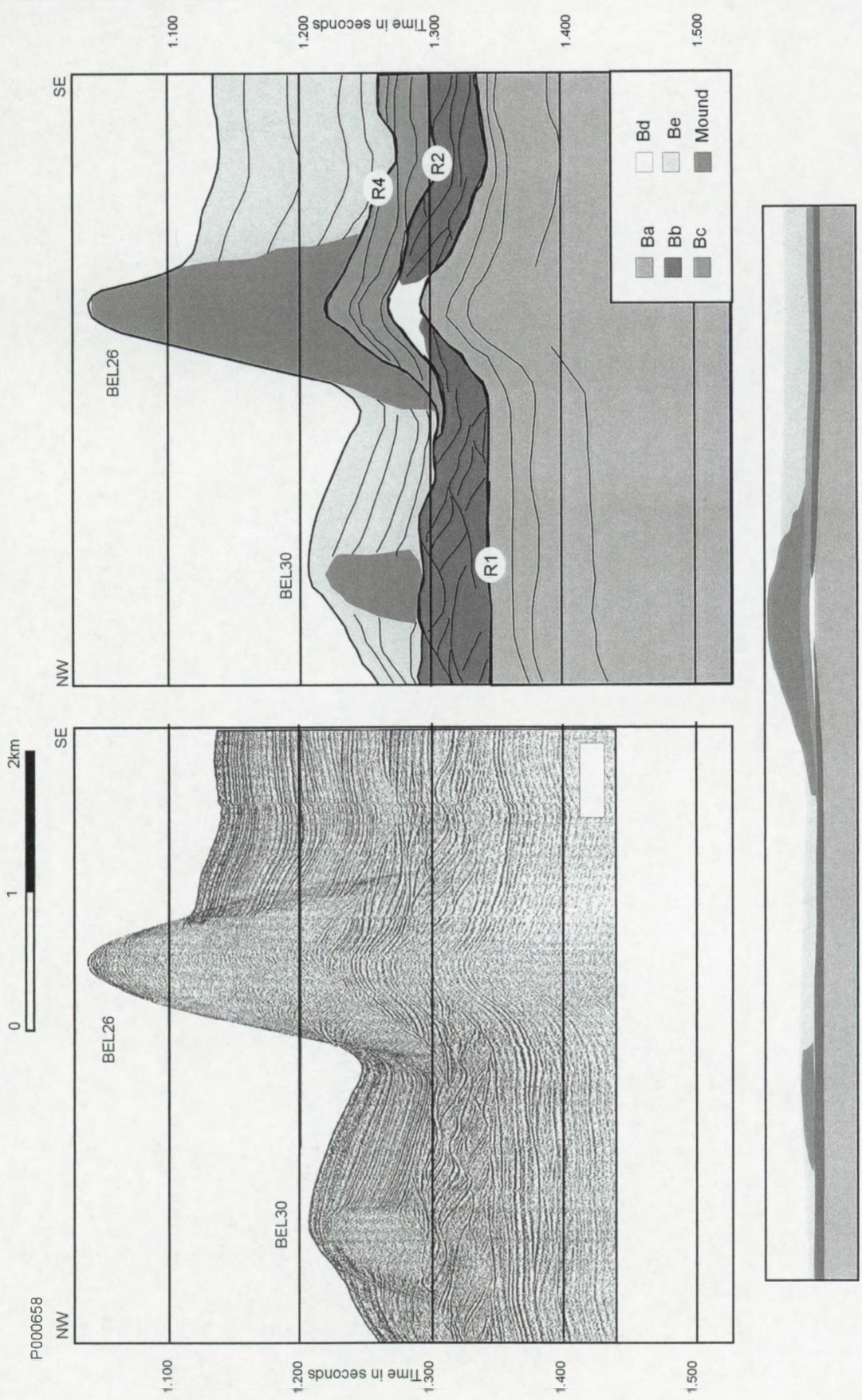
P000658
NW
SE
BEL26
BEL30
0
1
2km
Time in seconds
1.100
1.200
1.300
1.400
1.500
R1
R2
R4
Ba
Bb
Bc
Bd
Be
Mound

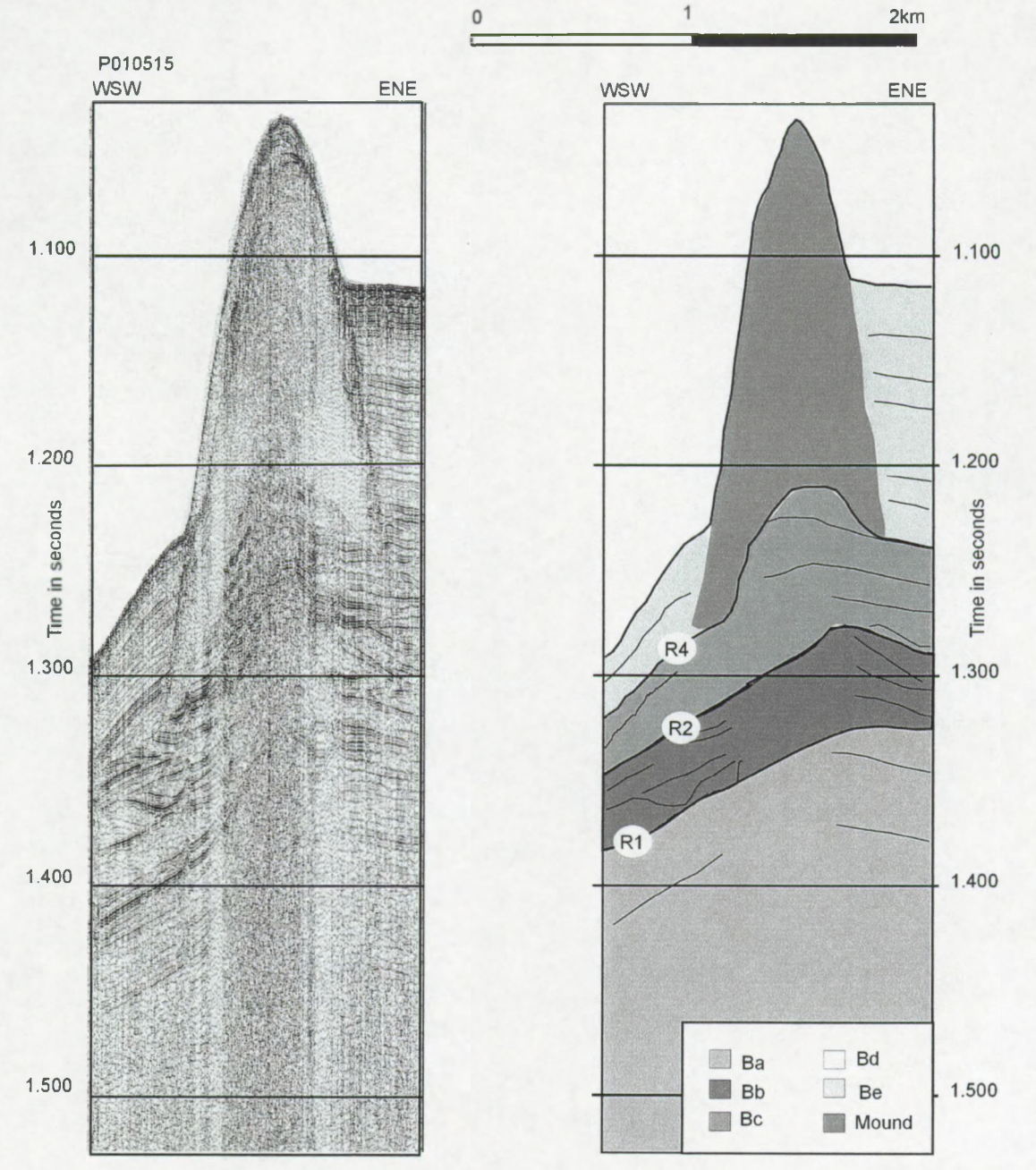
0
1
2km
P010515
WSW
ENE
WSW
ENE
1.100
1.200
1.300
1.400
1.500
Time in seconds
R4
R2
R1
Ba
Bb
Bc
Bd
Be
Mound

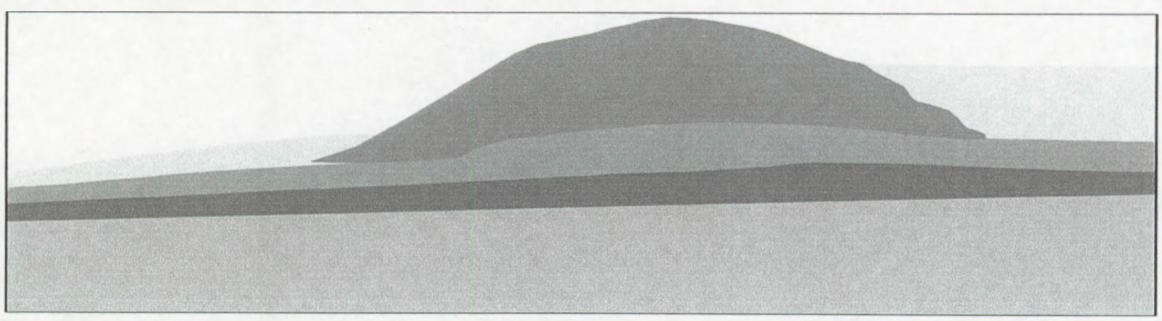

Appendix B
Case study Belgica mound province

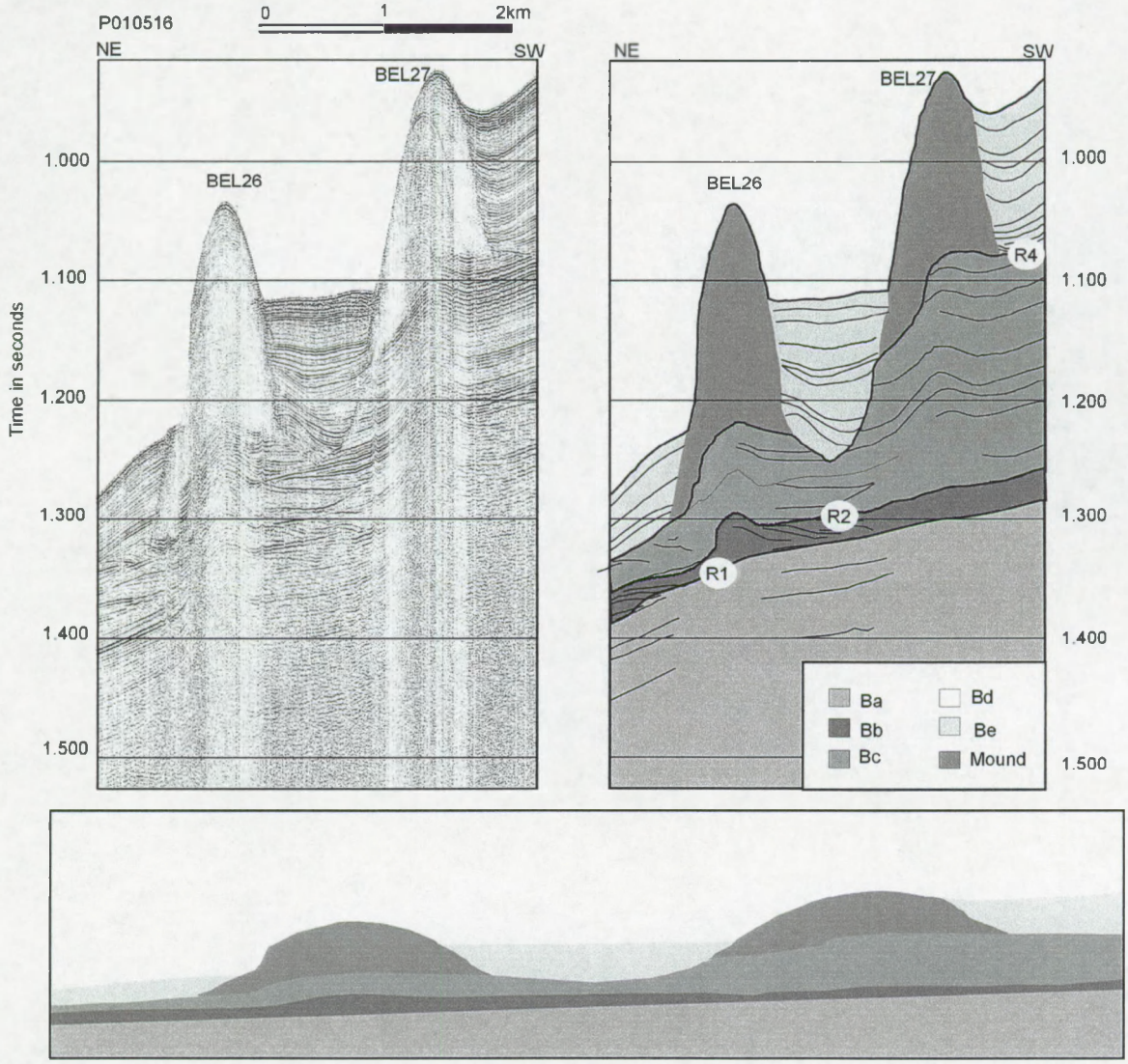

3. Case study of Thérèse mound and friends

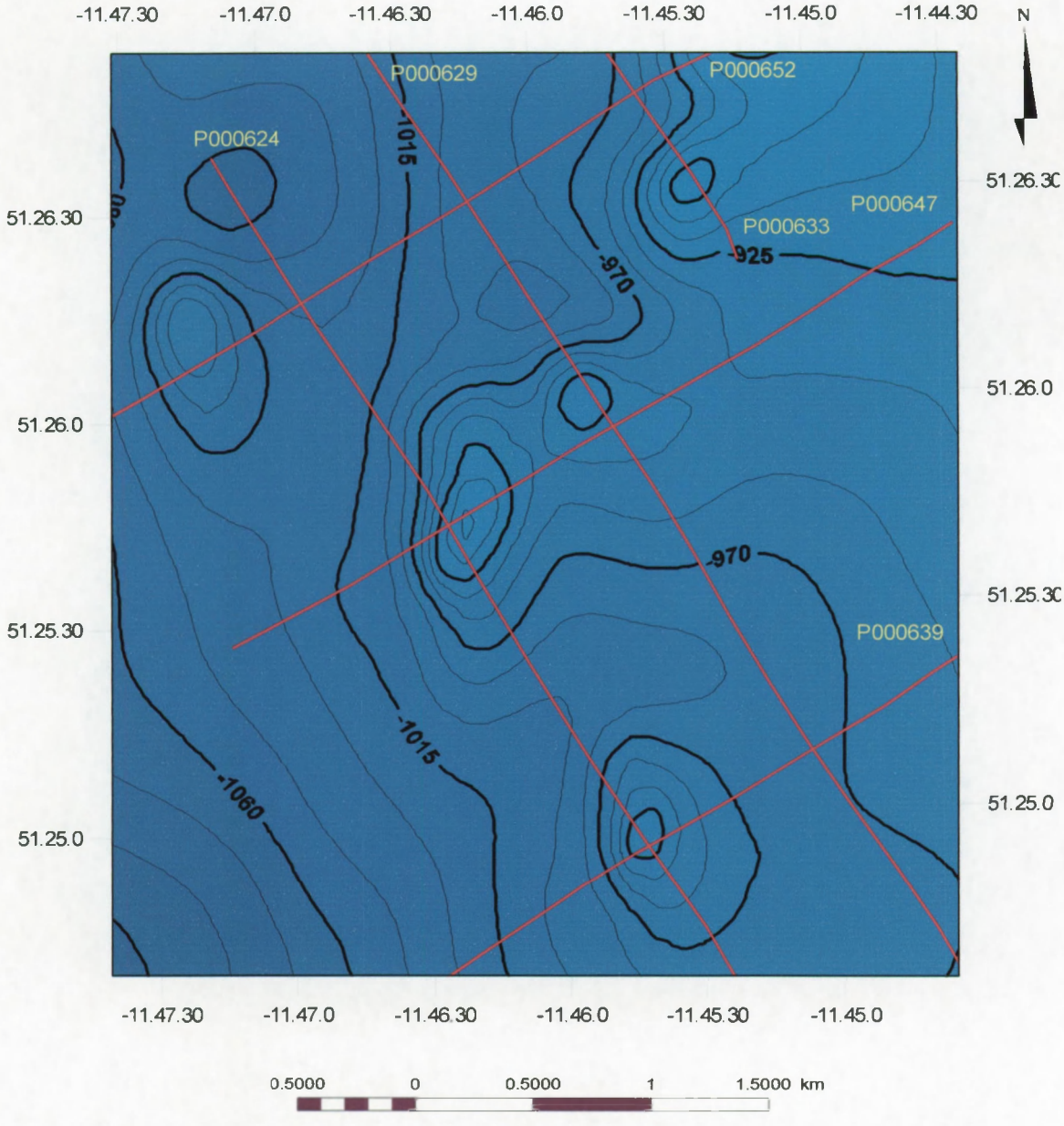

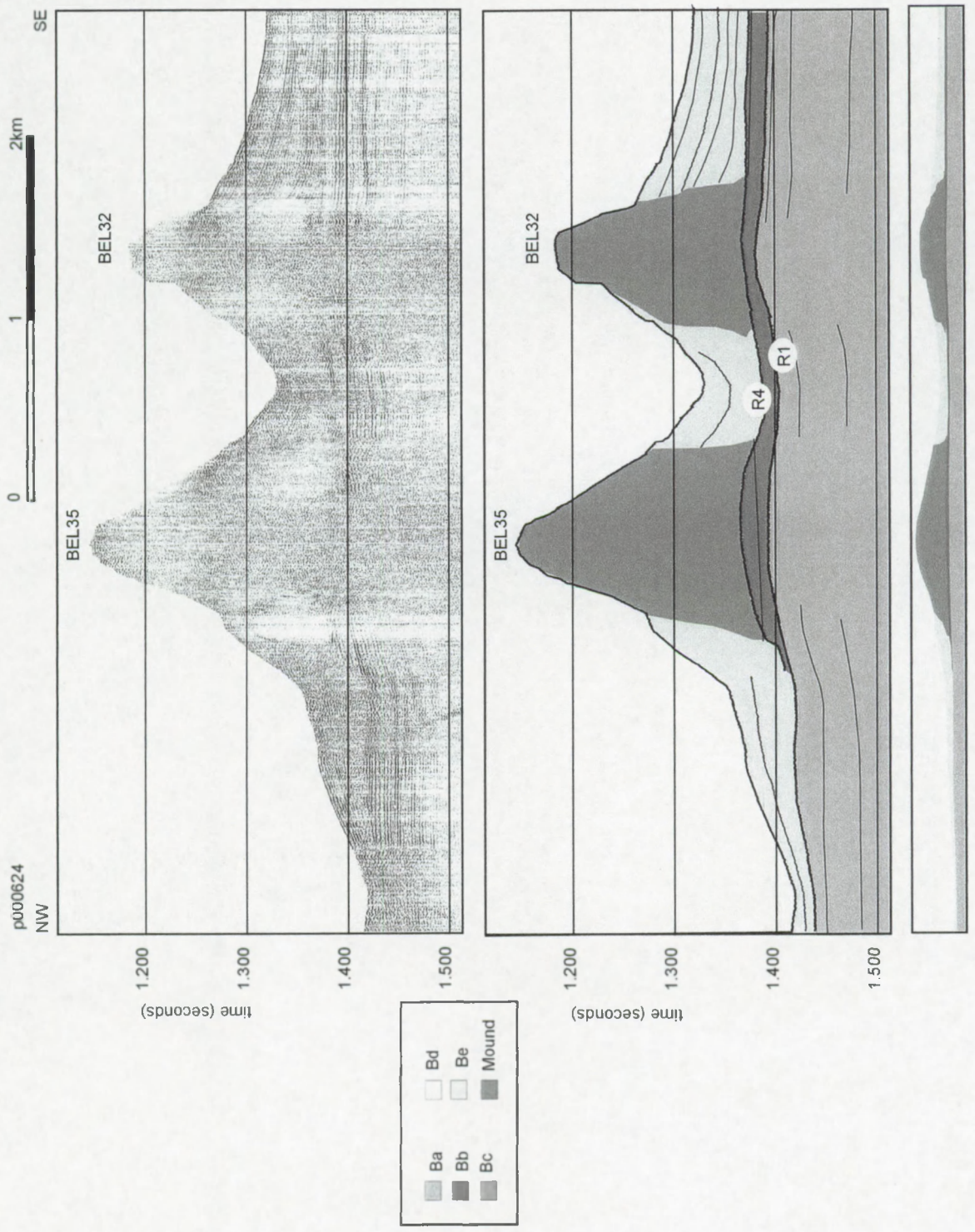
p000624
NW
SE
0
1
2km
BEL35
BEL32
1.200
1.300
1.400
1.500
time (seconds)
Ba
Bb
Bc
Bd
Be
Mound
R4
R1

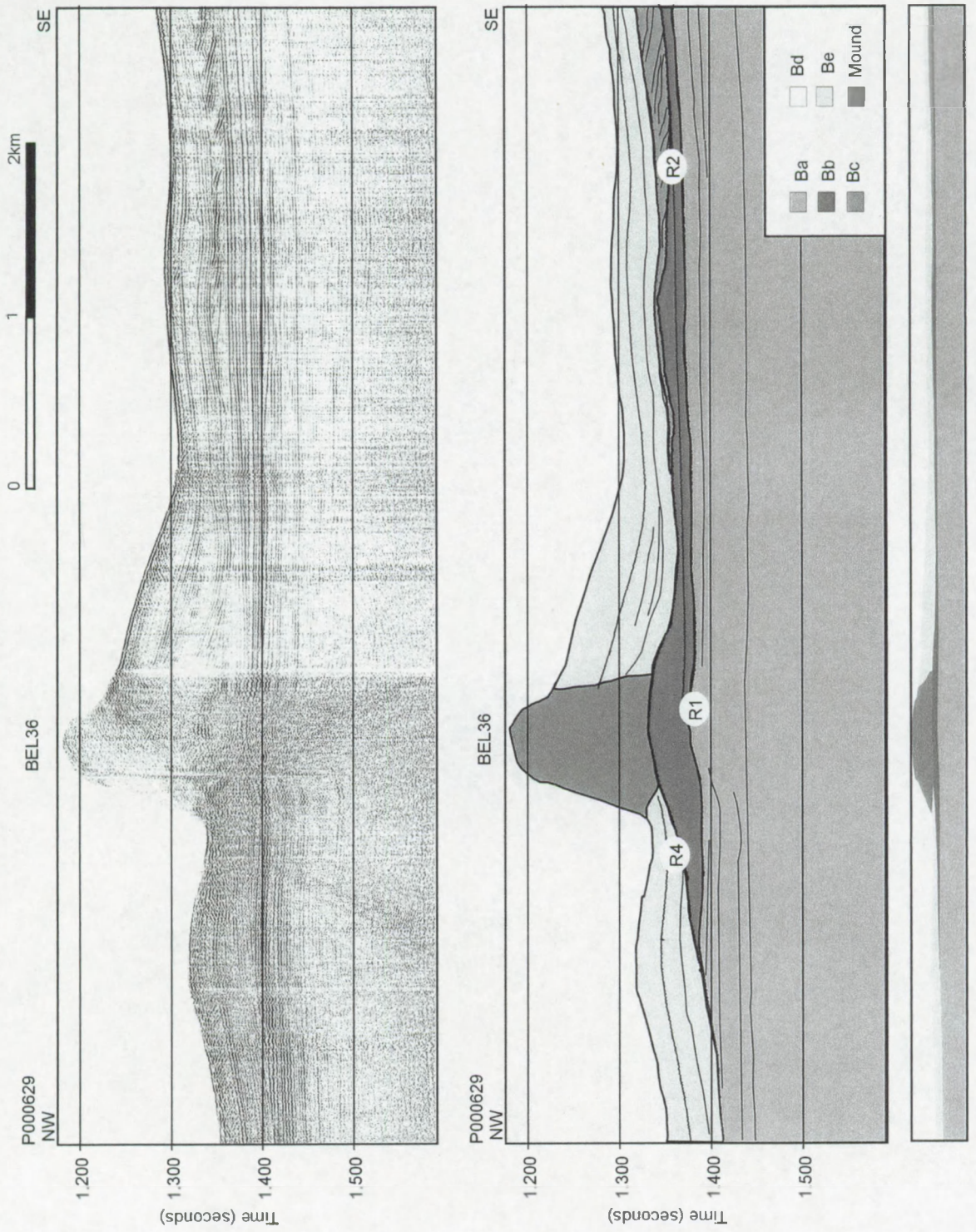
P000629
NW
BEL36
SE
0
1
2km
1.200
1.300
1.400
1.500
Time (seconds)
P000629
NW
BEL36
SE
R4
R1
R2
Ba
Bb
Bc
Bd
Be
Mound
1.200
1.300
1.400
1.500
Time (seconds)

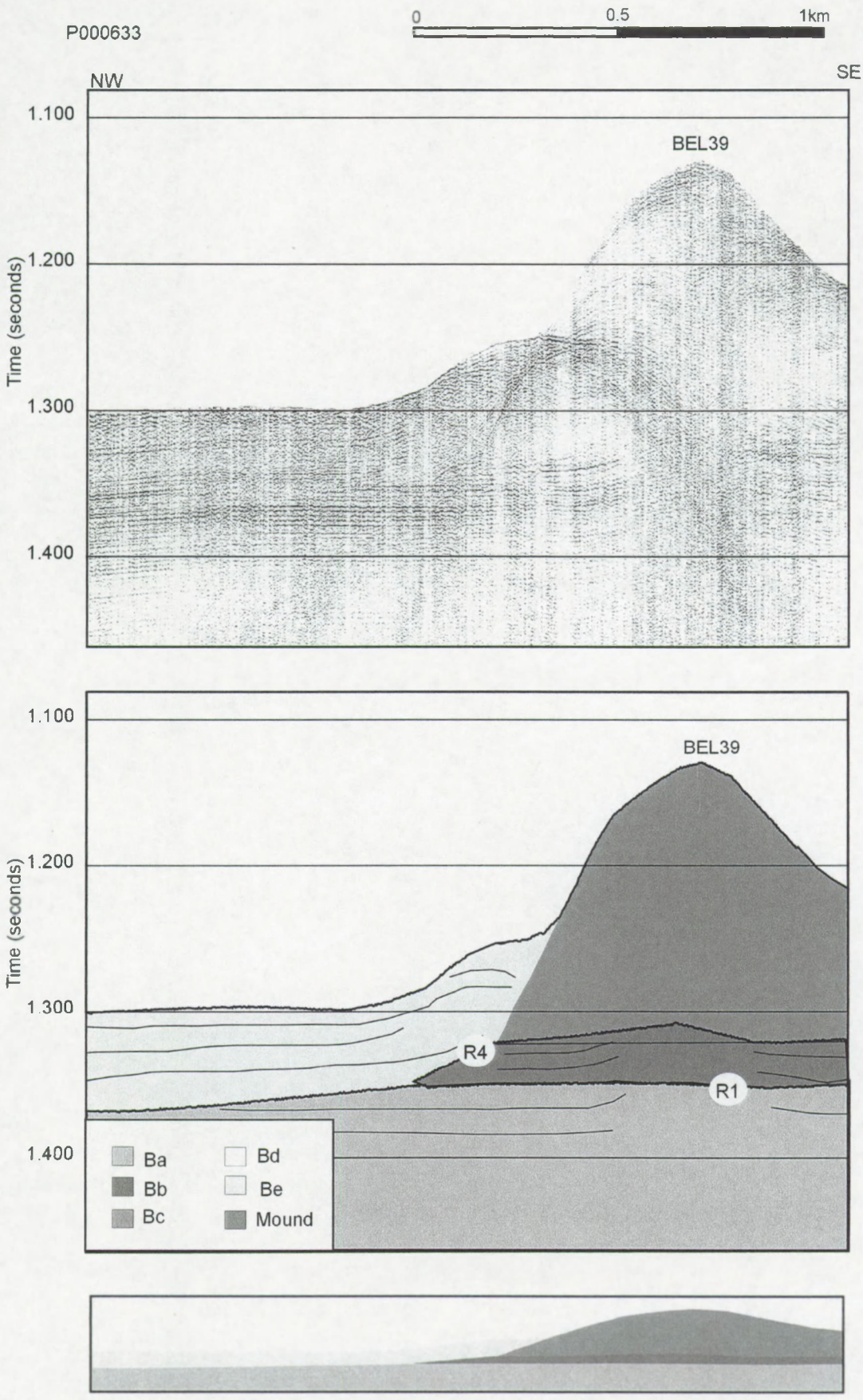
P000633
0
0.5
1km
NW
SE
1.100
1.200
1.300
1.400
Time (seconds)
BEL39
BEL39
R4
R1
Ba
Bb
Bc
Bd
Be
Mound

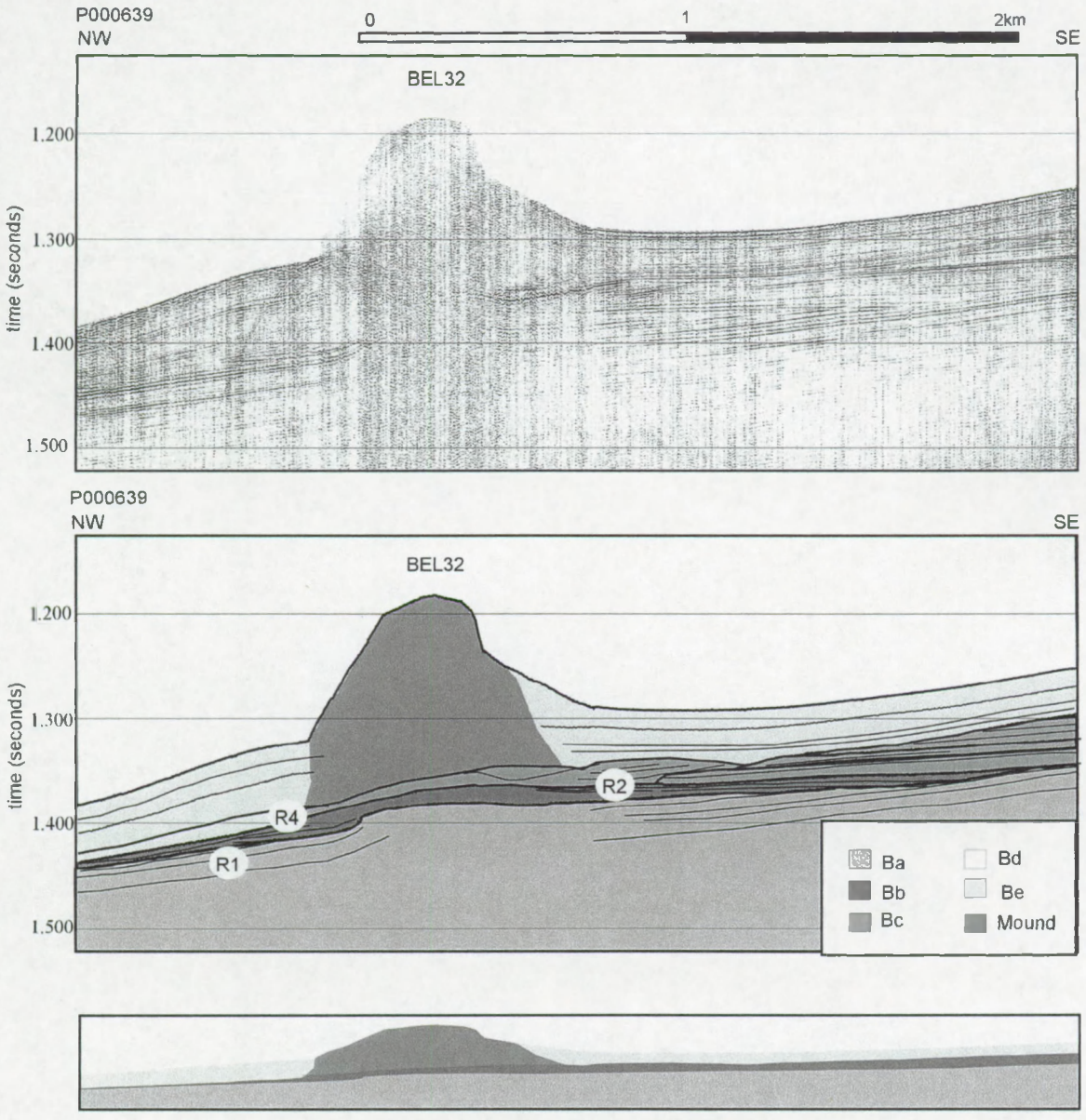
P000639
NW
0
1
2km
SE
BEL32
1.200
1.300
1.400
1.500
time (seconds)
P000639
NW
SE
BEL32
1.200
1.300
1.400
1.500
time (seconds)
R1
R2
R4
Ba
Bb
Bc
Bd
Be
Mound

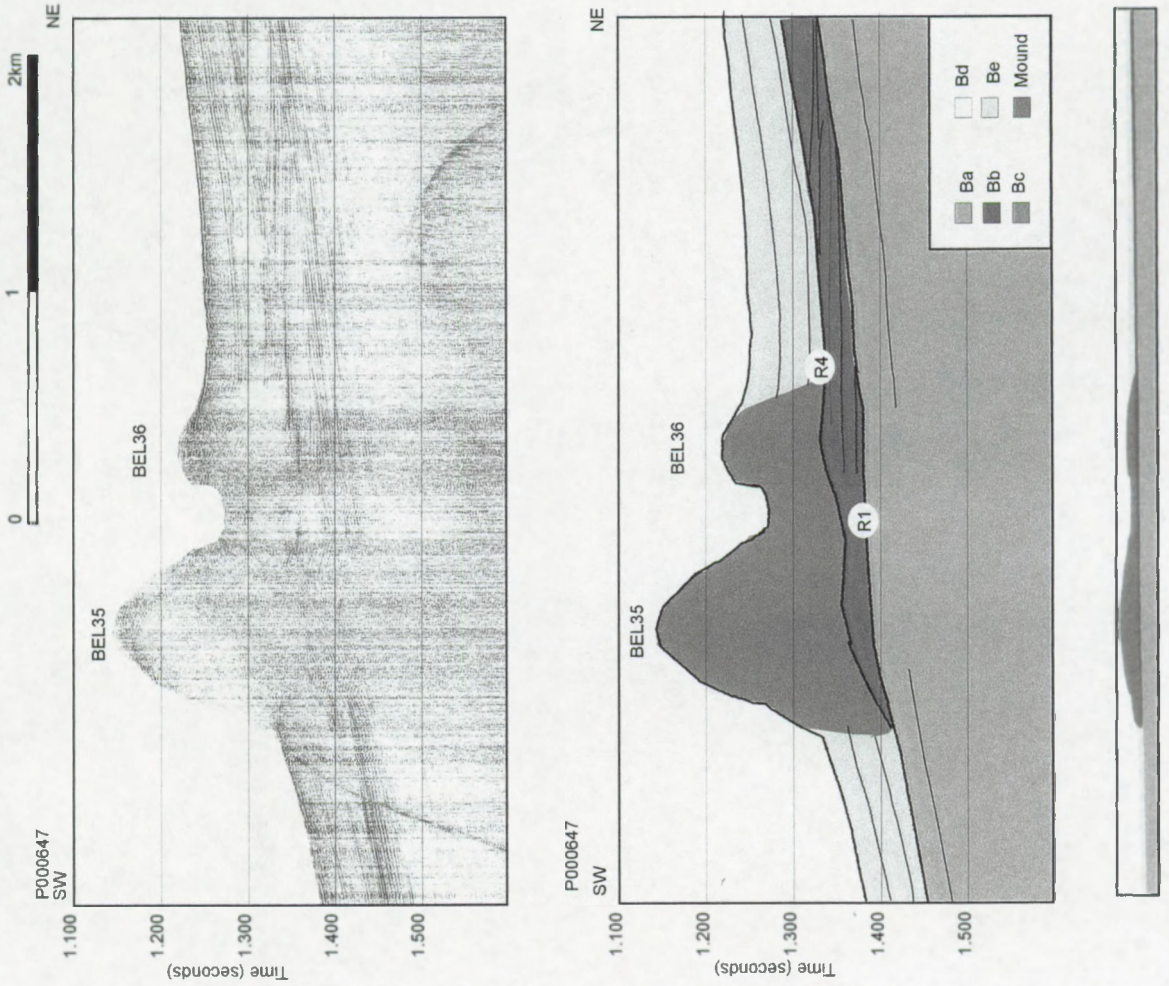
NE
2km
1
0
P000647
SW
BEL35
BEL36
1.100
1.200
1.300
1.400
1.500
Time (seconds)
NE
P000647
SW
BEL35
BEL36
R4
R1
Bd
Be
Mound
Ba
Bb
Bc
1.100
1.200
1.300
1.400
1.500
Time (seconds)

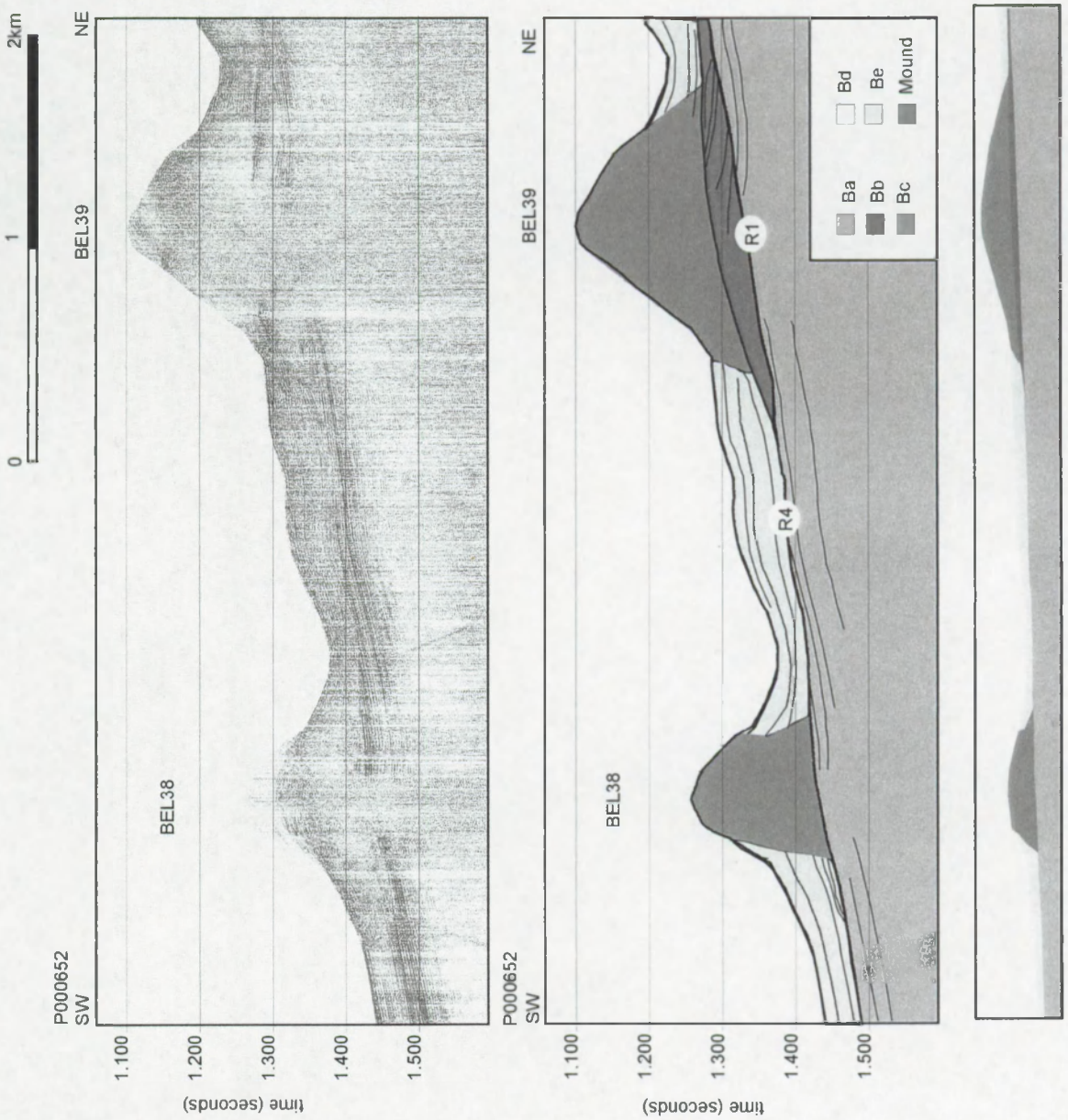
0
1
2km
P000652
SW
NE
BEL39
BEL38
1.100
1.200
1.300
1.400
1.500
time (seconds)
R1
R4
Ba
Bb
Bc
Bd
Be
Mound

Appendix C: Sedimentology Belgica mound province

1. Table of sample locations

2. Lithologs

3. Mineralogical and chemical data

1. Table of sample locations

GC: Gravity Core
PC: Piston Core
BC: Box Core
D: Dredge
GR: Grab

Data sort	Name	Latitude N	Longitude W	Depth m	Recovery cm	Target	Short description
GC	TTR7-AT-19G	51.2980	11.8098	1177	366	N-S channel	Pelagic core, foraminiferal sand, dark greyish clay
GC	TTR7-AT-20G	51.2970	11.6963	1008	275	foot of mound BEL10	Pelagic core, foraminiferal sand, dark greyish brown mud, silty clay
GC	TTR7-AT-21G	51.2980	11.6765	896	361	slope mound BEL10	Pelagic core, light olive brown foraminiferal sand, greyish brown silty clay
GC	TTR7-AT-22G	51.2983	11.6595	798	349.5	W slope mound BEL09	Pelagic core, olive brown foraminiferal sand, dark greyish silty clay, coral fargments
GC	TTR7-AT-23G	51.4547	11.7013	700	326	mound crest BEL42	foraminiferal sand, concentration of corals,greyish silty clay
GC	TTR7-AT-25G	51.2965	11.6192	686	281	mound flank BEL08	Pelagic core,sandy foraminiferal shells , lithic fragments, massive structureless clay
GC	TTR7-AT-26G	51.2943	11.6625	810	366	foot of BEL09	Pelagic core, foraminiferal sand, lithic fragments bioclasts, greyish brown clay
GC	TTR7-AT-33G	51.3000	11.6532	744	328	E flank BEL09	Pelagic core, foraminiferal sand, silty clay, dropstone and shells
GC	TTR7-AT-34G	51.3987	11.6997	785	0	W flank BEL28	No recovery, corals (Madrepora), coarse sand
GC	TTR7-AT-35G	51.3895	11.6982	774	328	mound crest BEL28	Coral core, greyish brown marl with corals, light grey marl with corals
GC	TTR7-AT-36G	51.3857	11.7028	830	339	Barchean shape bedforms on side scan sonar	Pelagic core, sand drape on top, dark grey, silty clay
GC	TTR8-AT-83G	51.4548	11.6988	715	322.5	mound flank BEL41	Sand, silty clay with pebbles, lag deposition
GC	TTR8-AT-84G	51.4549	11.7020	716	300	mound flank BEL41	Sand, silty clay with pebbles, lag deposition
BC	TTR8-AT-85B	51.4551	11.6987	712	26	mound flank BEL41	Sandy with Echinoderms, bryozoa, octocorals, brachipoda, bivalvia, gastropoda, hydrozoan, shell and coral fragments, dropstone, silty clay
BC	TTR8-AT-86B	51.4561	11.7608	930	22	W flank BEL42	Living corlas and associated fauna at surface, silty clay, coral debris in marly matrix

Data sort	Name	Latitude N	Longitude W	Depth m	Recovery cm	Target	Short description
PC	ENAM9901	51.4292	11.7662	948	635	E flank BEL35	Silty sand, shell fragments, silty with pebbles
PC	ENAM9902	51.4268	11.7713	961	675	S flank BEL35	Coral core, fine medium sand with coral debris
PC	ENAM9905	51.4397	11.7827	1025	633	NE of BEL38	Medium sand with coral debris, silty sand with pebble,
BC	Belgica2000 PB01	51.4255	11.7700	950	1	SE flank BEL35	Dead coral and associated epifauna 1cm sediment
BC	Belgica2000 PB2	51.4247	11.7733	940	2	SW flank BEL35	Dead coral and associated epifauna
BC	Belgica2000 PB04	51.4134	11.7654	1005	20	SW flank BEL32	25cm dead coral and associated epifauna, 20cm sediment
BC	Belgica2000 PB05	51.4137	11.7655	1000	20	SW flank BEL32	Partly covered with dead coral
BC	Pelagia 2000 BOX1 M2000-01	51.4080	11.7675	963		S of BEL32	80% of surface covered by coral, fine medium sand
BC	Pelagia 2000 BOX2 M2000-02	51.4292	11.7715	?		mound crest BEL35	80% of the surface is covered by coral debris, fine –medium sand
BC	Pelagia 2000 BOX3	51.4358	11.7768	1015		mound crest BEL35	Coral debris, fine-corarse sand
BC	Poseidon 2000 503-2	51.4523	11.7493	840		E upper slope BEL43	Living and dead coral, spongues 90% of surface, foramninifer sand
GR	TTR7-AT-24GR	51.4530	11.7010	736	1.5tonne	mound crest BEL42	Dead assemblage of Madrepora, echinoid, crinoids, alteraded Lophelia

2. Lithologs

Off-mound sediment samples

TTR7-AT-36G
TTR7-AT-19G

Near-mound sediment samples

TTR7-AT-20G
TTR7-AT-26G

On-mound sediment samples

TTR7-AT-22G
TTR7-AT-33G
TTR7-AT-25G
TTR7-AT-21G
ENAM99-01
ENAM99-02
ENAM99-05
TTR8-AT-84G

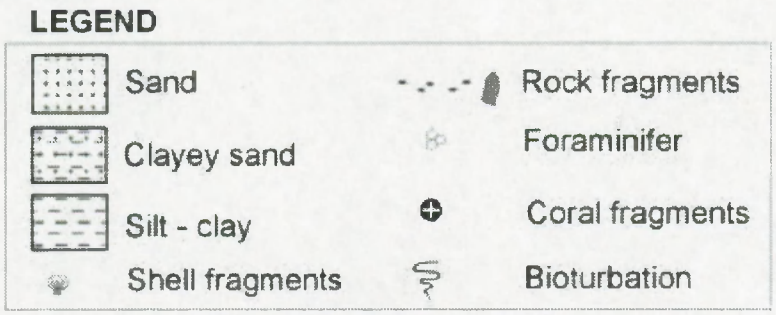

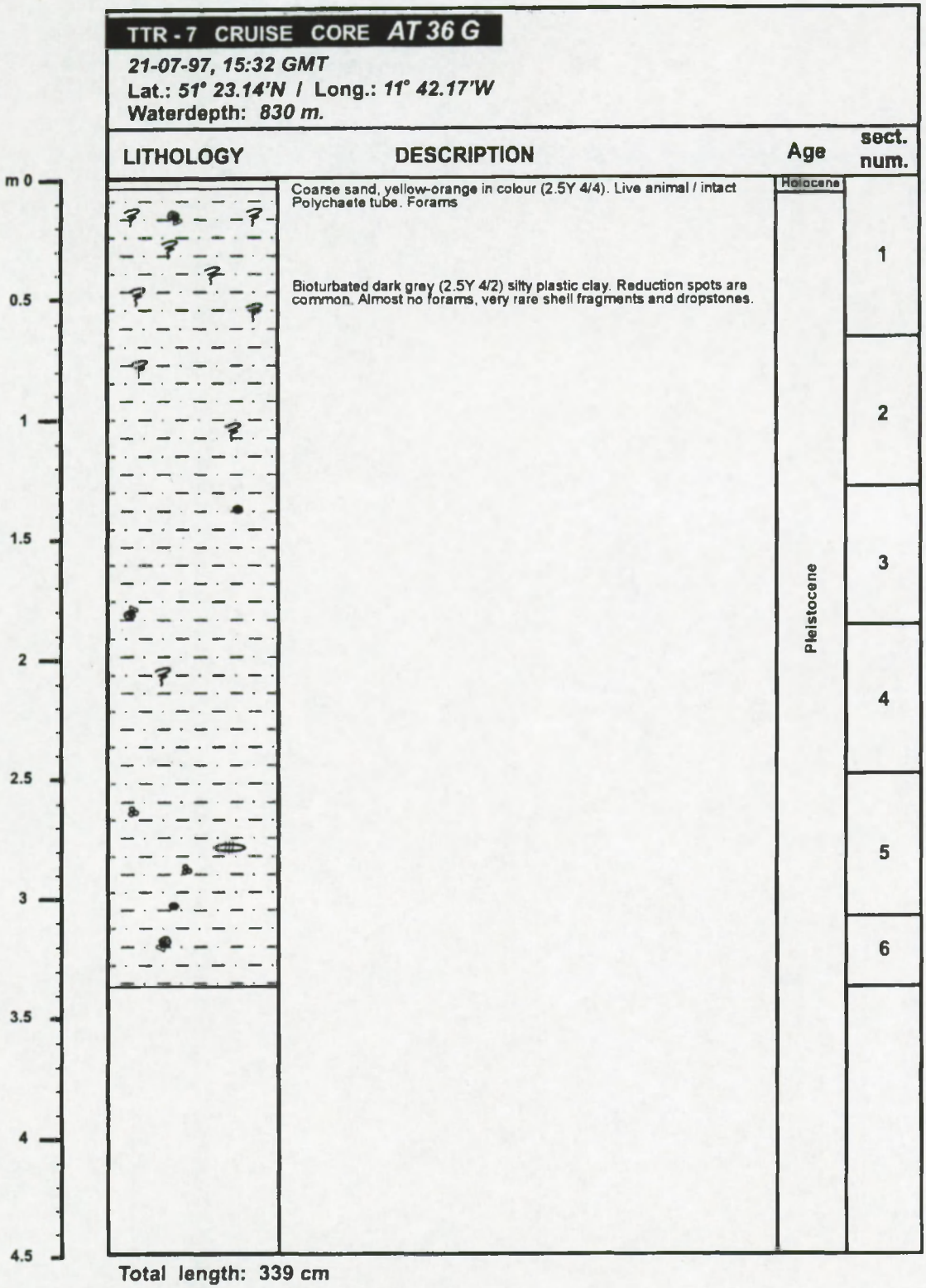
TTR - 7 CRUISE CORE AT 36 G
21-07-97, 15:32 GMT
Lat.: 51° 23.14'N / Long.: 11° 42.17'W
Waterdepth: 830 m.
LITHOLOGY
DESCRIPTION
Age
sect. num.
Coarse sand, yellow-orange in colour (2.5Y 4/4). Live animal / intact Polychaete tube. Forams
Bioturbated dark grey (2.5Y 4/2) silty plastic clay. Reduction spots are common. Almost no forams, very rare shell fragments and dropstones.
Holocene
Pleistocene
m 0
0.5
1
1.5
2
2.5
3
3.5
4
4.5
1
2
3
4
5
6
Total length: 339 cm

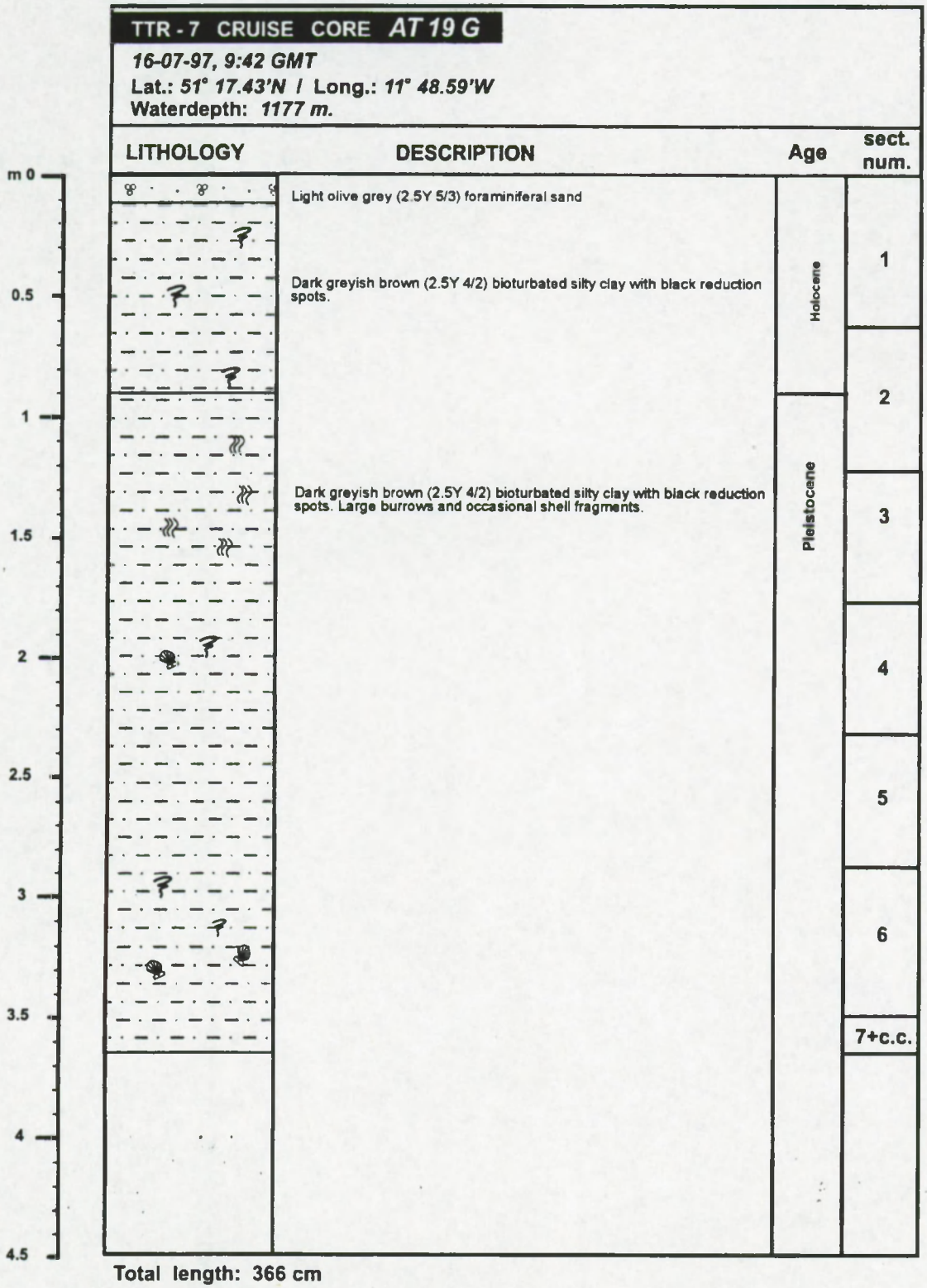
TTR - 7 CRUISE CORE AT 19 G
16-07-97, 9:42 GMT
Lat.: 51° 17.43'N / Long.: 11° 48.59'W
Waterdepth: 1177 m.
LITHOLOGY
DESCRIPTION
Age
sect. num.
m 0
0.5
1
1.5
2
2.5
3
3.5
4
4.5
Light olive grey (2.5Y 5/3) foraminiferal sand
Dark greyish brown (2.5Y 4/2) bioturbated silty clay with black reduction spots.
Dark greyish brown (2.5Y 4/2) bioturbated silty clay with black reduction spots. Large burrows and occasional shell fragments.
Holocene
Pleistocene
1
2
3
4
5
6
7+c.c.
Total length: 366 cm

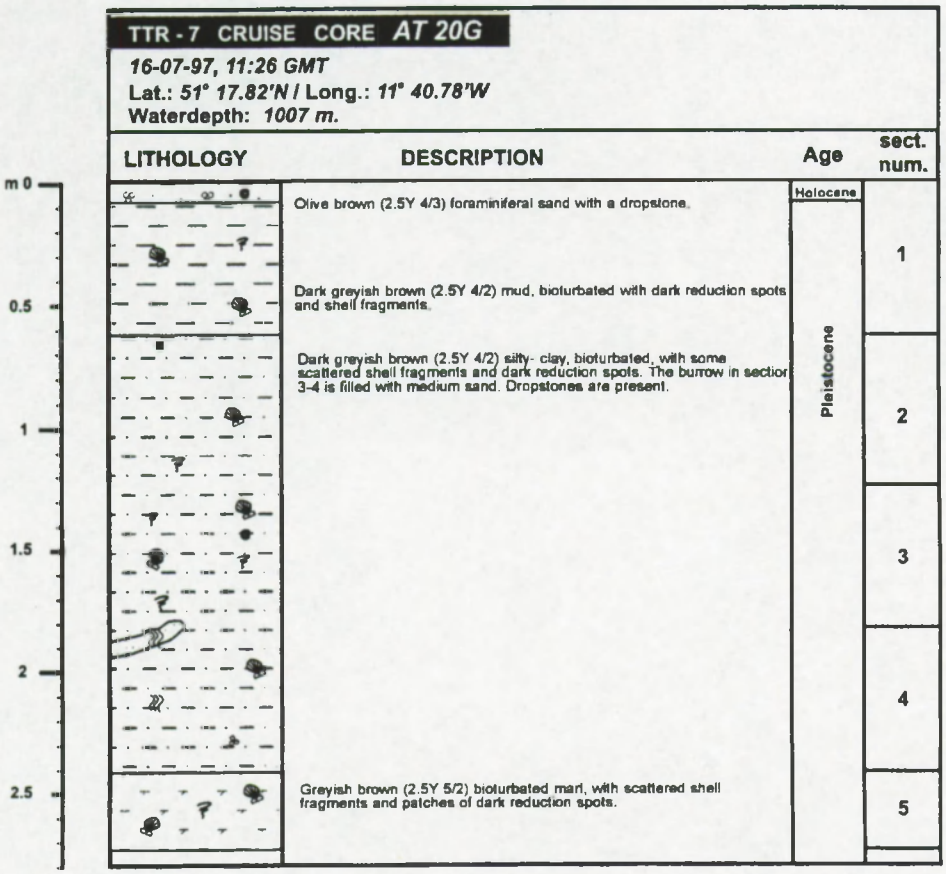

Total length: 275 cm

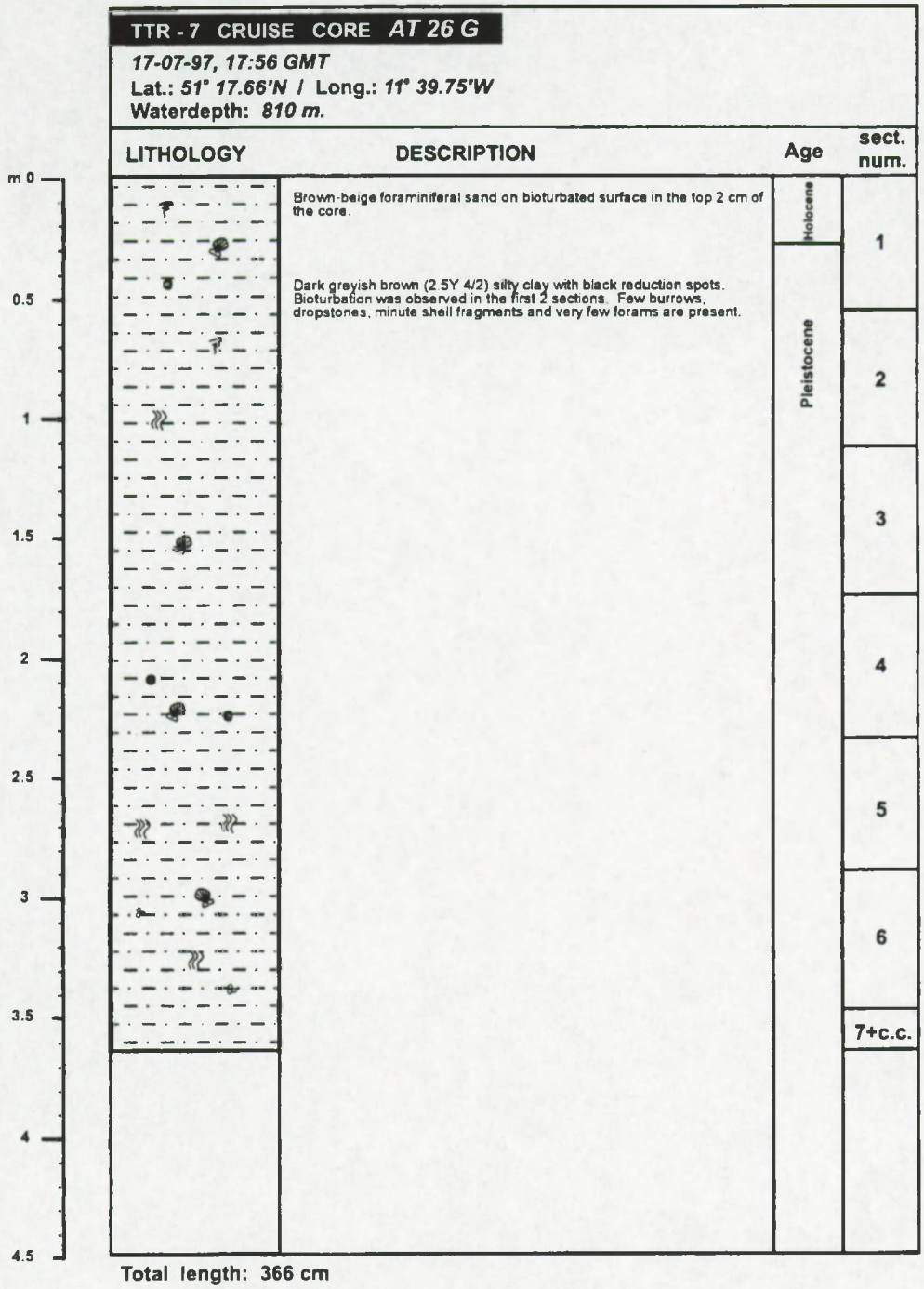
TTR - 7 CRUISE CORE AT 26 G
17-07-97, 17:56 GMT
Lat.: 51° 17.66'N / Long.: 11° 39.75'W
Waterdepth: 810 m.
LITHOLOGY
DESCRIPTION
Age
sect. num.
m 0
0.5
1
1.5
2
2.5
3
3.5
4
4.5
Brown-beige foraminiferal sand on bioturbated surface in the top 2 cm of the core.
Dark greyish brown (2.5Y 4/2) silty clay with black reduction spots. Bioturbation was observed in the first 2 sections. Few burrows, dropstones, minute shell fragments and very few forams are present.
Holocene
Pleistocene
1
2
3
4
5
6
7+c.c.
Total length: 366 cm

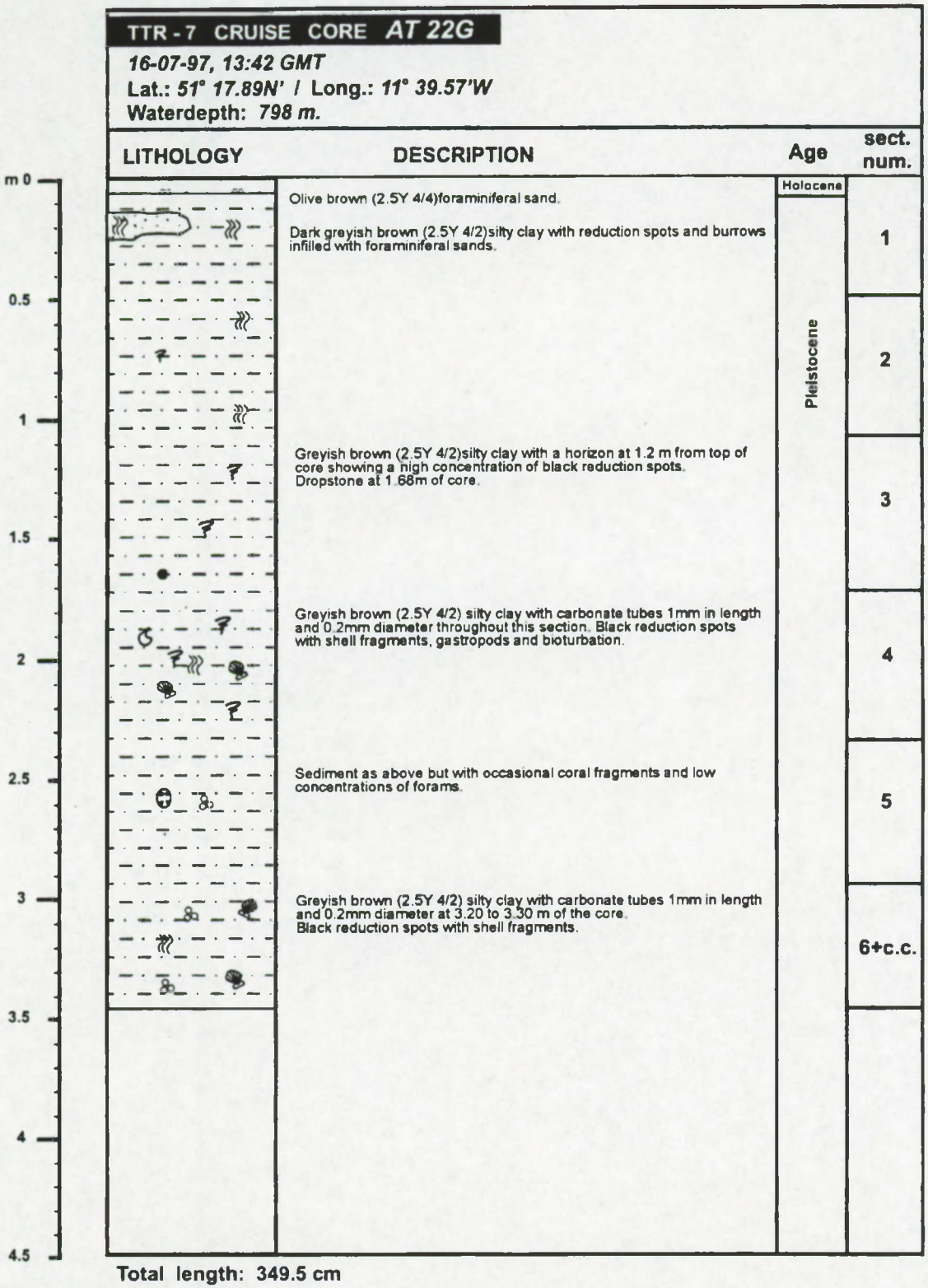
TTR - 7 CRUISE CORE AT 22G
16-07-97, 13:42 GMT
Lat.: 51° 17.89N' / Long.: 11° 39.57'W
Waterdepth: 798 m.
LITHOLOGY
DESCRIPTION
Age
sect. num.
m 0
0.5
1
1.5
2
2.5
3
3.5
4
4.5
Olive brown (2.5Y 4/4)foraminiferal sand.
Dark greyish brown (2.5Y 4/2)silty clay with reduction spots and burrows infilled with foraminiferal sands.
Greyish brown (2.5Y 4/2)silty clay with a horizon at 1.2 m from top of core showing a high concentration of black reduction spots. Dropstone at 1.68m of core.
Greyish brown (2.5Y 4/2) silty clay with carbonate tubes 1mm in length and 0.2mm diameter throughout this section. Black reduction spots with shell fragments, gastropods and bioturbation.
Sediment as above but with occasional coral fragments and low concentrations of forams.
Greyish brown (2.5Y 4/2) silty clay with carbonate tubes 1mm in length and 0.2mm diameter at 3.20 to 3.30 m of the core. Black reduction spots with shell fragments.
Holocene
Pleistocene
1
2
3
4
5
6+c.c.
Total length: 349.5 cm

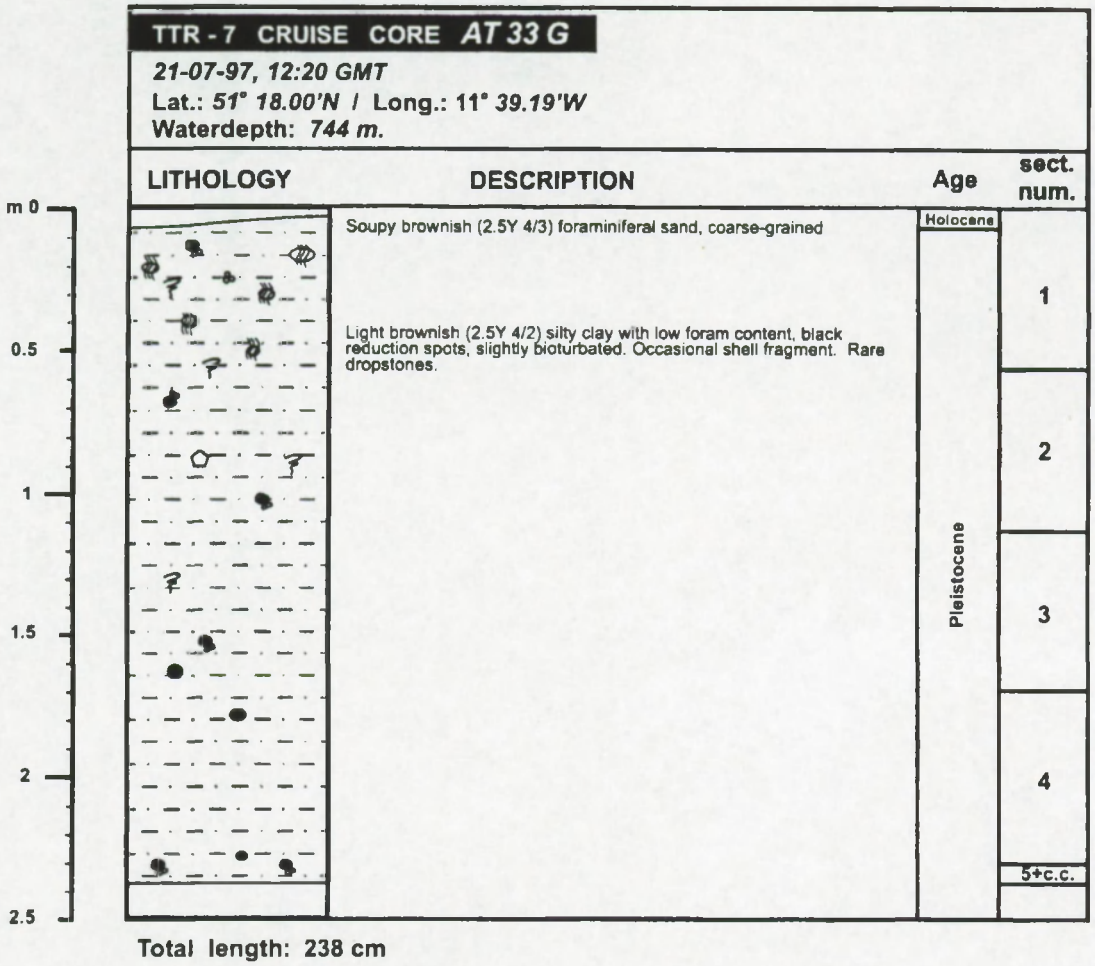
TTR - 7 CRUISE CORE AT 33 G
21-07-97, 12:20 GMT
Lat.: 51° 18.00'N / Long.: 11° 39.19'W
Waterdepth: 744 m.
LITHOLOGY
DESCRIPTION
Age
sect. num.
m 0
0.5
1
1.5
2
2.5
Soupy brownish (2.5Y 4/3) foraminiferal sand, coarse-grained
Light brownish (2.5Y 4/2) silty clay with low foram content, black reduction spots, slightly bioturbated. Occasional shell fragment. Rare dropstones.
Holocene
Pleistocene
1
2
3
4
5+c.c.
Total length: 238 cm

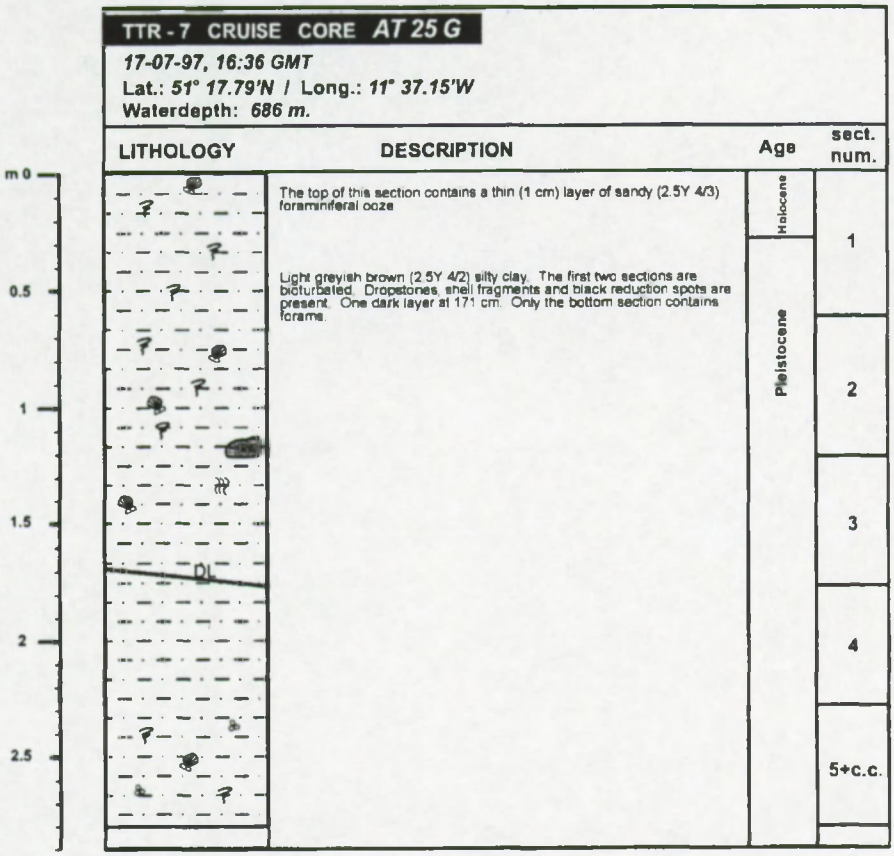

Total length: 281 cm

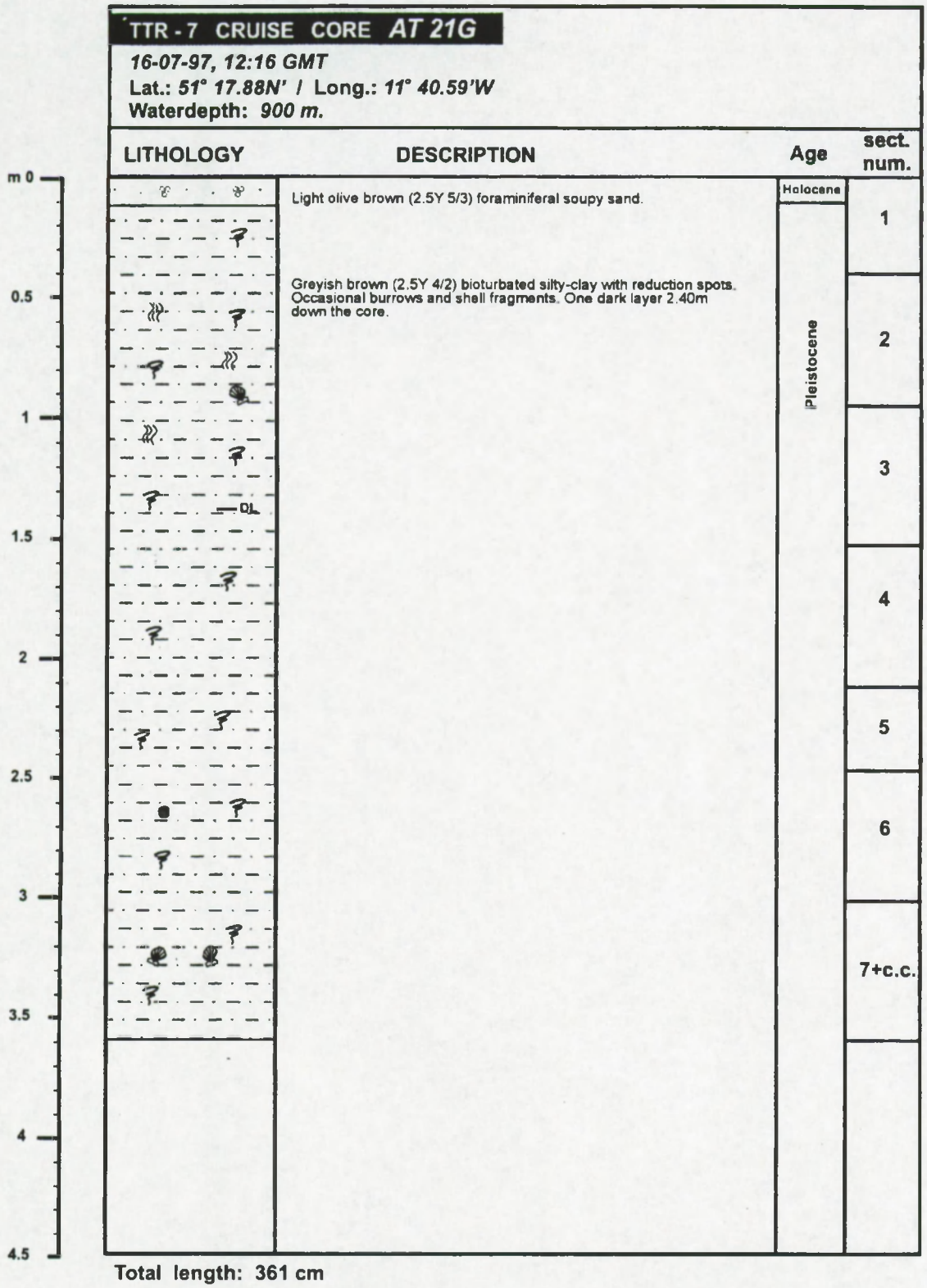
TTR - 7 CRUISE CORE AT 21G
16-07-97, 12:16 GMT
Lat.: 51° 17.88N' / Long.: 11° 40.59'W
Waterdepth: 900 m.
LITHOLOGY
DESCRIPTION
Age
sect. num.
m 0
0.5
1
1.5
2
2.5
3
3.5
4
4.5
Light olive brown (2.5Y 5/3) foraminiferal soupy sand.
Greyish brown (2.5Y 4/2) bioturbated silty-clay with reduction spots. Occasional burrows and shell fragments. One dark layer 2.40m down the core.
Holocene
Pleistocene
1
2
3
4
5
6
7+c.c.
Total length: 361 cm

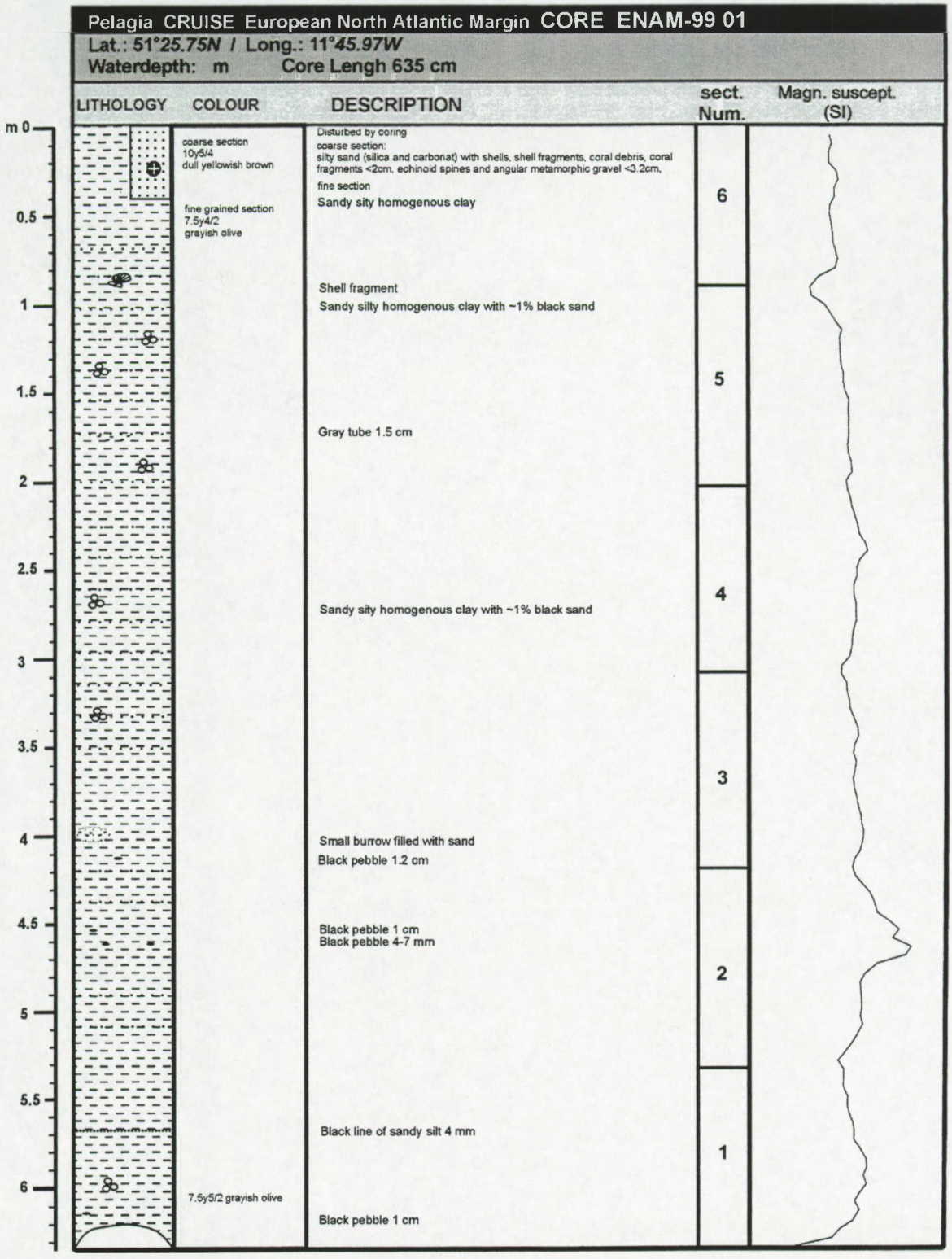
Pelagia CRUISE European North Atlantic Margin CORE ENAM-99 01
Lat.: 51°25.75N / Long.: 11°45.97W
Waterdepth: m Core Lengh 635 cm
LITHOLOGY
COLOUR
DESCRIPTION
sect. Num.
Magn. suscept. (SI)
m 0
0.5
1
1.5
2
2.5
3
3.5
4
4.5
5
5.5
6
coarse section
10y5/4
dull yellowish brown
fine grained section
7.5y4/2
grayish olive
7.5y5/2 grayish olive
Disturbed by coring
coarse section:
silty sand (silica and carbonat) with shells, shell fragments, coral debris, coral fragments <2cm, echinoid spines and angular metamorphic gravel <3.2cm,
fine section
Sandy sity homogenous clay
Shell fragment
Sandy silty homogenous clay with ~1% black sand
Gray tube 1.5 cm
Sandy sity homogenous clay with ~1% black sand
Small burrow filled with sand
Black pebble 1.2 cm
Black pebble 1 cm
Black pebble 4-7 mm
Black line of sandy silt 4 mm
Black pebble 1 cm
6
5
4
3
2
1

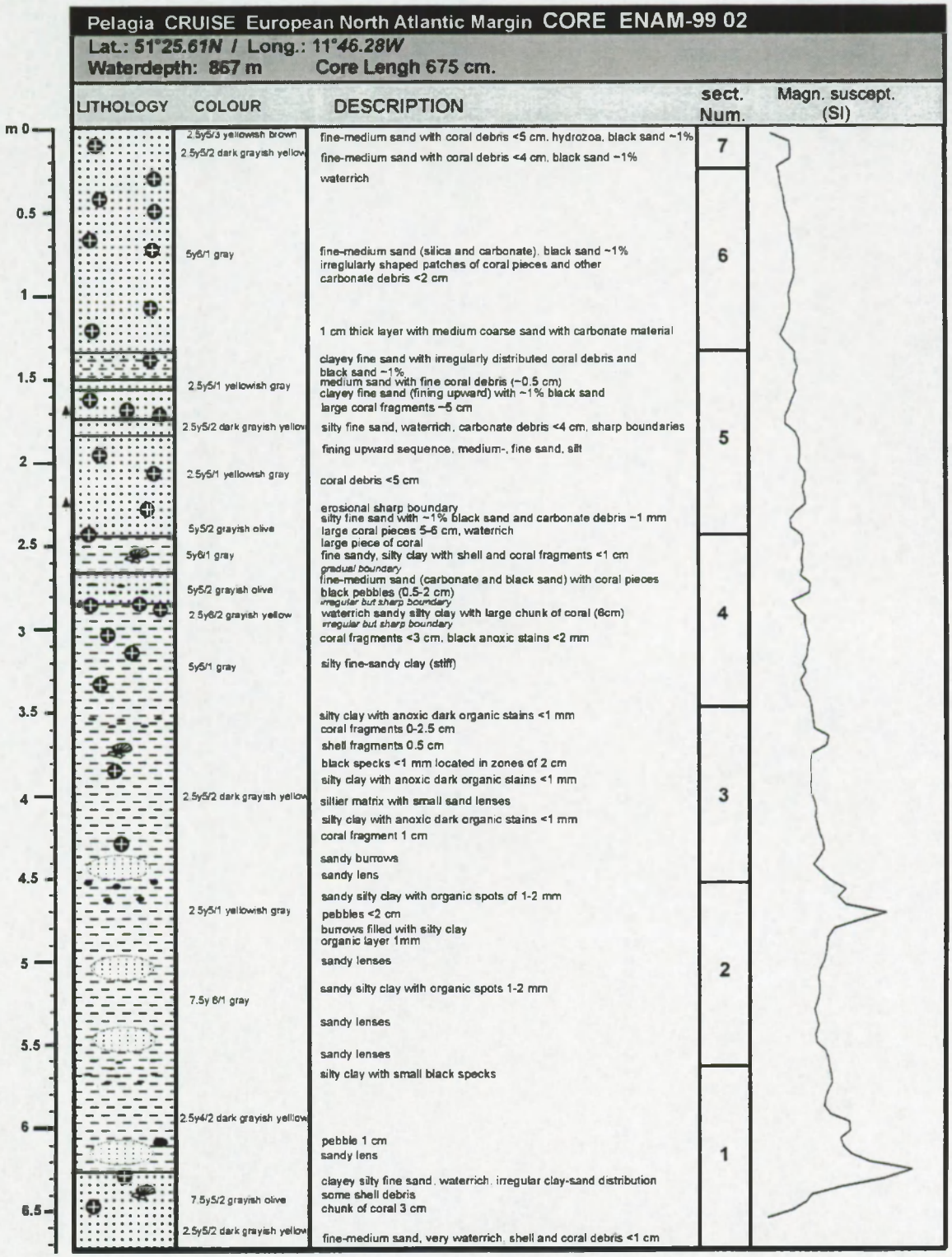
Pelagia CRUISE European North Atlantic Margin CORE ENAM-99 02
Lat.: 51°25.61N / Long.: 11°46.28W
Waterdepth: 867 m Core Lengh 675 cm.
LITHOLOGY
COLOUR
DESCRIPTION
sect. Num.
Magn. suscept. (SI)
m 0
0.5
1
1.5
2
2.5
3
3.5
4
4.5
5
5.5
6
6.5
2.5y5/3 yellowish brown
2.5y5/2 dark grayish yellow
5y6/1 gray
2.5y5/1 yellowish gray
2.5y5/2 dark grayish yellow
2.5y5/1 yellowish gray
5y5/2 grayish olive
5y6/1 gray
5y5/2 grayish olive
2.5y6/2 grayish yellow
5y5/1 gray
2.5y5/2 dark grayish yellow
2.5y5/1 yellowish gray
7.5y 6/1 gray
2.5y4/2 dark grayish yellow
7.5y5/2 grayish olive
2.5y5/2 dark grayish yellow
fine-medium sand with coral debris <5 cm, hydrozoa, black sand ~1%
fine-medium sand with coral debris <4 cm, black sand ~1%
waterrich
fine-medium sand (silica and carbonate), black sand ~1%
irregularly shaped patches of coral pieces and other carbonate debris <2 cm
1 cm thick layer with medium coarse sand with carbonate material
clayey fine sand with irregularly distributed coral debris and black sand ~1%
medium sand with fine coral debris (~0.5 cm)
clayey fine sand (fining upward) with ~1% black sand
large coral fragments ~5 cm
silty fine sand, waterrich, carbonate debris <4 cm, sharp boundaries
fining upward sequence, medium-, fine sand, silt
coral debris <5 cm
erosional sharp boundary
silty fine sand with ~1% black sand and carbonate debris ~1 mm
large coral pieces 5-6 cm, waterrich
large piece of coral
fine sandy, silty clay with shell and coral fragments <1 cm
gradual boundary
fine-medium sand (carbonate and black sand) with coral pieces
black pebbles (0.5-2 cm)
irregular but sharp boundary
waterrich sandy silty clay with large chunk of coral (6cm)
irregular but sharp boundary
coral fragments <3 cm, black anoxic stains <2 mm
silty fine-sandy clay (stiff)
silty clay with anoxic dark organic stains <1 mm
coral fragments 0-2.5 cm
shell fragments 0.5 cm
black specks <1 mm located in zones of 2 cm
silty clay with anoxic dark organic stains <1 mm
siltier matrix with small sand lenses
silty clay with anoxic dark organic stains <1 mm
coral fragment 1 cm
sandy burrows
sandy lens
sandy silty clay with organic spots of 1-2 mm
pebbles <2 cm
burrows filled with silty clay
organic layer 1mm
sandy lenses
sandy silty clay with organic spots 1-2 mm
sandy lenses
sandy lenses
silty clay with small black specks
pebble 1 cm
sandy lens
clayey silty fine sand, waterrich, irregular clay-sand distribution
some shell debris
chunk of coral 3 cm
fine-medium sand, very waterrich, shell and coral debris <1 cm
7
6
5
4
3
2
1

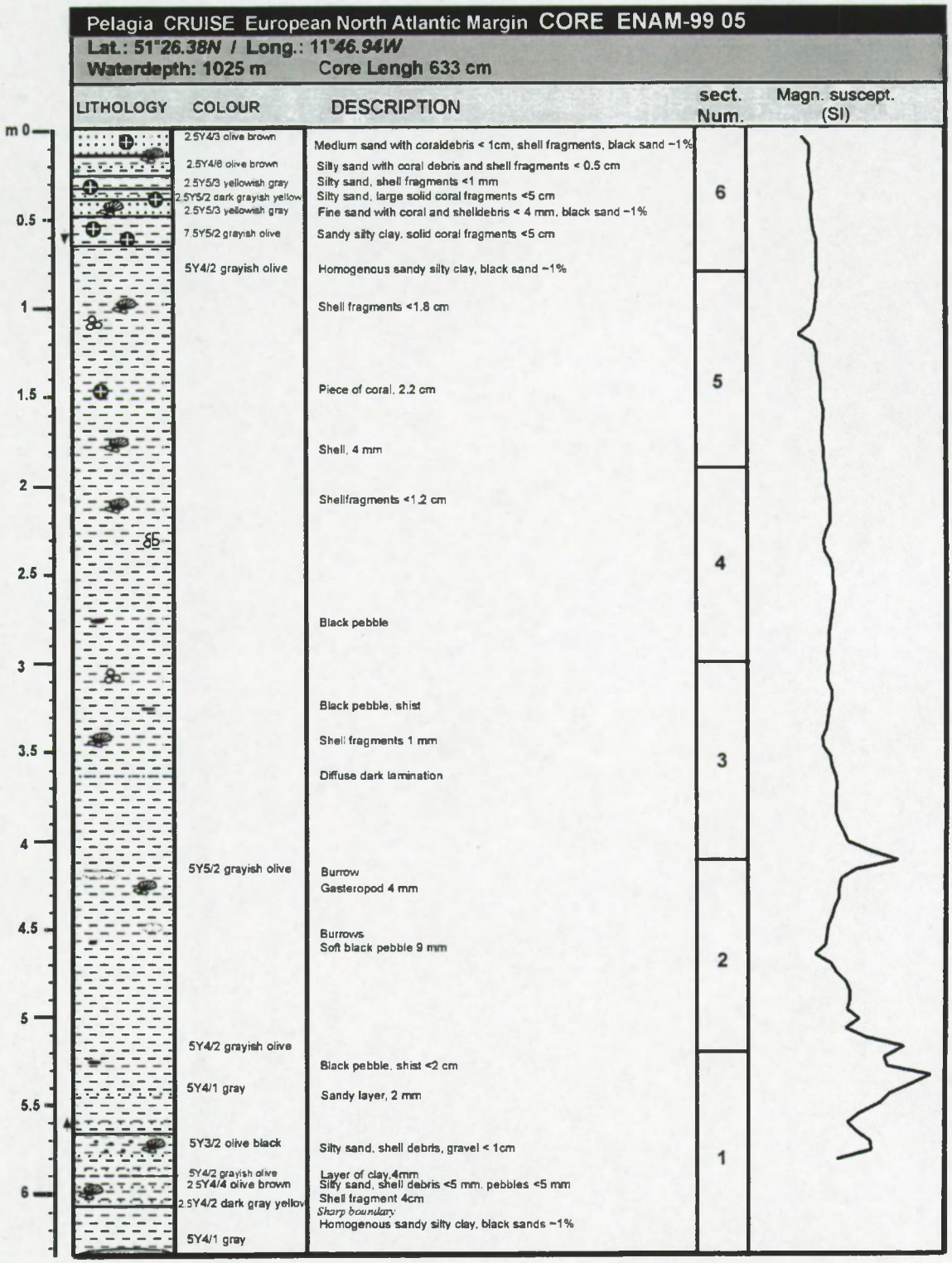
Pelagia CRUISE European North Atlantic Margin CORE ENAM-99 05
Lat.: 51°26.38N / Long.: 11°46.94W
Waterdepth: 1025 m
Core Lengh 633 cm
LITHOLOGY
COLOUR
DESCRIPTION
sect. Num.
Magn. suscept. (SI)
m 0
0.5
1
1.5
2
2.5
3
3.5
4
4.5
5
5.5
6
2.5Y4/3 olive brown
2.5Y4/6 olive brown
2.5Y5/3 yellowish gray
2.5Y5/2 dark grayish yellow
2.5Y5/3 yellowish gray
7.5Y5/2 grayish olive
5Y4/2 grayish olive
5Y5/2 grayish olive
5Y4/2 grayish olive
5Y4/1 gray
5Y3/2 olive black
5Y4/2 grayish olive
2.5Y4/4 olive brown
2.5Y4/2 dark gray yellow
5Y4/1 gray
Medium sand with coraldebris < 1cm, shell fragments, black sand ~1%
Silty sand with coral debris and shell fragments < 0.5 cm
Silty sand, shell fragments <1 mm
Silty sand, large solid coral fragments <5 cm
Fine sand with coral and shelldebris < 4 mm, black sand ~1%
Sandy silty clay, solid coral fragments <5 cm
Homogenous sandy silty clay, black sand ~1%
Shell fragments <1.8 cm
Piece of coral, 2.2 cm
Shell, 4 mm
Shellfragments <1.2 cm
Black pebble
Black pebble, shist
Shell fragments 1 mm
Diffuse dark lamination
Burrow
Gasteropod 4 mm
Burrows
Soft black pebble 9 mm
Black pebble, shist <2 cm
Sandy layer, 2 mm
Silty sand, shell debris, gravel < 1cm
Layer of clay,4mm
Silty sand, shell debris <5 mm, pebbles <5 mm
Shell fragment 4cm
Sharp boundary
Homogenous sandy silty clay, black sands ~1%
6
5
4
3
2
1

TTR8-AT-84G

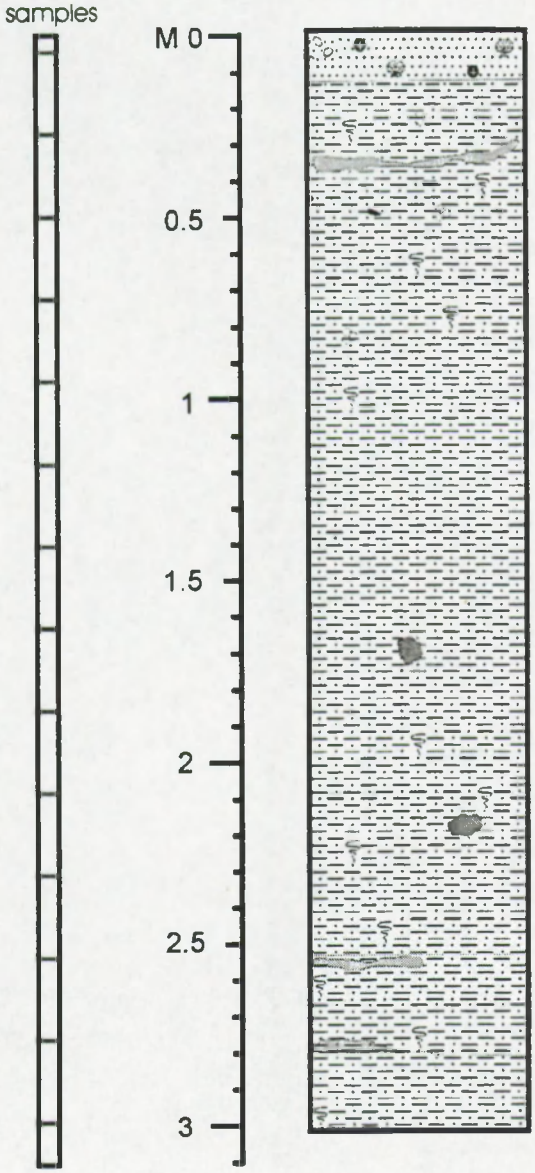

Upper centimeters contains shell and coral fragments in a brownish (2.5y7/6 bright yellow brown) sandy sediment. Several pebbels up to 2cm in diameter.

Homogeneous greyish (5Y5/3, greyish olive) bioturbated silty clay (no sedimentary structures), with some forams and black streams (organic matter)

Bioturbations are filled with bright yellow brown (2.5y6/6) silty sediment
Homogeneous silty clay with black spots and streams, less bioturbated (5y5/3)

Dark greyish yellow bioturbated silty clay
In general is this part less bioturbated and structureless

Slight increase of the bioturbation.

Spot with yellowish grey (2.5Y5/1),a little more sandy. Sandy fraction consists of darker terrigeneous grains and forams.

Bioturbations are filled with darker greyish yellow. (2.5Y6/6) In a silty greyish yellow clay (higher carbonate content)

Dark greyish yellow (2.5Y5/2) silty clay with traces of bioturbation

bioturbation
dropstone
foraminifera
coral fragments
shell fragments

	TTR84	TTR84	TTR84	TTR84	TTR84	TTR84	TTR84	TTR84	TTR84	TTR84
	S1top	S1	S1	S1	S1	S2	S2	S2	S2	S2
cm	3-5	23-25	43-45	63-65	83-85	10-12	30-32	50-52	70-72	90-92
depth	4	24	44	64	84	111	131	151	171	191
nummer	99/173	99/174	99/175	99/176	99/177	99/178	99/179	99/180	99/181	99/182
SiO_2	72.52	56.13	53.78	55.28	53.61	51.69	51.47	54.36	54.94	58.28
Al_2O_3	2.91	10.28	12.30	11.39	11.75	11.69	12.18	11.51	11.71	10.29
Fe_2O_3	1.10	3.81	4.63	5.02	5.38	5.39	5.21	4.79	4.65	4.08
TiO_2	0.29	0.92	0.78	0.97	1.19	1.17	1.08	1.01	0.76	0.67
MnO	0.02	0.04	0.04	0.05	0.05	0.05	0.05	0.05	0.05	0.05
CaO	11.20	7.57	6.99	7.20	7.71	8.27	8.58	8.22	8.29	8.31
MgO	0.53	2.10	2.38	2.32	2.40	2.69	2.57	2.40	2.54	2.19
Na_2O	0.83	2.06	2.12	1.71	1.82	1.66	1.63	1.53	1.62	1.51
K_2O	1.16	2.78	2.60	2.60	2.71	2.84	2.74	2.59	2.60	2.37
P_2O_5	0.07	0.12	0.12	0.13	0.13	0.15	0.13	0.13	0.13	0.13
H_2O^-	0.21	1.06	0.89	0.39	0.44	0.64	0.46	0.54	0.25	0.31
H_2O^+	8.59	12.45	13.03	12.93	13.10	13.30	13.70	12.61	12.54	11.58
Totaal	99.43	99.32	99.65	99.99	100.29	99.54	99.79	99.74	100.09	99.77
Carbonate content										
$CaCO_3$ calculated out of chemcial composition	19.99	13.51	12.48	12.85	13.76	14.76	15.31	14.67	14.80	14.83
CaO carbonate	11.20	7.57	6.99	7.20	7.71	8.27	8.58	8.22	8.29	8.31
Calculated Silicate fraction										
totale-H_2O-H_2O-P_2O_5-MnO-CaOcarbonate	79.34	78.08	78.59	79.29	78.86	77.13	76.88	78.19	78.82	79.39
factor	1.25	1.27	1.27	1.26	1.27	1.29	1.30	1.28	1.27	1.26
SiO_2	90.88	71.40	68.19	69.71	68.18	66.71	66.81	69.34	69.76	73.24
Al_2O_3	3.65	13.08	15.60	14.36	14.94	15.09	15.81	14.68	14.87	12.93
Fe_2O_3	1.38	4.85	5.87	6.33	6.84	6.96	6.76	6.11	5.90	5.13
TiO_2	0.36	1.17	0.99	1.22	1.51	1.51	1.40	1.29	0.97	0.84
MnO										
CaO	0.00	0.00	0.00	0.00	0.00	0.00	0.00	0.00	0.00	0.00
MgO	0.66	2.67	3.02	2.93	3.05	3.47	3.34	3.06	3.23	2.75
Na_2O	1.04	2.62	2.69	2.16	2.31	2.14	2.12	1.95	2.06	1.90
K_2O	1.45	3.54	3.30	3.28	3.45	3.67	3.56	3.30	3.30	2.98
P_2O_5										
Moleculaire ratio										
SiO2/Al2O3	42.29	9.27	7.42	8.24	7.74	7.50	7.17	8.01	7.96	9.61
SiO2/Fe2O3	175.22	39.16	30.87	29.27	26.48	25.49	26.26	30.16	31.40	37.96
SiO2/K2O	98.01	31.65	32.43	33.33	31.01	28.53	29.45	32.90	33.13	38.55
SiO2/MgO	91.77	17.93	15.16	15.98	14.98	12.89	13.43	15.19	14.51	17.85
SiO2/TiO2	332.45	81.11	91.66	75.76	59.89	58.73	63.36	71.55	96.10	115.64
Special ratio										
Fe/Ca	0.10	0.50	0.66	0.70	0.70	0.65	0.61	0.58	0.56	0.49
Ti/Ca	0.025892857	0.121532365	0.111587983	0.134722222	0.154345006	0.141475212	0.125874126	0.122871046	0.091676719	0.080625752
MgCa	0.047321429	0.277410832	0.340486409	0.322222222	0.311284047	0.325272068	0.2995338	0.291970803	0.306393245	0.263537906

Table C.3.1 Geochemical results of TTR8-AT-84G in oxide percentage. The silicate fraction is calculated from the total chemical results. Molecular ratios have been calculated to interpret the XRD diffractograms.

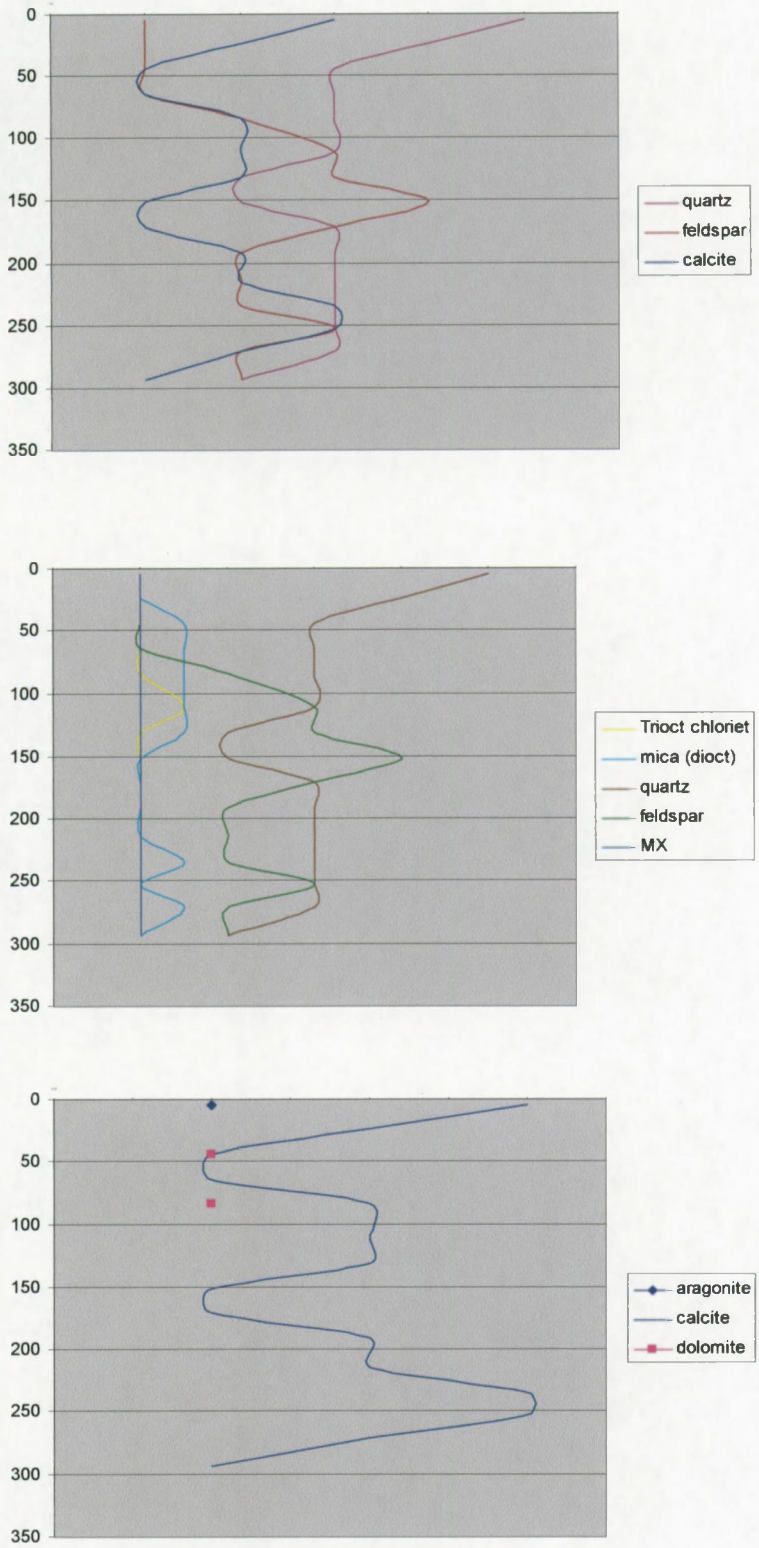

Fig. C.3.1: Mineralogical distribution in core TTR8-AT-84G.

Appendix D: Geometry Hovland mound province

1. Mound location and geometric database

2. Depth distribution: statistical parameters

3. Geometry: statistical parameters

Abbreviations:

SM: Surface mounds
BM: Buried mounds
HR: High-resolution seismic profiles
MP: Mid point
SP: Seismic profile

Database		HR	Orientation	Shot Points zone 28N WGS84					MP or highest Point			
number	Type	Profile		shot	Northing	Easting	Lat	Long	Northing	Easting	Lat	Long
HOV01	SM	P970512	NE-SW	3691	5778473	655115	52.135	-12.734				
				3812	5778929	655578	52.139	-12.727	5778929	655578	52.139	-12.73
				3936	5779395	656050	52.143	-12.719				
HOV02	SM	P970502c	NNW-SSE	4765	5778606	652775	52.137	-12.768				
				4883	5779147	652892	52.142	-12.766				
				5241	5780882	653308	52.157	-12.759				
		P970527	E-W	2845	5780088	652102	52.150	-12.777				
				2942	5780091	652546	52.150	-12.770				
				3165	5780097	653561	52.150	-12.755				
		P010535	N-S	1447	5778365	652608	52.135	-12.770				
		P1		1582	5779129	652581	52.142	-12.770				
				1667	5779619	652561	52.146	-12.770				
		P2		1782	5780286	652538	52.152	-12.770	5780286	652538	52.152	-12.77
		P3		1892	5780911	652517	52.158	-12.770				
				1987	5781439	652499	52.162	-12.770				
				2022	5781635	652493	52.164	-12.770				
HOV03	SM	P970527	E-W	1900	5779938	647826	52.150	-12.839				
				2006	5779955	648307	52.150	-12.832				
				2213	5780001	649242	52.150	-12.819				
		P970503b	N-S	4953	5778979	648556	52.141	-12.829				
		P1		4831	5779502	648557	52.146	-12.829				
		P2		4778	5779726	648557	52.148	-12.829	5779726	648557	52.148	-12.83
				4561	5780651	648568	52.156	-12.828				
		P970510a	NE-SW	7012	5778879	648701	52.140	-12.827				

Database number	Type	HR Profile	Orientation	Base (s)	Top (s)	SF TWT ms	Width m	Height (s)	Buried (s)	Waterdepth (m)	Slope deg	Orientation	Moat depth (ms)
HOV01	SM	P970512	NE-SW	1.174	1.150	1.150		0.024		863			
				1.207	0.936	0.936		0.271		702	18.88	SW	0.058
				1.265	1.212	1.212	1313	0.053		909	16.48	NE	0.004
HOV02	SM	P970502c	NNW-SSE	1.193	1.139	1.139		0.054		854			
				1.202	1.019			0.183		764	11.85	SSE	0.089
				1.236	1.186		2338	0.050		890	3.84	NNW	0.062
		P970527	E-W	1.116	1.072			0.044		804			
				1.140	0.900			0.240		675	21.67	W	0.09
				1.208	1.179		1459	0.029		884	10.60	E	depression
		P010535	N-S	1.177	1.15			0.027		1133			
		P1		1.184	1.052			0.132		789	11.84	N	0.057
				1.17	1.077			0.093		808	4.09		
		P2		1.154	0.885			0.269		664	13.35	S	0.093
		P3		1.157	1.072			0.085		804			
				1.159	1.034			0.125		776			
				1.166	1.093		3272	0.073		820	13.42	E	89
HOV03	SM	P970527	E-W	1.093	1.028			0.065		771			
				1.092	0.865			0.227		649	16.85	W	92
				1.097	1.097		1417	0.000		823	12.31	E	
		P970503b	N-S	1.084	1.084			0.000		813			
		P1		1.095	0.865			0.230		649	21.59	N	82
		P2		1.124	0.878			0.246		659			
				1.160	1.090		1672	0.070		818	9.72	S	100
		P970510a	NE-SW	1.088	1.088			0.000		816			

Database		HR	Orientation	Shot Points zone 28N WGS84					MP or highest Point			
number	Type	Profile		shot	Northing	Easting	Lat	Long	Northing	Easting	Lat	Long
HOV03		P1		6929	5779155	648976	52.143	-12.823				
				6828	5779495	649315	52.146	-12.818				
		P2		6884	5779308	649128	52.144	-12.821				
				6763	5779713	649532	52.148	-12.815				
HOV04	SM	P970527	E-W	3293	5780121	654136	52.150	-12.747				
				3356	5780124	654416	52.150	-12.743	5780124	654416	52.150	-12.74
				3528	5780191	655174	52.150	-12.732				
HOV05	SM	P970527	E-W	5795	5780577	665613	52.151	-12.579				
				5867	5780582	665955	52.151	-12.574	5780582	665955	52.151	-12.57
				5933	5780588	666328	52.151	-12.569				
HOV06	SM	P970510a	NE-SW	6021	5782156	652077	52.169	-12.776				
				5970	5782327	652252	52.170	-12.774	5782327	652252	52.170	-12.77
				5939	5782433	652360	52.171	-12.772				
		P010535	N-S	2225	5782752	652405	52.174	-12.771				
				2179	5782514	652438	52.172	-12.771				
				2150	5782356	652460	52.171	-12.771				
HOV07	SM	P970502c	NNW-SSE	5527	5782300	653618	52.170	-12.754				
				5642	5782867	653767	52.175	-12.751	5782867	653767	52.175	-12.75
				5697	5783138	653839	52.177	-12.750				
		P970524	NW-SE	3575	5783234	653626	52.178	-12.753				
				3490	5783048	653802	52.176	-12.751				
				3437	5782934	653922	52.175	-12.749				
HOV08	SM	P970528a	WNW-ESE	2329	5786949	681736	52.203	-12.340				
				2192	5786639	682070	52.200	-12.336	5786639	682070	52.200	-12.34
				2112	5786397	682330	52.198	-12.332				
HOV09	SM	P970510a	NE-SW	4876	5786005	656031	52.202	-12.717				
				4734	5786475	656542	52.206	-12.709	5786475	656542	52.206	-12.71
				4546	5787077	657187	52.212	-12.699				
HOV10	SM	P970512	NE-SW	6388	5788510	665158	52.222	-12.582				
				6508	5788934	665598	52.226	-12.575	5788934	665598	52.226	-12.58
				6718	5789745	666193	52.233	-12.566				
		P970522	NW-SE	7763	5789730	666435	52.233	-12.563				
				7841	5789442	666708	52.230	-12.559				
				7876	5789314	666836	52.229	-12.557				

Database number	Type	HR Profile	Orientation	Base (s)	Top (s)	SF TWT ms	Width m	Height (s)	Buried (s)	Waterdepth (m)	Slope deg	Orientation	Moat depth (ms)
HOV03		P1		1.094	0.981			0.113		736	14.63	SW	113
		P2		1.094	1.052			0.042		789			
				1.093	0.910			0.183		683	25.63		
				1.038	1.038		1177	0.000		779	16.06	NE	48
HOV04	SM	P970527	E-W	1.280	1.187			0.093		890			
				1.314	NA								depression
				1.334	1.235		1040	0.099		926			
HOV05	SM	P970527	E-W	1.380	1.346			0.034		1010			
				1.381	1.240			0.141		930	15.72	E	269
				1.298	1.298		715	0.000		974	18.79	W	200
HOV06	SM	P970510a	NE-SW	1.071	1.053			0.018		790			
				1.076	0.968			0.108		726	18.32	SW	75
				1.093	1.046		396	0.047		785	19.94	NE	depression
		P010535	N-S	1.168	1.152			0.016		864			
				1.171	1.089			0.082		817	13.89	N	NA
				1.176	1.164		400	0.012		873	21.55	S	NA
HOV07	SM	P970502c	NNW-SSE	1.199	1.141			0.058		856			
				1.176	0.984			0.192		738	11.62	SSE	13
				1.148	1.081		867	0.067		811	21.86	NNW	29
		P970524	NW-SE	1.136	1.094			0.042		821			
				1.156	1.078			0.078		809	7.21	NW	96
				1.142	1.089		421	0.053		817	7.74	SE	7
HOV08	SM	P970528a	WNW-ESE	1.226	1.193			0.033		895			
				1.192	0.977			0.215		733	19.77	ESE	103
				1.170	1.110		811	0.060		833	21.44	WNW	115
HOV09	SM	P970510a	NE-SW	1.111	1.111			0.000		833			
				1.127	0.874			0.253		656	18.16	SW	64
				1.090	1.053		1577	0.037		790	12.43	NE	111
HOV10	SM	P970512	NE-SW	1.139	0.997			0.142		748			
				1.141	0.866			0.275		650	11.08	SW	10
				1.149	1.105		1611	0.044		829	11.68	NE	144
		P970522	NW-SE	1.167	1.143			0.024		857			
				1.185	1.117			0.068		838	5.70	NW	128
				1.178	1.148		578	0.030		861	10.70	SE	147

Database		HR	Orientation	Shot Points zone 28N WGS84					MP or highest Point			
number	Type	Profile		shot	Northing	Easting	Lat	Long	Northing	Easting	Lat	Long
HOV11	SM	P970503b	N-S	2819	5787920	648720	52.222	-12.823				
				2691	5788469	648741	52.227	-12.822				
				2577	5788963	648773	52.231	-12.822				
		P970524b	NW-SE	1266	5789107	647484	52.233	-12.840				
		P1		1161	5788913	647662	52.231	-12.838				
				1070	5788742	647835	52.229	-12.835				
		P2		925	5788526	648091	52.227	-12.832				
				658	5788627	648607	52.228	-12.824				
		P970505	NE-SW	2645	5787999	647821	52.223	-12.836				
				2818	5788631	648478	52.228	-12.826				
				2926	5789031	648880	52.232	-12.820				
		P010536	E-W	489	5788506	649268	52.227	-12.814				
				620	5788497	648523	52.227	-12.825	5788497	648523	52.227	-12.83
				758	5788472	647736	52.227	-12.837				
HOV12	SM	P970502c	NNW-SSE	6832	5788940	655050	52.229	-12.730				
				6927	5789426	655142	52.233	-12.728				
				7008	5789840	655221	52.237	-12.727				
		P99024	NW-SE	3406	5789595	654735	52.235	-12.734				
				3496	5789293	655374	52.232	-12.725	5789293	655374	52.232	-12.72
				3576	5789024	655941	52.230	-12.717				
HOV13	SM	P980533	NE-SW	5602	5796393	690944	52.285	-12.201				
				5746	5796991	691496	52.290	-12.192	5796991	691496	52.290	-12.19
				5847	5797440	691858	52.294	-12.187				
HOV14	SM	P980535	NE-SW	493	5801736	689854	52.333	-12.213				
				407	5802058	690131	52.336	-12.209	5802058	690131	52.336	-12.21
				375	5802393	690438	52.339	-12.205				
HOV15	BM	P980533	NE-SW	5030	5794013	688406	52.264	-12.239				
				5281	5795072	689528	52.273	-12.222	5795072	689528	52.273	-12.22
				5370	5795429	688872	52.277	-12.231				
HOV16	BM	P980531	NE-SW	285	5796738	696700	52.286	-12.116				
				249	5796936	696867	52.287	-12.114	5796936	696867	52.287	-12.11
				224	5797073	696983	52.289	-12.112				

Database number	Type	HR Profile	Orientation	Base (s)	Top (s)	SF TWT ms	Width m	Height (s)	Buried (s)	Waterdepth (m)	Slope deg	Orientation	Moat depth (ms)
HOV11	SM	P970503b	N-S	1.072	1.040			0.032		780			
				1.037	0.805			0.232		604	18.14	S	79
				1.015	0.974		1044	0.041		731	19.15	N	90
		P970524b	NW-SE	0.999	0.967			0.032		725			
		P1		1.007	0.945			0.062		709	5.86	NW	92
				1.009	0.973			0.036		730	5.49		
		P2		1.020	0.828			0.192		621	22.74		
				1.081	1.040		1221	0.041		780	14.49	SE	111
		P970505	NE-SW	1.038	1.009			0.029		757			
				1.037	0.811			0.226		608	11.01	SW	110
				1.010	0.964		1479	0.046		723	15.94	NE	85
		P010536	E-W	1.009	0.972			0.037		729			
				1.023	0.79			0.233		593	13.32	E	71
				1.018	0.95		1532	0.068		713	10.68	W	84
HOV12	SM	P970502c	NNW-SSE	1.062	1.034			0.028		776			
				1.051	0.860			0.191		645	16.52	SSE	16
				1.043	1.015		916	0.028		761	19.19	NNW	22
		P99024	NW-SE	1.046	0.999			0.047		749			
				1.060	0.833			0.227		625	12.91	NW	108
				1.073	1.036		1334	0.037		777	15.24	SE	37
HOV13	SM	P980533	NE-SW	1.017	0.972	0.914		0.045		729			
				1.006	0.838	0.838		0.168		629	7.75	SW	NA
				1.009	0.937	0.937	1390	0.072		703	8.52	NE	115
HOV14	SM	P980535	NE-SW	0.938	0.909	0.836		0.029		682			
				0.929	0.784	0.784		0.145		588	13.81	SW	46
				0.923	0.820	0.820	879	0.103		615	4.76	NE	85
HOV15	BM	P980533	NE-SW	1.089	1.019	0.954		0.070	0.065	715		SW	41
				1.049	0.938	0.915		0.111	0.023	686			
				1.049	1.016	0.944	1491	0.033	0.072	708	5.37	NE	25
HOV16	BM	P980531	NE-SW	0.917	0.910	0.778		0.007	0.132	584			
				0.915	0.877	0.769		0.038	0.108	577	6.15	SW	16
				0.916	0.904	0.766	439	0.012	0.138	575	7.43	NE	NA

Database		HR	Orientation	Shot Points zone 28N WGS84					MP or highest Point			
number	Type	Profile		shot	Northing	Easting	Lat	Long	Northing	Easting	Lat	Long
HOV17	BM	P980539	NE-SW	237	5796798	702470	52.284	-12.032				
				273	5796975	702608	52.286	-12.029	5796975	702608	52.286	-12.03
				310	5797155	702748	52.287	-12.027				
HOV18	BM	P980539	NE-SW	510	5798211	703630	52.296	-12.014				
				817	5799677	705064	52.309	-11.992				
				902	5798362	703790	52.298	-12.011	5798362	703790	52.298	-12.01
HOV19	BM	P980541	NE-SW	1535	5801239	701341	52.324	-12.045				
				1368	5801953	702105	52.331	-12.034	5801953	702105	52.331	-12.03
				1292	5802363	702461	52.334	-12.028				
				1222	5802725	702806	52.337	-12.023				
				1210	5802780	702871	52.338	-12.022				
HVO20	BM	P980543	NE-SW	807	5805008	699129	52.359	-12.076				
				786	5804903	699030	52.358	-12.077	5804903	699030	52.358	-12.08
				739	5804690	698797	52.356	-12.081				
HOV21	BM	P980543	NE-SW	715	5804583	698681	52.355	-12.082				
				685	5804447	698532	52.354	-12.085	5804447	698532	52.354	-12.08
				672	5804385	698465	52.354	-12.086				
HOV22	BM	P980542	NW-SE	369	5799658	697150	52.312	-12.108	5799658	697150	52.312	-12.11
				221	5798828	697790	52.304	-12.099				
HOV23	BM	P980541	NE-SW	1908	5799574	699662	52.310	-12.071				
				1796	5800070	700110	52.314	-12.064				
				1733	5800352	700406	52.317	-12.060	5800352	700406	52.317	-12.06
HOV24	BM	P980543	NE-SW	185	5802247	696284	52.335	-12.119				
				245	5802485	696575	52.337	-12.115	5802485	696575	52.337	-12.11
				275	5802607	696725	52.338	-12.112				
				316	5802797	696897	52.340	-12.110				
				346	5802946	697017	52.341	-12.108				
HOV25	BM	P980545	NE-SW	2285	5805171	693270	52.363	-12.161				
				2204	5805510	693551	52.366	-12.157	5805510	693551	52.366	-12.16
				2151	5805705	693765	52.367	-12.154				
HOV26	BM	P980539	NE-SW	369	5797445	703035	52.290	-12.023				
				399	5797588	703179	52.291	-12.021	5797588	703179	52.291	-12.02
				426	5797730	703305	52.292	-12.019				

Database number	Type	HR Profile	Orientation	Base (s)	Top (s)	SF TWT ms	Width m	Height (s)	Buried (s)	Waterdepth (m)	Slope deg	Orientation	Moat depth (ms)
HOV17	BM	P980539	NE-SW	0.870	0.870	0.654		0.000	0.216	491			
				0.866	0.798	0.651		0.068	0.147	488	15.25	SW	20
				0.863	0.863	0.652	452	0.000	0.211	489	15.02	NE	25
HOV18	BM	P980539	NE-SW	0.859	0.791	0.637		0.068	0.154	478		SW	NA
				0.888	0.856	0.640		0.032	0.216	480			
				0.902	0.794	0.627	220	0.108	0.167	470	2.14	NE	NA
HOV19	BM	P980541	NE-SW	0.882	0.816	0.661		0.066	0.155	496			
				0.849	0.703	0.622		0.146	0.081	467	3.94	SW	39
				0.832	0.798	0.612		0.034	0.186	459	10.52		
				0.838	0.790	0.596		0.048	0.194	447	1.44		
				0.833	0.833	0.594	2172	0.000	0.239	446	26.90	NE	NA
HOV20		P980543	NE-SW	0.788	0.788	0.608		0.000	0.180	456			
				0.791	0.747	0.613		0.044	0.134	460	15.34	NE	NA
				0.794	0.794	0.622	460	0.000	0.172	467	7.15	SW	NA
HOV21		P980543	NE-SW	0.792	0.792	0.627		0.000	0.165	470			
				0.796	0.759	0.635		0.037	0.124	476	9.37	NE	NA
				0.797	0.797	0.637	293	0.000	0.160	478	20.04	SW	NA
HOV22	BM	P980542	NW-SE	0.897	0.818	0.782		0.079	0.036	587			
				0.904	0.846	0.749	1048	0.058	0.097	562	1.03		
HOV23	BM	P980541	NE-SW	0.887	0.854	0.689		0.033	0.165	517			
				0.895	0.84	0.684		0.055	0.156	513	1.70	SW	7
				0.9	0.84	0.674	1076	0.060	0.166	506	0.63	NE	NA
HOV24		P980543	NE-SW	0.866	0.843	0.693		0.023	0.150	520			
				0.863	0.759	0.699		0.104	0.060	524	10.97	SW	40
				0.861	0.808	0.696		0.053	0.112	522	13.35		
				0.846	0.792	0.691		0.054	0.101	518			
				0.843	0.843	0.689	1013	0.000	0.154	517	14.25	NE	NA
HOV25		P980545	NE-SW	0.815	0.815	0.67		0.000	0.145	503			
				0.809	0.727	0.661		0.082	0.066	496	9.51	SW	NA
				0.803	0.803	0.652	728	0.000	0.151	489	14.30	NE	NA
HOV26		P980539	NE-SW	0.862	0.862	0.647		0.000	0.215	485			
				0.867	0.8032	0.644		0.064	0.159	483	15.81	SW	NA
				0.861	0.861	0.645	392	0.000	0.216	484	16.84	NE	NA

Database		HR	Orientation	Shot Points zone 28N WGS84					MP or highest Point			
number	Type	Profile		shot	Northing	Easting	Lat	Long	Northing	Easting	Lat	Long
HOV27	BM	P980541	NE-SW	2161	5798442	698480	52.300	-12.089				
				2201	5798301	698281	52.299	-12.092				
		P980531	NE-SW	33	5798117	698028	52.298	-12.096				
				SOL	5798254	698188	52.299	-12.093				
		P950542	NW-SE	66	5797933	698332	52.296	-12.091				
				131	5798341	698224	52.300	-12.093	5798341	698224	52.300	-12.09
				161	5798498	698093	52.301	-12.095				
HOV28	BM	P980543	NE-SW	56	5801713	695681	52.331	-12.128				
		P980533	NE-SW	6641	5800896	694990	52.324	-12.139				
				6746	5801318	695395	52.327	-12.133	5801318	695395	52.327	-12.13
HOV29	BM	P980530	NW-SE	520	5797839	698937	52.295	-12.083				
				580	5798065	698668	52.297	-12.086				
				618	5798211	698500	52.298	-12.089	5798211	698500	52.298	-12.09
HOV30	BM	P980534	NW-SE	433	5803372	693321	52.347	-12.162				
				343	5802986	693821	52.343	-12.155	5802986	693821	52.343	-12.15
				377	5803145	693622	52.344	-12.157				
HOV31	BM	P980535	NE-SW	210	5803161	691359	52.345	-12.191				
				175	5803360	691551	52.347	-12.188	5803360	691551	52.347	-12.19
				160	5803445	691633	52.348	-12.186				
HOV32	BM	P980535	NE-SW	87	5803826	691962	52.351	-12.181				
				40	5804065	692164	52.353	-12.178				
				3	5804241	692312	52.355	-12.176				
		P980534	NW-SE	618	5804235	692511	52.355	-12.173	5804235	692511	52.355	-12.17
				562	5803968	692734	52.352	-12.170				
HOV33	BM	P980541	NE-SW	1128	5803162	703286	52.341	-12.016				
				1067	5803516	703585	52.344	-12.011	5803516	703585	52.344	-12.01
HOV34		P980539	NE-SW	1007	5800570	705938	52.317	-11.978				
				972	5800424	705772	52.316	-11.981	5800424	705772	52.316	-11.98
				945	5800309	705647	52.315	-11.983				
HOV35	BM	P980541	NE-SW	991	5803894	703952	52.347	-12.006				
				960	5804042	704100	52.349	-12.003	5804042	704100	52.349	-12.00
				927	5804219	704247	52.350	-12.001				

Database number	Type	HR Profile	Orientation	Base (s)	Top (s)	SF TWT ms	Width m	Height (s)	Buried (s)	Waterdepth (m)	Slope deg	Orientation	Moat depth (ms)
HOV27	BM	P980541	NE-SW	0.883	0.883	0.722		0.000	0.161	542		NE	
				0.883	0.814	0.726		0.069	0.088	545	14.29	SW	
		P980531	NE-SW	0.926	0.926	0.736		0.000	0.190	552	22.49	SW	16
				0.924	0.827	0.731	347	0.097	0.096	548		NE	
		P980542	NW-SE	0.927	0.866	0.719		0.061	0.147	539			
				0.926	0.827	0.727		0.099	0.100	545	4.63	SE	23
				0.868	0.868	0.736	614	0.000	0.132	552	23.51	NW	5
HOV28		P980543	NE-SW	0.888	0.774	0.743		0.114	0.031	557			
		P980533	NE-SW	0.904	0.886	0.745		0.018	0.141	559	4.62	SW	37
				0.896	0.768	0.752	487	0.128	0.016	564	9.61	NE	NA
HOV29		P980530	NW-SE	0.911	0.832	0.711		0.079	0.121	533		SE	NA
				0.914	0.838	0.720		0.076	0.118	540			
				0.911	0.823	0.714	574	0.088	0.109	536	2.78	NW	NA
HOV30	BM	P980534	NW-SE	0.872	0.859	0.731		0.013	0.128	548			
				0.868	0.801	0.728		0.067	0.073	546	4.40	SE	NA
				0.862	0.862	0.726	377	0.000	0.136	545	13.30	NW	
HOV31	BM	P980535	NE-SW	0.897	0.867	0.760		0.030	0.107	570			
				0.897	0.824	0.750		0.073	0.074	563	7.97	SW	7
				0.891	0.863	0.746	395	0.028	0.117	560	18.93	NE	NA
HOV32	BM	P980535	NE-SW	0.885	0.850	0.726		0.035	0.124	545			
				0.893	0.810	0.714		0.083	0.096	536	7.86	SW	NA
				0.883	0.836	0.708	543	0.047	0.128	531	8.02	NE	NA
		P980534	NW-SE	0.888	0.793	0.706		0.095	0.087	530		NW	NA
				0.886	0.818	0.710	348	0.068	0.108	533	4.00	SW	15
HOV33	BM	P980541	NE-SW	0.813	0.793	0.578		0.020	0.215	434		SW	NA
				0.813	0.777	0.564	463	0.036	0.213	423	1.78	NE	NA
HOV34		P980539	NE-SW	0.831	0.807	0.604		0.024	0.203	453		NE	NA
				0.834	0.783	0.608		0.051	0.175	456	6.27		NA
				0.835	0.835	0.611	391	0.000	0.224	458	15.12	SW	NA
HOV35	BM	P980541	NE-SW	0.787	0.750	0.542		0.037	0.208	407		NE	NA
				0.772	0.734	0.542		0.038	0.192	407			NA
				0.778	0.763	0.532	439	0.015	0.231	399	5.14	SW	NA

Database		HR	Orientation	Shot Points zone 28N WGS84					MP or highest Point			
number	Type	Profile		shot	Northing	Easting	Lat	Long	Northing	Easting	Lat	Long
HOV36	BM	P980539	NE-SW	1359	5802345	707681	52.33205	-11.95184				
				1314	5802105	707467	52.32997	-11.95513	5802105	707467	52.32997	-11.96
				1235	5801748	707062	52.32692	-11.96128				
HOV37	BM	P980539	NE-SW	1086	5801050	706280	52.32095	-11.97317				
				1127	5801217	706505	52.32236	-11.96977	5801217	706505	52.32236	-11.97
				1218	5801656	706973	52.32613	-11.96264				
HOV38	BM	P980530	NW-SE	294	5796897	699880	52.28603	-12.06941				
				271	5796819	699988	52.28529	-12.06788	5796819	699988	52.28529	-12.07
				243	5796706	700126	52.28422	-12.06592				
HOV39	BM	P980530	NW-SE	60	5795916	700993	52.27681	-12.0537				
				31	5795796	701126	52.27569	-12.05182	5795796	701126	52.27569	-12.05
				0	5795680	701261	52.2746	-12.04992				

Database number	Type	HR Profile	Orientation	Base (s)	Top (s)	SF TWT ms	Width m	Height (s)	Buried (s)	Waterdepth (m)	Slope deg	Orientation	Moat depth (ms)
HOV36		P980539	NE-SW	0.788	0.788	0.625		0.000	0.163	469			NA
				0.790	0.737	0.630		0.053	0.107	473	8.44	NE	NA
				0.800	0.800	0.620	860	0.000	0.180	465	5.05	SW	NA
HOV37		P980539	NE-SW	0.811	0.789	0.601		0.022	0.188	451			NA
				0.810	0.764	0.600		0.046	0.164	450	4.41	NE	NA
				0.805	0.805	0.618	921	0.000	0.187	464	3.69	SW	NA
HOV38		P980530	NW-SE	0.929	0.929	0.696		0.000	0.233	522			NA
				0.929	0.877	0.692		0.052	0.185	519	19.36	NE	NA
				0.929	0.929	0.688	311	0.000	0.241	516	14.70	SW	NA
HOV39		P980530	NW-SE	0.923	0.923	0.673		0.000	0.25	505			NA
				0.916	0.860	0.672		0.056	0.188	504	15.71	NE	NA
				0.919	0.886	0.673	357	0.033	0.213	505	6.63	SW	NA
										average	**11.74**		

2. Depth distribution: statistical parameters

Case Processing Summary

	Cases					
	Valid		Missing		Total	
	N	Percent	N	Percent	N	Percent
depth	27	100.0%	0	.0%	27	100.0%

Descriptives

			Statistic	Std. Error
depth	Mean		516.7778	12.2082
	95% Confidence Interval for Mean	Lower Bound	491.6834	
		Upper Bound	541.8722	
	5% Trimmed Mean		514.0658	
	Median		506.0000	
	Variance		4024.103	
	Std. Deviation		63.4358	
	Minimum		407.00	
	Maximum		686.00	
	Range		279.00	
	Interquartile Range		93.0000	
	Skewness		.674	.448
	Kurtosis		.627	.872

Table D.2.1: Statistical parameters of the depth distribution in the eastern part of the Hovland mound province.

Case Processing Summary

	Cases					
	Valid		Missing		Total	
	N	Percent	N	Percent	N	Percent
depth	12	100.0%	0	.0%	12	100.0%

Descriptives

			Statistic	Std. Error
depth	Mean		750.2500	32.4378
	95% Confidence Interval for Mean	Lower Bound	678.8548	
		Upper Bound	821.6452	
	5% Trimmed Mean		749.0000	
	Median		732.0000	
	Variance		12626.568	
	Std. Deviation		112.3680	
	Minimum		593.00	
	Maximum		930.00	
	Range		337.00	
	Interquartile Range		215.5000	
	Skewness		.365	.637
	Kurtosis		-1.168	1.232

Table D.2.2: Statistical parameters of the depth distribution in the central part of the Hovland mound province.

3. Geometry: statistical parameters

Case Processing Summary

		Cases					
		Valid		Missing		Total	
	Type	N	Percent	N	Percent	N	Percent
widthmax	BM	25	100.0%	0	.0%	25	100.0%
	SM	14	100.0%	0	.0%	14	100.0%

Descriptives

	Type			Statistic	Std. Error
widthmax	BM	Mean		660.6400	88.0050
		95% Confidence Interval for Mean	Lower Bound	479.0065	
			Upper Bound	842.2735	
		5% Trimmed Mean		607.9111	
		Median		463.0000	
		Variance		193622.2	
		Std. Deviation		440.0252	
		Minimum		220.00	
		Maximum		2172.00	
		Range		1952.00	
		Interquartile Range		499.0000	
		Skewness		2.064	.464
		Kurtosis		4.979	.902
	SM	Mean		1315.2143	182.8394
		95% Confidence Interval for Mean	Lower Bound	920.2139	
			Upper Bound	1710.2147	
		5% Trimmed Mean		1257.3492	
		Median		1323.5000	
		Variance		468023.3	
		Std. Deviation		684.1223	
		Minimum		400.00	
		Maximum		3272.00	
		Range		2872.00	
		Interquartile Range		732.5000	
		Skewness		1.762	.597
		Kurtosis		4.914	1.154

Table D.3.1: Statistic parameters of the maximum width distribution in the buried and surface Hovland mounds.

Case Processing Summary

		Cases					
		Valid		Missing		Total	
	Type	N	Percent	N	Percent	N	Percent
Heightmax	BM	25	100.0%	0	.0%	25	100.0%
	SM	13	92.9%	1	7.1%	14	100.0%

Descriptives

	Type			Statistic	Std. Error
Heightmax	BM	Mean		72.9200	6.0685
		95% Confidence Interval for Mean	Lower Bound	60.3953	
			Upper Bound	85.4447	
		5% Trimmed Mean		71.1000	
		Median		67.0000	
		Variance		920.660	
		Std. Deviation		30.3424	
		Minimum		36.00	
		Maximum		146.00	
		Range		110.00	
		Interquartile Range		48.5000	
		Skewness		.742	.464
		Kurtosis		-.166	.902
	SM	Mean		214.0769	16.6316
		95% Confidence Interval for Mean	Lower Bound	177.8399	
			Upper Bound	250.3140	
		5% Trimmed Mean		214.6410	
		Median		227.0000	
		Variance		3595.910	
		Std. Deviation		59.9659	
		Minimum		108.00	
		Maximum		310.00	
		Range		202.00	
		Interquartile Range		105.5000	
		Skewness		-.287	.616
		Kurtosis		-.781	1.191

Table D.3.2: Statistical parameters of the maximum height measured along the seismic profile for the surface and buried Hovland mounds.

Height - width correlation per profile orientation

Surface mounds

E-W profiles

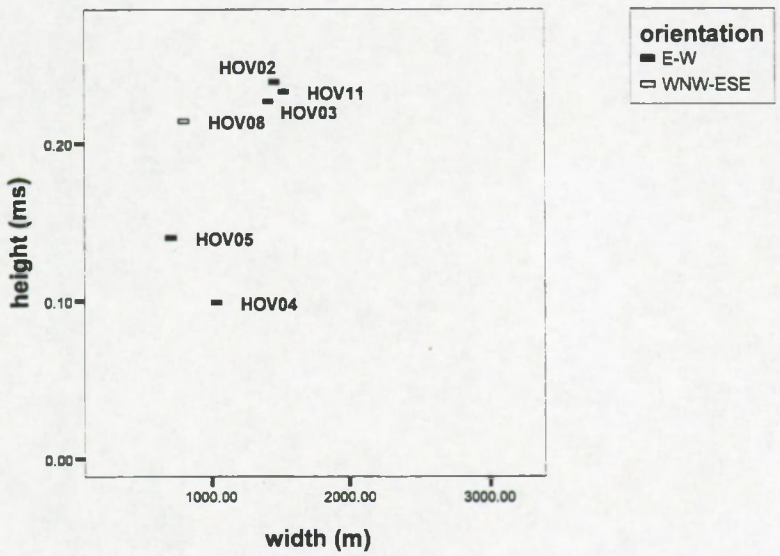

Fig. D.3.1: Scatter plot of the height and width of E-W orientated profiles.

N-S profiles

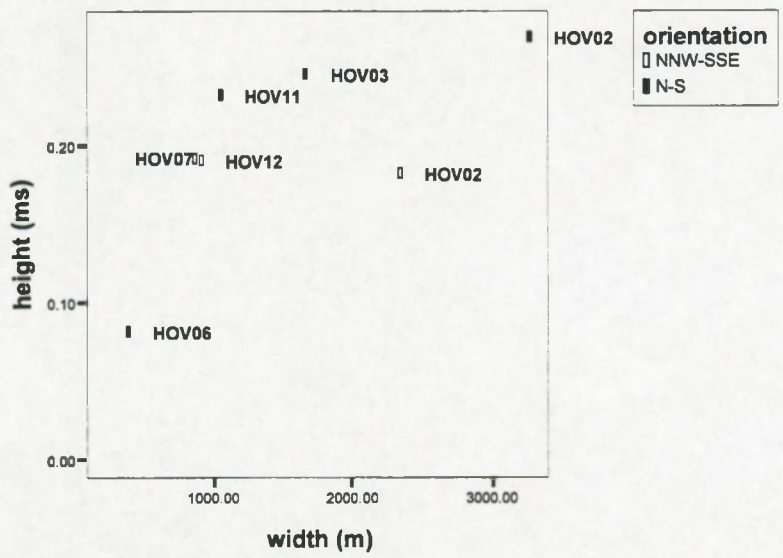

Fig. D.3.2: Scatter plot of the height and width of N-S orientated profiles.

NE-SW profiles

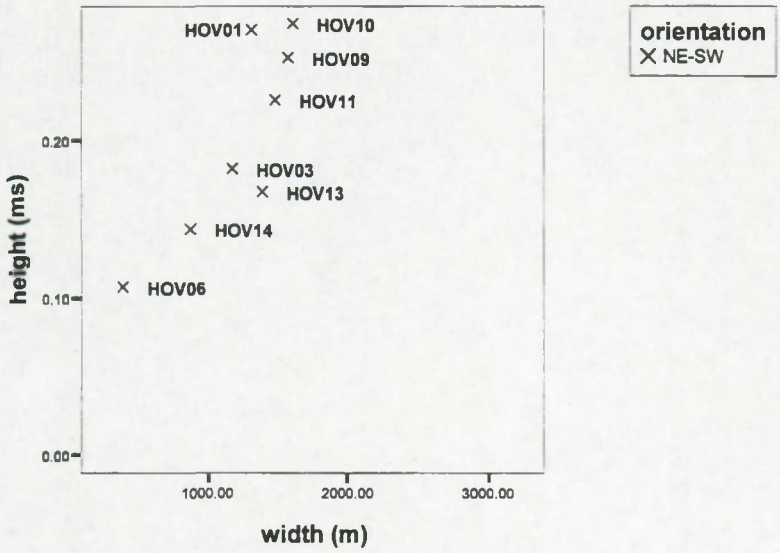

Fig. D.3.3: Scatter plot of the height and width of NE-SW profiles.

NW-SE profiles

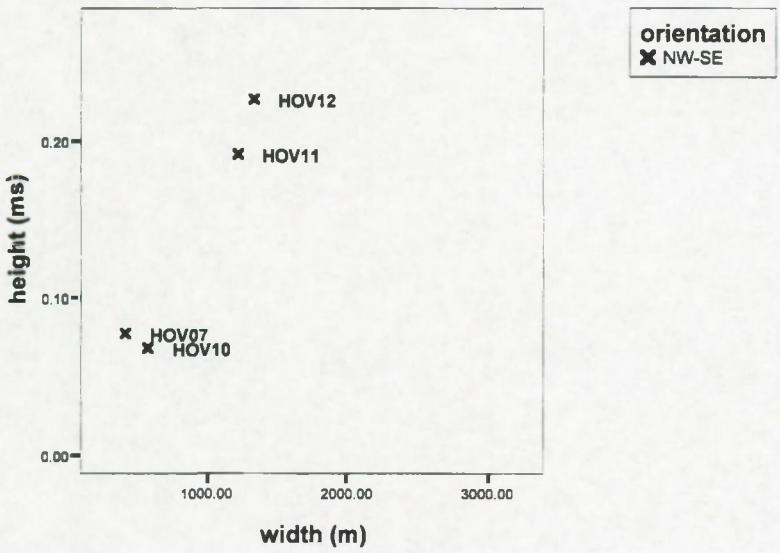

Fig. D.3.4: Scatter plot of the height and width of NW-SE profiles.

Buried mounds

NW-SE

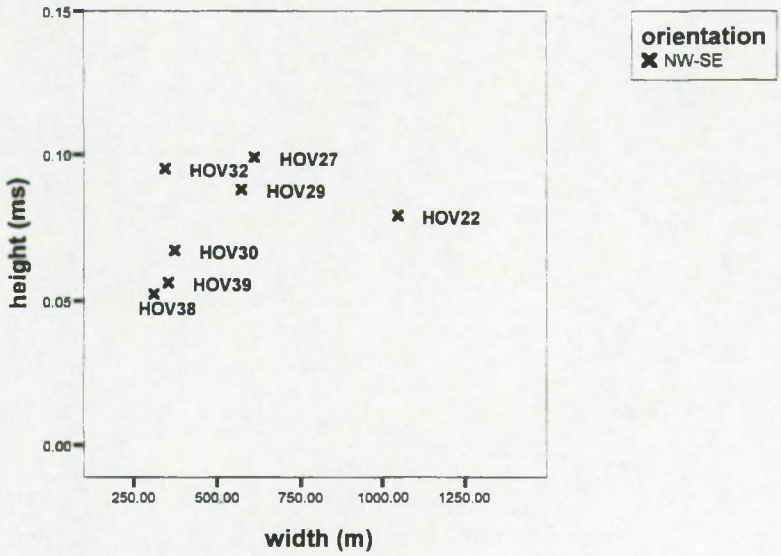

Fig. D.3.5: Scatter plot of the height and width of NW-SE profiles.

NE-SW

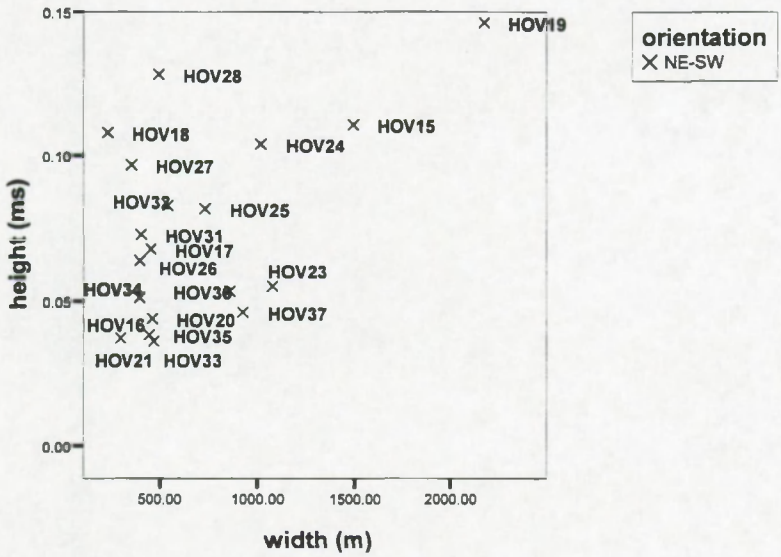

Fig. D.3.6: Scatter plot of the height and width of NE-SW profiles.

Height-width correlation for mounds crossed by more than one profile

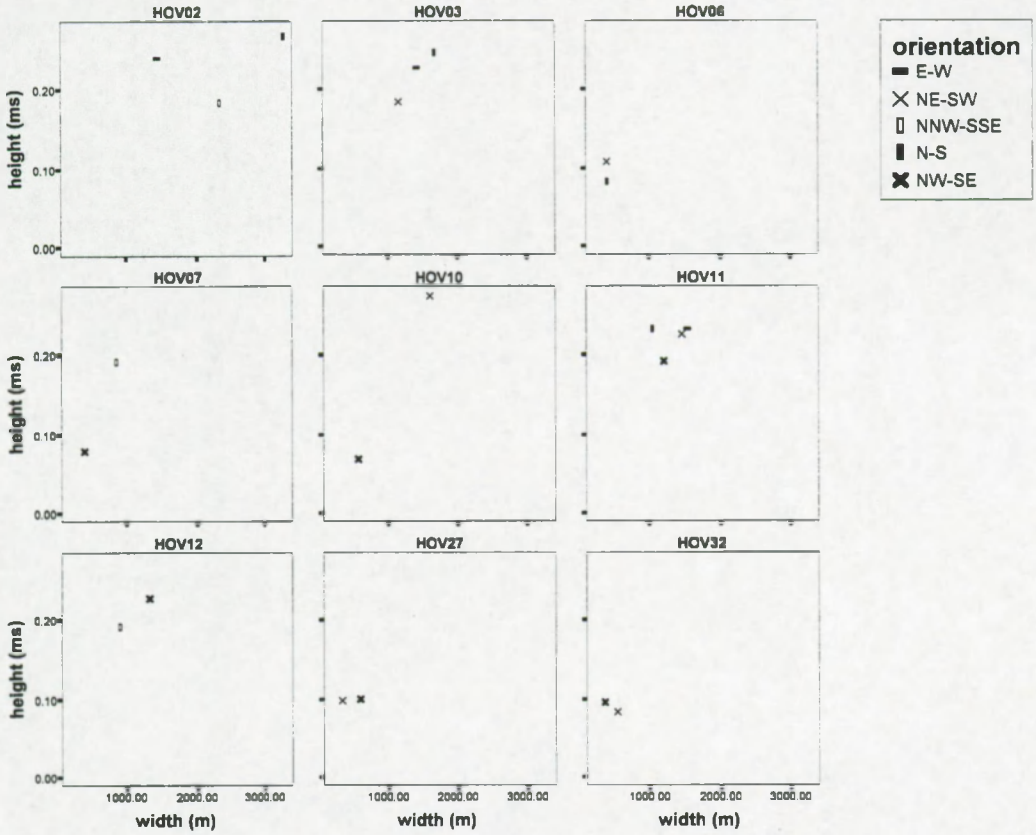

Fig. D.3.7: Panel of height-width scatter plots per mound. The symbols refer to the orientation of the profiles.

Mound flank

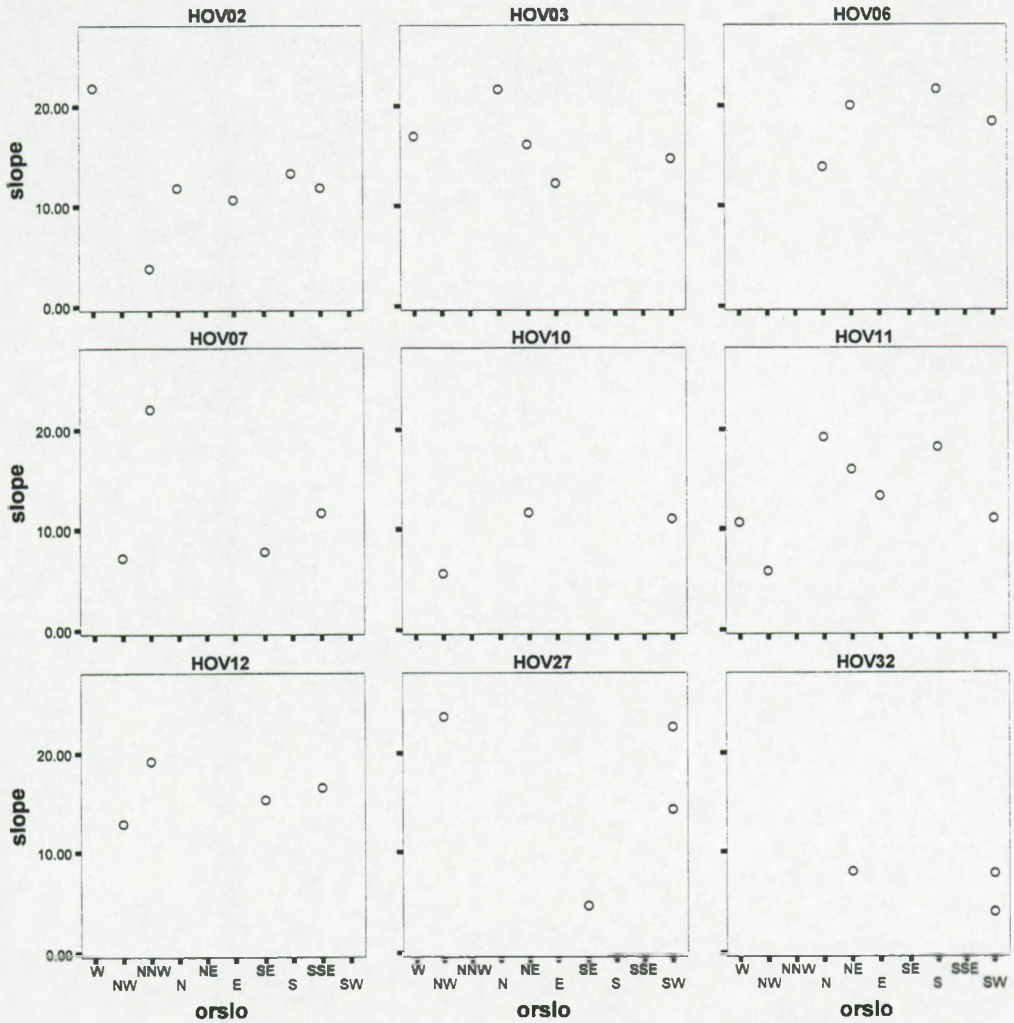

Fig. D.3.8: Slope angle of the mound against the orientation of the mound flank. In general, the northern flanks are steeper. Local variations are due to bathymetric variations.

Moat depth

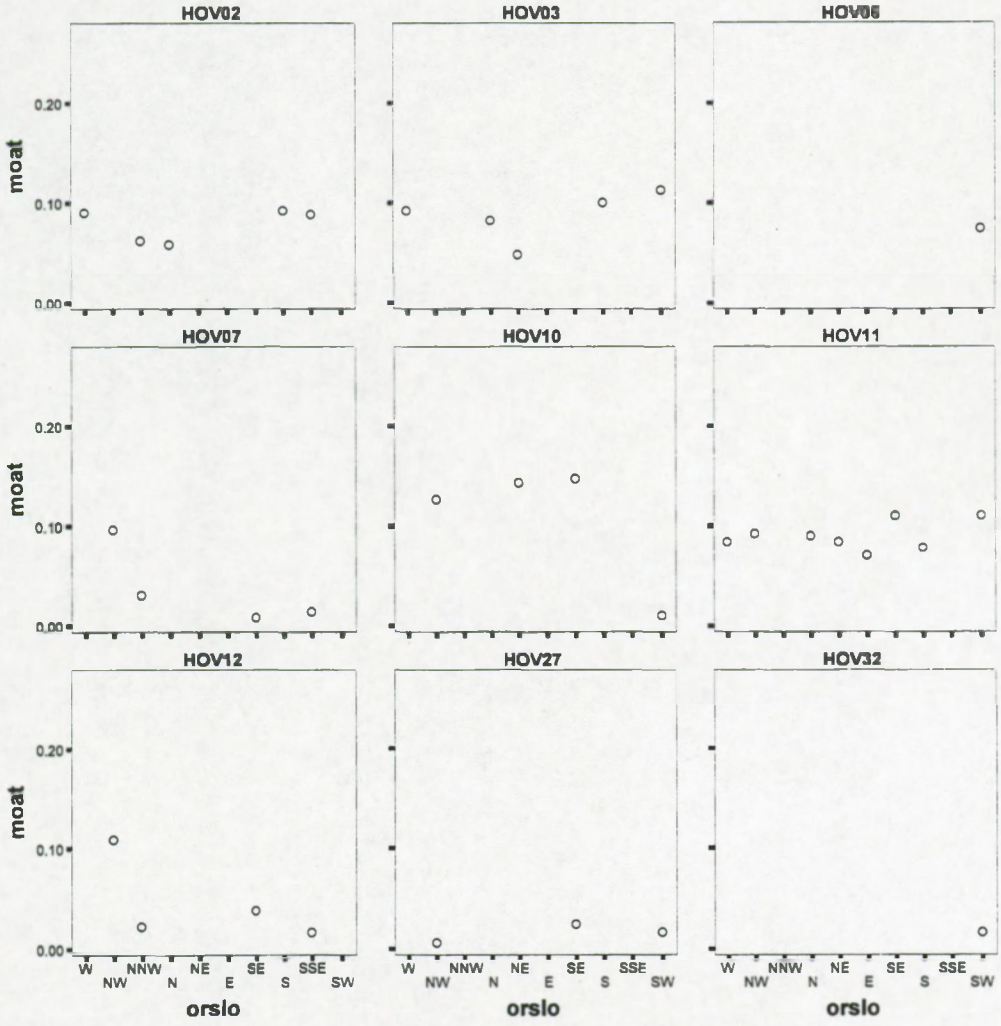

Fig. D.3.9: Moat depth plot against the flank orientation per mound. The moat depth is depending on the mound orientation and local bathymetric features.

Appendix E: Geology Hovland-Magellan mound province

Seismic profiles

- Bathymetric map with profile locations and mounds.
- P970502c
- P970503b
- P970505
- P970510a
- P970512
- P970514c-d
- P970514e
- P970514c-d-e
- P970522
- P970524b
- P970524c
- P970524b-c
- P970527
- P970528
- P980528
- P980533-43
- P990524
- P010536

Appendix E
Geology Hovland-Magellan mound province

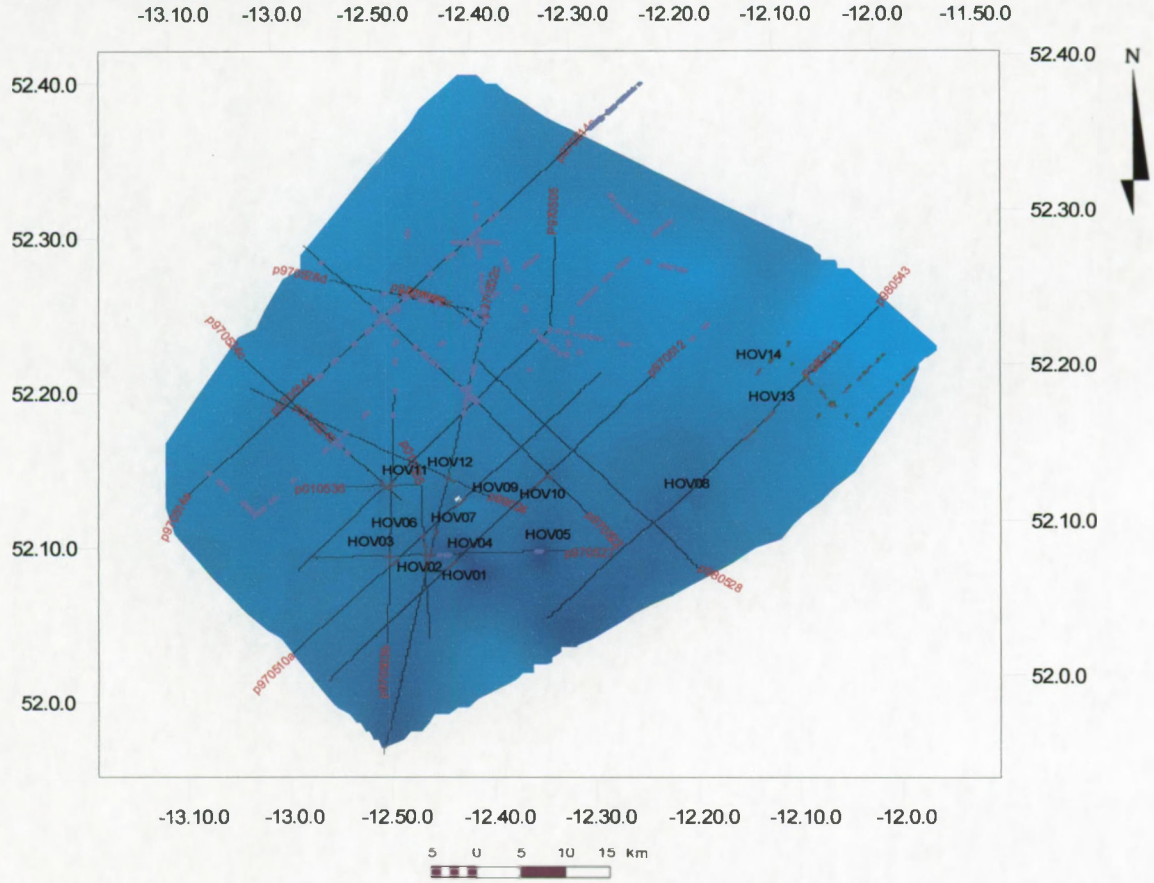

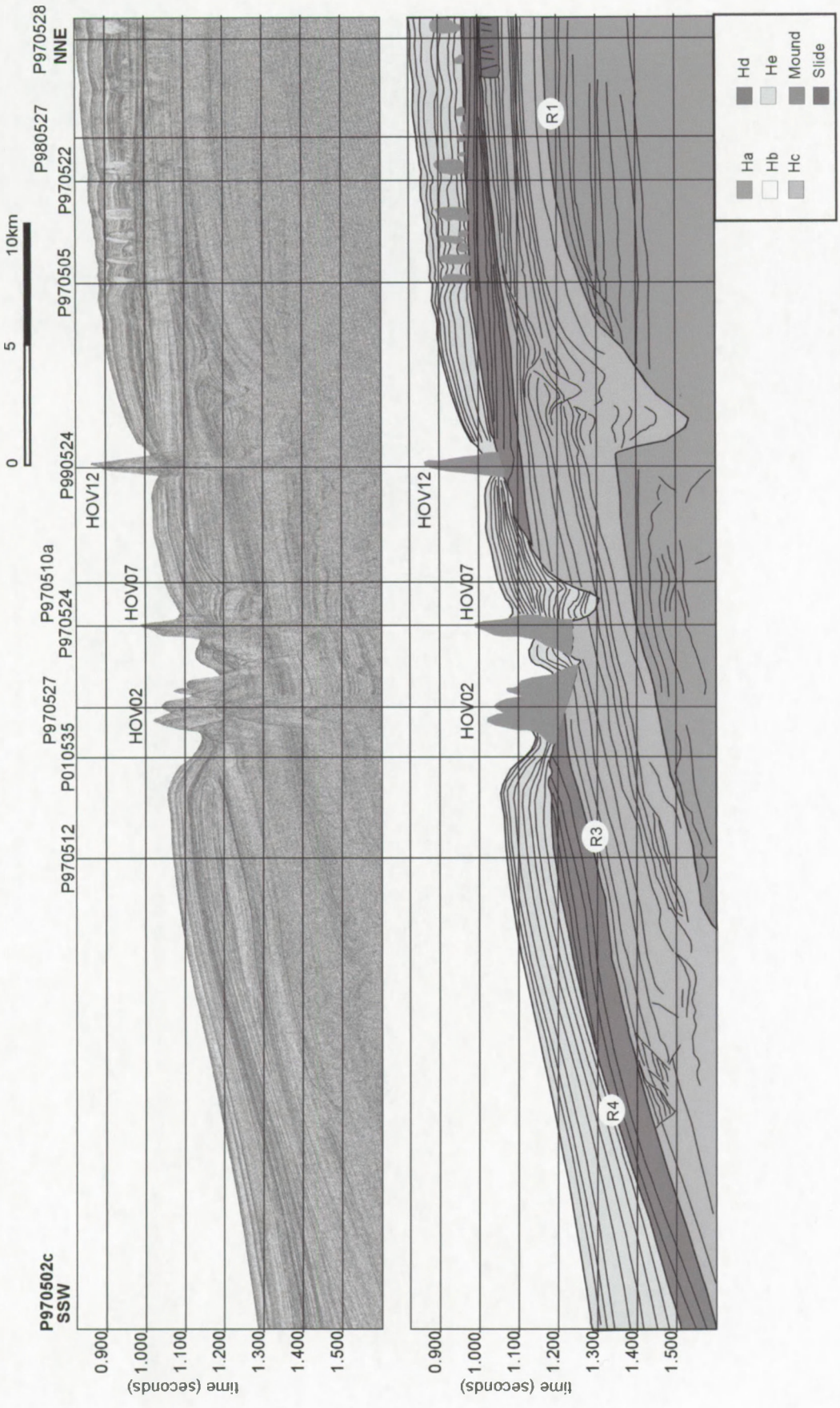
P970502c
SSW
P970512
P010535
P970527
P970524
P970510a
P990524
P970505
P970522
P980527
P970528
NNE
0
5
10km
HOV12
HOV07
HOV02
R1
R3
R4
Ha
Hb
Hc
Hd
He
Mound
Slide
time (seconds)
0.900
1.000
1.100
1.200
1.300
1.400
1.500

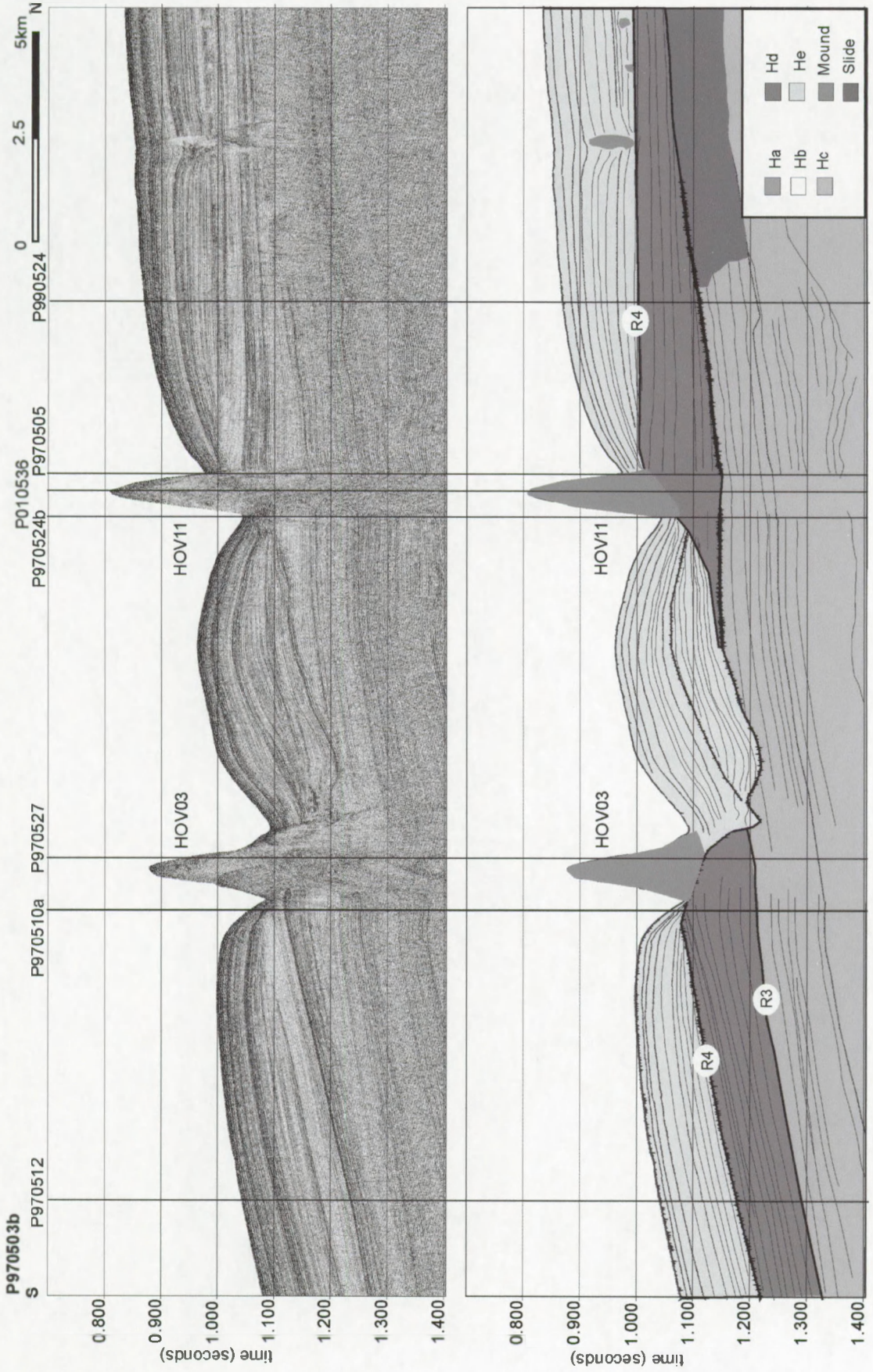
P970503b
S
P970512
P970510a
P970527
P970524b
P010536
P970505
P990524
N
0
2.5
5km
HOV03
HOV11
R3
R4
Hd
He
Mound
Slide
Ha
Hb
Hc
time (seconds)
0.800
0.900
1.000
1.100
1.200
1.300
1.400

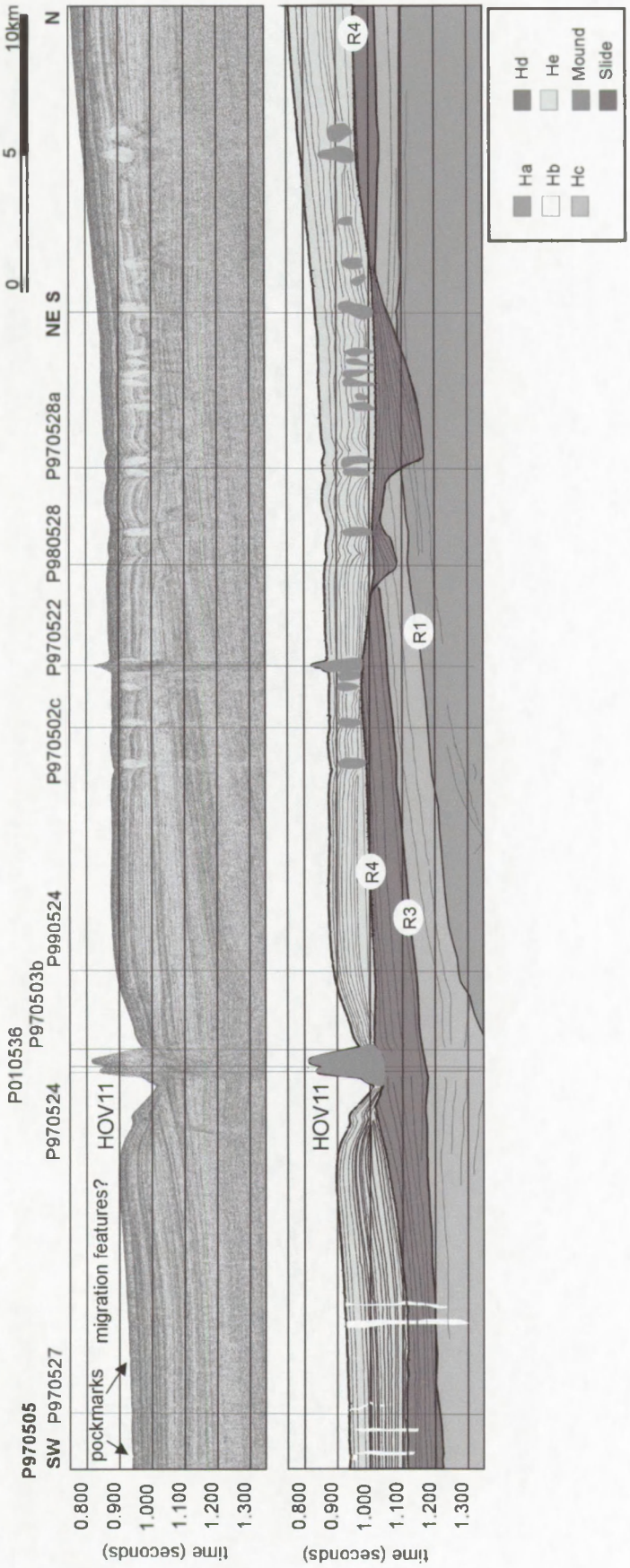
P970505
SW P970527
pockmarks
migration features?
HOV11
P970524
P010536
P970503b
P990524
P970502c
P970522
P980528
P970528a
NE S
N
0
5
10km
R4
R3
R1
HOV11
Ha
Hb
Hc
Hd
He
Mound
Slide
0.800
0.900
1.000
1.100
1.200
1.300
time (seconds)

0
5
10km
P970510a
SW
P970503b
P970527
P010535
P970502c
P970524
P990524
P970522
P980528
P970528
NE
HOV03
HOV06
HOV09
R1
R2
R3
R4
Ha
Hb
Hc
Hd
He
Mound
Slide
time (seconds)
0.800
0.900
1.000
1.100
1.200
1.300
1.400
1.500

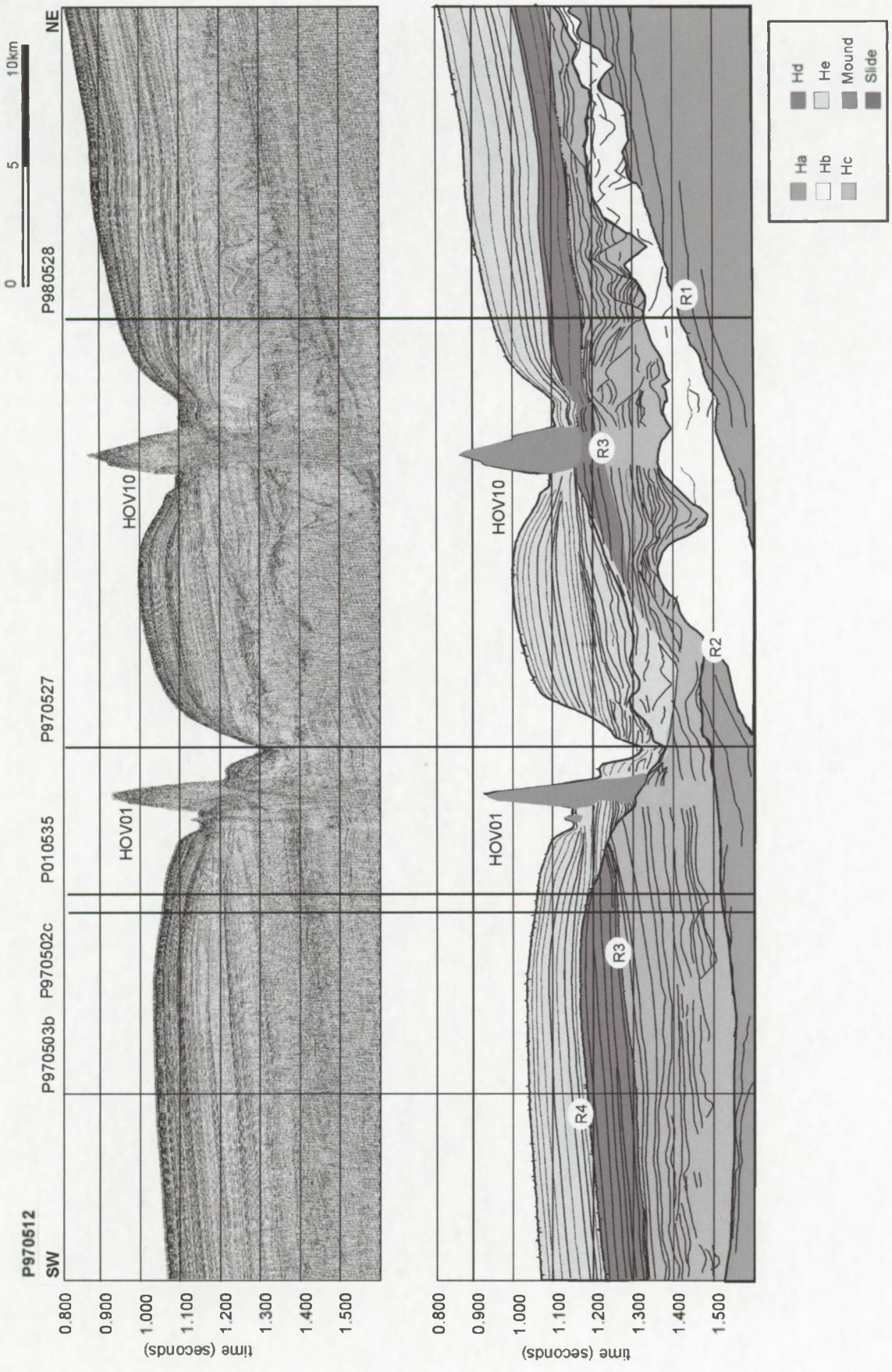
P970512
SW
P970503b
P970502c
P010535
P970527
P980528
NE
0
5
10km
HOV01
HOV10
R1
R2
R3
R4
Ha
Hb
Hc
Hd
He
Mound
Slide
time (seconds)
0.800
0.900
1.000
1.100
1.200
1.300
1.400
1.500

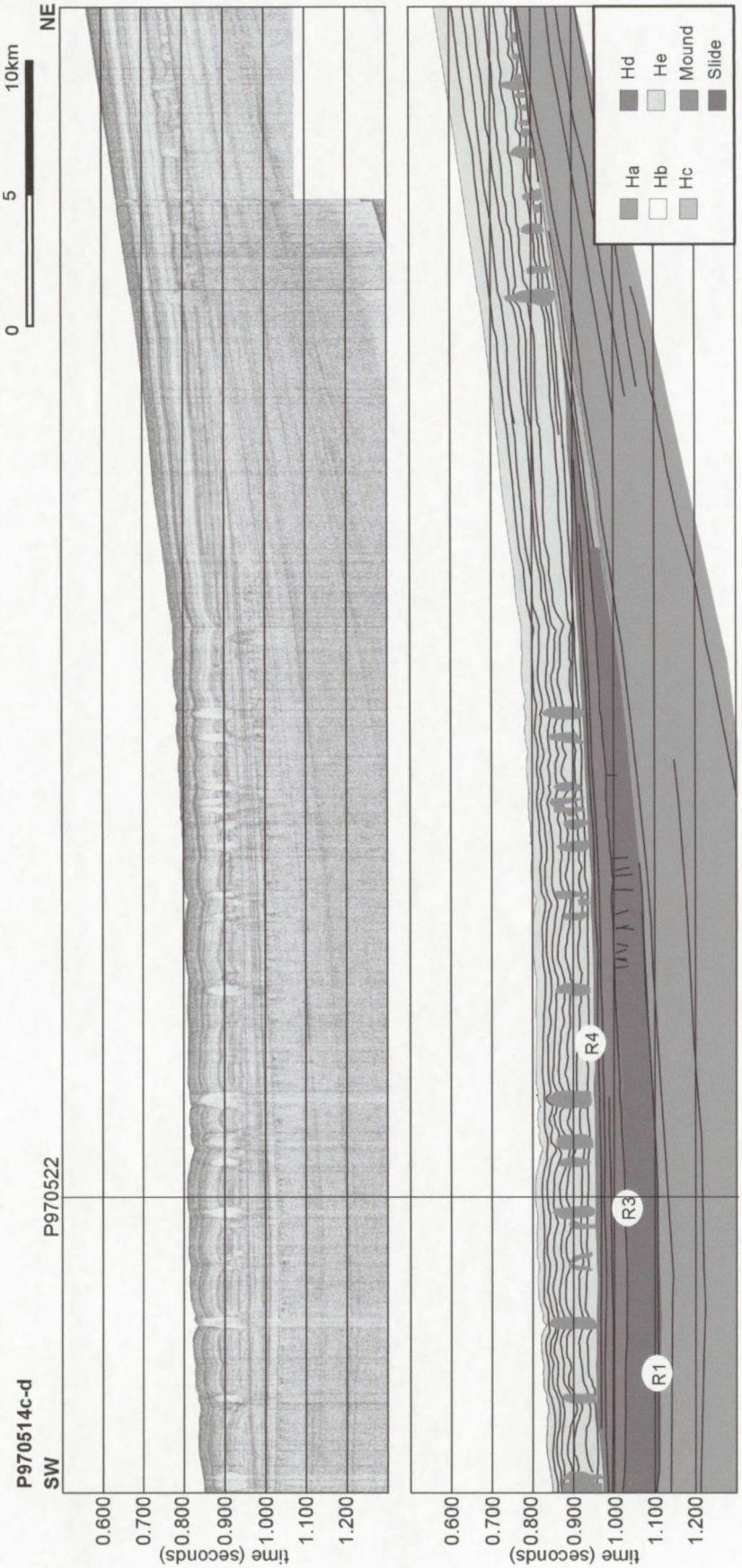
P970514c-d
SW
NE
P970522
0
5
10km
Ha
Hb
Hc
Hd
He
Mound
Slide
R1
R3
R4
time (seconds)
0.600
0.700
0.800
0.900
1.000
1.100
1.200

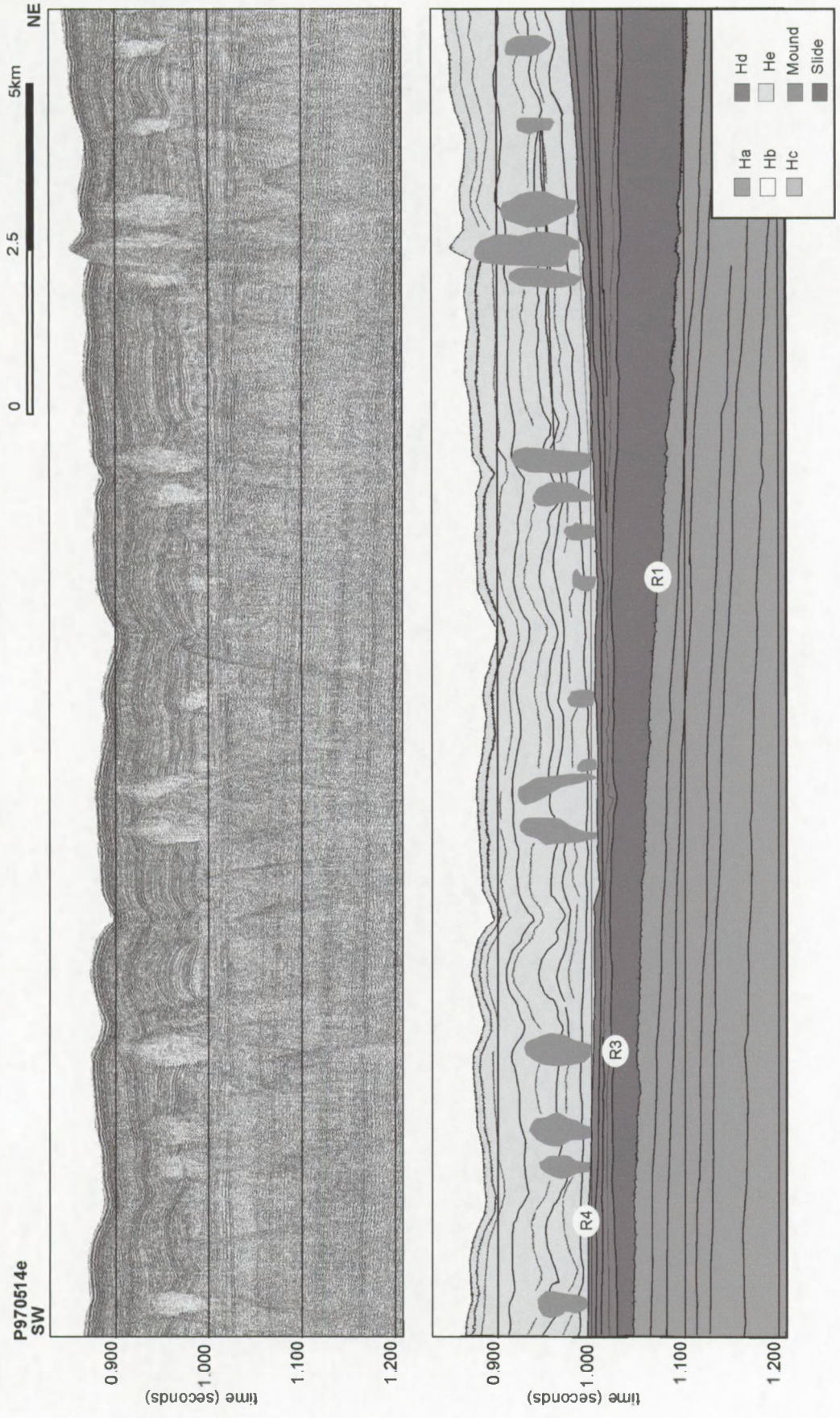
P970514e
SW
NE
0
2.5
5km
0.900
1.000
1.100
1.200
time (seconds)
R4
R3
R1
Ha
Hb
Hc
Hd
He
Mound
Slide

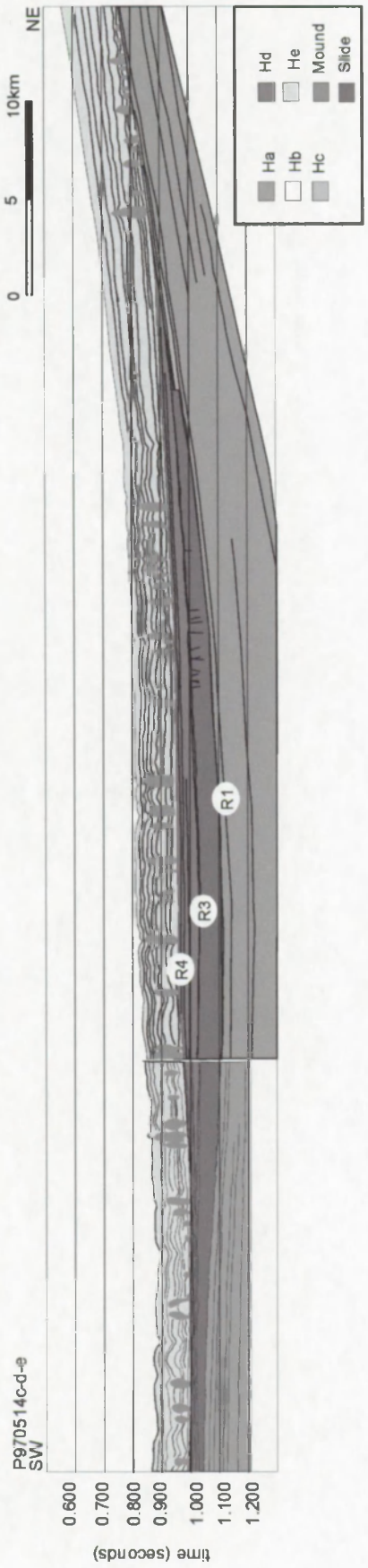
NE
0
5
10km
Hd
He
Mound
Slide
Ha
Hb
Hc
R1
R3
R4
P970514c-d-e
SW
0.600
0.700
0.800
0.900
1.000
1.100
1.200
time (seconds)

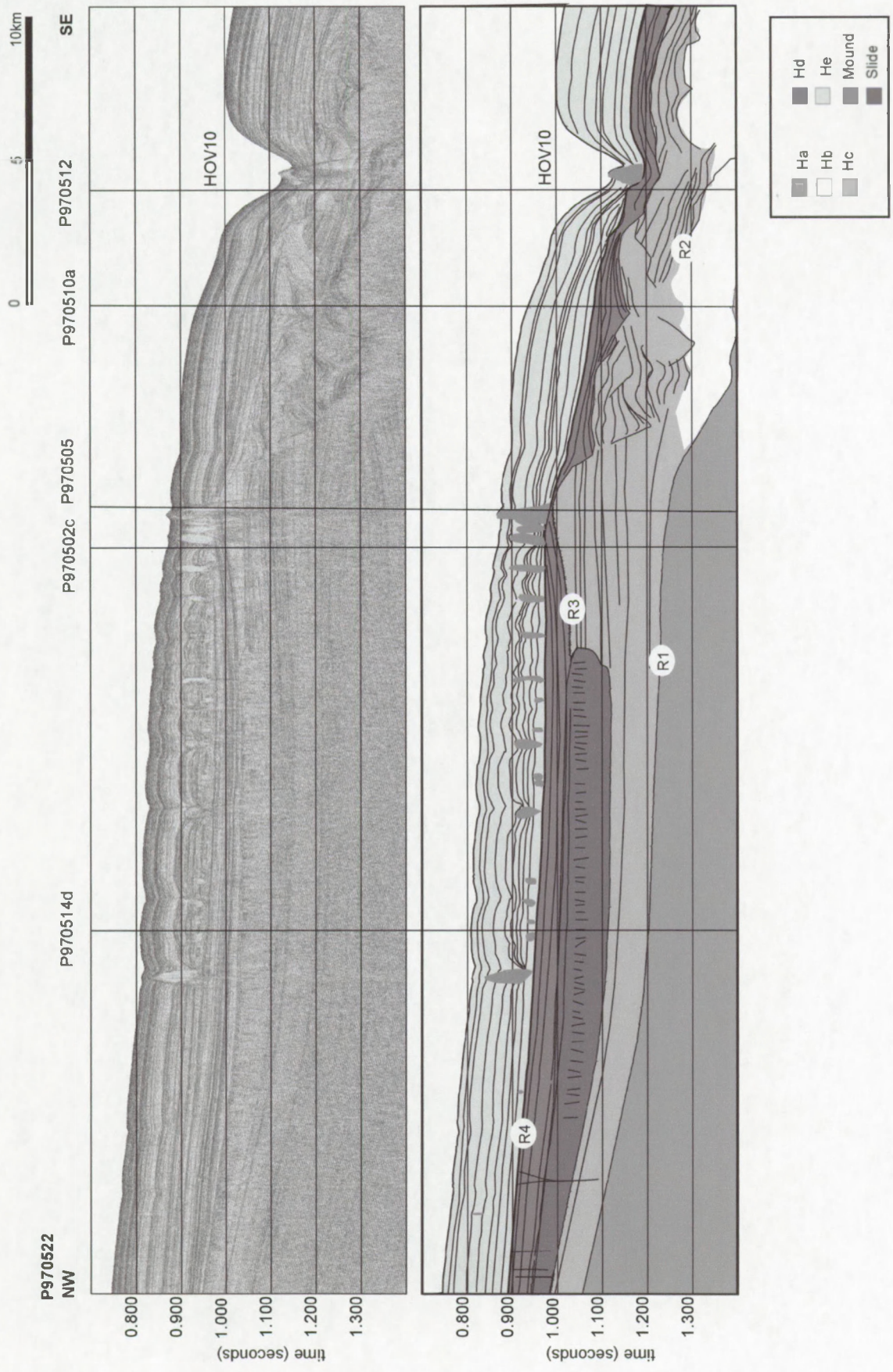
P970522
NW
P970514d
P970502c
P970505
P970510a
P970512
SE
0
5
10km
HOV10
HOV10
R1
R2
R3
R4
Hd
He
Mound
Slide
Ha
Hb
Hc
0.800
0.900
1.000
1.100
1.200
1.300
time (seconds)
time (seconds)

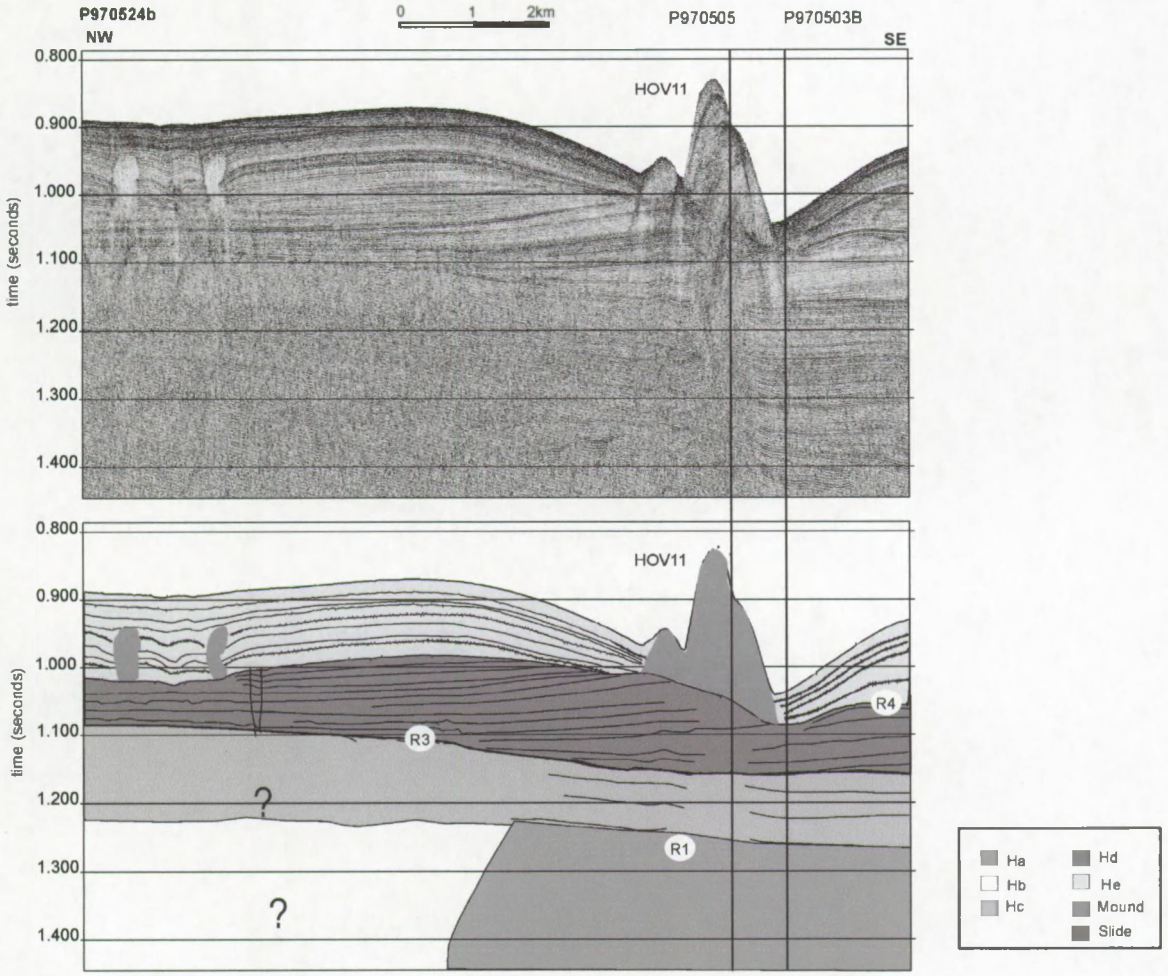
P970524b
NW
0
1
2km
P970505
P970503B
SE
0.800
0.900
1.000
1.100
1.200
1.300
1.400
time (seconds)
HOV11
HOV11
R4
R3
R1
?
?
Ha
Hb
Hc
Hd
He
Mound
Slide

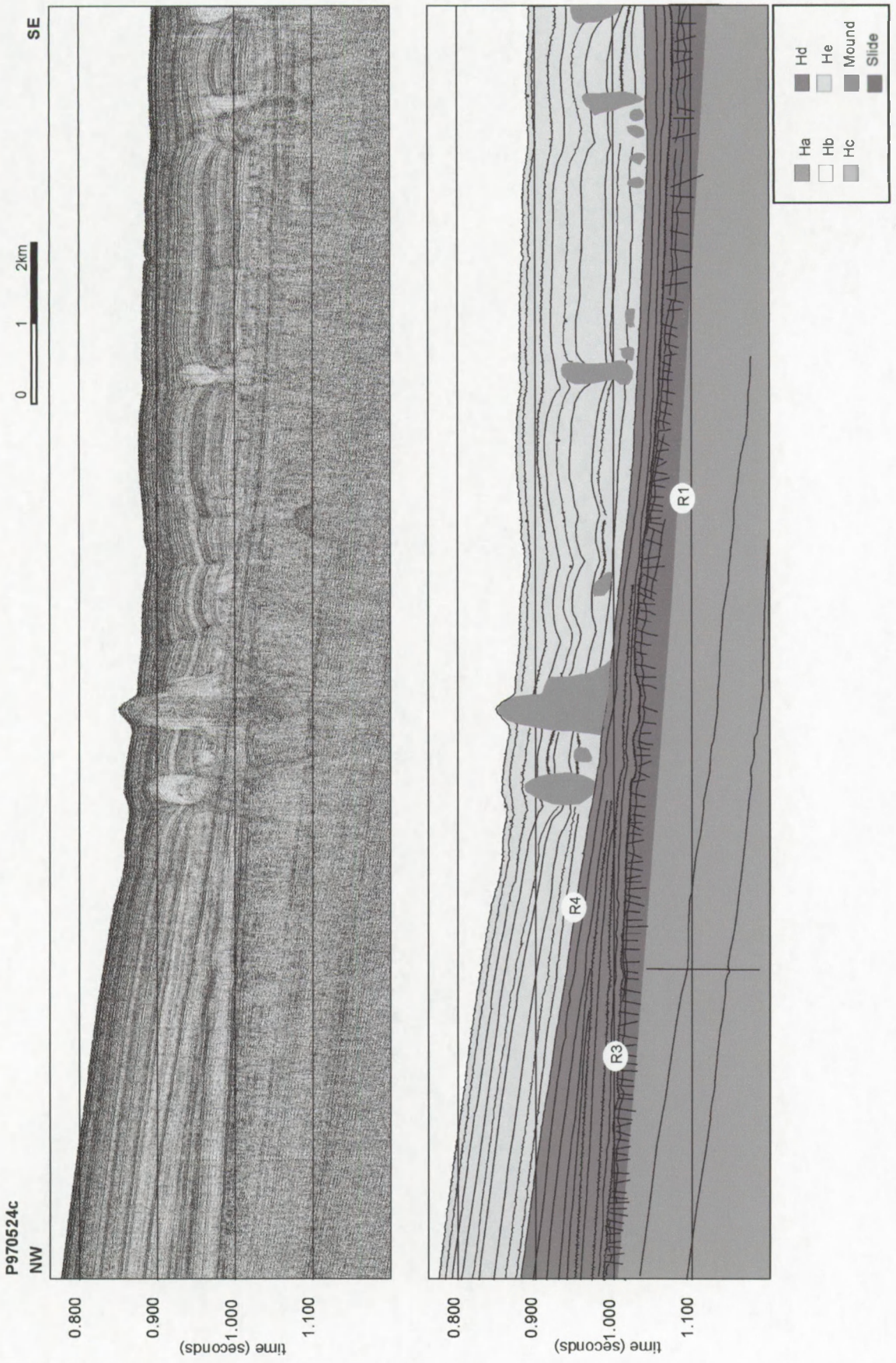
P970524c
NW
SE
0
1
2km
0.800
0.900
1.000
1.100
time (seconds)
R1
R3
R4
Hd
He
Mound
Slide
Ha
Hb
Hc

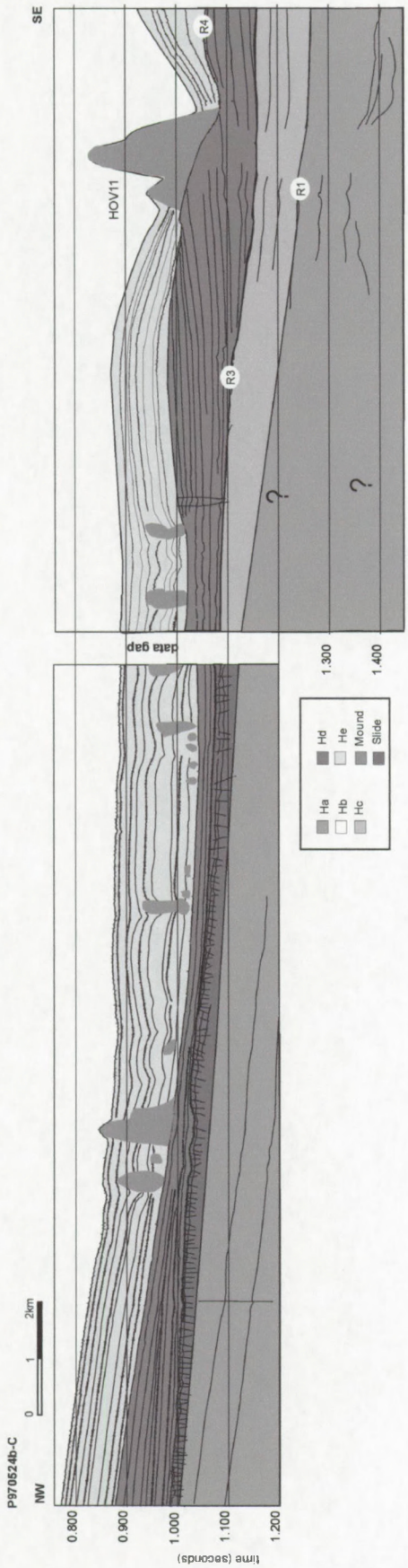
SE
NW
P970524b-C
0
1
2km
HOV11
R4
R1
R3
?
?
data gap
1.300
1.400
Hd
He
Mound
Slide
Ha
Hb
Hc
0.800
0.900
1.000
1.100
1.200
time (seconds)

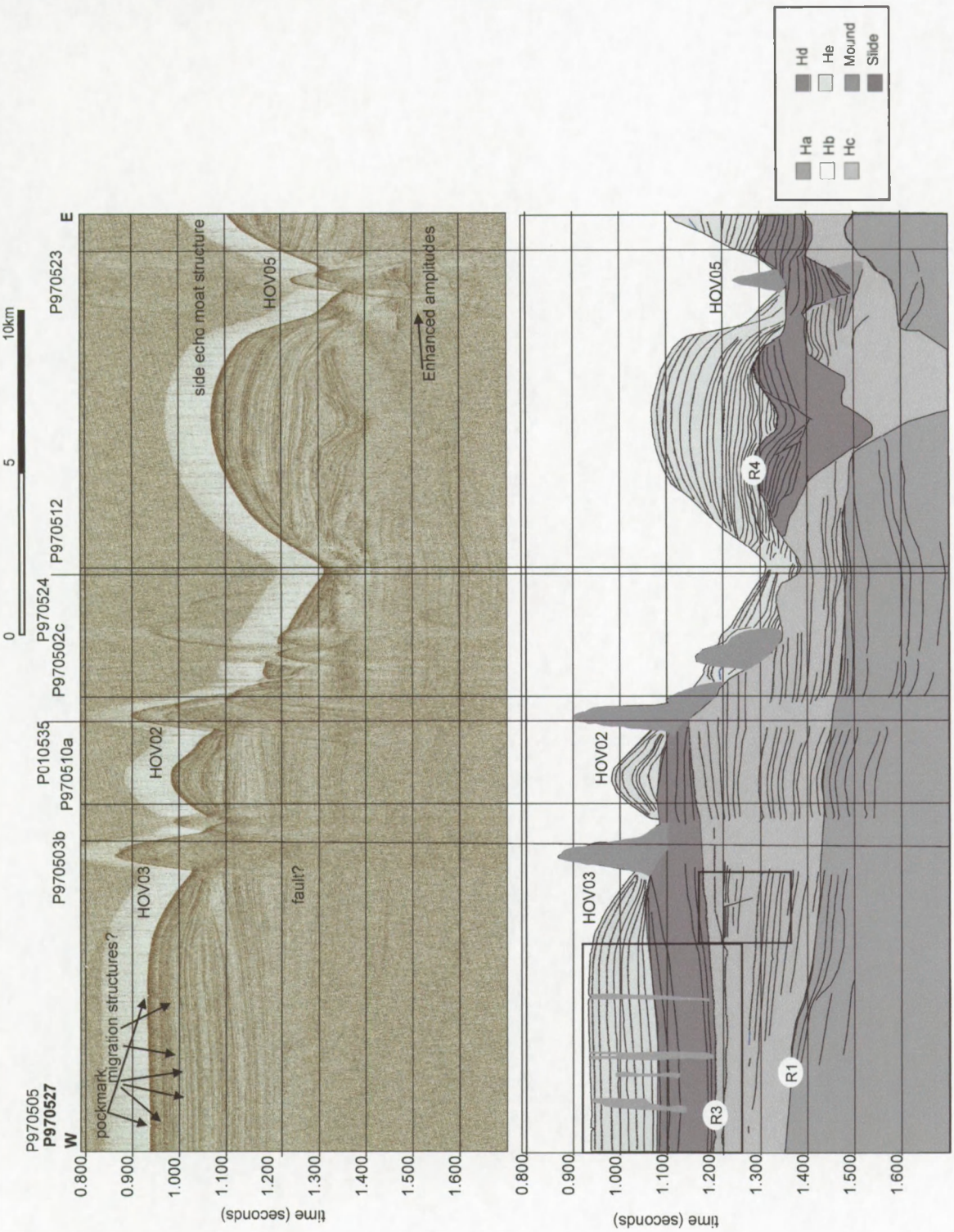
P970505
P970527
W
P970503b
P010535
P970510a
P970502c
P970524
P970512
P970523
E
0
5
10km
pockmark migration structures?
HOV03
HOV02
fault?
side echo moat structure
HOV05
Enhanced amplitudes
time (seconds)
0.800
0.900
1.000
1.100
1.200
1.300
1.400
1.500
1.600
R3
R1
R4
Hd
He
Mound
Slide
Ha
Hb
Hc

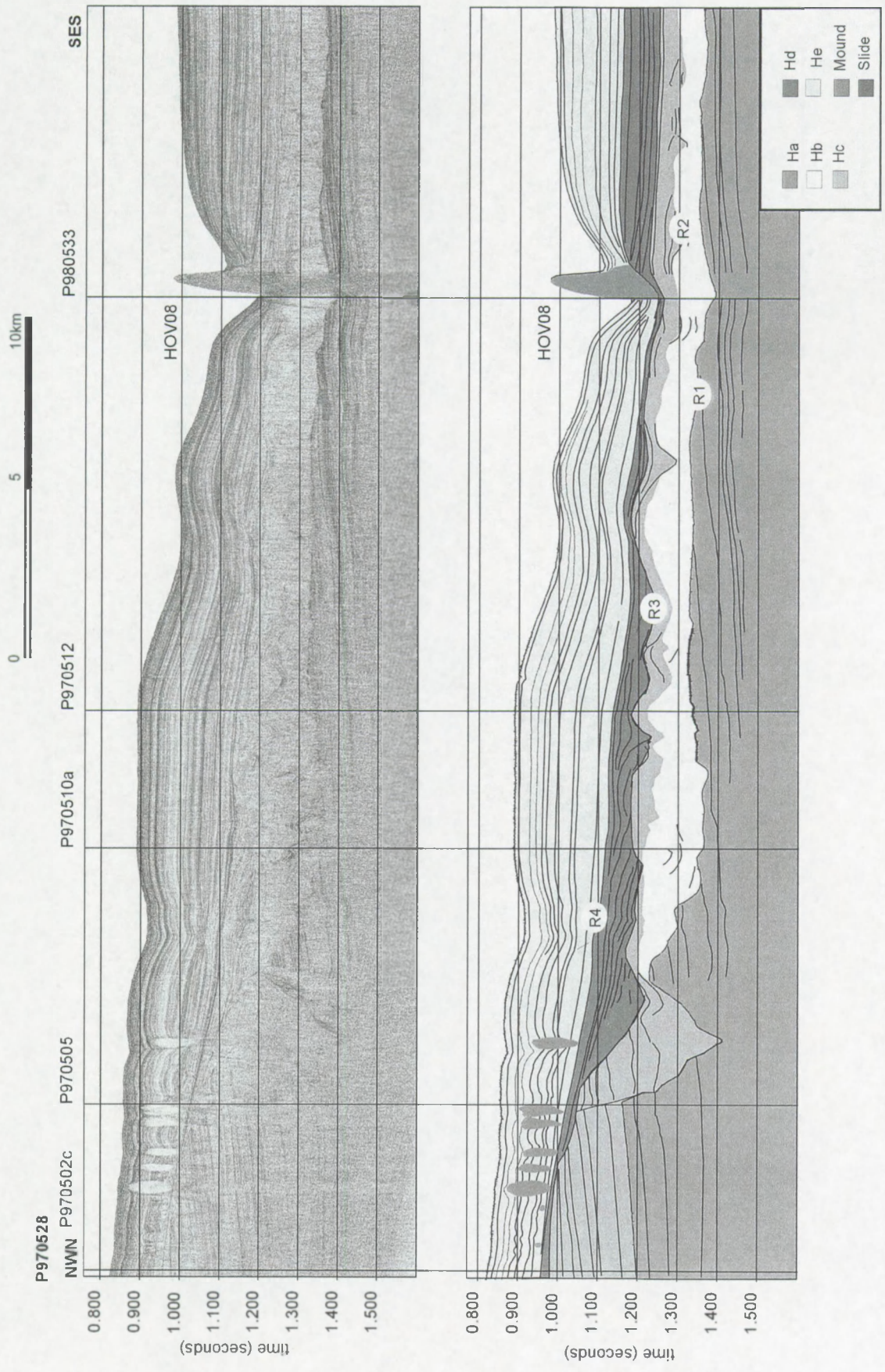
P970528
NWN
P970502c
P970505
P970510a
P970512
P980533
SES
0
5
10km
HOV08
HOV08
R1
R2
R3
R4
Hd
He
Mound
Slide
Ha
Hb
Hc
time (seconds)
0.800
0.900
1.000
1.100
1.200
1.300
1.400
1.500

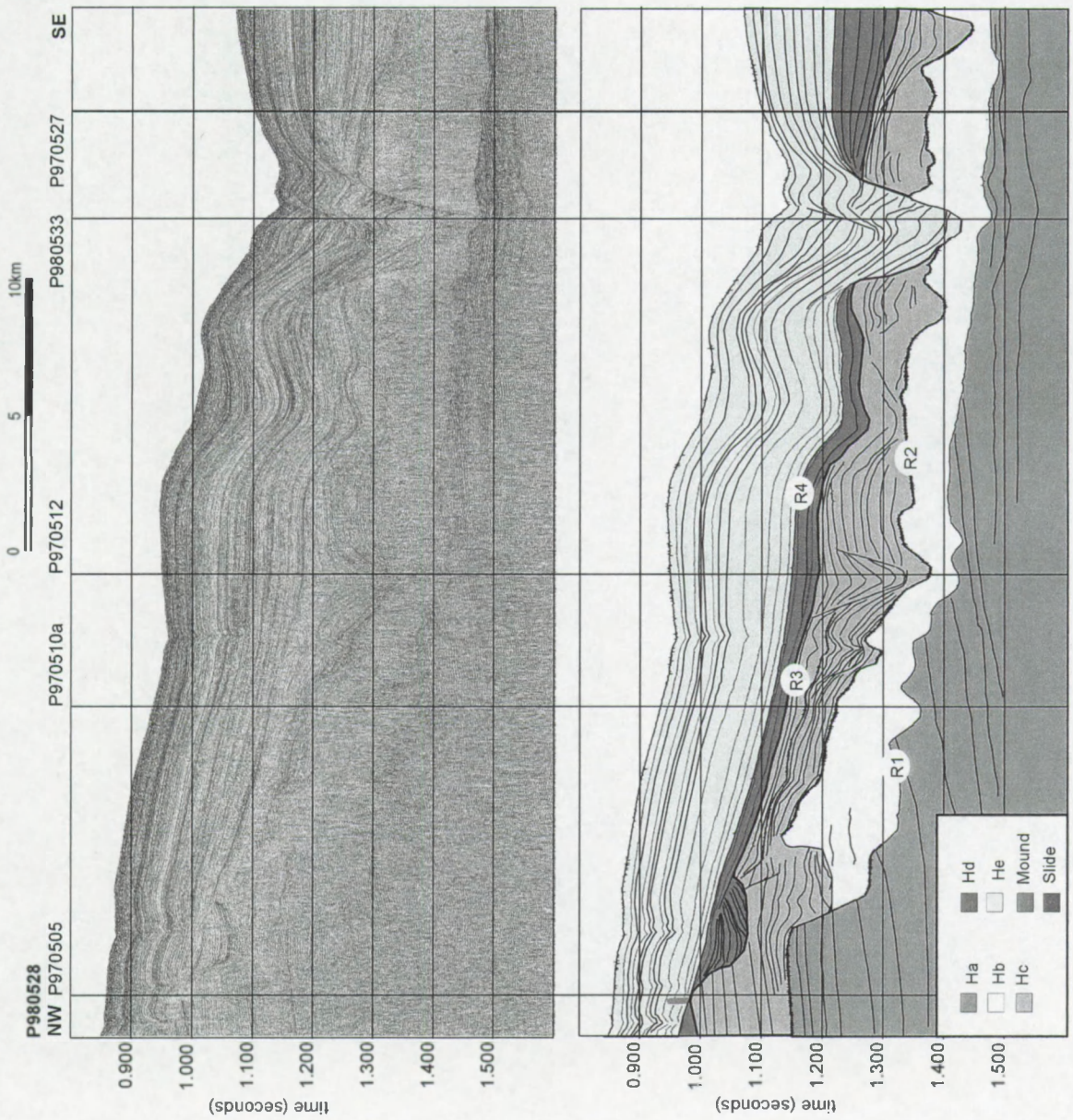
P980528
NW P970505
P970510a
P970512
P980533
P970527
SE
0
5
10km
R1
R2
R3
R4
Ha
Hb
Hc
Hd
He
Mound
Slide
time (seconds)
0.900
1.000
1.100
1.200
1.300
1.400
1.500

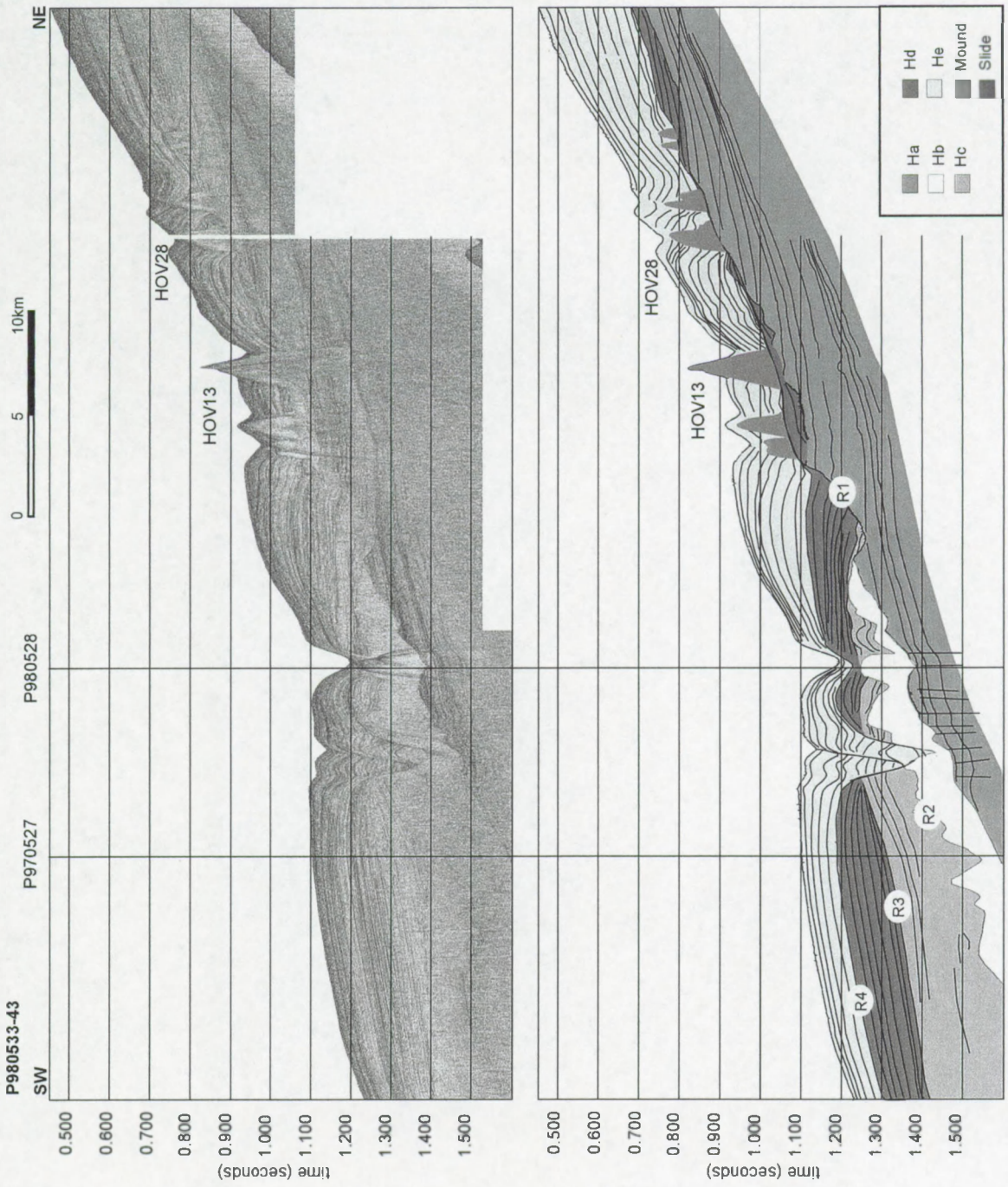
P980533-43
SW
NE
P970527
P980528
0
5
10km
HOV28
HOV13
R1
R2
R3
R4
Ha
Hb
Hc
Hd
He
Mound
Slide
time (seconds)
0.500
0.600
0.700
0.800
0.900
1.000
1.100
1.200
1.300
1.400
1.500

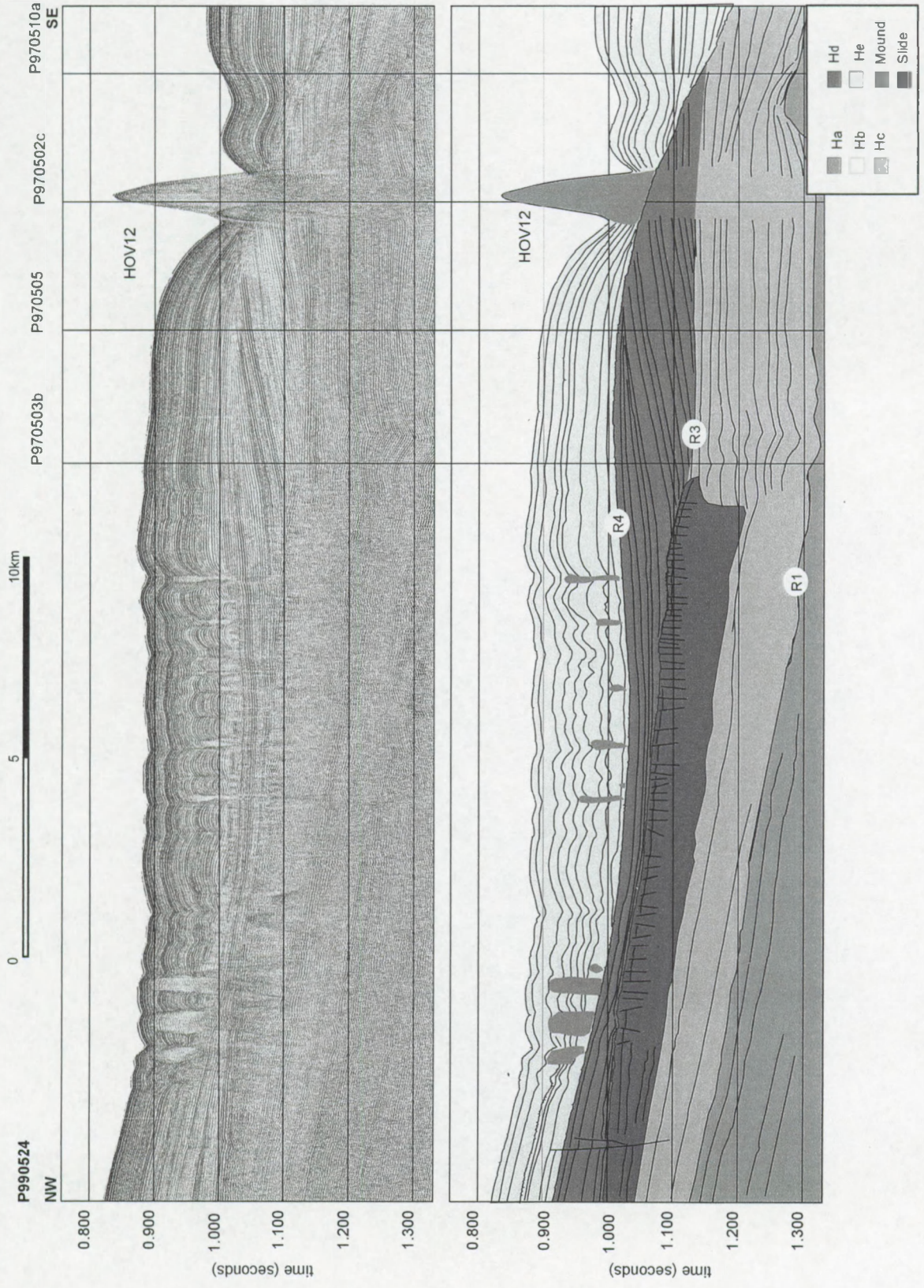
P990524
NW
P970503b
P970505
P970502c
P970510a
SE
0
5
10km
HOV12
HOV12
R1
R3
R4
Hd
He
Mound
Ha
Hb
Hc
Slide
0.800
0.900
1.000
1.100
1.200
1.300
time (seconds)
time (seconds)

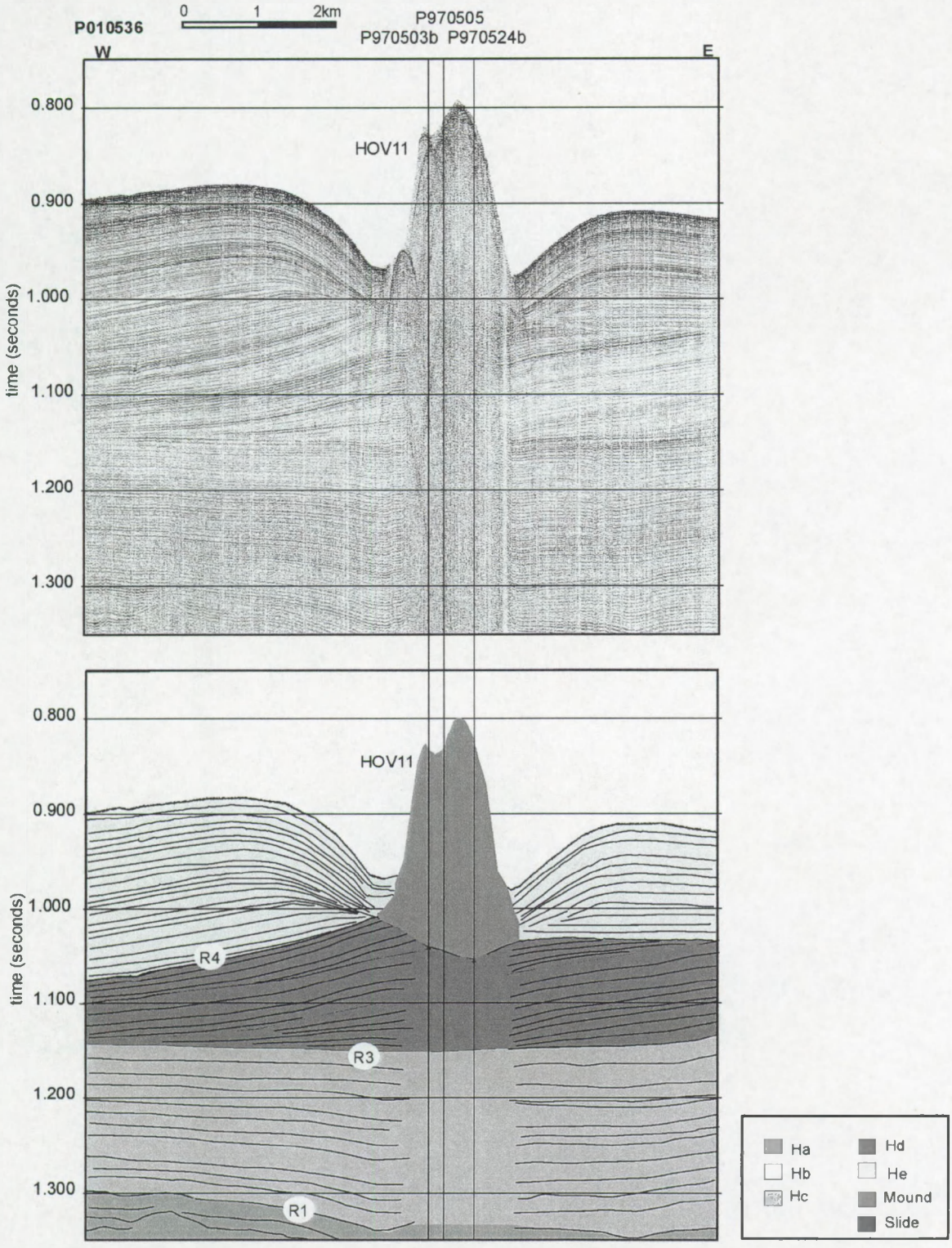
P010536
0
1
2km
P970505
P970503b P970524b
W
E
0.800
0.900
1.000
1.100
1.200
1.300
time (seconds)
HOV11
HOV11
R4
R3
R1
Ha
Hb
Hc
Hd
He
Mound
Slide

Appendix F: Sedimentology Hovland-Magellan mound province

1. Table of sample locations

2. Lithologs

3. Mineralogical and chemical data

4. Scanning electron microscopy

5. Petrographic and cathodoluminescent microscopy

6. Isotopic analysis

7. Gas analysis

1. Table of sample locations

Data sort	Name	Latitude N	Longitude W	Depth m	Recovery cm	Target	Short description
GC	TTR7-AT-2G	52.2277	12.5660	795	392	mound crest HOV10	Live and dead coral in foraminiferal ooze. Dense packed sandy coral intervals
GC	TTR7-AT-3G	52.2193	12.5672	840	369	moat of mound HOV10	Foramiferal sand, and marls down mud and dropstones
GC	TTR7-AT-5G	52.2332	12.7230	637	60.5	mound crest HOV12	Coral core, coarse bioccalstic sand including coral and epifauna, silty foraminiferal marl
GC	TTR7-AT-6G	52.2278	12.7260	790	247	moat of mound HOV12	Interbedded grey marls and sandy foramainfera an bioclastic layers
GC	TTR7-AT-7G	52.2188	12.7297	774	370	background	Pelagic core, silty foraminiferal marls, bioturbation
GC	TTR7-AT-9G	52.2122	13.0397	706	361	Magellan mound SE slope	Pelagic core, bioturbated
GC	TTR7-AT-10G	52.1990	13.0457	696	393.5	Magellan mound SE slope	Pelagic core silty foraminiferal marls, bioclastic debris scattered through core
GC	TTR7-AT-11G	52.2120	13.0410	703	388.5	Magellan mound SE slope	Bioturbaded pelagic core, one coral fragment
GC	TTR7-AT-12G	52.2733	13.0070	675	403.5	background core	Biorturbated pelagic core, greyish brown forminiferal silty marls, sandy bands
GC	TTR7-AT-13G	52.3198	12.9845	651	388.5	Magellan mound NNE side	Pelagic core foraminiferal sllty marls
GC	TTR7-AT-14G	52.3147	12.6783	624	145	Magellan mound	Coral core, band of dead coral interbedded with olive-grey silty foraminiferal mud.
GC	TTR7-AT-16G	52.1467	12.8800	691	389	mound crest HOV03	Mixed core, corals and pelagic sections
GC	TTR7-AT-17G	52.1453	12.8192	737	126	mound flank HOV03	Coral core, alternating foramineferal marls and coral fragments
GC	TTR7-AT-18G	52.1442	12.8315	786	198	mound flank HOV03	Bioturbated pelagic core with coral fragments
BC	TTR8-AT-87B	52.1513	12.7672	765	23	mound flank HOV02	Drop stone, coral branches, bivalve shells at surface, carbonate clay with coral debris

GC: Gravity Core

PC: Piston Core

BC: Box Core

D: Dredge

GR: Grab

Table F.1.1: Shallow sediment cores in the Hovland mound province. The cores yielding coral have been marked in grey.

Data sort	Name	Latitude N	Longitude W	Depth m	Recovery cm	Target	Short description
GC	TTR8-AT-88G	52.1516	12.7682	700	333	mound crest HOV02	Intercalation of silty marl and coral debris
GC	TTR8-AT-89G	52.1521	12.7704	706	200	mound crest HOV02	Intercalation of silty marl and coral debris
GC	TTR8-AT-90G	52.3128	12.9803	667	351	Magellan mound background sediment	Olive grey sandy/silt with foraminifera, heaviliy biturbated
BC	TTR8-AT-93B	52.3181	12.9901	658	33	Magellan mound background sediment	Olive grey with foraminifera, heavily bioturbated
BC	TTR8-AT-94B	52.3240	13.0001	659	35	Magellan mound background sediment	Olive grey with foraminifera, heavily bioturbated
BC	TTR8-AT-95B	52.3240	12.9602	658	36	Magellan mound background sediment	Olive grey with foraminifera, heavily bioturbated
BC	TTR8-AT-96B	52.3182	12.9703	670	35	Magellan mound background sediment	Olive grey with foraminifera, heavily bioturbated
BC	TTR8-AT-97B	52.3067	12.9703	663	33	Magellan mound background sediment	Olive grey with foraminifera, heavily bioturbated
BC	TTR8-AT-98B	52.3016	12.9606	680	33	Magellan mound background sediment	Olive grey with foraminifera, heavily bioturbated
BC	TTR8-AT-99B	52.3017	13.0005	665	36	Magellan mound background sediment	Olive grey with foraminifera, heavily bioturbated

Data sort	Name	Latitude N	Longitude W	Depth m	Recovery cm	Target	Short description
BC	TTR8-AT-100B	52.3074	12.9901	665	34	Magellan mound background sediment	Olive grey with foraminifera, heavily bioturbated
BC	Poseidon 468-1	52.1542	12.7698	742	31	flank of mound HOV02	Light brownish grey sandy mud
BC	Poseidon 468-2	52.1513	12.7703	657		crest of mound HOV02	Lophelia colonies
BC	Poseidon 469-2	52.2004	12.7000	817	40	southernflank of mound HOV2	Light brownish grey sandy mud
BC	Poseidon 477-1	52.1517	12.7706	686		flank of mound HOV2	Lophelia colonies plus silt and sand
BC	Poseidon 478-1	52.1596	12.7500	890	27	flank of mound HOV02	Light brownish grey sandy mud
BC	Poseidon 480-1	52.1521	12.7665	729		crest of mound HOV02	Lophelia and Desmophyllum
BC	Poseidon 481-1	52.1536	12.7719	696	22	flank of mound HOV02	Light brownish grey sandy mud
BC	Poseidon 482-1	52.1481	12.7717	890		crest of mound HOV02	Lophelia and Desmophyllum, partly living
GC	ST07	52.2718	13.2165	573	2.8	?	Grey silt, shell fragments
GC	ST16	52.1164	13.0412	615	2.7	on mound	Medium grey clay with abundant coral
GC	ST19	52.2835	13.0877	669	3.3	foot of seabed slope	Olive grey silt, clay
GC	ST29	52.1813	12.9531	695	2.8	background	Fine sand at top, silt ,clay
GC	ST40	52.1479	12.7549	857	2.4	foot of mound HOV07	Olive grey clay with abundant coral
GC	ST43	52.1481	12.7697	720	2.5	crest of mound HOV02	Olive grey silt with coral-coral sand
GC	ST44	52.1479	12.7746	809	2.2	crest of mound HOV02	Olive grey sand, olive grey silty clay
GC	ST45	52.1480	12.8112	769	2.3	crest of mound HOV03	Olive grey silt, clay

Data sort	Name	Latitude N	Longitude W	Depth m	Recovery cm	Target	Short description
GC	ST46	52.1438	12.8167	804	2.7	foot of mound HOV03	Olive grey silt, clay
GC	ST49	52.1479	12.8363	772	3	foot of mound HOV03	Olive grey silt, clay, shells
GC	ST71	52.1817	12.4134	805	2.7	foot of mound HOV08	Medium grey silt, shells
GC	ST78	52.2371	12.3232	693	3	crest of mound HOV08	Olive grey clay with corals, coral sand
GC	ST84	52.2702	12.3477	830	2.9	foot of mound HOV08	Olive grey sand with shells, silt and shells, clay
GC	ST92	52.2869	12.8498	640	2.8	Pockmark?	Grey silt, clay
GC	ST105	52.3207	13.1894	554	3	background	Medium grey silt and clay including shells
GC	ST108	52.3201	12.9815	649	2.9	Foot of mound	Medium grey silt and clay including shells
GC	ST110	52.2964	13.0795	616	2	on mound Magellan	Olive grey silt with corals, coral sand
GC	ST115	52.2363	12.9719	696	3	?	Light brown greyish silt
GC	ST116	52.2092	13.0569	678	3	?	Medium grey clayey silt
GC	ST121	52.1978	12.3300	848	2.7	slope HOV08	Fine sand, grey clay
GC	ST130	52.2271	12.3225		2.6	slope HOV08	Light olive grey coral sand with clay matrix
GC	ST133	52.2965	12.2317	632	0.8	on mound HOV15	Greenish grey sand with coral
GC	ST134	52.2465	12.2338	624	4	on mound HOV15?	Greenish grey snad with coral
GC	ST135	52.2477	12.2399	762	3	foot of mound HOV15?	Olive grey sand with rockfragments
GC	ST138	52.2463	12.3352	706	2.8	on mound HOV08	Abundant corals and coral sand
GC	ST139	52.2527	12.3351	800	2.1	crest of mound HOV08	Olive grey clay with abundant coral fragments
GC	ST142	52.2616	12.3467	857	2.2	foot of mound HOV08	Medium grey sand, some coral fragments
GC	ST143	52.2619	12.3366	665	3.6	on mound HOV08	Clay with abundant coral fragments

Data sort	Name	Latitude N	Longitude W	Depth m	Recovery cm	Target	Short description
GC	ST150	52.2861	12.2860	660	2.1	crest of mound HOV13	Corals
GC	ST151	52.2862	12.2897	709	3	foot of mound HOV15	Olive grey silt, clay
GC	ST154	52.1911	13.1539	654	3	?	Medium grey silt and clay
GC	ST166	52.2616	13.0355	670	2.7	on mound MAG?	Fine sand abundant coral fragments
GC	ST173	52.2139	12.4365	764	2.9	?	Medium grey silt with shells, clay
GC	ST175	52.2366	12.4367	823	3	?	Grey clay with shell fragments
GC	ST182	52.2761	12.2249	682	2.8	crest of mound HOV15	Olive grey silt
GC	ST190	52.2777	12.2372	645	2.6	crest of mound HOV15	Olive grey clay with lots of corals
GC	ST192	52.2774	12.2315	627	1.5	crest of mound HOV15	Olive grey clay with lots of corals
GC	ST195	52.2526	12.3397	877	2.7	foot of mound HOV08	Olive grey clay with few coral fragments
GC	PAD18	52.2285	12.5751		250	on-mound HOV04	Brownish silty clay coral fragments, silty clay abundant corals
GC	PAD25	52.2189	12.5785		280	on-mound HOV04	Olive green sity clay, plenty of corals
GC	PAD76	52.1543	12.5339		210	off mound	Sandy silt
GC	PAD81	52.1497	12.5783		215	on-mound HOV05	Coral, sandy silt, greyish silty clay, abundant corals
GC	PAD83	52.1477	12.5786		200	on-mound HOV05	Yellow silt, silty clay, shell and coral debris
GC	PAD2					background samples	Geochemical results
GC	PAD12					Absorbed gas anomaly samples	Geochemical results
GC	PAD13						Geochemical results
GC	PAD41					on-mound	Geochemical results
GC	PAD60					Biogenic mix	Geochemical results

Data sort	Name	Latitude N	Longitude W	Depth m	Recovery cm	Target	Short description
GC	PAD68						Geochemical results
GC	PAD75						Geochemical results
GC	PAD88					Background samples	Geochemical results
GC	PAD90					Background samples	Geochemical results
D	TTR7-AT-4D	52.225 to 52.223	12.565-12.566	822-886	N/A	HOV10	Carbonate ooze, echinoids, corals, sea urchins
D	TTR7-AT-8D	52.228-52.236	12.726-	789	N/A	HOV12	Carbonate ooze, echinoids, corals, sea urchins
GR	TTR7-AT-15GR	52.2270	12.5680	624	1.5tonne	BEL42	Corals and associated epifauna

2. Lithologs

Off-mound

Moat

TTR7-AT-3G
TTR7-AT-6G

Background

TTR7-AT-7G
TTR7-AT-9G
TTR7-AT-10G
TTR7-AT-11G
TTR7-AT-12G
TTR7-AT-13G

On-mound

HOV03

TTR7-AT-17G
TTR7-AT-18G

HOV04

PAD18
PAD25

HOV05

PAD81
PAD83

HOV10

TTR7-AT-2G

LEGEND

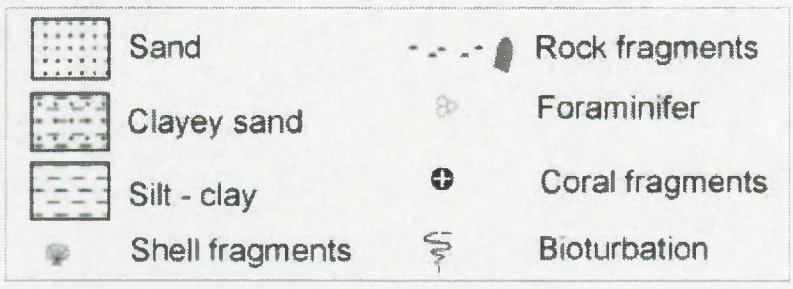

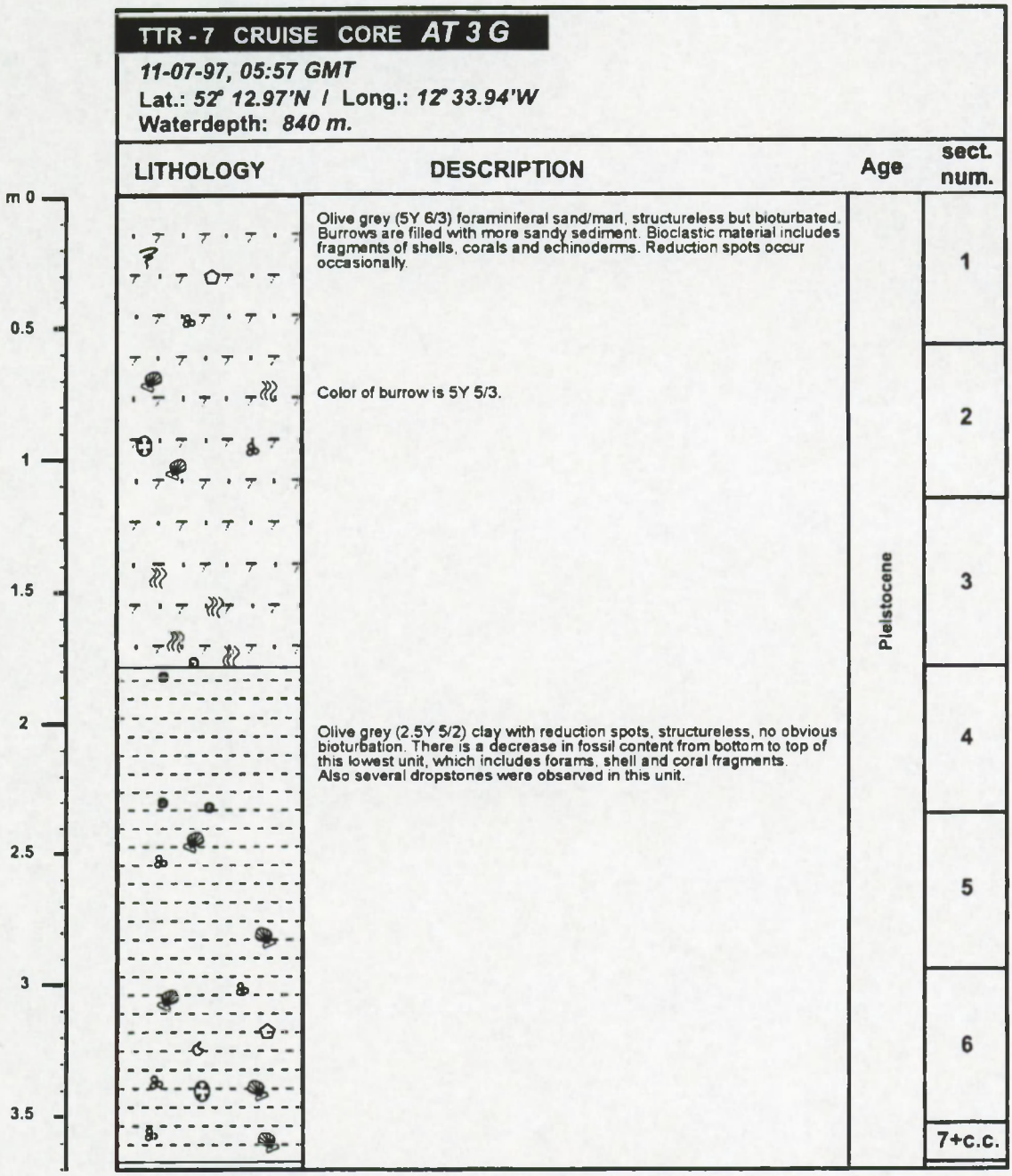
TTR - 7 CRUISE CORE AT 3 G
11-07-97, 05:57 GMT
Lat.: 52° 12.97'N / Long.: 12° 33.94'W
Waterdepth: 840 m.
LITHOLOGY
DESCRIPTION
Age
sect. num.
m 0
0.5
1
1.5
2
2.5
3
3.5
Olive grey (5Y 6/3) foraminiferal sand/marl, structureless but bioturbated. Burrows are filled with more sandy sediment. Bioclastic material includes fragments of shells, corals and echinoderms. Reduction spots occur occasionally.
Color of burrow is 5Y 5/3.
Olive grey (2.5Y 5/2) clay with reduction spots, structureless, no obvious bioturbation. There is a decrease in fossil content from bottom to top of this lowest unit, which includes forams, shell and coral fragments. Also several dropstones were observed in this unit.
Pleistocene
1
2
3
4
5
6
7+c.c.
Total length: 369 cm

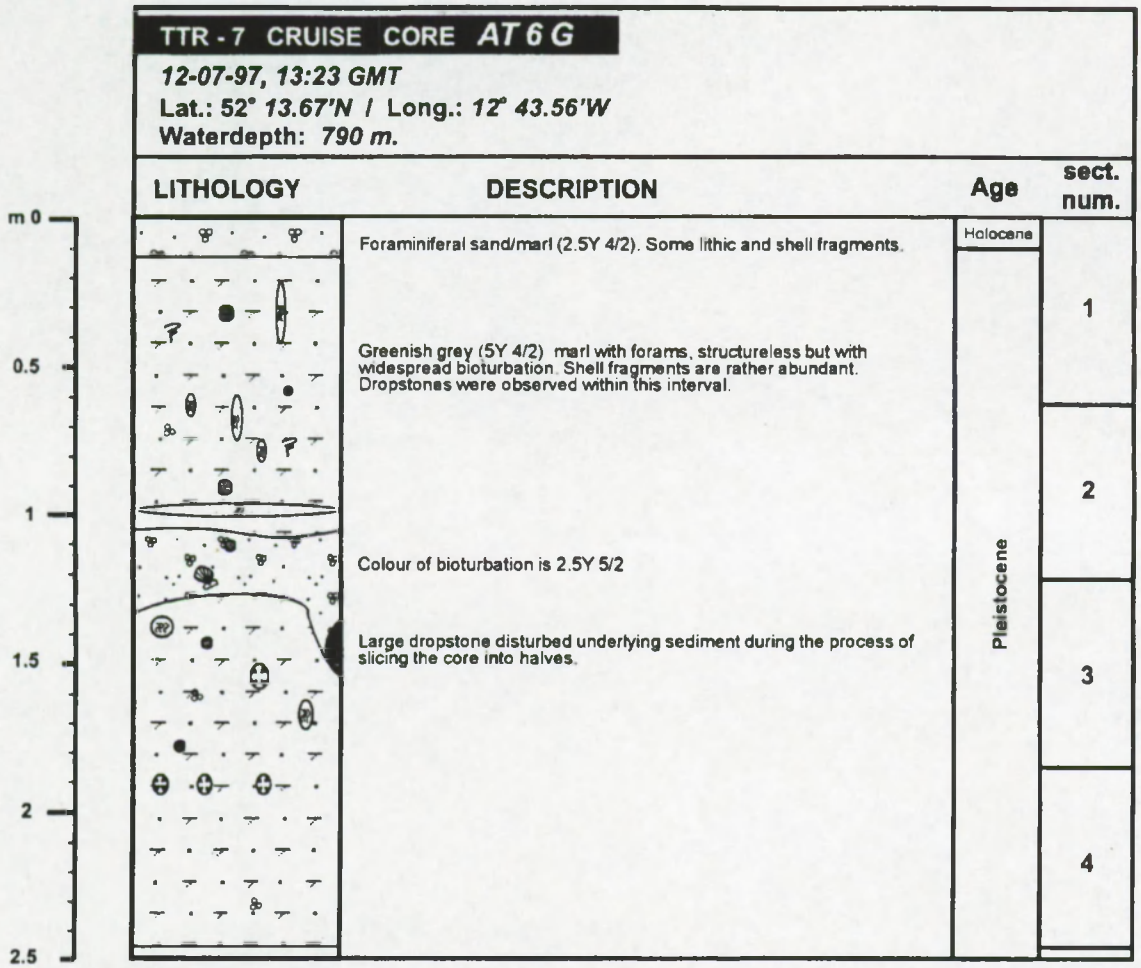

Total length: 247 cm

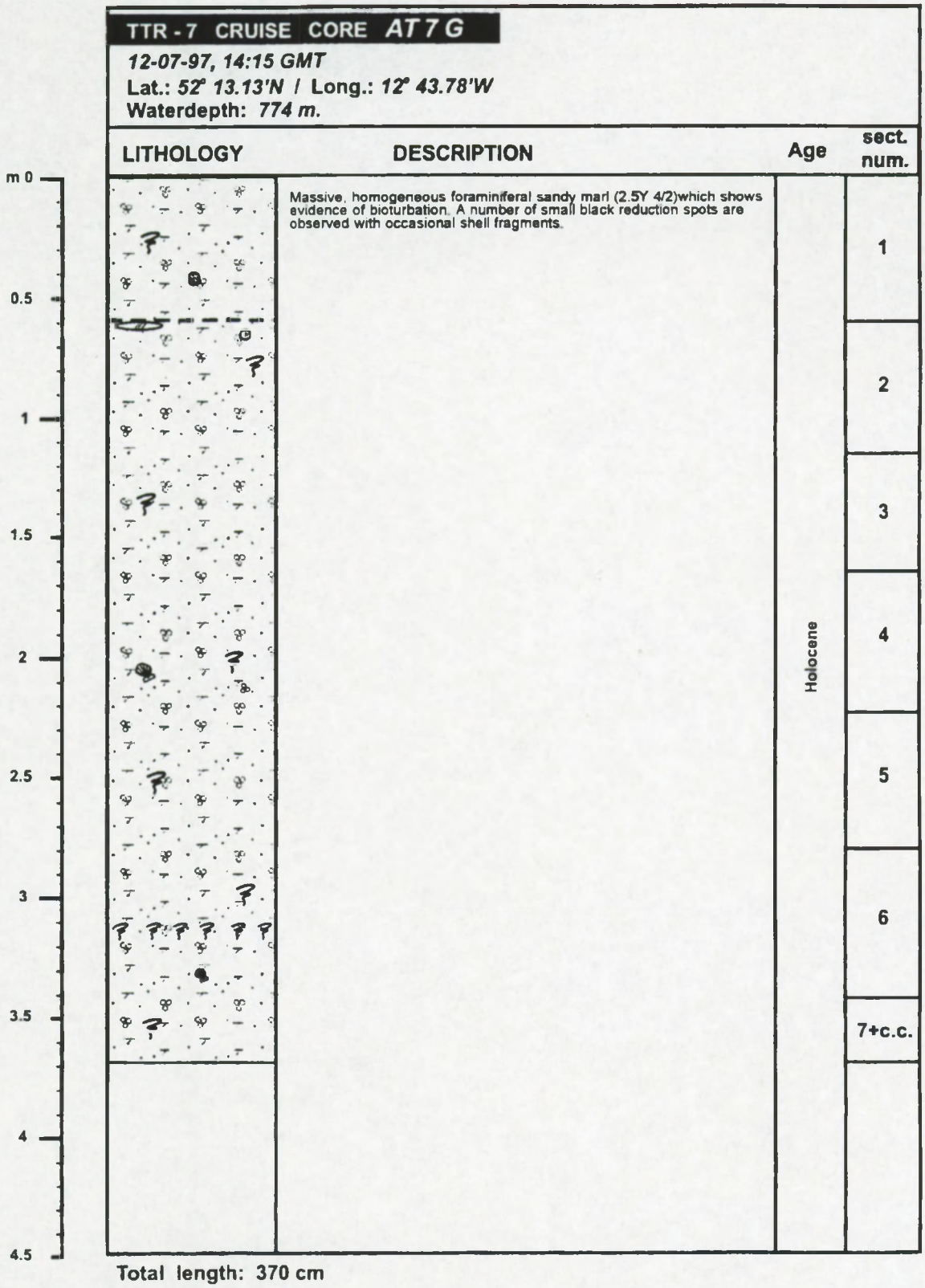
TTR - 7 CRUISE CORE AT 7 G
12-07-97, 14:15 GMT
Lat.: 52° 13.13'N / Long.: 12° 43.78'W
Waterdepth: 774 m.
LITHOLOGY
DESCRIPTION
Age
sect. num.
Massive, homogeneous foraminiferal sandy marl (2.5Y 4/2)which shows evidence of bioturbation. A number of small black reduction spots are observed with occasional shell fragments.
Holocene
m 0
0.5
1
1.5
2
2.5
3
3.5
4
4.5
1
2
3
4
5
6
7+c.c.
Total length: 370 cm

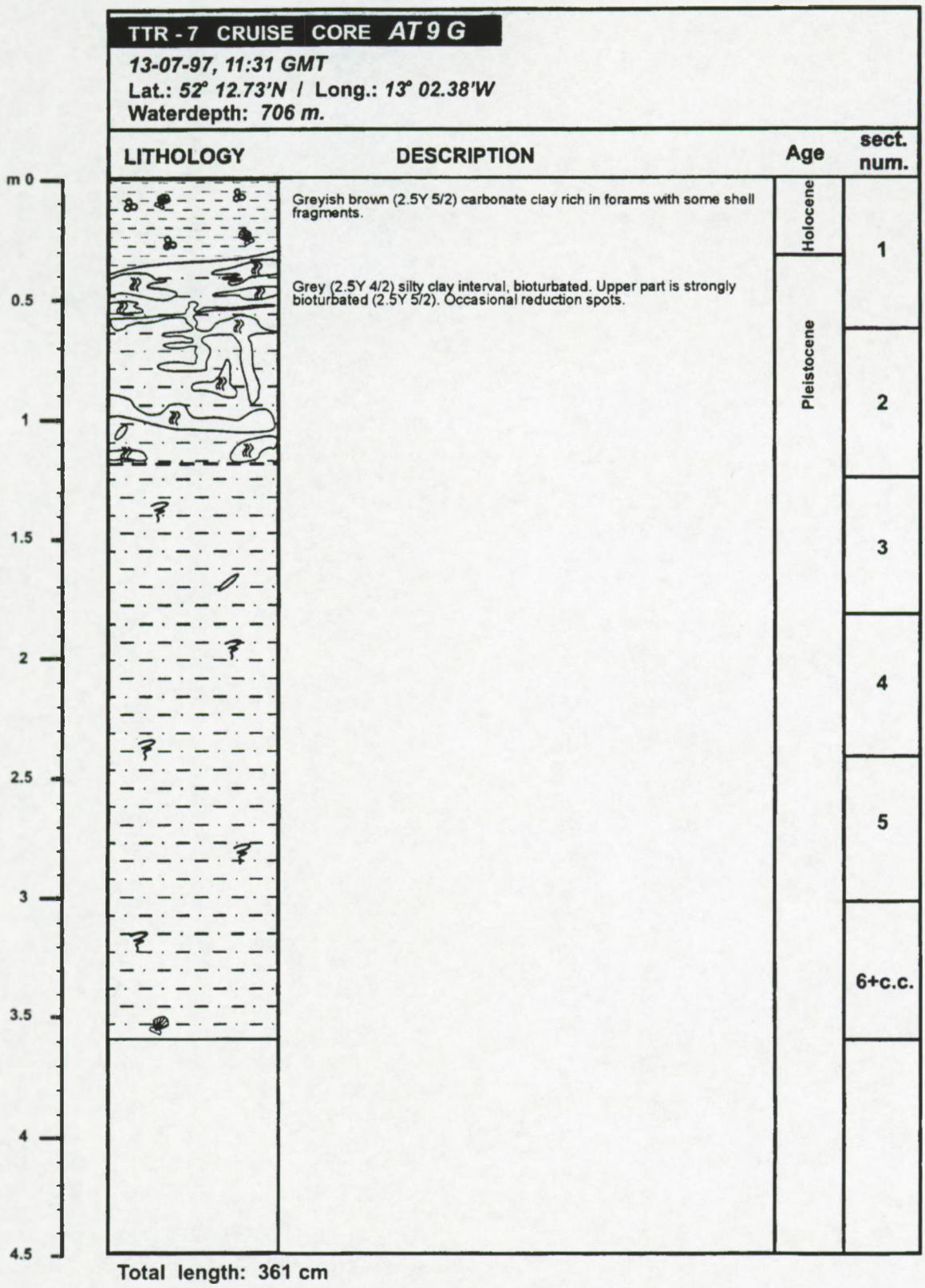
TTR - 7 CRUISE CORE AT 9 G
13-07-97, 11:31 GMT
Lat.: 52° 12.73'N / Long.: 13° 02.38'W
Waterdepth: 706 m.
LITHOLOGY
DESCRIPTION
Age
sect. num.
m 0
0.5
1
1.5
2
2.5
3
3.5
4
4.5
Greyish brown (2.5Y 5/2) carbonate clay rich in forams with some shell fragments.
Grey (2.5Y 4/2) silty clay interval, bioturbated. Upper part is strongly bioturbated (2.5Y 5/2). Occasional reduction spots.
Holocene
Pleistocene
1
2
3
4
5
6+c.c.
Total length: 361 cm

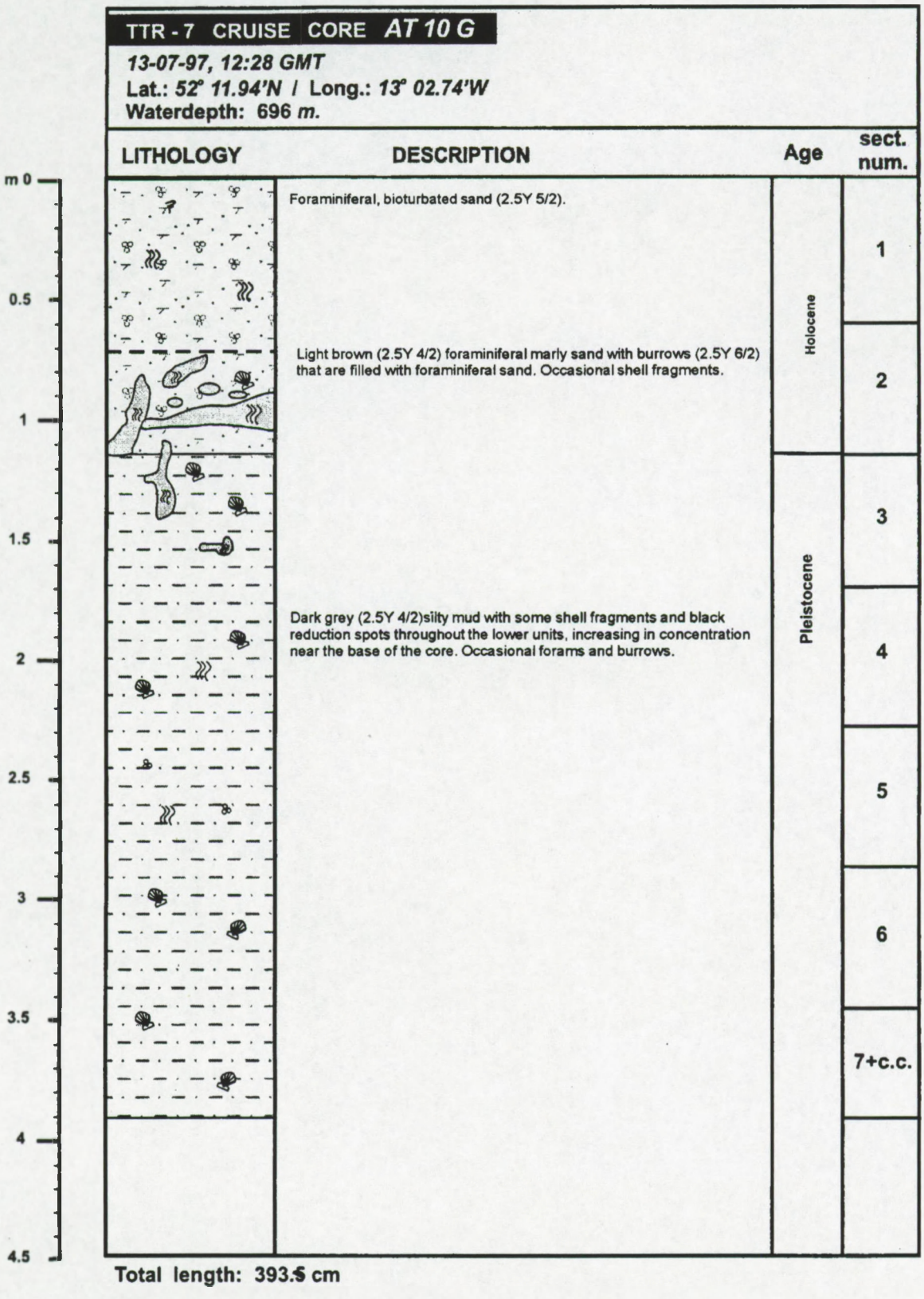
TTR - 7 CRUISE CORE AT 10 G
13-07-97, 12:28 GMT
Lat.: 52° 11.94'N / Long.: 13° 02.74'W
Waterdepth: 696 m.
LITHOLOGY
DESCRIPTION
Age
sect. num.
m 0
0.5
1
1.5
2
2.5
3
3.5
4
4.5
Foraminiferal, bioturbated sand (2.5Y 5/2).
Light brown (2.5Y 4/2) foraminiferal marly sand with burrows (2.5Y 6/2) that are filled with foraminiferal sand. Occasional shell fragments.
Dark grey (2.5Y 4/2)silty mud with some shell fragments and black reduction spots throughout the lower units, increasing in concentration near the base of the core. Occasional forams and burrows.
Holocene
Pleistocene
1
2
3
4
5
6
7+c.c.
Total length: 393.5 cm

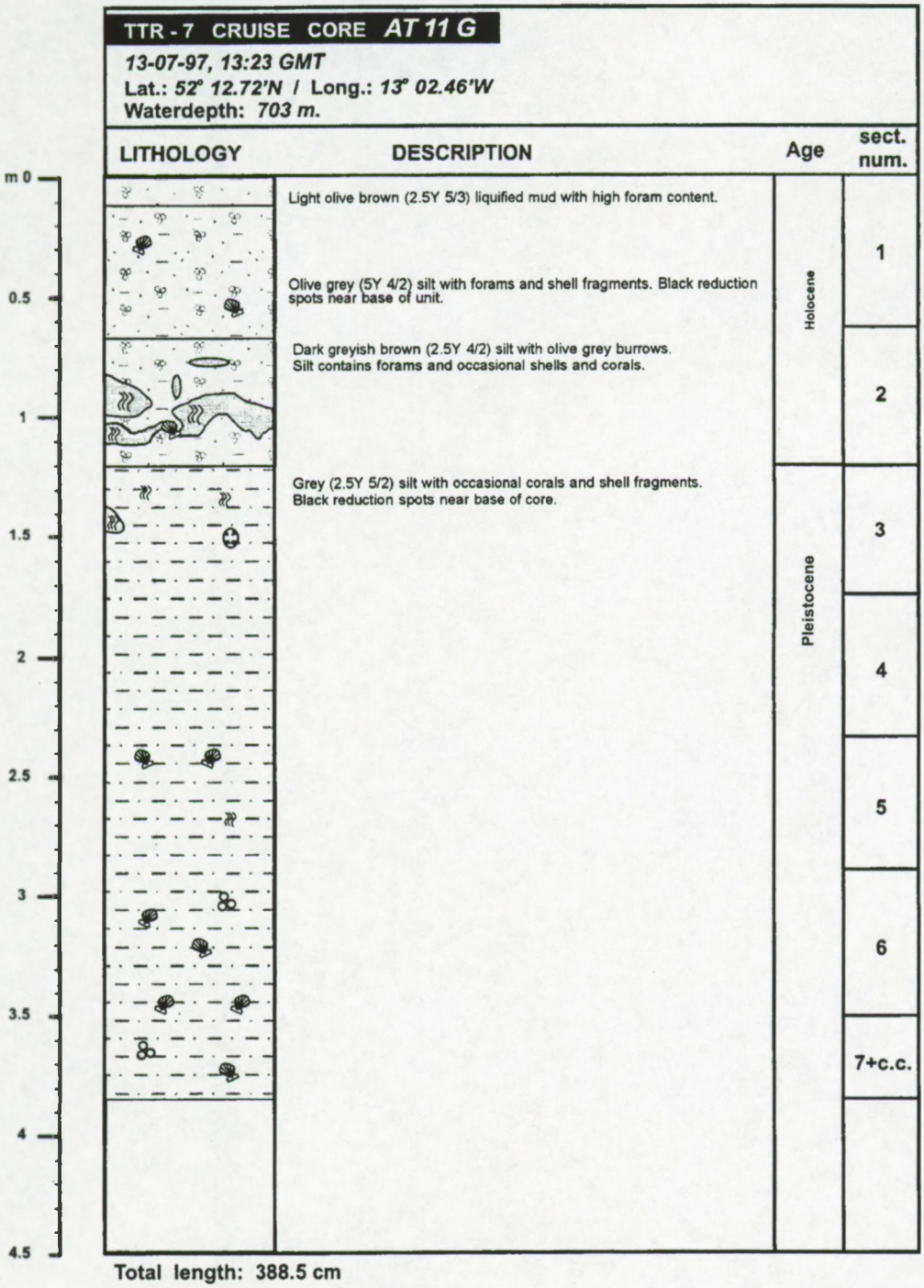

Total length: 388.5 cm

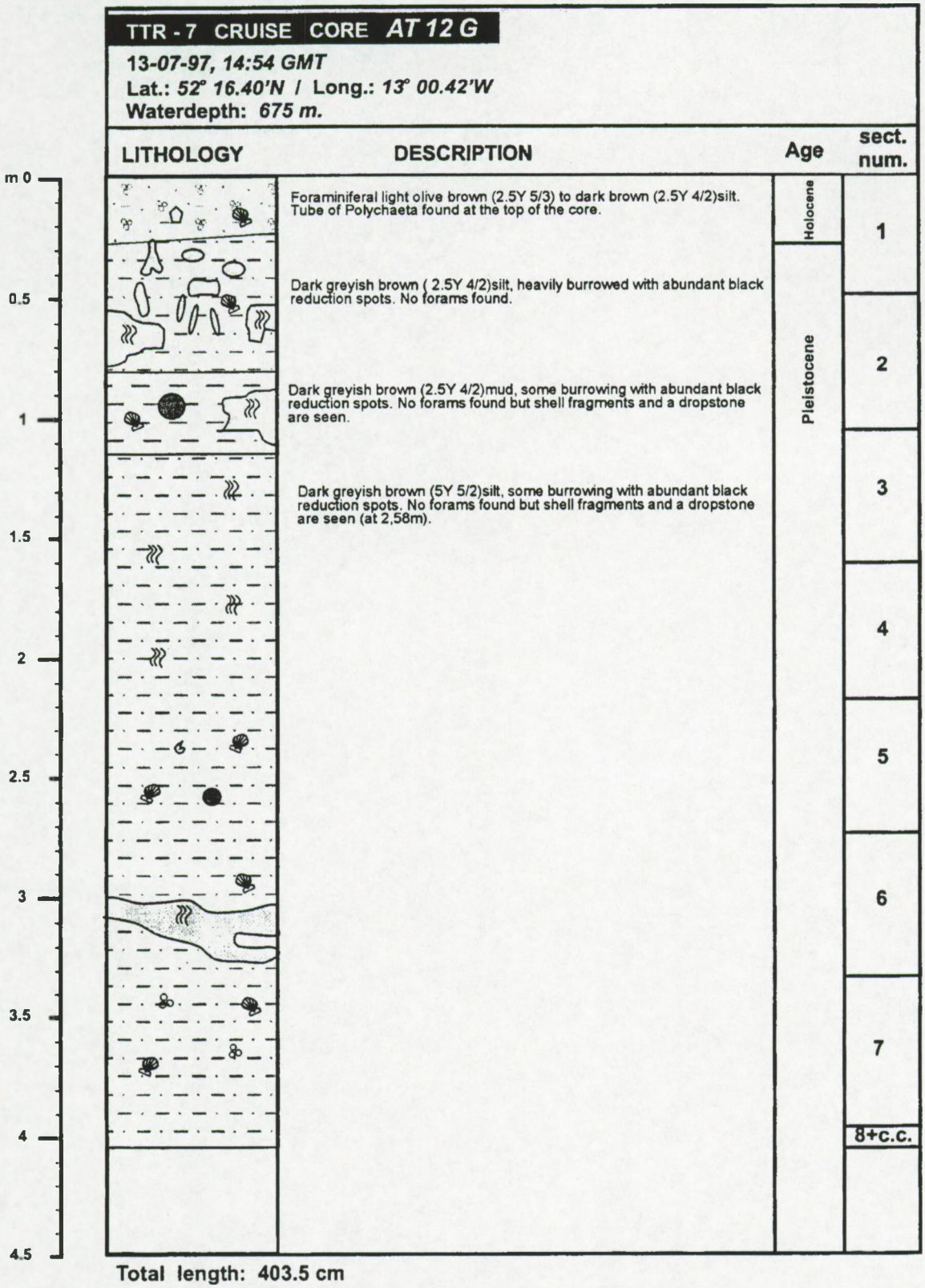
TTR - 7 CRUISE CORE AT 12 G
13-07-97, 14:54 GMT
Lat.: 52° 16.40'N / Long.: 13° 00.42'W
Waterdepth: 675 m.
LITHOLOGY
DESCRIPTION
Age
sect. num.
m 0
0.5
1
1.5
2
2.5
3
3.5
4
4.5
Foraminiferal light olive brown (2.5Y 5/3) to dark brown (2.5Y 4/2)silt. Tube of Polychaeta found at the top of the core.
Dark greyish brown (2.5Y 4/2)silt, heavily burrowed with abundant black reduction spots. No forams found.
Dark greyish brown (2.5Y 4/2)mud, some burrowing with abundant black reduction spots. No forams found but shell fragments and a dropstone are seen.
Dark greyish brown (5Y 5/2)silt, some burrowing with abundant black reduction spots. No forams found but shell fragments and a dropstone are seen (at 2,58m).
Holocene
Pleistocene
1
2
3
4
5
6
7
8+c.c.
Total length: 403.5 cm

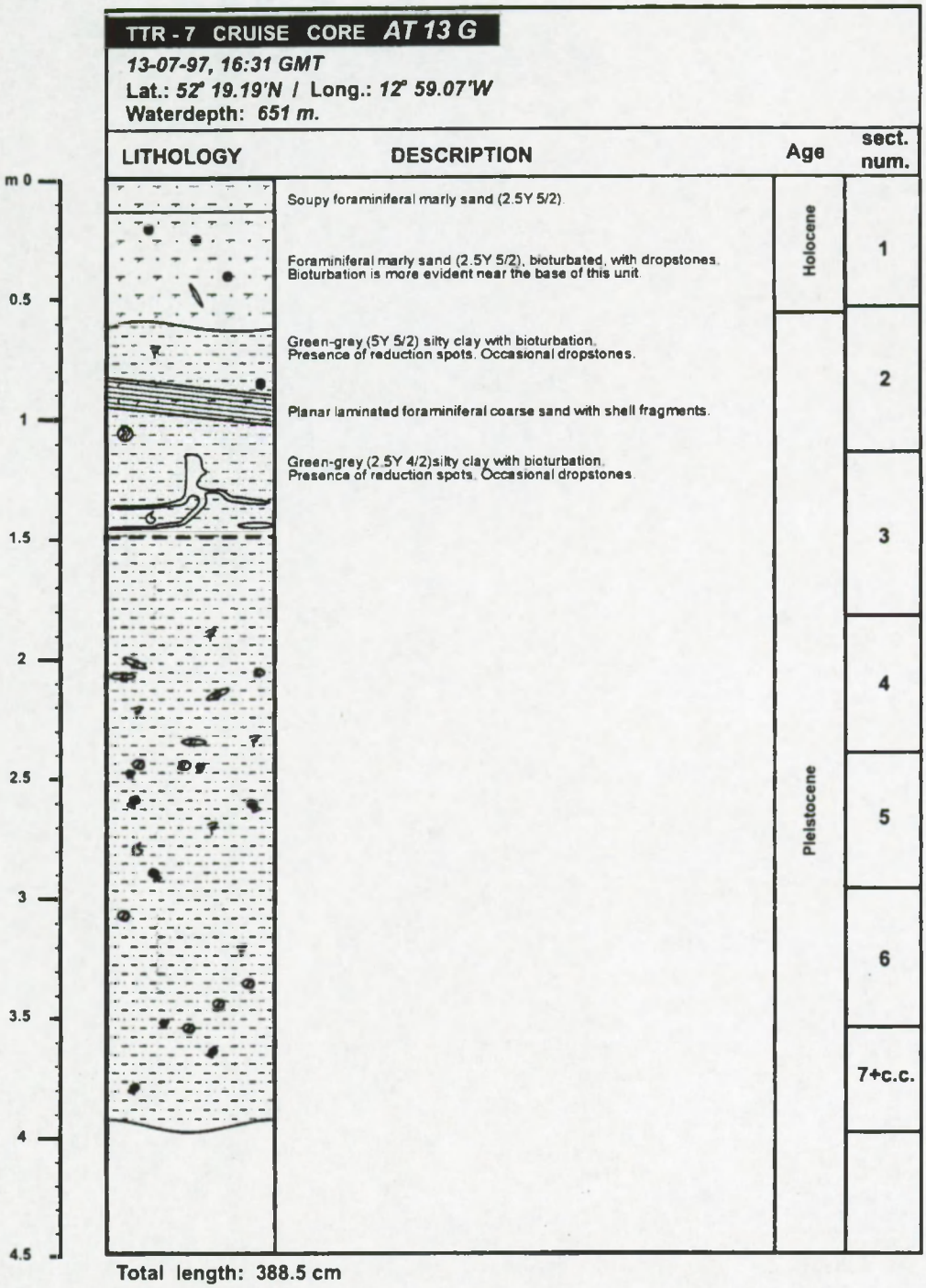

Total length: 388.5 cm

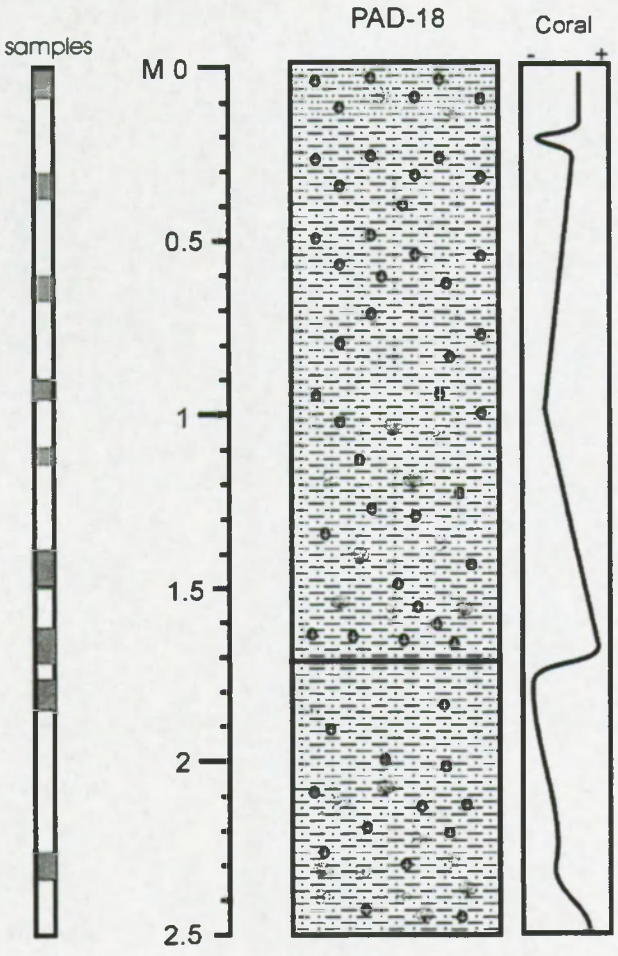

Brownish silty clay(marl) contains coral branches (Lophelia and Madrepora) Corals have a oxidised layer (Fe-Mn film) Down ward the colour changes slighty to white.

Brown-beige silty clay containing formas and coral fragments.

White marl with non oxidised coral branches, bioclasts (shells, forams, spicula)

No bioclast in a white marly sediment.

Greyish-white marl with an increasing bioclasts.

TTR - 7 CRUISE CORE *AT 17 G*

14-07-97, 12:56 GMT
Lat.: *52° 08.72'N* / Long.: *12° 49.15'W*
Waterdepth: *737 m.*

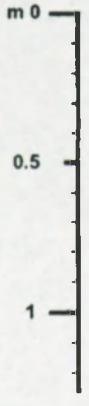

LITHOLOGY	DESCRIPTION	Age	sect. num.
	Silt (2.5Y 5/3) with high foraminiferal content. Shell and coral fragments are present.	Pleistocene + Holocene	1
	Light grey (2.5Y 7/0)marl with a very high shell content and some corals. Less forams than in the top layer.		
	Grey (5Y 6/1)silty clay with a high coral content and some black reduction spots. Shell fragments are present at the base of the unit.		2
			3+c.c.

Total length: 126 cm

TTR - 7 CRUISE CORE *AT 18G*

14-07-97, 13:46 GMT
Lat.: *52° 08.65N'* / Long.: *12° 49.89'W*
Waterdepth: *786 m.*

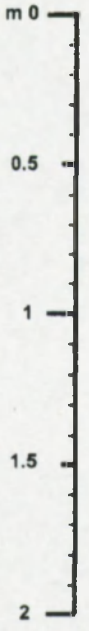

LITHOLOGY	DESCRIPTION	Age	sect. num.
	Sandy foraminiferal sediment (2.5Y 4/2) with dropstones.	Holocene	1
	Dark greyish brown (2.5Y 4/2) silty mud with dropstones, coral and shell fragments. The lower 30 cm of this unit has a variety of colors (2.5Y 6/6, 2.5Y 6/4, 5Y 7/1, 2.5Y 8/0) and has a very rich clay content. Complete shells are present.		
	Bioturbated and burrowed pale green (5Y 8/3)to brown (10Y 6/8)silty clay. No shell fragments visible.	Pleistocene	2
	Light grey (5Y 6/1) foraminiferal and bioturbated marl with echinoderm and shell fragments. Several cracks are present. Oxidated spots in the top 5 cm of this unit.		3
			4+c.c.

Total length: 198 cm

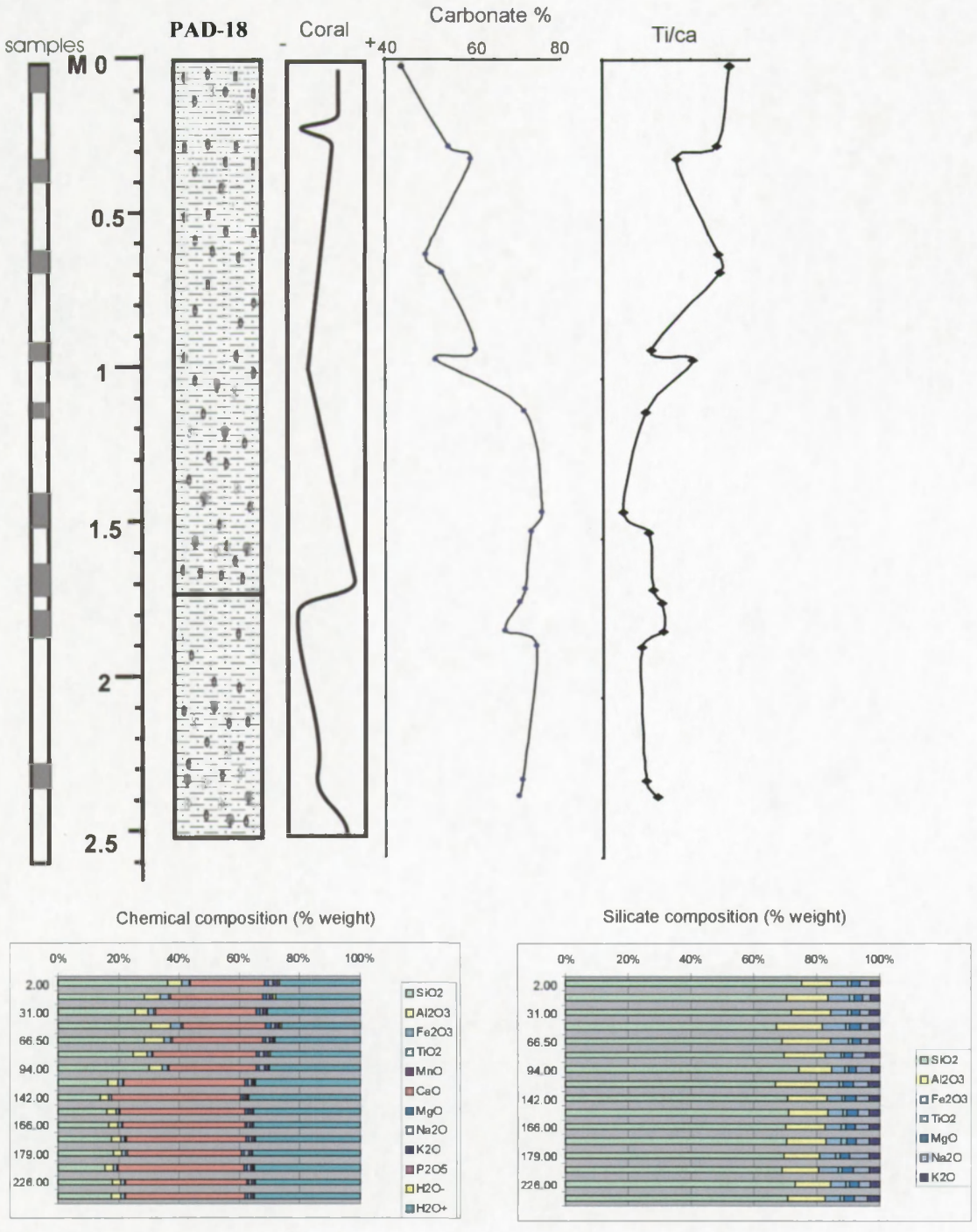

Fig. F.2.1: PAD 18 Carbonate distribution and Ti/Ca logs compared with the coral distribution and lithology. The tables illustrate the siliciclastic and total composition of the sediment.

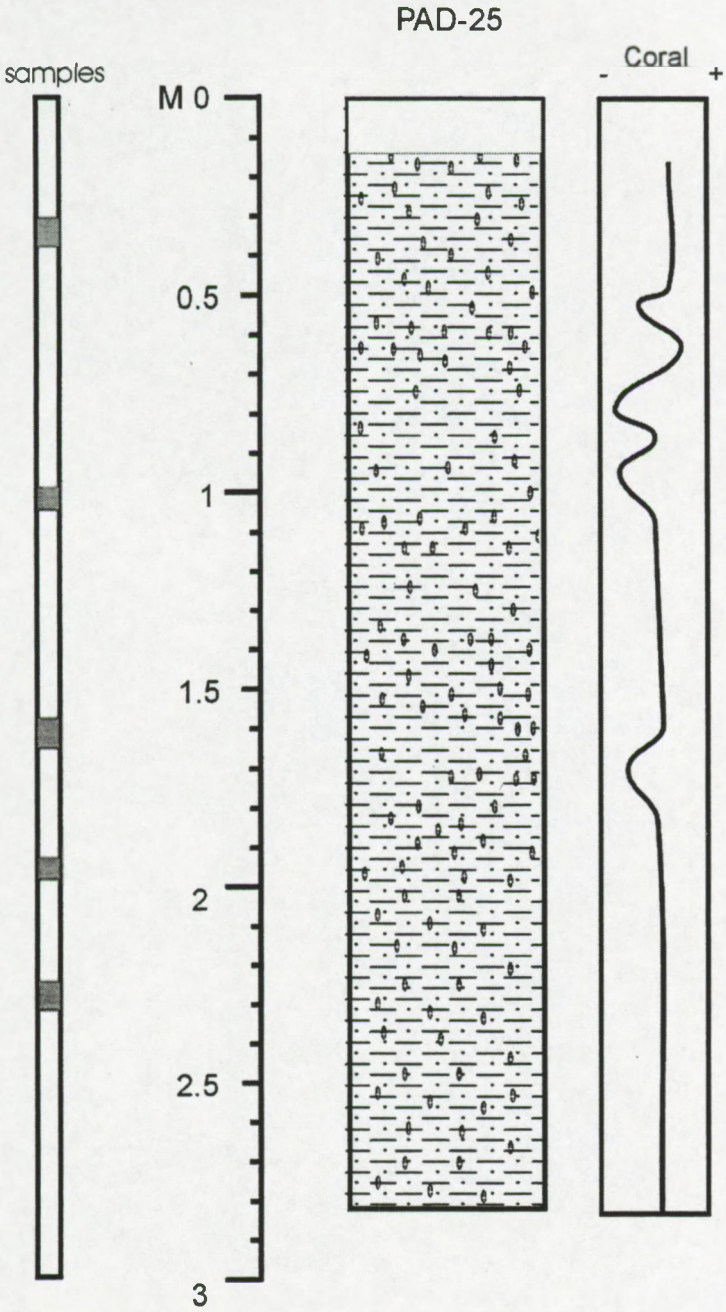

Olive green silty clay with plenty of coral fragments (lophelia) Coral fragments are well preserved and white (bioerosion is limited).

Less corals dominating Lophelia

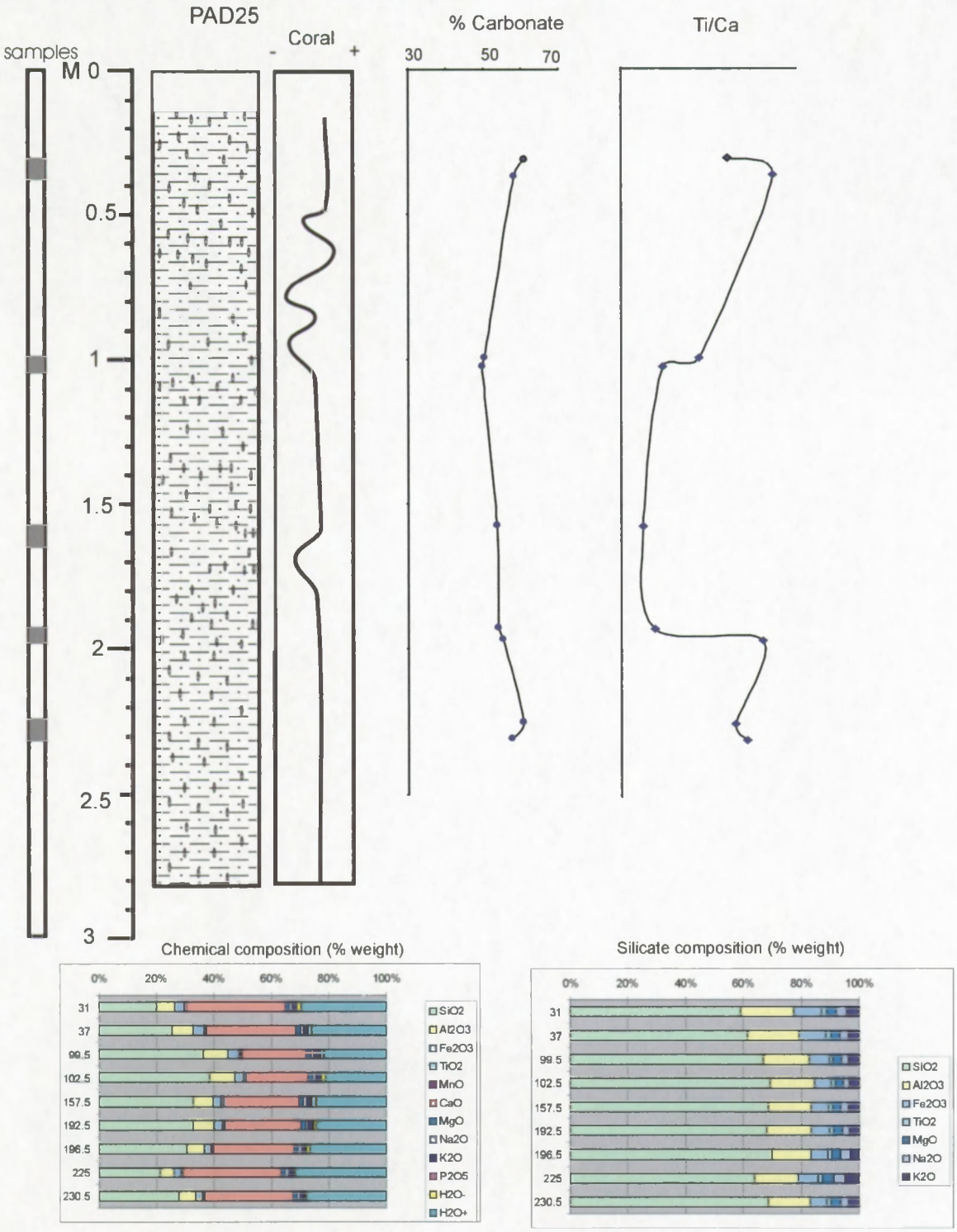

Fig. F.2.2: PAD 25 Carbonate distribution and Ti/Ca logs compared with the coral distribution and lithology. The tables illustrate the siliciclastic and total composition of the sediment.

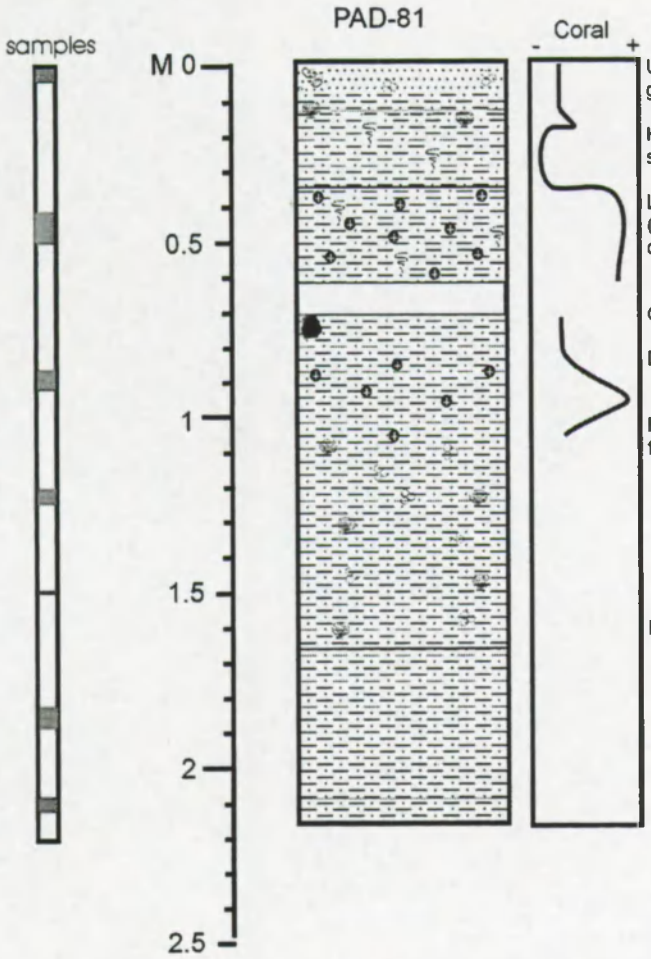

Upper centimeters contains shell and coral fragments in a grey yellowish sandy sediment.

Homogeneous greyish bioturbated silty clay (no sedimentary structures), with some forams and bioclasts

Light grey- yellowish layer consists of coral fragments (Lophelia) and shells. Reddish oxidation around the corals.

Quartz dropstone in yellowish sediment, less corals

Darker yellow, silty clay consists of coral fragments

Homogenous grey brown silty clay containing coral, shell fragments and forams.

Homogeneous brownish grey silty clay.

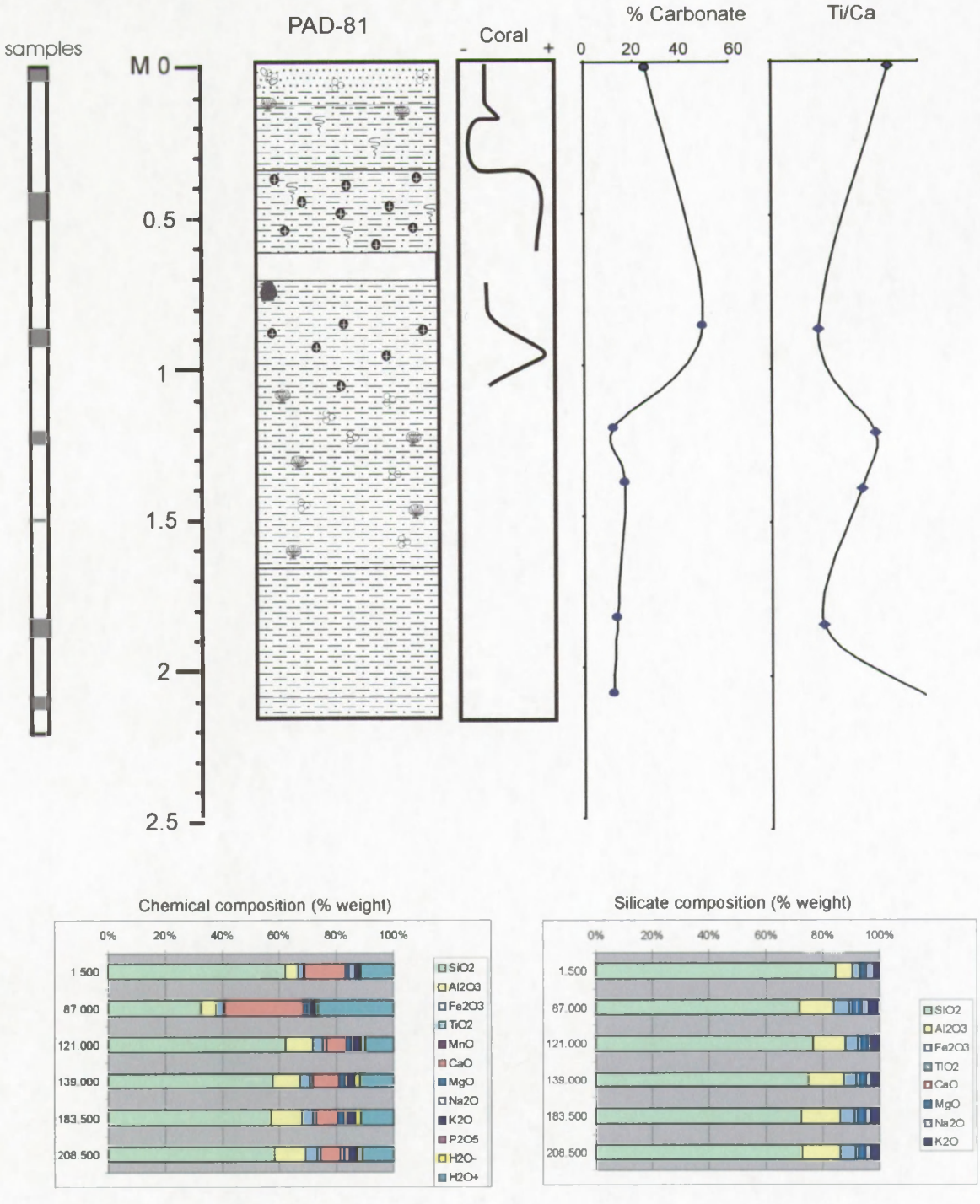

Fig. F.2.3: PAD 81 Carbonate distribution and Ti/Ca logs compared with the coral distribution and lithology. The tables illustrate the siliciclastic and total composition of the sediment.

PAD-83

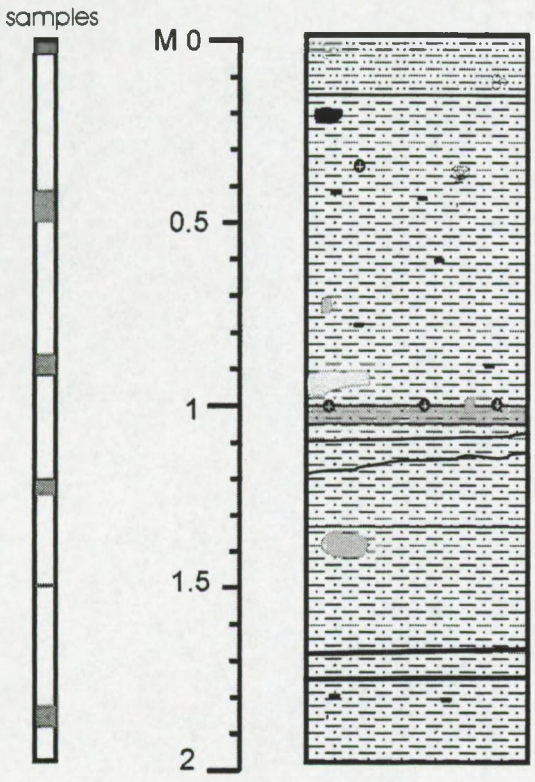

Upper centimeters (14cm) contains a dull yellow (2.5Y6/3) silty homogeous. The lower boundary of this unit is very sharp

Dull yellow (2.5Y6/3) homogenous silty clay
Lighter thin layers and spots are enriched in carbonate content (shell and coral fragments) and black streams (OM) characterizes this unit.

rockfragment

Bioturbation filled with a yellowish sandy sediment

Coral and bioclast layer, light yellow (2.5Y7/4) layer

Homogeneous greyish bioturbated silty clay (no sedimentary structures), with some forams and bioclasts

Light grey- yellowish layer consists of coral fragments (Lophelia) and shells. Reddish oxidation around the corals.

Quartz stone in yellowish sediment, less corals

Darker yellow, silty clay consists of coral fragments
Homogenous grey brown silty clay containing coral, shell fragments and forams.

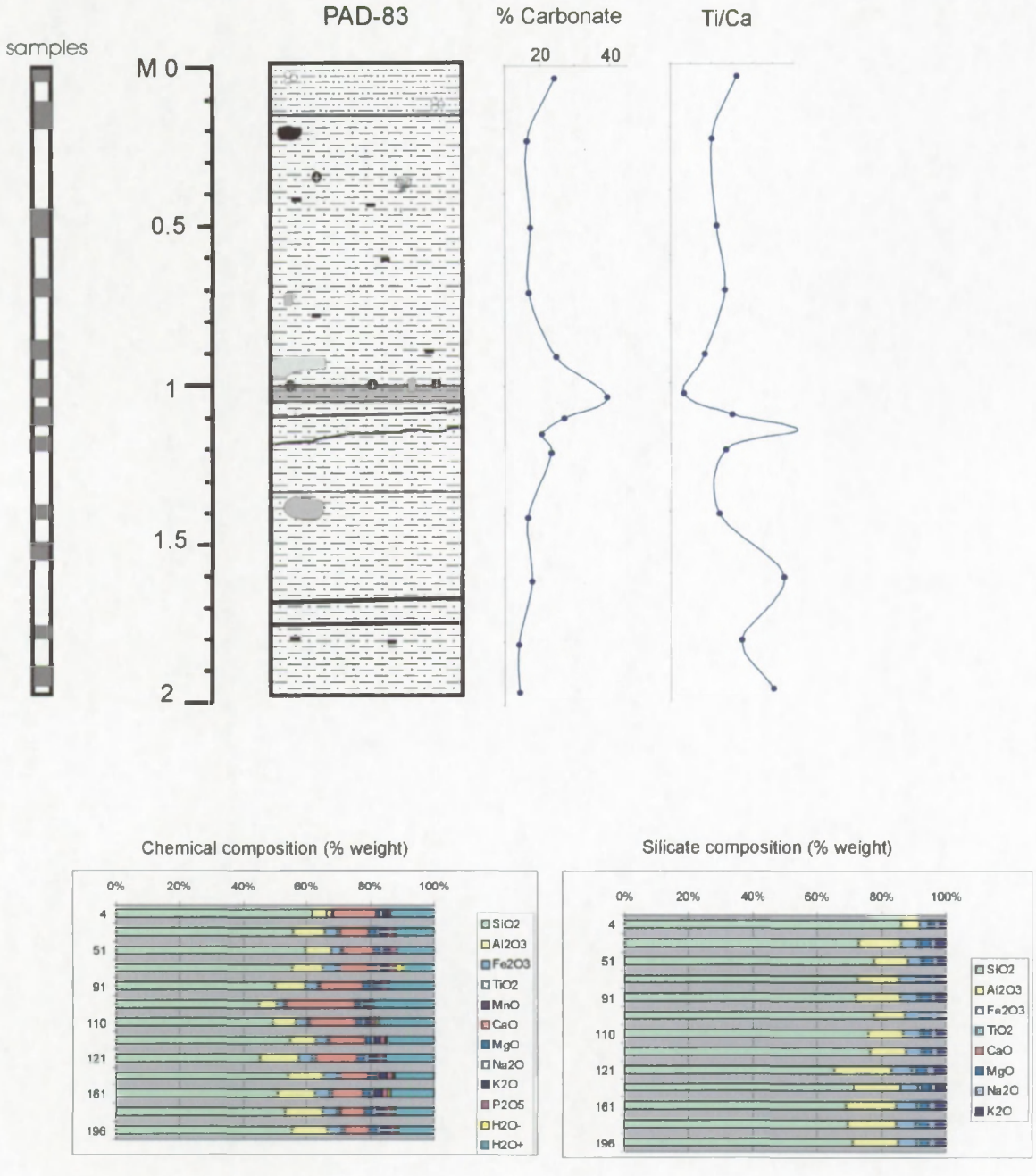

Fig. F.2.4: PAD 83 Carbonate distribution and Ti/Ca logs compared with the coral distribution and lithology. The tables illustrate the siliciclastic and total composition of the sediment.

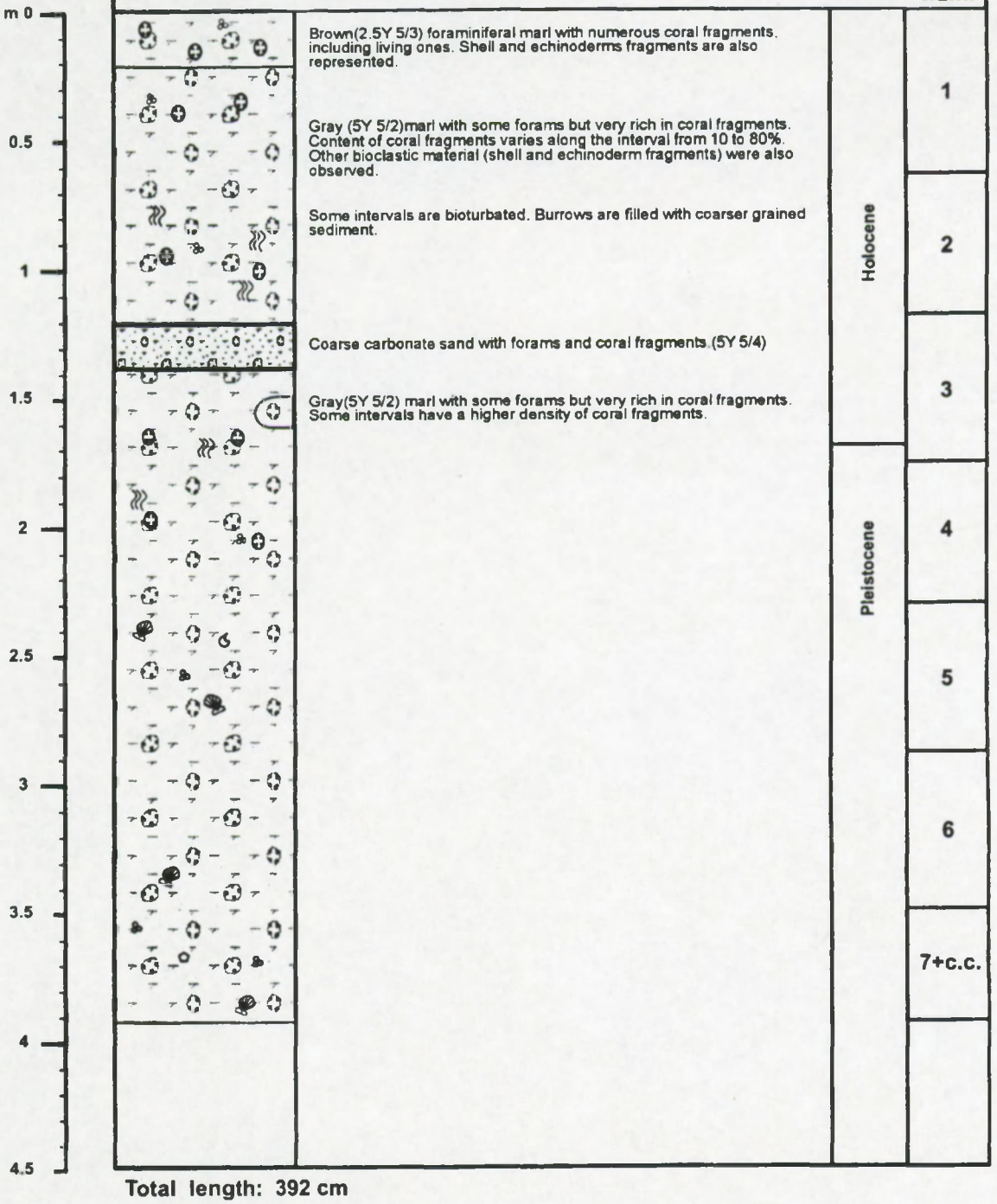
TTR - 7 CRUISE CORE AT 2 G
11-07-97, 04:48 GMT
Lat.: 52° 13.66'N / Long.: 12° 33.96'W
Waterdepth: 793 m.
LITHOLOGY
DESCRIPTION
Age
sect. num.
m 0
0.5
1
1.5
2
2.5
3
3.5
4
4.5
Brown(2.5Y 5/3) foraminiferal marl with numerous coral fragments, including living ones. Shell and echinoderms fragments are also represented.
Gray (5Y 5/2)marl with some forams but very rich in coral fragments. Content of coral fragments varies along the interval from 10 to 80%. Other bioclastic material (shell and echinoderm fragments) were also observed.
Some intervals are bioturbated. Burrows are filled with coarser grained sediment.
Coarse carbonate sand with forams and coral fragments.(5Y 5/4)
Gray(5Y 5/2) marl with some forams but very rich in coral fragments. Some intervals have a higher density of coral fragments.
Holocene
Pleistocene
1
2
3
4
5
6
7+c.c.
Total length: 392 cm

3. Mineralogical and chemical data

	PAD18	PAD18	PAD18	PAD18	PAD18	PAD18	PAD18	PAD18	PAD18	PAD18	PAD18	PAD18	PAD18
	S1	S1	S1	S1	S1	S1	S1	S2	S2	S2	S2	S2	S3
cm	1-3	26-28	30-32	60-62	66-67	90-92	93-95	14-17	46-48	52-54	70-72	74-76	3-5
depth	2.00	27.00	31.00	61.00	66.50	91.00	94.00	110.50	142.00	148.00	166.00	170.00	179.00
nummer	99/188	99/189	99/190	99/191	99/192	99/193	99/194	99/195	99/196	99/197	99/198	99/199	99/200
SiO_2	36.17	28.50	25.12	30.33	28.33	24.41	29.87	16.46	14.00	16.10	16.66	17.54	18.09
Al_2O_3	4.50	5.20	4.38	6.58	6.43	4.61	4.23	3.39	2.48	2.82	2.96	3.16	2.95
Fe_2O_3	2.49	2.81	1.96	3.37	2.28	1.80	1.70	1.63	0.97	1.06	1.21	1.23	1.27
TiO_2	0.53	0.59	0.42	0.54	0.59	0.28	0.44	0.29	0.14	0.32	0.34	0.39	0.38
MnO	0.03	0.04	0.03	0.03	0.02	0.02	0.02	0.03	0.03	0.03	0.02	0.02	0.02
CaO	24.58	30.52	33.33	27.55	29.64	33.95	28.84	40.13	42.40	41.04	40.16	39.58	37.66
MgO	1.29	1.05	0.95	1.56	1.09	0.99	0.95	0.82	0.76	0.77	0.69	0.75	0.84
Na_2O	1.58	0.99	1.03	1.22	1.05	1.47	1.93	1.18	0.78	0.81	1.06	1.04	1.62
K_2O	1.43	1.23	1.11	1.47	1.38	1.56	1.08	0.86	0.67	0.77	0.79	0.84	0.83
P_2O_5	0.10	0.15	0.11	0.13	0.08	0.07	0.09	0.15	0.19	0.15	0.13	0.12	0.11
H_2O^-	0.56	0.70	0.42	0.72	0.56	0.49	0.44	0.27	0.23	0.09	0.17	0.23	0.46
H_2O^+	26.57	27.84	30.31	25.81	27.85	29.42	29.67	34.69	36.75	35.12	35.04	34.55	35.33
Totale	99.83	99.63	99.17	99.31	99.30	99.06	99.25	99.89	99.40	99.08	99.24	99.45	99.57
Carbonate content													
Calcimeter													
TOC	0.34		0.24	0.20	0.25	0.23	0.36	0.18	0.15	0.18	0.58	0.65	0.68
$CaCO_3$	27.39		35.43	27.16	30.08	32.77	32.39	41.97	43.46	42.80	39.77	38.95	38.69
$CaCO_3$ calculated out of chemical composition	43.87	54.47	59.49	49.17	52.90	60.59	51.47	71.62	75.67	73.25	71.68	70.64	67.21
CaO carbonate	24.58	30.52	33.33	27.55	29.64	33.95	28.84	40.13	42.40	41.04	40.16	39.58	37.66
Calculated Silicate fraction													
totale-H_2O-H_2O-P_2O_5-MnO-CaOcarbonate	47.99	40.37	34.97	45.07	41.15	35.12	40.20	24.63	19.80	22.65	23.71	24.95	25.98
factor	2.08	2.47	2.84	2.20	2.41	2.82	2.47	4.06	5.02	4.37	4.19	3.99	3.83
SiO_2	75.24	70.33	71.24	66.83	68.36	68.85	73.75	66.75	70.27	70.43	69.74	69.91	69.32
Al_2O_3	9.36	12.83	12.42	14.50	15.52	13.00	10.44	13.75	12.45	12.34	12.39	12.60	11.30
Fe_2O_3	5.18	6.93	5.56	7.43	5.50	5.08	4.20	6.61	4.87	4.64	5.06	4.90	4.87
TiO_2	1.10	1.46	1.19	1.19	1.42	0.79	1.09	1.18	0.70	1.40	1.42	1.55	1.46
MgO	2.68	2.59	2.69	3.44	2.53	2.79	2.35	3.33	3.81	3.37	2.89	2.99	3.22
Na_2O	3.29	2.44	2.92	2.69	2.53	4.15	4.76	4.79	3.92	3.54	4.44	4.15	6.21
K_2O	2.97	3.04	3.15	3.24	3.33	4.40	2.67	3.49	3.36	3.37	3.31	3.35	3.18
Moleculaire ratio													
SiO2/Al2O3	13.64	9.30	9.73	7.82	7.48	8.99	11.98	8.24	9.58	9.69	9.55	9.42	10.41
SiO2/Fe2O3	38.61	26.96	34.06	23.92	33.02	36.04	46.70	26.84	38.36	40.37	36.59	37.90	37.86
SiO2/K2O	39.65	36.33	35.48	32.35	32.18	24.53	43.36	30.01	32.76	32.78	33.06	32.74	34.17
SiO2/MgO	18.81	18.20	17.73	13.04	17.43	16.54	21.09	13.46	12.36	14.02	16.19	15.69	14.44
SiO2/TiO2	90.73	64.22	79.51	74.67	63.84	115.90	90.25	75.46	132.94	66.89	65.14	59.79	63.29
Special ratio													
Fe/Ca	0.10	0.09	0.06	0.12	0.08	0.05	0.06	0.04	0.02	0.03	0.03	0.03	0.03
Ti/Ca	0.02	0.02	0.01	0.02	0.02	0.01	0.02	0.01	0.00	0.01	0.01	0.01	0.01
Mg/Ca	0.05	0.03	0.03	0.06	0.04	0.03	0.03	0.02	0.02	0.02	0.02	0.02	0.02

Table F.3.1: Chemical results and calculations of core PAD 18.

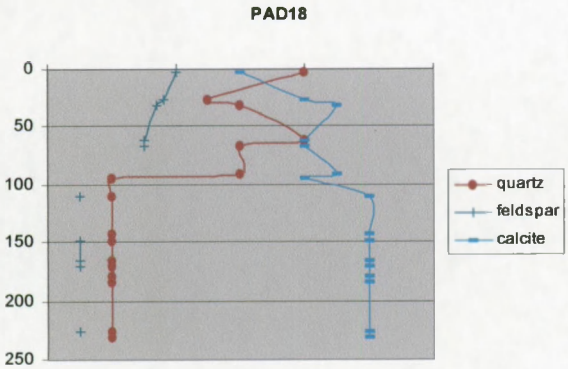

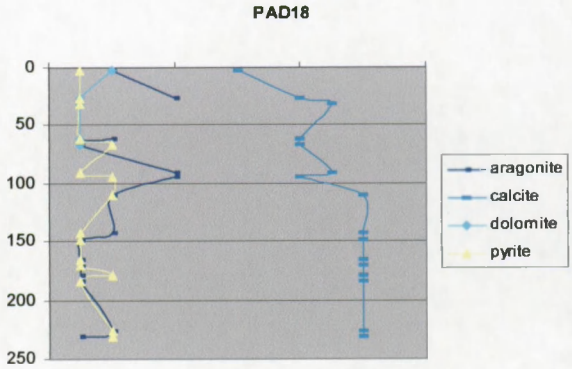

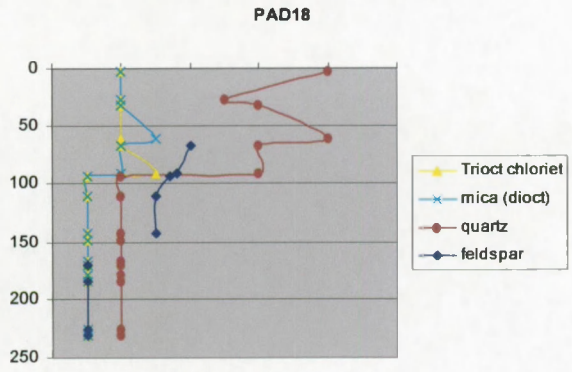

Fig. F.3.1: Mineral distribution in core PAD18 based on XRD and chemical results.

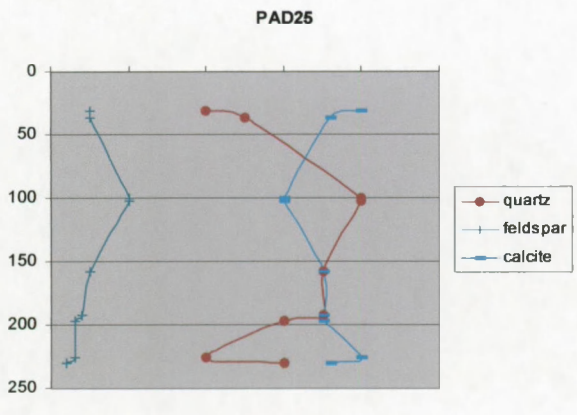

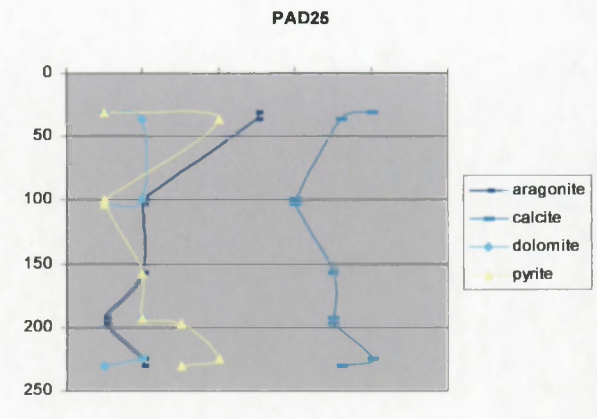

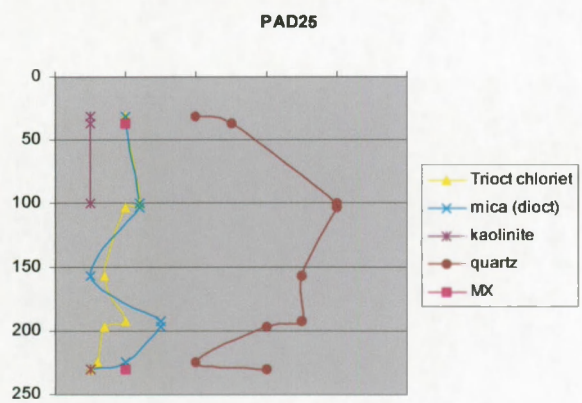

Fig. F.3.2: Mineral distribution in core PAD25 based on XRD and chemical results.

	PAD25	PAD25	PAD25	PAD25	PAD25	PAD25	PAD25	PAD25	PAD25
	S1	S1	S2	S2	S3	S3	S3	S3	S3
cm	30-32	36-38	99-100	102-103	157,5-158	192-193	196-197	224-226	230-231
depth	31	37	99.5	102.5	157.5	192.5	196.5	225	230.5
nummer	99/163	99/164	99/165	99/166	99/167	99/169	99/170	99/171	99/172
SiO_2	19.83	25.28	36.30	38.53	32.46	32.44	30.54	20.89	27.76
Al_2O_3	6.21	7.24	8.53	8.67	6.95	7.24	5.91	4.99	5.89
Fe_2O_3	3.25	3.88	3.83	3.17	2.80	3.01	2.49	2.24	2.35
TiO_2	0.60	0.68	0.72	0.78	0.70	0.77	0.59	0.54	0.62
MnO	0.03	0.03	0.04	0.04	0.04	0.04	0.02	0.02	0.02
CaO	34.66	31.46	22.70	21.91	26.54	26.68	28.17	34.25	30.84
MgO	1.16	1.35	1.56	1.57	1.36	1.46	1.29	1.23	1.36
Na_2O	1.16	1.24	1.33	1.09	1.28	1.12	1.47	1.32	1.09
K_2O	1.45	1.43	1.93	1.86	1.66	1.55	1.33	1.55	1.41
P_2O_5	0.06	0.07	0.11	0.11	0.10	0.11	0.10	0.15	0.12
H_2O^-	1.36	1.34	1.35	1.41	1.29	0.87	1.17	0.66	0.54
H_2O^+	29.47	25.88	21.62	21.30	24.45	24.53	26.61	31.34	27.92
Totale	99.24	99.89	100.02	100.43	99.63	99.82	99.69	99.18	99.93
Carbonate content									
Calcimeter									
TOC	0.41	0.41	0.92	0.83	0.93	0.87	0.92	0.62	0.61
$CaCO_3$	33.64	29.99	23.18	29.76	27.64	27.48	23.54	28.46	34.28
$CaCO_3$ calculated out of chemcial composition	61.86	56.15	40.51	39.10	47.37	47.62	50.28	61.13	55.04
CaO carbonate	34.66	31.46	22.70	21.91	26.54	26.68	28.17	34.25	30.84
Calculated Silicate fraction									
totale-H_2O-H_2O-P_2O_5-MnO-CaOcarbonate	33.66	41.10	54.20	55.67	47.21	47.59	43.62	32.76	40.48
factor	2.95	2.43	1.85	1.80	2.11	2.10	2.29	3.03	2.47
SiO_2	58.46	61.44	66.99	69.51	68.50	68.05	69.80	63.24	68.53
Al_2O_3	18.31	17.60	15.74	15.64	14.67	15.19	13.51	15.11	14.54
Fe_2O_3	9.58	9.43	7.07	5.72	5.91	6.31	5.69	6.78	5.80
TiO_2	1.77	1.65	1.33	1.41	1.48	1.62	1.35	1.63	1.53
MnO									
CaO	0.00	0.00	0.00	0.00	0.00	0.00	0.00	0.00	0.00
MgO	3.42	3.28	2.88	2.83	2.87	3.06	2.95	3.72	3.36
Na_2O	3.42	3.01	2.45	1.97	2.70	2.35	3.36	4.00	2.69
K_2O	4.27	3.48	3.56	3.36	3.50	3.25	3.04	4.69	3.48
P_2O_5									
Moleculaire ratio									
SiO2/Al2O3	5.42	5.93	7.22	7.54	7.93	7.60	8.77	7.10	8.00
SiO2/Fe2O3	16.22	17.32	25.19	32.30	30.81	28.64	32.60	24.79	31.40
SiO2/K2O	21.44	27.71	29.49	32.48	30.66	32.81	36.00	21.13	30.87
SiO2/MgO	11.47	12.56	15.61	16.46	16.01	14.90	15.88	11.39	13.69
SiO2/TiO2	43.94	49.42	67.03	65.67	61.65	56.01	68.82	51.43	59.52
Special ratio									
Fe/Ca	207.00	241.33	213.25	216.75	173.75	181.00	295.50	249.50	294.50
Ti/Ca	108.3333	129.3333	95.75	79.25	70	75.25	124.5	112	117.5
MgCa	1155.333	1048.667	567.5	547.75	663.5	667	1408.5	1712.5	1542

Table F.3.2: Chemical results and calculations of silicate fractions of core PAD25.

	PAD81	PAD81	PAD81	PAD81	PAD81	PAD81
	S1	S1	S2	S2	S2	S2
cm	1-2	86-88	10-12	38-40	73-74	98-99
depth	1.500	87.000	121.000	139.000	183.500	208.500
nummer	99157.000	99/158	99/159	99/160	99/161	99/162
SiO_2	62.220	32.270	62.240	57.910	57.580	58.650
Al_2O_3	4.590	5.460	9.400	9.430	10.670	10.940
Fe_2O_3	1.880	2.390	3.650	3.540	4.030	4.140
TiO_2	0.460	0.540	1.040	1.010	1.050	1.040
MnO	0.020	0.030	0.040	0.040	0.050	0.040
CaO	14.300	27.670	6.860	9.320	7.610	6.640
MgO	1.080	1.430	1.610	1.700	2.000	1.880
Na_2O	2.180	1.210	1.220	1.370	1.440	1.390
K_2O	1.310	1.320	2.190	2.190	2.610	2.680
P_2O_5	0.070	0.090	0.100	0.100	0.100	0.100
H_2O^-	0.486	1.110	1.785	1.705	2.102	2.145
H_2O^+	11.599	26.254	9.726	11.915	11.360	10.748
Totale	100.195	99.774	99.862	100.230	100.602	100.393
Carbonate						
Calcimeter						
TOC	0.38			0.57	0.75	0.85
$CaCO_3$	19.15			17.40	13.96	12.46
$CaCO_3$ calculated out of chemcial composition	25.52	49.99	12.24	16.63	13.58	11.85
CaO carbonate	14.30	28.01	6.86	9.32	7.61	6.64
Silicate fraction						
totale-H_2O-H_2O-P_2O_5-MnO-CaOcarbonate	73.72	44.28	81.35	77.15	79.38	80.72
factor	1.36	2.25	1.23	1.30	1.27	1.24
SiO_2	84.56	72.71	76.40	75.23	72.97	72.94
Al_2O_3	6.24	12.30	11.54	12.25	13.52	13.61
Fe_2O_3	2.56	5.38	4.48	4.60	5.11	5.15
TiO_2	0.63	1.22	1.28	1.31	1.33	1.29
MnO						
CaO	0.00	-0.76	0.00	0.00	0.00	0.00
MgO	1.47	3.22	1.98	2.21	2.53	2.34
Na_2O	2.96	2.73	1.50	1.78	1.82	1.73
K_2O	1.78	2.97	2.69	2.85	3.31	3.33
P_2O_5						
Moleculair ratio						
SiO2/Al2O3	23.00	10.03	11.24	10.42	9.16	9.10
SiO2/Fe2O3	87.96	35.89	45.32	43.48	37.97	37.65
SiO2/K2O	74.46	38.33	44.56	41.46	34.59	34.31
SiO2/MgO	38.64	15.14	25.93	22.85	19.31	20.92
SiO2/TiO2	179.82	79.45	79.56	76.23	72.90	74.97
Special ratio						
Fe/Ca	229.500	182.000	235.000	235.750	213.400	273.500
Ti/Ca	94.000	79.667	91.250	88.500	80.600	103.500
MgCa	715.000	922.333	171.500	233.000	152.200	166.000

Table F.3.3: Chemical results and calculations of silicate fractions for core PAD81.

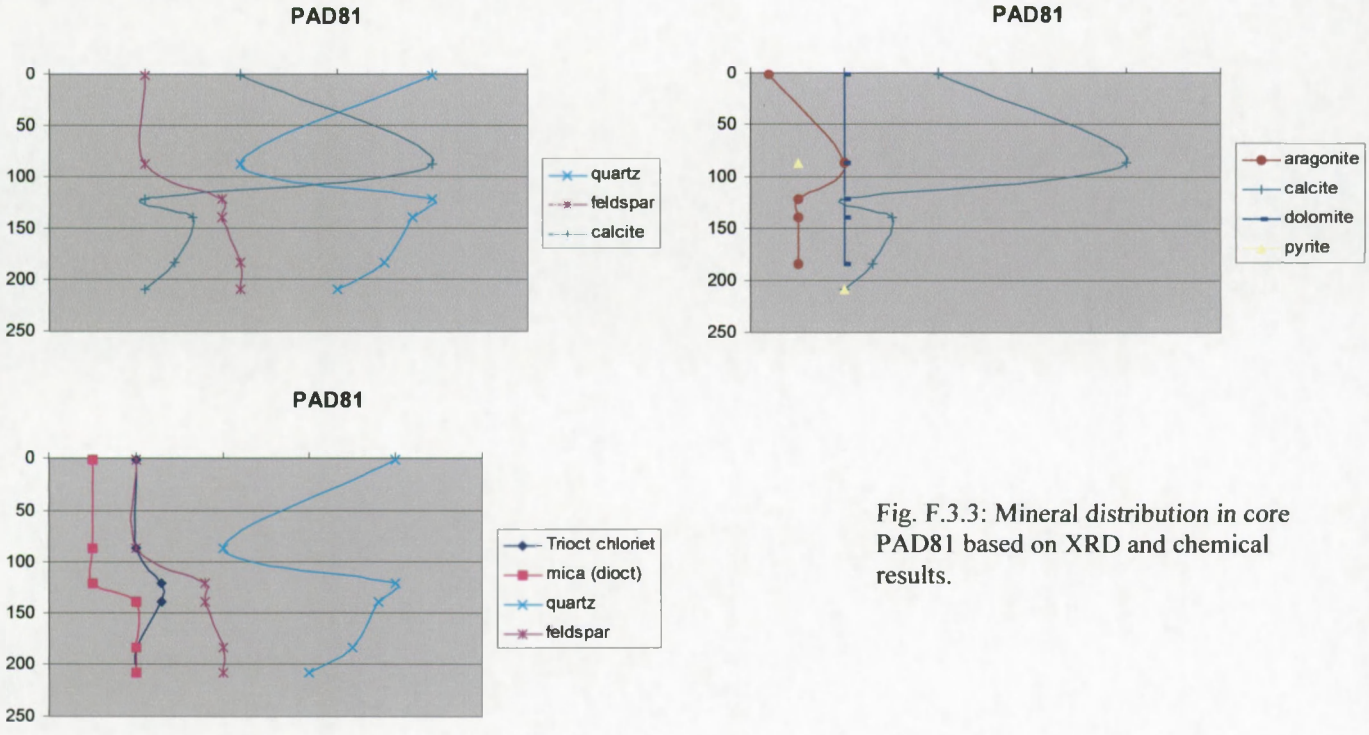

Fig. F.3.3: Mineral distribution in core PAD81 based on XRD and chemical results.

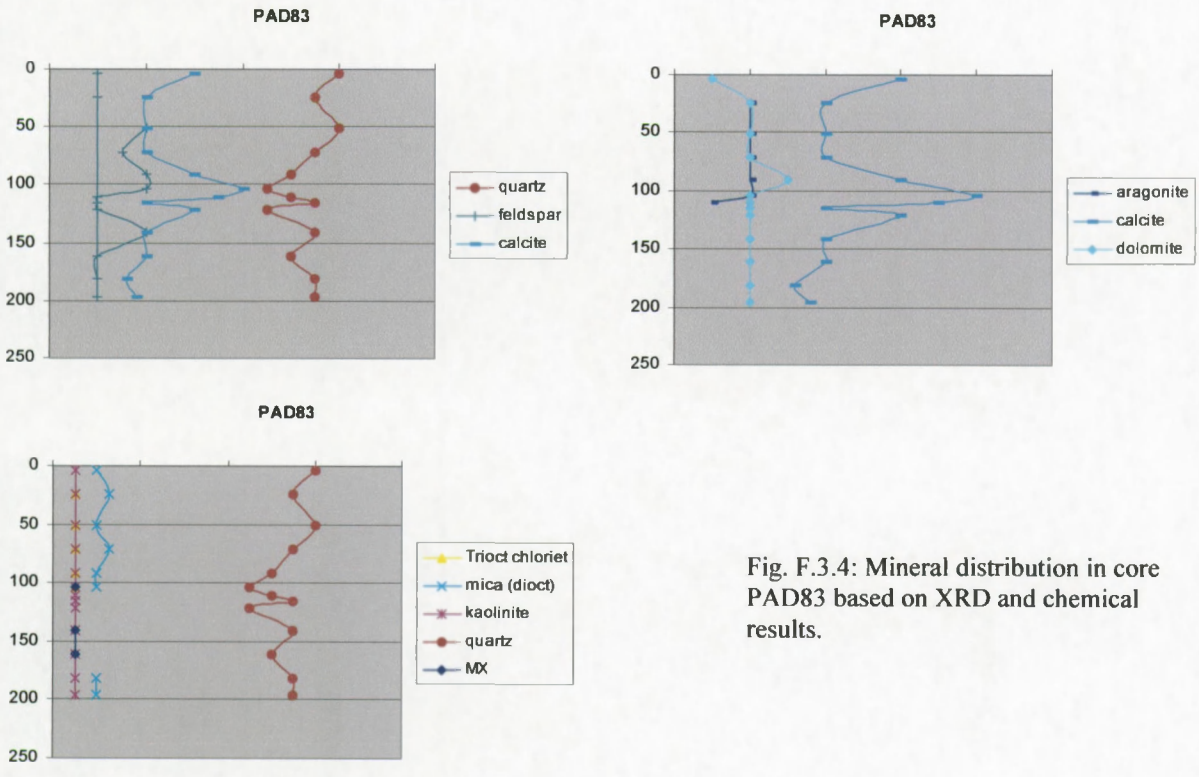

Fig. F.3.4: Mineral distribution in core PAD83 based on XRD and chemical results.

	PAD83	PAD83	PAD83	PAD83	PAD83	PAD83	PAD83	PAD83	PAD83	PAD83	PAD83	PAD83	PAD83
	S1	S1	S2	S2	S2	S3	S3	S3	S3	S3	S4	S4	S4
cm	3-5	23-25	0-2	20-22	40-42	3-4	9-11	14-16	20-22	40-42	10-12	30-32	45-47
depth	4	24	51	71	91	103.5	110	115	121	141	161	181	196
nummer	99/204	99/205	99/206	99/207	99/208	99/209	99/210	99/211	99/212	99/213	99/214	99/215	99/216
SiO_2	62.21	56.44	60.97	56.37	51.02	45.69	50.36	55.49	45.91	55.03	51.50	54.01	56.31
Al_2O_3	4.28	10.16	8.09	10.00	9.80	5.58	7.23	8.04	12.49	11.34	11.83	11.86	11.26
Fe_2O_3	1.85	4.02	3.30	4.32	3.84	2.66	3.60	3.65	4.34	4.19	4.59	4.73	4.40
TiO_2	0.39	0.81	0.64	0.78	0.57	0.58	0.61	0.66	1.10	0.93	0.92	0.97	0.92
MnO	0.02	0.05	0.04	0.05	0.05	0.04	0.04	0.03	0.05	0.05	0.04	0.05	0.04
CaO	13.56	9.2	9.65	9.42	13.86	21.88	15.10	11.51	13.02	9.28	9.92	7.92	8.04
MgO	0.96	2.14	1.94	2.27	2.16	1.38	1.46	1.51	2.15	1.97	2.00	2.08	1.99
Na_2O	1.24	1.54	1.46	1.67	1.45	1.35	1.43	1.4	1.88	1.42	1.59	1.78	1.91
K_2O	1.38	2.28	1.95	2.28	2.04	1.49	1.77	1.83	2.33	2.32	2.36	2.35	2.34
P_2O_5	0.07	0.12	0.11	0.12	0.11	0.17	0.13	0.09	0.12	0.12	0.13	0.12	0.11
H_2O^-	0.04	0.45	0.25	2.34	0.43	0.07	0.93	0.59	0.49	0.48	0.72	0.91	0.81
H_2O^+	13.63	12.29	11.89	10.07	14.42	19.42	17.72	14.88	15.46	12.61	13.84	12.63	11.36
totale-H2O-H2O-P2O5-MnO-CaOcarbonate	99.63	99.50	100.29	99.70	99.75	100.31	100.38	99.68	99.34	99.74	99.44	99.41	99.48
Carbonate content													
Calcimeter													
TOC	0.30	0.37	0.36	0.32	0.35	0.28	0.29	0.94		0.85	0.71	0.70	0.72
$CaCO_3$	26.80	18.53	19.32	18.47	23.63	37.89	32.26	20.54		16.02	17.76	15.59	13.32
$CaCO_3$ calculated out of chemical composition	24.20	16.42	17.22	16.81	24.74	39.05	26.95	20.54	23.24	16.56	17.70	14.14	14.35
CaO carbonaat	13.56	9.20	9.65	9.42	13.86	21.88	15.10	11.51	13.02	9.28	9.92	7.92	8.04
Calculated Silicate fraction													
totale-H_2O-H_2O-P_2O_5-MnO-CaOcarbonate	72.31	77.39	78.35	77.69	70.88	58.73	66.46	72.58	70.20	77.20	74.79	77.78	79.13
factor	1.38	1.29	1.28	1.28	1.41	1.71	1.51	1.37	1.42	1.29	1.33	1.28	1.26
SiO_2	85.71	72.56	78.04	72.34	71.80	78.04	76.07	76.21	64.97	71.10	68.47	69.03	70.79
Al_2O_3	5.90	13.06	10.36	12.83	13.79	9.53	10.92	11.04	17.67	14.65	15.73	15.16	14.16
Fe_2O_3	2.55	5.17	4.22	5.54	5.40	4.54	5.44	5.01	6.14	5.41	6.10	6.05	5.53
TiO_2	0.54	1.04	0.82	1.00	0.80	0.99	0.92	0.91	1.56	1.20	1.22	1.24	1.16
MgO	1.32	2.75	2.48	2.91	3.04	2.36	2.21	2.07	3.04	2.55	2.66	2.66	2.50
Na_2O	1.71	1.98	1.87	2.14	2.04	2.31	2.16	1.92	2.66	1.83	2.11	2.28	2.40
K_2O	1.90	2.93	2.50	2.93	2.87	2.54	2.67	2.51	3.30	3.00	3.14	3.00	2.94
Moleculaire ratio													
SiO2/Al2O3	24.67	9.43	12.79	9.57	8.83	13.90	11.82	11.71	6.24	8.23	7.39	7.73	8.49
SiO2/Fe2O3	89.37	37.32	49.10	34.68	35.31	45.65	37.18	40.41	28.12	34.91	29.82	30.35	34.01
SiO2/K2O	70.67	38.81	49.02	38.76	39.21	48.07	44.61	47.54	30.89	37.19	34.21	36.03	37.73
SiO2/MgO	43.46	17.69	21.08	16.66	15.84	22.21	23.13	24.65	14.32	18.74	17.27	17.42	18.98
SiO2/TiO2	212.06	92.63	126.65	96.08	119.00	104.73	109.76	111.77	55.49	78.67	74.42	74.02	81.37
Special ratio													
Fe/Ca	214.00	203.20	202.25	200.00	196.00	139.50	180.75	268.00	249.80	226.80	295.75	237.20	281.50
Ti/Ca	92.5	80.4	82.5	86.4	76.8	66.5	90	121.6667	86.8	83.8	114.75	94.6	110
MgCa	678	184	241.25	188.4	277.2	547	377.5	383.6667	260.4	185.6	248	158.4	201

Table F.3.4: Chemical results and calculations of core PAD83.

	TTR8-89G	TTR8-89G	TTR8-89G	TTR8-89G	TTR8-89G	TTR8-89G	TTR8-89G	TTR8-89G	TTR8-89G	TTR8-89G	TTR8-89G	TTR8-89G	TTR8-89G	TTR8-89G
	S1	S1	S1	S2	S2	S2	S3	S3	S3	S3	S4	S4	S4	S4
cm	9-11	29-31	49-50	20-21	29-31	40-42	10-12	30-32	36-38	44-47	0-3	20-22	40-42	48-49
depth	10.000	30.000	49.500	71.000	80.000	91.000	111.000	131.000	137.000	145.500	151.500	171.000	191.000	198.500
nummer														
SiO_2	29.100	32.590	30.220	35.470	33.150	36.110	34.280	34.010	17.800	24.130	24.570	27.110	21.910	25.640
Al_2O_3	6.220	7.060	6.200	8.190	7.160	9.300	9.400	7.320	3.600	4.250	4.240	5.730	3.720	5.800
Fe_2O_3	2.350	2.620	2.570	3.510	2.720	3.120	3.110	2.620	1.380	1.310	1.840	1.830	1.310	2.190
TiO_2	0.480	0.440	0.570	0.540	0.550	0.570	0.560	0.490	0.410	0.390	0.600	0.480	0.390	0.470
MnO	0.030	0.030	0.030	0.030	0.030	0.030	0.030	0.030	0.020	0.020	0.020	0.020	0.020	0.030
CaO	30.310	25.920	27.350	23.160	24.690	21.640	23.460	24.420	36.720	35.580	32.250	30.830	38.660	30.820
MgO	1.540	1.730	1.630	2.030	1.790	2.010	1.960	1.640	0.980	0.980	1.010	1.310	0.930	1.400
Na_2O	1.280	1.420	1.570	1.580	1.600	1.470	1.480	1.370	1.440	1.180	1.450	1.390	1.120	1.320
K_2O	1.510	1.760	1.610	2.170	1.870	2.110	2.110	1.750	0.890	0.980	1.080	1.260	0.940	1.490
P_2O_5	0.110	0.110	0.100	0.130	0.110	0.120	0.130	0.120	0.120	0.110	0.100	0.110	0.200	0.150
H_2O^-	0.280	0.530	0.470	0.320	0.450	0.570	0.670	0.500	0.840	0.310	0.770	0.290	0.190	0.340
H_2O^+	26.250	25.360	27.620	23.560	25.210	22.310	22.870	25.470	34.660	31.240	30.760	29.240	31.220	30.020
Totaal	99.470	99.570	99.940	100.690	99.330	99.360	100.060	99.740	98.860	100.480	98.690	99.600	100.610	99.670
Carbonate content														
Calcimeter														
TOC	1.22	0.57	0.46	0.64	0.62	0.73	0.70	0.60	0.66	0.52	0.46	0.55	0.22	0.85
$CaCO_3$	57.00	47.00	50.00	41.00	47.00	43.00	45.00	48.00	72.00	66.00	65.00	56.00	60.00	57.00
$CaCO_3$ calculated out of chemcial composition	54.10	46.26	48.81	41.34	44.07	38.62	41.87	43.58	65.54	63.50	57.56	55.02	69.00	55.01
CaO carbonate	30.31	25.92	27.35	23.16	24.69	21.64	23.46	24.42	36.72	35.58	32.25	30.83	38.66	30.82
Calculated Silicate fraction														
totale-H_2O-H_2O-P_2O_5-MnO-CaOcarbonate	42.49	47.62	44.37	53.49	48.84	54.69	52.90	49.20	26.50	33.22	34.79	39.11	30.32	38.31
factor	2.34	2.09	2.25	1.88	2.03	1.82	1.89	2.03	3.73	3.02	2.84	2.55	3.32	2.60
SiO_2	68.12	68.14	68.07	66.77	67.42	65.60	64.84	68.95	66.40	72.99	69.70	69.04	72.70	66.71
Al_2O_3	14.56	14.76	13.97	15.42	14.56	16.90	17.78	14.84	13.43	12.85	12.03	14.59	12.34	15.09
Fe_2O_3	5.50	5.48	5.79	6.61	5.53	5.67	5.88	5.31	5.15	3.96	5.22	4.66	4.35	5.70
TiO_2	1.12	0.92	1.28	1.02	1.12	1.04	1.06	0.99	1.53	1.18	1.70	1.22	1.29	1.22
MgO	3.61	3.62	3.67	3.82	3.64	3.65	3.71	3.32	3.66	2.96	2.87	3.34	3.09	3.64
Na_2O	3.00	2.97	3.54	2.97	3.25	2.67	2.80	2.78	5.37	3.57	4.11	3.54	3.72	3.43
K_2O	3.53	3.68	3.63	4.08	3.80	3.83	3.99	3.55	3.32	2.96	3.06	3.21	3.12	3.88
Moleculaire ratio														
SiO2/Al2O3	7.94	7.83	8.27	7.35	7.86	6.59	6.19	7.88	8.39	9.63	9.83	8.03	9.99	7.50
SiO2/Fe2O3	32.91	33.06	31.25	26.86	32.39	30.76	29.30	34.50	34.28	48.96	35.49	39.37	44.45	31.12
SiO2/K2O	30.21	29.03	29.43	25.63	27.79	26.83	25.47	30.47	31.35	38.60	35.67	33.73	36.54	26.98
SiO2/MgO	12.67	12.63	12.43	11.72	12.42	12.05	11.73	13.91	12.18	16.51	16.32	13.88	15.80	12.28
SiO2/TiO2	80.60	98.47	70.48	87.32	80.13	84.22	81.38	92.27	57.72	82.26	54.44	75.09	74.69	72.53
Special ratio														
Fe/Ca	0.078	0.101	0.094	0.152	0.110	0.144	0.133	0.107	0.038	0.037	0.057	0.059	0.034	0.071
Ti/Ca	0.016	0.017	0.021	0.023	0.022	0.026	0.024	0.020	0.011	0.011	0.019	0.016	0.010	0.015
MgCa	0.051	0.067	0.060	0.088	0.072	0.093	0.084	0.067	0.027	0.028	0.031	0.042	0.024	0.045

Table F.3.5: Chemical results and calculations of core TTR8-AT-89G.

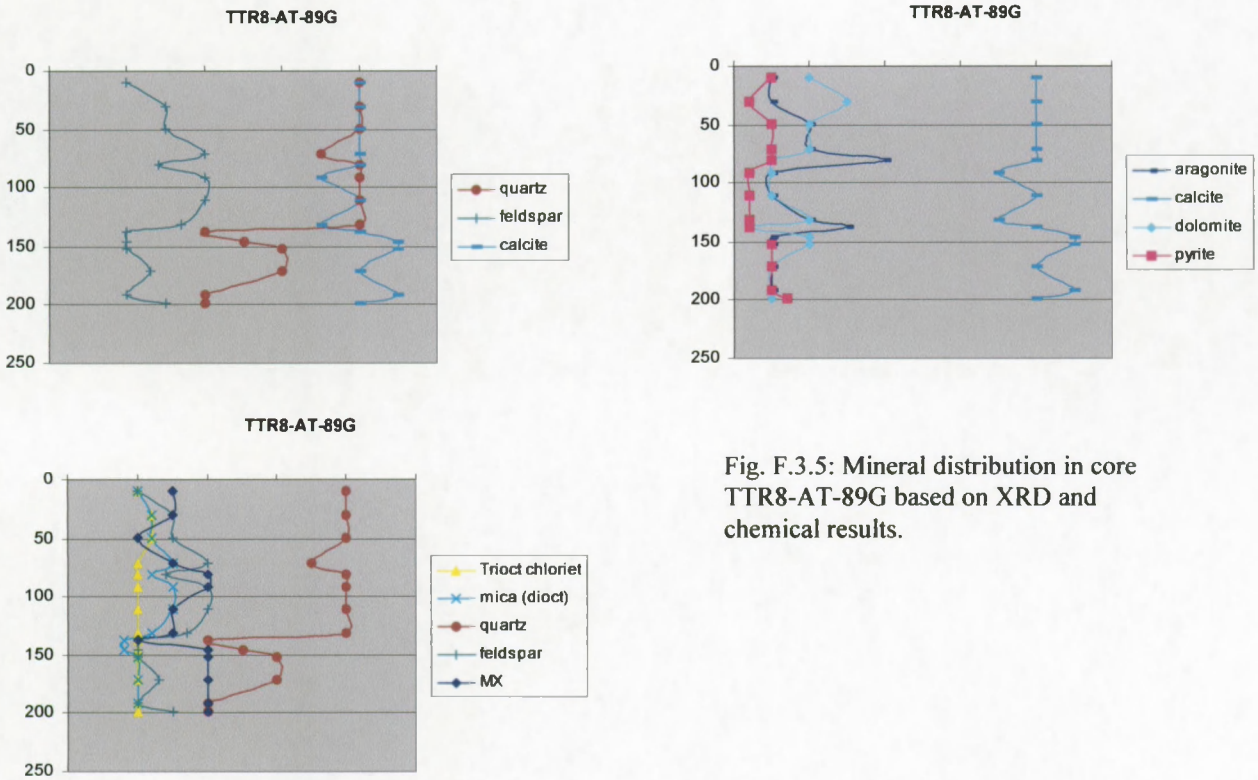

Fig. F.3.5: Mineral distribution in core TTR8-AT-89G based on XRD and chemical results.

	STATOIL ST43B	STATOIL STO110A	STATOIL ST130B	STATOIL ST154A	STATOIL ST44B	STATOIL ST134B	STATOIL ST43A
nummer	**99/217**	**99/218**	**99/219**	**99/221**	**99/222**	**99/223**	**99/225**
SiO_2	23.34	15.38	29.89	25.32	46.55	15.40	48.97
Al_2O_3	4.52	2.96	5.21	4.46	6.29	1.78	11.08
Fe_2O_3	1.91	1.19	2.11	2.00	2.90	0.91	4.21
TiO_2	0.38	0.07	0.48	0.22	0.53	0.23	0.77
MnO	0.04	0.02	0.02	0.02	0.03	0.01	0.04
CaO	36.13	38.49	31.38	33.76	19.03	42.08	11.84
MgO	0.96	0.86	0.94	1.13	1.42	0.68	1.98
Na_2O	1.22	1.03	1.01	1.21	1.29	1.28	1.41
K_2O	1.21	0.78	1.32	1.10	1.56	0.58	2.23
P_2O_5	0.16	0.08	0.07	0.09	0.08	0.15	0.11
H_2O^-	0.37	6.67	0.29	0.38	2.33	0.16	1.13
H_2O^+	30.33	32.82	27.21	29.56	17.46	36.77	15.84
Totaal	100.57	100.36	99.94	99.25	99.47	100.02	99.60
Carbonate content							
Calcimeter							
$CaCO_3$	35.23	36.01	32.01	37.61	17.92	44.93	12.91
TOC	0.26	0.58	0.17		0.28	0.56	0.32
$CaCO_3$ calculated out of chemcial composition	64.48	68.70	56.01	60.25	33.96	75.10	21.13
CaO carbonate	36.13	38.49	31.38	33.76	19.03	42.08	11.84
Calculated Silicate fraction							
totale-H_2O-H_2O-P_2O_5-MnO-CaOcarbonate	33.54	22.27	40.96	35.44	60.54	20.86	70.65
factor	3.00	4.51	2.44	2.80	1.64	4.79	1.41
SiO_2	69.99	69.31	72.93	70.91	76.49	73.84	69.04
Al_2O_3	13.55	13.34	12.71	12.49	10.34	8.54	15.62
Fe_2O_3	5.73	5.36	5.15	5.60	4.77	4.36	5.94
TiO_2	1.14	0.32	1.17	0.62	0.87	1.10	1.09
CaO	0.00	0.00	0.00	0.00	0.00	0.00	0.00
MgO	2.88	3.88	2.29	3.16	2.33	3.26	2.79
Na_2O	3.66	4.64	2.46	3.39	2.12	6.14	1.99
K_2O	3.63	3.52	3.22	3.08	2.56	2.78	3.14
Moleculaire ratio							
SiO_2/Al2O3	8.76	8.82	9.74	9.63	12.56	14.68	7.50
SiO2/Fe2O3	32.48	34.35	37.65	33.65	42.66	44.98	30.92
SiO2/K2O	30.24	30.91	35.50	36.09	46.78	41.63	34.43
SiO2/MgO	16.31	11.99	21.33	15.03	21.99	15.19	16.59
SiO2/TiO2	81.66	292.10	82.79	153.01	116.77	89.02	84.55

Table F.3.6: Chemical results and calculations of silicate fractions of cores used in the gas analysis of Statoil.

4. Scanning electron microscopy

Fig. F.4.1: TTR7-AT-16G-97cm. Foraminifer in a carbonate matrix showing early marine diagenesis and micritic cement.

Fig. F.4.2: TTR7-AT-16G-97cm. Foraminifer in a carbonate matrix. On top of the foraminifer: an euhedral dolomite crystal of 10μm.

Fig. F.4.3: Zoom of the dolomite crystal on top of the foraminifer.

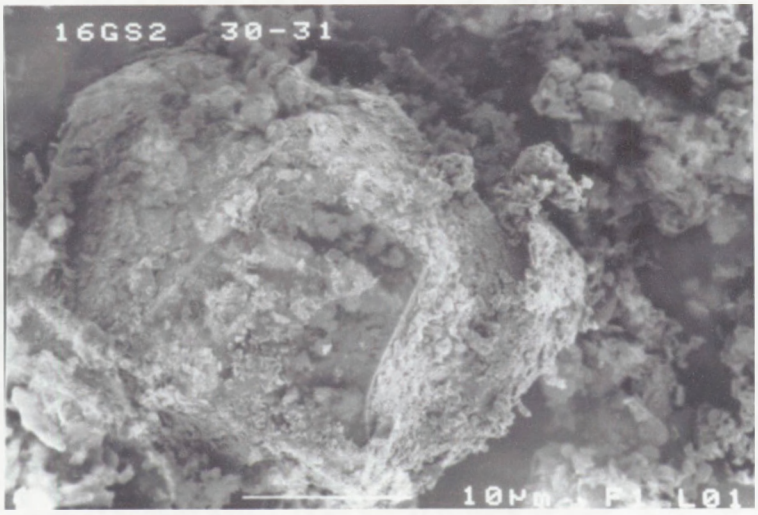

Fig. F.4.4: TTR7-AT-16G-85.5cm. Carbonate dominating matrix with an angular quartz crystal covered with carbonate.

Fig. F.4.5: TTR7-AT-16G-186cm. Fibrous aragonite needles in a coccolith matrix. The aragonite needles are most probably of the coral fragments.

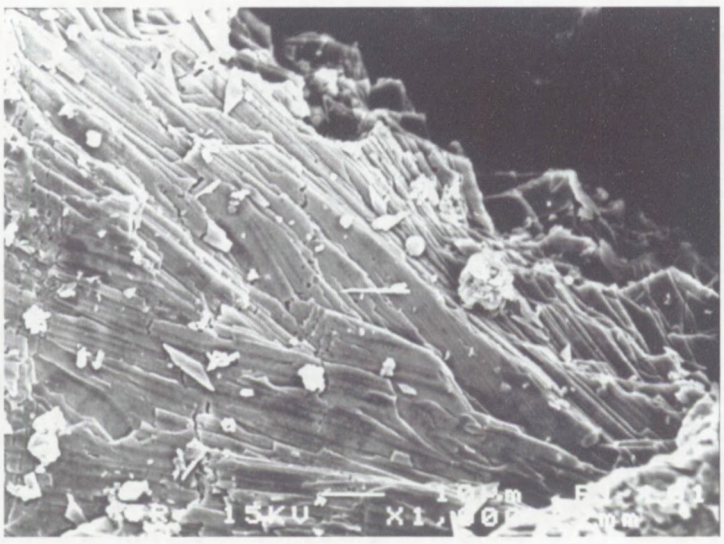

Fig. F.4.6: TTR7-AT-16G-186cm. Plate shaped aragonite needles. A variation of growth in the aragonite crystals is seen in the backscattering. Spherical shaped structures on top of the aragonite might represent calcified bacteria. These bacteria might be involved in the bioerosion of the coral skeleton (reddish colouring of Fe and Mn bacteria).

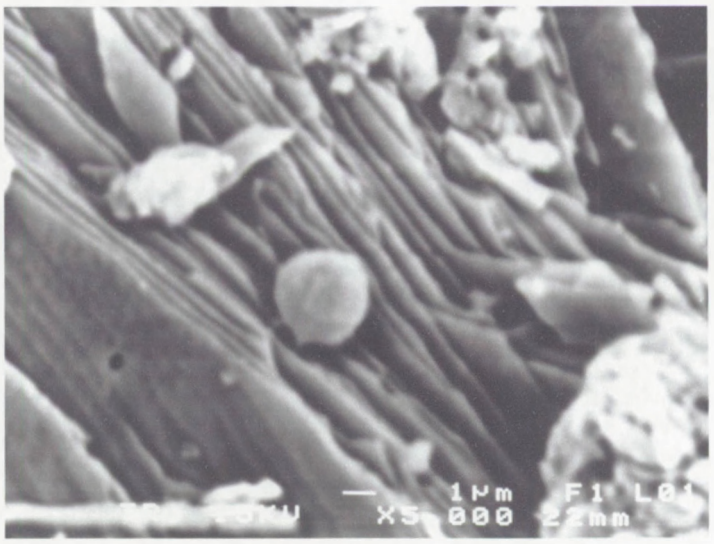

Fig. F.4.7: Zoom of F.4.6. On top of the plate shaped aragonite needles spherical shaped structures of 1µm might represent calcified bacteria. Those bacteria might be involved in the bioerosion of the coral skeleton.

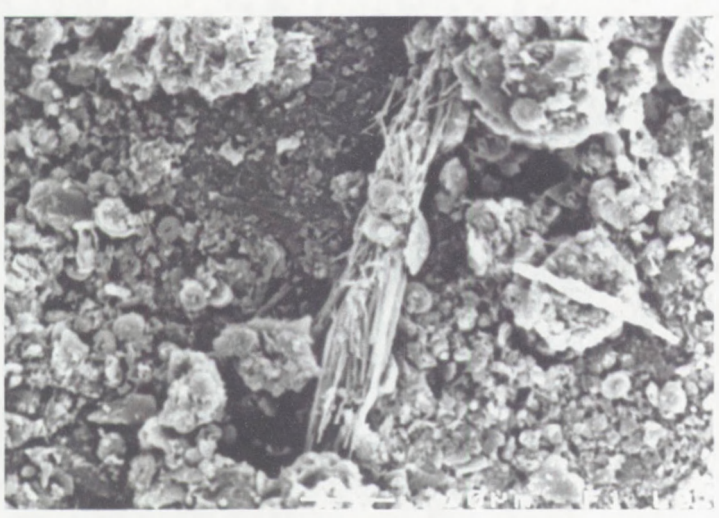

Fig. F.4.8: TTR7-AT-16G-186cm. Overview of the coccolith-rich matrix and coral fragment in the central part consisting of aragonites and calcite. The coccolith in the background are *Emilania huxleyi.*

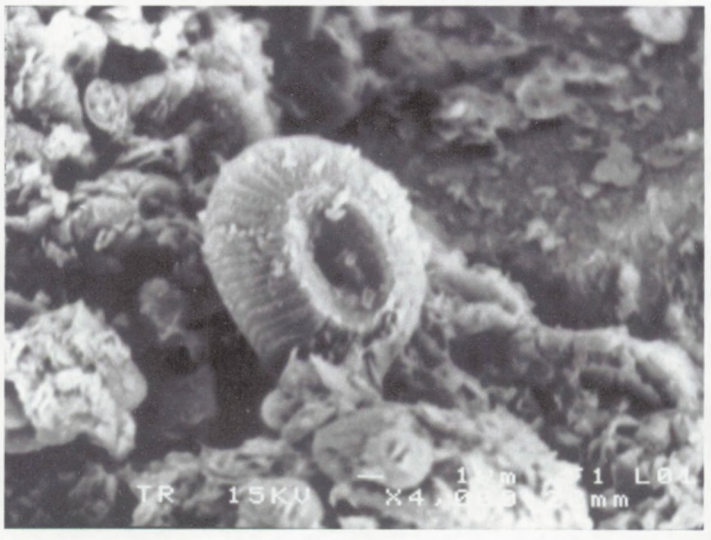

Fig. F.4.9: Zoom on *Coccolithus pelagicus* with a formation of micritic cement.

5. Petrographic and cathodoluminescent microscopy

X: crossed nicles
Scale (white line): 0.5mm

Fig. F.5.1: **A.** X of sample ST192A located on the crest of HOV15. An overview of the lithological facies in a bioclastic-rich layer. Coral fragments are seen in the middle and on the lower right side of the picture. The carbonate-rich matrix imbeds quartz, feldspar and glauconite. Large benthic and small pelagic foraminifera have been observed in the matrix.

B. X of STT110 has been taken on an outcropping Magellan mound. The thin section illustrates the fine-grained matrix with glauconite, benthic and pelagic foraminifera and shell debris. Angular quartz grains and feldspar have been observed in the carbonate-rich matrix.

C. ST28 is a background core. The matrix is similar to that of the on-mound cores. Pyrite and benthic foraminifera are very common in the sample. Bioclastic material comprises echinoderm needles, coccoliths and small coral fragments.

D. X of TTR7-AT-16G, 23-24cm, is a coral-rich zone with large bioclasts of corals. Benthic and pelagic foraminifera are omnipresent. Coarse angular grains of quartz and feldspar have been observed between the bioclasts. The texture can be defined as a mud supported packstone.

E. ST110A Organic rich matrix with bioclasts of coral and pelagic foraminifera.

F. X of E. ST110A. The fine-grained matrix is composed of quartz, feldspar and carbonate (foraminifera and coccoliths). Bioclasts occur scattered in the matrix.

G. X of ST44B located on the crest of HOV02. A coral fragment is embedded in a matrix-rich zone with angular quartz, feldspar and calcite.

H. X of TTR7-AT-16G S1, 23-24cm. Coral fragments and large benthic foraminifera are common in this zone. Glauconite has been observed inside the molds of bioclasts.

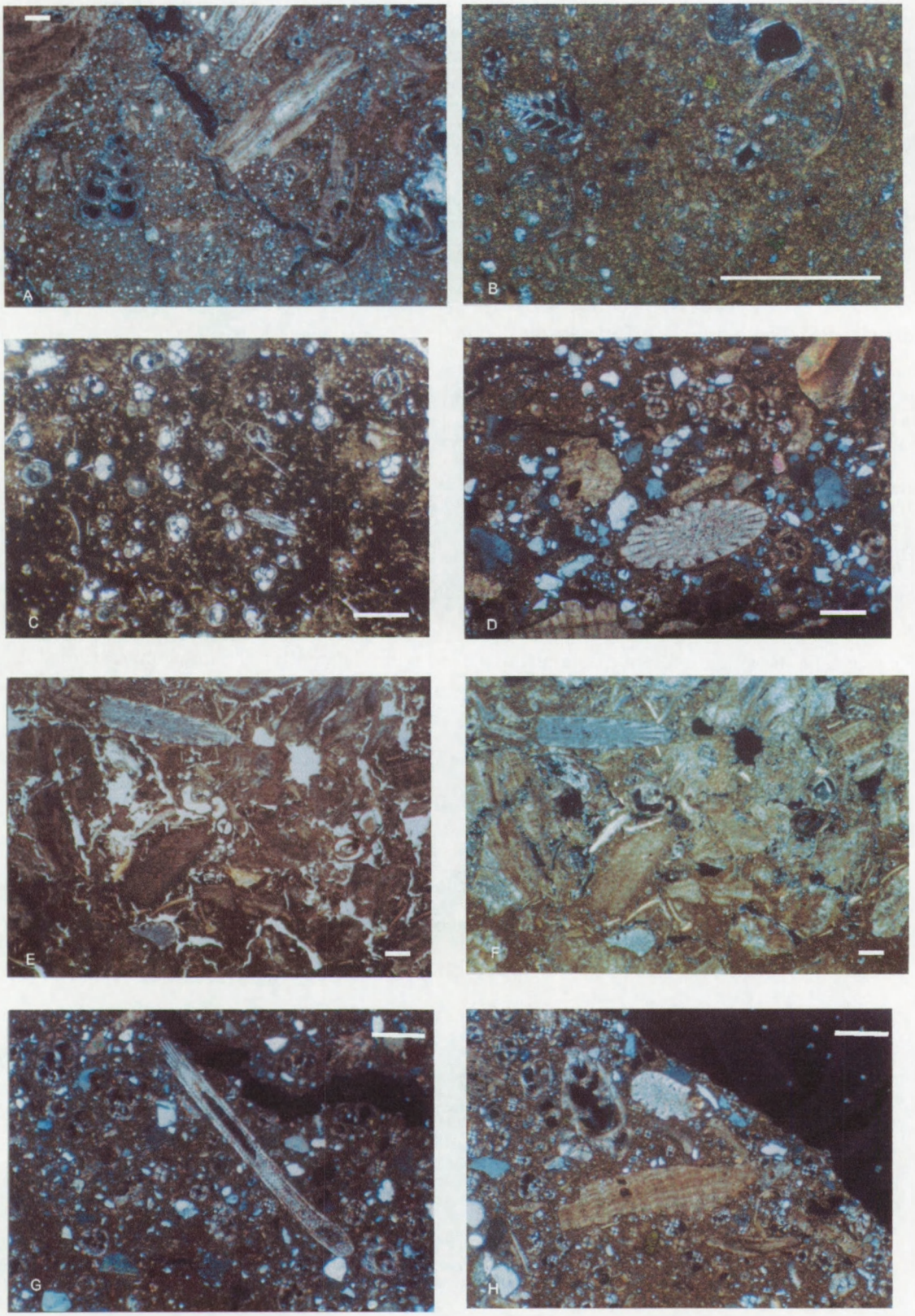
A
B
C
D
E
F
G
H

Fig. F.5.2: **A.** X Overview of the matrix in ST130 on HOV08 in a coral poor zone. The matrix is composed of quartz, feldspar and carbonates. In the matrix large and small glauconite minerals have been observed. Many fine-grained bioclasts such as coral fragments, shell fragments and echinoderm needless occur in the matrix.

B. X of ST44 located on the crest of HOV02. In the lower left corner of the picture a bioturbation with a dense concentration of quartz and feldspar has been observed. Outside the bioturbation, the matrix has a large value of carbonate and bioclasts. The quartz grains are larger outside the bioturbation than inside.

C. X of ST44B. Large angular and well-rounded quartz and feldspar grains occur in the carbonate-rich matrix. Small bioclasts of coral fragments and gastropods are embedded in the matrix.

D. X of ST44B. Detail of C. with metasediment rock fragments composed of plagioclase, quartz, mica and feldspar. Detrital calcite has been found in the matrix.

E. X of ST44B. Pelagic foraminifera test are filled with glauconite. The glauconite seemed to be authigenic formed inside the bioclastic cavities. Around and inside the forams, micritic cements have been observed.

F. X of TTR7-16G-S6, 22-22,5cm. A glauconite formation in a carbonate-rich matrix bioclast.

G. ST44B Bioclastic fragments, detrital carbonate fragments, quartz and feldspar in a carbonate-rich matrix. Inside the detrital carbonate chlorite or glauconite is formed. Bioclasts are composed of benthic foraminifera and coral fragments.

H. X idem as G.

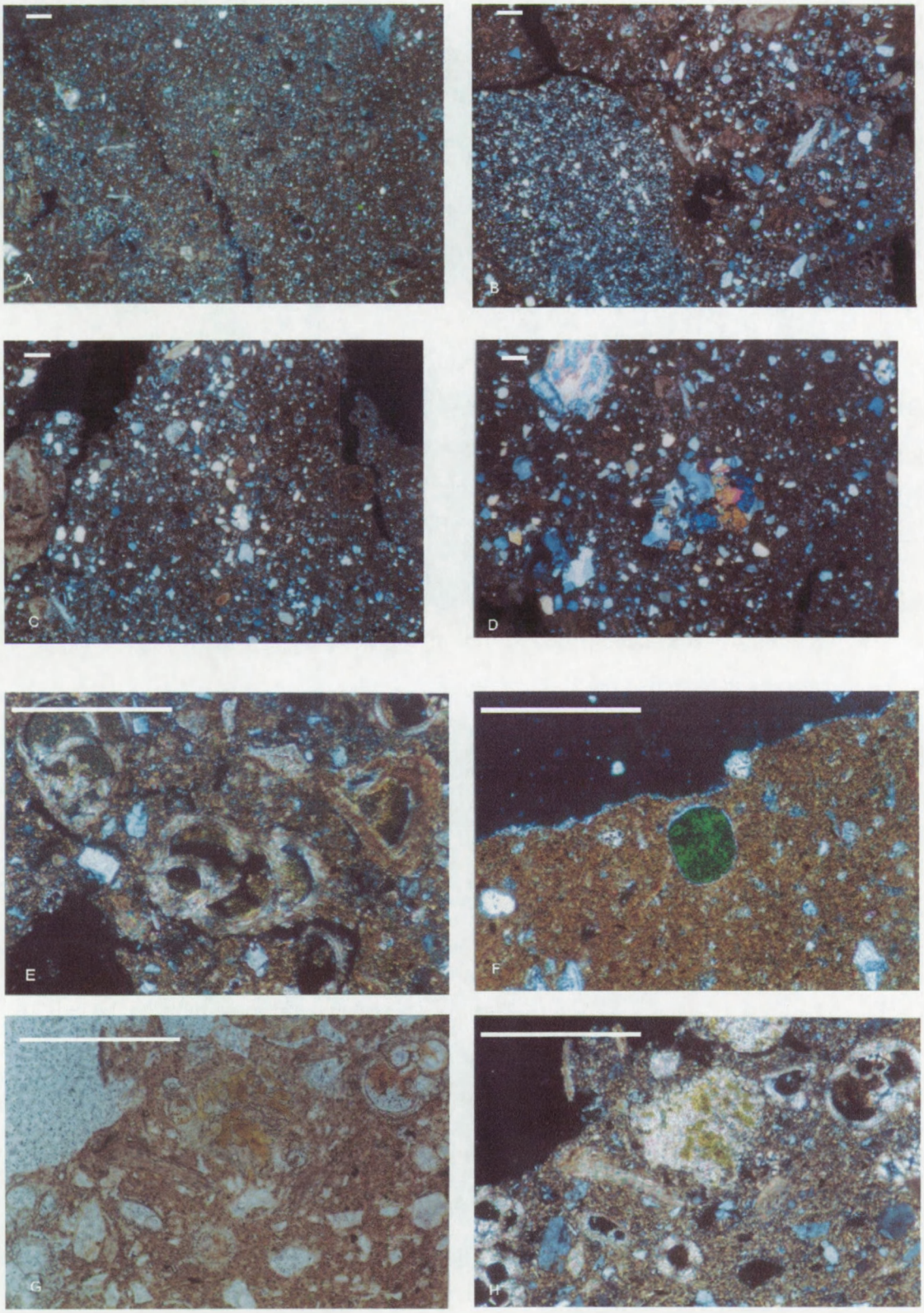
A
B
C
D
E
F
G
H

Fig. F.5.3: **A.** X of ST133A. Coral fragment in a carbonate-rich matrix. The coral fragment has dark spots at the rim, which has been interpreted as pyrite. In the embedding matrix, pyrite clusters near bioclasts. In the left cavity of the coral, a large cluster of pyrite has been observed indicating a local sulphate reduction zone.

B. Zoom of A illustrating the encrusting of pyrite at the rim of the coral. Mn and Fe bacteria are probably responsible for the formation of pyrite. Micritic calcite has been formed as early cement inside the cavities.

C. X of ST190 taken on HOV15. Coral fragment cavities have been infilled with the same sediment composition as the matrix. The coral is bioeroded by boring foraminifera and sponges weakening the skeleton. In the rim of the coral, pyrite and secondary calcite has been formed. The colour banding in the coral probably illustrates growth patterns or alteration of aragonite.

D. X of TTR7-AT-16G S3, 52-53cm. Occurrences of pyrite in the upper surface of a coral clast. Pyrite is mostly orientated parallel to the rim. Colour banding of the coral has been interpreted as growth patterns.

E. X of ST110''. Pyrite has been formed parallel with the aragonite minerals, perpendicular to the rim of the coral.

F. X of ST133A on-mound of HOV15. Pyrite concentration in association with glauconite in a carbonate-rich matrix.

G. Cathodoluminescent image illustrating the weak luminescence of the matrix. Bioclasts are brighter. No colour variation has been observed in the carbonate fraction, indicating a uniform chemical composition for all carbonates. K-feldspars (blue) and quartz have been observed in the matrix. The bright green spots in the matrix are unidentified heavy minerals. Reddish colours represent dolomite.

H. Cathodoluminescent image with a bright luminescence yellow-orange coral stem. The bright colour is formed by the high Fe/Mn ratio in the corals. Bright spots in the matrix have been interpreted as small coral fragments. Quartz, feldspar and heavy minerals have been observed in the matrix. Reddish colours indicate small dolomite minerals and some larger clasts of dolomite.

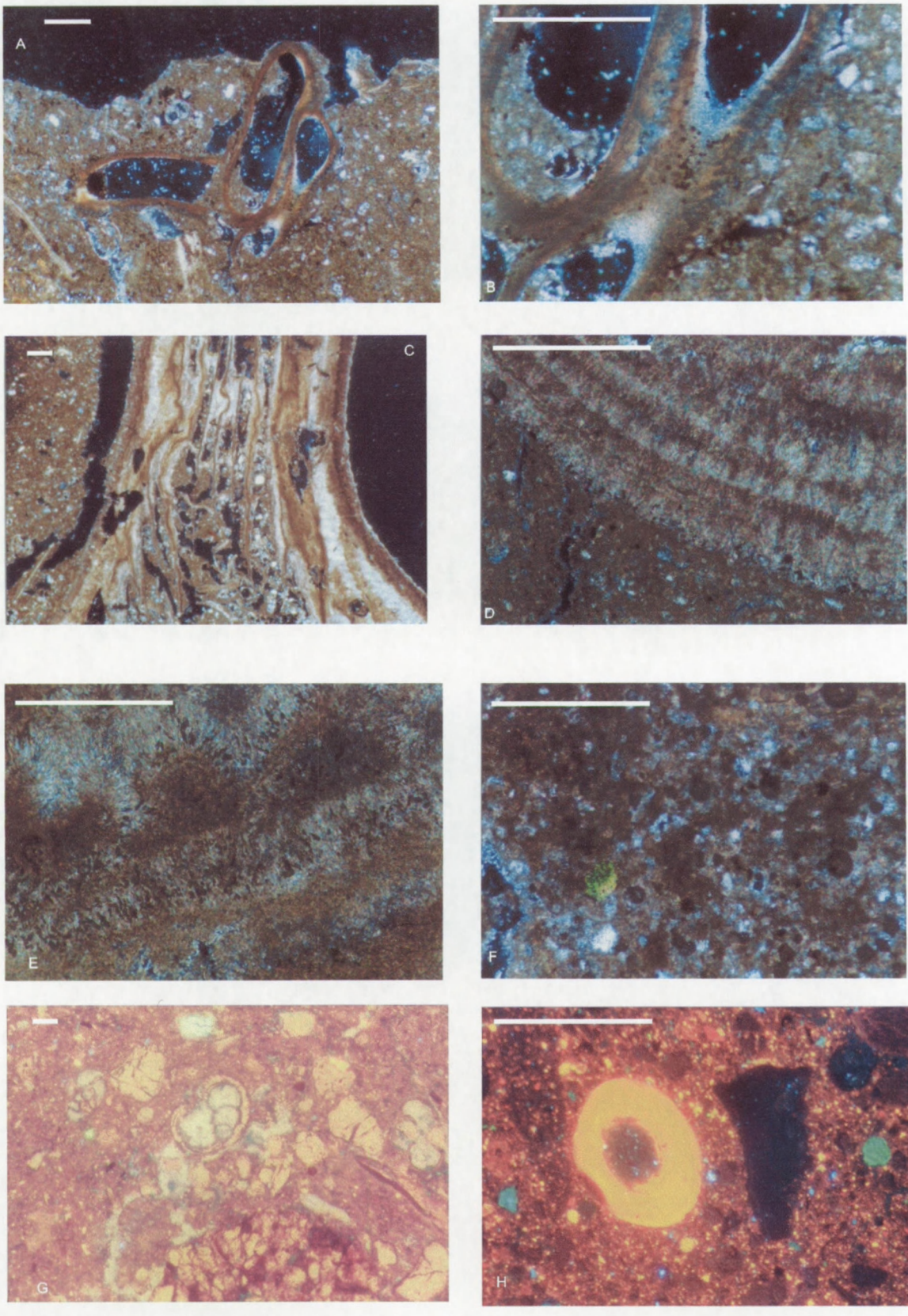
A
B
C
D
E
F
G
H

6. Isotopic analysis

Core	Depth (mm)	Description	$\delta^{13}C$	$\delta^{18}O$
TTR7-AT-16G	50	carbonate	-0.268	-1.541
TTR7-AT-16G	245	carbonate	-1.134	1.228
TTR7-AT-16G	605	carbonate	-0.354	-0.184
TTR7-AT-16G	675	M. oculata	1.677	4.314
TTR7-AT-16G	855	carbonate	0.69	-3.584
TTR7-AT-16G	965	carbonate	-1.1085	0.23
TTR7-AT-16G	975	M. oculata	-3.505	1.794
TTR7-AT-16G	1145	carbonate	-0.272	2.563
TTR7-AT-16G	1405	shell bivalv	2.247	4.114
TTR7-AT-16G	1625	M. oculata	-3.5	2.044
TTR7-AT-16G	1625	carbonate	0.355	2.435
TTR7-AT-16G	1708	carbonate	0.887	2.367
TTR7-AT-16G	1768	carbonate	-0.568	2.528
TTR7-AT-16G	1858	M. oculata	0.499	2.086
TTR7-AT-16G	1858	carbonate	0.526	2.145
TTR7-AT-16G	1928	M. oculata	-3.644	1.645
TTR7-AT-16G	1928	carbonate	0.009	2.001
TTR7-AT-16G	1998	carbonate	-1.01	1.566
TTR7-AT-16G	2058	carbonate	-1.724	1.875
TTR7-AT-16G	2168	carbonate	0.091	1.196
TTR7-AT-16G	2238	carbonate	0.602	0.834
TTR7-AT-16G	2498	carbonate	0.674	-2.124
TTR7-AT-16G	2698	carbonate	0.469	-2.871
TTR7-AT-16G	2948	carbonate	0.541	-3.155
TTR7-AT-16G	3108	carbonate	0.246	-1.604
TTR7-AT-16G	3158	carbonate	0.234	2.101
TTR7-AT-16G	3288	carbonate	0.654	0.871

Table F.6.1: Stable isotopic analysis of $\delta^{13}C$ and $\delta^{18}O$ in core TTR7-AT-16G for the sediment and bioclasts.

	$\delta^{13}C$	$\delta^{18}O$	Genus	Description
KR1	-5.389	-0.649	L. pertusa	coral
KR2A	-2.163	1.846	L. pertusa	coral
KR2B	-1.159	2.267	L. pertusa	coral
KR3A	-1.941	1.71	M. oculata	coral
KR3B	-4.614	0.405	M. oculata	coral
KR5A	0.466	2.329	L. pertusa	bryozoa
KR5B	1.363	2.325	L. pertusa	bryozoacrust
KR5C	-1.569	1.295	L. pertusa	polype
KR6A	-5.095	0.33	M. oculata	fresh aragonite
KR6B	0.748	2.08	M. oculata	contact alternated and fresh zone
KR6C	-0.665	2.731	M. oculata	inside polype
KR7A	-5.639	-0.144	L. pertusa	polype
KR8C	-1.567	2.39	M. oculata	wormtube
KR9A	-2.563	1.612	M. oculata	living mucus
KR9B	-3.462	0.485	M. oculata	connection wormtube-coral
KR9C	-3.093	1.018	M. oculata	inside stem
KR9D	-1.747	1.856	M. oculata	inside wormtube
KR10A	0.761	2.647	M. oculata	outside wormtube
KR10B	0.093	2.091	M. oculata	tip of coral
KR10C	1.548	2.401	M. oculata	bryozoa yellow
KR10D	1.414	2.39	M. oculata	bryozoa white
KR11A	-0.676	1.897	M. oculata	fresh near living polype
KR11B	-0.251	2.419	M. oculata	core of stem
KR11C	0.155	2.926	M. oculata	red polype tissue
KR12B	-2.554	1.007	M. oculata	main stem
KR12C	-1.336	1.607	M. oculata	branch
KR13A	-0.001	1.018	M. oculata	inside branch
KR13B	0.211	1.582	M. oculata	sediment filled worm tube
16G-675	1.677	4.314	M. oculata	coral
16G-975	-3.513	1.79	M. oculata	coral
16G-1625	-3.5	2.044	M. oculata	coral
16G-1858	0.499	2.086	M. oculata	coral
16G-1928	-3.778	1.645	M. oculata	coral
16G-2058	0.887	2.67	M. oculata	coral
KR4A	1.579	-1.748	shell bivalv	
KR4B	1.979	2.103	shell bivalv	
E1	1.073	1.737	echinoderm needle	
16G-140,5	2.247	4.114	shell bivalv	

Table F.6.2: Stable isotopic analysis of $\delta^{13}C$ and $\delta^{18}O$ of coral fragments.

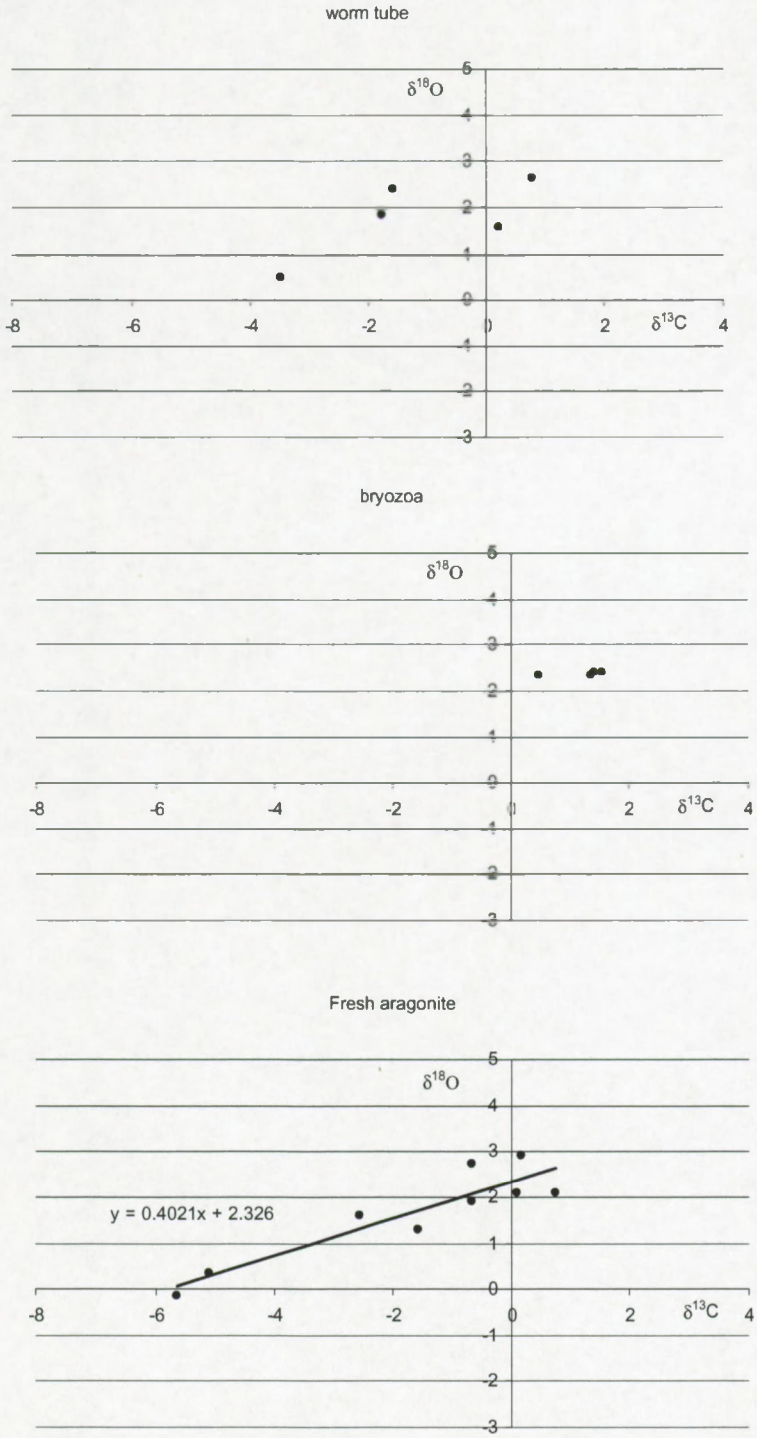

Fig. F.6.1: Isotopic analysis of Eunices tubes associated with the corals, bryozoans and fresh aragonite near the calyx of the corals. The wormtubes have a similar isotopic composition as the coral stem and as fresh aragonite. This illustrates an influence of the coral mucus on the precipitation of these carbonate minerals. Bryozoans have a normal marine signature.

7. Gas analysis

Sample	TOC	Sand fraction Weight %	Clay fraction Weight %	Head gas Me mg/g sed	Occluded gas Me mg/g sed	[SUM SATS] mg/g sed	[SUM CYCS] mg/g sed	[SUM ENES] mg/g sed	Isotopes methane	CO2	Minerals	Location
ST16A	0.19	31.20	68.80	0.46		0.18	0.02	0.05				on mound
ST40A	0.48	32.10	67.90	0.23		0.09	0.01	0.04				foot of mound
ST43A	0.32	23.70	76.30	0.70	54.29	0.19	0.02	0.09				on mound
ST43B	0.26	28.30	71.70	0.67	24.37	0.41	0.02	0.12				on mound
ST44A	0.50	2.60	97.40	0.79		0.00	0.00	0.02			-5.2	crest of mound
ST44B	0.28	39.30	60.70	1.02	101.88	0.37	0.07	0.05	-33.10	-8.60		crest of mound
ST45A											-1.1	foot of mound
ST46B	0.72	16.90	83.10	0.69	81.26	0.55	0.04	0.09				foot of mound
ST49A											-0.1	foot of mound
ST71B									-45.70	-10.80		foot of mound
ST78A	0.19	46.10	53.90	0.14		0.05	0.00	0.01				on mound
ST78B	0.54	41.10	58.90	0.79		0.18	0.03	0.11				on mound
ST110A	0.58	33.60	66.40	0.51	24.41	0.23	0.02	0.11				on mound
ST110B	0.25	46.30	53.70	0.20		0.11	0.01	0.11				on mound
ST116B	0.34	3.10	96.90	0.83		0.00	0.00	0.04				?
ST130B	0.17	27.90	72.10	0.25		0.11	0.01	0.04				slope of mound
ST133S								0.04				on mound
ST133A	0.54	25.20	74.80	1.15		0.17	0.01					on mound
ST134A	0.52	43.80	56.20	0.82		0.00	0.00	0.10				on mound
ST134B	0.56	58.60	41.40	0.32		0.00	0.00	0.04				on mound
ST135B	0.39	8.90	91.10	0.75		0.00	0.00	0.00			-1.6	foot of mound
ST138 A	0.53	48.40	51.60	0.41	22.81	0.01	0.00	0.00				on mound
ST139A	0.51	11.60	88.40	0.75		0.01	0.00	0.00				crest of mound
ST142A									-51.00	-14.00		foot of mound
ST142B									-70.30	-10.60		foot of mound
ST143A	0.22	31.70	68.30	0.78	10.94	0.82	0.08	0.05				on mound
ST150A	0.22	40.00	60.00	0.43	7.56	0.55	0.00	0.00				crest of mound
ST166A	0.57	5.20	94.80	0.49		0.00	0.00	0.00				on mound
ST166B	0.27	23.10	76.90	0.59	52.89	0.35	0.15	0.13				on mound
ST175B									-34.70	-16.40		crest of mound
ST182A									-67.90	-12.50		crest of mound
ST190A	0.48	44.60	55.40	1.03		0.16	0.03	0.01				crest of mound
ST192A	0.45	49.20	50.80	0.58	9.48	0.19	0.01	0.02				crest of mound
ST195A	0.50	7.60	92.40	1.25	11.22	0.22	0.04	0.08				foot of mound
PAD18									-33.60			on-mound
PAD25									-34.80			on-mound
PAD41									-35.50			on-mound
PAD83									-37.70			on-mound
PAD12									-37.30			Absorbed gas anomaly samples
PAD13									-37.50			
PAD60									-37.10			Biogenic mix
PAD75									-36.90			
PAD68									-36.90			
PAD2									-37.80			Background samples
PAD88									-3.7.0			Background samples
PAD90									-36.90			Background samples

off mound												
intermound			n=6	0.83	46.24					n=3	-55.66666667	
on-mound			n=21	0.63	35.73					n=3	-45.23333333	
Dataset PAD												
Mean			Interstitial methane (ppmv)	Interstitial ethane ppmv	Interstitial propane (ppmv)	Absorbed methane (ppbw)	Absorbed methane (ppmw)	Absorbed ethane (ppbw)	Absorbed ethane (ppmw)	Absorbed propane (ppbw)	Absorbed propane (ppmw)	
Off-mound (n=20)			6.8	0.1	0.08	625	0.625	87	0.087	43.5	0.0435	
Inter mound (n=20)			9.8	0.1	0.11	655	0.655	79	0.079	39.5	0.0395	
on-mound (n=37)			7	0.2	0.1	437	0.437	65	0.065	34.9	0.0349	

Table F.7.1: Results of gas analysis of potential hydrocarbon seeps. The results include headspace gas, occluded gas, biomarkers and isotopic analysis. Source Hovland et al., 1994 and Statoil (UL) Ltd., Seabed Coring, Porcupine Licence 8/95, Offshore Ireland, 1996.Report No 6096/7.

Appendix G: Oceanography Hovland-Magellan mound province

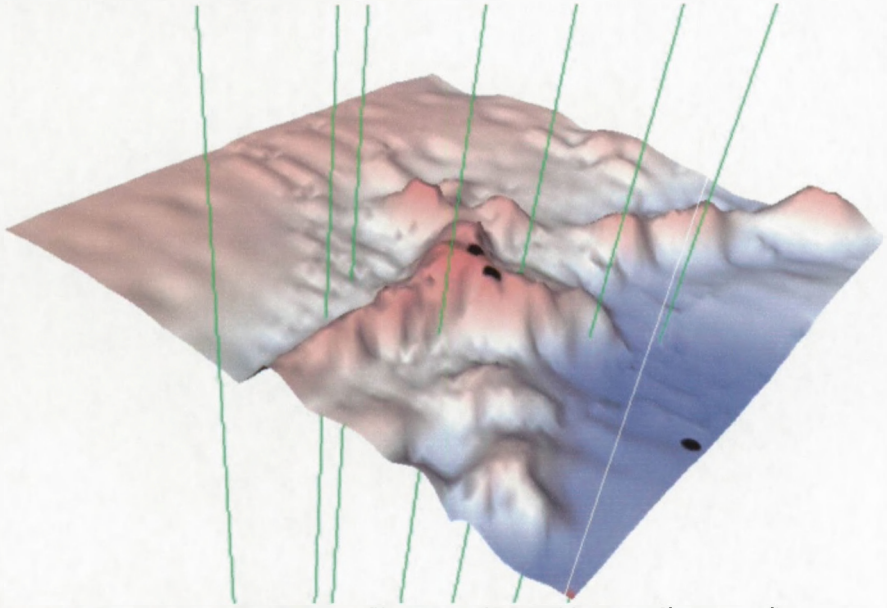

Fig. G.1: Location of the CTD profiles around HOV02 (Propeller mound).

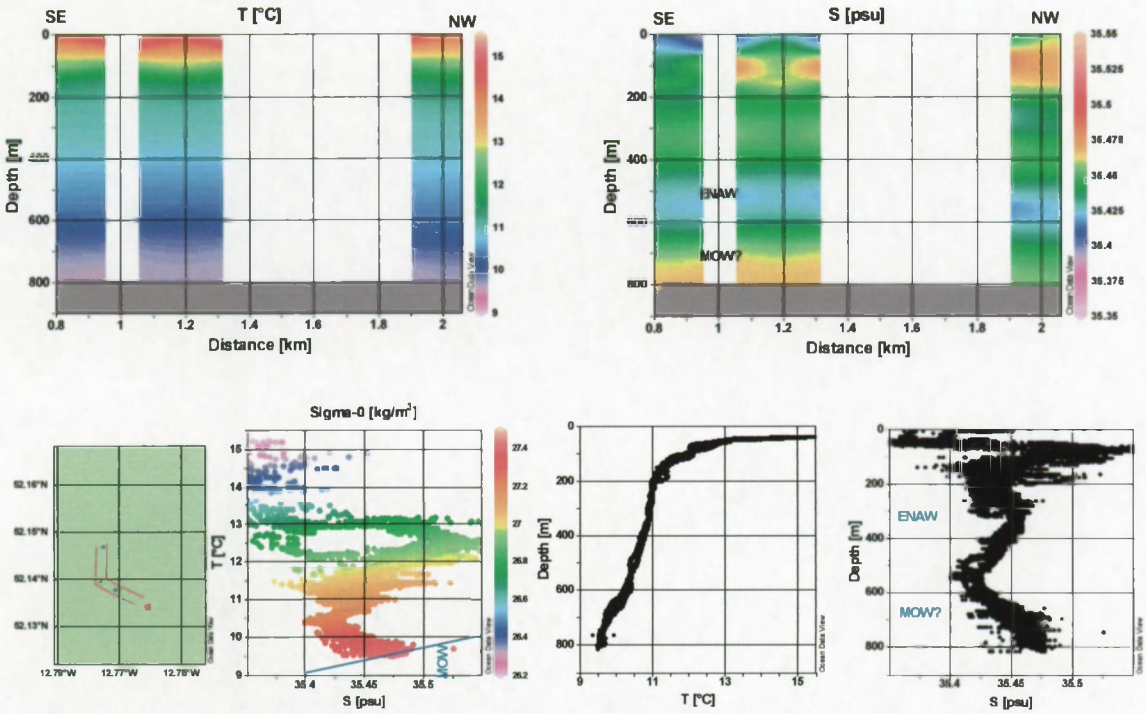

Fig. G.2: SE-NW temperature and salinity profile of the CTD data on HOV02. The water masses characteristics have been plotted in a temperature-salinity-density plot. On the northwestern side a lower salinity and temperature has been observed near the bottom.

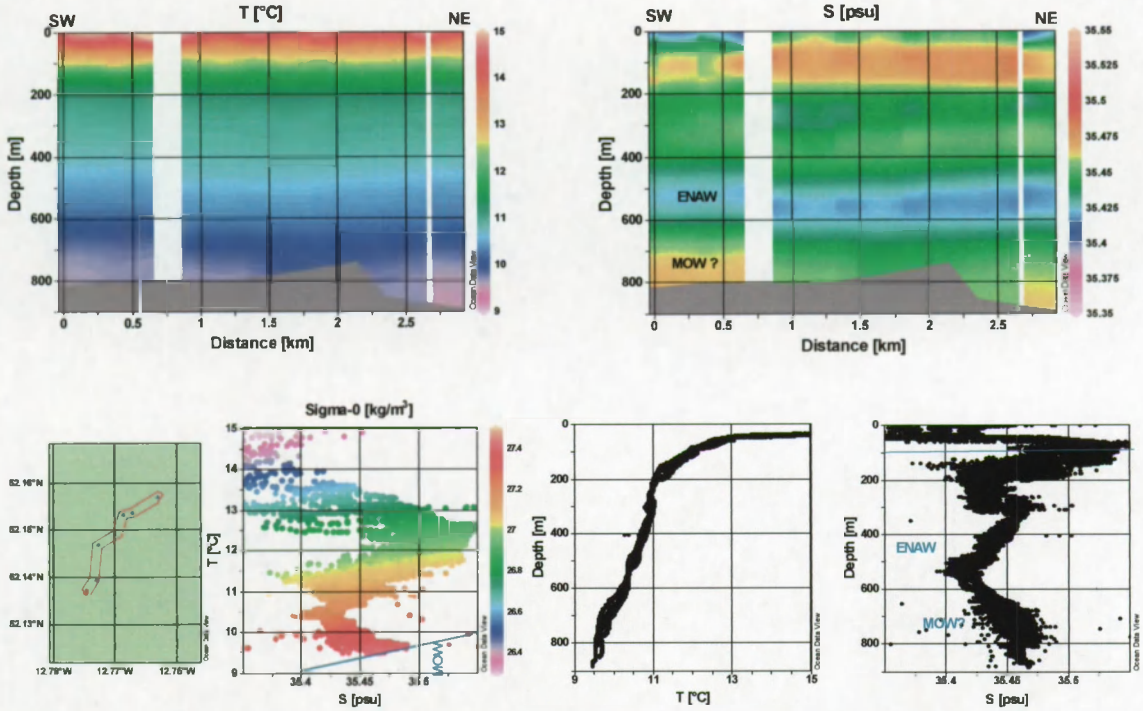

Fig. G.3: NE-SW temperature and salinity profile of the CTD data profiles on HOV02. The water masses characteristics have been plotted in a temperature-salinity-density plot. On the southern side a higher salinity and temperature than on the northern side have been observed.

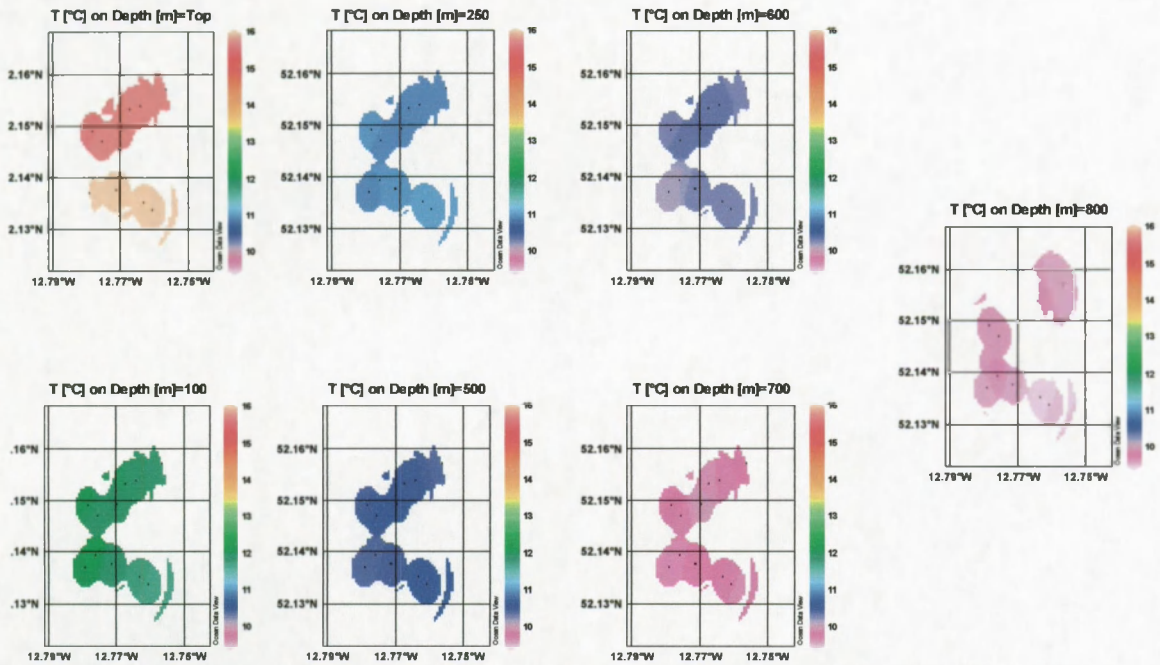

Fig. G.4: Temperature surfaces for several depth levels. Near the bottom and at 600m slight variations in temperature have been observed between the northern and southern flank of the mound.

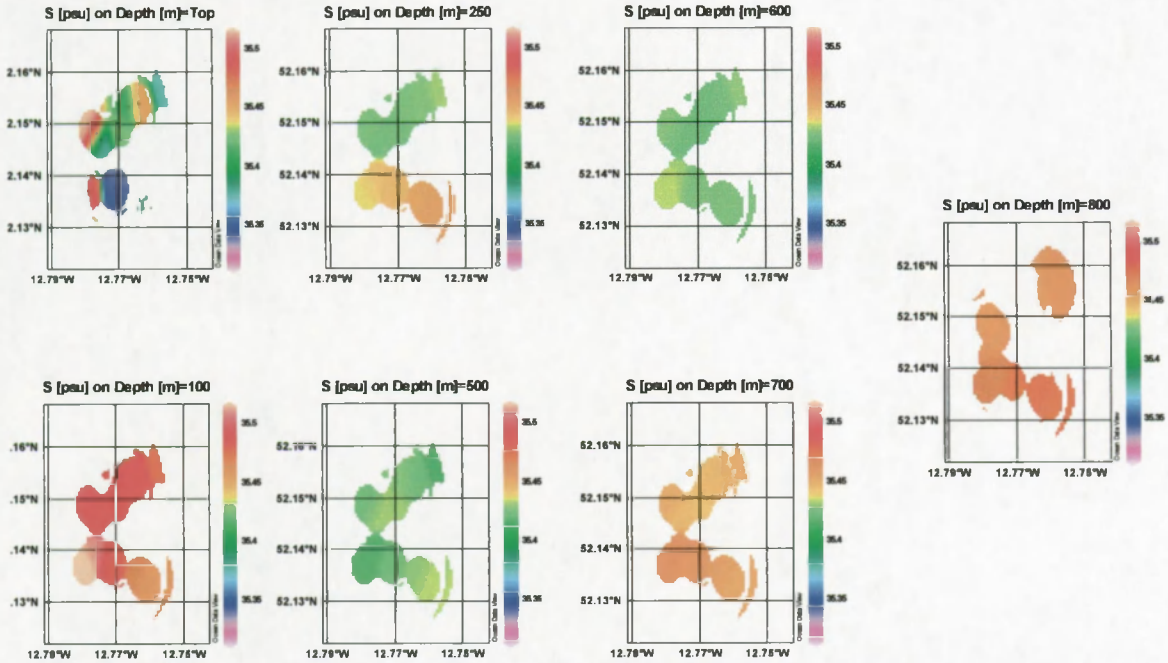

Fig. G.5: Salinity surfaces around HOV02. Higher salinities have been observed near the seabed of the southern flank of the mound.